A Study of Axial Joint Behaviour in a High Power Ultrasonic Device Through Transfer Function Synthesis

John William Russell

Submitted to the College of Science and Engineering,

University of Glasgow

This dissertation is submitted for the degree of

Doctor of Philosophy

Declaration

I declare that, except where explicit reference is made to the contribution of others, this dissertation is the result of my own work and has not been submitted for any other degree at the University of Glasgow or any other institution.

John William Russell
May 2015

Acknowledgements

Foremost I would like to extend my sincerest gratitude to Professor Matthew Phillip Cartmell for his encouragement and insight throughout the course of the work. My appreciation is also extended to Professor Margaret Lucas for her guidance throughout my studies and her resourcefulness at all times. Further to this I would like to recognise Doctor Andrew Mathieson for giving up his time to discuss my experimental set ups. I would like to thank the Engineering and Physical Sciences Research Council (EPSRC) (grant EP/P504937/1) for providing the support to carry out the work. I would also like to thank Mister Adrian Walker from the EPSRC Engineering Instrument Pool for supplying me with access to the ultra-high speed camera. I would like to thank the other researchers in the Systems, Power and Energy group for sharing their work with me and engaging with my work. In particular I would like to thank Doctor Andrew Feeney for his friendship and advice. I am extremely grateful to the University of Glasgow workshop and technicians for their support, which made my experimental work possible. Finally I would like to thank my family and friends for their encouragement throughout my studies.

Abstract

Further development of an open loop control strategy for High Power Ultrasonic (HPU) devices requires investigation of the dynamic behaviour of its interfaces. These interfaces exist between components that are assembled through a screwed threaded axial joint. An unknown prestress permeates from this bearing surface due to the tension in the stud. It is well known that the vibration of bolted interfaces is highly nonlinear. It is assumed that the axial joint will not loosen to the extent that the entire contacting surfaces will slip. Therefore the characteristic behaviour of this interface descends from the microscopic motions, of asperities in and out of contact, as slipping occurs locally. A review of the literature suggests that this physical mechanism will contribute to second harmonics in the response of the jointed system. This complex constitutive behaviour is not amenable to dynamical modelling. Instead the Bouc-Wen (BW) model for hysteresis is adopted to capture the phenomenology. The force-displacement behaviour of the axial joint is required to identify the parameters to this model.

Dynamic force behaviour of a component that is subjected to high power ultrasonic loading cannot be obtained directly through conventional measurement systems. Force estimation of a set of ultrasonic test assemblies is attempted through a hybrid analytical-experimental scheme. The test assemblies consist of a Commercial Piezoelectric Actuator (CPA) or an In-House Piezoelectric Actuator (IHPA) with a stepped ultrasonic horn attached. Stepped ultrasonic horns are produced with and without an additional axial joint that is set to three different tightnesses. These are named the Jointed Horns (JH) or the Monolithic Horn (MH) respectively. The model of an actuator with the MH attached is named the linear calibration model. This is formulated through a Distributed Transfer Function Method that describes waveguides, with discontinuous parameters, that behave according to Love Rod Theory. This is too limited to represent the behaviour of a piezoelectric rod, so the electromechanical nature of the piezoelectric actuator is not considered in detail. Instead the parameters of the model are updated based on results from Experimental Modal Analysis through the

Genetic Algorithm. The force at the foremost point of the piezoelectric stack is deconvolved from the distributed parameter rod model. Stable solutions to the ill-posed inverse problem are achieved by means of the Truncated Singular Value Decomposition or Tikhonov regularisation schemes. Electrical impedance analysis of the piezoelectric actuators, with a JH attached, demonstrate that the introduction of the joint to an equivalent assembly, made with the MH attached, will significantly modify the impedance behaviour.

Input forces are deconvolved from the linear calibration assembly when the output is the measured response of the IHPA with the MH attached. The response of the IHPA with the JH attached is then assumed as the output and the joint force is estimated for the input force that corresponds to the voltage that was applied for the JH test. This force will be out of phase with the true linear input force to the JH assembly. The responses of the test assemblies are measured at 2 or 3 locations through Laser Doppler Vibrometry (LDV). Simultaneous images of a portion of the ultrasonic horn are recorded through an ultra-high speed camera. Digital Image Correlation (DIC) is applied to estimate a displacement field that can be compared to a LDV measurement. Good agreement in phase is found, but there are significant errors in the amplitude. It is suggested that this is the result of projection error. The strain fields are obtained from the displacement field through bi-cubic interpolation. It is not possible to achieve comparable results through the force estimation scheme.

The BW model of hysteresis is defined by four shape parameters that are not straightforwardly related to physical quantities. The influence of these parameters on the hysteresis loop, and the frequency response of the model, is demonstrated through a sensitivity analysis. This suggests that the model will fit to the softening overhang behaviour that was associated with the looseness of the axial joint in the literature. Two interpretations of identifying the model are discussed. Firstly the limit cycle is fitted to experimental data through a set of MATLAB functions that make use of analytical solutions to each branch of the loop. Secondly a minimisation is carried out between the output of the model and the measured response of the IHPA with a JH attached. This is achieved through Differential Evolution. It is not possible to identify a reliable model without an improved estimation of the input to the model.

To make progress with this problem a number of contributions have been made. Simulations of the BW model have demonstrated that it is capable of describing the softening overhang behaviour that has been observed in the response of HPU devices and the subharmonic generation that descends from Contact Acoustic Nonlinearity. A methodical attempt to identify the parameters to this model from measurements of HPU test assemblies has been presented.

A new force estimation scheme has been developed, which is based on a recent formulation of the Distributed Transfer Function Method. This provides a closed form route to estimating the force at an axial joint in a rod-like system. Regularisation methods have been applied to stabilise these estimations. An experimental configuration has been presented to test the force estimation scheme with observations from HPU test assemblies. These test assemblies have been analysed through electrical impedance analysis and Experimental Modal Analysis. This demonstrates changes in the behaviour of the assembly due to the introduction of the joint and its set tightness. Digital Image Correlation is presented as an alternative to finding the hysteresis behaviour at the axial joint which is subject to ultrasonic loading. Recommendations are made towards improving this set up.

Contents

List of Figures

List of Tables

Nomenclature

Roman Symbols

A	Bouc-Wen shape parameter	
a	Amplitude of displacement response	m
A_i	Cross sectional area	m^2
c	Damping coefficient	Nsm^{-1}
c^D	Piezoelectric elastic constant measured at constant electric charge	Nm^{-2}
D	Electric charge density displacement	Cm^{-2}
E	Electric field	NC^{-1}
E_i	Young's Modulus	Nm^{-2}
F	External load	N
f	Excitation force	N
$\mathbf{F}_i$	State matrix	
$\hat{\mathbf{G}}$	Distributed transfer function	
$\mathbf{G}$	Response observation for force deconvolution	m
$\mathbf{g}$	Green function matrix	

$\hat{\mathbf{H}}$	Distributed transfer function	
h	Piezoelectric constant that is the ratio of mechanical stress to applied electric displacement	NC^{-1}
$\mathbf{I}$	Identity matrix	
I	Current	A
J	Polar moment of area	m^4
j	Imaginary unit	
k	Stiffness coefficient	Nm^{-1}
K_i	Retarding force that is proportional to displacement	Nm^{-1}
k_n	Wavenumber	m^{-1}
k_3	Cubic stiffness coefficient	Nm^{-3}
l_i	Length of a component in a distributed parameter system	m
m	Inertial mass	kg
$\mathbf{M}_b$	Boundary matrix at zero node	
$\mathbf{N}$	Joint force	N
N	Number of samples	
n	Bouc-Wen shape parameter	
n	Total number of components in a distributed parameter system	
$\mathbf{N}_b$	Boundary matrix at maximum node	
$\mathbf{p}_i$	Input matrix	
$\mathbf{Q}_k$	Real matrix of the transfer function residues of the k^{th} mode	

Q	Q factor	
$q_i(t)$	Nodal boundary load	s
r	Radius of rod	m
S	Strain	
T	Kinetic energy	J
T	Stress	Nm^{-2}
$\mathbf{T}_i$	Matching matrix	
$\mathbf{U}$	Fundamental matrix	
U	Strain energy	J
u	Displacement	m
V	Loading energy	J
V^E	Potential difference	V
$\bar{\mathbf{v}}_i$	Nodal load	N
W	Electric energy	J
x	Axial location	m
x_a	Starting location of the joint force distribution	m
x_b	Ending location of the joint force distribution	m
x_i	Node of a distributed parameter system	m
x_j	Location of the bearing surface	m
X_m	Axial location of measurement point for m = 1, 2, or 3	m

$\mathbf{Z}$	Impedance matrix	
Z	Electrical impedance	
z	Hysteretic displacement	

Greek Symbols

α	Bouc-Wen shape parameter	
β^S	Inverse of the electric permittivity	mF^{-1}
β	Bouc-Wen shape parameter	
Γ	Tikhonov regularisation parameter	
γ	Bouc-Wen shape parameter	
γ_L	Boundary load at node x_0	N
γ_R	Boundary load at node x_n	N
Γ_Z	Power reflection coefficient	
δ	Variation parameter	
ΔT	Discretisation rate	s
$\Delta\tau$	Width of the impulse response	s
$\Delta\xi$	Spatial discretisation of the distributed parameter system	m
ϵ	Small parameter	
ζ	Damping ratio	
η_i	Retarding that is force proportional to velocity	Nsm^{-1}
θ	Diameter	m

λ	Lamé's 1st parameter	Nm^{-2}
λ_{LM}	Lagrange multiplier	
μ	Lamé's 2nd parameter	Nm^{-2}
ν	Poisson's ratio	
ξ	Spatial distribution of deconvolved force	
ρ	Density	kgm^{-3}
τ	Temporal distribution of the deconvolved force	
$\boldsymbol{\phi}$	State transition matrix	
$\boldsymbol{\chi}_i$	Spatial state vector	
ω	Angular frequency	$rads^{-1}$
ω_k	Modal frequency	$rads^{-1}$
ω_n	Discrete frequency	$rads^{-1}$
ω_p	Damped resonant frequency	$rads^{-1}$

Superscripts

$\bar{}$	Frequency domain quantity as a result of the Laplace Transform
$\check{}$	Predicted quantity
$\dot{}$	Time derivative
$'$	Spatial derivative
$\tilde{}$	Frequency domain quantity as a result of a Fourier Transform
$\hat{}$	Transfer function

Subscripts

i	Component of a distributed parameter system
k	Vibration mode
p	Sample point in time
q	Sample of impulse response

Other Symbols

@	When accompanied with a torque setting (Ti@12Nm) it denotes the type of joint and the tightness
:	When used to separate St@16Nm:Ti@8Nm it denotes the axial joint at the piezoelectric actuator (left) and within the ultrasonic horn (right)
$H(\dots)$	Heaviside step function
$sign(\dots)$	Signum function
Ti	Titanium Grade 5 alloy (Ti90Al16Va4)
$w()$	Time warping function

Acronyms / Abbreviations

BW	Bouc-Wen
CAN	Contact Acoustic Nonlinearity
CCD	Charged Coupled Device
CMIF	Complex Modal Indicator Function
CPA	Commercial Piezoelectric Actuator
DE	Differential Evolution

DIC	Digital Image Correlation
DSP	Digital Signal Processing
DTFM	Distributed Transfer Function Method
DTW	Dynamic Time Warping
EMA	Experimental Modal Analysis
ERT	Elementary Rod Theory
FE	Finite Element
FRF	Frequency Response Function
GA	Genetic Algorithm
HPU	High Power Ultrasonic System
IHPA	In-House Piezoelectric Actuator
JH	Jointed (ultrasonic) Horn
LDV	Laser Doppler Vibrometry
LRT	Love Rod Theory
MATLAB	Matrix Laboratory
MH	Monolithic (ultrasonic) Horn
MSD	Mass Spring Damper
MSE	Mean Squared Error
ODE	Ordinary Differential Equation
PSO	Particle Swarm Optimisation

PZT	Lead Zirconate Titanate piezoelectric ceramic	
RMS	Root Mean Square	
ROI	Region Of Interest	pixels×pixels
SEM	Spectral Element Method	
SM	Similarity Matrix	
STFT	Short Time Fourier Transform	
TEP	Transcendental Eigenvalue Problem	
TSVD	Truncated Singular Value Decomposition	

Chapter 1

Introduction

Unpredictable behaviour is a known consequence of exciting High Power Ultrasonic (HPU) devices by means of high voltage signals. However, this level of excitation is necessary to produce the vibration amplitudes that are required to supersede, or improve, the action of competing tools for the same process. It is well known that, at these levels of vibration, the device will exhibit a variety of nonlinear behaviour, such as: resonance shifting, phase and amplitude modulations, bifurcations and chaos [1]. In order to produce repeatable and stable designs, it is important to understand the predominant nonlinear phenomena. This can be approached through the development of a simplified dynamical model [2]. A model of this kind can be employed to explore the response of a device for a variety of design parameters. However, it is only relevant for a limited operating range, which must be specified, based on the set of assumptions that have been applied. Many HPU devices feature a stacked piezoelectric actuator, which is also known as a Langevin transducer, to which components are serially connected through the use of screwed threaded joints. The influence of these joints on the response of the device is not well understood. However, it is well known that the joints in any structure will contribute to a high proportion of the overall damping and a variety of nonlinear dynamic phenomena will descend from these discontinuities [3, 4]. Accurately modelling these axial joints will develop further understanding of the overall response of HPU devices.

A typical HPU vibration system is composed of a tool, horn and piezoelectric actuator, all of which are attached, in turn, through screwed threaded axial joints. Such connections offer a significant advantage over other joining methods because the components can quickly be assembled or disassembled. This means that different tools can be utilised through the

same HPU transduction system. The Langevin transducer is a stacked piezoelectric actuator that has found wide spread use in HPU applications. However, its operation depends on applying a prestress through the centre of a piezoelectric stack. Without this prestress the piezoelectric exciter will not obtain a narrow enough bandwidth to transmit useful levels of acoustic power. However the contact and interaction of these prestressed interfaces, as well as other prestressed interfaces in the device, are not well understood. Furthermore the application of the ultrasonically vibrating tool, to a medium, requires that the tool is held under some prestress so that it can affect a change in the medium. Therefore, the processes that are activated, at a prestressed site, may be better understood through some estimation of the force behaviour that is occurring within the tool over time.

For this study the test subject is an ultrasonic horn that is attached to a stacked piezoelectric actuator by means of a screwed threaded axial joint. Although it is often desirable to make this connection with a set screw, which is driven by an internal wrenching drive, in the following, a screw of uniform nominal diameter throughout its length is considered. A typical HPU assembly is depicted in Figure 1.1. The assembly is tuned to operate with a longitudinal motion when it is excited at 20 kHz. The approximate locations of the vibration nodes, and a sketch of the output, are shown below the assembly. A step change in cross section produces gain in the vibrational output of the device. The attachment of the horn to the stacked piezoelectric actuator is through an axial joint. Without a detailed understanding of the HPU exciter, it is not possible to isolate the behaviour of this axial joint in the system. Therefore the axial joint behaviour is tested by manufacturing two horns that are both identical apart from the inclusion of an additional axial joint in one horn. The assembly to be modelled, and the location of the joint, are indicated in Figure 1.2. The axial joint has been introduced close to the front of the HPU assembly, so that it is subjected to operating conditions that would not normally be experienced by an axial joint in the device. It is necessary to maximise the amplitude of vibration at the joint in order to improve the possibility that any of its characteristic behaviour will be observable above the measurement noise floor.
Lim [5] investigates the nonlinear behaviour exhibited by a HPU cutting device with components that are thought to produce opposing softening and hardening overhang frequency behaviours. Overhang frequency behaviour has been observed by Cardoni [6] and Mathieson [7] in their studies of the nonlinear behaviour of HPU devices. They excite the device at discrete frequencies around its resonant operating mode to reveal the shape of frequency response. Exciting the HPU device at a voltage, which is considered to be characteristically low, will produce a bell curve shaped response. Whereas a voltage that is considered to be high will typically produce a bell curve that has been skewed towards the negative end of the

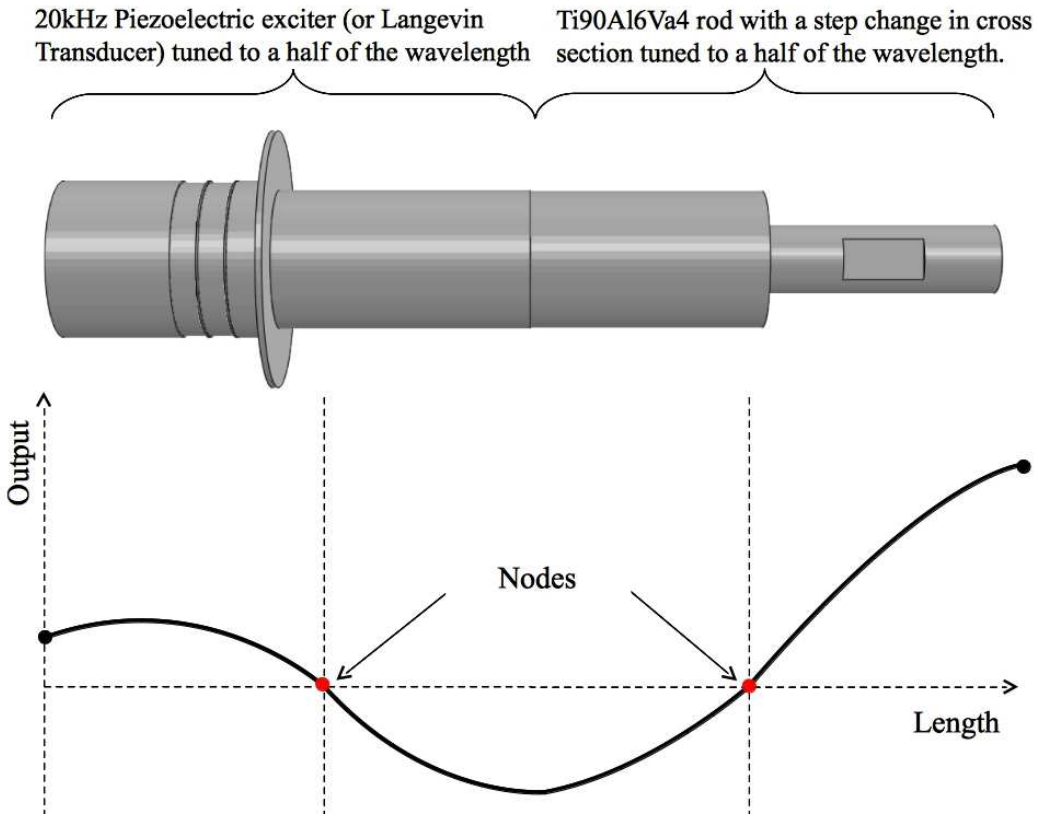

Fig. 1.1 The nodes of vibration in the High Power Ultrasonic test assembly possessing a 20kHz operating resonance.

measured spectrum. This results in a jump characteristic, in the magnitude of the spectrum, as the discrete excitation frequency is varied close to the frequency at which the amplitude of the spectrum has saturated. This softening overhang behaviour has been associated with the constitutive behaviour of the piezoelectric material [8], the heating of the device during continuous operation [7] and the tightness of the axial joints in the assembly [6]. Jump behaviour is a very important characteristic in the application of any HPU device because of the way that the power supply operates. As an ultrasonic tool is loaded, the power supply will change in frequency to match the impedance behaviour of the device, so that it is operating close to resonance. However, sweeping through the excitation frequency can result in unstable behaviour if no control is in place to maintain the operation of the device. Lim [5] demonstrates that by connecting components with opposing overhang behaviour in series, it is theoretically possible to mitigate the overhang behaviour in the overall response of the device. This is achieved by analysing the effect of coupling within a two degree of freedom nonlinear oscillator. The classical Duffing equation is adopted as a theoretical vehicle

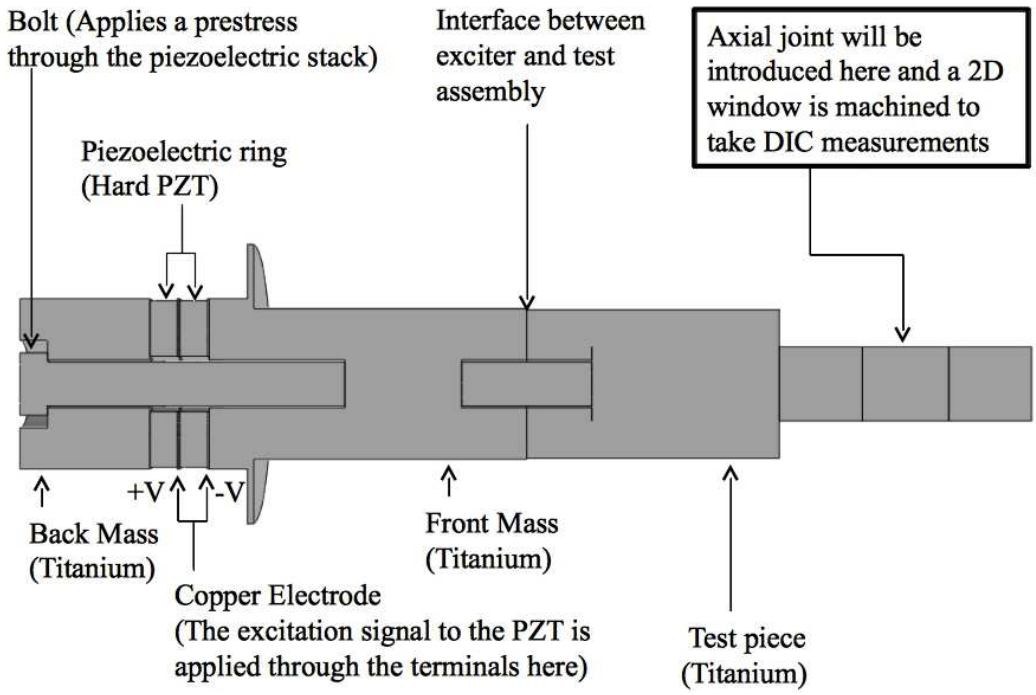

Fig. 1.2 Cross section of the High Power Ultrasonic test assembly.

for this exploration. It is well known that the cubic stiffness term gives rise to overhang frequency behaviour:

$$m\ddot{u} + c\dot{u} + ku + k_3u^3 = F\cos\Omega t \tag{1.1}$$

where u is displacement, t is time, F and Ω are the amplitude and angular frequency of excitation force respectively, m is the inertial mass, c is the viscous damping coefficient and k and k_3 are the linear and nonlinear stiffness coefficients. For the study of an energy harvesting device, Green *et al.* [9] derived the following solution to the Duffing equation through the perturbation technique of multiple scales:

$$\omega = \frac{3k_3a^2}{8m\omega_k} \pm \sqrt{\left(\frac{F^2}{4\omega_k^2a^2} - \frac{c^2}{4}\right)} + \omega_k \tag{1.2}$$

where a and ω are the amplitude and angular frequency of the displacement response, $\omega_k = \frac{k}{m}$ is the natural frequency and the damping ratio ζ has been used to calculate c according to $c = 2\zeta\sqrt{km}$. Equation (1.2) has been applied to compute the frequency response that is displayed in Figure 1.3, based on the values given in Table 1.1. This shows that the Duffing equation is capable of simulating the amplitude jump phenomenon that has been observed in the frequency response of HPU systems. As the excitation frequency is swept downwards

from 30kHz, the response follows the path from A to B, at which the amplitude saturates, and then jumps from B to C as it continues to 10kHz. A frequency sweep upwards from 10kHz would instead follow the path C to A before continuing to 30kHz. Therefore the loop ABC represents an area of hysteresis, in the frequency response of the system, where bifurcation occurs. Under the condition that the stiffnesses in Equation (1.1) are $k < 0$ and $k_3 > 0$, an increase in the amplitude of excitation may cause the system to exhibit a sequence of bifurcations, which can lead to chaotic behaviour through period doubling. Two further responses are computed in Figure 1.4 by varying the value of the cubic stiffness coefficient k_3. Lim [5] coupled two Duffing oscillators with frequency behaviour that featured the characteristics of the curves shown for $k_3 = -1 \times 10^{20}\text{Nm}^{-3}$ and $k_3 = +1 \times 10^{20}\text{Nm}^{-3}$. With these components connected serially it was possible to mitigate the overhang frequency behaviour, that is demonstrated by each of the components individually, and produce the linearised response equivalent to the $k_3 = 0$ curve.

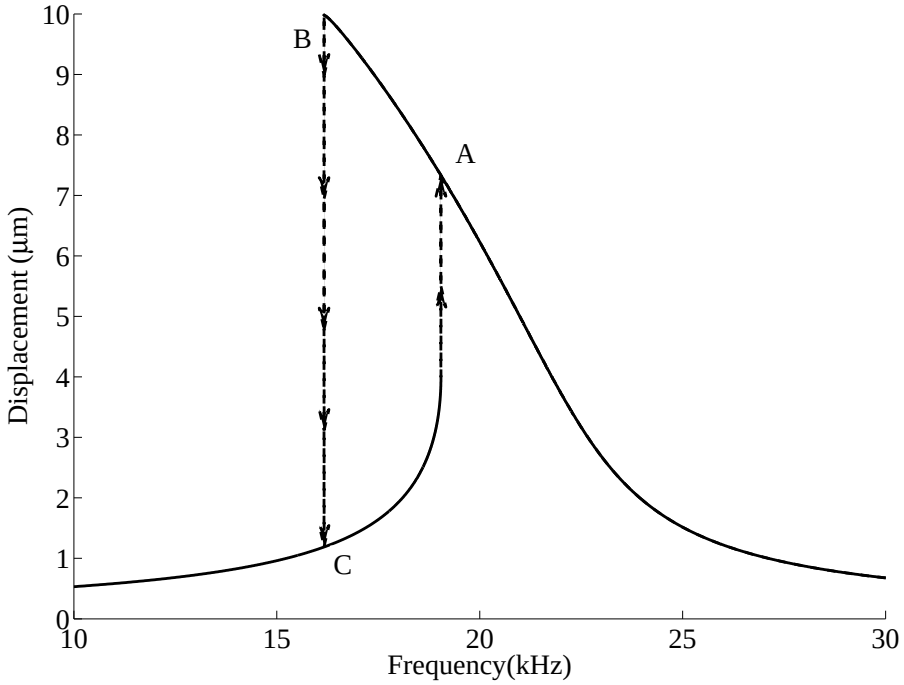

Fig. 1.3 Amplitude jump phenomenon in the frequency response of the Duffing equation.

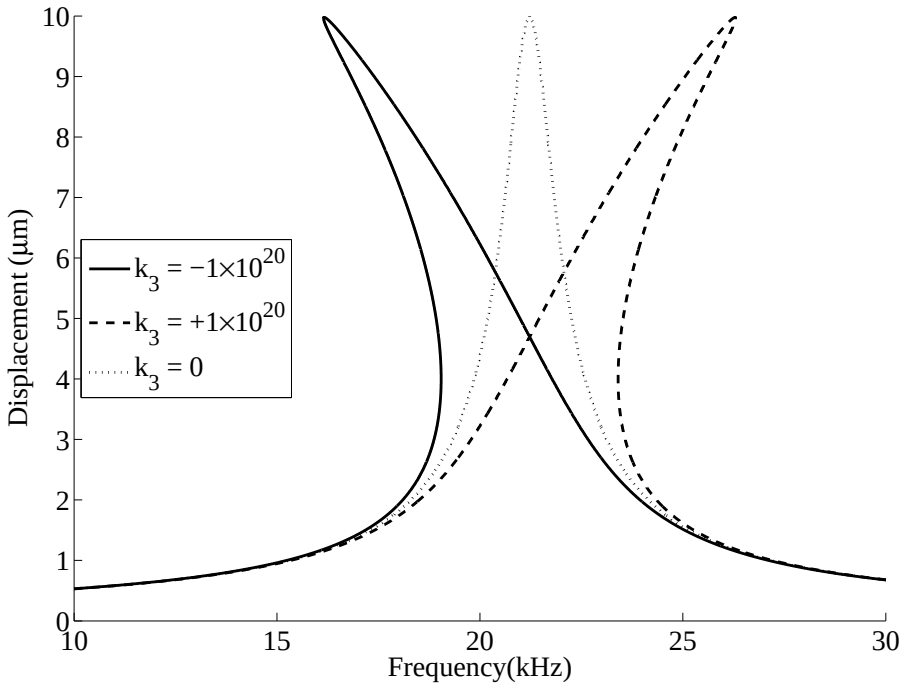

Fig. 1.4 Frequency response of the Duffing equation as the cubic stiffness coefficient is varied.

1.1 Outline

The investigation that follows seeks further development of the open loop control strategy, for High Power Ultrasonic (HPU) systems, by considering the interfaces within the system. These interfaces are made through screwed threaded axial joints where a prestress with unknown axial distribution permeates from the bearing surface due to the tension in the stud.

The aims of the investigation can be summarised as follows:

(I) Investigate the behaviour of a simplified dynamic model that can be related to the physical behaviour of the axial joint within a HPU device.

(II) Present a force identification scheme that may facilitate the estimation of the axial joint behaviour within a HPU device.

(III) Develop a test assembly that may be used as part of a controlled experiment to investigate the characteristics of an axial joint within a HPU device.

Table 1.1 Parameters that determine the frequency response of the Duffing equation

Parameter	Value	Units	Description
m	880.66	g	Inertial mass
ζ	0.032		Damping ratio
ω_k	$21.225 \times 2\pi$	$\times 10^3 \text{rads}^{-1}$	Natural frequency
k_3	-1×10^{20}	Nm^{-3}	Cubic stiffness coefficient
f	10	kN	Excitation amplitude
a	$\in [0, 10]$	μm	Displacement amplitude

(IV) Define the limitations in describing this controlled experiment through the hybrid force identification scheme.

(V) Identify an alternative experimental method that may be used to verify any estimation of the axial joint behaviour through the force identification scheme.

The following steps are attempted in order to make progress with understanding the complex nonlinear dynamics associated with the vibration of this interface as it is subjected to high frequency ultrasonic vibration.

(I) Estimation of the force in rod-like piezoelectric actuators:

(i) The exact transfer function from force to displacement in a distributed parameter rod is formed through the Distributed Transfer Function Method (DTFM).

(ii) This requires the definition of a one dimensional homogeneous rod waveguide that can be connected in series for either isotropic or transverse isotropic materials.

(iii) It is found that there are severe limitations in attempting to formulate a one dimensional piezoelectric rod.

(iv) The HPU assembly is predominantly composed of materials that may be considered isotropic and a formulation of the DTFM for waveguides featuring coupled PDEs remains an open question.

(v) The Transcendental Eigenvalue Problem (TEP) appears to be a key component in minimising the error in the force identification scheme as it may be applied to optimise the parameters of the system based on evidence obtained through Experimental Modal Analysis (EMA).

(vi) Formulating an Inverse TEP that can uniquely identify a distributed parameter rod with free-free end conditions remains an open question.

(vii) The estimation of the axial joint force requires that the exact transfer function, obtained through the DTFM, is discretised. A set of MATLAB scripts and functions are written to achieve this.

(viii) The force estimation relies on the inversion of a discretised form of the convolution integral. This is an ill-posed problem, so regularised inversion techniques are summarised and applied to obtain the least squares regularised solution.

(II) The linear calibration model for the HPU test assemblies

(i) Manufacture the test assemblies that are required for the force identification scheme: The Monolithic and Jointed (ultrasonic) Horns (MH and JH). The In-House Piezoelectric Actuator (IHPA) is manufactured with comparable characteristics to a the Commercial Piezoelectric Actuator (CPA) that is tested.

(ii) Observe the magnitude and phase of the electrical impedance of each test assembly. This knowledge is required to understand the power efficiency of each assembly in relation to its power supply. Unless the electrical impedance of the power supply is matched to the assembly, power will be reflected back from the device and must be dissipated by the supply. This impedance behaviour varies significantly around each of the axial vibration resonance frequencies and these are confirmed through Experimental Modal Analysis (EMA). The influence that the tightness of the additional joint has on this spectrum behaviour is also demonstrated. For the purpose of the joint force identification scheme it is important to give a comparison between the electrical behaviours of the monolithic and jointed assemblies. Without a large number of manufactured horns it is not possible to suggest the pattern that might be observed by tightening the additional joint.

(iii) EMA of each test assembly is carried out to identify the natural frequencies and mode shapes of the axial modes. Bending/twisting modes are observed to be more predominant in the response of the test assembly when it is made with the IHPA. However, the amplitude of the unwanted modes are too small to identify them accurately. Overall four axial modes dominate the response of both piezoelectric actuators over the range 0-40kHz.

(iv) The DTFM models of the HPU test assemblies are defined and the associated assumptions are stated.

(v) The difference between the eigenvalues and the natural frequencies of each assembly is minimised through the Genetic Algorithm (GA). The homogeneous stiffness of each component in the DTFM model is modified to account for the unknown prestresses that exist in the assembly.

(vi) When the DTFM model is applied to describe a piezoelectric actuator with a MH attached, this is considered to be a linear calibration model for the force identification scheme.

(vii) For each linear calibration model the transient response is computed for both a boundary load, applied at the foremost location on the piezoelectric stack, and the boundary load with an additional joint force applied. The distribution of the additional force is defined as along a component, after the step change in cross section, through the Heaviside step function.

(III) Force estimation via Laser Vibrometry and High Speed Imaging

(i) Hysteresis loops are obtained from two methods that involve recording the vibration over an area where each equivalent ultrasonic horn has been machined flat.

(ii) A speckle pattern is applied to each flat in order to observe its vibration with an ultra-high speed camera. Some introductory analysis of the speckle patterns, and the measurement set up, are presented.

(iii) Laser Doppler Vibrometry (LDV) measurements are recorded at more than one location for use with the force identification scheme.

(iv) The LDV measurements are integrated using omega arithmetic and filtered to produce displacements that share the same frequency and temporal characteristics as the original measurements.

(v) The post processing of the ultra-high speed camera is discussed alongside the smoothing of the obtained displacement field and the estimated measurement noise floor.

(vi) The displacement measurements obtained through LDV and Digital Image Cor-

relation (DIC) are presented for an equivalent location at simultaneous samples. These are associated with testing each of the piezoelectric actuators with each of either the MH or JH attached.

(vii) The strain field is calculated through bicubic interpolation of the displacement field that was obtained through DIC. The interpolation is made through Finite Element shape functions. Uniaxial strain is transformed to axial force through the Young's Modulus of the horn material.

(viii) The linear calibration force is the boundary force which is estimated from the tests of each piezoelectric actuator with the Monolithic Horn attached. This is computed through the force identification scheme from the displacements obtained when a range of excitation voltages are applied to the piezoelectric actuator terminals.

(ix) The electrical characteristics of the IHPA are discussed. The ratio of the impedance between the MH and JH is applied to scale the boundary force that was estimated from the tests of the MH assembly.

(x) The regularised inversion schemes are applied to each set of displacements that have been obtained from testing the horns with an additional axial joint.

(IV) The dynamic response of the Bouc-Wen model for hysteresis

(i) The formulation of the Bouc-Wen (BW) model for hysteresis is discussed as a suitable simplified model that can fit to the hysteresis behaviour exhibited in a system that features interfaces.

(ii) Analytical solutions to the model are given along with a discussion of the modifications that have been applied to the hysteresis functional in the literature.

(iii) The state space form of the model is presented along with a Simulink block diagram, which can be used to numerically integrate the model in MATLAB.

(iv) A parameter identification scheme is presented for the model with an algorithm that has been implemented in MATLAB. The MATLAB code is given as an appendix. This is a demonstration of the problems associated with both the identification of parameters in the hysteresis model and the DTFM model because both cases form transcendental equation problems.

(v) The parameter identification scheme is applied to the data obtained through DIC and this does not yield positive results. Measurement noise that was present in the displacement field derivation had been amplified when the strain field was obtained and this obscured the true hysteresis behaviour.

(vi) A sensitivity analysis of the BW model is given and shows the influence that varying one of the parameters has on the hysteresis solution vectors as well as the displacement spectrum.

(vii) The analysis of the model yields some constraints that are relevant to the parameter identification in the next chapter.

(V) Identification of the Bouc-Wen model parameters from experimental results

(i) Power spectrum analysis is given for each horn attached to the IHPA. The Q factor is calculated in each case and used to find the damping ratio for each response.

(ii) The BW model is fitted to the displacement and boundary load that has been found for each of the tests assemblies involved in the linear calibration. In this case assume $\alpha = 1$ so that the contribution from the hysteretic spring is removed to leave a linear mass-spring-damper system. Apart from the linear viscous damping coefficient c, it is assumed that all of the parameters have been measured. To obtain a suitable value for c a metric is required to minimise the error in the measured and the modelled displacement. Dynamic Time Warping (DTW) is found to be a suitable scheme to form this metric and a similar value for c is identified for each set of displacement-force data that has been obtained for the test assembly.

(iii) The parameters to the BW model for some of the JH test assemblies are estimated by minimising the error between the modelled and the experimentally measured displacements. Differential Evolution (DE) is applied to obtain the best solution that was available based on very limited information. Various input signals are assumed for this analysis.

Chapter 2

Review of the literature

2.1 Introduction

High Power Ultrasonic (HPU) devices are driven at high power in order to generate the large vibration velocities required to perform cutting, drilling and welding. However at these levels of vibration their dynamic behaviour tends to exhibit detrimental nonlinear effects. This inherent unreliability is a barrier to extending the applicability of HPU technology. Lucas *et al.* [10] state the necessity for nonlinear models of the complex physical mechanisms that dominate HPU applications.

HPU devices conventionally make use of threaded joints for quick and easy assembly and disassembly. An early study by Kumehara *et al.* [11] asserts that this leads to problems such as self-loosening and propagation loss of acoustic power at the joint. An experimental technique is developed to characterise the effect of joint dimensions, accuracy of bearing surface and preload on the propagation of vibration through an HPU device. It is shown that detecting a critical stress amplitude at the bearing surface can be used as an indication of the quality of the joint. Investigations by Lim [5] and Cardoni [6] demonstrate how the joint in an HPU cutting device influences its dynamic response. It is shown that a looser joint gives rise to stronger nonlinear behaviour. This is attributed to the quality of the interface at the joint. Clearly further investigation is required to understand the problematic mechanisms involved. Evaluating the response for two different levels of torque in the joint indicates that the response exhibits a more severe softening frequency overhang behaviour with increasing looseness. It is also shown that the frequency response becomes softer when

a higher proportion of the threaded stud is fitted into the transducer base as opposed to being fitted further into the tool base. These results show that the instability region of the response can be manipulated through adjustments to the joint.

The study of an HPU cutting device by Lim [5] explores the nonlinear behaviour exhibited by an HPU exciter and a tuned blade connected in series. A previous study by Aurelle *et al.* [8] has shown that softening frequency behaviour descends from the ultrasonic piezoelectric actuator when it is driven at high voltages because the nonlinear domain of the piezoelectric element is reached. Measuring the response of the tuned blade, when it is attached to the ultrasonic actuator, allowed Cardoni [6] to deduce that the blade exhibits a hardening overhang frequency nonlinearity. This conclusion is reinforced in the study by Chakraborty *et al.* [12] where it is demonstrated that beam-like structures exhibit hardening frequency response behaviour. The softening overhang effect, from the HPU exciter, is coupled with the hardening overhang effect, from the tuned blade, in the phenomenological model created by Lim [5]. These effects arise in the model as a result of a negative and a positive cubic stiffness. The threaded connection is said to be contribute to the hardening overhang behaviour, so it is lumped with the behaviour of the cutting blade. This leads to a two degree of freedom Duffing oscillator, which can be used to represent an open loop control strategy for linearising the response of HPU tools. It is shown that the softening nonlinearity can be mitigated by attaching components that exhibit a hardening nonlinearity. However, the complex nonlinear behaviour, at the joint interface in the assembly, does not feature in the model. The effect of the joint in the assembly must be fully understood to produce a model that is a better representation of the nature of an HPU device.

2.2 Nonlinearities at Joints

Joints represent discontinuities in structures where elevated stresses and complex behaviours occur. They influence dynamic characteristics such as: natural frequencies, mode shapes and nonlinear response to external excitation. Stresses and slip at a joint determine the static strength, cyclic plasticity, frictional damping and vibration levels of a structure. In a study of a bolted lap joint by Hartwigsen *et al.* [13] it is shown that natural frequencies tend to diminish in bolted structures. This suggests that they exhibit softening stiffness behaviour. It is also found that energy is dissipated in a power law relationship with applied force. The power law exponent is close to 2 and 3 for equivalent monolithic and jointed structures

respectively. It is demonstrated that the mode shapes of a jointed structure are distorted compared to their monolithic counterparts. In two separate studies by Ma *et al.* [14] and Ouyang *et al.* [15] an odd number of superharmonics are found in the frequency response of a jointed system. This indicates that a cubic stiffness would be useful in modelling the dynamic behaviour of a bolted lap joint. Ahmadian & Jalali [16] suggested a cubic stiffness would be effective in modelling the softening behaviour and saturation phenomenon of a bolt excited at high-level vibration. It is unclear if these results, from tests of bolted lap joints, relate to joints of different geometry, such as the joint found in an HPU device. However the vast amount of work on harmonic excitation of joints is based on the bolted lap joint and reviewing it has highlighted possible sources of nonlinearity such as:

- Damping due to nonlinear interface friction, viscosity of lubricants, microimpacts between bolted components and mechanical hysteresis.
- Nonlinear contact stiffness.
- Shearing motions that are functions of joint loading and geometry.
- Relaxation of bolts leading to clearance.
- Prying load.

Joints are responsible for a large proportion of damping in an assembled structure. There are two prevailing mechanisms responsible for energy dissipation in joints. These are commonly referred to as slip and slap processes [17]. Both processes are fundamentally nonlinear and difficult to measure. They are depicted in Figure 2.1. There are two stages involved in the slip of threaded joints: microslip and macroslip. One reason for these distinct slipping mechanisms is the non-uniformity of the preload through a joint. The preload (or clamping pressure) is the highest near to the hole, where it is applied by the threads of the bolt, and decreases with distance from the hole. Microslip occurs when regions away from the hole begin to slip locally, whilst those near to the hole do not slip. This causes energy dissipation, due to friction, whilst the integrity of the joint is maintained. When slip occurs over the entire contact surface this is called macroslip. This happens when the microslip builds up to a point where the overall force of friction has diminished so that it is lower than the loading of the joint. Slip processes tend to damp the vibration amplitude. In comparison slap processes occur at high vibration amplitudes when parts of the joint experience dynamic contact. This causes energy to be transferred to higher frequencies than those that excited the slap process.

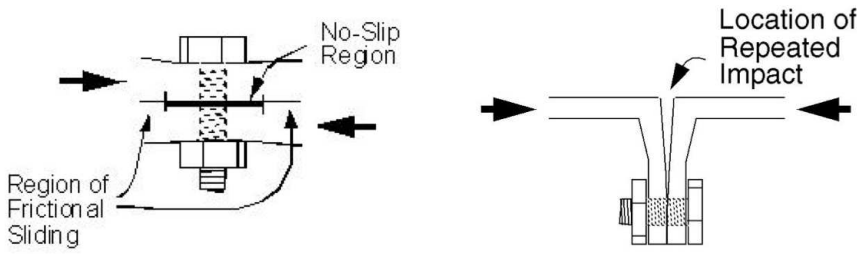

(a) Slip (b) Slap

Fig. 2.1 Energy dissipation due to slip and slap processes [17].

2.3 Interfacial friction

On the endeavour of analysing the nature of friction Oden & Martins [18] state:

> *" . . . dynamic friction is not a single phenomenon but is a collection of many complex and chemical phenomena entwined in a mosaic whose features cannot be grasped through simple experiments."*

Therefore to make progress with analysing the friction at the joint it is important to typify the friction behaviour that is most prominent. The discussion here follows the analysis put forward by Oden & Martins [18] in considering the dynamic contact and relative sliding of dry, metallic surfaces with engineering finishes. This case of friction concentrates on dynamic interactions such as: frictional damping, dynamic sliding, stick-slip motion and chattering.

The dynamic friction forces that are developed between two surfaces, in contact, descend from a wide variety of factors. The factors of interest here include: constitution of the interface, roughness of the contacting surfaces, response of the interface to normal forces and the time scales and frequency of contact. Frictional behaviour arises as a result of the true nature of the interface that is formed when two surfaces are in contact. Understanding the geometry of the surface profile has proven to be vital in producing accurate representations of contact. It is clear that the first stage of analysing this dynamic friction problem is to develop a suitable model of the contact interface. This interface is regarded as a separate entity from the materials of which it is composed. Constitutive equations must be defined for the interface that are independent of those used to describe these materials. The drawback of this approach is that the model can become too complex to be amenable to a full

analysis of the interface dynamics. Alternatively, the use of phenomenological models is one route to understanding the effects of time scales and frequency of contact on the friction behaviour. Stick-slip motion is not explicitly analysed, but the hysteresis that occurs as a result of this motion is captured. This reduces the number of parameters that are required to describe a system. It can be difficult to relate the physical nature of the interface to the resulting model.

A highly polished metal surface will appear flat upon ocular observation. However magnification of the surface will reveal hills and valleys that are large in comparison to molecular dimensions. These undulations on the surface are named asperities. When two asperity covered surfaces come into contact the true area of contact will always be smaller than the nominal area of the surfaces that are touching. The surface roughness arising from the distribution of asperities, and the true area of contact, are key ideas in the study of Tribology. Tribology is the contact mechanics of moving interfaces and is mostly concerned with friction and wear. The classical laws for friction state:

1. The force of friction is directly proportional to the applied load (Amontons 1st law.)
2. The force of friction is independent of the apparent area of contact (Amontons 2nd law.)
3. Kinetic friction is independent of sliding velocity (Coulomb's law.)

Early theories for frictional behaviour attempted to explain it in terms of the interlocking of asperities. However this does not account for the fact that friction is a dissipative process. Bowden & Tabor [19] suggested that the true area of contact arose from the plastic deformation of asperities, which resulted in the formation of metallic junctions. The force of friction was attributed to the shearing of these junctions. The resulting relations from Archard [20] are:

$$W = AH \tag{2.1}$$

$$F = sA \tag{2.2}$$

$$\mu = \frac{s}{A} \tag{2.3}$$

where W is the normal load, A is the true area of contact, H is the hardness, F is the force due to friction, s is the shear strength of junctions and μ is the coefficient of friction.

Archard [20] disagreed with the idea of a fully plastic flow of all asperities during frictional sliding. However, this conclusion was drawn from considering the wear of the surfaces where asperities were assumed to deform plastically. Archard's relations for wear are:

$$\frac{V}{L} = \frac{1}{3}KA = \frac{1}{3}K\frac{W}{H} \tag{2.4}$$

where V is the worn volume, L is the sliding distance and K is a constant named the wear coefficient.

Archard found typical values for K between 10^{-3} and 10^{-6}. This suggested that only a small proportion of contacts between asperities result in a worn particle. This lead to the conclusion that although plastic deformation of asperities may occur at first contact, their relaxation would be elastic, and subsequent contacts will bear the same load entirely by elastic deformation. Therefore, plastic deformation may not occur predominantly during continuous and repeated rubbing cycles on the same surface. Bowden & Tabor [19] also investigated friction behaviour through a simplified single asperity model, which was based on Hertzian elastic theory. However the resulting nonlinear friction-load relation seemed to contradict Amontons 1st law. This was resolved by Archard through modifying the model so that each asperity was covered with microasperities and many asperities were involved in contact. It was assumed that this number of asperities depended on the load and they had a uniform distribution of heights. This yields the result that additional load creates new areas of contact rather than enlarging the existing areas. Both of these models were later verified through the use of the atomic and friction force microscopes [20]. Archard's model was later improved by Greenwood & Williamson [21] by assuming a Gaussian distribution of asperity heights. They subsequently used their model to study the limits of the elastic deformation of rough surfaces. They supplied a criterion which determines the mode of deformation of a surface over a wide range of loads. It takes the form:

$$\psi = \frac{E'}{H}\sqrt{\frac{\sigma^*}{R}} \tag{2.5}$$

$$E' = \frac{E}{1-\nu^2} \tag{2.6}$$

where $\sigma*$ is the standard deviation of the distribution of asperity heights, R is the mean radius of curvature of asperity tips and E' is the plane stress modulus for the material with Young's modulus E and Poisson's ratio ν. The plasticity index ψ can be used to indicate the mode of deformation of the asperities:

- $\psi < 0.6 \implies$ There is a low probability of plastic contact. It will only occur at very large nominal pressures.
- $\psi > 1 \implies$ Plastic flow will occur at trivial nominal pressures.

Therefore Equation (2.5) indicates that the probability of plastic contact is almost entirely dependent on material properties and surface finish rather than applied load. The true area of contact is dependent on the load and the mean contact pressure is independent of load [20]. For most engineering materials and surface finishes $\psi > 1$. During the polishing of metallic surfaces, the loading-unloading and sliding of metal surfaces will produce changes in the shape of the asperities and a reduction in σ^*/R. Therefore subsequent deformations will tend towards being of an elastic nature.

From an investigation to identify the dynamic stiffness of joints, Andrew *et al.* [22] found that upon the application of prestress to a joint its stiffness would increase rapidly. However, when the joint is unloaded, the dynamic stiffness will decrease to a value which is higher than it was when the joint was initially loaded. This confirms Archard's finding that the initial loading resulted in some plastic flow at the contact surface. This causes a bedding in effect of the asperities at the surface, which increases the area of contact and therefore the stiffness. This shows that stiffness is strongly dependent on preload that has been experienced by the surfaces.

Oden & Martins [18] state that when considering dynamic sliding friction problems, the constitution of the interface is deemed stable. This is because the friction forces due to the dynamic sliding, of the surfaces in contact, are much larger than the friction forces arising from the plastic deformations of asperities. This is due to the difference in scales between the two friction phenomena. When two surfaces are pressed together the local friction forces depend upon surface displacements of the order of magnitude of 10μm. Comparatively two sliding surfaces will develop much larger relative motions and therefore larger friction forces. These forces will also change in direction. It is clear that the application of preload to the joint, in an HPU device, will cause permanent local deformation at the contact surfaces. However, the dynamic response of the joint will depend on continual loading-unloading of the contact interface that is of an elastic nature.

2.4 Phenomenological models for friction

A number of phenomenological models have been adopted to represent the dissipative behaviour and the dynamic response of a joint. These represent the friction force as a function of relative displacement.

Phenomenological models for friction behaviour include:

- Coulomb friction
- Jenkins element
- Lund-Grenoble (LuGre) model
- Valanis model
- Bouc-Wen model

Stick-slip phenomena are classically represented using Coulomb's law of friction. This requires the frictional force to change direction when the relative sliding velocity passes through zero. This is a signum type function which represents computational difficulties due to multi-valuedness of the friction force at zero velocity. This is shown in Figure 2.2 [23]. This approach does not take microslip into account.

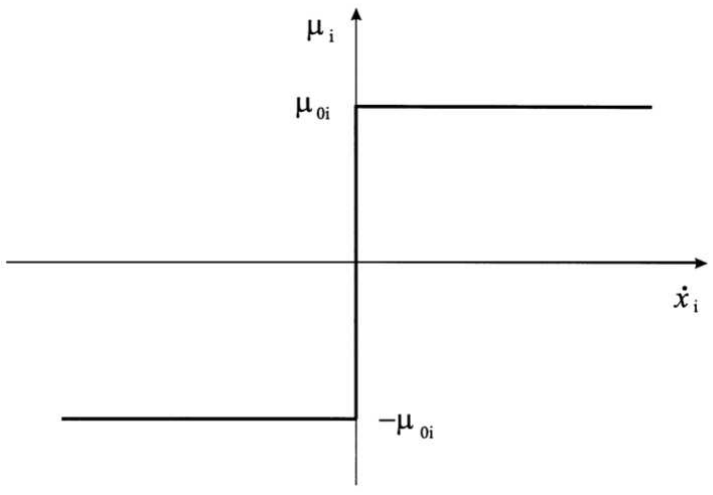

Fig. 2.2 Signum-type characteristic function for the frictional force [23].

A Jenkins element is a spring and a Coulomb damper, which are connected in series, and

is discussed in detail by Oldfield [24]. As long as the Coulomb element is sticking, it will provide a force that is equal to the input force and opposite in direction. It will slip when the input force equals the product of the normal contact force and the coefficient of friction to provide a resistive force of this magnitude during the slip phase. Under harmonic excitation the Jenkins element will produce an elastic perfectly-plastic hysteresis curve. One element alone is not sufficient to create a model representing microslip because it still only exhibits stick and slip behaviour. However, connecting Jenkins elements of varying stiffness, and threshold force, in parallel can simulate realistic behaviour exhibited by joints. The element is illustrated in Figure 2.3. Microslip occurs in regions away from the hole where the clamping pressure is lowest. Each Jenkins element can be considered as representing a discrete point on the contact surface. Elements further away from the hole will have a low threshold for slipping, so that these local regions can dissipate energy. The regions closer to the hole will have higher thresholds and will not slip until a large number of the elements with a lower threshold have been allowed to slip. The total joint force can be calculated by summing the contributions by the Jenkins elements:

$$F_{joint} = k_0 x + \sum_{i=1}^{n} \begin{cases} r_i(t) & abs(r_i(t)) < R_i \\ R_i sgn(\dot{x}) & \text{else} \end{cases}$$
$$r_i = k_i(x - x_{rev}) + R_i sgn(\dot{x}) \tag{2.7}$$

where k_0 is the permanent spring stiffness, k_i is the constant of the spring attached to the Coulomb element i, R_i is the threshold force of the Coulomb element i and x_{rev} is the displacement immediately prior to velocity reversal. The dot over a symbol represents the derivative with respect to time [25].

The LuGre model is a dynamic friction model, presented by Canudas [26], where the friction interface between two surfaces is thought of as elastic bristles moving over rigid bristles, as shown in Figure 2.4. When a tangential force is applied, the bristles will deflect like springs. For larger deflections the bristles will begin to slip. The model captures various aspects of friction behaviour such as: the Stribeck effect, hysteresis, spring-like characteristics for stiction and varying breakaway force. The Stribeck effect is mostly associated with lubricated sliding contacts where at low velocities friction will decrease with increasing velocity, as displayed in Figure 2.5. The LuGre model also accounts for varying breakaway force and

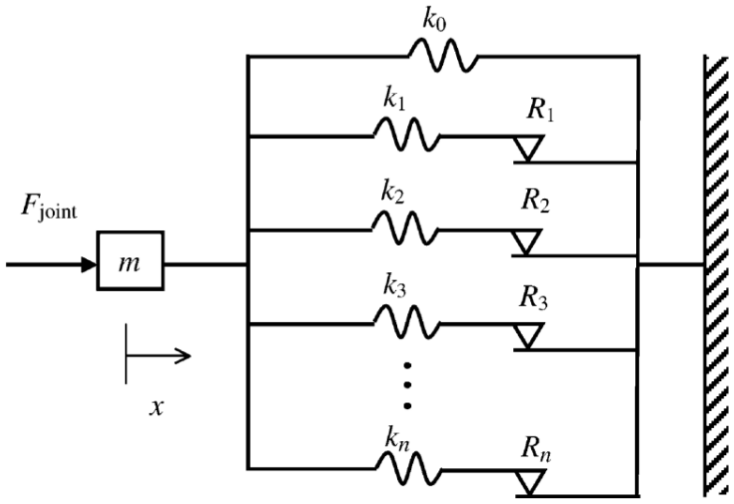

Fig. 2.3 Multiple Jenkins elements in parallel to represent a joint interface [25].

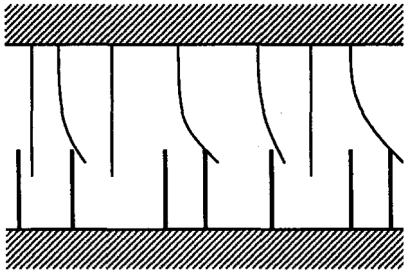

Fig. 2.4 The bristle interpretation of friction [26].

frictional lag [27]. The model has the form:

$$\frac{dz}{dt} = \upsilon - \sigma_0 \frac{|\upsilon|}{g(\upsilon)} z \tag{2.8}$$

$$F = \sigma_0 + \sigma_1(\upsilon)\frac{dz}{dt} + f(\upsilon) \tag{2.9}$$

where z is average bristle deflection, υ is velocity, σ_0 is stiffness of the bristles, $\sigma_1(\upsilon)$ is damping and both $g(\upsilon)$ and $f(\upsilon)$ are functions to model the Stribeck effect and viscous damping respectively.

The Valanis [29] model is adopted from plasticity by Gaul & Lenz [30] to reduce the complexity of analysing a space structure containing many joints. This produces a joint model simulation that only requires three material parameters. The model accounts for both mi-

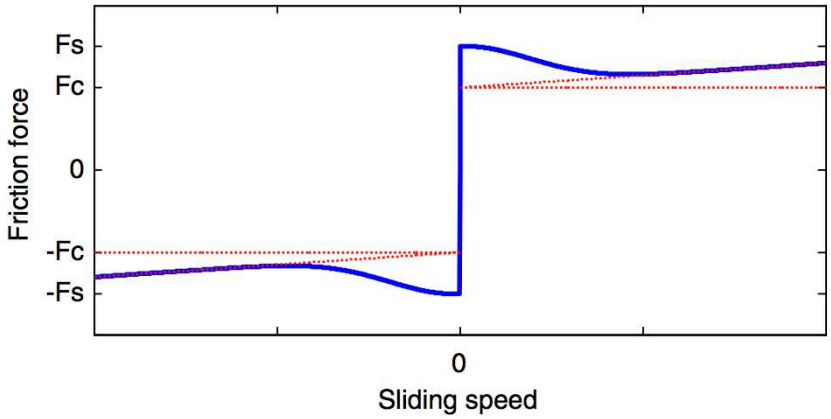

Fig. 2.5 A comparison of friction force as modelled using Stribeck friction (-) and Coulomb friction (- -) [28].

croslip and macroslip and is governed by the differential equation:

$$F'(z) + \lambda F(z) = E_0 q'(z) + \lambda E_t q(z) \tag{2.10}$$

where F is the generalised force, q is the generalised coordinate and E_0, E_t and λ are material parameters. The prime denotes differentiation with respect to an internal variable $z(t)$. The relationship between $z(t)$ and physical time is given as:

$$\dot{z}(t) = \left| \dot{q}(t) - \chi \frac{\dot{F(t)}}{E_0} \right| \tag{2.11}$$

where χ is a coordinate on the contact area and the dot denotes differentiation with respect to time. Through manipulation of these equations, Gaul & Lenz [30] develop a first order differential equation for joint hysteresis:

$$\dot{F} = \frac{E_0 \dot{q} \left[1 + \frac{\lambda}{E_0} \frac{\dot{q}}{|\dot{q}|} (E_t q - F) \right]}{1 + \chi \frac{\lambda}{E_0} \frac{\dot{q}}{|\dot{q}|} (E_t q - F)} \tag{2.12}$$

The hysteresis loops generated using the Valanis model are shown in Figures 2.6 and 2.7. The Bouc-Wen model is adopted by Oldfield *et al.* [25] as a simplified model to investigate the dynamics of a harmonically excited bolted joint. Similar to the Valanis model, the Bouc-Wen model was originally intended for modelling plastic behaviour, however there are parallels between this and friction behaviour. The joint exhibits elastic behaviour during

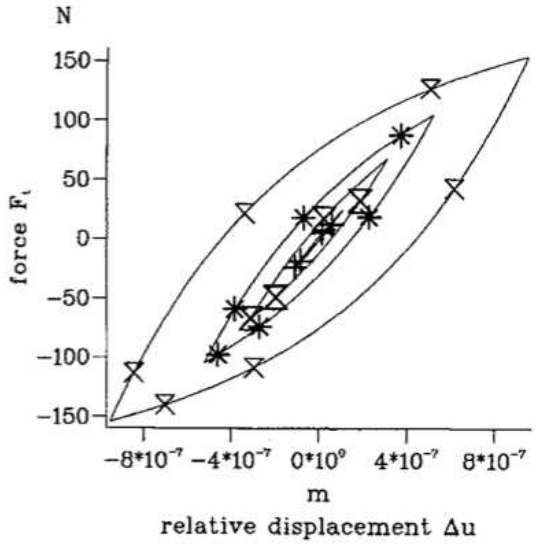

Fig. 2.6 Hysteresis loops generated from the Valanis model for microslip [30].

stiction and yielding of a material can be likened to slippage of the contact surfaces. The model describes the restoring force in a hysteretic system as:

$$Q(x,\dot{x}) = g(x,\dot{x}) + z(x,\dot{x},t) \tag{2.13}$$

where g is a nonhysteretic function and z is a hysteretic function dependent on the displacement history of the model. The function z is given as:

$$\dot{z} = -\alpha|\dot{x}||z|^{m-1}z - \beta\dot{x}|z|^{m} + A\dot{x} \tag{2.14}$$

where α and β define the shape of a hysteresis loop that is generated through tuning the parameters in the equation. The initial stiffness is A and m is used to manipulate the smoothness of the loop. Unlike the Jenkins element model, the parameters α and β possess no physical meaning. They are identified to fit the curve of the model to measured data.

From reviewing these phenomenological models for friction behaviour it is clear that analogising friction behaviour to plastic behaviour is useful when considering the mechanisms involved. It is likely that the friction behaviour occurring at the joint in an HPU device could be modelled using one of the methods outlined above. However these models have mostly been used to investigate transverse loading of bolted joints, so the axially excited joint in an HPU tool may exhibit behaviours that have not been observed in these studies.

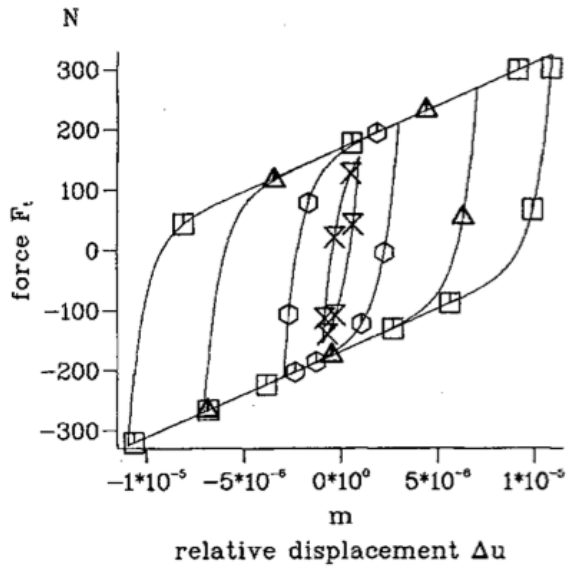

Fig. 2.7 Hysteresis loops generated from the Valanis model for macroslip [30].

2.5 Relaxation of bolted joints

Nonlinearities arise due to looseness of joints because this is a departure from their ideal behaviour. This small amount of play could be a precursor to chaos when the joint is subjected to harmonic excitation. Looseness of a bolt can occur through a number of relaxation mechanisms. Firstly vibration will increase relaxation through wear and hammering. This will reduce the preload and eventually friction forces will drop low enough to cause the bolt to slip. A study by Basava & Hess [31] demonstrates that a bolt can loosen or tighten under these conditions. The physical explanation for this behaviour involves the nonlinear dynamic interaction of the vibration and friction, and the resulting patterns of momentary sliding, sticking and separation between the threaded components. Figure 2.8 shows the evolution of either loosening or tightening behaviour in the clamping force as a result of varying vibration accelerations. An initial preload of 20N is applied to a bolt which is then subjected to axial vibration accelerations ranging from 10-2000ms^{-2}. For vibration levels of 250ms^{-2} and lower, the clamping force will reduce due to loosening behaviour, until it settles around a steady state. Similarly tightening behaviour occurs for vibration accelerations of 500ms^{-2} and greater. The maximum decrease or increase in clamping force possible from axial vibration levels was not determined.

Loosening of the joint will lead to clearance and subsequent nonlinear behaviour. Self-

loosening behaviour will lead to undesirable responses in HPU tooling and eventually failure of the system because the operating frequency will shift beyond the bandwidth of the power supply. A study by Zadoks & Yu [32] investigates the loosening behaviour of a transversely

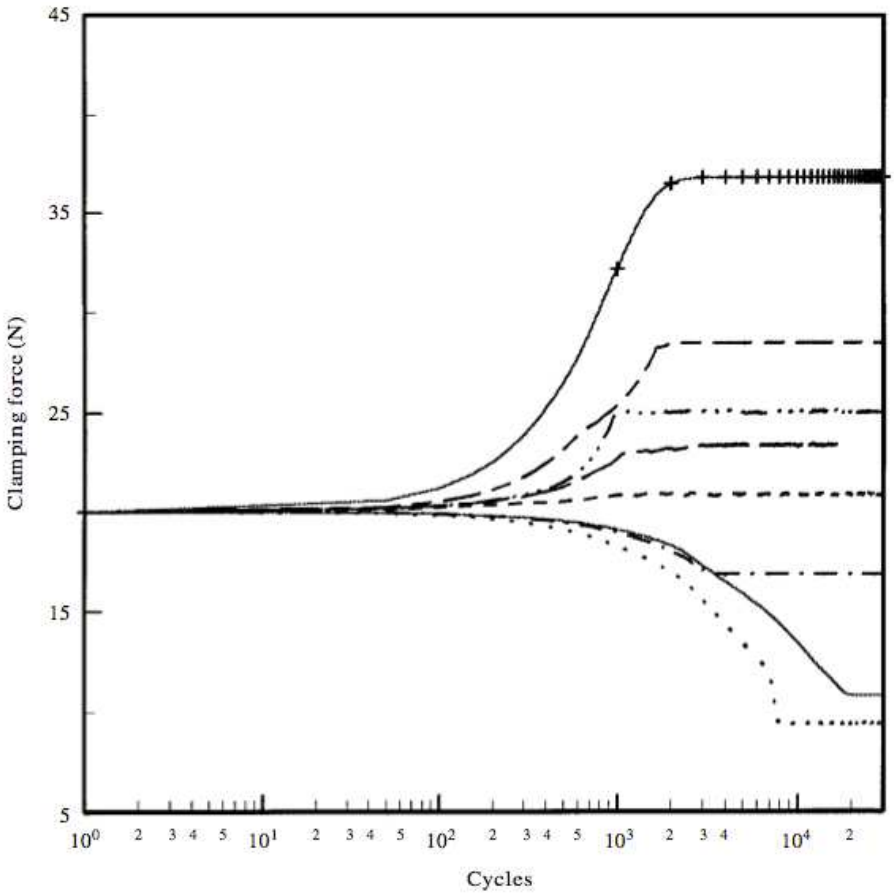

Fig. 2.8 Clamping force versus cycles of vibration for different vibration acceleration levels: 10ms^{-2} (–); 80ms^{-2} (...); 250ms^{-2} (–.–.); 500ms^{-2} (- - -); 600ms^{-2} (— —); 750ms^{-2} (–...–...); 1000ms^{-2} (— – — –); 2000ms^{-2} (–+–+) [31].

loaded bolt connection. This reveals that only the occurrence of impacts can generate the torque required to overcome the friction between the threads, bolt head and clamped component to cause slip. It is also shown that the larger friction surface area, between the bolt head and the component, dominates the response. This implies that the threads are less significant in this case. In the study of loosening due to axial vibration, Hess & Sudhirkashyap [33], produce an analytical model of a bolt loaded by gravity, which is shown in Figure 2.9. This is used to demonstrate that loosening occurs when the moment generated by the normal contact force of the threads overcomes the frictional moments.

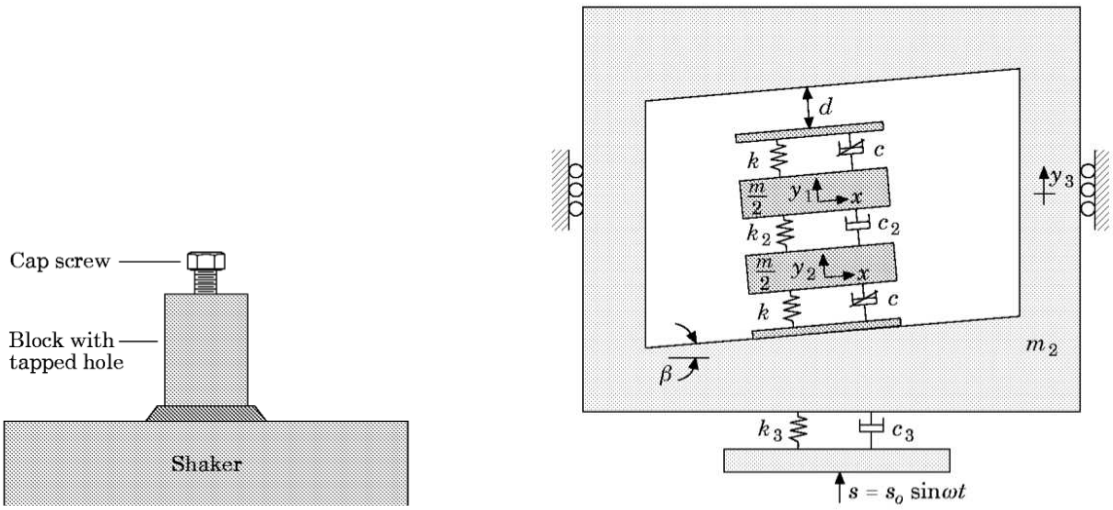

(a) Experimental set up (b) Analytical model

Fig. 2.9 Axial vibration of a bolt: Experimental set up and analytical model [33].

The study by Hess & Sudhirkashyap [33] represents the physical system shown in Figure 2.9a as an analytical model shown in Figure 2.9b. The threads of the tapped hole are unwrapped and viewed as upper and lower inclined constraints. The screw is constrained between these inclines, its threads are also unwrapped, and represented as upper and a lower inclines. This model successfully predicts loosening behaviour of the screw with and against load for varying vibration frequencies. It demonstrates the dependency of loosening and tightening behaviour on: vibration amplitude and frequency, thread fit, screw mass, component material and thread friction. However the effect of varying the thread pitch and pitch angle is not investigated to show how applicable the model is to different screw types. This model is extended to investigate the variation in clamping force due to applied vibration by Basava & Hess [31]. They incorporate a Karnopp [34] friction model and simulate a steady clamping force over a large number of cycles for various degrees of preload and vibration levels applied to the bolt. The model also predicts the loosening then tightening behaviour that occurs when preload decreases or vibration levels increase. They predict a maximum loss of 52.9% in clamping force due to axial vibration as well as a maximum increase of 83.4%. However both incarnations of this model are only applicable to situations where moderate preload is applied to the bolt.

Another common nonlinearity found in bolted interfaces is prying load. This arises because load is not applied directly along the axis of the bolt, but is offset to one side. This can dramatically increase the amount of tensile and bending stress produced in the bolt [35].

Prying is significant for certain joint configurations, such as the setup shown in Figure 2.1b, when an excitation force is not applied directly along the bolt axis. It is unclear if this behaviour will occur significantly at the joint in an HPU device, but it may arise if the device operates in a bending mode.

2.6 Joint identification

Joint identification is the process of estimating the joint parameters to minimise the difference between the measured response characteristics of an assembly and those found analytically or numerically. Direct measurement of a joint is usually not possible because it is inaccessible and the addition of sensors will affect the response. Experimental measurements of Frequency Response Functions (FRF) are employed in most approaches. Some of these depend on the ability to accurately measure modal parameters. However this is difficult when modes are closely coupled or strongly damped. Of the various methods used to get around this problem, most involve a hybrid of experimental data and numerical analysis through the Finite Element (FE) method. This can be applied to produce improved FE models. Discrepancies between experimental and numerical techniques often arise due to uncertainty in the FE model. This is the result of unmodelled variability in joint properties, and boundary conditions, as well as unmodelled nonlinearities [35].

The strategy utilised to identify joints, through measured FRFs, involves extracting properties of the structure with and without joints. The latter may involve measuring the response of the substructures, to be assembled, or a monolithic structure before it is decomposed into substructures. Tsai & Chou [36] extract the joint properties of a bolted lap joint through measurement of the FRFs of the substructures and the assembled structure. The method involves using measured receptances without the need for mathematical models of the mass, stiffness and damping matrices. The joint properties extracted from one assembled structure can be used to predict the result for another structure assembled with the same joint condition. In a similar approach, Ren & Beards [37] stress the importance of developing techniques which are insensitive to measurement error. Unlike the previous study, this study does not model the joint as a massless lumped spring-damper, but it is assumed that the dynamic characteristics of joints are linear and can be represented in the form of mass, stiffness and damping matrices. This method is also not limited to the identification of assemblies composed of one joint and two substructures.

A combination of FE modelling and measured FRFs is used by Hong & Lee [38] to predict the accurate dynamics of an assembly. This technique is based on the assumption that the dynamic properties of the structure are completely known apart from the joint parameters, which are to be determined. FRFs are measured experimentally and generated by an equivalent FE model, which is missing the joint parameters. This is a cost effective way of identifying linear joint parameters because only a few FRFs are required. These techniques are known as direct methods when the joint parameters are determined by solving a set of characteristic or dynamic equations. These consist of the mass and stiffness matrices, generated from a FE model, and measured frequency response data. Comparatively, penalty techniques minimise the errors or residuals that are used to assess the discrepancies between FE models and experimental measurements. One such case of this is the study by Li [39], which explains a method for the identification of joint stiffness. This involves defining a characteristic polynomial composed in terms of: the measured natural frequency, the partial modal properties predicted by a flawed FE model and the model parameters to be identified. By extracting the modal frequencies of the structure, and using data generated by the FE model, the remaining modal parameters can be determined.

A different approach, called force state mapping, can be used to identify the stiffness and damping properties of a nonlinear joint. Consider a single degree of freedom nonlinear vibrating system. The restoring force can be found by subtracting the terms representing inertial force from the terms representing the excitation force as long as material damping is negligible in the system:

$$\omega^2 q(t) + h(q, \dot{q}) = Q(t) - \ddot{q}(t) \tag{2.15}$$

Most of the terms can then be determined experimentally, which allows the nonlinear parameters to be identified. The study by Jalali *et al.* [40] identified the presence of a cubic softening spring, and damping dependent on vibration level, in a bolted lap joint model.

Unlike the previous studies in this section, Kashani & Nobari [41] seek to develop a method for identifying nonlinear joints without the need to pre-assume a model for the joint behaviour. It must also not require sophisticated techniques and equipment and be applicable for nonlinearities located at inaccessible or indeterminate degrees of freedom. They propose the use of a method based in the frequency domain, which is known as Optimum Equivalent Linear Frequency Response Function (OELF). The premise of this theory is that a nonlinear system will have a displacement time history containing nonlinearities that would not be

produced by a linear system. The nonlinear system output can be replaced by an equivalent linear system output with an added correction term. This method depends on finding an optimum model for the equivalent linear system. They make use of two different methods to extract the nonlinear elements of the dynamic behaviour. The first technique is Direct Identification Method (DIM) and the second is the Model Based Identification Method (MBIM). The process is as follows:

The equation of motion for a MDoF system is written as:

$$\mathbf{M}\mathbf{x}_n + \mathbf{C}\dot{\mathbf{x}}_n + \mathbf{K}\mathbf{x}_n + \mathbf{f}_n(\mathbf{x}_n, \dot{\mathbf{x}}_n) = \mathbf{f} \tag{2.16}$$

where **M**, **C** and **K** are the mass, viscous damping and stiffness matrices respectively. The nonlinear system response is $\mathbf{x}_n$, the internal force of the nonlinear element is $\mathbf{f}_n$ and the excitation force is **f**.

By considering harmonic excitation, and setting $\mathbf{Z}_n\left(\mathbf{X}_n, \dot{\mathbf{X}}_n\right)$ as the nonlinear impedance of the system, the frequency domain representation of Equation (2.16) can be written as Equation (2.17). Here $\dot{\mathbf{X}}_n$ is the Fourier transform of $\dot{\mathbf{x}}_n$ and $\mathbf{Z}\left(\mathbf{X}_n, \dot{\mathbf{X}}_n\right)$ is the impedance of the nonlinearity:

$$-\omega^2\mathbf{M} + i\omega\mathbf{C} + \mathbf{K} + \mathbf{Z}\left(\mathbf{X}_n, \dot{\mathbf{X}}_n\right) = \mathbf{Z}_n \tag{2.17}$$

Equation (2.17) implies that $\mathbf{Z}(\mathbf{X}_n, \dot{\mathbf{X}}_n)$ can be determined from:

$$\mathbf{Z} = \mathbf{Z}_n - \mathbf{Z}_l \tag{2.18}$$

where $\mathbf{Z}_l$ is the impedance of the underlying linear system. However this technique is not practical because impedances are difficult to measure. Equation (2.18) can be rewritten using FRF matrices to produce an expression where the only impedance required is that of the overall nonlinear system:

$$\mathbf{H}_n\mathbf{Z}\mathbf{H}_l = \mathbf{H}_l - \mathbf{H}_n \tag{2.19}$$

where $\mathbf{H}_n$ is the FRF of the nonlinear system and $\mathbf{H}_l$ is the FRF of the underlying linear system.

Instead of extracting $\mathbf{Z}(\mathbf{X}_n, \dot{\mathbf{X}}_n)$ directly, the following models of **Z** are introduced for viscous and hysteretic damping respectively:

$$\mathbf{Z}(\bar{\mathbf{X}}) = \begin{cases} \mathbf{K}_n\left(\bar{X}\right) + i\omega\mathbf{C}_n\left(\bar{X}\right) \\ \mathbf{K}_n\left(\bar{X}\right) + i\boldsymbol{\eta}_n\left(\bar{X}\right) \end{cases} \tag{2.20}$$

where:

$$\bar{X} = x_{RMS} \tag{2.21}$$

$\mathbf{K}_n$, $\mathbf{C}_n$ and $\boldsymbol{\eta}_n$ are the nonlinear stiffness, viscous damping and structural damping respectively and x is the relative displacement of two ends of the nonlinear element. The nonlinear stiffness and damping depend on the Root Mean Square (RMS) response value because the OELF are derived for each level of random excitation RMS value. The nonlinearity in the frequency domain can be represented as a function of displacement RMS. This can then be related to the amplitude of an equivalent harmonic signal, X, so the stiffness and loss factors can be related to the amplitude of harmonic excitation:

$$X = \sqrt{2}x_{RMS} \tag{2.22}$$

Overall this method involves measuring $\mathbf{H}_n$ and $\mathbf{H}_l$ to make use of Equation (2.19). Then assuming a form for the nonlinearity from the damping models that are stated in Equation (2.20). The equations are then converted into a standard form where they can be frequency weighted to correct for fluctuations in the OELF, which can cause errors. In this weighted form a least squares problem is formulated and solved.

Nonlinear acoustics also offers sensitive techniques which can be used to identify joint parameters. Nonlinear elastic and dissipative parameters can be found by looking at changes in resonance frequency and damping with the level of excitation. In a study to understand the physical process at the interface of a screw tightened into a plate, Rivière *et al.* [42] evaluate the sensitivity of nonlinear acoustic resonance spectroscopy to torque changes. They identify the existence of nonlinear behaviour between the screw and the plate, which is cubic and hysteretic in nature. These nonlinearities coexist at lower torques and decrease with increasing torque. The effect of the cubic nonlinearity becomes less pronounced at higher torques, so the hysteretic behaviour is more significant. They speculate that models derived from Hertz-Mindlin theory would encapsulate these nonlinearities. An example of this type of model is detailed by Aleshin & Van Den Abeele [43].

2.7 Transmission of ultrasound at joints

Ultrasonic methods play an important role in quality control and monitoring of engineering systems by providing non-destructive evaluation (NDE) techniques. A great deal of this

research has been aimed towards assessing the strength and quality of the bond in an adhesive joint [44]. A relatively new area of study is named Contact Acoustic Nonlinearity (CAN) [45]. This arises from the nonlinear interaction between an elastic wave and a contact interface. CAN has shown promise for use in applications of NDE. The transmission and reflection characteristics of ultrasonic waves are sensitive to contact conditions such as contact pressure and true area of contact. This occurs because the load at the contact interface is supported by surface asperities. Upon the application of preload these asperities will change in configuration and flatten. This discussion is limited to purely elastic behaviour of asperities because no damping terms are included to account for the energy dissipation that would occur due to plastic deformation of asperities. Following on from the discussion in Section 2.3, this assumption can be justified for bearing surfaces with high precision finishes. With increased load more asperities will come into contact and flatten, causing an overall change in the configuration of the surface, and an increase in the true area of contact. The mechanical response of the contact interface will involve nonlinear behaviour. A wave interacting with the interface will generate second or higher order harmonics. CAN is the predictor of significantly more harmonic generation than classical material nonlinearities [45]. A study by Guo *et al.* [46] seeks to quantitatively evaluate the interfacial stiffness of

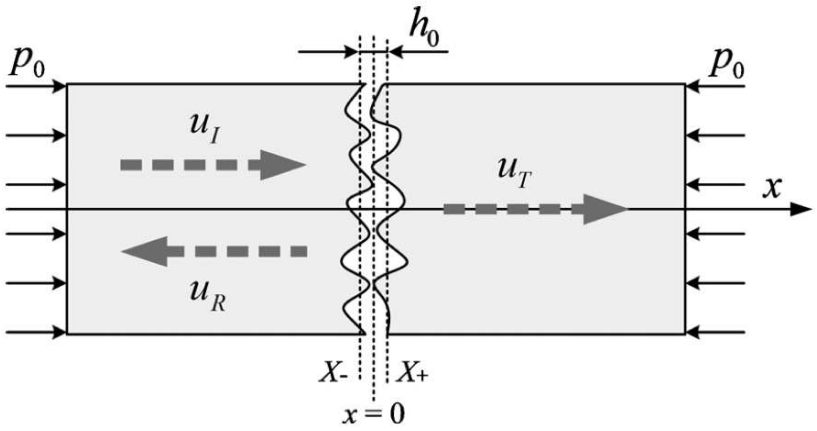

Fig. 2.10 Geometrical sketch of contacting rough interfaces under pressure located at the origin on the x-axis, together with the propagation of ultrasonic waves [46].

contacting interfaces with a dual-frequency ultrasonic technique. The CAN model is shown in Figure 2.10. In this model two identical material surfaces with density ρ and longitudinal stiffness E are pressed together by a pressure p_0. The uncertainty of the contact surface is not considered here, but aspects of this have been reviewed by Ibrahim & Pettit [35]. Instead the reference planes $x = X_-$ and $x = X_+$ average the certain roughness of each contact

surface.

In the absence of ultrasonic waves, the gap has an equilibrium position h_0 for a pressure p_0. When a wave interacts with the contact interface, the gap displacement h varies with time:

$$h(t) = h_0 + u(X_+, t) - u(X_-, t) \tag{2.23}$$

where $u(X_-, t)$ and $u(X_+, t)$ and are the displacements of the contact surfaces on the left hand side and the right hand side of the gap respectively. For a longitudinal wave propagating, in the positive x direction, the equation of motion is:

$$\rho \frac{d^2u}{dt^2} = \frac{d\sigma}{dx} \tag{2.24}$$

Assume that the vibrating system has continuously distributed mass and elasticity and there is negligible damping. The stress-strain relation is:

$$\sigma = E\frac{du}{dx} - p_0 \tag{2.25}$$

where $u(x,t)$ is the displacement in the x-direction, $\sigma(x,t)$ is the stress and t denotes time. Elimination of σ between Equations (2.24) & (2.25) yields:

$$\frac{d^2u}{dt^2} = c^2\frac{d^2u}{dx^2} \tag{2.26}$$

where c is the longitudinal wave velocity:

$$c = \sqrt{\frac{E}{\rho}} \tag{2.27}$$

The following terms are considered as a solution to Equation (2.26):

$$u(x,t) = u_I(x - ct) + u_R(x + ct) \qquad x < X_- \tag{2.28}$$

$$u(x,t) = u_T(x - ct) \qquad x > X_+ \tag{2.29}$$

where u_I, u_R and u_T are displacement fields of the incident, reflected and transmitted waves respectively.

For the open contact interface:

$$u(X_+,t) > u(X_-,t) \tag{2.30}$$

$$\sigma(X_+,t) = \sigma(X_-,t) = 0 \tag{2.31}$$

For the closed contact interface:

$$u(X_+,t) = u(X_-,t) \tag{2.32}$$

$$\sigma(X_+,t) = \sigma(X_-,t) = -p(h(t)) \tag{2.33}$$

$$p(h_0) = p_0 \tag{2.34}$$

The stress is continuous across the interface and obeys a functional relationship between the gap distance h and the contact pressure $p(h(t))$, which is in general a nonlinear relationship [45].

The initial conditions must be considered to find the forms of the incident, reflected and transmitted waves. These are supplied by Richardson [47] for a planar interface in a semi-infinite media. At time, $t = 0$, the right hand side of the gap is in an unperturbed state and an incident wave is propagating in the positive x direction of the left hand side of the gap. These conditions are expressed as:

$$u(x,0) = 0 \qquad X_+ \leq x < \infty \tag{2.35}$$

$$= u_I(x-ct) \qquad -\infty < x < X_- \tag{2.36}$$

$$\frac{du}{dt}(x,0) = 0 \qquad X_+ \leq x < \infty \tag{2.37}$$

$$= -cu_I'(x-ct) \qquad -\infty < x < X_- \tag{2.38}$$

The prime denotes differentiation with respect to the spatial coordinate x. The initial conditions are satisfied if $u_R(x+ct)$ vanishes when $x \leq 0$ and $u_T(x-ct)$ vanishes when $x \geq 0$. The function $u_I(x-ct)$ is considered to be known and functions $u_R(x+ct)$ and $u_T(x-ct)$ are to be determined by the boundary conditions.

The stresses due to the propagating wave can be found by differentiating Equations (2.28) and (2.29), with respect to space, and substituting them into Equation (2.25). At this point

the closed interface boundary condition Equation (2.33) is also applied:

$$\sigma = E\left[u_I'(x-ct) + u_R'(x+ct)\right] + p(h(t)) - p_0 \qquad x < X_- \tag{2.39}$$

$$\sigma = Eu_T'(x-ct) + p(h(t)) - p_0 \qquad x > X_+ \tag{2.40}$$

For the right hand side of the gap:

$$X_+ = u_T(x-ct) \tag{2.41}$$

$$\dot{X}_+ = -cu_T'(x-ct) \implies u_T'(x-ct) = -\frac{1}{c}\dot{X}_+ \tag{2.42}$$

The dot represents differentiation with respect to time, t. Equation (2.40) becomes:

$$\sigma(X_+,t) = -\frac{E}{c}\dot{X}_+ + p(h(t)) - p_0 \tag{2.43}$$

From Equation (2.27)

$$\frac{E}{c} = (E\rho)^{0.5} = \rho c \tag{2.44}$$

From Richardson [47], Equation (2.43) becomes:

$$\sigma(X_+,t) = -\rho c\dot{X}_+ + p(h(t)) - p_0 \tag{2.45}$$

For the left hand side of the gap:

$$X_- = u_I(x-ct) + u_R(x+ct) \tag{2.46}$$

$$\dot{X}_- = -cu_I'(x-ct) + cu_R'(x+ct) \tag{2.47}$$

$$\implies u_R'(x+ct) = \frac{\dot{X}_-}{c} + u_I'(x-ct) \tag{2.48}$$

Equation (2.39) becomes:

$$\sigma(X_-,t) = 2Eu_I'(x-ct) + \rho c\dot{X}_- + p(h(t)) - p_0 \tag{2.49}$$

$$\text{Let:} \quad 2Eu_I'(x-ct) = -F \tag{2.50}$$

where F is the driving force per unit area due to the incident wave $u_I(x-ct)$.

From Richardson [47], Equation (2.49) becomes:

$$\sigma(X_-, t) = -F + \rho c \dot{X}_- + p(h(t)) - p_0 \tag{2.51}$$

For the open contact interface:

$$X_+ > X_- \tag{2.52}$$

Equation (2.31) leads to:

$$\rho c \dot{X}_+ = p(h(t)) - p_0 \tag{2.53}$$

$$\rho c \dot{X}_- = F - p(h(t)) + p_0 \tag{2.54}$$

For the closed contact interface:

$$X_+ = X_- \tag{2.55}$$

$$-\rho c \dot{X}_+ + p(h(t)) - p_0 = \rho c \dot{X}_- - F + p(h(t)) - p_0 < 0 \tag{2.56}$$

Analysis by Richardson [47] and Biwa *et al.* [45] has defined two variables: $X(t)$ "centre of gravity" of the contacting surfaces and $Y(t)$ "the dynamic gap distance".

$$X(t) = \frac{u(X_-, t) + u(X_+, t)}{2} \tag{2.57}$$

$$Y(t) = u(X_+, t) - u(X_-, t) = h(t) - h_0 \tag{2.58}$$

From Equations (2.57) and (2.58):

$$X = \frac{X_- + X_+}{2} \tag{2.59}$$

$$Y = X_+ - X_- \tag{2.60}$$

Rearranging Equations (2.59) and (2.60) gives:

$$X_+ = X + \frac{1}{2} Y \tag{2.61}$$

$$X_- = X - \frac{1}{2} Y \tag{2.62}$$

Equation (2.57) with the conditions in Equations (2.53) and (2.54) yields:

$$\rho c \dot{X} = \frac{1}{2} F \tag{2.63}$$

Richardson [47] states that this is valid for all time regardless of whether the gap is open or closed. Similarly Equation (2.58) gives:

$$\text{Open gap:} \quad \rho c\dot{Y} = -F + 2p(h(t)) - 2p_0 \qquad Y \geq 0 \tag{2.64}$$

$$\text{Closed gap:} \quad F - 2p(h(t)) + 2p_0 \geq 0 \qquad Y = 0 \tag{2.65}$$

According to the initial conditions in Equations (2.36) and (2.38) the original continuous system at $t = 0$ is in an unperturbed state except for an incident wave that has not yet reached the point $x = 0$. The initial conditions for X and Y are therefore:

$$X(0) = 0 \tag{2.66}$$

$$Y(0) = 0 \tag{2.67}$$

Equation (2.66) $\implies$

$$X = u_I(x - ct) \tag{2.68}$$

$$\dot{X} = -cu_I'(x - ct) \tag{2.69}$$

Equation (2.64) $\implies$

$$\dot{Y} = -\frac{F}{\rho c} + \frac{2p(h(t))}{\rho c} - \frac{2p_0}{\rho c} \tag{2.70}$$

$$= 2cu_I'(x - ct) + \frac{2}{\rho c}\left\{p(h(t)) - p_0\right\} \tag{2.71}$$

By considering Equations (2.23) and (2.58), Equation (2.71) becomes:

$$\dot{Y} = 2cu_I'(x - ct) + \frac{2}{\rho c}\left\{p(h_0 + Y) - p_0\right\} \tag{2.72}$$

The forms of the reflected and transmitted waves can be defined using the transformed coordinates with arguments retained. Equations (2.28), (2.62) and (2.68) can be combined to give:

$$u_R(x + ct) = -\frac{1}{2}Y\left(t + \frac{x}{c}\right) \tag{2.73}$$

Equation (2.41), (2.61) & (2.68) can be combined to give:

$$u_T(x-ct) = X_+\left(t-\frac{x}{c}\right) \tag{2.74}$$

$$= X\left(t-\frac{x}{c}\right)+\frac{1}{2}Y\left(t-\frac{x}{c}\right) \tag{2.75}$$

$$= u_I(x-ct)+\frac{1}{2}Y\left(t-\frac{x}{c}\right) \tag{2.76}$$

Restate Equation (2.72):

$$\dot{Y} = 2cu_I'(x-ct)+\frac{2}{\rho c}\Big\{p(h_0+Y)-p_0\Big\}$$

To analyse Equation (2.77), the term $p(h(t))$ must be treated further. Biwa *et al.* [45] use a Taylor expansion of $p(h(t))$ near h_0 up to the second order term:

$$p(h(t)) = p(h_0+Y) = p_0 - K_1Y + K_2Y^2 \tag{2.77}$$

where the first-order and second-order interfacial stiffness are defined as:

$$K_1 = -\left.\frac{dp}{dh}\right|_{h=h_0} \tag{2.78}$$

$$K_2 = -\left.\frac{d^2p}{dh^2}\right|_{h=h_0} \tag{2.79}$$

Equation (2.77) becomes:

$$\dot{Y} = 2cu_I'(x-ct)+\frac{2}{\rho c}\Big\{-K_1Y+K_2Y^2\Big\} \tag{2.80}$$

The K_2 term gives rise to nonlinear ultrasonic responses in the reflected and transmitted waves. Analytical solutions are found using a perturbation method and predict that both reflected and transmitted waves contain second harmonics. The joint in an HPU device could exhibit CAN at the contact between the connecting faces of the transducer and the tool, as well as the threads of the screwed connector.

2.8 Outcomes

A summary of engineering literature that is related to bolted joints has been compiled to identify the relevant avenues that should be explored when considering the behaviour of an axial joint in a High Power Ultrasonic (HPU) device. This demonstrates the breadth of the problem in terms of the nonlinear vibration phenomena as well as the analytical and experimental techniques that may be employed for the analysis. Previous studies, that have been carried out to test this axial joint, have shown the difficulties that will be encountered during experiments. Loosening the joint will impede the ultrasonic standing wave. As a result the displacement response will be limited. The upper limit of this response is represented by a critical stress amplitude at the bearing surface. Encouraging the nonlinear behaviour of the axial joint, through loosening, will tend to diminish the level to which observations can be made above the noise floor of the measurement equipment.

It is clear that the chief concern to the open loop operation of an HPU device is its frequency behaviour. Loosening the joint will tend to increase the bandwidth of the instability region, which was depicted as the loop ABCA in Figure 1.3. This is problematic because the power supply to the HPU will typically track the impedance of the device in an effort to excite it close to its operating resonance. As the power supply adjusts the excitation frequency, towards the operating resonance, it can lead to the failure of its useful output behaviour. This instability region can be detected by exciting the HPU device at discrete frequencies, over a frequency range, that is expected to contain the operating vibration mode. Through controlled experiments, the width of the region can be associated with characteristics of the HPU device, based on empirical evidence. This is a costly process because it requires high temporal and frequency resolution to achieve reliable results. It is clear that any attempt to relate the behaviour of the axial joint to the nonlinear vibration behaviour of the device must be capable of matching the softening overhang behaviour that has been observed previously. A nonlinear system of equations is necessary to mimic this frequency behaviour

The literature that is available on bolted joints is extensive and only a small number of studies have been discussed in an effort to illustrate the potential for vibration phenomena. These empirical results are presented in order to provide some guidance to the subsequent experimental schemes in this study. This details results that have been observed from a dynamic perspective before discussing its direct relationship to frictional behaviour. It is clear that observation of the force-displacement loops of the axial joint will illustrate the behaviour of the joint most concisely. Lack of knowledge of the input force to the axial joint in an HPU

system means that a model cannot be formed using measured FRF matrices. It is expected that microimpacts at the bearing surface will give rise to second harmonics in the vibration response whereas stick-slip behaviour might give rise to odd superharmonics.

Discussion of the constitutive behaviour of surfaces is juxtaposed with details of various phenomenological models that have been employed to describe interface behaviour. It is clear that detailed dynamical analysis of a joint will rely on an austere model to clarify the the pertinent behaviour that is occurring. Furthermore, if a detailed description of the piezoelectric behaviour is necessary, then a simplified model of the joint will be required to complete analyses within a manageable time scale. The discussion of the relaxation of bolted joints relates to some of the most direct studies of axial joint behaviour that is available. The self loosening phenomenon was the main driving source behind the investigation. Literature on the nature of axial joints is relatively rare and their implementation in HPU devices is a niche application. A great deal of the bolted joint literature discusses the behaviour of bolted lap joints or the stick-slip motion of two frictional surfaces held by a bolt. The application of the outcomes of these studies to axial joint behaviour is not prevalent in the literature.

Due to the inaccessibility of the axial joint to direct measurement, the application of a suitable joint identification scheme is essential. However, such schemes demand the direct observation of the input force to the system in order to measure appropriate Frequency Response Functions. The excitation force for an HPU system descends from its piezoelectric stack under the application of high electrical power. This does not fit in with conventional vibration testing schemes. The force identification literature [13, 14] has suggested that observation of an unknown nonlinear subsystem can be achieved if its output is balanced with a system that is considered to be its monolithic counterpart. It is very unlikely that the force occurring within a HPU device will be measured reasonably by a sensor that is attached nearby to its axial joint. Furthermore, force sensors with a linear frequency response up up to 40kHz are not available to make this observation. This means that noncontact measurement systems are necessary. Therefore, a method that can extract the behaviour of the axial joint from indirect observations is required. This implies that a hybrid analytical-experimental scheme must be developed for the HPU device.

Chapter 3

Force estimation in rod-like piezoelectric actuators

3.1 Introduction

The direct measurement of the force or strain that is occurring within a High Power Ultrasonic (HPU) device is not usually required for its application. However, without this observation, it is not possible to discuss the true behaviour of its interfaces. The behaviour of a mechanical interface is predominantly a matter of the frictional processes that are occurring. Due to the complexity of these processes it is not possible to separate them and instead it is more useful to consider the interface as a black box with input-output behaviour. An HPU device can only maintain its dynamic equilibrium if its interfaces do not self loosen. Otherwise it is unlikely that the bandwidth of its power supply will be able to excite a vibration mode, of the newly separated structure, that will produce motion that is observable above the noise floor of the measurement system. Therefore the frictional process at the interface is best thought of as slapping process relating to the microslip of the asperities at the bearing surface. Attempting to place a sensor between the two contact surfaces, or across their circumferences, will modify their interaction. The observation of this behaviour must be made through non-contact optical methods.

The Distributed Transfer Function Method (DTFM) is applied, as the underpinning to a hybrid experimental technique, that is required to estimate the behaviour of an axial joint in an HPU device. PZT (piezoelectric ceramic) and Titanium Grade 5 components are con-

nected serially through the prestress developed by one, or more axial joints, throughout the assembled device. Estimations of the linear and nonlinear behaviour of this assembly are discussed in Chapters 4 and 5 respectively. The DTFM is designed for the vibration analysis and feedback control of the elastic continua. It features a spatial state formulation, where it is assumed that each component in the structure supports waves that propagate according to a spectrum relationship, which is obtained analytically. The current state space formulation is first order, which means that the governing differential equations of elastic continua must depend on one variable only. Therefore, to apply the DTFM scheme to higher order waveguide theories, it would need to be reformulated. For single mode wave theories, the transient solution to an elastic continuum, which contains discontinuities in its parameters, can be obtained symbolically through the evaluation of the transfer function residues. This application is attributed to the work by Yang [48, 49] and following a specific case of the work given in Yang [50].

Yang's analytical work has been generalised as a set of MATLAB scripts and functions. This introduces numerical errors into the exact analytical method. However, this facilitates the tests of a configuration that contains many discontinuities, of varying type, without the need for the explicit formulation of the transfer function each time. The time discretisation of the method is also necessary, so that it can be applied to experimental data. The method can now be applied more readily to complex problems, such as parameter identification and force identification, through the use of numerical algorithms. However, the number of samples, N, which may be considered in the force estimation, is limited by the memory available to MATLAB. This determines the largest contiguous virtual address space that is available to form the one dimensional convolution matrix. For 64-bit MATLAB, running on 64-bit Windows 7, the memory available to the computation is determined by the system memory. This is the sum of the physical memory and the size of the swap file. There is 16GB of RAM physical memory available and 32GB of virtual memory allocated. This gives a maximum size of $N \times N$ for a double precision array where $N = 5681$. However, the virtual memory is accessed slower than the physical memory. Therefore it incurs a significant cost in computation time. The nature of the force identification problem that follows is determined by the number of samples involved in the computation. The number of samples was limited to approximately half of the expected maximum to allow the computation to progress in a manageable timescale.

The application of the DTFM, which follows, differs from the examples given by Yang [50] because it makes use of a higher order spectrum relationship, which is derived from a

waveguide defined by Love Rod Theory (LRT). Also, in order to describe a piezoelectric component, a potential difference is applied through the length of the waveguide. To achieve this, the formulation of a two mode theory piezoelectric rod, which is given by Shatalov *et al.* [51], is reformulated for a one mode piezoelectric rod. A retarding force that is proportional to velocity is also included in an attempt to allow the linear model to dissipate energy. The implementation of the DTFM to a rod-like electromechanical transducer, the discretisation of the technique and the inversion of the transfer function, for the purpose of force identification, distinguishes this particular example. The overall goal is that some useful observation of axial joint behaviour can be derived relative to this formulation. Suggestions are given throughout on the limitations that must be addressed.

3.2 Waveguides

It is assumed that the vibration of the i^{th} serially connected component, in the assembly of the HPU device, is dictated by a particular waveguide theory. The exact solution of waves propagating in waveguides requires some in depth mathematical analysis that has not been attempted here. This analysis can be found in Doyle [52] and Żak & Krawczuk [53], and provides much more insight into the vibration of structural rods. The exact representation of an infinite continuum is found by representing the displacements in three Cartesian directions, u_1, u_2 and u_3, with four potential functions ϕ, H_1, H_2 and H_3, by means of a Helmholtz decomposition. These are then substituted into Navier's equations. When a particular waveguide is constructed from this exact analysis, it reveals that the waveguide supports an infinity of modes, and akin to vibration theory, the higher order modes become more significant in the behaviour of the waveguide at higher frequencies. Żak & Krawczuk [53] derive new two, three and four mode theories, for rod behaviour, and compare these with classical examples of single mode Love Rod Theory (LRT), two mode Mindlin-Herrmann Theory and three mode theories. They demonstrate that each of the theories agrees well with the exact Pochhammer analytical solution for different limited frequency ranges.

The exact solution is only suitable for the description of an assumed infinite continuum. Therefore, it is not suitable for structural problems where elements are subject to boundary and external conditions. The waveguide theory, proposed in Doyle [52], assumes that the elements are semi-infinite and this results in the need for a throw off element. This throw off element allows energy to be propagated and reflected from a free end condition, so that some

energy proceeds to infinity, whilst reflected energy still modifies the structural response. This is an effective assumption when the time of interest is short and the structure is large. In comparison, Transfer Element methods, such as the DTFM, define the solution space to the structure through a Transcendental Eigenvalue Problem (TEP), which is constrained by explicit boundary and matching condition matrices [54].

The simplest rod theory, that is an improvement over Elementary Rod Theory (ERT), is the classical single mode Love Rod Theory (LRT). This is a modified rod theory, where the transverse strain $S_{11} = S_{22}$ is related to the axial strain S_{33} through the Poisson's ratio ν: $S_{33} = -\nu S_{11}$. Through the application of Hamilton's principle, the following governing equation of motion can be derived:

$$EA\frac{\partial^2 u}{\partial x^2} + \nu^2 \rho J \frac{\partial^2 \ddot{u}}{\partial x^2} - \rho A \frac{\partial^2 u}{\partial t^2} = 0 \tag{3.1}$$

where E and ρ are the Young's modulus and the density of the waveguide material respectively, u is the displacement in the axial direction, J is the polar moment of area and t is time.

The Spectral Element Method (SEM), which was developed by Doyle [52], is built on the assumption that once an equation of motion has been chosen to represent the waveguide, it is then assumed that any time input or response can be represented using the discrete Fourier transform:

$$F(t) = \sum_{n=0}^{N-1} \tilde{C}_n e^{+j\omega_n t} \qquad n = 0, 1, \ldots, N-1 \tag{3.2}$$

where $F(t)$ is an arbitrary function in the time domain and $\tilde{C}_n$ are the Fourier coefficients that are sampled at discrete frequencies given by $\omega_n = 2\pi n/T$. The tilde accent denotes a quantity that has been transformed into the frequency domain. T is the period of the signal and it is sampled up to N points. The imaginary unit is denoted by j. A discretisation rate can be defined as: $\Delta T = T/N$. This is useful in defining the Nyquist frequency [52]:

$$f_N = \frac{1}{2\Delta T} \tag{3.3}$$

The Nyquist frequency determines the minimum sampling rate that should be adopted to avoid aliasing of an observed signal.

Equation (3.2) implies the form of the axial displacements in the frequency domain:

$$u(x,t) = \sum_n \tilde{u}_n(x,\omega_n)e^{+j\omega_n t} \tag{3.4}$$

The governing differential Equation (3.1) can be represented as:

$$\sum_n \left\{ (EA - \nu^2 \rho J \omega_n^2)\frac{d^2\tilde{u}_n}{dx^2} + (\rho A \omega_n^2)\tilde{u}_n \right\} e^{+j\omega_n t} = 0 \tag{3.5}$$

The above equation must be solved at each discrete frequency ω_n. Doyle [52] assumes a solution of the form $\tilde{u}_n = Ce^{-jk_1 x}$. This can be substituted into Equation (3.5) to give the characteristic equation:

$$\sum_n \left[\left\{ (EA - \nu^2 \rho J \omega_n^2)k_1^2 - (\rho A \omega_n^2) \right\} Ce^{-jk_1 x} \right] e^{+j\omega_n t} = 0 \tag{3.6}$$

This can be used to extract the spectrum relation for the longitudinal mode represented by LRT. The spectrum relation describes the spatial variation of the travelling wave. The wavenumber is derived from Equation (3.6):

$$k_1 = \pm\omega_n \sqrt{\frac{\rho A}{EA - \rho\nu^2 J\omega_n^2}} \tag{3.7}$$

As the frequency is increased the wavenumber can go to infinity when $\rho\nu^2 J\omega_n^2 = EA$ and after this critical frequency the wavenumber is imaginary because all of the input energy is converted to transverse motion. The solution to equation (3.1) can be expressed as:

$$u(x,t) = \sum_n B_1 e^{-j(k_1 x - \omega_n t)} + \sum_n C_1 e^{+j(k_1 x + \omega_n t)} \tag{3.8}$$

where B_1 and C_1 are the amplitudes of a forward moving wave and a backward moving wave respectively. For both of these the amplitudes and the wavenumber must be determined at each frequency ω_n.

Equation (3.8) is only applicable for a semi-infinite rod. To introduce discontinuities into the behaviour of this rod, a dynamic stiffness matrix is formed. This grows in complexity for each parameter change that is included, and it can be assembled to give the transfer function between the input force and the output displacement in the frequency domain. As an alternative to this, the DTFM approach is applied, and requires only the manual assembly

of 2×2 matrices to form a Transcendental Eigenvalue Problem (TEP).

The state space formulation of the DTFM restricts it to a single equation of motion to describe the vibration of the i^{th} component. Therefore higher rod theories are not explored in this case. Doyle [52] has shown that the dispersion behaviour of LRT agrees significantly better, with the exact Lamb solution, than ERT as the frequency of interest is increased. The dispersion relationship is defined as the group speed c_g normalised by the wave speed given by ERT, c_0. The group speed is expressed as $c_g = \frac{d\omega_n}{dk}$. The dispersion relationship of ERT is constant with frequency and LRT begins to diverge from this significantly after 5kHz, whilst agreeing with the exact Lamb solution. LRT diverges from the exact Lamb solution at around 13kHz, along with Mindilin-Herrmann theory. The Mindilin-Hermann theory is closer in agreement with the exact Lamb than LRT, but the error for both is minimal at around 20kHz. A further modification that has been implemented by Doyle [52] is the introduction of retarding forces proportional to velocity and displacement in the waveguide. This approach is adopted here to allow the model to dissipate energy.

3.3 Electromechanical rod elements

In order to describe a stacked piezoelectric actuator, which features changes in its geometrical, material and loading parameters along its length, there is a need for a rod element that is admissible to both electrical and mechanical conditions at its boundaries. It must also be simplified enough so that it is suitable for computations that feature many discontinuities. For this purpose, the element has been limited to a one mode deformation field. However, Shatalov *et al.* [51] suggest that a two mode deformation field is necessary for most transducer models. They adopt the Mindlin-Herrmann two mode deformation field, where $u_1(x_1, x_3, t) = u_2(x_2, x_3, t) = \psi(x_3, t)$ with $u_3(x_3, t)$ as the axial displacement field and $\psi(x_3, t)$ as the radial displacement field in three dimensional Cartesian coordinates. This is more realistic for thick rod-like elements, however this will result in spatial derivatives for two dependent variables.

A DTFM scheme is required to describe piezoelectric rod elements. However, the piezoelectric stacked actuator features many discontinuities, so a DTFM scheme that could admit more than one mode would feature a significant number of terms. The result of this would be to limit the calculation of transient behaviour to a smaller number of samples than the one mode theory. Therefore the extension of the force identification scheme for higher

wave mode theory is not attempted at this stage. Later it will be shown that a state transition matrix is computed to obtain the eigenvalues for a distributed parameter system. This is based on a first order state space formulation, which is not capable of describing coupled equations of motion. This would need to be replaced with a scheme where this is possible. The transient response of the distributed parameter system is computed as the sum of the transfer function residues. Yang [50] found an exact expression for this because the inverse Laplace Transform was available. However it is unlikely that this would be available for a higher order waveguide, so the inverse Laplace Transform would have to be computed numerically.

The linear theory of piezoelectricity may be adopted to describe small vibrations in piezoelectric crystal type materials. The dynamic mechanical motion is coupled to the quasi-static electric field through assumed piezoelectric material constants. However, this relationship depends on the crystalline symmetry of the chosen material. Many materials exhibit the direct piezoelectric effect of tending to generate an internal charge from an induced mechanical stress, and the vice versa converse piezoelectric effect. Fotiadis *et al.* [55] modelled a long dry bone as a hollow piezoelectric cylinder, with crystal class 6 (hexagonal) symmetry, based on previous experimental evidence. This naturally occurring symmetry is also found in synthetic piezoelectric ceramics.

Lead Zirconate Titanate (PZT) is a piezoelectric ceramic that is commonly adopted in engineering applications for use as resonators in sensors and actuators. It is offered as either hard or soft PZT, where the former suggests that the ceramic suffers lower electromechanical losses, at a cost of generating a smaller electrical field per unit mechanical stress, than its counterpart [56]. Hard PZT is favoured for HPU applications. Below a temperature, which is known as the Curie point, PZT is a mass of ceramic crystals, where each crystal has a dipole moment, and each of these moments is randomly distributed. Under these conditions, it is unlikely that the ceramic will be able to develop a piezoelectric effect that can do any useful work. To solve this problem the ceramic is held just below the Curie point and a strong direct current electric field is applied through its axis. This tends to align adjacent dipoles to generate an axis for which the PZT can be considered net polarised. Once the electric field is removed, the PZT is permanently polarized and elongated through its axis. This produces hexagonal crystalline symmetry that results in transverse isotropic constitutive behaviour. This means that the PZT is anisotropic in the polarisation direction, x_3, whilst it is isotropic in the two other directions, x_1, x_2. An example PZT ring is shown in Figure 3.1. In the case of a piezoelectric rod this material behaviour may be thought of

as the rod having rotational symmetry about its axis of poling.

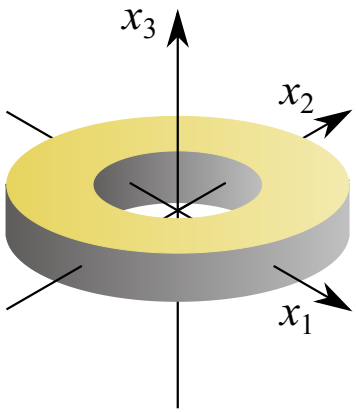

Fig. 3.1 Piezoelectric disc poled in in the x_3 direction.

The wave motion analysis will be based on the one mode Love Rod Theory (LRT), which assumes that the radial strain is related to the axial strain through Poisson's ratio. The displacement field can be stated as:

$$\begin{aligned} u_1 &= u_1(x_1, x_3, t) = -x_1 \nu_{13} u_{3,3} \\ u_2 &= u_2(x_2, x_3, t) = -x_2 \nu_{23} u_{3,3} \\ u_3 &= u_3(x_3, t) \end{aligned} \tag{3.9}$$

where u_3 is the displacement along the axis of poling x_3 and u_1 and u_2 are the transverse displacements perpendicular to the poling axis; along x_1 and x_2. The Poisson's ratio is denoted by $\nu_{ij} = \frac{\partial u_{i,i}}{\partial u_{j,j}}$ with the comma derivative $u_{i,i} = \frac{\partial u_i}{\partial x_i}$. Repeated indices after the comma indicates higher order partial derivatives, so $u_{3,33} = \frac{\partial^2 u_3}{\partial x_3^2}$.

The subsequent strain field can be derived following:

$$S_{ij} = \frac{1}{2}(u_{i,j} + u_{j,i}) \tag{3.10}$$

$$
\begin{aligned}
S_{11} &= u_{1,1} = -\nu_{13} u_{3,3} \\
S_{22} &= u_{2,2} = -\nu_{23} u_{3,3} \\
S_{33} &= u_{3,3} \\
S_{23} &= -\frac{1}{2} x_2 \nu_{23} u_{3,33} \\
S_{13} &= -\frac{1}{2} x_1 \nu_{13} u_{3,33} \\
S_{12} &= 0
\end{aligned} \tag{3.11}
$$

Relating the transverse strain to the axial strain implies that the shear strains are a function of the axial strain gradient. Recent advances in strain gradient elasticity theory have shown that higher order gradients of the displacement field can produce significant corrections to the wave number when very small length scales are involved [57].

Tiersten [58] derives the first law of thermodynamics for a piezoelectric medium that conforms to the assumption of a quasi-static electric field. This is valid if the wavelengths of the elastic waves are much shorter than the electromagnetic wavelengths for the same frequency. The following electric enthalpy function is derived for a linear piezoelectric medium:

$$
\begin{aligned}
H(\mathbf{S}, \mathbf{E}) &= \frac{1}{2} c^E_{ijkl} S_{ij} S_{kl} - \frac{1}{2} \kappa^S_{ij} E_i E_j - e_{kij} S_{ij} E_k \\
c^E_{ijkl} &= c^E_{ijlk} = c^E_{jikl} = c^E_{klij} \\
e_{ijk} &= e_{ikj} \\
S_{ij} &= S_{ji}
\end{aligned} \tag{3.12}
$$

where e_{kij} are the piezoelectric constants, κ^S are the dielectric constants measured at constant strain and c^E_{ijkl} are the elastic constants measured at constant electric field E_i, which implies that the electric terminals are short circuited. The stress charge form of the piezoelectric constitutive equations can be obtained by differentiating Equation (3.12) as follows [59]:

$$
\begin{aligned}
T_{ij} &= \frac{\partial H(\mathbf{S}, \mathbf{E})}{\partial S_{ij}} = c^E_{ijkl} S_{kl} - e_{kij} E_k \\
D_i &= \frac{\partial H(\mathbf{S}, \mathbf{E})}{\partial E_i} = e_{ikl} S_{kl} + \kappa^S_{ik} E_k
\end{aligned} \tag{3.13}
$$

Equation (3.13) can be converted into stress-voltage form through the following matrix

Table 3.1 Conversion from tensor to matrix notation

p or q	ij or kl
1	11
2	22
3	33
4	23
5	13
6	12

transformations:

$$\begin{aligned}
\boldsymbol{\beta}^S &= (\boldsymbol{\kappa}^S)^{-1} \\
\mathbf{e} &= \mathbf{c}^E\mathbf{d} \\
\mathbf{c}^D &= \mathbf{c}^E - \mathbf{c}^E\mathbf{d}\boldsymbol{\beta}^S\mathbf{d}'\mathbf{c}^E \\
\mathbf{h} &= -\mathbf{c}^E\mathbf{d}\boldsymbol{\beta}^S
\end{aligned} \tag{3.14}$$

where the stiffness parameter is now measured at constant electric charge, c^D_{ijkl}, and the piezoelectric coupling is now related to charge D_k through h_{kij}. This implies that the electric terminals of the piezelectric are open. Given the notation contained in Equation (3.12) it is more compact to replace the tensor description of Equation (3.13) with a matrix form according to Table 3.1. The substitution of Equation (3.14) into Equation (3.13) gives the stress-voltage form:

$$\begin{aligned}
T_p &= c^D_{pq}S_{ij} - h_{kp}D_k \\
E_i &= -h_{iq}S_q + \beta^S_{ik}D_k
\end{aligned} \tag{3.15}$$

For transverse isotropic material behaviour Equation (3.15) can be expanded to [58]:

$$\begin{Bmatrix} T_1 \\ T_2 \\ T_3 \\ T_4 \\ T_5 \\ T_6 \end{Bmatrix} = \begin{bmatrix} c_{11}^D & c_{12}^D & c_{13}^D & 0 & 0 & 0 \\ c_{12}^D & c_{11}^D & c_{13}^D & 0 & 0 & 0 \\ c_{13}^D & c_{13}^D & c_{33}^D & 0 & 0 & 0 \\ 0 & 0 & 0 & c_{44}^D & 0 & 0 \\ 0 & 0 & 0 & 0 & c_{44}^D & 0 \\ 0 & 0 & 0 & 0 & 0 & \frac{1}{2}(c_{11}^D - c_{12}^D) \end{bmatrix} \begin{Bmatrix} S_1 \\ S_2 \\ S_3 \\ S_4 \\ S_5 \\ S_6 \end{Bmatrix} + \\ - \begin{bmatrix} 0 & 0 & h_{31} \\ 0 & 0 & h_{31} \\ 0 & 0 & h_{33} \\ 0 & h_{15} & 0 \\ h_{15} & 0 & 0 \\ 0 & 0 & 0 \end{bmatrix} \begin{Bmatrix} D_1 \\ D_2 \\ D_3 \end{Bmatrix}$$

$$\begin{Bmatrix} E_1 \\ E_2 \\ E_3 \end{Bmatrix} = \begin{bmatrix} 0 & 0 & 0 & 0 & -h_{15} & 0 \\ 0 & 0 & 0 & -h_{15} & 0 & 0 \\ h_{31} & h_{31} & h_{33} & 0 & 0 & 0 \end{bmatrix} \begin{Bmatrix} S_1 \\ S_2 \\ S_3 \\ S_4 \\ S_5 \\ S_6 \end{Bmatrix} + \\ + \begin{bmatrix} \beta_1^S & 0 & 0 \\ 0 & \beta_2^S & 0 \\ 0 & 0 & \beta_3^S \end{bmatrix} \begin{Bmatrix} D_1 \\ D_2 \\ D_3 \end{Bmatrix} \tag{3.16}$$

Isotropic material constitutive behaviour can be recovered by setting the piezoelectric coupling constants to zero and assuming the following relationships:

$$\begin{aligned} c_{12}^D &= c_{13}^D \\ c_{11}^D &= c_{33}^D \\ c_{44}^D &= c_{66}^D \\ \beta_1^S &= \beta_3^S \end{aligned} \tag{3.17}$$

The stiffness constants can be given in terms of Lamé constants:

$$\begin{aligned} c_{11}^D &= \lambda + 2\mu \\ c_{12}^D &= \lambda \\ c_{44}^D &= \mu \end{aligned} \tag{3.18}$$

where Lamé constants are written in terms of Young's modulus E and Poisson's ratio ν of the isotropic material:

$$\begin{aligned} \lambda &= \frac{\nu E}{(1+\nu)(1-2\nu)} \\ \mu &= \frac{E}{2(1+\nu)} \end{aligned} \tag{3.19}$$

With these constitutive relationships in place it is possible to define a general waveguide that may accept mechanical or electric boundary conditions based on a choice of material parameters. To derive this waveguide the generality of the piezoelectric rod must be retained and the Extended Hamilton Principle is applied to establish the equilibrium and compatibility requirements [52]:

$$\delta \int_{t_1}^{t_2} [T - (U+V) + W]\, dt = 0 \tag{3.20}$$

where T, U, V and W are the kinetic, strain, loading and electric energies respectively and δ is the variation parameter. Equation (3.20) is a variational statement that describes the work done by the system as it progresses from its state at time t_1 to a state at time t_2. A full introduction to variational approaches is given by Lanczos [60]. Equations (3.11) and (3.16) imply that the strain energy for the element can be written as:

$$\begin{aligned} U = \frac{1}{2} \int_0^{l_i} \Bigg[&\left\{ 2\left(c_{11}^D + c_{12}^D\right)\nu^2 A - 4c_{13}^D \nu A + c_{33}^D A \right\} u_{3,3}^2 + \\ &+ \frac{1}{2} c_{44}^D \nu^2 J u_{3,33}^2 + (2h_{31}\nu - h_{33}D_3 A) u_{3,3} \Bigg] dx_3 \end{aligned} \tag{3.21}$$

where $x_1 = x_2 = r$ is the radius of the rod, $A = \pi r^2$ is the area, $J = \frac{\pi}{2} r^4$ is the second polar moment of area and $\nu_{23} = \nu_{13} = \nu$ is the Poisson's ratio. The kinetic energy for the rod with rotational symmetry can be written as:

$$T = \frac{1}{2} \int_0^{l_i} \left[\rho A \dot{u}_3^2 + \rho \nu^2 J \dot{u}_{3,3}^2 \right] dx_3 \tag{3.22}$$

where the dot accent denotes differentiation with respect to time. The electric behaviour of the medium is only assumed to be significant along the poled x_3 axis. Therefore $D_1 = D_2 = 0$ and the electric energy is the product of the electric field E_3 and the displacement of charge D_3. From Shatalov *et al.* [51] the electric energy can be written as:

$$W = \frac{1}{2}\int_0^{l_i}\left[(2h_{31}\nu - h_{33})D_3 A u_{3,3} + \beta_3^S D_3^2 A\right]dx_3 \tag{3.23}$$

By definition a potential difference, $V^E(t)$, is:

$$V^E(t) = \int_0^{l_i} E_3 dx_3 = \int_0^{l_i}\left[(2h_{31}\nu - h_{33})u_{3,3} + \beta_3^S D_3\right]dx_3 \tag{3.24}$$

The work due to a potential difference along the axis of polarisation may be written as:

$$V^W = \int_0^{l_i}\left[(2h_{31}\nu - h_{33})u_{3,3} + \beta_3^S D_3\right]dx_3 - V^E \tag{3.25}$$

It is assumed that the element is in compression through applied loads F_0 and F_{l_i} at either end. These are associated with the displacements $u_3(x_3 = 0)$ and $u_3(x_3 = l_i)$ respectively, so the overall work done is $Fu_3|_0^{l_i} = F_0 u_3(x_3 = 0) - F_{l_i} u_3(x_3 = l_i)$. A distributed load $f(x_3, t)$ is also applied along the length of the element. The potential of these external loads may be written as:

$$V^U = -\int_0^{l_i} f(x_3, t)dx_3 + Fu_3\Big|_0^{l_i} \tag{3.26}$$

Equations (3.21)-(3.31) are integrated by parts so that all of the terms are multiplied by a common variation δu.

$$\begin{aligned}\delta U = \frac{1}{2}\int_0^{l_i}\Bigg[&-\left\{2\left(c_{11}^D + c_{12}^D\right)\nu^2 A - 4c_{13}^D \nu A + c_{33}^D A\right\}\frac{\partial^2 u_3}{\partial x^2} + \\ &+\frac{1}{2}c_{44}^D \nu^2 J\left\{\frac{\partial^4 u_3}{\partial x_3^4} - \frac{\partial^3 u_3}{\partial x_3^3}\right\}\Bigg]\delta u_3 dx_3 + \\ &+\frac{1}{2}\Bigg[\left\{2\left(c_{11}^D + c_{12}^D\right)\nu^2 A - 4c_{13}^D \nu A + c_{33}^D A\right\}\frac{\partial u_3}{\partial x_3} + \\ &+\frac{1}{2}c_{44}^D \nu^2 J\left\{\frac{\partial^2 u_3}{\partial x_3^2} - \frac{\partial^3 u_3}{\partial x_3^3}\right\} + \\ &+(2h_{31}\nu - h_{33}D_3 A)\Bigg]\delta u_3\Bigg|_0^{l_i}\end{aligned} \tag{3.27}$$

$$\delta T = \frac{1}{2}\int_0^{l_i}\left[\rho\nu^2 J\frac{\partial\ddot{u}_3}{\partial x_3^2} - \rho A\ddot{u}_3\right]\delta u_3 dx_3 + \frac{1}{2}\left[\rho\nu^2 J\left\{\frac{\partial^2\dot{u}_3}{\partial x_3^2} - \frac{\partial\ddot{u}_3}{\partial x_3}\right\} + \rho A\dot{u}_3\right]\delta u_3\Bigg|_0^{l_i} \tag{3.28}$$

$$\delta W = \frac{1}{2}\left[(2h_{31}\nu - h_{33})D_3 A\right]\delta u_3\Big|_0^{l_i} + \beta_3^S D_3^2 l_i A \tag{3.29}$$

$$\delta V^W = \frac{1}{2}\left[2h_{31}\nu - h_{33}\right]\delta u_3\Big|_0^{l_i} + \beta_3^S D_3 l_i - V^E(t) \tag{3.30}$$

$$\delta V^U = -\int_0^{l_i} f(x_3)\delta u_3 dx_3 + F\delta u_3\Big|_0^{l_i} \tag{3.31}$$

Shatalov *et al.* [51] minimises the an energy functional that is equivalent to Equation (3.20) with Equations (3.27)-(3.30). They constrain the minimisation of this functional subject to the constraint in Equation (3.30) through the use of the Lagrange multiplier λ_{LM}. The Lagrange multiplier is adopted into the virtual work of the external forces through: $\delta V = \delta(V^U + \lambda_{LM}V^W)$. The substitution of this along with Equations (3.27)-(3.29) into the extended Hamilton's principle in Equation (3.20) suggests that for a stationary value of the integral the following relationship is true:

$$\left\{2\left(c_{11}^D + c_{12}^D\right)\nu^2 A - 4c_{13}^D\nu A + c_{33}^D A\right\}\frac{\partial^2 u_3}{\partial x_3^2} + \rho\nu^2 J\frac{\partial\ddot{u}_3}{\partial x_3^2} - \rho A\ddot{u}_3 + \\ -\frac{1}{2}c_{44}^D\nu^2 J\left\{\frac{\partial^4 u_3}{\partial x_3^4} - \frac{\partial^3 u_3}{\partial x_3^3}\right\} = f \tag{3.32}$$

It is assumed that the spatial derivatives of order greater than 2 will not provide a significant correction to the spectral behaviour of the waveguide element because it will be applied to describe components with greater than microscopic length scales. On dropping the subscripts the governing differential equation for the element can be written as:

$$\left\{2\left(c_{11}^D + c_{12}^D\right)\nu^2 - 4c_{13}^D\nu + c_{33}^D\right\}A\frac{\partial^2 u}{\partial x^2} + \rho\nu^2 J\frac{\partial\ddot{u}}{\partial x^2} - \rho A\ddot{u} = f \tag{3.33}$$

Shatolov *et al.* [51] find similar terms in their derivation of a piezoelectric rod by considering two deformation fields, for the axial and transverse motion, which are independent of one another. This results in a coupled set of differential equations that govern the deformation of the rod. In their formulation the first two terms in Equation (3.33) appear coupled to the transverse displacement field instead of being subject to a scalar transformation through

the Poisson's ratio. The coefficient of the third term in Equation (3.33) acts to couple the two fields and appears in both of the governing differential statements for each field in making the product with the spatial derivative of the other field. The substitution of Equations (3.17) and (3.18) into Equation (3.33) gives:

$$\left\{-\nu(2\nu+1)E+E\right\}A\frac{\partial^2 u}{\partial x^2}+\rho\nu^2 J\frac{\partial \ddot{u}}{\partial x^2}-\rho A\ddot{u}=f \tag{3.34}$$

Clearly it is necessary to set the terms in the curly braces to E in order to recover Love rod theory for an isotropic rod. This suggests that it is not physically viable to include the transverse strain estimations in the Hamiltonian formulation of the element. Therefore it is not possible to represent the transverse isotropic behaviour of a piezoelectric rod through this scheme despite the similarities in the terms that arise between this and the equivalent two mode deformation theory. The DTFM is limited to a single dependent variable in the governing equation for its waveguides. Therefore the classic Love rod theory is applied to describe both the isotropic and transverse isotropic components that are connected in series for the piezoelectric actuator assembly:

$$EA\frac{\partial^2 u}{\partial x^2}+\rho\nu^2 J\frac{\partial \ddot{u}}{\partial x^2}-\rho A\ddot{u}=f \tag{3.35}$$

where $E=c_{33}^D$ for the piezoelectric elements. The remaining terms in Equations (3.27)-(3.31) must be zero and these specify the boundary conditions for $u_3(x_3,t)=u(x,t)$:

$$u=0 \tag{3.36}$$

$$F=c_{33}^D A\frac{\partial u}{\partial x}+\rho\nu^2 J\frac{\partial \ddot{u}}{\partial x}+\lambda_{LM}h_{33} \tag{3.37}$$

$$0=\beta_3^S D_3 l_i(D_3 A-\lambda_{LM}) \qquad x\in(0,l_i) \tag{3.38}$$

Therefore $\lambda_{LM}=D_3A$ and this implies the boundary condition:

$$F=c_{33}^D A\frac{\partial u}{\partial x}+\rho\nu^2 J\frac{\partial \ddot{u}}{\partial x}+D_3 A h_{33} \tag{3.39}$$

An impedance analyser can measure the impedance of the rod as follows:

$$\bar{Z}(s)=\frac{\bar{V}^E(s)}{\bar{I}(s)} \tag{3.40}$$

where the bar accent denotes that the quantities are represented in the frequency domain,

through Laplace Transform, with the complex argument s. The electrical characteristics of a piezoelectric element are often modelled as a parallel plate capacitor. Under the assumption that the plates are large in comparison to the distance between them, the charge density can be written as: $\rho = \frac{Q}{A}$. Where Q is the total charge and A is the perpendicular area of the plate [61]. Guass's Law states that the electric field is $E = \frac{\rho}{\kappa}$ where κ is the permittivity of the dielectric. The electric current through the thickness can be written as:

$$I(t) = \frac{dQ}{dt} = \kappa A \frac{dE}{dt} = A \frac{dD}{dt} \tag{3.41}$$

The Laplace Transform of Equation (3.41):

$$\bar{I}(s) = sAD - D_0 \tag{3.42}$$

where D_0 is the electric displacement at time $t = 0$.

3.4 Formulation of the problem

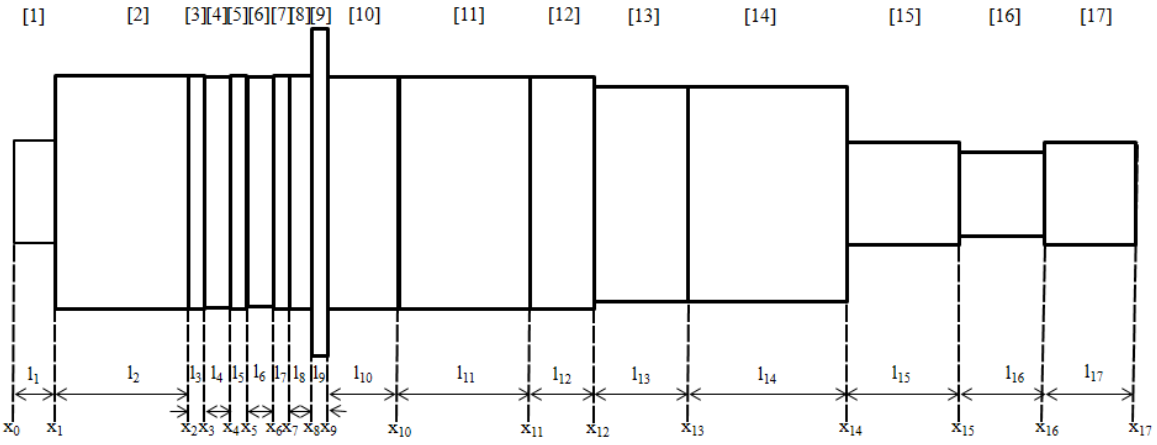

Fig. 3.2 Schematic of the stepped distributed dynamic rod.

The formulation of the DTFM will be carried out with reference to the stepped rod shown in Figure 3.2. The interior nodes are labelled x_i for $i = 1, 2, \ldots, n-1$ with n as the number of components. The extremities of the system have the boundary nodes x_0 and x_n. The length of the i^{th} component can be written in terms of the nodes through the expression: $l_i = x_{i+1} - x_i$ so that when $x_0 = 0$ the nodes can be written as: $x_i = l_1 + l_2 + \cdots + l_i$ for $i = 1, 2, \ldots, n$. The leftmost and rightmost nodes in Figure 3.2 will never be associated with piezoelectric

elements directly. Therefore the boundary conditions of the assembly require no electrical characteristics whereas the matching nodes may have to allow for this.

The vibration of the i^{th} component in the DTFM will be governed by the following governing equation of motion:

$$(EA)_i \frac{\partial^2 u_i(x,t)}{\partial x^2} + (\nu^2 \rho J)_i \frac{\partial^2 \ddot{u}_i(x,t)}{\partial x^2} - (\rho A)_i \frac{\partial^2 u_i}{\partial t^2} - (\eta A)_i \frac{\partial u_i(x,t)}{\partial t} - K_i u_i(x,t) = f_i(x,t) \quad (3.43)$$

where i denotes a component through which the parameters are considered to be constant. The damping factors η_i and K_i are defined such that they are the coefficients to retarding forces that are proportional to velocity and displacement respectively. An external force $f_i(x,t)$ is defined that is spatially distributed throughout the component. This external force will be used as a tool to investigate the behaviour of an axial screwed threaded joint that has an assumed spatial distribution.

It is assumed that the displacement and the force is preserved at the nodes that connect the i^{th} and the $i^{th}+1$ components. This yields the following matching conditions.

$$u_i(x_i,t) = u_{i+1}(x_i,t)$$

$$\begin{aligned}(EA)_i \frac{\partial u_i(x_i,t)}{\partial x} + (\nu^2 \rho J)_i \frac{\partial \ddot{u}_i(x_i,t)}{\partial x} - (\eta A)_i \frac{\partial u_i(x_i,t)}{\partial t} - K_i u_i(x_i,t) \\ = (EA)_{i+1} \frac{\partial u_{i+1}(x_i,t)}{\partial x} + (\nu^2 \rho J)_{i+1} \frac{\partial \ddot{u}_{i+1}(x_i,t)}{\partial x} + \\ -(\eta A)_{i+1} \frac{\partial u_{i+1}(x_i,t)}{\partial t} - K_{i+1} u_{i+1}(x_i,t) + q_i(t)\end{aligned} \quad (3.44)$$

where $q_i(t)$ is an external force applied to the interface. This may take the form of force in a piezoelectric material due to an applied electric field through Equations (3.39) and (3.42), which implies:

$$q_i(t) = \mathcal{L}^{-1}\left\{ \frac{1}{s} \frac{h_{33}}{\bar{z}(s)} \bar{V}^E(s) \right\} \quad (3.45)$$

where $\mathcal{L}^{-1}\{\dots\}$ denotes the inverse Laplace Transform and zero initial conditions have been assumed.

The boundary conditions are synthesised from the following expressions for $x = x_0$ and

$x = x_n$ respectively:

$$\begin{aligned}(EA)_1\frac{\partial u_1(x,t)}{\partial x} + (\nu^2\rho J)_1\frac{\partial \ddot{u}_1(x,t)}{\partial x} + K_1 u_1(x,t) = \gamma_L(t)\\ (EA)_n\frac{\partial u_n(x,t)}{\partial x} + (\nu^2\rho J)_n\frac{\partial \ddot{u}_n(x,t)}{\partial x} + K_n u_n(x,t) = \gamma_R(t)\end{aligned} \tag{3.46}$$

where $\gamma_L(t)$ and $\gamma_R(t)$ are the boundary loads at $x = x_0$ and $x = x_n$ respectively. It is straightforward to add a mass-spring-damper force boundary condition to Equation (3.46) by adding the appropriate terms. However the aim here is to assume fixed-fixed, fixed-free and free-free boundary conditions of the rod. The fixed boundary condition is implemented by setting $K_i = 1$ and all other terms to zero to give $u(x_0,t) = 0$ or $u(x_n,t) = 0$ for $x = x_0$ or $x = x_n$ respectively. Comparatively the free boundary condition $\frac{\partial}{\partial x}u(x,t) = 0$ is found by setting $K_i = 0$ and the boundary load to zero to give the natural boundary condition. For the boundary condition at $x = x_0$ this must also be multiplied by -1.

Initial spatial distributions for displacement and velocity can also be set for each component $x \in (x_{i-1}, x_i)$:

$$\begin{aligned}u_i(x,0) &= u_{0,i}(x)\\ \frac{\partial u_i(x,0)}{\partial t} &= v_{0,i}(x)\end{aligned} \tag{3.47}$$

The governing conditions that are expressed in Equations (3.43)-(3.47) are transformed into the frequency domain in order to find the s-domain solution of the stepped distributed system. The procedure is given in Yang [50] and the s-domain quantities are denoted by the bar accent.

Laplace Transform of Equation (3.43) with respect to time gives:

$$\begin{aligned}\frac{1}{\partial x}\frac{\partial \bar{u}_i(x,s)}{\partial x} = \left(\frac{s^2(\rho A)_i + s(\eta A)_i + K_i}{s^2(\nu^2\rho J)_i + (EA)_i}\right)\bar{u}_i(x,s) +\\ + \left(\frac{1}{s^2(\nu^2\rho J)_i + (EA)_i}\right)\left\{\bar{f}_i(x,s) + (\nu^2\rho J)_i(s\iota_0 + \kappa_0) - (\rho A)_i(su_0 - v_0) - (\eta A)_i u_0\right\}\end{aligned} \tag{3.48}$$

where two new initial conditions, ι_0 and κ_0 have emerged as a result of the coupling between the transverse strain and the axial strain. These are an initial strain and strain rate which are

defined as follows:

$$\begin{aligned} \iota_{0,i} &= \left.\frac{du_i(x,t)}{dx}\right|_{t=0} \\ \kappa_{0,i} &= \left.\frac{1}{\partial t}\frac{\partial u_i(x,t)}{\partial x}\right|_{t=0} \end{aligned} \tag{3.49}$$

It is assumed that the initial strains in the rod are small enough for the influence ι_0 to be negligible. This may be problematic because some portions of the HPU device are joined through an applied prestress. If the external force is set to zero and all initial conditions are zero then the homogeneous part of Equation (3.48) remains:

$$\frac{1}{\partial x}\frac{\partial \bar{u}_i(x,s)}{\partial x} = \left(\frac{s^2(\rho A)_i + s(\eta A)_i + K_i}{s^2(\nu^2\rho J)_i + (EA)_i}\right)\bar{u}_i(x,s) \tag{3.50}$$

A comparison of Equations (3.7) and (3.50) shows the equivalent spectrum relationship found in the SEM. However the way that the boundary conditions are built into the DTFM solution will distinguish it from SEM.

The Laplace Transform is applied to the matching conditions in Equation (3.44) to give:

$$\bar{u}_{i+1}(x_i,s) = \bar{u}_i(x_i,s)$$

$$\begin{aligned} \frac{d\bar{u}_{i+1}}{dx} = &\left(\frac{s^2(\nu^2\rho J)_i + (EA)_i}{s^2(\nu^2\rho J)_{i+1} + (EA)_{i+1}}\right)\frac{d\bar{u}_i}{dx} + \left(\frac{s\eta_i + K_i}{s^2(\nu^2\rho J)_{i+1} + (EA)_{i+1}}\right)\bar{u}_i(x,s) + \\ &- \left(\frac{1}{s^2(\nu^2\rho J)_{i+1} + (EA)_{i+1}}\right)\bar{q}(s)\begin{pmatrix}0\\1\end{pmatrix} \end{aligned} \tag{3.51}$$

The Laplace Transform is applied to the boundary conditions in equation (3.46) to give:

$$\begin{aligned} (EA + s^2\nu^2\rho J)_1\frac{d\bar{u}_1(x,s)}{dx} + K_1\bar{u}_1(x,s) &= \gamma_L(t) - (\nu^2\rho J)_1(s\iota_{0,1} + \kappa_{0,1}) \\ (EA + s^2\nu^2\rho J)_n\frac{d\bar{u}_n(x,t)}{dx} + K_n\bar{u}_n(x,t) &= \gamma_R(t) - (\nu^2\rho J)_n(s\iota_{0,n} + \kappa_{0,n}) \end{aligned} \tag{3.52}$$

Equations (3.48) - (3.52) are recast in first order state form. To achieve this the spatial state vector is defined as follows:

$$\bar{\boldsymbol{\chi}}_i(x,s) = \begin{Bmatrix} \bar{u}_i(x,s) \\ \dfrac{\partial \bar{u}_i(x,s)}{\partial x} \end{Bmatrix} \tag{3.53}$$

Therefore the waveguide in Equation (3.48) becomes:

$$\frac{\partial}{\partial x}\bar{\boldsymbol{\chi}}_i(x,s) = \mathbf{F}_i(s)\bar{\boldsymbol{\chi}}_i(x,s) + \bar{\mathbf{p}}_i(x,s) \tag{3.54}$$

where:

$$\mathbf{F}_i(s) = \begin{bmatrix} 0 & 1 \\ \left(\frac{s^2(\rho A)_i + s(\eta A)_i + K_i}{s^2(\nu^2\rho J)_i + (EA)_i}\right) & 0 \end{bmatrix} \tag{3.55}$$

$$\bar{\mathbf{p}}_i(x,s) = \left(\frac{1}{s^2(\nu^2\rho J)_i + (EA)_i}\right) \left\{\bar{f}_i(x,s) + (\nu^2\rho J)_i(su_0 + \kappa_0) - (\rho A)_i(su_0 - v_0) - (\eta A)_i u_0\right\}\begin{pmatrix}0\\1\end{pmatrix} \tag{3.56}$$

The matching conditions in Equation (3.51) become:

$$\bar{\boldsymbol{\chi}}_{i+1}(x,s) = \mathbf{T}_i\bar{\boldsymbol{\chi}}_i(x,s) - \bar{\mathbf{v}}_i(x,s) \tag{3.57}$$

where:

$$\mathbf{T}_i = \begin{bmatrix} 1 & 0 \\ \frac{s\eta_i + K_i}{s^2(\nu^2\rho J)_{i+1} + (EA)_{i+1}} & \frac{s^2(\nu^2\rho J)_i + (EA)_i}{s^2(\nu^2\rho J)_{i+1} + (EA)_{i+1}} \end{bmatrix}$$

$$\bar{\mathbf{v}}_i(x,s) = \left(\frac{1}{s^2(\nu^2\rho J)_{i+1} + (EA)_{i+1}}\right)\bar{q}(s)\begin{pmatrix}0\\1\end{pmatrix} \tag{3.58}$$

Finally the boundary conditions are written as:

$$\mathbf{M}_b\bar{\boldsymbol{\chi}}(x_0,s) + \mathbf{N}_b\bar{\boldsymbol{\chi}}(x_n,s) = \boldsymbol{\gamma}_b(s) \tag{3.59}$$

$$\mathbf{M}_b = \begin{bmatrix} (EA + s^2\nu^2\rho J)_1 & K_1 \\ 0 & 0 \end{bmatrix}$$

$$\mathbf{N}_b = \begin{bmatrix} 0 & 0 \\ (EA + s^2\nu^2\rho J)_n & K_n \end{bmatrix}$$

$$\bar{\boldsymbol{\gamma}}_b(s) = \begin{pmatrix} \bar{\gamma}_L(s) \\ \bar{\gamma}_R(s) \end{pmatrix} \tag{3.60}$$

3.5 Wave propagation solution

Chi-Tsong Chen [62] discusses finding the solutions to dynamical equations that are cast in first order state form. The first step is to find the solution to the homogeneous part of the equation and this is achieved through the use of the state transition matrix, $\boldsymbol{\phi}(x,\xi,s)$. The homogeneous part of the DTFM formulation can be found in Equation (3.54) when zero initial conditions are assumed. The state transition matrix is the unique solution of:

$$\frac{\partial}{\partial x}\boldsymbol{\phi}(x,\xi,s) = \mathbf{F}_i(x,s)\boldsymbol{\phi}(x,\xi,s) \tag{3.61}$$

Yang [50] states that it must also satisfy the matching conditions:

$$\boldsymbol{\phi}(x_{i+1},\xi,s) = \mathbf{T}_i(x,s)\boldsymbol{\phi}(x_i,\xi,s) \tag{3.62}$$

Chi-Tsong Chen [62] proves that the state transition matrix is a linear transformation that maps the state $\bar{\boldsymbol{\chi}}_{0,i}$ at time t_0 to $\bar{\boldsymbol{\chi}}_i$ at time t. Where $\bar{\boldsymbol{\chi}}_{0,i}$ contains the initial conditions defined in Equation (3.47). It is shown that this relationship can be found from:

$$\boldsymbol{\phi}(x,\xi,s) = \mathbf{U}(x,s)\mathbf{U}^{-1}(\xi,s) \tag{3.63}$$

where $\mathbf{U}$ is the fundamental matrix of $\frac{1}{\partial t}\bar{\boldsymbol{\chi}} = \mathbf{F}\bar{\boldsymbol{\chi}}$. This fundamental matrix can be found as the nonsingular solution to:

$$\frac{\partial}{\partial x}\mathbf{U}(x,s) = \mathbf{F}(x,s)\mathbf{U}(x,s) \tag{3.64}$$

Chi-Tsong Chen [62] proves that an exponential matrix can be used to form the fundamental matrix to a linear time invariant dynamical equation. The exponential matrix $e^{\mathbf{A}t}$ is nonsingular for all t and has the following properties:

$$\begin{aligned} \frac{d}{dt}e^{\mathbf{A}t} &= \mathbf{A}e^{\mathbf{A}t} \\ \left(e^{\mathbf{A}t}\right)^{-1} &= e^{-\mathbf{A}t} \end{aligned} \tag{3.65}$$

Yang [50] states that it is possible to show that a fundamental matrix of Equation (3.64) is:

$$\mathbf{U}(x,s) = \begin{cases} e^{\mathbf{F}_1(s)(x-x_0)} & x \in (x_0,x_1) \\ e^{\mathbf{F}_i(s)(x-x_{i-1})}\mathbf{T}_{i-1}e^{\mathbf{F}_{i-1}(s)l_{i-1}}\ldots\mathbf{T}_1e^{\mathbf{F}_1(s)l_1} & x \in (x_{i-1},x_i), 2 \le i \le n \end{cases} \tag{3.66}$$

The exponential matrix is found by finding the resolvent of $\mathbf{F}_i$:

$$(s\boldsymbol{I}-\mathbf{F}_i)^{-1}=\frac{1}{s^2-a(s)^2}\begin{bmatrix} s & 1 \\ a(s)^2 & s \end{bmatrix} \tag{3.67}$$

where $\mathbf{I}$ is the identity matrix and $a(s)$ is found from:

$$a(s)^2=\left(\frac{s^2(\rho A)_i+s(\eta A)_i+K_i}{s^2(\nu^2\rho J)_i+(EA)_i}\right) \tag{3.68}$$

Then by taking the inverse Laplace Transform of each element in Equation (3.67) the exponential matrix can be found as:

$$e^{\mathbf{F}_i(s)x}=\begin{bmatrix} cosh(a(s)x) & \frac{1}{a(s)}sinh(a(s)x) \\ a(s)sinh(a(s)x) & cosh(a(s)x) \end{bmatrix} \tag{3.69}$$

3.6 Distributed Transfer Functions

It is not within the scope of this study to derive the Distributed Transfer Function Method. The derivation can be found in Yang [50] and is stated here for completeness. The s-domain response of the stepped system that is defined by the state transition matrix in Equation (3.63) is found from the following set of expressions:

$$\begin{aligned}
\bar{\boldsymbol{\chi}}(x,s)&=\int_{x_0}^{x_n}\hat{\mathbf{G}}(x,\xi,s)\bar{\mathbf{p}}(\xi,s)d\xi+\hat{\mathbf{H}}(x,s)\bar{\boldsymbol{\gamma}}_b(s)-\sum_{i=1}^{n-1}\hat{\mathbf{G}}(x,x_i+,s)\bar{\mathbf{v}}_i(s)\\
\hat{\mathbf{G}}(x,\xi,s)&=\begin{cases}\hat{\mathbf{H}}(x,s)\mathbf{M}_b\boldsymbol{\phi}(x_0,\xi,s) & \xi\le x\\ -\hat{\mathbf{H}}(x,s)\mathbf{N}_b\boldsymbol{\phi}(x_n,\xi,s) & \xi>x\end{cases}\\
\hat{\mathbf{H}}(x,s)&=\boldsymbol{\phi}(x,x_0,s)\mathbf{Z}^{-1}(s)
\end{aligned} \tag{3.70}$$

The transfer functions are $\hat{\mathbf{G}}(x,\xi,s)$ and $\hat{\mathbf{H}}(x,s)$ and $\mathbf{Z}$ is the impedance matrix, which is defined as:

$$\mathbf{Z}(s)=\mathbf{M}_b+\mathbf{N}_b\boldsymbol{\phi}(x_n,x_0,s) \tag{3.71}$$

The impedance matrix contains information about the stepped waveguide and the boundaries in a 2×2 matrix.

3.7 Transcendental Eigenvalue Problem

With the impedance matrix derived it is now possible to set up a Transcendental Eigenvalue Problem (TEP) by finding the roots of the following characteristic equation [50]:

$$|\boldsymbol{Z}(s)| = |\boldsymbol{M}_b + \mathbf{N}_b\boldsymbol{\phi}(x_n, x_0, s)| = 0 \tag{3.72}$$

The roots are taken to be $s_k = j\omega_k$ for $k = 1, 2, \ldots, \infty$. Each root yields an eigenvalue ω_k that is real under the condition $\eta = 0$. To identify the roots an iterative scheme is adopted as in Singh & Ram [63] and Singh [64]. To seek a minima in (3.72) expand $|\mathbf{Z}(j\omega_k)|$ in the neighbourhood of $\omega_k^{(0)}$:

$$\omega_k = \omega_k^{(0)} + \epsilon \tag{3.73}$$

where ϵ is a small parameter that allows for the application of Taylor expansion to the characteristic equation as follows:

$$\left|\mathbf{Z}\left(\omega_k^{(0)} + \epsilon\right)\right| = \left|\mathbf{Z}\left(\omega_k^{(0)}\right)\right| + \epsilon\frac{d\left|\mathbf{Z}\left(\omega_k^{(0)}\right)\right|}{d\omega_k} + O(\epsilon^2) \tag{3.74}$$

where $O(\epsilon^2)$ shows that the series has been truncated to remove the higher order terms. Following Singh [64], rewrite (3.74) with $\mathbf{A}(\omega_k) = \left|\mathbf{Z}\left(\omega_k^{(0)}\right)\right|$ and $\mathbf{B}(\omega_k) = -\frac{d\left|\mathbf{Z}\left(\omega_k^{(0)}\right)\right|}{d\omega_k}$ to give an algebraic eigenvalue problem:

$$(\mathbf{A}(\omega_k) - \epsilon\mathbf{B}(\omega_k))\mathbf{a} = 0 \tag{3.75}$$

where $\mathbf{a}$ is a vector that may be determined if the eigenfunctions are required. To adopt an iterative procedure the search for the k^{th} eigenvalue can be written at the n^{th} iteration as:

$$\omega_k^{(n)} = \omega_k^{(n-1)} + \epsilon^{(n)} \tag{3.76}$$

where ϵ^n is an eigenvalue of:

$$\left(\mathbf{A}\left(\omega_k^{(n-1)}\right) - \epsilon^{(n)}\mathbf{B}\left(\omega_k^{(n-1)}\right)\right)\mathbf{a}^{(n)} = 0 \tag{3.77}$$

The eigenvalue can be found through the operation:

$$\epsilon^{(n)} = \frac{\mathbf{A}\left(\omega_k^{(n-1)}\right)}{\mathbf{B}\left(\omega_k^{(n-1)}\right)} \tag{3.78}$$

Applying a Newton iterative method for a range of initial guesses $\omega_k^{(0)}$ will yield a set of estimated ω_k for $k = 1, 2, \ldots, \infty$ that is subject to the chosen range of guesses. This set is then rounded to a degree that is only significant in the neighbourhood of each ω_k and the unique values are taken as the set of eigenvalues for the system.

The TEP facilitates a comparison of the model to data obtained through Experimental Modal Analysis (EMA). Comparisons can be made based on minimisations between the DTFM estimated eigenvalues and eigenfunctions and the experimentally obtained natural frequencies and mode shapes. This is discussed further in Chapter 4. The TEP is the focus of fundamental research towards the inversion of second order systems and is summarised in the monograph by Gladwell [65]. The archetype to this problem is the classical Sturm-Liouville equation which can be written so that it that describes the vibration of a rod:

$$(A(x)u'(x))' + \lambda_{SL}A(x)u(x) = 0 \tag{3.79}$$

where the prime denotes differentiation with respect to the position x. From this model Gladwell concludes that two spectra associated with two different end conditions are required to uniquely estimate a parameter $A(x)$ with piecewise behaviour throughout the length of the rod. Singh [64] developed a procedure to apply this principle to various reconstruction problems by means of a distributed parameter model. This inverse problem is defined as: Estimate the axial rigidity and the density of n components in the distributed parameter rod system from the knowledge of the lowest spectrum longitudinal modes of a fixed-free and fixed-fixed rod along with the total mass of the rod. The free-fixed eigenvalues are $\omega_{r,i}$ and the fixed-fixed eigenvalues are $\omega_{s,j}$. Under the assumption that the lowest spectrum of each configuration is known the eigenvalues will be ordered according to: $\omega_{r,1} < \omega_{s,1} < \omega_{r,2} < \omega_{s,2} \ldots$ until $i = n$ or $j = n$.

Singh [64] developed a Newton Eigenvalue iterative algorithm to search for the eigenvalues in his TEP. He replaces the determinants of the matrices involved in terms of their left and right eigenvectors. This has not been implemented here, but it would be beneficial scheme for use with the DTFM. However, in the case of applying the inverse solution scheme to HPU systems, it is not realistic to clamp either end of the assembly so that it can be assumed

fixed-free. Therefore another set of boundary conditions must be chosen that are relevant to the device. A suggestion would be open and closed circuit boundary conditions for the piezoelectric stack, whilst the mechanical boundaries remain free-free. However this would require a more detailed formulation of the electromechanical rod element than has been presented so far.

3.8 Transfer function residues

The transfer function residues are required for the calculation of the transient response through the DTFM. Yang [50] derives the Green's function formula by taking the inverse Laplace Transform of Equation (3.70). Through the application of residue theorem it is possible to rewrite the Green's function integrals in terms of transfer function residues. The details of this are given in Yang [50]. Subsequent calculations descending from the transfer function residues are attributed to the following matrix:

$$\mathbf{Q}_k = \frac{adj(\mathbf{Z}(\omega_k))}{Z_D(\omega_k)} \tag{3.80}$$

where the $adj(\mathbf{Z}(\omega_k))$ is the adjoint of the impedance matrix and $Z_D(\omega_k)$ is given as:

$$\frac{d}{ds}|\mathbf{Z}(s)|_{s=\pm j\omega_k} = \pm Z_D(\omega_k) \tag{3.81}$$

In order to find $Z_D(\omega_k)$ the Characteristic Equation (3.72) can be differentiated explicitly to yield a general matrix expression and this is given in Yang [50]. The exact transient solution is given analytically as follows:

$$\boldsymbol{\chi}(x,t) = 2\sum_{k=1}^{\infty} \mathbf{U}(x, j\omega_k)\mathbf{Q}_k(\mathbf{I}_{Ext}(t) + \mathbf{I}_{ExcBC}(t) + \mathbf{I}_{ExcIC}(t)) \tag{3.82}$$

where the vectors $\mathbf{I}_{Ext}(t)$, $\mathbf{I}_{ExcBC}(t)$, $\mathbf{I}_{ExcIC}(t)$ represent the contributions of the external loads, boundary excitations and initial disturbances respectively. For now it is assumed that there are no initial disturbances so $\mathbf{I}_{ExcIC}(t) = 0$. The remaining terms can be expanded

as:

$$\mathbf{I}_{Ext}(t) = -\mathbf{M}_b \sum_{i=1}^{n} \left(\frac{1}{(EA)_i - (\nu^2 \rho J)_i \omega_k^2} \right) \mathbf{U}^{-1}(x_{i-1}+, j\omega_k) \int_0^t \int_{x_{i-1}}^{x_i} e^{-\mathbf{F}_i(j\omega_k)(\xi - x_{i-1})} sin\omega_k(t-\tau) f_i(\xi, \tau) d\xi d\tau \begin{pmatrix} 0 \\ 1 \end{pmatrix} \tag{3.83}$$

$$\mathbf{I}_{ExcBC}(t) = \int_0^t sin\omega_k(t-\tau) \begin{pmatrix} \gamma_L(\tau) \\ \gamma_R(\tau) \end{pmatrix} d\tau - \mathbf{M}_b \sum_{i=1}^{n} \left(\frac{1}{(EA)_i - (\nu^2 \rho J)_i \omega_k^2} \right) \mathbf{U}^{-1}(x_{i-1}+, j\omega_k) \int_0^t sin\omega_k(t-\tau) q_i(\tau) d\tau \begin{pmatrix} 0 \\ 1 \end{pmatrix} \tag{3.84}$$

3.9 Estimation of axial joint force

The axial joint is thought of as being composed of two interfaces: the bearing surface and the contact areas of the internal and external threads between the component and the fastener respectively. The contact of the threads may extend in both directions, from the bearing surface, if a threaded rod has been chosen to make the joint. They may also only extend in one direction if each component has female and male threads that mate. A further assumption that must be made to apply the DTFM, in its current formulation, is the spatial distribution of the joint force. Ma *et al.* [14] assumed that the joint force was pointwise in nature, requiring its distribution to be represented by the Dirac delta function. To extend this the joint force will be distributed according to Heaviside step functions, $H()$. However a means to determine this distribution has not been formulated.

An interesting prospect would be to be able to infer this spatial distribution through the use of an Inverse Transcendental Eigenvalue Problem. The distribution would be the clamping force, which is emanating from the bearing surface, so this length of rod would have to be split into many components. It would need to be possible to reliably estimate the stiffness of each of these components in order to estimate the force distribution. For the current architecture the ill-conditioned inverse problem will most likely obscure any attempt to achieve this even through the well behaved scheme that has been applied in Singh [64]. A Bayesian approach to this could alleviate the ill-posed problem by instead representing the estimation through probability density functions. An introduction to these methods is covered by Yuen [66] where the model updating problem is discussed for a lumped parameter model based on eigendata.

The results of the estimated joint force will be compared to results that descend from Digital Image Correlation (DIC) of a 2D plane. The DIC method improves with spatial resolution so it should be compared to an estimated force with the same assumed spatial distribution. This spatial distribution can take any form, that can be synthesised from Heaviside step functions within the i^{th} component, to give an identified force that is denoted as $N_i(\xi,\tau)$; where ξ is the spatial distribution and τ is the temporal distribution. The external force applied to the i^{th} component in Equation (3.83) can be represented as:

$$f_i(\xi,\tau) = [H(\xi-(x_j-x_a)) - H(\xi-(x_j+x_b))]N_i(\tau) \tag{3.85}$$

where x_j is the position of the bearing surface and x_a to x_b is the length through which the joint force is distributed uniformly.

If it is assumed that the rod is initially at rest, and is not subjected to any initial disturbances, then a substitution of the relevant terms in Equation (3.83) & (3.84) into Equation (3.82) gives:

$$\begin{aligned}\boldsymbol{\chi}^{JH}(x,t) = 2\sum_{k=1}^{\infty}\mathbf{U}(x,j\omega_k)\mathbf{Q}_k\Bigg(-\mathbf{M}_b\sum_{i=1}^{n}\left(\frac{1}{(EA)_i-(\nu^2\rho J)_i\omega_k^2}\right)\mathbf{U}^{-1}(x_{i-1},j\omega_k)\\ \int_0^t\int_{x_{i-1}}^{x_i} e^{-\mathbf{F}_i(j\omega_k)(\xi-x_{i-1})}[H(\xi-(x_j-x_a))-H(\xi-(x_j+x_b))]\\ sin\omega_k(t-\tau)N(\tau)d\xi d\tau\begin{pmatrix}0\\1\end{pmatrix}-\mathbf{M}_b\sum_{i=1}^{n}\left(\frac{1}{(EA)_i-(\nu^2\rho J)_i\omega_k^2}\right)\\ \mathbf{U}^{-1}(x_{i-1},j\omega_k)\int_0^t sin\omega_k(t-\tau)q_i(\tau)d\tau\begin{pmatrix}0\\1\end{pmatrix}\Bigg)\end{aligned} \tag{3.86}$$

where the superscript ^{JH} denotes that the spatial state vector is observed from the response of the jointed system, which in this case is the Jointed Horn (JH). If the restoring force due to the joint is removed from Equation (3.86) then the solution can be found for a linear rod subjected to a boundary load:

$$\begin{aligned}\boldsymbol{\chi}^{MH}(x,t) =& 2\sum_{k=1}^{\infty}\mathbf{U}(x,j\omega_k)\mathbf{Q}_k\Bigg(-\mathbf{M}_b\sum_{i=1}^{n}\left(\frac{1}{(EA)_i-(\nu^2\rho J)_i\omega_k^2}\right)\\ &\mathbf{U}^{-1}(x_{i-1},j\omega_k)\int_0^t sin\omega_k(t-\tau)q_i(\tau)d\tau\begin{pmatrix}0\\1\end{pmatrix}\Bigg)\end{aligned} \tag{3.87}$$

where the response of the unjointed system is known by the spatial state vector and the superscript ^{MH} denotes that this is the Monolithic Horn (MH) in this instance. If the boundary load could be applied simultaneously, so that both the jointed and unjointed systems experienced the exact same loading, then the subtraction of Equation (3.87) from Equation (3.86) gives:

$$\boldsymbol{\chi}^{JH}(x,t) - \boldsymbol{\chi}^{MH}(x,t) = 2\sum_{k=1}^{\infty} \mathbf{U}(x, j\omega_k)\mathbf{Q}_k \Bigg(-\mathbf{M}_b \sum_{i=1}^{n} \frac{1}{K_i} \mathbf{U}^{-1}(x_{i-1}, j\omega_k) \int_0^t \int_{x_{i-1}}^{x_i} e^{-\mathbf{F}_i(j\omega_k)(\xi - x_{i-1})} [H(\xi - (x_j - x_a)) - H(\xi - (x_j + x_b))] sin\omega_k(t-\tau) N(\tau) d\xi d\tau \begin{pmatrix} 0 \\ 1 \end{pmatrix} \Bigg) \tag{3.88}$$

Clearly Equation (3.88) may be applied to isolate the temporal distribution of the joint force if the convolution integrals can be evaluated.

3.10 Discretisation scheme

The first simplification that is necessary to isolate the joint force is to choose whether to identify the force from displacement or velocity measurements of the assembly. The spatial state vector for the jointed system is:

$$\boldsymbol{\chi}_i^{JH}(x,t) = \begin{Bmatrix} u_i^{JH}(x,t) \\ \frac{\partial u_i^{JH}(x,t)}{\partial x} \end{Bmatrix} \tag{3.89}$$

The displacement is chosen because the characterisation of the joint will be made from hysteresis loops that are plotted as: $(x,y) = (u(\tau), N(\tau))$. Therefore the following operation is carried out:

$$\begin{pmatrix} 1 & 0 \end{pmatrix} \cdot \boldsymbol{\chi}_i^{JH}(x,t) = u_i^{JH}(x,t) \tag{3.90}$$

If Equation (3.86) is rearranged along with the previous substitution, and the right hand side terms are enclosed in the temporal integral, then it becomes:

$$u_i^{JH}(x,t) - \begin{pmatrix}1 & 0\end{pmatrix} \cdot 2 \sum_{k=1}^{\infty} \mathbf{U}(x, j\omega_k)\mathbf{Q}_k \left(-\mathbf{M}_b \sum_{i=1}^{n} \left(\frac{1}{(EA)_i - (\nu^2 \rho J)_i \omega_k^2} \right) \right.$$
$$\mathbf{U}^{-1}(x_{i-1}, j\omega_k) \int_0^t sin\omega_k(t-\tau) q_i(\tau) d\tau \left. \begin{pmatrix}0\\1\end{pmatrix} \right) = \begin{pmatrix}1 & 0\end{pmatrix} \cdot 2 \sum_{k=1}^{\infty}$$
$$\mathbf{U}(x, j\omega_k)\mathbf{Q}_k \left(-\mathbf{M}_b \sum_{i=1}^{n} \left(\frac{1}{(EA)_i - (\nu^2 \rho J)_i \omega_k^2} \right) \right) \mathbf{U}^{-1}(x_{i-1}, j\omega_k)$$
$$\int_{x_{i-1}}^{x_i} e^{-\mathbf{F}_i(j\omega_k)(\xi - x_{i-1})} [H(\xi - (x_j - x_a)) - H(\xi - (x_j + x_b))] d\xi$$
$$\left. \begin{pmatrix}0\\1\end{pmatrix} \right) \int_0^t sin\omega_k(t-\tau) N(\tau) d\tau \tag{3.91}$$

At this point the spatial integral, with respect to ξ, can be evaluated through the use of a numerical integration procedure. Trapezoidal integration will be applied over the length of the i^{th} component that has been discretised into a number of observation points separated by $\Delta\xi$. The exponential matrix is skew-symmetric so three independent integrals must be calculated. Finally the convolution integrals must be discretised to allow us to isolate the magnitude of the joint force. The time variable is discretised according to $t_p = p\Delta t$ for $p = 1, \ldots, N$. The integral is discretised by setting τ to discontinuous values τ_q. Therefore the joint force is isolated under the assumption that it is a series of impulses of magnitude $N(\tau)\Delta\tau$. The temporal integrals become:

$$\int_0^t sin\omega_k(t-\tau) N\left(u(\tau), \frac{\partial u(\tau)}{\partial \tau}\right) d\tau \rightarrow \sum_{q=1}^{p} sin\omega_k(t_p - \tau_q) N(\tau_q) \Delta t \tag{3.92}$$

$$\int_0^t sin\omega_k(t-\tau) q_i(\tau) d\tau \rightarrow \sum_{q=1}^{p} sin\omega_k(t_p - \tau_q) q_i(\tau_q) \Delta t \tag{3.93}$$

Both of these integrals can be written analogously in the form that follows:

$$\frac{1}{\Delta t}\left\{\mathbf{m}(t_p)\right\} = \left[\mathbf{A}(t_p,\tau_q)\right]\cdot\left\{\mathbf{f}(\tau_q)\right\} \tag{3.94}$$

$$\begin{Bmatrix} m(t_1)/\Delta t \\ \vdots \\ m(t_p)/\Delta t \\ \vdots \\ m(t_N)/\Delta t \end{Bmatrix} =$$

$$\begin{bmatrix} sin\omega_k(t_1-\tau_0) & 0 & \dots & 0 & \dots & 0 \\ \vdots & \vdots & \vdots & \vdots & \vdots & \vdots \\ sin\omega_k(t_p-\tau_0) & \dots & \dots & sin\omega_k(t_p-\tau_{q-1}) & \dots & 0 \\ \vdots & \vdots & \vdots & \vdots & \vdots & \vdots \\ sin\omega_k(t_N-\tau_0) & \dots & \dots & sin\omega_k(t_N-\tau_{q-1}) & \dots & sin\omega_k(t_N-\tau_{N-1}) \end{bmatrix} \cdot \begin{Bmatrix} f(\tau_0) \\ \vdots \\ f(\tau_q) \\ \vdots \\ f(\tau_{N-1}) \end{Bmatrix} \tag{3.95}$$

The matrix that relates the measurement **m** to the unknown **f** here is known as the impulse-response matrix. This means that Equation (3.91) can be written as:

$$\mathbf{G}(x,t_p,\tau_q) = \mathbf{g}(x,x_a,x_b,t_p,\tau_q)\mathbf{N}(\tau_q) \tag{3.96}$$

where:

$$\mathbf{G}(x,t_p,\tau_q) = u_i^{JH}(x,t_p) - \begin{pmatrix}1 & 0\end{pmatrix}\cdot 2\sum_{k=1}^{\infty}\mathbf{U}(x,j\omega_k)\mathbf{Q}_k\left(\sum_{q=1}^{p} sin\omega_k(t_p-\tau_q)\mathbf{q}_i(\tau_q)\Delta t\right) \tag{3.97}$$

$$\begin{aligned}\mathbf{g}(x,x_a,x_b,t_p,\tau_q) = \sum_{q=1}^{p}\begin{pmatrix}1 & 0\end{pmatrix}\cdot 2\sum_{k=1}^{\infty}\mathbf{U}(x,j\omega_k)\mathbf{Q}_k\Bigg(-\mathbf{M}_b\sum_{i=1}^{n}\frac{1}{K_i}\mathbf{U}^{-1}(x_{i-1}+,j\omega_k) \\ \int_{x_{i-1}}^{x_i} e^{-\mathbf{F}_i(j\omega_k)(\xi-x_{i-1})}[H(\xi-(x_j-x_a))-H(\xi-(x_j+x_b))]d\xi\cdot\begin{pmatrix}0\\1\end{pmatrix}\Bigg) \\ sin\omega_k(t_p-\tau_q)\Delta t\end{aligned} \tag{3.98}$$

If both the jointed and unjointed systems experienced the exact same loading then Equation (3.96) could be reduced to:

$$\mathbf{G}(x,t_p,\tau_q) = \mathbf{u}_i^{JH}(x,t_p) - \mathbf{u}_i^{MH}(x,t_p) = \mathbf{g}(x,x_a,x_b,t_p,\tau_q)\mathbf{N}(\tau_q) \tag{3.99}$$

In order to identify the joint force an inversion of the Green's function matrix is required:

$$\mathbf{N}(\tau_q) = \mathbf{g}^{-1}(x, x_a, x_b, t_p, \tau_q)\mathbf{G}(x, t_p, \tau_q) \tag{3.100}$$

Any attempt to reconstruct the force at this stage would be naive because the inversion of the impulse response matrix is ill-posed. Instead Equation (3.100) is written as a restricted inverse problem.

3.11 Inverse problems

3.11.1 Direct and indirect operations

Inverse problems occur in science and engineering when there is a need to characterise the behaviour of a system from indirect or incomplete measurements. To appreciate the difficulty associated with this procedure it is beneficial to first define a problem that would be considered its opposite. This is named an analysis problem in Neto & da Silva Neto [67], but may also be known as a direct problem. Historically these types of problem have been tackled first because the solution methods are generally more straightforward. If the discussion is restricted to the subject of differential equations then analysis problems are concerned with obtaining the distribution of some variables in a domain of a given size and shape which can be time dependent. If any information is missing from the analysis problem then it is thought of as an inverse problem because now this missing information must be determined in addition to solving the the original analysis problem [67].

3.11.2 Linear measurement model

A discrete linear model can be constructed to represent a measurement as follows [68]:

$$\mathbf{m} = \mathbf{A}\mathbf{f} + \boldsymbol{\epsilon} \tag{3.101}$$

where $\mathbf{m}$ and $\mathbf{f}$ are vectors representing the measurement data and the unknown quantity that can be observed $N \times p$ and $N \times q$ times respectively with N as the number of sample points. The linear operator $\mathbf{A}$ is a $p \times q$ matrix that models the analysis problem of converting $\mathbf{m}$ to $\mathbf{f}$. The remaining term $\boldsymbol{\epsilon}$ represents the modelling error in $\mathbf{A}$ as well as the error in

observing $\mathbf{m}$. It may appear that if the objective is to determine the unknown quantity $\mathbf{f}$ then an approximation may be obtained by:

$$\mathbf{f} \approx \mathbf{A}^{-1}\mathbf{m} \tag{3.102}$$

However this is not the case and this becomes clear if Equation (3.101) is multiplied by $\mathbf{A}^{-1}$ to give:

$$\mathbf{A}^{-1}\mathbf{m} = \mathbf{A}^{-1}\mathbf{A}\mathbf{f} + \mathbf{A}^{-1}\boldsymbol{\epsilon} \tag{3.103}$$

The modelling error is now being manipulated by the linear operator $\mathbf{A}^{-1}$. This shows that in attempting to apply Equation (3.102) it is being assumed that both operators $\mathbf{A}$ and $\mathbf{A}^{-1}$ have the same properties that will permit the operations in Equations (3.101) and (3.103).

3.11.3 Ill-posed problems

Awareness of the operator properties is fundamental to the solution of the inverse problem. They were interpreted by Jacques Hadamard who introduced the notion of a well-posed problem as one which has the following features [69]:

1. *Existence*: There should be at least one solution
2. *Uniqueness*: There should be at most one solution
3. *Stability*: The solution must depend continuously on the data

From this point on the focus will be on a forward mapping $\mathbf{A}$ that is well-posed because it satisfies Hadamard's conditions and a backwards mapping $\mathbf{A}^{-1}$ that is ill-posed because it does not. As a result of the ill-posed indirect problem, in Equation (3.103), asymptotic behaviour can obscure the reconstruction $\mathbf{f}$ and the instability of the operation exacerbates errors due to noise, modelling and truncation. To obtain a meaningful estimation of $\mathbf{f}$ a strategy must be found that accepts the inherent uncertainties in the calculation, at the same time as treating the operator $\mathbf{A}^{-1}$, so that it conforms to Hadamard's provisions.

The adherence of a problem to Hadamard's conditions can be analysed through the Singular Value Decomposition (SVD). This allows the linear operator $\mathbf{A}$ to be written in the form:

$$\mathbf{A} = \hat{\mathbf{U}}\mathbf{S}\hat{\mathbf{V}}^T \tag{3.104}$$

where $\mathbf{S}$ is a $p \times q$ matrix that contains the singular values of $\mathbf{A}$ along its diagonal and $\hat{\mathbf{U}}$ and $\hat{\mathbf{V}}$ are $p \times p$ and $q \times q$ orthogonal matrices that satisfy:

$$\hat{\mathbf{U}}^T \hat{\mathbf{U}} = \hat{\mathbf{U}} \hat{\mathbf{U}}^T = \mathbf{I} \tag{3.105}$$

$$\hat{\mathbf{V}}^T \hat{\mathbf{V}} = \hat{\mathbf{V}} \hat{\mathbf{V}}^T = \mathbf{I} \tag{3.106}$$

To develop some intuition about the SVD its application can be visualised as three geometric operations. This is demonstrated in Figure 3.3. Each step can be distinguished from the greyscale plots as follows:

1. *Black*: The circle is represented by the standard basis vectors and is defined by the matrix $\mathbf{C}$.

2. *Dark grey*: The circle is rotated through the transformation $\hat{\mathbf{V}}\mathbf{C}$ so that it is represented by the new basis in dark grey.

3. *Medium grey*: The circle is transformed by $\mathbf{S}\hat{\mathbf{V}}^T\mathbf{C}$ and as a result the components of $\mathbf{C}$ have been contracted by the magnitude of the singular values in the new basis. The singular values are the square roots of the eigenvalues of $\mathbf{A}^T\mathbf{A}$. The linear transformation $\mathbf{A}$ has been applied to the circle data $\mathbf{C}$ in this new basis to produce an output in that basis.

4. *Light grey*: The transformed circle is now rotated back into the standard basis through the operation $\hat{\mathbf{U}}\mathbf{S}\hat{\mathbf{V}}^T\mathbf{C}$

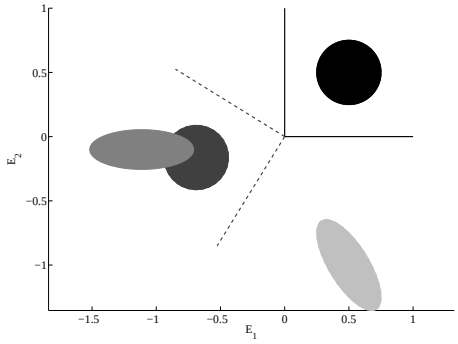

Fig. 3.3 The steps of the singular value decomposition in black to light grey.

The operations that constitute the SVD have been omitted here as they are included in the MATLAB function `svd()`, which will always be applied for any proceeding problems, or as part of the Moore-Penrose pseudo inverse that may be used to find Truncated Singular

Value Decomposition (TSVD) solution to operations that take the form of Equation (3.102). Hadamard's conditions can now be applied to determine whether or not a problem is well-posed. If $\mathbf{A}$ is not a square matrix then it can be shown that the existence and uniqueness conditions are not met [68]. In the proceeding analysis the transfer function matrix will always be square and invertible. The error in the reconstruction of Equation (3.103) is bounded by the sub-multiplicative norm:

$$||\mathbf{A}^{-1}\boldsymbol{\epsilon}|| \leq ||\mathbf{A}^{-1}||\,||\boldsymbol{\epsilon}|| \tag{3.107}$$

where $||$ denotes the norm of the matrix. Assuming the sub-multiplicative norm implies the matrix p-norm:

$$||\mathbf{A}^{-1}||_P = \sup_{\boldsymbol{\epsilon}\neq 0} \frac{||\mathbf{A}^{-1}\boldsymbol{\epsilon}||_P}{||\boldsymbol{\epsilon}||_P} \tag{3.108}$$

where P indicates the choice of norm and the p-norm for vectors can be written as:

$$||\boldsymbol{\epsilon}||_P = \left(\sum_{i=1}^{n} |\boldsymbol{\epsilon}_i|^P\right)^{1/P} \tag{3.109}$$

Equation (3.107) demonstrates that ill-conditioning of the problem can immediately be detected by checking the magnitude of $||\mathbf{A}^{-1}||$. If $||\mathbf{A}^{-1}||$ is large then the error in the reconstruction $||\mathbf{A}^{-1}\boldsymbol{\epsilon}||$ can become significant even if $\boldsymbol{\epsilon}$ contains small terms. Instead of calculating $||\mathbf{A}^{-1}||$ it is more common to define the condition number of the matrix as:

$$Cond(\mathbf{A}) = \frac{s_1}{s_p} \tag{3.110}$$

where the SVD has been utilised in the sense that the singular values matrix $\mathbf{S}$ will always contain a diagonal of positive numbers that decrease in order from the first element s_1 to the last element s_p. Therefore the condition of the matrix is the ratio of the largest to the smallest singular value. This number can be thought of as a measure of the relative change in output for a relative change in input. With this tool it is now possible to detect ill-posedness in the sense of the continuity condition. As more measurement points p of the forward problem are computed it is possible to define a failure in the continuity of the reconstruction through the condition given by Mueller & Siltanen [68]:

$$\lim_{p\to\infty} Cond(A_p) = \infty \tag{3.111}$$

This failure of the continuity condition will be shown in the simulations in Chapter 5. This shows that failure of continuity can only be detected by observing a sequence of events and attempting the reconstruction with each A_p.

On realising that a problem is ill-conditioned there are now two main routes that the analysis can follow. These are regularisation strategies and statistical inversion. Sometimes both strategies will produce estimations that are equivalent. However, the statistical inversion approach is more general and gives qualitative information about the uncertainties when compared with regularisation. In the analysis that follows regularisation strategies have been applied in order to estimate input force signals and to interpret this inverse problem.

3.11.4 Regularised inversion

The least squares method is the most generally accepted strategy for obtaining an optimal estimate of the linear inverse problem. However, simply minimising the least squares cost function of an ill-posed linear system is not guaranteed to satisfy Hadamard's conditions. Instead the condition of the problem can be improved by adding some levity to the minimisation by means of a regularisation method. This can be visualised as drawing a radius δ around the forward map of the reconstructed unknown $\mathbf{Af}$; where the true solution $\mathbf{m}$ is one point inside the resulting area. Tikhonov regularised inversion is the simplest method available to linear problems beyond the TSVD [68]. The Tikhonov regularised solution is a vector $\mathbf{z}_\Gamma(\mathbf{m})$ with a small ℓ^2 norm that gives a small residual $\mathbf{Az}_\Gamma(\mathbf{m}) - \mathbf{m}$ so that it minimises the expression:

$$\|\mathbf{Az}_\Gamma(\mathbf{m}) - \mathbf{m}\|^2 + \Gamma\|\mathbf{z}_\Gamma(\mathbf{m})\|^2 \tag{3.112}$$

A computationally attractive form of this is:

$$\min_{\mathbf{f}^q} \left\| \begin{pmatrix} \mathbf{A}^{p\times q} \\ \sqrt{\Gamma}\mathbf{L}^{p\times q} \end{pmatrix} \mathbf{f}^q - \begin{pmatrix} \mathbf{m}^p \\ \mathbf{0} \end{pmatrix} \right\|^2 \tag{3.113}$$

This is known as the stacked form of the regularisation where $\Gamma > 0$ is the regularisation parameter that must be chosen to compute the Tikhonov regularised solution and $\mathbf{L}$ is the discrete derivative operator. The least squares solution of $\mathbf{f}^q$ is computed in this form at each iteration q. However this depends on the guess of the regularisation parameter. Too much regularisation will tend to cause the model updating method to converge close to the

initial guess, whereas too little regularisation can result in an unstable search. It is generally accepted that a good solution can be found by viewing a plot of the residual norm against the regularised norm, (x,y) = (log $\|\mathbf{Af}-\mathbf{m}\|$, $log\|\mathbf{Lf}\|$), for a specified range of the regularisation parameter Γ [70]. This will typically form a smooth curve in a L shape, so it is known as the L-curve method. The best solution is thought to be found as near to the corner of the L as possible. Example L-curves are shown in Figure 3.4. These have been generated for the reconstruction of the boundary load for the Commercial Piezoelectric Actuator simulation in Section 4.5.3. The value of Γ that has been selected is associated with the point on the L-curve that has been marked ♦.

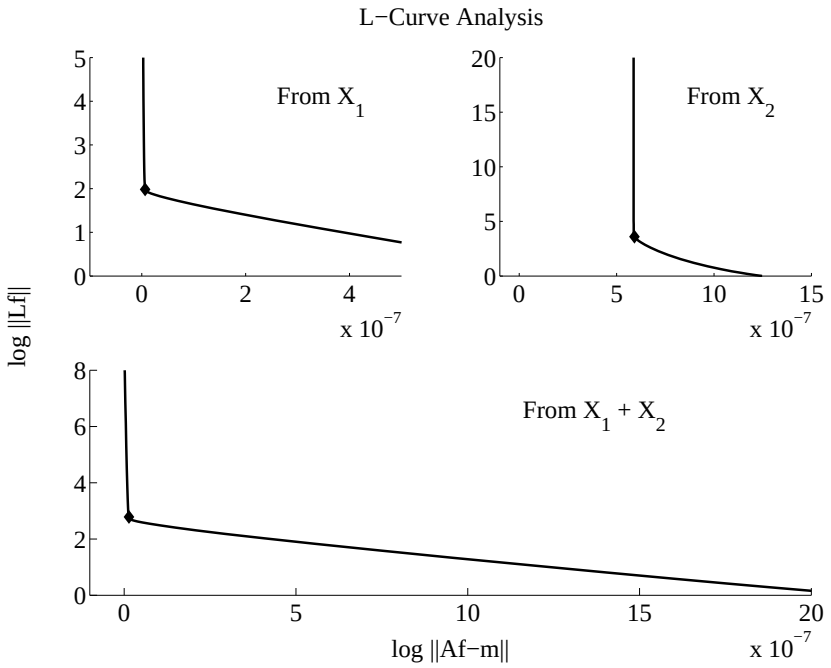

Fig. 3.4 Typical L-curves.

3.12 Outcomes

It is clear that observation of the axial joint behaviour in a High Power Ultrasonic (HPU) device demands indirect methods. It is inaccessible to measurement instruments and the response of the HPU device would be significantly altered by their attachment. Indirect observations will always be incomplete. Therefore the task of the analysis is to ascertain whether these observations can be justified through meaningful application. The meaning

of an indirect observation can be obscured disproportionately by approximations that are acceptable in the formulation of the equivalent direct problem. These observations insist on knowledge of the exact waveguide, which can be represented as a distributed parameter system.

A Fast Fourier Transform based Spectral Element Method (SEM) was discussed alongside the Laplace Transform based Distributed Transfer Function Method (DTFM). Equivalent distributed parameter models of a rod may be formulated through both methods and subsequently multiple reflections in the waveguide will lead to sharp spectral peaks in the system transfer functions. As a result, each model will be very sensitive to discrepancies between the experimental modelling and the measured data [71]. However the formulation of the SEM requires a throw-off element to determine the reflection of waves from their source. The DTFM does not require this and it is possible to formulate a Transcendental Eigenvalue Problem (TEP) for the waveguide. Singh [64] has demonstrated the power of the Inverse TEP for identifying the parameters of a distributed parameter model of a fixed-free beam. However a form of this is not yet available for a free-free rod or a piezoelectric rod. A scheme of this nature is necessary to estimate the distribution of the prestress that is developed at an axial joint in a free-free rod. However this requires that the the axial response of the rod is measurable for two different boundary conditions. Distributed parameter models of the HPU device, for open and closed electric boundary conditions, might be the best direction for this investigation. It will be difficult to obtain matching experimental data. The method by Singh [64] is effective because of the existence of the free-free resonant frequencies of the beam as the the anti-resonant frequencies of the fixed-free beam. An equivalent set of interlaced boundary conditions for a piezoelectric rod are unknown.

A disadvantage of selecting the DTFM, instead of the SEM, is that it was not possible to extend it so that it could describe higher order waveguides. The first order state space formulation must be replaced with a scheme where the waveguide can be described by coupled equations of motion. The SEM does not suffer from this, but it cannot be employed to form a TEP. Spectral Elements is an open area of research, so other formulations should be investigated. The analysis of the electromechanical rod element suggested that a one mode wave theory is too simplistic for piezoelectric behaviour. The forward problem of predicting the response, for the distributed parameter model of an HPU device, will not be implemented for applied electrical boundary conditions. Therefore the subsequent analysis is reduced to considering whether a distributed parameter rod, that is based on Love Rod Theory (LRT), will be suitable to describe the mechanical behaviour of the HPU device.

LRT is expected to provide a reasonable correction to Elementary Rod Theory and it is not known how much of a correction a higher mode theory would achieve for the HPU device model when it is operating at 20kHz.

The details of the DTFM have been presented and this has been reproduced as a set of MATLAB functions and scripts. The discretisation of the convolution integral is required for force estimation and the interpretation of this requires the tools from the field of inverse problems, which have been presented. Any distribution of the joint force can be assumed using Heaviside step functions, within the spatial discretisaion that is chosen for the elements of the distributed parameter rod. Without a better understanding of the prestress that is developed at an axial joint there is no route to determining this distribution. If it cannot be measured directly then an Inverse TEP is necessary to estimate the stiffness of the distributed parameter rod so that the prestress can be estimated. Without this the next best option is a very detailed 3D Finite Element model to visualise the nature of the prestress. Trapezoidal integration of the distributed load was necessary to incorporate it into the DTFM program.

The force estimation scheme, through the LRT distributed parameter model, requires point wise displacement response data from the HPU assemblies. To determine whether the assumptions that have been made are appropriate, the force estimations must be verified through another experimental method. However, before this can be carried out. the model must be optimised by means of its TEP.

Chapter 4

The linear calibration model for the High Power Ultrasonic test assemblies

4.1 Introduction

Ultrasonic horns have been manufactured in order to test the proposed force identification scheme. They are manufactured to the same geometric specification. Then all but one of the horns is modified to include an additional axial joint. This joint will experience ultrasonic vibration of higher amplitude than the vibration experienced at the joint between the horn and the piezoelectric actuator. This is achieved by manufacturing each horn with a step change in cross section, and including the joint after this, close to the front radiating face of the overall High Power Ultrasonic (HPU) assembly. The horns are initially tested with a Commercial Piezoelectric Actuator (CPA), however full access to the properties of the components in this assembly is not available. Therefore the In-House Piezoelectric Actuator (IHPA) is manufactured to a known specification. Every combination of ultrasonic horn and piezoelectric actuator is tested through electrical impedance analysis and Experimental Modal Analysis (EMA). This reveals that the CPA features four axial vibration modes that dominate its behaviour. The IHPA is also dominated by four axial modes, however other closely spaced modes are also significant. When the additional joint of a Jointed Horn (JH) is tighter, the natural frequencies of the HPU assembly tend toward the equivalent natural frequencies of the piezoelectric actuator with the Monolithic Horn (MH) attached.

Limited information is available to define the distributed parameter models of each piezo-

electric actuator with the MH attached. These models are considered to be the linear calibration to the estimation of the joint force. A set of assumptions is required to estimate the remaining unknowns of each model. This is achieved by minimising the difference between its eigenvalues and the natural frequencies of the physical system, which are obtained through EMA. Due to the inhomogeneity of the minimisation problem, the Genetic Algorithm (GA) is applied to search efficiently for suitable models. Without a stricter search method it is not possible to optimise the linear calibrations models. It is suggested that a suitable formulation of an Inverse Transcendental Eigenvalue Problem (TEP) is necessary. Despite the errors in the resulting linear models, the eigenvectors agree well with the experimentally measured mode shapes. The force identification is based on the sum of the transfer function residues, so the models appear to be appropriate.

A set of simulations are completed to test the force estimation scheme under ideal conditions. A boundary load is applied to each linear calibration model at the foremost node of the piezoelectric stack. This represents the input force that is generated when an electrical excitation signal is applied. The transient response of each assembly is computed at two locations for the same analytical input force. Each displacement is then downsampled through interpolation and the input force is reconstructed through the force identification scheme. This is a least squares problem that requires the inversion of an ill-conditioned matrix. The solutions that are obtained through forward substitution are numerically unstable.

Two regularisation methods are applied to recover stable solutions: Truncated Singular Value Decomposition (TSVD) and Tikhonov regularisation. Both schemes provide a reasonable reconstruction of the input signal. The most significant errors occur at the end of the observation window. Amplitude is also lost at the crests and troughs of the sinusoidal signals. Attempts are made to reconstruct the input force when the stiffness to the model is reduced. It is not possible to recover a stable solution in the examples that are given. An error, which increases with time, masks any approximation of the input force that might be obtained. Transient responses are also calculated when each model is excited by the boundary load, as well as an additional load, that is uniformly distributed over the component that represents the flats of the ultrasonic horn. The attempts to reconstruct this force through the regularisation schemes are successful. However the joint identification scheme requires that both HPU assemblies, featuring a MH or JH, should produce a measurable response for the same input signal. Due to the sharp spectral behaviour of the HPU assemblies it is clear that this condition would be difficult to cultivate experimentally.

4.2 Ultrasonic horn test pieces and piezoelectric actuators

In order to test the force identification scheme a range of ultrasonic horns, with a step change in cross section, are manufactured to the same geometrical specification. All but one of the horns are then modified to include an additional axial joint. Each horn will be excited through either a Commercial Piezoelectric Actuator (CPA), the L500 ultrasonic process system that is produced by Sonic Systems, or a stacked Piezoelectric Actuator that has been manufactured In-House (IHPA).

To do useful work, with either of the devices, it is necessary to continuously track the principal operating frequency and adjust the excitation signal accordingly. For both devices this operating frequency is associated with the second longitudinal vibration mode of the assembly. This has narrow bandwidth and, assuming that the CPA and IHPA cannot be modified, the resonant frequency depends on the geometry of the ultrasonic horn, as well as the tightness of any axial joints, for low power excitation.

Each of the electrical impedance minima of the device that is measured is identified as being close to a mechanical resonance frequency for low voltage excitation. It is common to assume that a HPU device that is driven at one of its mechanical eigenfrequencies can be described through a Mason [72] equivalent circuit of the form that is given in Figure 4.1. The input voltage V is applied across the electrical branch, which consists of a capacitor C and a resistor R. The electromechanical transformation factor N_m describes the transmission ratio between the electrical and mechanical branches through the analogue of an ideal transformer. The mechanical branch is a RLC circuit where the resistor R_m represents the modal stiffness, the inductor L_m represents the modal mass, the capacitor C_m represents the modal damping and F is the input force. Under the condition that $R = 0$ in the electrical branch, the mechanical resonance is approximately equal to the frequency of the minimum electrical impedance [73].

For the CPA, acquisition of the electrical characteristics are incorporated into its power supply, so that the frequency of the excitation signal is adjusted to actuate the device at its operating mode [74]. The CPA is supplied with its own power supply that tracks the operating frequency. This also controls a cooling fan, that is stored in its casing, in order to reduce the temperature of the piezoelectric stack. This casing, and the additional electronics, mean that the full behaviour of the device cannot be observed because most of the components are hidden from view. The device cannot be powered using burst excitation signals because this

could cause permanent damage to the cooling fan components. For these reasons an equivalent stacked piezoelectric actuator was manufactured in house with no casing or additional electronics.

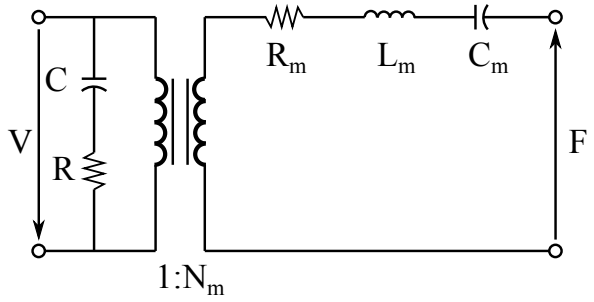

Fig. 4.1 Equivalent Circuit of a High Power Ultrasonic device.

Increased temperature of the piezoelectric stack, during continuous operation, has been associated with softening overhang behaviour in the frequency response of the device by Mathieson [7]. At low levels of vibrational amplitude the temperature in the piezoceramic stack does not change significantly and the response of the High Power Ultrasonic (HPU) device is not altered noticeably. This is true whether burst or continuous excitation is employed. However a train of burst excitations at higher power will induce a temperature change in the piezoceramic stack. The time delay between each burst is shown to contribute to softening frequency overhang behaviour. Therefore, without additional cooling, it is important to test the IHPA through burst excitation signals to minimise any heating of the device. The force identification scheme requires that one HPU assembly is tested over a range of excitation power levels, which will not cause a significant shift in the operating mode. Results of this nature are then assumed to be the linear calibration for a comparison to test pieces that are exhibiting the behaviour that is associated with nonlinear dynamic systems. This behaviour may include resonance shifting, phase and amplitude modulations, bifurcations and chaos.

The main focus of this investigation is to assume the nonlinear subsystem of an axial screwed threaded joint and expose it to extreme levels of ultrasonic vibration. The force identification scheme is then applied to isolate a force signal that is relative to a force signal occurring in a system with assumed linear behaviour. This linear system must maintain its resonant operating frequency over the same range of electrical stimulation for which the nonlinear subsystem exhibits behaviour that is distinctly separate. To achieve this a range of ultrasonic stepped horns are manufactured from Titanium Grade 5 alloy (Ti90Al6Va4) for a

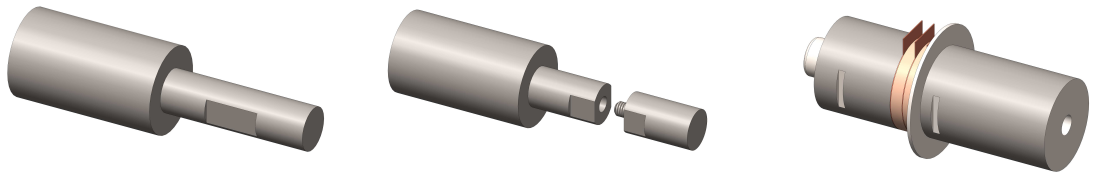

(a) Monolithic Horn (b) Jointed Horn (c) In-House Piezoelectric Actuator

Fig. 4.2 The ultrasonic horn test pieces.

comparison through the same geometric specification. This material is commonly adopted for applications in ultrasonics due to its low specific acoustic impedance, which results in low losses of acoustic energy, as well as its high stiffness to mass ratio and high toughness. All but one of the ultrasonic horns have an additional axial joint that is close to the radiating tip of the horn. The exploded view of this interface is shown in Figure 4.2b. There are four Jointed Horns (JH); each of which has its own matching cap that is tightened to its front radiating face. The radiating face contains a set of internal M6 threads through which the axial joint is formed with the cap. Three of the horns have a cap with a set of matching external threads machined from its rear face. The remaining horn has a cap with a set of internal threads. The first three horns have been set to 8, 12 or 16Nm at the axial joint. A flat has been machined over the interface to leave a 10×20mm window that will be observed using an ultra-high speed camera in Chapter 5. The torque settings are applied by means of a calibrated torque wrench with a quoted accuracy of ± 0.5Nm. The remaining JH has been set to 8Nm through a M6 steel stud between the cap and the rest of the horn. There is also one further horn which has no joint over the flat portion. This is referred to as the Monolithic Horn (MH) and is displayed in Figure 4.2a. Each of the ultrasonic horns must be attached to a piezoelectric actuator through its M10 internal threads at its rear face.

Each horn features a step change in cross section to ensure that the amplitude of vibration experienced by the additional joint, in each JH, is significantly higher than the vibration encountered through the larger diameter bearing surface, between the piezoelectric actuator and the horn. The horn is always attached to the IHPA, which is shown in Figure 4.2c, through a joint that is set to 16Nm. The CPA assembly is equivalent, however some features of the design have not been provided and cannot be ascertained through non-destructive testing. Initially a set of male threads was machined out of extra material at the rear face

of each JH, so that they were composed solely of the Grade 5 titanium alloy. However incorporating this alloy at the threaded connection is associated with a risk of thread galling occurring between the male threads of the horn and the female threads of the piezoelectric exciter [75]. This cold welding process can occur when two surfaces with oxide film are held under a heavy pressure that causes a break down of their oxide coatings. Without this protective layer there is an increase in friction at the joint and this can generate enough heat to fuse the external and internal threads together. Therefore it was necessary to remove the external threads and replace them with internal threads so that the joint could be made through a steel threaded rod. The high vibrational amplitude developed in the HPU device may have encouraged galling to occur, so this stage ensured that different horns could be attached and unattached from a piezoelectric exciter, during a single run of the experiments that follow in Chapter 5.

In the plots and tables that follow a shorthand has been adopted to specify the configuration of the axial joint. For Grade 5 Titanium male and female threads that are set to 8Nm the axial joint is specified as: Ti@8Nm. If this is written as St@16Nm:Ti@8Nm then the notation the the left and right of the semi colon is that of the joint to the piezoelectric actuator and the joint within JH respectively. Where St represents an axial joint made through tightening a Steel stud.

4.3 Impedance Analysis Results

Each horn is attached to either the Commercial Piezoelectric Actuator (CPA) or the In-House Piezoelectric Actuator (IHPA) through a joint set to 16Nm and the impedance of the assembly was evaluated through an Agilent 4294A impedance analyser using the 42941A impedance probe. The analyser, probe and any additional cabling required must be calibrated together before performing any tests. The piezoelectric actuator is supported through its flange and the probe is connected to its terminals. A 500mV excitation signal is swept over a frequency range of 1-80kHz and the magnitude and phase of the impedance is recorded. Only 5kHz of the total range is measured at a time because the impedance analyser is limited to 801 measurement points per sweep. This gives an artificial resolution of $\approx$ 6Hz. Evaluating the impedance of the device gives a comparison of the electrical behaviour of the device for different joint settings. For the low level excitation signal it is appropriate to assume that the frequency of minimum impedance is a good approximation

of the resonant frequency of the device [73].

4.3.1 Commercial Piezoelectric Actuator

The impedance measurements of the CPA assemblies reveal that each spectrum is dominated by 4 minima/maxima pairs over a frequency range of 10-45kHz whilst the 45-80kHz range contains maxima/minima pairs of smaller amplitude. Initially three of the JHs were manufactured with external Grade 5 Titanium threads at their back face for connection to the CPA. Limited frequency spectra are shown for this assembly in Figure 4.3. As explained in Section 4.2, the external threads were removed, so they must be replaced with a steel threaded rod. In the case of an HPU device, this has a significant influence on its modal characteristics. It can be seen that increasing the applied torque to the cap has increased the frequency of the 2^{nd} minimum impedance, which is associated with the operating mode of the device. However the sharpest spectral characteristics are achieved for the medium tightness of 12Nm. This may indicate that the tightness of 16Nm, at this joint, has resulted in a loss of stiffness through the elongation of the external threads. Due to the complexity of setting the torque at both cap or the actuator joint, and the limited accuracy of utilising the torque wrench, it is not possible to characterise the device behaviour through torque changes. This has been implemented here to create three distinct assemblies for which the force identification scheme in Chapter 3 can be applied. Therefore it is not possible to accurately deduce the level of torque that will fail to comply with the assumption that the JH can tend towards to the MH as its joint is tightened.

The impedance traces for the ultrasonic horns, when they are connected to the CPA through a steel threaded rod, are displayed in Figure 4.4. A comparison of these results to the previous results in Figure 4.3 suggests that the operating frequency has not changed significantly. The most significant frequency shift is ≈ 0.4kHz between the impedance minima that are associated with the 4^{th} longitudinal mode. A comparison of the traces measured from the JHs, with the Grade 5 Titanium threads, shows that ≈ 0.4kHz is the maximum frequency shift incurred through modifying the tightness. The JH that is set to 12Nm produces the sharpest spectral characteristics out of the jointed horns, but the MH achieves a significantly sharper electrical impedance at the operating mode.

Before tightening any JH, onto either piezoelectric actuator, its axial joint is set independently to the rest of the assembly. The horn is clamped tightly into a bench vice with soft

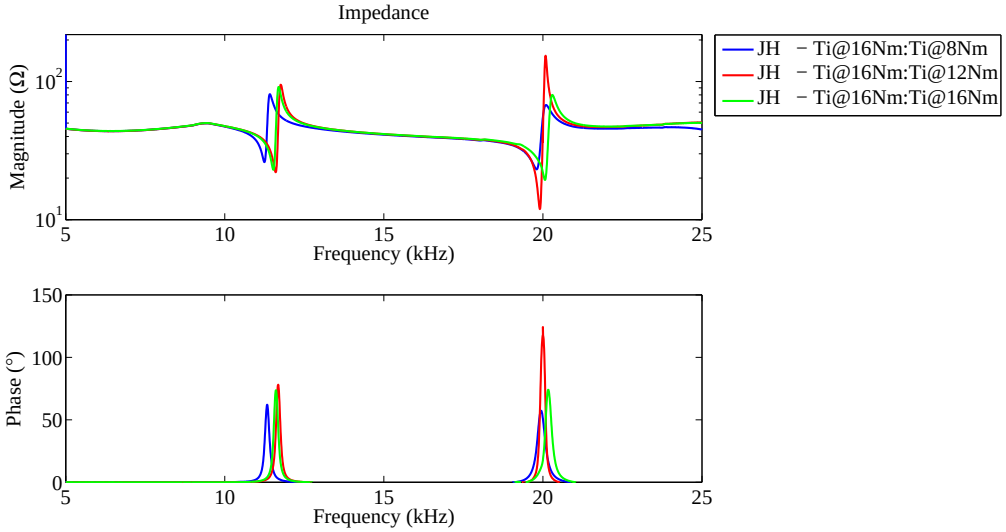

Fig. 4.3 Impedance behaviour of test pieces attached to the Commercial Piezoelectric Actuator through Grade 5 Titanium external threads.

jaws vice pads. The torque is then set using a custom torque drive adapter which grips the flat portions of the cap. Once the cap torque has been set its flats are mirrored, over the bearing surface, and machined to produce the JH shown in Figure 4.2b. Then a different torque drive adapter is employed to grip that new flat, so that the torque of the joint between the horn and the piezoelectric exciter can be set independently. For each new test, in any of the experiments that follow, different ultrasonic horns will have been unattached from, or attached to, the same piezoelectric actuator. Due to inaccuracies in applying this torque each time it is not possible to draw reliable conclusions from the shift that may be incurred in either the electrical or mechanical spectrum behaviour of an HPU device. Therefore the torque of each JH has been set once and is not loosened or tightened before performing any of the experiments. The torque of the joint to the piezoelectric actuator is set using the explained protocols in order to maintain consistency between experiment runs, however this prestress will not be treated explicitly in any of the following analysis. It is therefore assumed that when this joint is set to 16Nm the frequency spectrum of the assembly will not be influenced significantly by tightening it any further. As has been mentioned previously, the thickness of the rod at this bearing surface impedes the acoustic waves, in the device, more than the thickness of the rod at the JH axial joint, which is the subject of the force identification experiment.

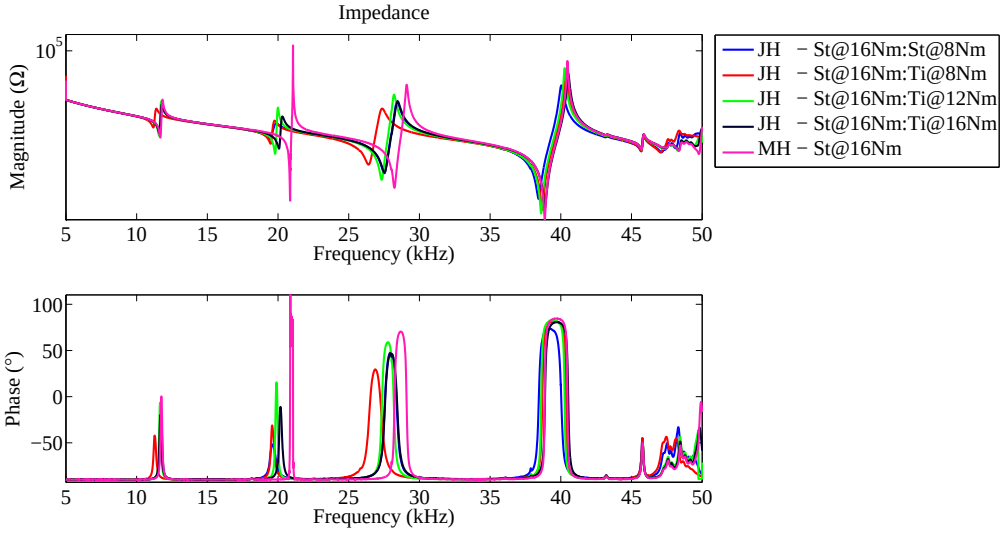

Fig. 4.4 Impedance behaviour of each test piece attached to the Commercial Piezoelectric Actuator through a threaded Steel rod.

4.3.2 In-House Piezoelectric Actuator

The impedance behaviour of the IHPA is measured with each of the ultrasonic horns attached. The titanium studs at the rear of each horn have been removed before this stage, so a set of results are not obtained for a titanium threaded connection between the IHPA and the horn. The results for a steel stud between each horn and the IHPA are shown in Figure 4.5. A comparison of these, to the results given in Figure 4.4, shows that the four axial modes in this assembly are not as predominant as they were in the case of the CPA assembly. The most significant deviation from this requirement is the close spacing of modal behaviour around the third longitudinal mode. Therefore, to fully describe this device, the transfer element scheme requires a higher order mode rod theory to account for coupling of its axial motion to radial and tangential motions. Experimental Modal Analysis (EMA) is required to identify the mode shapes before it can be determined whether it is appropriate to base the transfer element model solely on the axial modal behaviour. It is clear that the IHPA is not as well behaved as the CPA, so it would be desirable to manufacture more IHPAs. The properties of the individual components must be ascertained and the impedance behaviour should feature four predominant modes, in the 0-50kHz range, with the 2nd longitudinal resonance located as close as is possible to 20kHz.

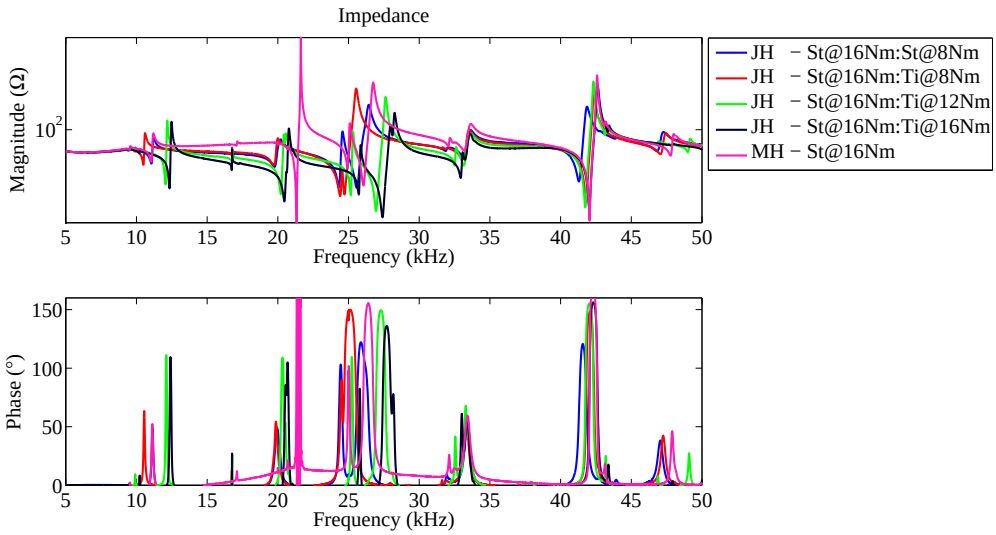

Fig. 4.5 Impedance behaviour of each test piece attached to the In-House Piezoelectric Actuator through a threaded Steel rod.

4.3.3 Discussion

The impedance minima that are shown in Figures 4.3-4.5 are summarised in Table 4.1. Only the four most predominant minima are tabulated because it is likely that these are the four longitudinal modes. This will be verified through EMA. The errors between the impedance of the equivalent JH and MH assemblies is given in Table 4.2. From this it can be seen that changing the tightness of the joint in a JH assembly will, in most cases, adjust the impedance frequencies so that they tend towards those of the equivalent MH assembly. The most significant disagreement to this is the behaviour of the 1^{st} axial mode in the IHPA results. However the repeatability of each test depends on setting the axial joint between the IHPA and the horn to 16Nm. This depends on the use of the torque wrench as well as its calibration. The sharpest spectral characteristics appear to be associated with the 12Nm tightness. This may suggest that the 16Nm torque setting is tending to overtighten the stud causing too much movement of its threads. Importantly tightening the JH is tending to adjust the 2^{nd} longitudinal mode of the assembly towards agreement with equivalent MH assembly. The force identification experiments will always involve adjusting the excitation frequency around the obtained 2^{nd} longitudinal frequency, to maximise the resonant response, so it is not necessary to predict this frequency for each instance of assembly.

Table 4.1 Summary of the impedance minima that are associated with the dominant axial behaviour for each test assembly

Actuator	Horn	Actuator Joint	Horn Joint	Frequency of minimum impedance (kHz)			
				1st	2nd	3rd	4th
CPA	JH	Ti@16Nm	Ti@8Nm	11.244	19.806	26.563	39.044
CPA	JH	Ti@16Nm	Ti@12Nm	11.600	19.906	27.475	39.050
CPA	JH	Ti@16Nm	Ti@16Nm	11.525	20.069	27.338	39.231
CPA	JH	St@16Nm	St@8Nm	11.650	19.413	27.513	38.438
CPA	JH	St@16Nm	Ti@8Nm	11.188	19.481	26.406	38.694
CPA	JH	St@16Nm	Ti@12Nm	11.588	19.800	27.331	38.613
CPA	JH	St@16Nm	Ti@16Nm	11.600	20.069	27.531	38.881
CPA	MH	St@16Nm	-	11.675	20.856	28.238	38.869
IHPA	JH	St@16Nm	St@8Nm	11.056	19.750	24.313	41.300
IHPA	JH	St@16Nm	Ti@8Nm	10.494	19.675	24.363	41.813
IHPA	JH	St@16Nm	Ti@12Nm	12.056	20.219	24.869	41.744
IHPA	JH	St@16Nm	Ti@16Nm	12.344	20.463	24.750	42.038
IHPA	MH	St@16Nm	-	11.050	21.331	24.944	42.050

4.4 Experimental Modal Analysis Results

Modal analysis is the study of the dynamic properties of a structure subject to vibrational excitation. These properties include resonant and anti-resonant frequencies, damping and mode shapes. These are analysed for a dynamic input over the frequency range that is of interest. The ratio of the subsequent response to this input is found after taking the Fast Fourier Transform (FFT) of both signals to obtain a Frequency Response Function (FRF). Many FRFs must be windowed and averaged before a reliable transfer function can be accepted for a point on the structure. This represents the conversion of an input to an output at two collocated or non collocated points in the state space of the structure. Transfer functions can be measured in three orthogonal directions, at multiple locations on the structure, and the results can be superimposed on top of one another to view the resonant frequencies and their relative contributions at each point. This may be used to determine the natural frequencies and damping factors of the structure. In the tests that follow the anti-resonant frequencies will not be observable due to the noise floor of each measured FRF. The anti-resonant frequencies are of interest in some of the most exciting applications of dynamic data to practical problems such as model updating, damage identification and damage location [76, 77]. A discussion towards the practical aspects of modal analysis can be found by

Table 4.2 Error between the impedance minima of the Jointed Horns and the Monolithic Horn assemblies

Actuator	Actuator Joint	Horn Joint	Error (%)				Mean (%)
			1st	2nd	3rd	4th	
CPA	Ti@16Nm	Ti@8Nm	3.7	5.0	5.9	0.5	3.8
CPA	Ti@16Nm	Ti@12Nm	0.6	4.5	2.7	0.5	2.1
CPA	Ti@16Nm	Ti@16Nm	1.3	3.8	3.2	0.9	2.3
CPA	St@16Nm	St@8Nm	0.2	6.9	2.6	1.1	2.7
CPA	St@16Nm	Ti@8Nm	4.2	6.6	6.5	0.5	4.5
CPA	St@16Nm	Ti@12Nm	0.7	5.1	3.2	0.7	2.4
CPA	St@16Nm	Ti@16Nm	0.6	3.7	2.5	0.03	1.7
IHPA	St@16Nm	St@8Nm	0.1	7.4	2.5	1.8	3.0
IHPA	St@16Nm	Ti@8Nm	5.0	7.8	2.3	0.6	3.9
IHPA	St@16Nm	Ti@12Nm	9.1	5.2	0.3	2.7	3.8
IHPA	St@16Nm	Ti@16Nm	12	4.1	0.8	0.1	4.1

Avitabile [78] and the main discussion is summarised in [79]. A theoretical framework to Experimental Modal Analysis can be found in Ewins [80].

Experimental Modal Analysis (EMA) of each HPU assembly is performed through the apparatus that is displayed in Figure 4.6. The Data Physics Quattro performs the role of both the function generator and the analogue to digital data acquisition. It produces a low power random excitation signal over the 0-80kHz range, which is then boosted through the QSC Audio RMX 4050HD power amplifier, to excite the piezoelectric actuator. The velocity response at a point on the HPU assembly is observed through Laser Doppler Vibrometry (LDV). The chosen LDV system is the Polytec CLV-3D, which is comprised of a controller unit that is coupled to an optical sensor head. This sensor head contains three independent LDV systems. Each of these rely on measuring the frequency shift in the reflection of a coherent light source from the measurement surface in motion. According to the Doppler effect, this frequency shift, f_D, can be related to the velocity of the surface, $\dot{u}$, through the wavelength of the emitted wave, λ_e, as follows:

$$f_D = 2\frac{\dot{u}}{\lambda_e} \tag{4.1}$$

The laser controller produces a voltage in proportion to the velocity response at a measurement point on the surface. When this is divided by the simultaneous random voltage, that is produced by the Quattro function generator, it gives the transfer function for that point.

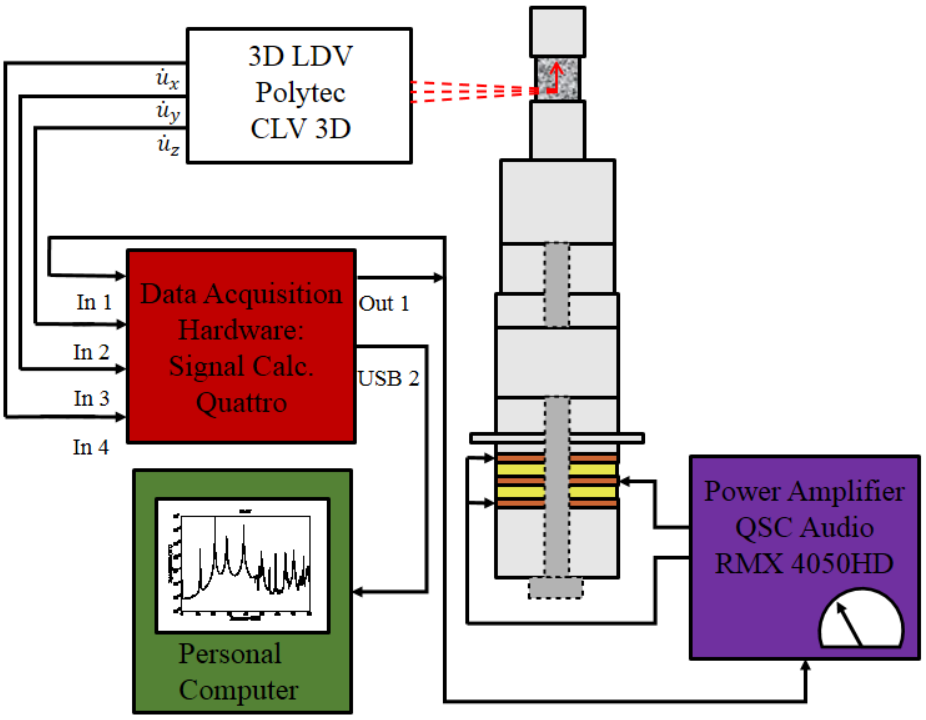

Fig. 4.6 Apparatus for the Experimental Modal Analysis.

Transfer functions are measured at each point subject to 100 stable averages. The points are spaced every 7mm from the front of the horn to its step change in cross section. After which the spacing is increased to 14mm. For the CPA the points only extend to above its flange. After that the casing hides the rest of the actuator from view. The IHPA has points that extend to below the back of the piezoelectric stack, after which the platform for the laser cannot travel further to cover the full device. Each test has a line of these points along the length of the assembly for every $\pi/2$ rotation around its longitudinal axis. The measured transfer functions are assigned to the equivalent points of a scaled spatial model in the software package ME'scopeVES. Observing the amplitude of each of these points, for a sinusoidal excitation at a set frequency, reveals the mode shapes. The reliability of this depends on whether the grid of measurement points is dense enough to estimate the locations of the vibration nodes.

The distributed parameter system model is limited to longitudinal modal behaviour because it contains only rod elements. Optimisation of this description requires that its real eigenvalues match the natural frequencies that are identified through the EMA. Independent EMAs are performed for either of the MH or the JH attached to either of the CPA or IHPA as it is driven by a random voltage signal. The joint to the piezoelectric actuator must be set

to 16Nm through a calibrated torque wrench for each test. The Complex Modal Indicator Function (CMIF) is fitted to the overlaid transfer functions obtained during an EMA. This shows the existing modes and their relative magnitudes [81]. The data that is derived from this, and is to be taken forward, is associated with the most significant resonance peaks. It is assumed that these can be identified as being associated with longitudinal mode shapes.

4.4.1 Commercial Piezoelectric Actuator

The first set of EMA results corresponds to the CPA with either of the MH or JHs attached. Only one JH has been tested in this case because the impedance traces in Figures 4.3 and 4.4 suggest that there are only four dominant modes for all of the JH and the MH. If these modes are all longitudinal then it is assumed that the minimum impedances measured from the CPA assemblies in Table 4.1 correspond to four longitudinal modes that dominate the assumed linear vibration behaviour of the assembly. The frequencies of the dominant peaks are listed in Table 4.3 and show good agreement with the minimum impedance frequencies listed in Table 4.1. The CMIF is displayed in Figure 4.7 and shows that the 1^{st}, 2^{nd} and 4^{th} modes are far more significant than their neighbouring modes. The 3^{rd} mode appears to be closely spaced with another mode. Incomplete 3D mode shapes are displayed as 2D contour maps in Figure 4.8 and, although the full length of the CPA assembly has not been observed, they show clear axial behaviour with bending motions that are not discernible from measurement noise. The mode that is closely spaced with the 3^{rd} axial mode appears to have a bending motion.

For the purpose of comparing the experimental results to the distributed parameter model, it is useful to plot the mode shapes that are obtained through the transfer function measured in the axial direction. The model updating process seeks a minimum error in the measured eigenvalues and those of the distributed parameter system for a set of unknown variables. If this is successful then the measured mode shapes should agree with the eigenvectors of the distributed parameter system. Displaying these in one dimension is the clearest comparison that can be made from the limited information. It is assumed that each of the axial mode shapes will be maximum at the front radiating face of the horn due to the step change in cross section. Therefore each of the one dimensional plots have been normalised by setting the maximum magnitude to unity and scaling the other components relative to this. The 1D axial mode shapes are displayed in Figures 4.9 and 4.10. These 1D plots suggest that

the bending mode close to the 3rd axial mode is not modifying the longitudinal motion significantly.

Table 4.3 Results for the Experimental Modal Analysis of the Monolithic Horn with joint made through a steel stud set to 16Nm

Mode	Frequency (kHz)	Error to minimum impedance (%)
1st Longitudinal	11.7	0.2
2nd Longitudinal	20.8	0.3
3rd Longitudinal	28.1	0.5
4th Longitudinal	38.9	0.1

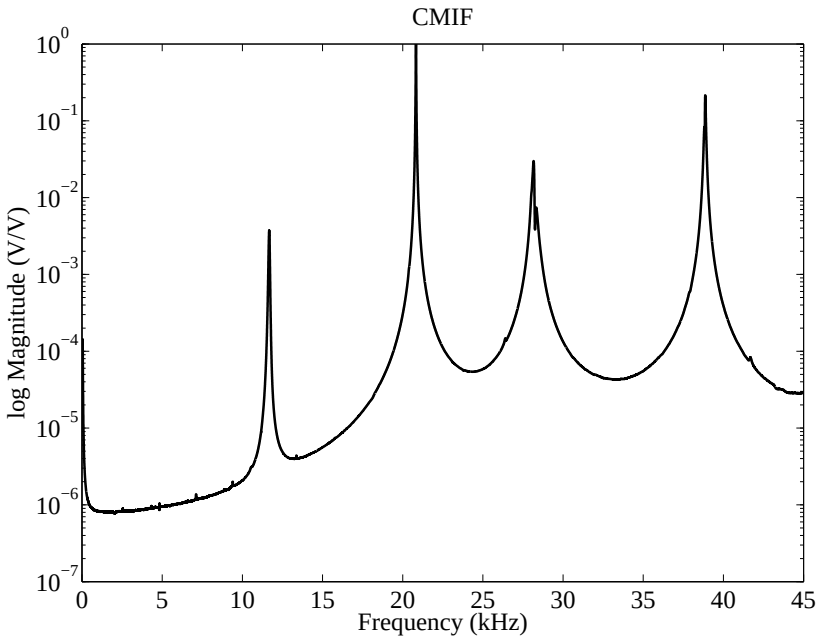

Fig. 4.7 Complex Modal Indicator Function for the Commercial Piezoelectric Actuator with Monolithic Horn attached through a steel stud.

The following results for a JH with cap set to 12Nm represents the most homogeneous jointed assembly possible because both the cap joint and the joint to the piezoelectric actuator are made through external Grade 5 Titanium threads that protrude from the back of both the horn and the cap. The CMIF in Figure 4.11 is qualitatively similar to the CMIF given in Figure 4.7, however the sharpness of each of the peaks is reduced due to the introduction of additional modal damping. This descends from the joint. As a result there is a more prominent bending mode close to the 3rd longitudinal mode. Table 4.4 shows that the

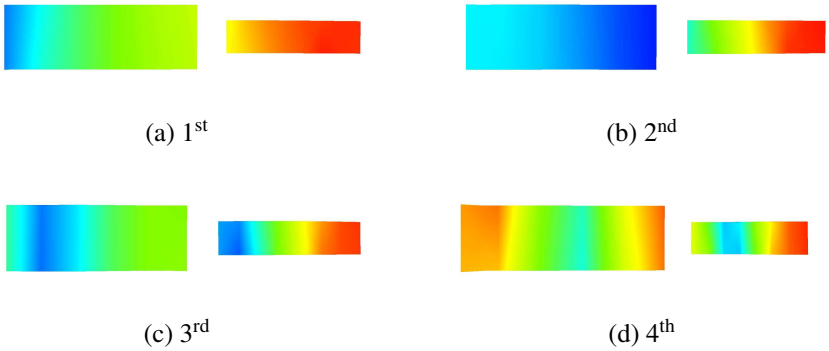

(a) 1st (b) 2nd

(c) 3rd (d) 4th

Fig. 4.8 Measured longitudinal mode shapes of the Monolithic Horn attached to the Commercial Piezoelectric Actuator through a screwed threaded steel rod. The vibration nodes and anti-nodes are indicated following the colour map: ■ → ■.

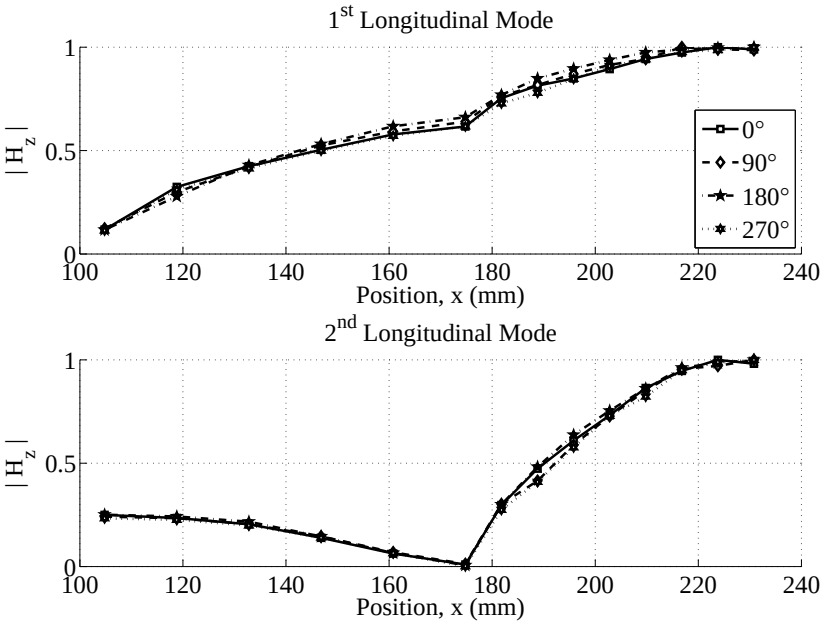

Fig. 4.9 Measured 1st and 2nd 1D longitudinal mode shapes evaluated along four lines of the Monolithic Horn attached to the Commercial Piezoelectric Actuator through a screwed threaded steel connector.

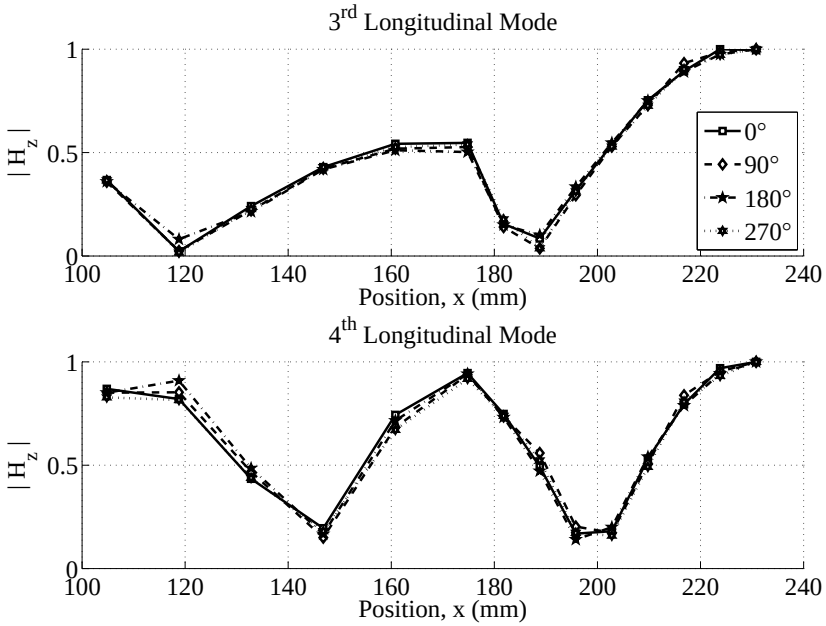

Fig. 4.10 Measured 3rd and 4th 1D longitudinal mode shapes evaluated along four lines of the Monolithic Horn attached to the Commercial Piezoelectric Actuator through a screwed threaded steel connector.

identified modes agree well with the impedance minima in Table 4.1. In comparison to the MH results, it appears that the change in the configuration with the JH has influenced the 2nd and 3rd longitudinal modes most significantly. On viewing the 3D mode shapes, from which the 2D plots in Figure 4.13 have been obtained, it is clear that this assembly has some bending motion after the step change in cross section, at the 2nd longitudinal mode. The 3rd longitudinal mode does not display this, despite the nearby bending mode that is shown on the CMIF. The 1D mode shapes that are shown in Figures 4.13 and 4.14 do not show a significant difference in qualitative behaviour to the 1D mode shapes from the MH tests that are given in Figures 4.9 and 4.10. However the measurement of these, from each rotation around the longitudinal axis of the assembly is less consistent. This may be expected because the inclusion of the joint increases the overall modal damping, which means that measurement noise becomes more significant in each line of points.

4.4.2 In-House Piezoelectric Actuator

The IHPA is tested so that 3 variations of the JH can be compared to the MH. The IHPA was one attempt at producing a piezoelectric actuator for the force identification experiments,

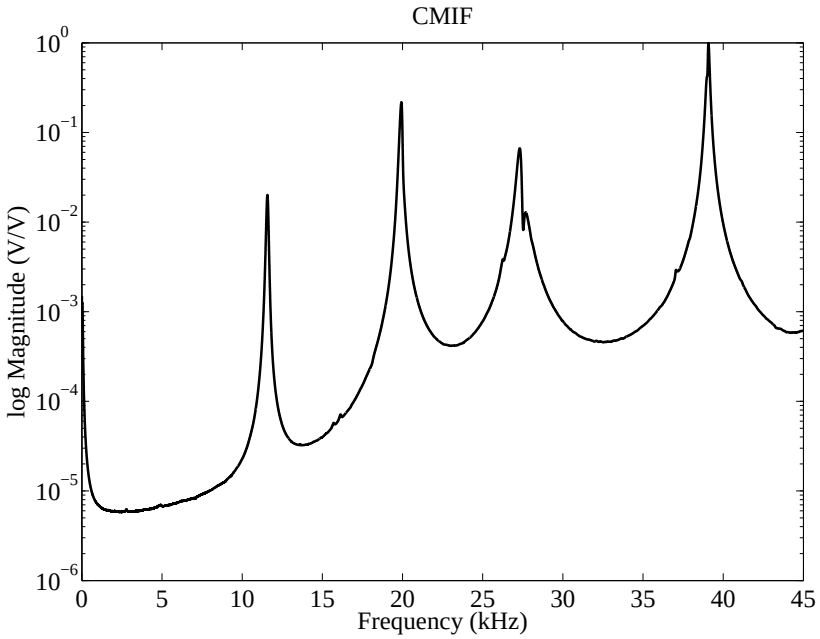

Fig. 4.11 Complex Modal Indicator Function for the Commercial Piezoelectric Actuator with Jointed Horn attached through titanium external threads.

Table 4.4 Results for the Experimental Modal Analysis of the Jointed Horn with joint set to 12Nm through Grade 5 titanium external threads

Mode	Frequency (kHz)	Error to minimum impedance (%)
1st Longitudinal	11.6	0.0
2nd Longitudinal	19.9	0.1
3rd Longitudinal	27.3	0.2
4th Longitudinal	39.0	0.1

(a) 1st (b) 2nd

(c) 3rd (d) 4th

Fig. 4.12 Measured longitudinal mode shapes of the Jointed Horn attached to the Commercial Piezoelectric Actuator through Grade 5 titanium external threads.

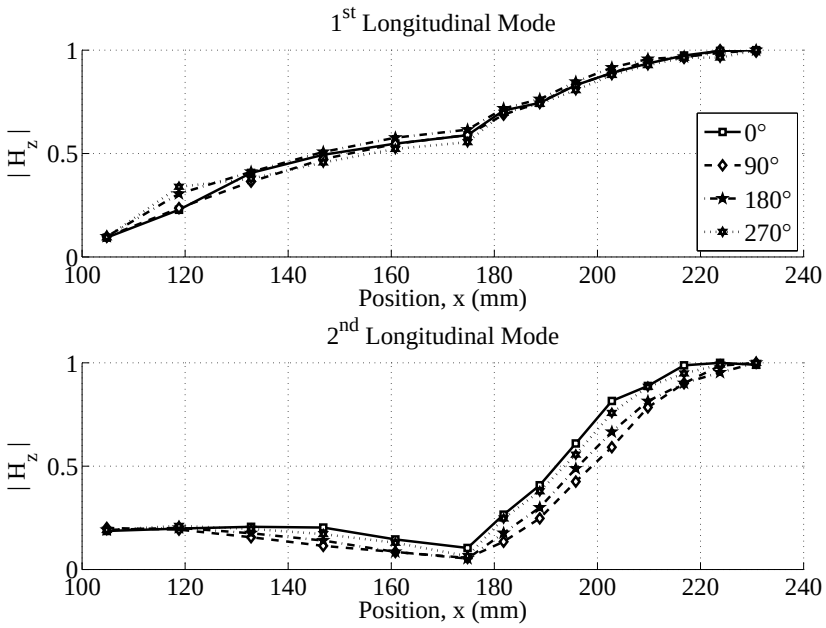

Fig. 4.13 Measured 1st and 2nd 1D longitudinal mode shapes evaluated along four lines of the Jointed Horn with cap tightened to 12Nm attached to the Commercial Piezoelectric Actuator through Grade 5 titanium external threads.

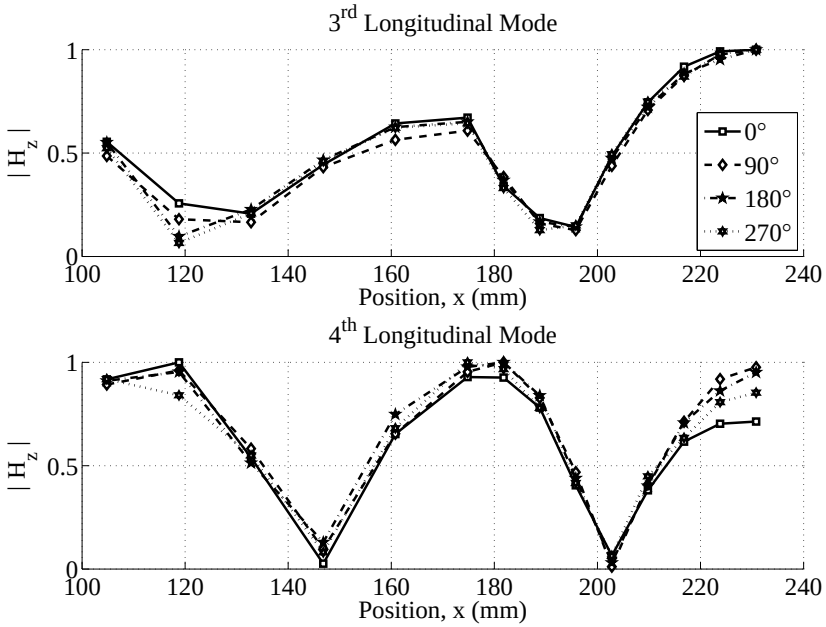

Fig. 4.14 Measured 3rd and 4th 1D longitudinal mode shapes evaluated along four lines of the Jointed Horn with cap tightened to 12Nm attached to the Commercial Piezoelectric Actuator through Grade 5 titanium external threads.

however it is not as well behaved as the CPA, in the sense that more modal activity is captured. This is clear in the CMIF that is shown in Figure 4.15. Any of the axial modes that are identified are most likely in close proximity to bending or torsional behaviour. The identified modal frequencies are given in Table 4.5 with a comparison to the equivalent impedance results. The error in the first mode suggests that the true longitudinal frequency has been obscured by a neighbouring mode. On viewing the 3D mode shape, from which a 2D image has been taken in Figure 4.16, it is clear that the 1st identified mode is strongly coupled to a torsional mode. The 2nd mode shape, however, does not appear to be perturbed by any nearby modes. The 3rd mode is difficult to distinguish from nearby modes and the 4th mode is very clear in comparison. The significant errors in identifying the 1st and 3rd modes will limit any model updating scheme that is applied to the calibration assembly of the IHPA with MH attached. To mitigate this error it would be necessary to redesign the IHPA until it exhibits behaviour that is closer to the CPA when the MH is attached. The 1D mode shapes that are plotted in Figures 4.17 and 4.18 show that the 2nd and 4th longitudinal mode shapes have been obtained reliably whereas the 1st and 3rd modes are distorted. The design of this assembly would need to be iterated to decouple the distorted axial modes and this would improve the rod description of the system. However these discrepancies are absorbed into the application of the least squares schemes. Whether they are admissible depends on what an application of the scheme requires.

Table 4.5 Results for the Experimental Modal Analysis of the Monolithic Horn attached to In-House Piezoelectric Actuator with joint made through a steel stud set to 16Nm

Mode	Frequency (kHz)	Error to minimum impedance (%)
1st Longitudinal	9.98	9.7
2nd Longitudinal	21.3	0.1
3rd Longitudinal	24.6	1.4
4th Longitudinal	42.1	0.1

For comparison to the results of the IHPA with MH attached, EMAs are carried out when each JH with a Grade 5 Ti joint is instead attached. The obtained CMIFs for each test are shown in Figures 4.19-4.21; where the additional axial joint is set to 8, 12 or 16Nm. It is clear that for an amplitude threshold of $\approx 10^{-1}$V/V there are 5 modes that dominate the spectrum, instead of the desired 4 modes. This additional mode is coupled closely to the 3rd longitudinal mode and appears to have a torsional component. The peak that extends the most is identified as the longitudinal mode shape, however the mode shape is clearly

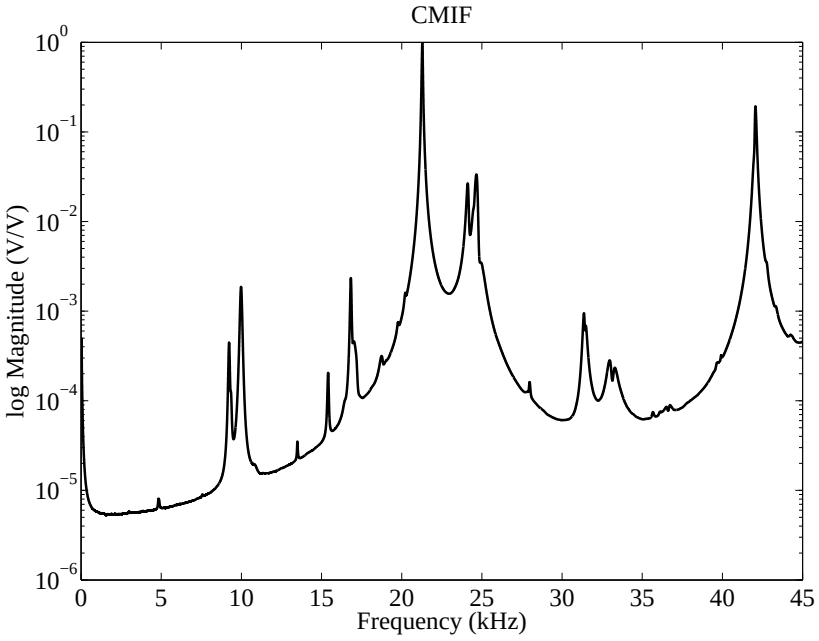

Fig. 4.15 Complex Modal Indicator Function for the In-House Piezoelectric Actuator with Monolithic Horn attached through a steel stud.

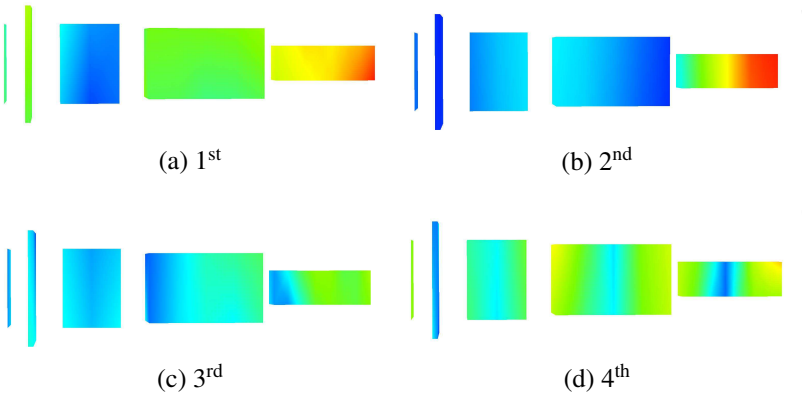

(a) 1st (b) 2nd

(c) 3rd (d) 4th

Fig. 4.16 Measured longitudinal mode shapes of the Monolithic Horn attached to the In-House Piezoelectric Actuator through a screwed threaded steel connector. The vibration nodes and anti-nodes are indicated following the colour map: ■ → ■.

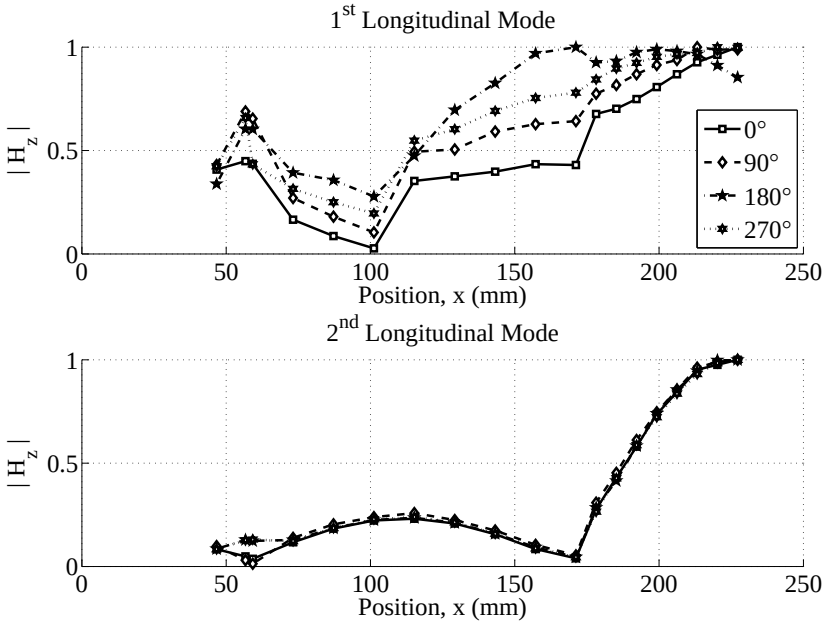

Fig. 4.17 Measured 1st and 2nd 1D longitudinal mode shapes evaluated along four lines of the Monolithic Horn attached to the In-House Piezoelectric Actuator through a screwed threaded steel connector.

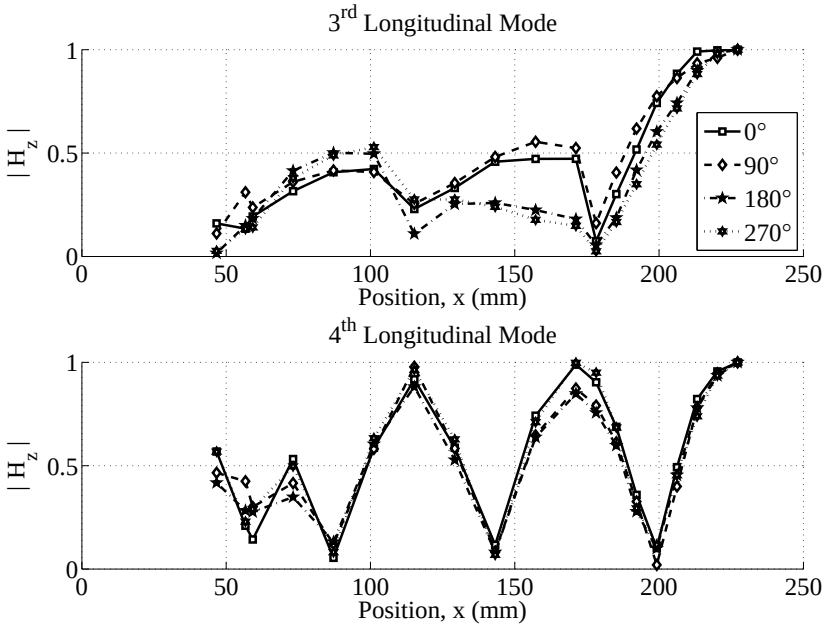

Fig. 4.18 Measured 3rd and 4th 1D longitudinal mode shapes evaluated along four lines of the Monolithic Horn attached to the In-House Piezoelectric Actuator through a screwed threaded steel connector.

distorted by the neighbouring mode. Other than this it should be noted that the mode that precedes the 2nd mode appears as motion limited to the measurement points of the flange. Therefore this is identified as a systematic measurement error. The flange is resting on a burnished aluminium holder that has been lined with felt, so the flange measurement is occasionally masked by tufts of felt. In order to include the flange on the 3D mode shape plots it was necessary to measure two points over the 2.5mm thickness. This thickness is in contact with the holder so there should be little movement at this location. Despite the dense modal behaviour of each CMIF, the 1D mode shapes displayed in Figures 4.22-4.27 show that the 2nd and 4th modes are comparable to the modes that are given in Figures 4.17 and 4.18. The second and third points from the left of each 1D mode shape are associated with the erroneous measurements from the flange. The 1st 1D mode shape from each EMA appears reasonably clear and it is possible to estimate the location of the vibration node. The 3rd axial mode shapes are clearly distorted, however they do give estimates of the nodal locations that are sufficient for comparison to the equivalent eigenvector derived through the distributed parameter model.

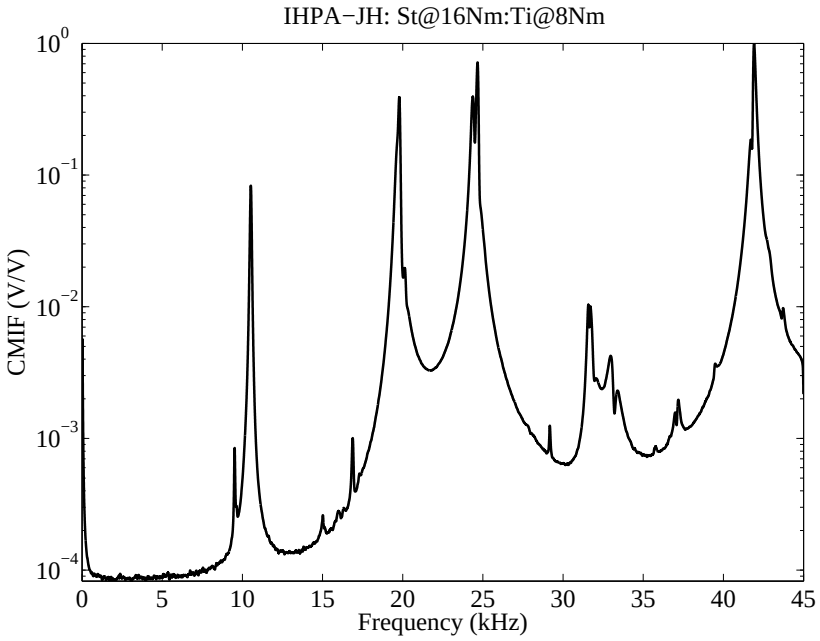

Fig. 4.19 Complex Modal Indicator Functions for the In-House Piezoelectric Actuator with a Jointed Horn set to 8Nm attached through a steel stud.

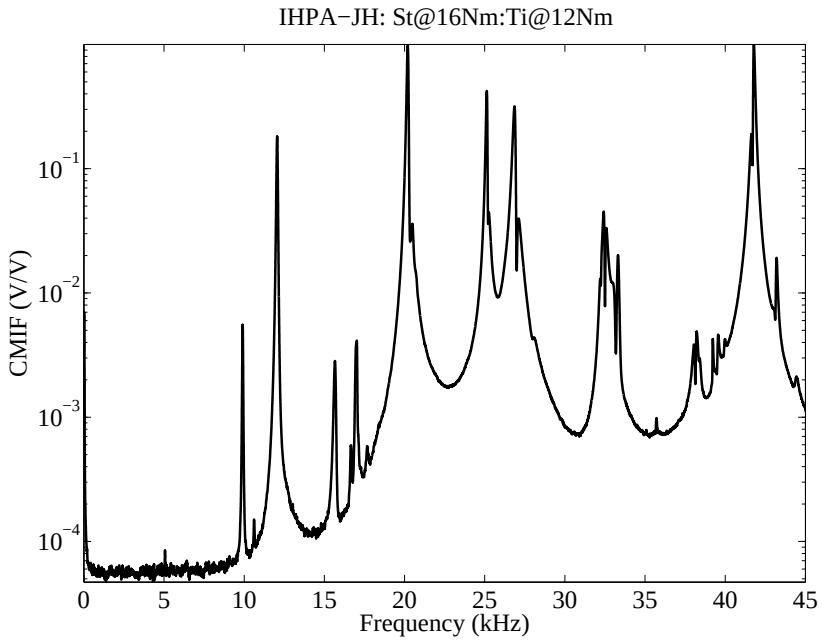

Fig. 4.20 Complex Modal Indicator Functions for the In-House Piezoelectric Actuator with a Jointed Horn set to 12Nm attached through a steel stud.

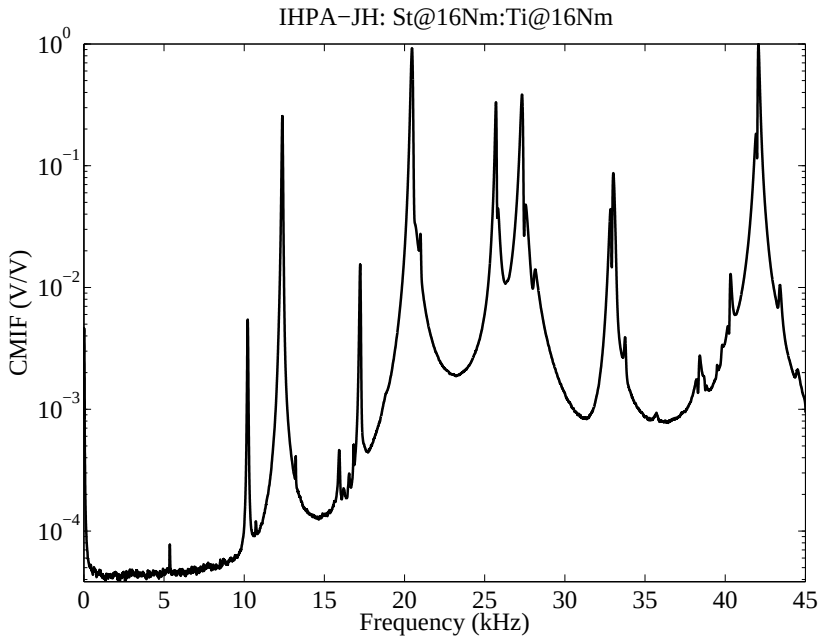

Fig. 4.21 Complex Modal Indicator Functions for the In-House Piezoelectric Actuator with a Jointed Horn set to 16Nm attached through a steel stud.

Table 4.6 Results of the Experimental Modal Analysis for each Jointed Horn attached to the In-House Piezoelectric Actuator with a joint made through a steel stud set to 16Nm

Longitudinal mode	Frequency (kHz) at torque		
	8Nm	12Nm	16Nm
1	10.5	12.1	12.3
2	19.8	20.2	20.5
3	24.4	26.9	27.3
4	43.1	41.7	41.9

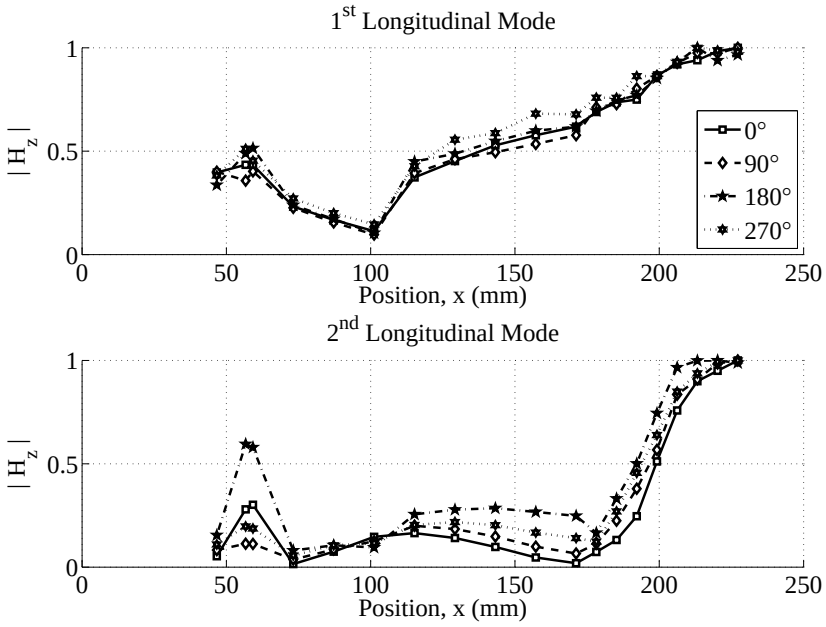

Fig. 4.22 Measured 1st and 2nd 1D longitudinal mode shapes evaluated along four lines of the Jointed Horn with cap tightened to 8Nm as it is attached to the In-House Piezoelectric Actuator through a screwed threaded steel connector.

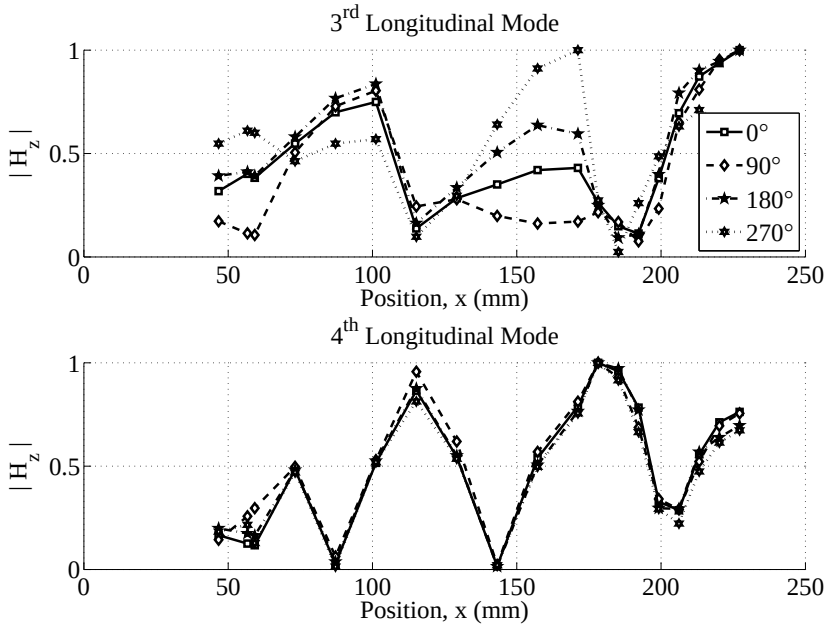

Fig. 4.23 Measured 3rd and 4th 1D longitudinal mode shapes evaluated along four lines of the Jointed Horn with cap tightened to 8Nm as it is attached to the In-House Piezoelectric Actuator through a screwed threaded steel connector.

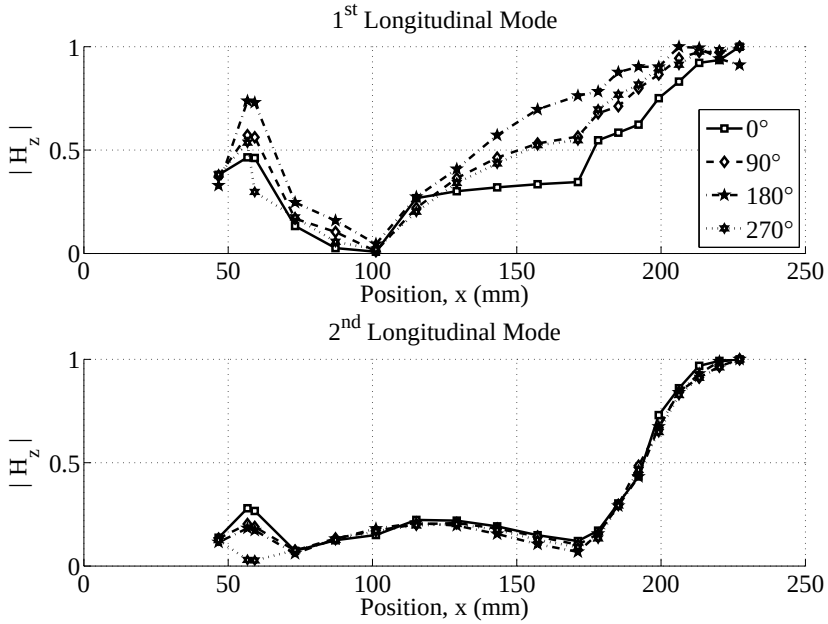

Fig. 4.24 Measured 1st and 2nd 1D longitudinal mode shapes evaluated along four lines of the Jointed Horn with cap tightened to 12Nm as it is attached to the In-House Piezoelectric Actuator through a screwed threaded steel connector.

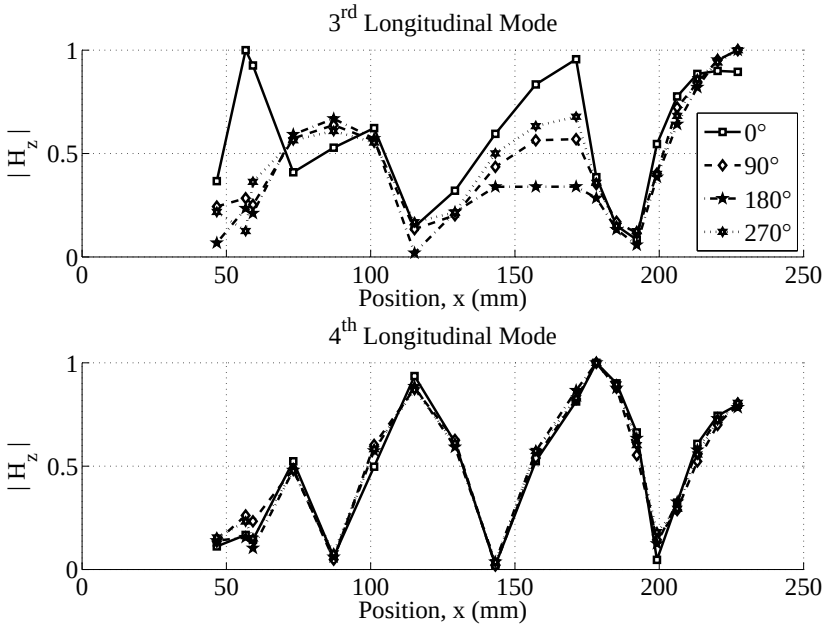

Fig. 4.25 Measured 3rd and 4th 1D longitudinal mode shapes evaluated along four lines of the Jointed Horn with cap tightened to 12Nm as it is attached to the In-House Piezoelectric Actuator through a screwed threaded steel connector.

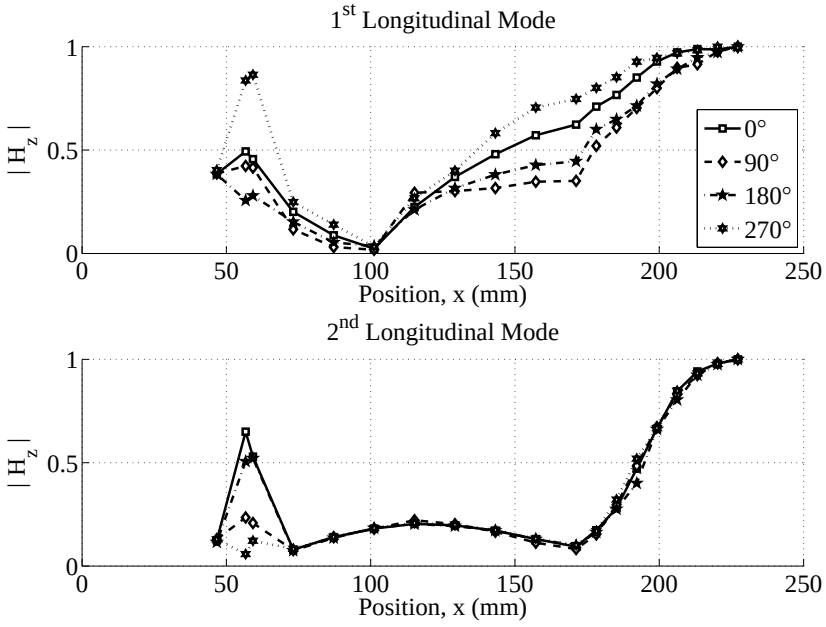

Fig. 4.26 Measured 1st and 2nd 1D longitudinal mode shapes evaluated along four lines of the Jointed Horn with cap tightened to 16Nm as it is attached to the In-House Piezoelectric Actuator through a screwed threaded steel connector.

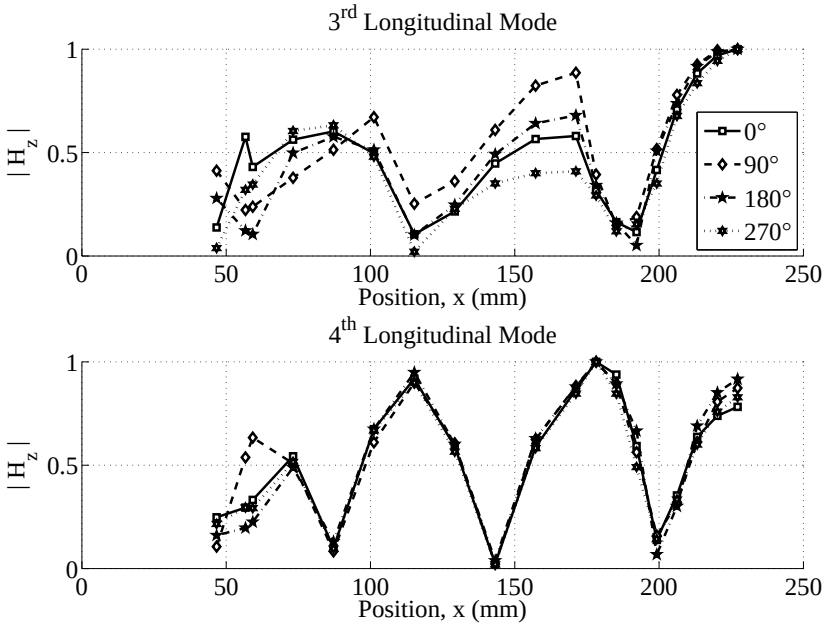

Fig. 4.27 Measured 3rd and 4th1D longitudinal mode shapes evaluated along four lines of the Jointed Horn with cap tightened to 16Nm as it is attached to the In-House Piezoelectric Actuator through a screwed threaded steel connector.

4.4.3 Discussion

It is clear that an assembly made through attaching an ultrasonic horn to the Commercial Piezoelectric Actuator (CPA) suits the proposed force identification scheme better than an equivalent assembly made with the In-House Piezoelectric Actuator (IHPA). The CMIF results from testing the CPA show four clear peaks over a frequency range where it is expected that four axial modes will exist. Matching the modal characteristics of a 3D Finite Element model to the manufactured IHPA would be a economical route to amending the design until better spacing of the modes is achieved. Despite the dense modal behaviour of each configuration that was tested, it was possible to identify a clear 2nd Longitudinal operating mode. Therefore, as long as the JH assemblies are excited at a frequency that is close to the operating mode of the equivalent MH assembly, then it should be appropriate to describe the system through the proposed distributed parameter rod schemes.

4.5 Numerical analysis through the linear calibration model

In order to apply the force identification framework, to experimental data, it must be assumed that it is appropriate to describe the High Power Ultrasonic (HPU) assemblies, made with the Monolithic Horn (MH), through the linear distributed parameter model. To achieve this it is assumed that the distributed parameter model should match the EMA results, that were given in Section 4.4, with minimal error. There are a set of homogeneous material parameters that define the components of the distributed parameter model and these will yield a unique set of eigenvalues through the solution to the Transcendental Eigenvalue Problem (TEP) in Section 3.7. These will only be obtained under the condition that the axial modes are the only modes that are excited and the measurement errors are negligible. For the indirect problem this set of eigenvalues does not represent a unique rod. A unique rod model will yield an infinite number of eigenvalues and each eigenvalue is associated with a unique eigenvector. However the converse is that a set of eigenvalues will yield an infinite set of rod parameter specifications. As a result, the eigenvector of the rod at an eigenvalue may not correspond to the expected mode shape at that frequency.

For a distributed parameter system, that is composed of waveguides governed by the wave equation [64] identified the unique parameters to reasonable accuracy. To do this the inverse problem for the rod was defined following theory from Gladwell [65]. The distributions of density and rigidity along a rod may be determined if two complete sets of spectral data associated with two different boundary conditions are known as well as the total mass. Singh [64] refines this to identifying the parameters of a stepped rod for which the two lowest fixed-free eigenvalues are known along with the lowest interlaced eigenvalue of the fixed-fixed configuration. Specifying the lowest eigenvalues of each configuration ensures that the unique rod is identified instead of solutions that are multiples of the rod. These solutions will feature the eigenvalues, but the spectrum will be shifted so that these eigenvalues do not align with the true eigenvectors. This scheme works well in identifying the wave speed of components based on the wave equation. However the analysis in Chapter 3 assumes that the rod elements have a spectrum relationship that is a function of the frequency. This added complexity means that the scheme by Singh [64] cannot be applied. As part of the current study a scheme was implemented to identify the Young's Modulus of components through the DTFM method and an Inverse Transcendental Eigenvalue Problem. However this was not successful because the ill-conditioning of the defined Jacobian matrix introduced large errors into the identified Young's Modulus and made it unsuitable for the current application.

Instead the complexity of the waveguide that has been adopted means it is more appropriate to calculate the forward TEP. This is calculated many times during each iteration of the Genetic Algorithm (GA). The evolutionary framework attempts to minimise the errors in the modal properties of the model within a set of given constraints. More background to this is the subject of Section 7.3.2.

The GA seeks to minimise a fitness function through a process that is allegorical to biological evolution. If this function can be applied to a point in the state space, then this point can be called an individual. In this analogy the individual can be thought of as a genome. The solver scores each individual through the application of the fitness function and these scores are found for a group of individuals at each iteration. This group is then known as a population. A larger population implies that there will be more diversity between individuals. Where diversity is calculated as the average distance between each individual in a population. At each iteration the GA will produce a new population by selecting individuals that have a good fitness score and using these to produce new individuals. When a new population is produced this counts as a generation. This process is distinctly separate to the inverse TEP because if the TEP is properly formulated it will converge on the true solution. The Genetic algorithm is not guaranteed to converge on a global optimum, so it is more likely fall into a minimum solution that is somewhere in the neighbourhood around the true solution [82].

4.5.1 Optimisation through the Genetic Algorithm

The linear calibration models are required to describe either the Commercial Piezoelectric Actuator (CPA) or the In-House Piezoelectric Actuator (IHPA) attached to the Monolithic Horn (MH). This is a linear calibration in the sense that the operating mode of these configurations does not shift significantly as the level of electrical excitation is increased. Whereas the same range of electrical excitation, to a configuration composed of a piezoelectric exciter and a Jointed Horn, will result in significant frequency overhang behaviour. The assumed distributed parameter model of the IHPA with the MH attached is shown in Figure 4.28. The CPA schematic is the same, but the copper electrode component 3 is not required, so there are only 16 components in the description. Due to the number of parameters in the model, it is not possible to estimate all of them through a model updating scheme. Appropriate assumptions must be chosen before any attempt to reconcile the model with the EMA data. The mass of the assembly can be measured and this will help to constrain the values of the

densities that are chosen for each component. For the CPA the mass of the outer casing and additional electronics cannot be reconciled and the actuator cannot be disassembled without causing damage. The mass of the MH is $m = 282.78 \pm 0.005$g. The assumed density for the Grade 5 Titanium is $\rho = 5500\text{kgm}^{-3}$. It is not possible to assume a single material density when a portion of a threaded bolt or stud passes through another diameter because the model is restricted to one dimension. Therefore an average density must be assumed as follows:

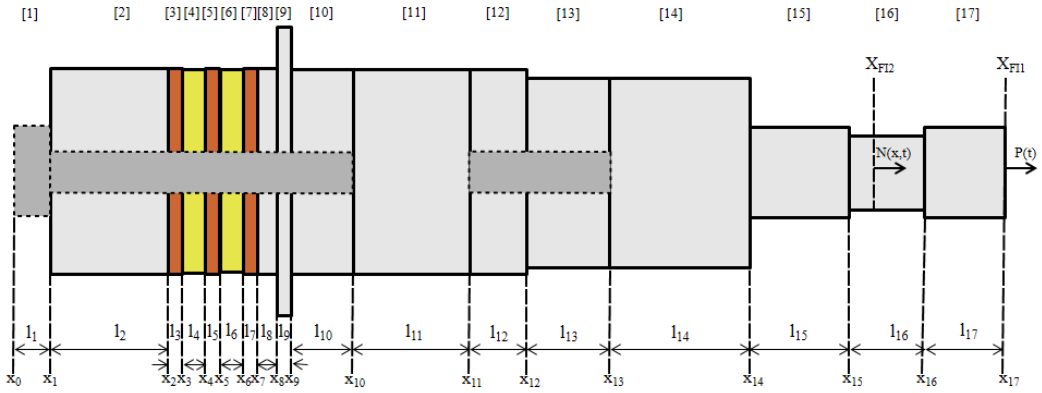

Fig. 4.28 Schematic of the stacked Piezoelectric Actuator that has been manufactured In-House with the Monolithic Horn attached.

$$\rho_i = \frac{(\rho_i A_i)_{in} + (\rho_i A_i)_{out}}{(A_i)_{in} + (A_i)_{out}} \tag{4.2}$$

where the material density is ρ_i and the cross sectional area is A_i for the ith component. The parameters denoted by $()_{in}$ are those associated with the bolt whereas those denoted by $()_{out}$ are the components that are held by the bolt. An average Young's modulus of the cross section is also assumed.

$$E_i = \frac{(E_i A_i)_{in} + (E_i A_i)_{out}}{(A_i)_{in} + (A_i)_{out}} \tag{4.3}$$

With these relations in place the main application of the GA is to estimate the Young's Modulus of the components that are held under an applied prestress in the actuator and assume that standard material data from MatWeb [83] represents a good estimate for the remaining components. The exact area of the flat portion of the horn is calculated by removing the area of the segments associated with the flats from the circular area of the horn. The following formula can be applied to calculate the area of the cross section at the flats [84]:

$$A_{Flat} = A_{Rod} - 2A_{Segment} \tag{4.4}$$

where:

$$A_{Rod} = \pi r_{16}^2 \tag{4.5}$$

$$A_{Segment} = \frac{r_{16}^2}{2} cos^{-1}(\frac{r_{16}-h}{r_{16}}) - (r_{16}-h)\sqrt{2r_{16}h-h^2} \tag{4.6}$$

where $r_{16} = \frac{\theta_{16}}{2}$ is the radius of the 16$^{\text{th}}$ component in the distributed parameter system and h = 1.626mm is the radial depth of the flat. For all of the horns that were tested A_{Flat} = 204.85 mm^2.

Commercial Piezoelectric Actuator

The full specification of the CPA is unknown so additional parameters must be estimated through the application of the GA. The optimisation can be constrained through the following details that are available in the customer specification and these are supplemented with some practical assumptions:

1. Prestress is applied to the piezoelectric stack through a 3/8 x 2 UNF Cap bolt. A common assumption is to assume an effective diameter for the bolt that is the mean of the major and minor diameters: $\theta = \frac{9.525+8.265}{2}$ = 8.895mm. The length of the shank is l = 50.8mm and it is assumed that the cap head has length l = 12.7mm and diameter θ = 19.05mm according to the bolt design guidelines given in Shigley [85].

2. The length of the back mass, two PZT disks, two copper electrodes and an unknown portion of the front mass is given as l = 52.5mm. All of these components, apart from the PZT, has an outer diameter of θ = 39mm.

3. The back mass is countersunk so that the rear face is flush with the bolt cap head. If it is assumed that the length of the bolt head is known then the remaining length of the back mass is taken as an unknown.

4. The front mass is composed serially of an unknown length, a length l = 1.5mm with a diameter θ = 64mm flange and a length l = 63mm with diameter θ = 34.5mm. The unknown length of the front mass is assumed to be shorter than the unknown length of the back mass. This should be true because the front of the piezoelectric stack should be reasonably close to the leftmost vibration node of the 2$^{\text{nd}}$ longitudinal mode. This should be positioned close to the flange.

5. From the end of the front mass a set of M10 internal threads have been machined to a depth of $l = 15$mm. The assumed effective diameter is: $\theta = \frac{9.85+8.14}{2} = 9.00$mm.

6. MatWeb [83] gives values of $E = 200\text{GNm}^{-2}$ and $\rho = 7850\text{kgm}^{-3}$ for the typical high tensile strength carbon steel that would be used to manufacture the cap bolt and the threaded rod. Grade 5 titanium has a listed modulus of $E = 114\text{GNm}^{-2}$ from which both the back and front masses have been manufactured. The assumed properties for the copper electrode are $E = 110\text{GNm}^{-2}$ and $\rho = 8930\text{kgm}^{-3}$.

7. It is assumed that the properties of the piezoceramic are the same as those that have been obtained for the PZT disks that are used in the IHPA. The PZT was supplied by CeramTec and is Sonox P8 with the following properties: Length $l = 5.02$mm, mass $m = 35.84$g, outer diameter $\theta_o = 37.92$mm and inner diameter $\theta_i = 16$mm. This yields $\rho = 7691\text{kgm}^{-3}$. The compliance matrix for the assumed transverse isotropic material be written as:

$$\mathbf{c}^E = \begin{bmatrix} c_{11}^E & -\nu_{12}c_{11}^E & -\nu_{31}c_{33}^E & 0 & 0 & 0 \\ -\nu_{12}c_{11}^E & c_{11}^E & -\nu_{31}c_{33}^E & 0 & 0 & 0 \\ -\nu_{13}c_{11}^E & -\nu_{13}c_{11}^E & c_{33}^E & 0 & 0 & 0 \\ 0 & 0 & 0 & (1+\nu_{13})c_{11}^E & 0 & 0 \\ 0 & 0 & 0 & 0 & (1+\nu_{13})c_{11}^E & 0 \\ 0 & 0 & 0 & 0 & 0 & \frac{1}{2}(1+\nu_{12})c_{11}^E \end{bmatrix} \tag{4.7}$$

where the elastic stiffnesses, c_{11}^E and c_{33}^E, are assumed to be the inverse of the elastic compliances, s_{11}^E and s_{33}^E, that are supplied by the manufacturer. This yields the following parameters: $c_{11}^E = 8.77\times10^{10}\text{Nm}^{-2}$ and $c_{33}^E = 7.30\times10^{10}\text{Nm}^{-2}$. The same assumption provided a good fit for Finite Element and analytical models of a Langevin Transducer by Al-Budairi [86]. Here the following Poisson's ratios were assumed: $\nu_{13} = 0.3$ and $\nu_{12} = 0$. This implies that $\nu_{31} = \frac{c_{33}^E}{c_{11}^E}\nu_{13} = 0.25$. To obtain the stiffness matrix at constant electric displacement Equation (3.14) can be invoked. This requires that the $\mathbf{d}$ and $\boldsymbol{\beta}^S$ matrices are also known. The material parameters that are required are summarised in Table 4.7 and have been obtained through MatWeb [83]. The stiffnesses at constant electric displacement are obtained as: $c_{11}^D = 4.88\times10^{10}\text{Nm}^{-2}$ and $c_{33}^D = -2.59\times10^{10}\text{Nm}^{-2}$. However the PZT will always be prestressed to a high degree in any HPU actuator, so the material parameters here can only be assumed as an initial guess in the optimisation of the model. The piezoelectric strain constants are given by the manufacturer as $d_{31} = -95\times10^{-12}\text{CN}^{-1}$, $d_{33} = 240\times10^{-12}\text{CN}^{-1}$,

$d_{15} = 380 \times 10^{-12}$CN^{-1} can be converted to piezoelectric stiffness constants through Equation (3.14). These are obtained as: $h_{31} = 26.6 \times 10^{8}$NC^{-1}, $h_{33} = -47.1 \times 10^{8}$ NC^{-1}, $h_{15} = -61.2 \times 10^{8}$ NC^{-1}.

8. Instead of assuming an unknown for each prestressed component, a homogeneous stiffness is assumed for each prestressed material, which is associated with each component that is tightened. This includes the bolt applying a prestress to the piezoelectric stack and the stud forming the joint between the actuator and the horn. Therefore five unknown stiffness, each written as a modulus, are estimated through an application of the GA for the following components:

   - The modified stiffness of the Grade 5 titanium of the front and back mass, which are held by the bolt that prestresses the piezoelectric stack.
   - The modified stiffness of the Grade 5 titanium of the front mass that is held by the stud that forms the joint between the actuator and the horn.
   - The modified stiffness of the high tensile steel from which the bolt that prestresses the piezoelectric stack is composed.
   - The modified stiffness of the high tensile steel from which the stud that makes the joint between the actuator and the horn is composed.
   - The modified stiffness of the PZT that is held under a prestress bolt.

Table 4.7 Assumed material parameters for Sonox P8

Parameter	Value	Units
s_{11}^{E}	11.4	$\times 10^{-12}$ m^{2}N^{-1}
s_{33}^{E}	13.7	$\times 10^{-12}$ m^{2}N^{-1}
d_{15}	3.80	$\times 10^{-10}$ CN^{-1}
d_{31}	-0.95	$\times 10^{-10}$ CN^{-1}
d_{33}	2.40	$\times 10^{-10}$ CN^{-1}
κ_{1}^{S}	7.08	$\times 10^{-9}$ Fm^{-1}
κ_{2}^{S}	7.08	$\times 10^{-9}$ Fm^{-1}
κ_{3}^{S}	4.78	$\times 10^{-9}$ Fm^{-1}

Table 4.8 lists the assumed parameters and where necessary these have been averaged through Equations (4.2) and (4.3). The values that are considered an initial guess, subject to the constraints in the numbered list above, have been asterisked. By choosing five

unknown stiffness's for each prestressed material, the initial guesses are updated through an application of the GA to give the results in Table 4.9. A set of MATLAB scripts and functions define a TEP inside the MATLAB solver `ga()`. The fitness function for the analysis compares the eigenvalues produced by the model to the modal analysis until its best identified value and mean evaluation value for all of the population reach a tolerance of 1×10^{-15}. The fitness function is as follows:

Table 4.8 1D approximation of the Commercial Piezoelectric Actuator with the Monolithic Horn attached.

i	E_i (GNm^{-2})	ρ_i (kgm^{-3})	θ_i (mm)	l_i (mm)	Description
1	134.52*(193.71)	6061	39.00	12.7	back mass and bolt head
2	118.47*(217.23)	5622	39.00	17.71*	back mass and bolt
3	35.48*(91.07)	7700	37.92	5.02	PZT and bolt
4	114.68	8874	39.00	0.50	copper electrode and bolt
5	35.48*(91.07)	7700	37.92	5.02	PZT and bolt
6	114.68	8874	39.00	0.50	copper electrode and bolt
7	118.47*(217.23)	5622	39.00	11*	front mass and bolt before flange
8	115.66*(221.35)	5545	64	1.50	front mass flange and bolt
9	119.72*(215.41)	5656	34.5	9.5	front mass and bolt after flange
10	114	5500	34.5	38.5	front mass
11	119.85*(90.36)	5660	34.5	15.00	front mass and stud
12	120.03*(90.48)	5665	34.00	17.00	stepped horn stud
13	114	5500	34.00	41.40	stepped horn before step
14	114	5500	17.00	18.20	stepped horn after step before flat
15	114	5500	16.15	20.90	stepped horn after step with flat
16	114	5500	17.00	16.30	stepped horn after step after flat

$$J = \frac{100}{4} \sum_{k=1}^{4} \left(\frac{\check{\omega}_k - \omega_k}{\omega_k} \right)^2 \tag{4.8}$$

where ω_k are the first four natural frequencies that are identified through a modal analysis of the device and $\check{\omega}_k$ are the eigenfrequencies that are found when the DTFM TEP is evaluated for an individual out of the population. The unique frequencies are isolated by rounding the results to the nearest 0.1Hz.

The update to the initial guesses have been given in brackets in Table 4.8 by accepting the estimates in Table 4.9. Clearly the GA has not identified the true parameters and this problem

cannot be solved without more information of the true distribution of the prestress through each tightened set of components. A scheme similar to the method that was applied by Singh [64] is likely to be that only way to achieve this estimate. However this scheme requires that the resonance and anti-resonance frequencies of the rod can be observed for two free-fixed and fixed-fixed boundary conditions. Fixing the HPU assembly through heavy clamping will likely dampen its response so that it is not distinguishable from the measurement noise floor. Another approach may be to test the assembly when the piezoelectric stack is under short or open circuit conditions. However this would mean that tests cannot be carried through electrical stimulation. This electrical stimulation is required to excite a reasonable number of longitudinal modes for the estimation. A standard impact test could excite the device from $\approx 0-7$kHz and therefore would not excite the lowest mode. Therefore for model updating purposes it would be more useful to consider a distributed parameter system that considered transverse vibration. EMAs with a very dense grid of measurement points and a high number of averages would be required to estimate the bending mode shapes. The antiresonance frequencies would likely be masked by the measurement noise floor.

Table 4.9 Parameters updated for the Commercial Piezoelectric Actuator with Monolithic Horn attached by application of the Genetic Algorithm

Parameter	Component	$\in i$	Stiffness (GNm^{-2})
$E_{Ti@Bolt}$	CPA back mass/front mass	1,2,7-9	223.79
$E_{St@Bolt}$	CPA bolt	1-9	97.70
$E_{PZT@Bolt}$	CPA PZT	3,5	90.68
$E_{Ti@Stud}$	CPA front mass/MH	11,12	86.24
$E_{St@Stud}$	CPA front mass/MH stud	11,12	146.81

The parameters in Table 4.8 are used to define a distributed parameter system according to Chapter 3 and the eigenvalues computed from the TEP are given in Table 4.10. These show that although the model has been tuned towards agreeing with the experimental results, there is no pattern in the errors to suggest that the optimal distributed parameter model has been identified. It is known that the adopted waveguide has a frequency range over which it will agree reasonably with an exact rod waveguide. It is less accurate as higher frequency rod behaviour is considered, so it would be expected that the error in its longitudinal modes should increase when higher modes are considered. Despite this, the comparison of the DTFM calculated eigenvectors to the experimental mode shapes in Figure 4.29 is reasonable. Any force estimation is made on the basis of these transfer function residues so it is

attempted based on this verification.

Table 4.10 Eigenvalues computed for the Commercial Piezoelectric Actuator with Monolithic Horn attached through the Distributed Transfer Function Method

Mode	Frequency (kHz)	Error to Experimental Modal Analysis (%)
1st Longitudinal	11.00	5.9
2nd Longitudinal	20.32	2.3
3rd Longitudinal	28.04	0.2
4th Longitudinal	38.84	0.2

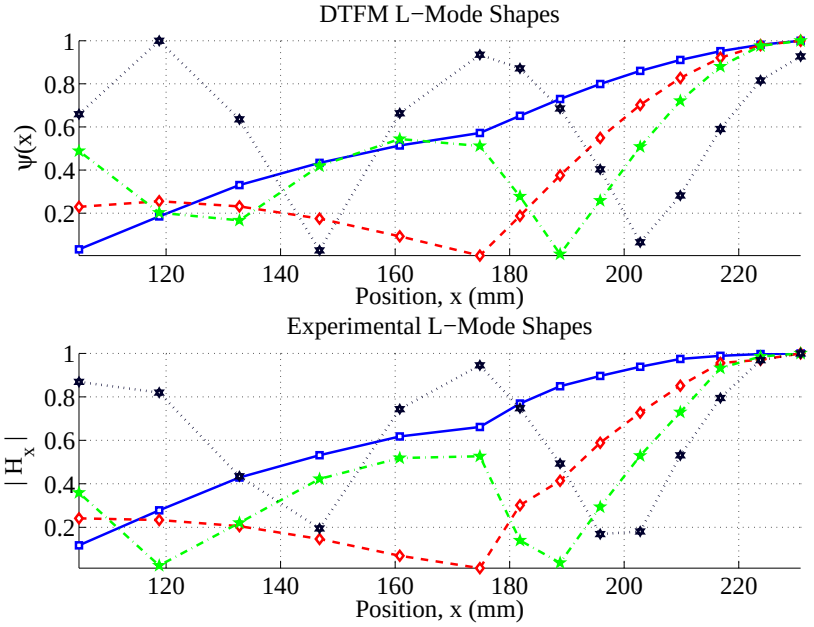

Fig. 4.29 Mode shapes found through the Distributed Transfer Function Method and Experimental Modal Analysis for the Commercial Piezoelectric Actuator with Monolithic Horn attached

In-House Piezoelectric Actuator

The In-House Piezoelectric Actuator is of similar construction to the Commercial Piezoelectric Actuator. However, there is no casing that masks the piezoelectric stack from view, so EMA measurement points can extend from its rear to the front of the Monolithic Horn.

The 3/8 UNF bolt is replaced with a M10 bolt of the same type that was machined to produce the M10 threaded stud. The length of each component can also be measured before the actuator is assembled, so the estimations made for the CPA dimensions are not required. Following the assumptions that have been set out in Section 4.5.1 yields the DTFM model given in Table 4.11. The estimations, that are are considered initial guesses to the optimisation, have been marked with an asterisk. The updated parameters are given in brackets and the stiffnesses, that have been obtained through application of the GA, are given in Table 4.12. As in the previous optimisation, it is clear that the obtained stiffnesses do not represent the true stiffnesses that have been induced through the components by prestress. However Table 4.13 shows that the error in the EMA identified eigenvalues and the DTFM estimated eigenvalues has been minimised to some extent. The comparison of the DTFM eigenvectors to the EMA mode shapes in Figure 4.30 confirms that there is good agreement in the location of the vibration nodes.

Table 4.11 1D approximation of the In-House Piezoelectric Actuator with Monolithic Horn attached.

i	E_i (GNm^{-2})	ρ_i (kgm^{-3})	θ_i (mm)	l_i (mm)	Description
1	200*(92.76)	7850	16.00	9.90	steel bolt head
2	118.82*(285.99)	5632	38.00	34.00	back mass and bolt
3	115.05*(103.83)	8869	38.00	0.50	copper electrode and bolt
4	35.71*(32.62)	7700	37.92	5.02	PZT and bolt
5	115.05*(103.83)	8869	38.00	0.50	copper electrode and bolt
6	35.71*(32.62)	7700	37.92	5.02	PZT and bolt
7	115.05*(103.83)	8869	38.00	0.50	copper electrode and bolt
8	118.82*(285.99)	5632	38.00	1.00	front mass and bolt before flange
9	116.30*(294.86)	5563	55.00	2.50	front mass flange and bolt
10	118.82*(292.01)	5632	38.02	19.00	front mass and bolt after flange
11	114	5500	38.02	25.50	front mass
12	118.82*(53.49)	5632	38.02	10.00	front mass and stud
13	120.03*(54.08)	5665	34.00	17.00	stepped horn stud
14	114	5500	34.00	41.40	stepped horn before step
15	114	5500	17.00	18.20	stepped horn after step before flat
16	114	5500	16.15	20.90	stepped horn after step with flat
17	114	5500	17.00	16.30	stepped horn after step after flat

Table 4.12 Parameters updated for the In-House Piezoelectric Actuator with Monolithic Horn attached by application of the Genetic Algorithm

Parameter	Component	$\in i$	Stiffness (GN/m^2)
$E_{Ti@Bolt}$	CPA back mass/front mass	1,2,8-10	297.47
$E_{St@Bolt}$	CPA bolt	1-10	92.76
$E_{PZT@Bolt}$	CPA PZT	4,6	34.57
$E_{Ti@Stud}$	CPA front mass/MH	12,13	51.16
$E_{St@Stud}$	CPA front mass/MH stud	12,13	92.76

Table 4.13 Eigenvalues computed for the In-House Piezoelectric Actuator with Monolithic Horn attached through the Distributed Transfer Function Method

Mode	Frequency (kHz)	Error to Experimental Modal Analysis (%)
1st Longitudinal	10.83	8.5
2nd Longitudinal	20.40	4.3
3rd Longitudinal	24.95	1.4
4th Longitudinal	38.49	8.6

Discussion

The discussion of the linear calibration models has demonstrated the difficulty in taking full advantage of the exactness of distributed parameter models from an experimental view point. Confidence in any implementation of an exact rod model to describe a physical system is limited if it is not possible to restrict the model updating problem so that it converges towards the true solution. In the case of a fixed-free rod, the mathematical theory for estimating the true distribution of parameters has been available for some time. Recently numerical schemes to exploit this have been developed. However finding the conditions under which an HPU device may be uniquely identified as a distributed parameter system remains an open question. A scheme of this type would indicate the true distribution of the prestress that is imbued in the components through the screwed axial joints. Without this information it is possible to form a good representation of the eigenvectors through general assumptions. However these estimations will have consequences in the proceeding chapter when the force identification will destabilise due to modelling errors.

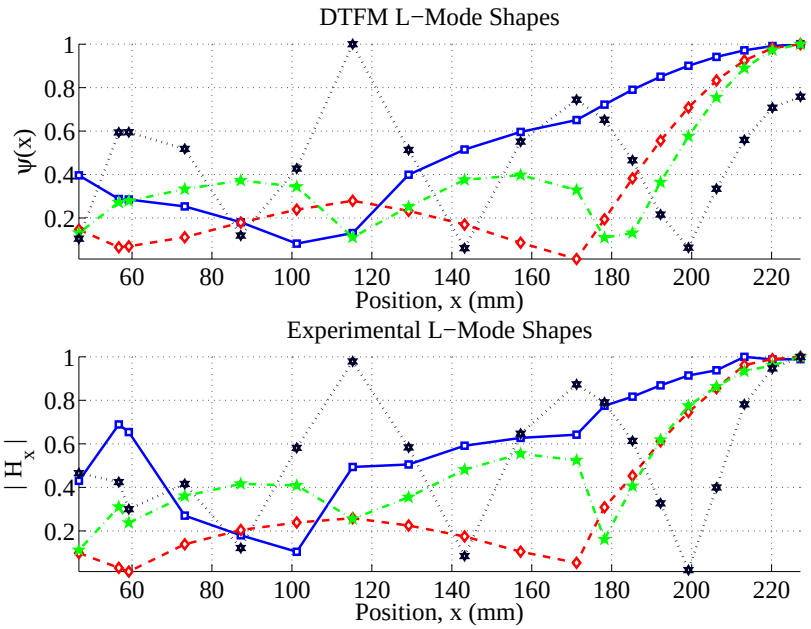

Fig. 4.30 Mode shapes found through the Distributed Transfer Function Method and Experimental Modal Analysis for the In-House Piezoelectric Actuator with Monolithic Horn attached.

4.5.2 Transient response

Each of the linear calibration models are excited through an electrical boundary condition that is applied as an external force at either node 5 or 6 for the CPA or IHPA respectively. This is where the foremost cross section of PZT is positioned. According to Equation (3.45) the force takes the form:

$$q_i(\tau) = G\frac{h_{33}}{|Z|}V sin(\omega_2 \tau) \tag{4.9}$$

where the assumed parameter values are given in Table 4.14. A set gain of G has been chosen to produce an undamped transient response that is representative of the amplitude that is observed when the excitation signal is set similarly in the experiments of the proceeding chapter. For the IHPA experiments this excitation signal is the voltage output from a function generator, which is then amplified through a power amplifier with a gain of 53dB. The power amplifier is not impedance matched to the IHPA, so there is reflected power that cannot be acquired real time. The real time voltage signal that is experienced by the stack has not been observed, so the gain in Table 4.14 has been applied as a correction factor.

The results for both piezoelectric actuators are shown in Figures 4.31 and 4.32. The CPA

assembly has been evaluated over a shorter time window than the IHPA assembly and it does not reach steady state vibrations. For the longer time window the IHPA assembly has not reached steady state vibrations either and only a small portion of the total response has been shown. Albareda *et al.* [87] described that the limitation of testing the transient vibration of a High Power Ultrasonic (HPU) device is the occurrence of beat phenomenon due to closely spaced vibration modes around the operating resonance. This represents a serious limitation in the accuracy of the current waveguide model, which can only be improved by introducing a waveguide that features coupled equations of motion to represent higher order wave modes. A zero header is applied to the input signal, in the current study, so that the first 170 samples are zero. This can be very instructive when testing the inverse scheme because instabilities are most predominant at the boundaries of the time window that is being evaluated. Therefore, when the signal is reconstructed, these instabilities can be viewed directly. This can be applied directly to experimental tests and clarifies the results artificially without a change in the the modelling assumptions. With a set of simulated transient responses, the ability of the inverse DTFM reconstruction can be evaluated to some extent. However, it is not possible to account for the mismatch between the assumed model and the physical system through simulated results.

Table 4.14 Parameters for transient simulations of the linear calibration models

Parameter	Value for assembly		Units	Description
	CPA	IHPA		
τ_0	0		µs	Initial time
τ_f	808	7336	µs	Final time
N	200	1835	-	Number of samples
$\Delta\tau$	4	6	µs	Time step
h_{33}	-47.1		$\times 10^8$ NC^{-1}	Piezoelectric strain constant
V	$100, 200, 300, 400, 450$		mV	Applied voltage
G	1.5		$\times 10^{-6}$	Gain
$\|Z\|$	43.0	3.6	Ω	Stack impedance at operating mode
ω_2	20.32	20.4	$\times 10^3 \cdot 2\pi rad s^{-1}$	Operating mode frequency
X_1	0.2307	0.2272	m	1st Observation location
X_2	0.2037	0.1960	m	2nd Observation location

In order to test the reconstruction of an axial joint force, which is relative to the linear calibration model, further transient simulations of the IHPA assembly are carried out with an additional distributed load applied over the length of the model that contains the flats. The

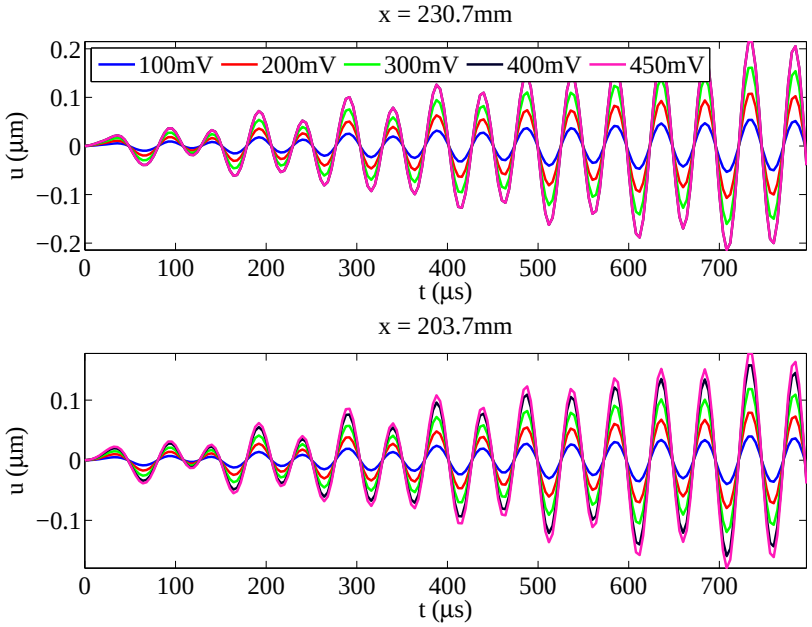

Fig. 4.31 Simulated transient response of the Commercial Piezoelectric Actuator with Monolithic Horn attached through the Distributed Transfer Function Method

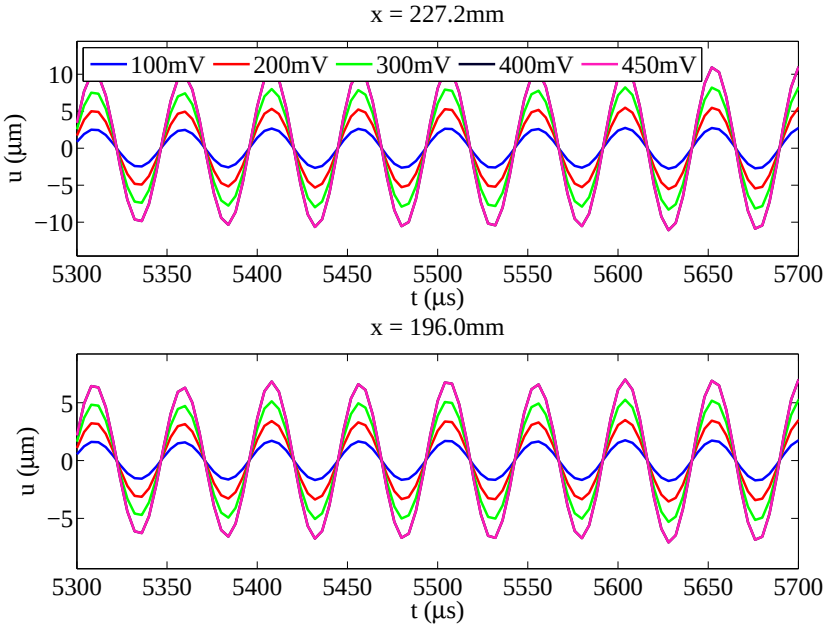

Fig. 4.32 Simulated transient response of the In-House Piezoelectric Actuator with Monolithic Horn attached through the Distributed Transfer Function Method

model is again defined through the parameters in Table 4.14. When the MH is replaced with a JH, the mechanical impedance will increase, due to the presence of the joint. This will in turn change the overall electrical characteristics of the device. For example, a comparison of the impedance results in Figure 4.5 shows that for an axial joint that is set to 8Nm, through Grade 5 Titanium threads, the change in the electrical impedance characteristics of the operating mode are as follows: minimum $|Z| = 3.6\Omega \rightarrow 29\Omega$ and maximum $arg(Z) = 150° \rightarrow 100°$. However, in order to test the proposed scheme for joint force identification, the JH assembly must be actuated through the same input force as the MH assembly. Therefore, for the purpose of this test, the model is subjected to the same input excitation that is given in Equation 4.9 and defined in Table 4.14. An additional load is applied over component $i = 16$ through the following form:

$$f_i(\xi,\tau) = H[\xi - (x_j - x_a)] - H[\xi - (x_j + x_b)]N_i(\tau) \tag{4.10}$$

where ξ is an assumed uniform spatial distribution through the i$^{\text{th}}$ component that starts at $x = x_a$ and ends at $x = x_b$. Also x_j is the x position of the bearing surface. It is assumed the most practical joint force identification would require the force to be estimated for a spatial distribution that is equivalent to the static prestress, which emanates from the bearing surface, due the tension of the screwed threads. Without a scheme whereby this can be estimated accurately, it is only possible to estimate the temporal distribution of the joint force for an assumed prestress. Clearly the prestress will be highest at the bearing surface and will decay with distance. An initial estimate, that is part of a least squares inference, is the uniform distribution that gives some mean between the dynamic force and the applied prestress. In the proceeding simulations the joint force is applied as a sinusoidal force that is modulated by a low frequency wave:

$$N(\tau) = a[1 + b \cdot sin(\omega_b \tau)]sin(\omega_j \tau); \tag{4.11}$$

where arbitrary values are chosen qualitatively based on the experimental observations of Chapter 5. They are as follows: Amplitude $a = 1$kN, modulation $b = 0.1$, frequency of JH response $\omega_j = 2\pi \cdot 20 \times 10^3 \text{rads}^{-1}$ and modulation frequency $\omega_b = 2\pi \cdot 5 \times 10^3 \text{rads}^{-1}$. It is expected that these parameters will vary for a change in the input excitation to the HPU device. However, for the following test, the same joint force has been applied for all input excitations. The responses are shown in Figure 4.33 and the assumptions that have been made are equivalent to those that will be applied in the proceeding Chapter 5.

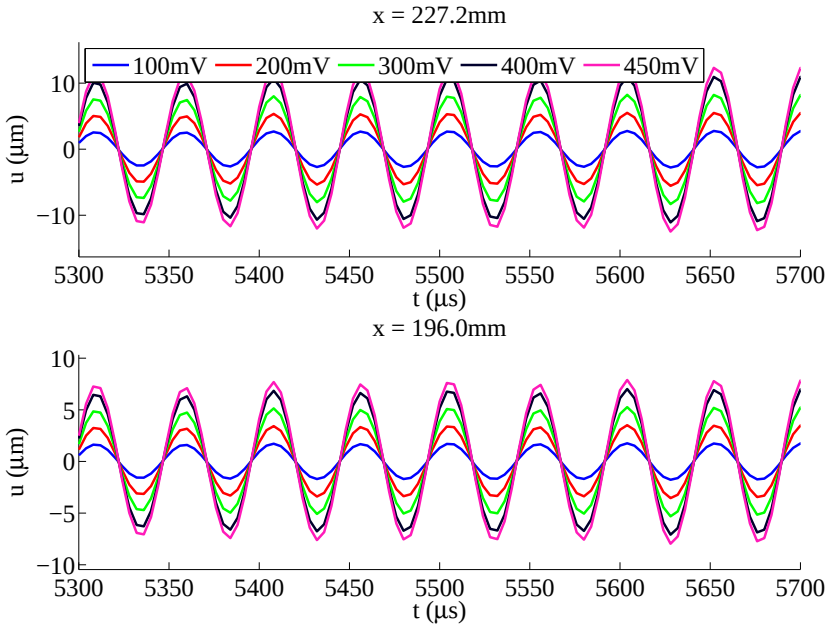

Fig. 4.33 Simulated transient response of the In-House Piezoelectric Actuator with a Jointed Horn attached calculated through the Distributed Transfer Function Method.

Only the real eigenvalues of the model have been considered so far. Introducing a retarding force that is proportional to velocity will produce complex eigenvalues. This will change the state space of the model, which may have some influence on the reconstruction problem. To develop some insight of this, the input excitation only tests of the IHPA are repeated for $V = 450\text{mV}$ and the retarding force is varied. A uniform damping coefficient is assumed for each component in the model with the form: $\eta_i = 2\pi \cdot 40 \cdot \rho_i \cdot d$. Where d is varied to modify the level of damping, ρ_i is the density of the i^{th} component and 40kHz is the frequency range. This form has been recommended by Doyle [52] where it improved the stability of the inverse estimations. For the SEM or DTFM this will increase the bandwidth of each peak in the transfer function. Figure 4.34 demonstrates that successful energy dissipation is not achieved through this method. Without an outlet for the dissipated energy to propagate, it is reflected back through the waveguide. Therefore it is necessary to modify the boundary conditions of the distributed parameter system or incorporate an alternative damping strategy. The investigation by Spak *et al.* [88] implements both viscous damping and hysteresis damping into distributed parameter beam models to describe space flight cables.

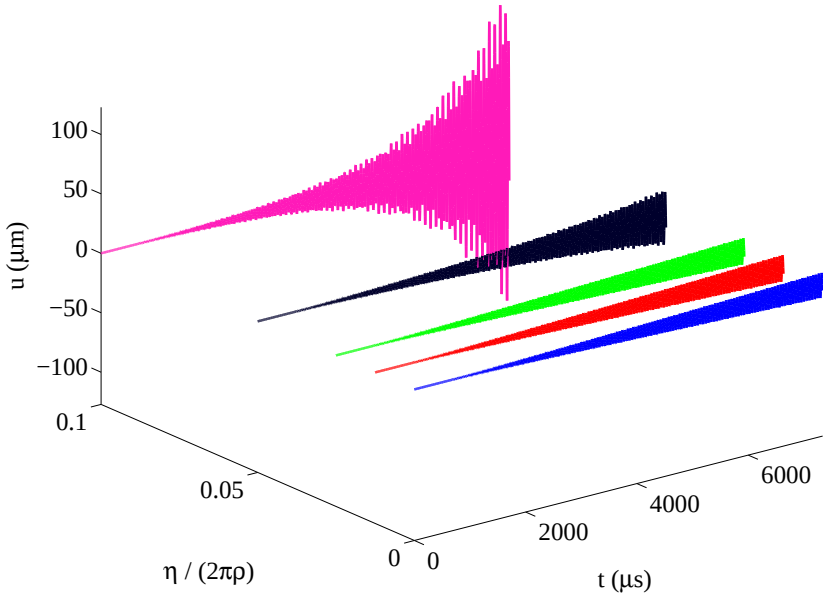

Fig. 4.34 Damped transient response of the In-House Piezoelectric Actuator with the Monolithic Horn attached calculated through the Distributed Transfer Function Method.

4.5.3 Reconstruction of the input

The inverse problem is computed from simulated data by means of a discretised model. This is known as an inverse crime when the discretisation of the problem is the same forwards as it is backwards. In order to produce an appropriate test of the distributed parameter model, the temporal distribution of the forwards problem is downsampled, through interpolation, before attempting to recover the input from simulated transient data. An in-built MATLAB function, `interp1()`, is applied to achieve this. The results associated with the CPA and the IHPA are downsampled to $N = 150$ and $N = 1500$ temporal points respectively. The input to be reconstructed is represented through Equation (4.9) and the original signals that are used in the transient simulations are given in Figure 4.35.

The reconstruction of the input is attempted via three methods: least squares inversion of an ill-conditioned system, Truncated Singular Value Decomposition (TSVD) regularisation and Tikhonov regularisation. As discussed in the previous chapter, the condition of the system is the ratio of the non-zero values in the first and last rows of the matrix of singular values. The least squares inversion is handled by the MATLAB backslash operator algorithm. The impulse response matrix will always be a lower triangular matrix, so the backslash operator algorithm makes the implicit choice of solving the system through a for-

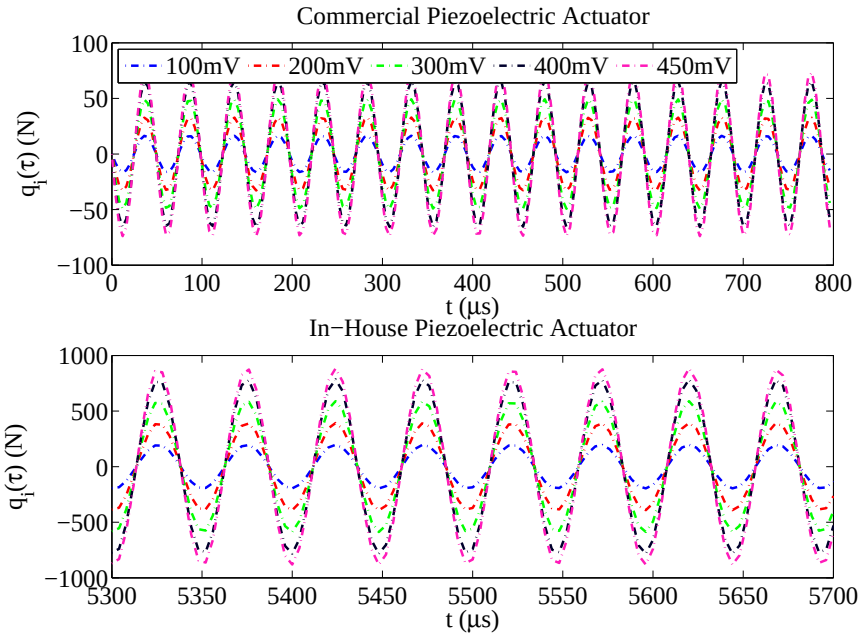

Fig. 4.35 Input signals for simulated transient responses of the linear calibration models.

ward substitution algorithm [89]. Higham [90] suggests that this may not be the optimal decision for solving a triangular system and recommends that LU, QR and Cholesky factorisations are implemented. However, as part of a large set of scripts and functions, the use of the backslash operator is most efficient. Testing of the factorisation methods directly is omitted in favour of regularisation strategies. TSVD regularisation can be carried out through the pseudoinverse function in MATLAB, `pinv()`. This involves first calculating the Singular Value Decomposition (SVD) and then forming a pseudoinverse that satisfies four matrix conditions. Implementing the TSVD involves setting singular values below a specified tolerance to zero before calculating the pseudoinverse [91]. The Tikhonov regularisation has been implemented manually through the algorithm provided in Mueller & Siltanen [68] that has been given at the end of Chapter 3.

The results of reconstructing the input from the CPA transient responses are given in Figure 4.36. It is clear that the solution through forward substitution is very unstable at the end of the distributed rod system. The solution at the point, which is situated closer to the application of the load, achieved a more stable solution. However the error is clearly increasing as more samples are evaluated. In the case of both solutions it appears that the reconstruction is tending to become more asymptotic closer at the upper edge of the observation time window. This feature is retained in results obtained through the regularisation methods.

These are shown in Figures 4.37 and 4.38. Both regularisation methods obtain a reasonable reconstruction of the input signal. The TSVD regularised solutions were obtained by zeroing all of the singular values below the set tolerance $\epsilon = 3.1623 \times 10^{-11}$. The Tikhonov regularised solutions have been found through the L-curve method that is given in Section 3.11.4. For locations X_1 and X_2, the optimal values of the regularisation parameter were $\Gamma_{X_1} = 3.4305 \times 10^{-17}$ and $\Gamma_{X_2} = 2.1544 \times 10^{-17}$. Evaluating the inverse problem at a location that is closer to the location of the estimated signal requires less regularisation. Less regularisation implies that the identified solution is closer to the true solution. Both of the regularisation methods obtain solutions of sufficient accuracy for the requirements of the force identification problem. The Tikhonov solution is better at retaining the amplitude of the samples at the extremity of the observation window. This is due to the availability of a method to optimise the regularisation parameter in this case.

An equivalent set of results are produced by reconstructing the input that was applied to the IHPA model through the transient responses in Figure 4.32. The solutions that are obtained through forward substitution are given in Figure 4.39. The solutions that are associated with X_1 are significantly unstable. They grow to an increased amplitude as a result of evaluating a longer time interval. Only a small number of samples have been displayed, so the extremities of the observation window are not shown. The solutions obtained from X_2 follow a similar pattern to the solutions that were found from X_2 in the previous example. However, the amplitude has greatly exceeded the expected level that is found from the input signals that are shown in Figure 4.35. The TSVD and Tikhonov regularisation strategies recover the input signals with reasonable accuracy. The tolerance of the TSVD regularisation is selected so that it is the same as the previous example. Only a small number of samples out of the total observation window are displayed in Figure 4.40. The results associated with location X_1 show that the TSVD regularisation does not succeed in preserving the edges of the signals. The phases of the signals are faithfully reconstructed, but it is not possible to recover the uniform amplitude that was defined in Figure 4.35. The amplitudes that are associated with X_2 are improved, but the exact input is not recovered due to losses at the edges of the signals. The Tikhonov regularised solutions, that are associated with X_1, improve on the TSVD regularised solutions. Better edge preservation is achieved. However the results from X_2 appear to be worse. When Tikhonov regularisation is applied, the regularisation parameter is chosen manually by selecting a point on the L-curve. There is some interpretation involved in selecting the corner of the L-curve, so it is not guaranteed that the optimal value of regularisation parameter will be chosen. Therefore the quality of the solutions can vary.

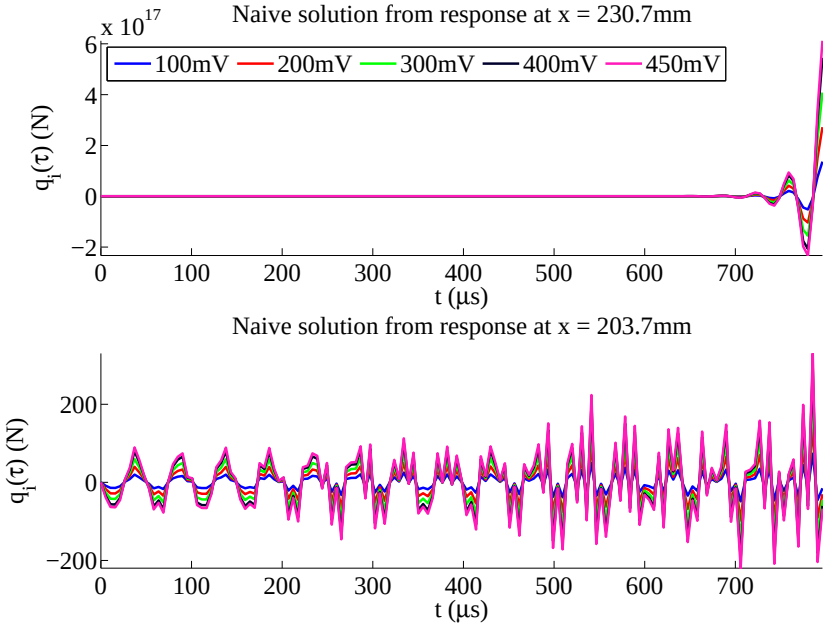

Fig. 4.36 Reconstruction through Forward Substitution of the input force for the linear calibration model of the Commercial Piezoelectric Actuator.

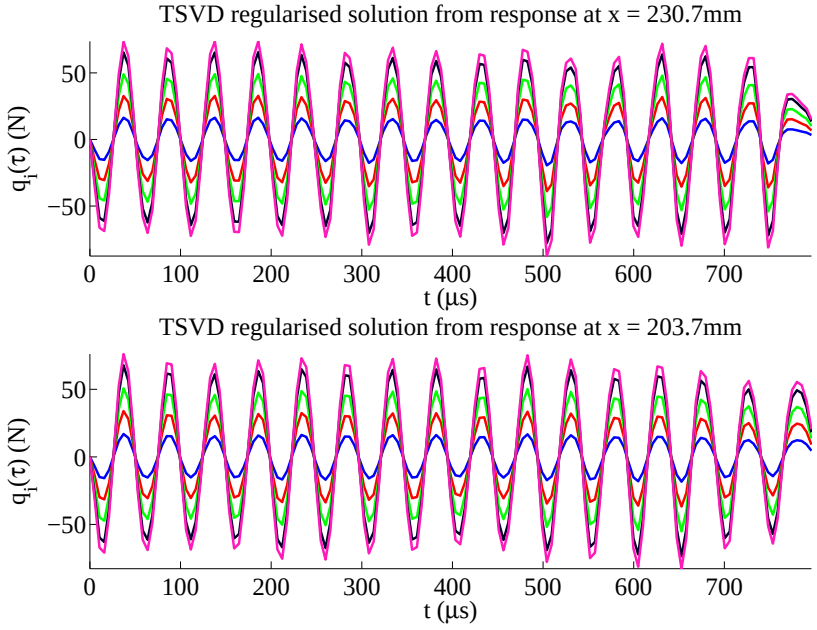

Fig. 4.37 Reconstruction through Truncated Singular Value Decomposition of the input force for the linear calibration model of the Commercial Piezoelectric Actuator.

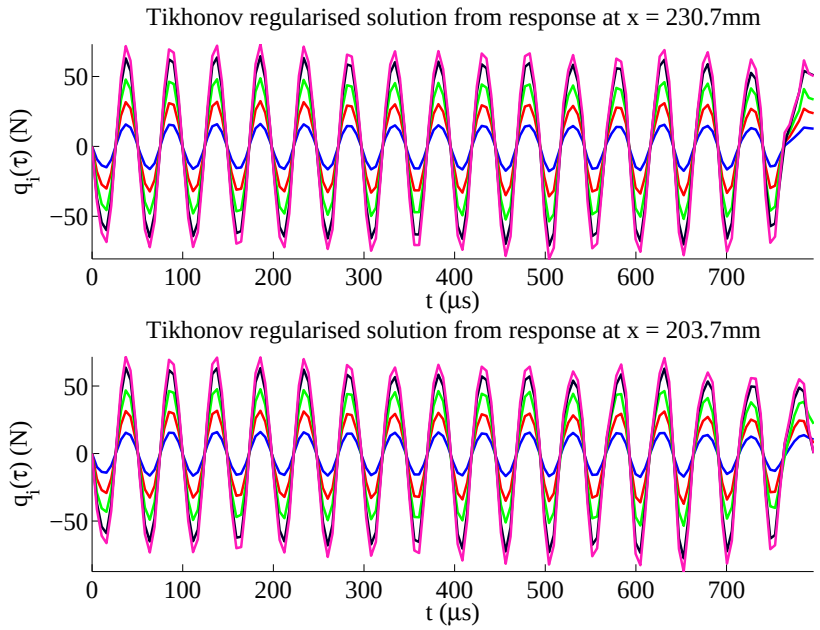

Fig. 4.38 Reconstruction through Tikhonov Regularisation of the input force for the linear calibration model of the Commercial Piezoelectric Actuator.

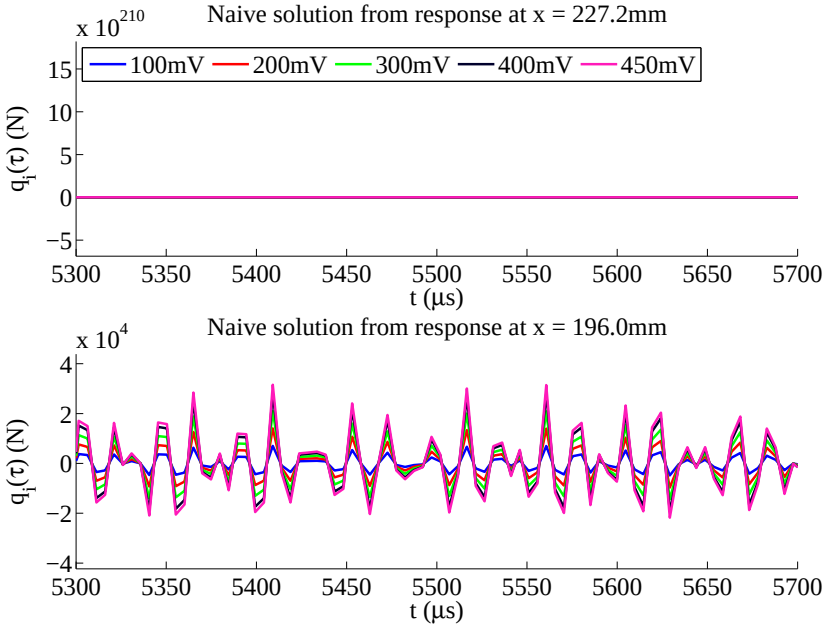

Fig. 4.39 Reconstruction of the input force $q_6(t)$ through forward substitution for the linear calibration model of the In-House Piezoelectric Actuator.

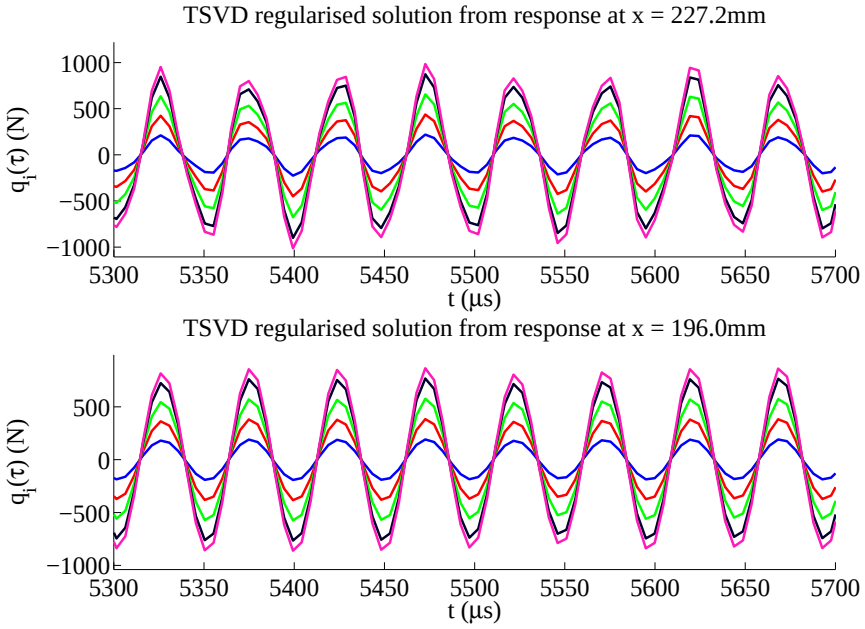

Fig. 4.40 Reconstruction of the input force $q_6(t)$ through Truncated Singular Value Decomposition for the linear calibration model of the In-House Piezoelectric Actuator.

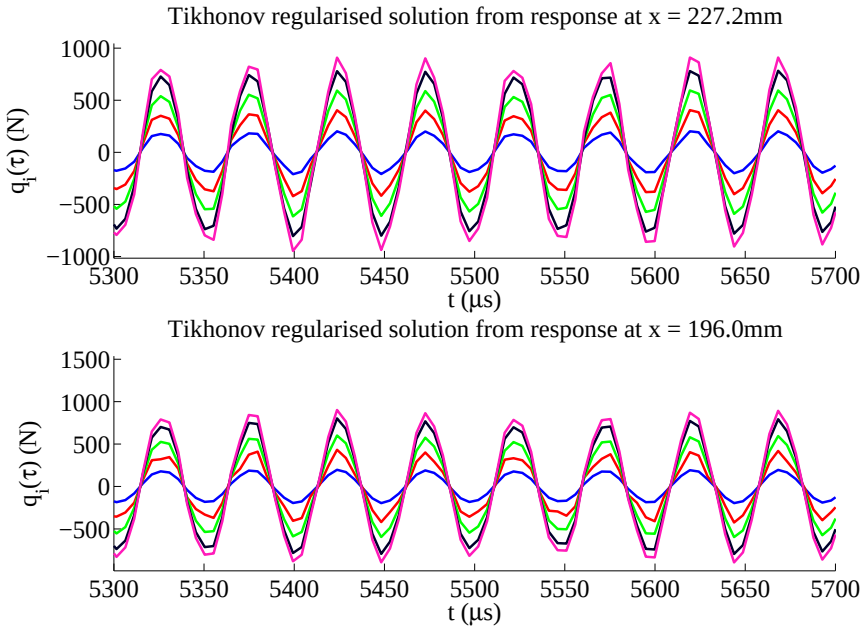

Fig. 4.41 Reconstruction of the input force $q_6(t)$ through Tikhonov Regularisation for the linear calibration model of the In-House Piezoelectric Actuator.

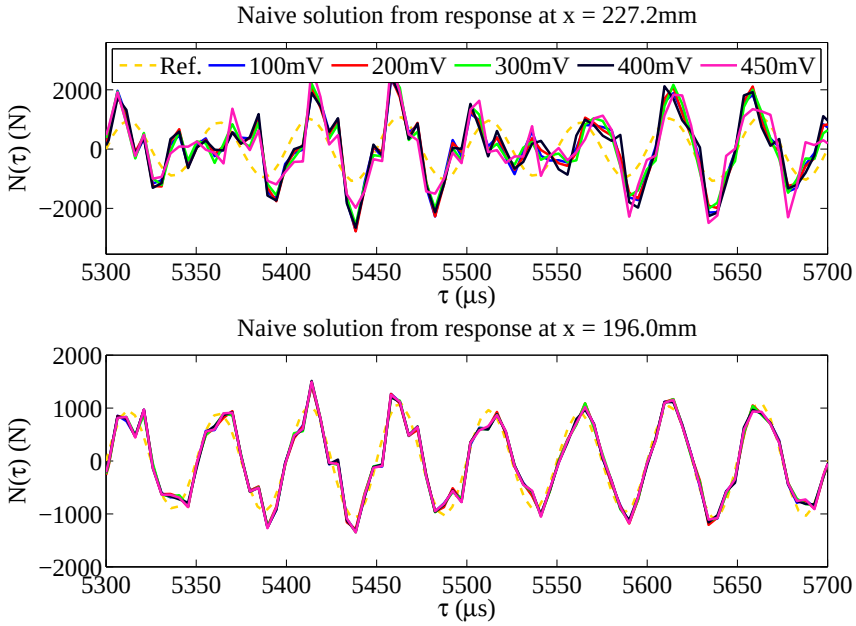

Fig. 4.42 Reconstruction of the joint force $N(x,t)$ through forward substitution for the linear calibration model of the In-House Piezoelectric Actuator.

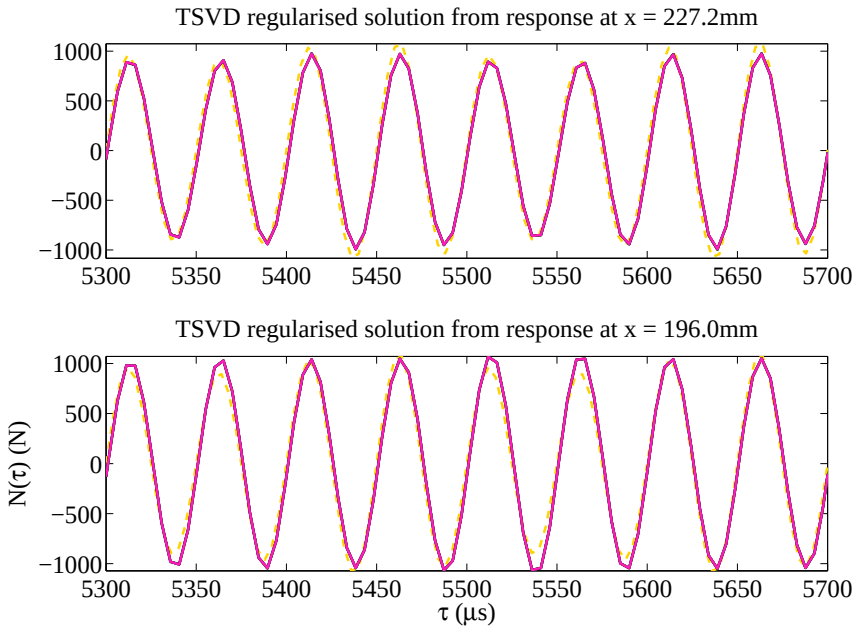

Fig. 4.43 Reconstruction of the joint force $N(x,t)$ through Truncated Singular Value Decomposition for the linear calibration model of the In-House Piezoelectric Actuator.

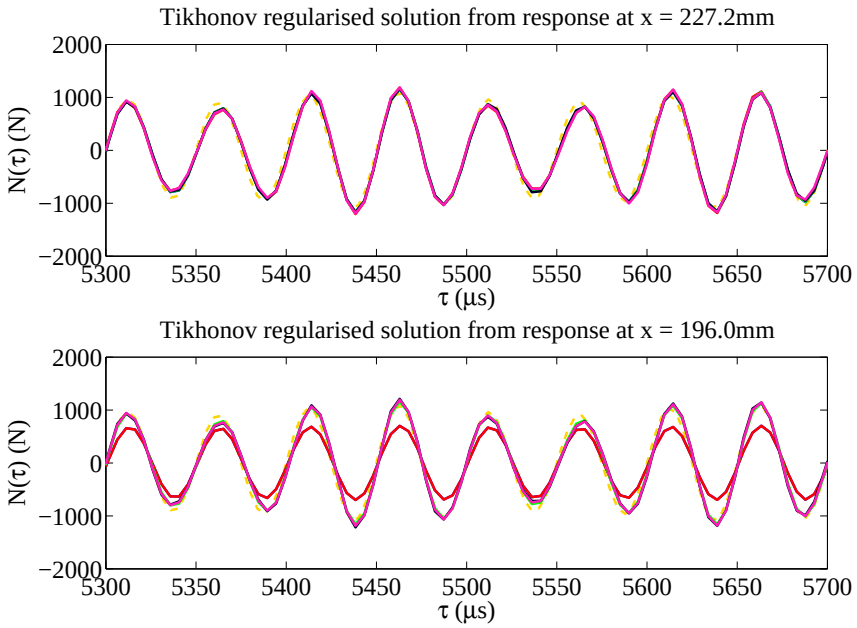

Fig. 4.44 Reconstruction of the joint force $N(x,t)$ through Tikhonov Regularisation for the linear calibration model of the In-House Piezoelectric Actuator.

A further question that must be asked about reconstructing the input through the proposed method is: What happens to the estimation due to errors between the model and the physical system? The simplifications that were required to make use of the current Distributed Transfer Function Method (DTFM) meant that each waveguide component could only be described by a single equation of motion. This rules out the physical coupling of the axial, transverse and rotational motions of the rod-like HPU system. Attempts to take full advantage of the exact DTFM description were also hindered from the lack of a hybrid experimental method to estimate the parameters of the distributed parameter system through its modal characteristics. Therefore, it is difficult to minimise the error between the EMA and DTFM results.

To evaluate the influence of modelling errors, the input force is reconstructed from models of the IHPA, that have been modified relative to the original model, which has the eigenvalues listed in Table 4.13. In Modification 1 the Young's Modulus of each component is reduced by 10% and this yields the eigenvalues that are given in Table 4.15. The input force is recovered from the transient responses that are associated with the 450mV excitation. Figures 4.45 and 4.46 show a comparison of the reconstructions from the original and modified models. Each figure only shows a small number of samples associated with the beginning of the estimation or the observation time window that is of interest. When the

first 2ms is viewed, the desired result is obtained over the time period 950 – 1250μs. This is only successful when the reconstruction is associated with location X_1 and not X_2. This is to reconstruct close to the correct amplitude of signal, whilst accepting that there will be a error in the phase because of the error in the eigenvalues. However, due to the ill-conditioning of the computation, the estimation error is amplified as the number of samples increases. The trend of the error is not linear, however a best line fit to the error yields a growth rate of 1.8N/μs. When the observation window of interest is viewed, as shown in Figure 4.46, the erroneous signal is approximately 9 times the amplitude of the actual signal. However over this window the phase error is constant.

For Modification 2 the Young's modulus of the component, which is associated with the flat portion of the assembly, is reduced by 40 GNm^{-2}. This yields the eigenvalues in Table 4.16 and the subsequent reconstructions are shown in Figures 4.47 and 4.48. The initial portion of the estimation shows some partial reconstruction associated with location X_1 and not X_2. The growth rate of the error in this case is 1.7N/μs and for the observation window, that is of interest, the erroneous signal is approximately 9 times the actual signal. The phase error is reasonably constant for this length of time, which is shown in Figure 4.48. Overall, these examples have shown that the reconstruction of a relatively steady signal from an erroneous model will result in a reconstruction that is masked by an error that increases steadily as the number of evaluated samples increases.

Table 4.15 Modification 1 eigenvalues computed for the In-House Piezoelectric Actuator with Monolithic Horn attached through the Distributed Transfer Function Method

Mode	Frequency (kHz)	Error relative to original model (%)
1st Longitudinal	10.27	5.17
2nd Longitudinal	19.35	5.15
3rd Longitudinal	23.67	5.13
4th Longitudinal	36.52	5.12

4.5.4 Reconstruction of the joint force

The final set of reconstructions involves obtaining the force that has been simulated through the temporal and spatial descriptions in Equations (4.10) and (4.11) respectively. This has been applied to the IHPA model, as it is excited through the boundary load q_6, that takes

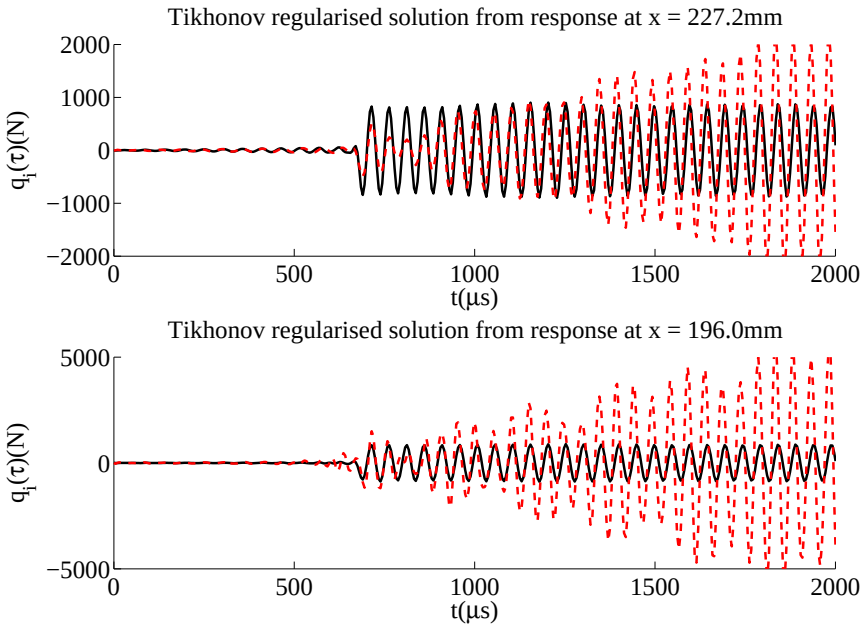

Fig. 4.45 Initial samples from the reconstruction of the input force from Modification 1 of the linear calibration model of the In-House Piezoelectric Actuator.

Table 4.16 Modification 2 eigenvalues computed for the In-House Piezoelectric Actuator with Monolithic Horn attached through the Distributed Transfer Function Method

Mode	Frequency (kHz)	Error relative to original model (%)
1st Longitudinal	7.03	35.1
2nd Longitudinal	19.72	3.33
3rd Longitudinal	22.38	10.3
4th Longitudinal	49.61	28.9

the form of Equation (4.9). In this case the exact input force is known, however in the case of the physical experiment, this force will have to be estimated from testing the MH assembly.

When the force is estimated through this method there will be an error between the frequency of the unknown force and the obtained estimation. This is equal to the difference between the resonance frequencies of the JH and MH assemblies. Ideally the MH assembly would be excited at the same frequency as the JH assembly, so that both assemblies experience the same frequency of input force. However, at this frequency, the MH assembly would not resonate sufficiently to achieve the axial vibration amplitude that is necessary to be observable above the measurement noise floor of a Digital Image Correlation exper-

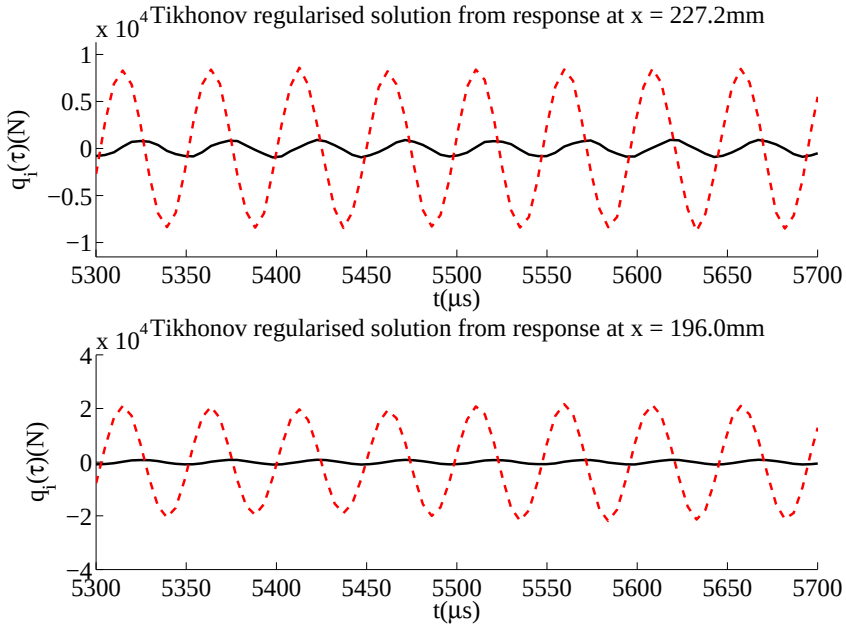

Fig. 4.46 Reconstruction of the observation window of the input force from Modification 1 of the linear calibration model of the In-House Piezoelectric Actuator.

iment (≈ 1μm) [92]. As a result it would not be possible to verify any results that are obtained through laser vibrometry. If both assemblies were excited at the same frequency they would not develop the same input force when the same excitation signal is produced from a function generator. This is due to the difference in the electrical impedance of the two assemblies. The JH assembly will have a greater mechanical impedance than the MH assembly because of the additional axial joint. Therefore both assemblies will have different amplitudes of electrical impedance at the same excitation frequency. As a result, the power that is drawn by each assembly will be different. A power amplifier boosts the signal from the function generator before it is applied to the piezoelectric stack. A mismatch between the output impedance of the amplifier and the load impedance of the stack will result in a different power draw because power will be reflected back to the amplifier at different levels.

When the same input force is applied to both the monolithic and the jointed assemblies, the joint force can be deconvolved through the expression that is given in Equation (3.100). This involves computing the impulse response matrix of the linear calibration model, $\boldsymbol{g}^{-1}$ (x, x_a, x_b, t_p, τ_q), and the difference between the response of the Monolithic and jointed assemblies, $\boldsymbol{G}(x, t_p, \tau_q) = \boldsymbol{u}_i^{JH}(x,t_p) - \boldsymbol{u}_i^{MH}(x,t_p)$ for $p = 1, 2, \ldots, N$ and $q = 1, 2, \ldots, N-1$. The inversion

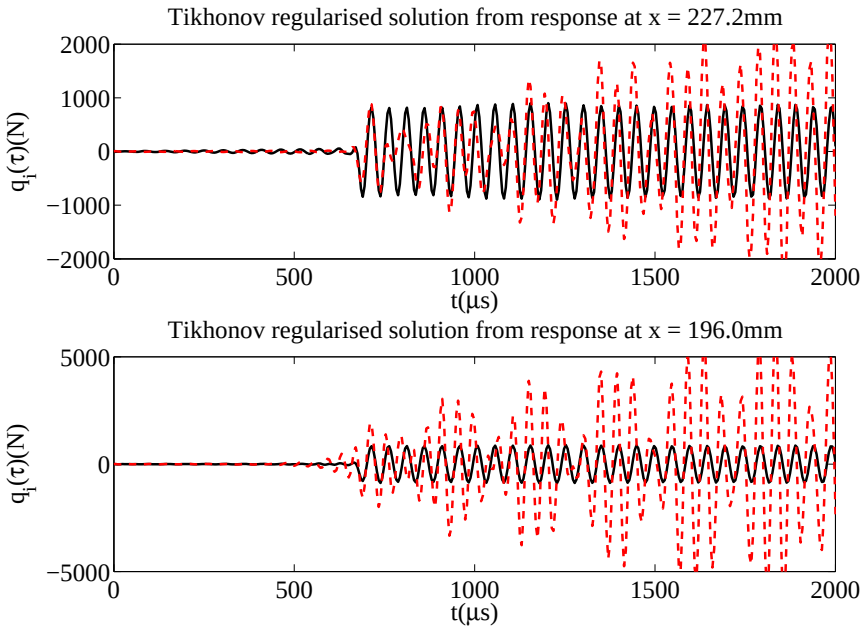

Fig. 4.47 Initial samples from the reconstruction of the input force from Modification 2 of the linear calibration model of the In-House Piezoelectric Actuator.

of the impulse response matrix is carried out using forward substitution as well as TSVD and Tikhonov regularisation. The results are given in Figures 4.42 - 4.44. It is not expected that the joint force would be constant for different amplitudes of input excitation to HPU system, however in the current simulation the joint force signal is identical in each test. It has been plotted as a dotted line in each of the figures. When the results match the original signal it is obscured. The solutions that are obtained through forward substitution, from location X_1, are clearly badly conditioned. However they appear to follow the phase of the original signal. These solutions improve when they are obtained equivalently from location X_2, but there is some amplification of noise in the reconstruction. The TSVD regularised solutions in Figure 4.43 give a good estimation of the original signal, however close inspection shows that the edges of the signal are not completely preserved. The Tikhonov solutions in Figure 4.44 do not offer significant improvement in preserving the edges of the original signal. One solution associated with location X_2 differs significantly from the other solutions. This demonstrates the range in the quality of solutions that might be obtained from a reasonable guess of the regularisation parameter.

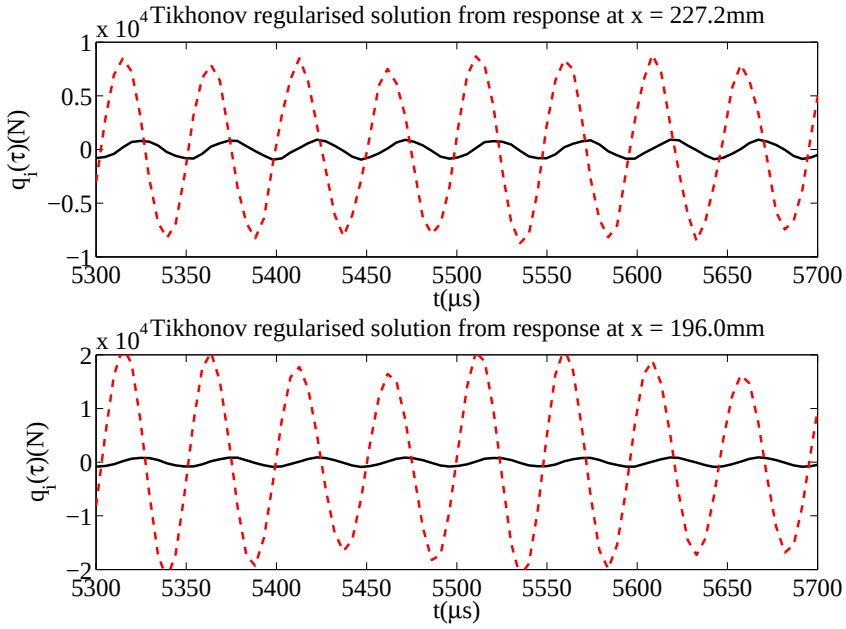

Fig. 4.48 Reconstruction of the observation window of the input force from Modification 2 of the linear calibration model of the In-House Piezoelectric Actuator.

4.6 Outcomes

The linear calibration models are a necessary step towards isolating the behaviour of an axial joint in a HPU system. A set of ultrasonic horns were designed and a piezoelectric actuator was manufactured towards facilitating this comparison. The force estimation is based on mechanical observations due to the difficulty of incorporating piezoelectric behaviour into the DTFM model. The impedance analysis results show that the electrical characteristics of the device are strongly influenced by its mechanical constitution. However the ability to observe the mechanical behaviour of the device depends on being able to apply electrical excitation close to its minimum impedance behaviour. This is close to the desired axial vibration operating mode. It is shown that four axial modes can be estimated reliably through both the electrical impedance analysis and EMA of the HPU assemblies. Increasing the tightness of the axial joint tends to adjust the axial modes of a JH assembly towards those identified for a MH assembly. However, over-tightening can result in loss of output. Looseness of the joint decreases the amplitude of the minimum impedance of a JH assembly and will increase the significance of other closely spaced modes in the response of the device. Therefore, to apply the distributed rod description, it is important to ensure that bending and torsional modes do not contribute significantly at the operating frequency of the JH

assembly.

It is not possible to measure all of the parameters that are necessary to define the linear calibration model that describes the CPA. Furthermore, both the CPA and IHPA assemblies, with the MH attached, will feature unknown prestress through components. The possibility of addressing this with a TEP has already been discussed and remains the only route to estimating the true values of the parameters. The evolutionary approach that was implemented succeeded in minimising the error between the DTFM eigenvalues and the measured natural frequencies. However this does not give any insight to the nature of the unknown parameters in the model. Despite this, a comparison of the DTFM with the measured mode shapes, suggested good agreement and reasonable estimates of the nodal locations.

The force estimation scheme was tested by computing transient response of each linear calibration model, and applying the subsequent signals, to reconstruct the input force or the joint force. The signals were interpolated to avoid committing an inverse crime during this simulation. These reconstructions do not account for the mismatch between the distributed parameter model and the physical system. Therefore the stiffness of the model is modified to demonstrate the influence of this discrepancy on the reconstruction. Every effort has been made to optimise the linear calibration models and it has been demonstrated that the regularisation schemes can facilitate force reconstruction for an ill-conditioned inverse problem. True insight into the limitations of this scheme requires experimental data that can be verified.

Chapter 5

Force estimation via Laser Vibrometry and High Speed Imaging

5.1 Introduction

The analysis in Chapters 3 and 4 has been set out to give context to the least squares estimation of a force, with assumed spatial distribution, in a rod system with distributed parameters. Two rod models have been defined to describe the linear axial vibration behaviour of each piezoelectric actuator with the Monolithic Horn (MH) attached. Clearly there are many limitations in applying this exact deterministic representation of a physical system to measured data. The preceding discussion has highlighted these limitations, so that they might be tackled individually as future work. In particular the problem of updating the distributed parameters of a free-free rod from modal data requires detailed mathematical analysis that has not been attempted here. The solution to this problem is required to give a clearer representation of the stiffness distribution at the axial joint due to an applied prestress. Despite the aforementioned problems it is still possible to proceed with applying the scheme to measured data with the goal of obtaining a least squares inference of force behaviour from limited information about the system. If this information provides a route to suggesting overhang behaviour in the frequency domain, due to an isolated subsystem, then the scheme has some practical application to the operation of High Power Ultrasonic (HPU) devices.

In order to develop confidence in the reconstructed data, another method to obtain equivalent

data is required for verification. An ultra-high speed camera has been introduced to acquire images of a portion of an ultrasonic horn during axial motion. By tracking pixels, throughout a progression of these images in time, the Digital Image Correlation (DIC) method can be applied to obtain full field displacements and strains. There are many factors involved when obtaining these measurements. These include:

- The speed and resolution of the ultra-high speed camera with respect to the spatial and temporal scale of the dynamic phenomena that are under observation.
- The surface properties of the 2D area that is under observation. Most often this involves the application of a speckle pattern to the surface.
- Post processing of the acquired images through a DIC algorithm. This involves relating the pixels in each image, which is obtained after a known step in time, to the pixels in an initial reference image. To achieve this, the pixels to be tracked must be specified and then grouped into a subset. The reliability of the tracking depends on being able to identify how each subset in the reference image transforms after each step in time. The subsets must be chosen so that they are uniquely identifiable between images.

Force estimations are obtained through the 1D DTFM model for comparsion to the DIC estimations. Laser Doppler Vibrometer (LDV) measurements are acquired at a point on a flat of the ultrasonic horn, which has symmetry with the flat that the ultra-high speed camera observes. The measured velocity must be post processed using Digital Signal Processing (DSP) tools in order to obtain the desired observation of displacement. The DIC obtained displacement and strain fields are averaged over a line that is coincident to the x position of the LDV measurement, but perpendicular to the longitudinal axis of the flat. To improve the force identification measurements, at least two LDVs will acquire data simultaneously to the camera. The camera has a maximum sample rate of 1×10^6 frames per second (Mfps) at which it can only record 102 sequential images. Comparatively the LDV measurements can be sampled far more often, for a very long time window, through the use of a phosphor oscilloscope. However, instead of observing the camera time window more often with the LDVs, the sample rate of the camera is matched and a time window that extends before and after the camera time window is observed. This is useful because the force identification can suffer from edge effects at the beginning and end of the measurement window. This was illustrated through the simulations in Section 4.5.3.

For tests of the HPU assemblies, the difference between the JHs and the MH are clear during the experiments. For the assemblies made with the Commercial Piezoelectric Ac-

tuator (CPA), its power supply will lock on to the frequency of the maximum phase of the impedance, over a limited bandwidth centred on ≈ 20kHz. The actuation frequency of the JH will always be lower in comparison to the MH. It must be assumed that the response is dominated by the 2^{nd} longitudinal mode for both types of horns. The evidence for this assumption is given in Chapter 4. In the case of the In-House Piezoelectric Actuator (IHPA) assemblies, the excitation frequency is adjusted through a function generator to produce a resonant response. This frequency will vary from that of the 2^{nd} longitudinal mode that was observed through the Experimental Modal Analysis (EMA) in Chapter 4. However, it is assumed that the correct resonance has been actuated if the maximum amplitude occurs close to the identified frequency and then decreases for an increase in excitation voltage to a JH assembly.

The isolation of the axial joint force is attempted based on very limited information. The level of regularisation that is required to obtain a stable solution to the reconstruction gives an indication of its appropriateness. This estimation can be graphed with displacement to draw hysteresis loops that represent the force behaviour that is isolated through the scheme. The DIC obtained strain field in the axial direction is converted to force through an assumed material stiffness. This may be considered appropriate for the MH tests because there are no macro-scale discontinuities over the length that is evaluated. However the JHs will have an unknown stiffness distribution, over the axial distance, because of the prestress that emanates from the axial joint. Therefore, the usefulness of the DIC method for observing the axial joint, subjected to ultrasonic vibration, is limited. However, of the experimental methods that are available for non-contact strain measurement, the DIC method has the most flexible and straightforward configuration. The complexity of the DIC method is associated with the post processing of data. This is approached through a set of freely available and modifiable MATLAB scripts and functions.

5.2 Experimental procedure

High quality displacement measurements are required in order to be able to compute force estimations through the one dimensional deconvolution scheme, as well as the displacement and strain fields, by means of Digital Image Correlation (DIC). However, in the case of both experiments, displacement is not measured directly. The Laser Doppler Vibrometer (LDV) produces a voltage that is directly proportional to the axial velocity component for a known

scale factor. The images captured by the ultra-high speed camera cannot be associated with the experiment until the post processing stage. Each run of the physical experiment takes less than a second to acquire both simultaneous sets of data for both methods. However the post processing of this data requires a variety of numerical tools, which are applied in series to the separate data sets. Initially the High Power Ultrasonic (HPU) assembly is tested with no excitation signal, so that any transient noise features can be identified in the LDV signal. The LDV is repositioned to obtain steady state noise. In the case of the high speed camera there is little direct feedback to provide an idea of the appropriateness of the configuration. A set of images are obtained when no excitation signal is applied to the HPU assembly. This set of images is processed with the DIC algorithm to check the noise level. This test is repeated and small adjustments are made to both the camera settings and the positioning of the camera and light source. This process is thought of as enhancing the speckle pattern observation. This gives some confidence that the ultra-high speed camera has been configured correctly with respect to the other equipment that is involved in the experiment. Optimising the configuration can be difficult because the DIC algorithm performs best for images with a distribution of grey values that covers the entire range of the camera's palette.

5.2.1 Speckle pattern

It is unlikely that it will be possible to obtain any successful correlation between images of the flat portion of the horn without modifying the appearance of the metallic surface. Correlation of images depends on being able to track pixels. Each of these is a digitised light intensity, which is assigned a value that depends on the bit depth of the camera. Tracking a single pixel is unreliable because in isolation it does not contain any information that is not shared by many other pixels. If pixels are grouped together then this is known as defining a subset. Each subset contains all of the values that have been assigned to each pixel in the subset, but it also has the feature that each pixel is now spatially defined by its adjacent pixels. The uniqueness of the subset depends on its distribution of grey values because a higher distribution implies more spatial relationships between pixels. This distribution is limited by the bit depth of the Charge Coupled Device (CCD) sensor of the camera. This is the palette of tones from which the camera can record the image. Subtle changes in light intensity, over a featureless surface, will not be recorded by the camera. Therefore the best solution is to artificially induce some non uniform changes in reflectivity across the area that

is of interest. There are two main aspects of this problem. Firstly, the application of a paint speckle pattern, to the flat portion of the horn, will have a direct effect on distinguishing adjacent pixels. Secondly, during the acquisition of the images, the speckle pattern must be illuminated to match best with the spectral characteristics of the CCD sensor. It must also be focussed onto the sensor so that the spatial qualities of the pattern are distinguishable.

The speckle patterns that have been applied to the flat portion of the ultrasonic horns are shown in Figure 5.1. The camera settings that have been employed are given in Section 5.2.2. The horns are covered with masking tape so that only a $10 \times 20.9\text{mm}^2$ window remains exposed. This is helpful in determining the microns per pixel in each image, so that displacement can be obtained from the movements of the pixels. White Italian Kobra spray paint is applied liberally to obtain an even layer over the exposed area. This paint has a 100% acrylic formula and is fast drying, with immediate adherence, so that no dripping occurs. It can be removed easily with an acetone solution if necessary. After the paint has been left for some time a layer of black droplets is applied to the white background by spraying black spray paint at an approximate distance of 90cm from the surface. Too much black spray paint can render the pattern useless because this tends to reduce the possibility of grey tones in the image far more than if a pattern is predominantly white. These grey tones can be instigated unintentionally because any blurring that occurs in focussing the pattern onto the CCD sensor can be perceived as a range of tones by the camera. The configuration of the camera and the illumination of the speckle pattern is crucial to obtaining good correlation under the very fast time scales involved in testing the HPU devices. From the feedback that is available, during a run of the experiment, it will not be clear whether the chosen configuration is successful until after the post processing of the images. To provide some guidance, in this decision, all dynamic experiments begin with a static test of the speckle pattern for a chosen configuration.

The static image set is processed in MATLAB to obtain a histogram of each image that will feature in the correlation. It is straightforward to check the uniformity of the illumination, of the specimen, over the acquisition time window. A histogram of Figure 5.1a is shown in Figure 5.2a. This shows that the grey values are distributed approximately as a positive skew bell curve. Ideally the grey values should have a normal distribution that covers the entire range. The bias of the curve is influenced by the positioning of two flash lamps at a perpendicular distance from the speckle pattern. Reducing this distance will tend to increase the intensity of the reflections from the surface that are recorded by the camera. These reflections tend to saturate images during the acquisition of the sequential images.

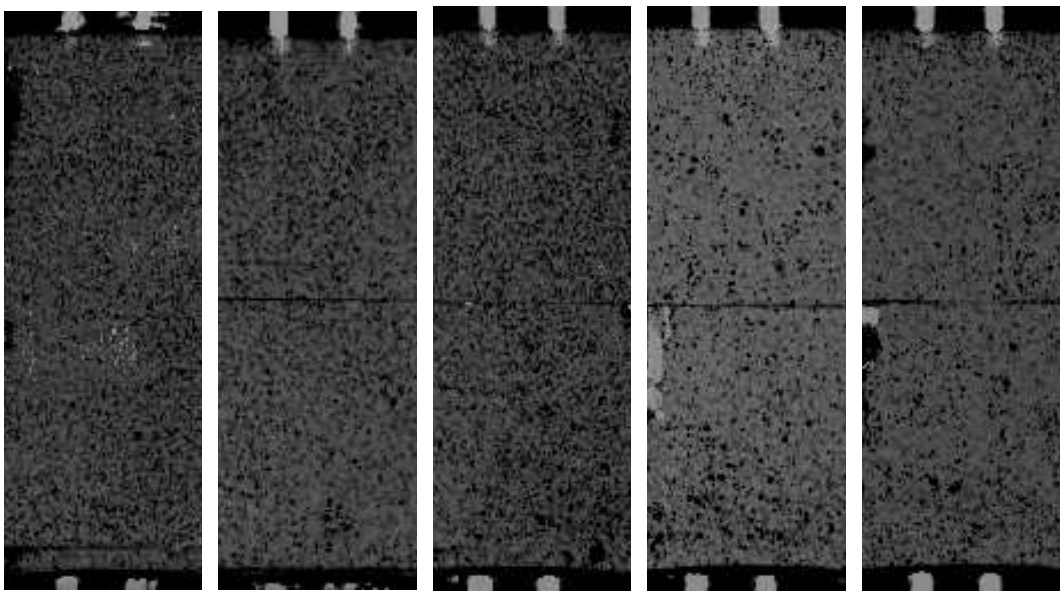

(a) MH (b) JH: St@8Nm (c) JH: Ti@8Nm (d) JH: Ti@12Nm (e) JH: Ti@16Nm

Fig. 5.1 The speckle patterns applied to the Monolithic Horn (MH) and each of the Jointed Horns (JH).

Without these images the sample rate of the camera is diminished. Therefore, it is better to acquire images that are biased towards the 0 end of the spectrum, instead of suffering distortion due to reflections. A diffuser may be placed between the speckle pattern, and the source of illumination, in order to reduce the influence of reflections. However this will also reduce the intensity of the illumination over the pattern. In the subsequent experiments horticultural fleece is layered over the light source in order to diffuse the light.

A 2D Fast Fourier Transform (FFT) of the speckle pattern can be employed to assess it for use in the DIC. The image is windowed so that its boundaries fade gradually to black and this removes their spectral characteristics from the FFT map. This is applied here separately and is not part of the DIC analysis. In the case of the FFT of the JH, in Figure 5.2d, the joint appears clearly as a vertical line. This demonstrates that the DIC method cannot be applied across a joint because the bearing surface will introduce spectral artefacts into the correlation process that are not physical. Instead these images must be assessed based on the pixels on one side of the joint. The FFT is applied to compare the spectral content of the speckle patterns. Lecompte *et al.* [93] concluded that high spectral content in an image would will lead to a larger random and systematic error in any displacements estimated through DIC. Therefore, for a given speckle pattern, it can be valuable to not focus it onto the CCD sensor too sharply. However, sharpness of the speckle pattern image is required to define the pattern

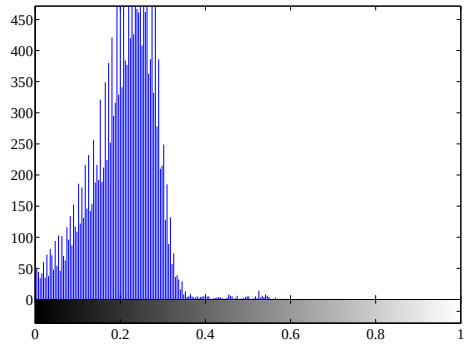

(a) MH: Histogram

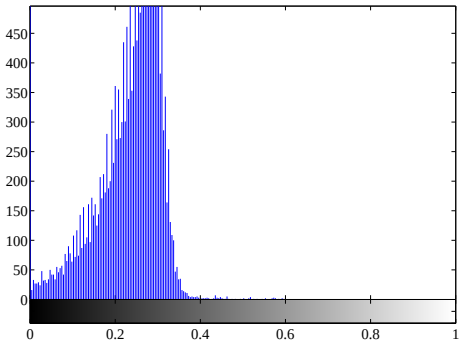

(b) JH: Histogram

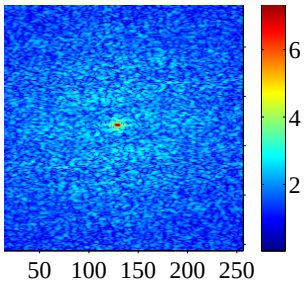

(c) MH: 2D FFT

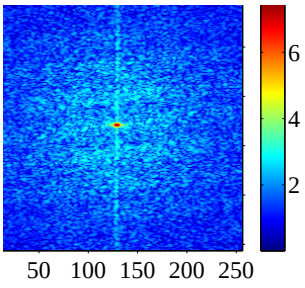

(d) JH: 2D FFT

No. Speckles: 1584 Average Size: 13 pixel x pixel

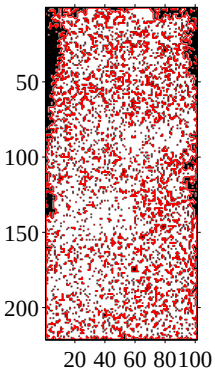

(e) MH: Speckle no. and area

No. Speckles: 1267 Average Size: 17 pixel x pixel

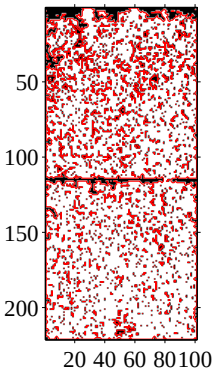

(f) JH: Speckle no. and area

Fig. 5.2 A speckle pattern comparison by means of 3 methods: Histogram, two dimensional Fast Fourier Transform (FFT) as well as number and average area of speckles. The patterns are to the Monolithic Horn (MH) and the Jointed Horn (JH); where the joint has been made through a steel threaded rod.

spatially. The grayscale images are transformed into binary images using the MATLAB `graythresh()` function. This makes use of Otsu's [94] method to optimise the choice of the gray threshold based on integration of the histogram of the image. With the obtained binary image, MATLAB can draw boundaries around the zero valued pixels. Each closed boundary that is stored is counted as a speckle, with the exception of the boundary around the image, which is discarded. The area inside these closed boundaries can be calculated to plot the distribution of speckle areas and the average area of the speckles in the image. It can be seen from Figures 5.2e and 5.2f that the images of the speckle patterns on the different horns are similar. However, replacing the spray paint with a method that deploys paint with better average resolution, might yield more definition to each image. A solution to this would be to try an airbrush instead.

5.2.2 Apparatus and configuration

Two experiments are triggered alongside one another in order to acquire data at the same points in time. The symmetry of the test for the Commercial Piezoelectric Actuator (CPA) assembly is displayed in Figure 5.3. The CPA can be clamped horizontally through its casing with negligible influence on its operating mode. The casing is attached to the flange on the front mass, which is at a node of vibration. A similar configuration is implemented for the tests of the In-House Piezoelectric (IHPA) assembly, however, instead of aligning the IHPA in parallel with the optical table, it is supported perpendicularly. This is due to the difficulty of avoiding a short circuit to the piezoelectric stack, through the holder, because the stack is not electrically insulated from the flange of the actuator. Only two 3D LDVs are available, so the IHPA tests feature two LDVs instead of three. Aligning the remaining 1D LDV with the end of the IHPA assembly was impractical whereas it is straightforward when measuring the horizontal CPA assembly. The configuration of the lasers for both set ups are shown in Figure 5.4. The CPA set up has the LDVs resting on top of the optical table, whereas the IHPA set up requires each of the LDVs to be positioned through the use of a scissor jack platform. In both cases the HPU assembly is supported by a holder, which is bolted onto the optical table, so that the axis of the assembly intersects a line of holes. The LDVs are aligned to this axis by pressing them into bolts that have been inserted into the table. The HPU assembly and LDVs are then checked for alignment with the surface of the table by means of a spirit level. It is assumed that the planes of the LDV sensor are perpendicular to the appropriate velocity components of the HPU assembly.

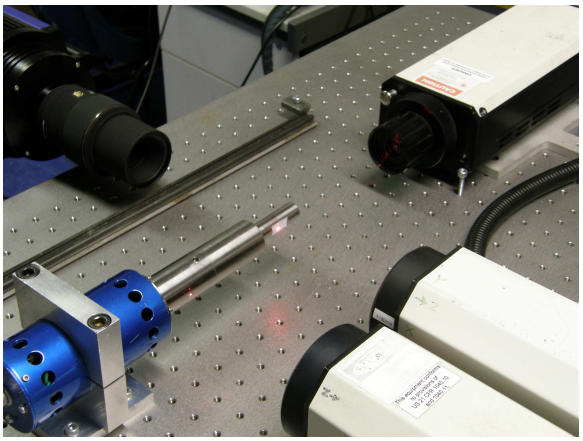

(a) LDV view

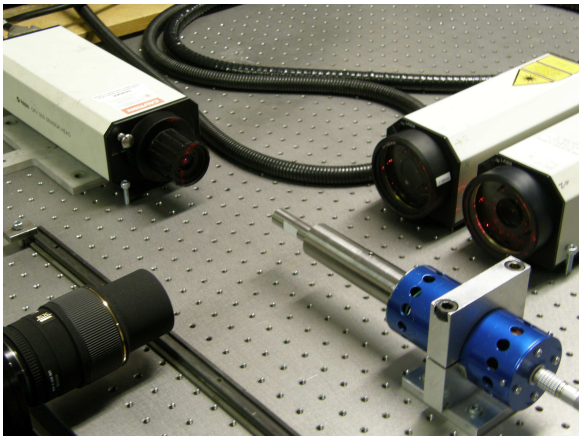

(b) DIC view

Fig. 5.3 Alignment of the ultra-high speed camera and the laser vibrometers to the Commercial Piezoelectric Actuator with the Monolithic Horn attached.

The LDV measurements are obtained simultaneously by 2 or 3 LDVs for the IHPA and the CPA configuration respectively. All 3 LDVs are manufactured by Polytec. Each LDV has a controller unit where the voltage measurement signal is converted to velocity through the chosen scale of $125 \text{mms}^{-1}\text{V}^{-1}$ at the post processing stage. Each controller is coupled to a sensor head from which it receives the measurement signal. For the two 3D LDV systems (CLV-3D) this sensor head contains three independent LDVs, whereas the 1D LDV system features one only. The output voltage from each LDV controller is fed to the measurement channel of a Tektronix DPO 7054 Digital Phosphor Oscilloscope 500MHz. Four channels are available and the data sheet states a delay of $\leq$ 100ps between any two channels. The data from each LDV is acquired with no excitation signal applied to the piezoelectric actuator. The noise level of each channel is assessed and the LDVs can be adjusted to remove any

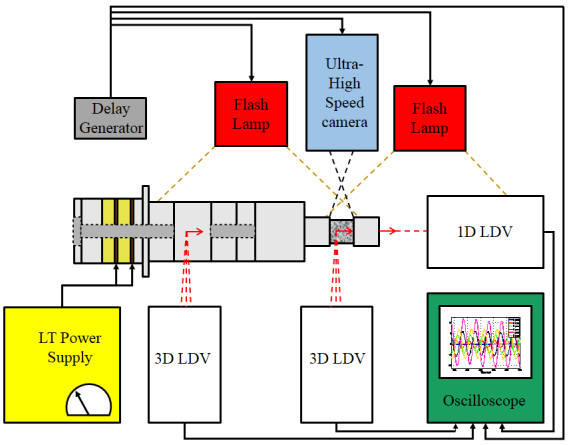

(a) Horizontal setup for the CPA

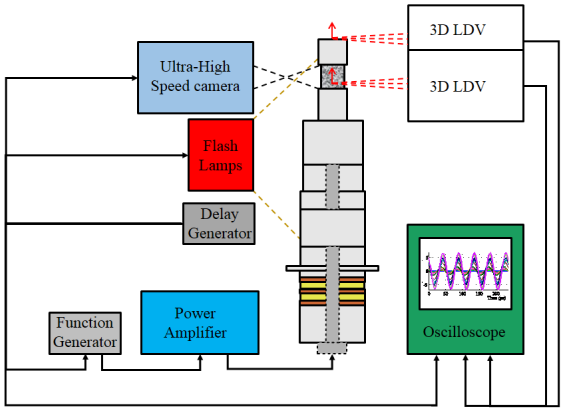

(b) Vertical setup for the IHPA

Fig. 5.4 Experimental configurations for testing the Commercial Piezoelectric Actuator (CPA) or the In-House Piezoelectric Actuator (IHPA) with a test horn.

transient noise artefacts. The acquisition of up to 3 LDVs is triggered through a rising edge signal that is produced by a delay generator. The CPA power supply cannot be activated/de-activated through an external signal, so it must be switched on/off manually before/after the LDV acquisition has completed. Therefore this assembly will always achieve steady state vibrations when observations are recorded. The LDV acquisition window is matched to the camera record period for these tests. In the case of the IHPA tests, the LDV acquisition is triggered prior to the camera and continues after the camera stops recording images. The parameters that are associated with the LDV measurements are summarised in Table 5.1. This gives the x position that each LDV was focussed onto each HPU assembly. This was

determined by tracing the LDV focus onto the assembly, so that it could be measured after the experiment, with a set of digital callipers. The time window parameters will be applied to post-process the velocity data to obtain displacement. The settings are also important in aligning the LDV sampled data to the data that is obtained through DIC. The function generator, which provides the excitation signal to the IHPA, was triggered with the LDV acquisition. Each run of the IHPA experiment involved adjusting the voltage of this excitation signal and varying its frequency, close to the impedance minima that were identified in Table 4.1, in order to locate a resonance. The experiment was then carried out for the identified frequency.

Table 5.1 Acquisition of Laser Doppler Vibrometry measurements

Parameter	Value for assembly		Units	Description
	CPA	IHPA		
X_1	230.75	227.24	mm	LDV focal point at front
X_2	203.75	195.97	mm	LDV focal point at flat
X_3	86.95	-	mm	LDV focal point at front mass
f_s	250		kS/s	Sample rate
N	202	4096	S	Number of recorded samples
t_i	0	0	µs	Start of acquisition window
t_f	368	16 380	µs	End of acquisition window
t_D	440	652	µs	Pre-record time to acquisition window

The images that will be processed by the DIC algorithm are recorded by a Shimadzu HPV-1 ultra-high speed camera. A Sigma 105mm f/2.8 Macro lens focusses the image onto the CCD sensor. Ideally the 2D observation area should be illuminated with uniform intensity throughout the acquisition time period. To achieve this, two U shape Xenon flashtubes were positioned either side of the camera head at an approximate perpendicular distance of 90cm to the measurement area. Horticultural fleece was layered in a plane over the face of the flashtube to provide some diffusion of the expelled light. Both flashtubes are activated simultaneously through an ADAPT 500 joule flash controller. This controller is triggered by a delay generator, which also activates the camera acquisition. The configuration of the camera is summarised in Table 5.2 with respect to the time window of the LDV measurements, which was given in Table 5.1. The resolution of the CCD sensor is 312×260 pixels and, as was discussed previously, it has a grey level dynamic range of 8-bit. The axis of the test assembly is always aligned with the shorter dimension of the sensor because in this direction the fill factor is the highest. The fill factor indicates the percentage of a pixel on

the solid state CCD sensor that is sensitive to light - or covered by photodiode. Modern ultra-high speed cameras suffer from very low fill factors because storage memory must be physically close to photodiodes in order to minimise the storage time of each image. In order to achieve this the Shimadzu makes use of the In-situ Storage Image Sensor (ISIS) architecture, which is discussed in Goji Etoh *et al.* [95] and shown in Figure 5.5. Pierron *et al.* [96] characterised the performance of the Shimadzu for use in DIC. They found that the sensor saturates far below its 8-bit limit where a characteristic saturation pattern is encountered around 110-130. This saturation pattern was also encountered during the tests of the static speckle patterns in Section 5.2.1. However, the results that were obtained required the set up to be reconfigured to minimise the influence of reflections on the image set. These reflections could only be reduced by moving the flash heads further away from the measurement area. This resulted in generally darker images, where the saturation of the sensor was not approached. Pierron *et al.* [96] also observed that the low fill factor of the sensor can induce a spatial fringe pattern into the images. This is remedied by smooth transitions between the black and white zones of the observed areas. This has also been discussed previously for the current configuration. It was suggested that the speckle pattern should be observed slightly out of focus so that the spectral content displayed in the 2D FFT is less sharp.

Table 5.2 Parameters for the High Speed Imaging set-up

Parameter	Value for assembly		Units	Description
	CPA	IHPA		
X_a	193.55	190.04	mm	Starting x position of speckle pattern
X_b	214.45	210.94	mm	Ending x position of speckle pattern
f_s	250		kfps/s	Sample rate
N	102		S	Number of recorded samples
-	1/8		×4µs	Exposure time
t_i	0	5 308	µs	Start of acquisition window
t_f	404	5 712	µs	End of acquisition window
t_D	440	4 920	µs	Delay of trigger to acquisition window
-	340	4 820	µs	Delay of trigger to flash lamps

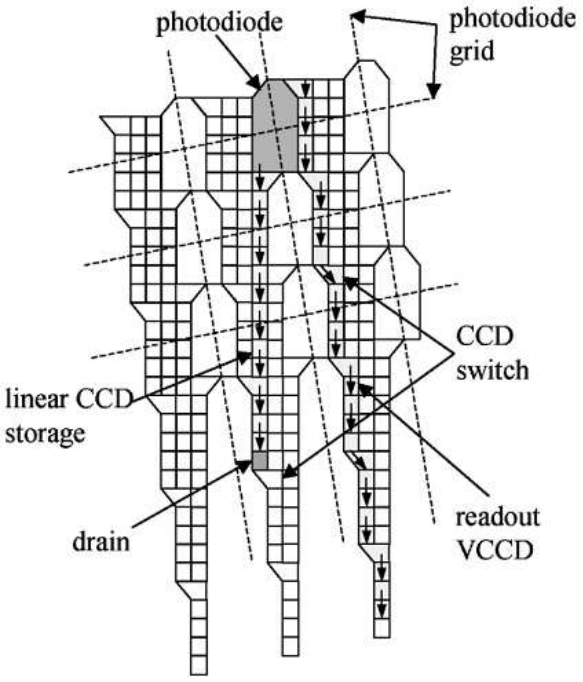

Fig. 5.5 The In-situ Storage Image Sensor architecture from Goji Etoh *et al.* [95].

5.2.3 Optical Metrology and Digital Image Correlation

Digital Image Correlation (DIC) is an optical metrology that involves a combination of digital image processing and numerical computing. The development of it is attributed to the work by a group of researchers at the University of Carolina in the 1980s, which included: Peters & Ranson [97], Chu *et al.* [98], Sutton *et al.* [99] and Peters *et al.* [100]. DIC was preceded by other non-contact optical techniques that are capable of finding full-field displacements. The geometric and interferometric Moiré methods were among the earliest from around 1954 [101, 102]. Speckle methods came later in 1970 [103] and the most recent was Holography in 1971 [104]. As was discussed by Sciammarella [105], all of the above techniques have certain elements in common and it is of interest to present this as a generalised body of technological knowledge towards optical metrology. Contrasting the techniques gives some perspective to the overall field of study. If the discussion is restricted to include 2D DIC, or measurements through the use of a single camera, then each of the above techniques involves the transformation of a 3D space into a 2D space through some projection centre. The laws of projective geometry are required for an in depth understanding of this process. However some aspects of this can be illustrated by considering the ideal pinhole camera model in Figure 5.6. If the aperture of the camera

is at O then the projection of the real world point P to the projected point Q involves the relationship of two similar triangles. If this argument is extended into the perpendicular direction, X_2, then the following expression can be found in the 3D coordinate system:

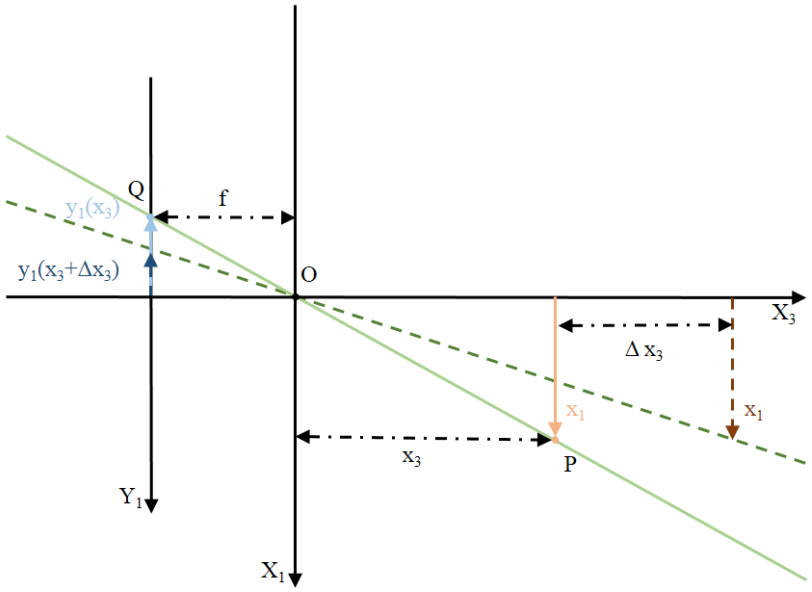

Fig. 5.6 Schematic of the ideal pinhole camera model, adapted from Sutton *et al.* [106].

$$\begin{pmatrix} y_1(x_3) \\ y_2(x_3) \end{pmatrix} = -\frac{f}{x_3}\begin{pmatrix} x_1 \\ x_2 \end{pmatrix} \tag{5.1}$$

where f is the focal length of the pinhole camera, x_3 is the perpendicular distance from the aperture to the point P and x_i and y_i for $i = 1,2$ correspond to coordinates of points on the orthogonal axes that are associated with planes in the real world and the photo sensor respectively. If further points are observed either side of P, in the 3 direction, then it can be shown that length scales are not preserved in the projection of these points. Each of the measurement techniques that rely on a single light sensor will suffer considerably from out of plane motions. In practice it is not possible to absolutely align the measurement axis of the sensor so that it is completely perpendicular to the measurement surface. There will always be some perspective error present in the observations. Furthermore, due to Poisson's effect, any vibration experiment will exhibit out of plane motions even if the in-plane vibration is predominant. In the case of the current experimental configurations, the HPU assemblies will typically feature high modal density. The likelihood that bending modes will contribute to their overall motion is high. Sutton *et al.* [106] have studied the influence of out of plane motion on both 2D and 3D DIC measurements. They make use of

the ideal pinhole model to provide approximate strain errors due to out of plane translations and rotations. It follows from Figure 5.6 that Equation (5.1) can be expressed for an out of plane translation as:

$$\begin{pmatrix} y_1(x_3+\Delta x_3) \\ y_2(x_3+\Delta x_3) \end{pmatrix} = -\frac{f}{x_3}\left\{\frac{1}{1+\left(\frac{\Delta x_3}{x_3}\right)}\right\}\begin{pmatrix} x_1 \\ x_2 \end{pmatrix} \tag{5.2}$$

A first order Taylor series expansion of the term $\{\ldots\}$ gives the approximation:

$$\frac{1}{1+\left(\frac{\Delta x_3}{x_3}\right)} \approx \left(1-\frac{\Delta x_3}{x_3}\right) \tag{5.3}$$

Therefore the displacement field can be written as:

$$\begin{pmatrix} u_1(\Delta x_3) \\ u_2(\Delta x_3) \end{pmatrix} = \begin{pmatrix} y_1(x_3+\Delta x_3) \\ y_2(x_3+\Delta x_3) \end{pmatrix} - \begin{pmatrix} y_1(x_3) \\ y_2(x_3) \end{pmatrix} \approx -\frac{f}{x_3}\left\{-\frac{\Delta x_3}{x_3}\right\}\begin{pmatrix} x_1 \\ x_2 \end{pmatrix} \tag{5.4}$$

This follows onto an estimation for the strain field of:

$$\begin{pmatrix} S_{11} \\ S_{22} \end{pmatrix} = \begin{pmatrix} \frac{\partial u_1(\Delta x_3)}{\partial y_1(x_3)} \\ \frac{\partial u_2(\Delta x_3)}{\partial y_2(x_3)} \end{pmatrix} \approx -\frac{\Delta x_3}{x_3}\begin{pmatrix} 1 \\ 1 \end{pmatrix} \tag{5.5}$$

It is clear that unavoidable out of plane displacements will be amplified as the distance between the real world point P and the aperture O is reduced. In the case of the current set up, the camera has very limited resolution, so it is desirable to project the speckle pattern so that it fills most of the (260) pixels of the vertical axis. Unfortunately, in the absence of a telecentric lens, the barrel of the Sigma macro lens must be extended almost fully to fill the CCD sensor with the speckle pattern. This takes it close to its minimum focus distance of $f = 312.4$mm, which gives a working distance of $x_3 = 122$mm. Therefore, an out of plane displacement of $\Delta x_3 = 1\mu$m is expected to introduce a displacement of $\approx 0.1\mu$m to the displacement observed in the 1 direction; at a point that is offset from O by 5mm in the 1 direction. However, this will also induce a strain of $S_{11} \approx -8.2\times10^{-6}$. Another aspect of mapping the real world, to the projected image space, is that angles are not preserved. If the vertices of the flats in Figure 5.1 are not shown as a meeting of two perpendicular lines, in the image, then some misalignment or distortion has been inherited through the measurement set up. The extreme of this would be observed if two real world parallel lines intersect in the projection at a vanishing point. The convexity of the cylindrical portion of the horn, that is shown in each image, is also a clue to image errors. However it is difficult to identify these errors clearly in the current set of images. The best approach would be to

eliminate these errors by application of 3D DIC through a stereovision high speed camera system. If this is not possible, then a telecentric lens should be introduced. Otherwise more material could be removed from the ultrasonic horn to form longer flats. The CCD sensor could be filled with a longer speckle pattern, that is observed at a greater working distance, x_3. Increasing this distance can significantly reduce out of plane errors and will approximate a telecentric imaging system [106].

5.3 Post processing applied to the recorded data

5.3.1 DIC method

In general the Digital Image correlation (DIC) method involves the extraction of displacement information from the recorded irradiance of deformed bodies. Displacement is obtained directly from point trajectories and the process is more successful when random carriers are utilised. These carriers are in the form of speckle images that have been digitised and recorded. Example images are shown in Figure 5.1. For a set of images that is taken throughout a deformation, at known intervals of time, a subset of pixels of the image is tracked to obtain the point trajectories. This is achieved by a cross correlation of the subset before and after the time step; where the position of a correlation peak gives the local displacement of the subset. All of the subsets in an image are correlated and merged into lines that are tangent to the trajectories of the points of the surface. Clearly this will not result in a realistic displacement field due to small variations in the correlations of each subset in the image. Therefore further information must be imposed on the scheme based on knowledge of surface behaviour. From single camera observations this behaviour is limited to in plane deformations, so only 2D DIC is considered.

In the results that follow the DIC analysis is performed through a MATLAB based program that has been developed by Jones [107]. This program was designed as an improvement to the implementation by Eberl *et al.* [108, 109]. In both cases the correlation between the reference and deformed images is achieved through the MATLAB image registration function `cpcorr()`. This performs normalised cross correlation to obtain the adjustment to control points in the deformed image with respect to the reference image. The control points are generated through a user specified grid and specify the locations at which the displacement vectors will be computed. The outline of the grid specifies the Region Of Interest

(ROI) from the reference image for the DIC process. Jones [107] has modified `cpcorr()`, however the principle remains the same, so a subset of pixels around each control point in the deformed image is correlated to a larger subset around each corresponding control point in the reference image. The size of the reference subset is defined as a search zone which specifies the gain in its area with respect to the deformed subset. The search zone is set to 2 for all subsequent calculations. The normalised cross correlation coefficient is computed through the MATLAB function `normxcorr2()` for a range of theoretical displacements $(\check{u}_1, \check{u}_3)$. This convolves the pixels in the subset of the deformed image from those of the reference image. From Jones [107] this is written as:

$$C(\check{u}_1,\check{u}_3) = \frac{\sum_{\check{u}_1,\check{u}_3}\left[\left(r(\check{x}_1,\check{x}_3)-\mu(r_{\check{u}_1,\check{u}_3})\right)(d(\check{x}_1-\check{u}_1,\check{x}_3-\check{u}_3)-\mu(d))\right]}{\left\{\sum_{\check{u}_1,\check{u}_3}\left[\left(r(\check{x}_1,\check{x}_3)-\mu(r_{\check{u}_1,\check{u}_3})\right)^2\right]\sum_{\check{u}_1,\check{u}_3}\left[(d(\check{x}_1-\check{u}_1,\check{x}_3-\check{u}_3)-\mu(d))^2\right]\right\}^{\frac{1}{2}}} \tag{5.6}$$

where r and d are the intensities of the pixels in the reference and deformed subsets respectively and the mean intensity of each matrix is denoted by $\mu()$. Each subset has a control point at its centre and this coincides with the origin to a local coordinate system $(\check{x}_1, \check{x}_3)$. However the control points of the deformed subset might require sub-pixel accuracy to locate. Therefore a second order polynomial interpolation scheme is adopted. To calculate displacements to within $\frac{1}{100}$ of a pixel the correlation is performed nine times around the maximum coefficient. Then it is assumed that, at a control point, the actual displacement (u_1, u_3) is the theoretical displacement $(\check{u}_1, \check{u}_3)$ that is associated with the maximum interpolated correlation coefficient. A more detailed explanation can be found in Sutton *et al.* [110] and the review by Pan *et al.* [111] gives an overall summary.

Once the displacements have been estimated for the control points, it is now possible to derive the strain field from the displacement gradients. The strains can be computed via numerical differentiation of the displacement field, however this will amplify inherent measurement noise. Jones [107] has circumvented the need to differentiate the displacement field by defining a Finite Element (FE) that deforms according to a bicubic interpolated surface. The computation is summarised here for completeness, but the full details can be found in the documentation with the MATLAB program. Bicubic interpolation is an extension of cubic interpolation for interpolating a two dimensional regular grid of control points. Shreier *et al.* [112] found that a bilinear interpolation scheme can introduce systematic phase errors of up to 40% into the obtained strain field. Replacing bilinear interpolation with a cubic scheme is therefore necessary. Higher order schemes will improve accuracy,

but not as dramatically. Furthermore Cheng *et al.* [113] found that, instead of estimating the displacement field through tracking subsets, representing the surface deformation by the B-spline function produced more accurate deformation fields. Where the accuracy now depends on the minimisation of interpolation errors in the deformed image and on controlling the Guassian noise levels of the images. This ensures the continuity of displacements and displacement gradients between the control points. Bicubic interpolation is implemented over a 4×4 grid of the control points defined for the correlation process. For the implementation by Jones [107] the control points are mapped to a master element through a two dimensional isoparametric mapping [114]:

$$(x,y) = f^i(\xi,\eta) = \hat{\boldsymbol{N}}(\xi,\eta)\boldsymbol{X}^i \tag{5.7}$$

This transforms the image coordinates (x,y) to the local coordinates of the master element (ξ,η) through the matrix multiplication of the FE shape functions $\hat{\boldsymbol{N}}$ and the image coordinates of the 16 control points for the i$^{\text{th}}$ group that is being mapped. Sixteen bicubic FE shape functions are then defined as follows:

$$N_j(\xi,\eta) = (a\xi^3 + b\xi^2 + c\xi + d)(e\eta^3 + f\eta^2 + g\eta + h) \tag{5.8}$$

$$N_j(\xi,\eta) = \begin{cases} 1 & \text{at node } j \\ 0 & \text{at all other nodes} \end{cases} \tag{5.9}$$

where $a,b,c,\ldots,h$ are the constant coefficients of the polynomial. Displacements are interpolated over the master element as a function of the image coordinates to give $\boldsymbol{U}^I(x,y)$. These can now be mapped back to the original element:

$$\boldsymbol{U}^I(x,y)|_{(x,y)=f^i(\xi,\eta)} = \hat{\boldsymbol{N}}(\xi,\eta)\boldsymbol{U}^i_{EL} \tag{5.10}$$

where $\boldsymbol{U}^i_{EL}$ represents the displacements of the i$^{\text{th}}$ group of control points in the x and y direction. The Jacobian of the mapping function can be computed as:

$$\boldsymbol{J}^i(\xi,\eta) = [f^i(\xi,\eta)]' = \nabla\hat{\boldsymbol{N}}(\xi,\eta)\boldsymbol{X}^i \tag{5.11}$$

This can be used to find the first order partial derivatives of the interpolated displacements:

$$\nabla\boldsymbol{U}^I(x,y)|_{(x,y)} = \nabla\hat{\boldsymbol{N}}(\xi,\eta)[\boldsymbol{J}^i(\xi,\eta)]^{-1}\boldsymbol{U}^i_{EL} \tag{5.12}$$

Barlow [115] investigated commonly used Finite Elements to identify the unique points at

which stresses could be most accurately evaluated. It was found that the Gauss quadrature points have the same degree of accuracy as the nodal displacements within a model. The code by Jones [107] involves calculating the displacement gradients at these points. This involves averaging Gauss points that overlap, when adjacent groups of control points are interpolated, before calculating the small strain tensor in Equation (3.10). This produces strains that are evaluated over a reduced grid, that resides within the overall ROI, where each Gauss point is defined on the master element through combinations of $(\xi, \eta) = \left\{-\sqrt{\frac{3}{5}}, 0, \sqrt{\frac{3}{5}}\right\}$.

5.3.2 Digital Signal Processing of the laser vibrometry observations

Essential to the waveguide spectral analysis approach is the assumption that all of the involved signals may be integrated or differentiated. In this case the DTFM has been applied to provide the transfer function from force to displacement for the rod with distributed parameters. This can easily be changed for force to velocity through a modification of Equation (3.90). It may be preferable to do this because errors that propagate from the post processing that follows will not be included in the force estimation. However, the displacement form has been chosen. Before any estimations of force are carried out, the pointwise displacements, which are obtained through laser vibrometry, can be compared to the average axial displacements that are derived through DIC. To characterise the axial joint, 2D portions of hysteresis loops can be shown between velocity reversal points as: $(u(\tau), N(\tau))$.

The LDVs produce a voltage that is proportional to the vibration of the surface being observed. These signals must be integrated before the force estimation can take place. A typical set of results from testing the CPA is shown in Figure 5.7 for the parameters in Table 5.1. The MH is attached to the CPA through a steel stud set to 16Nm. The device is excited through its own power supply for a nominal output setting of 3μm. This locks on to the maximum phase of the impedance at 20.752 kHz. This is consistent with the results from both the impedance analysis and the EMA of the configuration that are shown in Tables 4.1 and 4.3. The assembly has been disassembled and reassembled before each of the three resonances have been observed. The velocity recorded at X_3, from the front mass, has smaller amplitude than the vibration after the step change in cross section. It is also the only measurement that is taken from a curved surface. As a result there is a DC offset to this response and this is corrected by removing a best fit straight line from the signal vector through the MATLAB function `detrend()`. Omega Arithmetic is applied to the velocity signals, $\dot{u}_3$, to

obtain displacements, u_3. Continuing the discussion in Section 3.2, the axial displacement in Equation (3.4) is restated as:

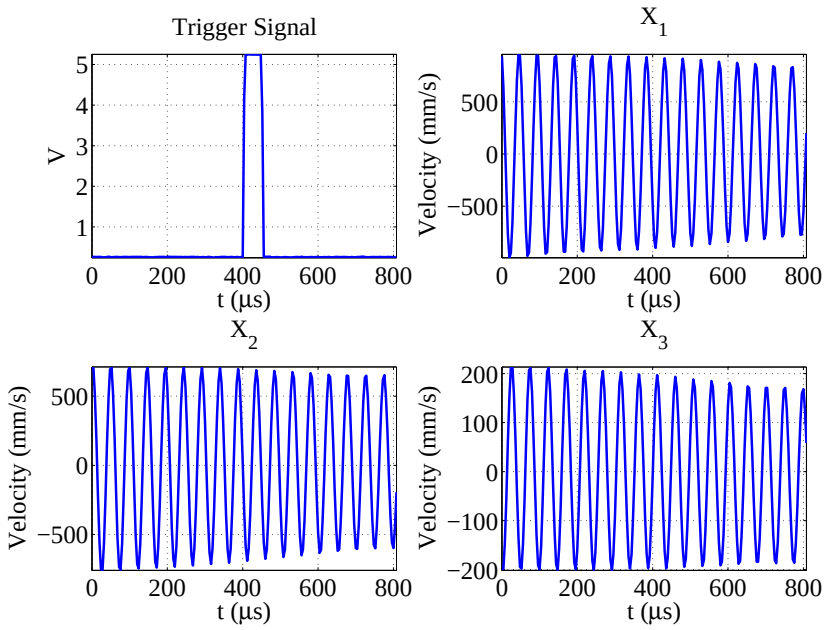

Fig. 5.7 Typical velocity measurements obtained from three points of the Commercial Piezoelectric Actuator with Monolithic Horn attached through a steel stud set to 16Nm.

$$u(x,t) = \sum_n \tilde{u}_n(x,\omega_n)e^{i\omega_n t} \tag{5.13}$$

This implies that the velocity can be found from:

$$\dot{u}(x,t) = \sum_n i\omega_n \tilde{u}_n(x,\omega_n)e^{i\omega_n t} \tag{5.14}$$

This transformation is achieved through the in-built MATLAB Fast Fourier Transform (FFT) function. This obtains the coefficients of the Discrete Fourier Transform (DFT) of the velocity vector. The operation is fastest when the length of the transform contains a number of points that is a power of 2 and the transform of any signal is padded with zeros to meet this condition. The vector containing ω_n is formed for $\pm f_{Nyquist}$, following Equation (3.3), and the zero frequency component of the signal FFT is shifted to the centre of the spectrum. The displacement is obtained in the frequency domain through the division of each component in the velocity FFT by the each component of the frequency vector. The inverse FFT is then applied to recover the time domain signal. However, the constants of integration must also

be known to obtain the true displacements.

Figure 5.8 shows the displacements that have been recovered from the velocities shown in Figure 5.7 through Omega Arithmetic. From the integral of the rectangular pulse trigger signal, it is clear that without the proper constants of integration, there are errors inherited through the integration of the signals. These errors are due to the enforced periodicity that is assumed of the data when a portion of the total signal is sampled. This is related to the continuous Fourier Transform (CFT), which requires that signals are known analytically over the complete domain. In order to implement the DFT it must be assumed that the sampled portion of the signal, or the window, is repeated for $\pm\infty$. This means that there must be a continuous transition from the end of a time window the beginning of the next (identical) time window. This characteristic is clear in all of the integrated signals.

The FFTs of the velocity and displacement signals are shown in Figure 5.9 and 5.10 respectively. Before taking the FFT, each signal has been windowed with a Hann function and padded with zeros up to 2^9 sampled points. This gives some artificial definition to the FFT plot. A comparison of the displacement and velocity spectra suggests that the integration has generated spectral behaviour that is low frequency and reasonably isolated from the frequency of interest. The spectrum of the integrated rectangular trigger signal is not separable from the integration scheme, however it is not required, and has been shown purely for demonstration. To remove the low frequency components each signal is filtered through a 3^{rd} order Butterworth high pass filter with a cutoff frequency of 4kHz. The filter characteristics are displayed in Figure 5.11. The filtered displacement signals, and their FFTs, are shown in Figures 5.12 and 5.13. The peak-to-peak amplitudes are consistent between the filtered and unfiltered displacements, however some distortion remains at the beginning of the time window. For this reason the high speed camera images are recorded starting close to the middle of the time window that is observed through the LDVs. This procedure is applied to all of the recorded velocities, whilst close attention is paid to the frequency characteristics of each measurement.

Only the 3D LDVs are employed to record the axial response of the assemblies made with the In-House Piezoelectric Actuator (IHPA). The excitation signal is sent to the amplifier that powers the device. The signal always begin with a quiescent period before the function generator is triggered. The period of excitation ends before the mid point of the time window in order to capture the response as it settles. Typical velocity measurements for a 300mV peak-to-peak excitation voltage are given in Figure 5.14. It is clear that at this rate of sampling it is not possible to excite the device from rest to steady state and back to

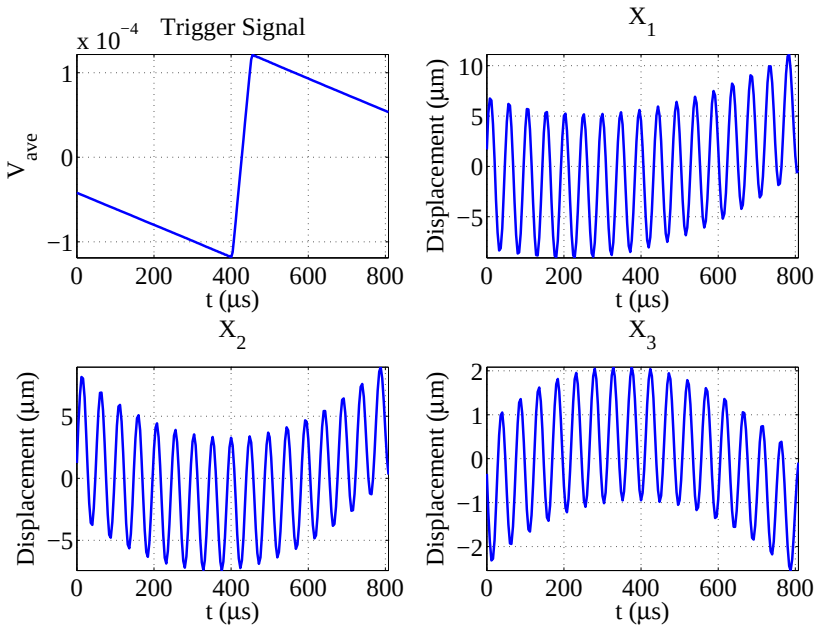

Fig. 5.8 Obtained displacements from three points on the Commercial Piezoelectric Actuator with Monolithic Horn attached through a steel stud set to 16Nm.

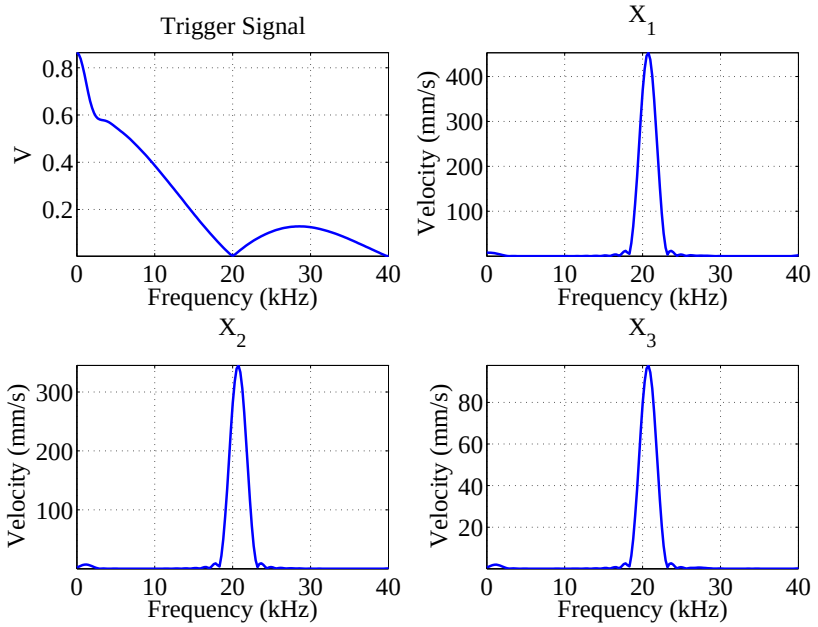

Fig. 5.9 Fast Fourier Transforms of typical velocity measurements obtained from three points on the Commercial Piezoelectric Actuator with Monolithic Horn attached through a steel stud set to 16Nm.

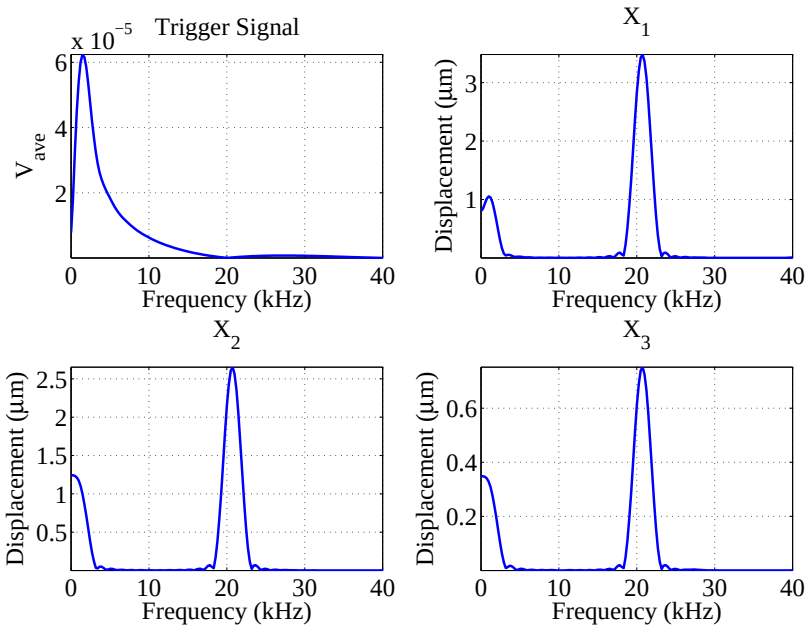

Fig. 5.10 Fast Fourier Transforms of obtained displacements from three points on the Commercial Piezoelectric Actuator with Monolithic Horn attached through a steel stud set to 16Nm.

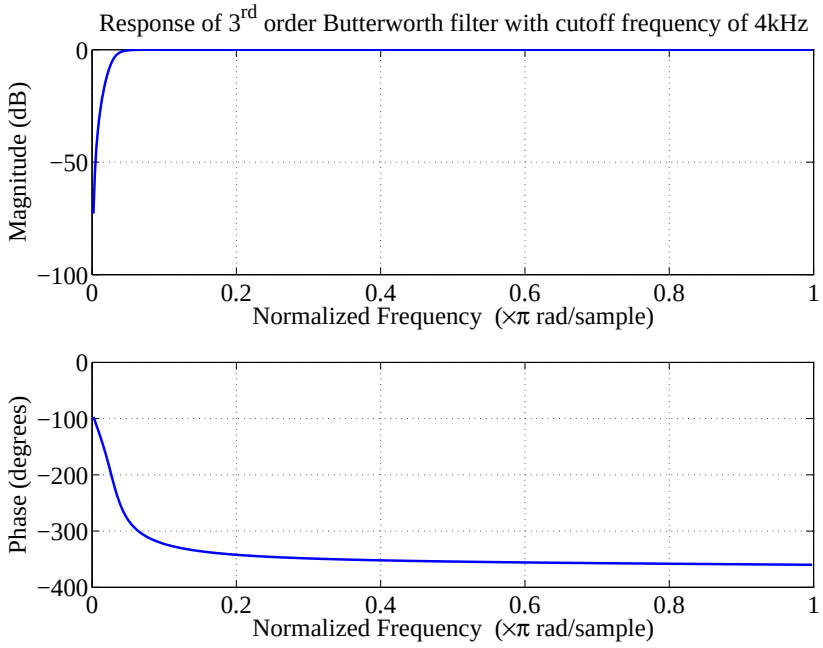

Fig. 5.11 The Butterworth high pass filter that is applied to correct the integrated displacements.

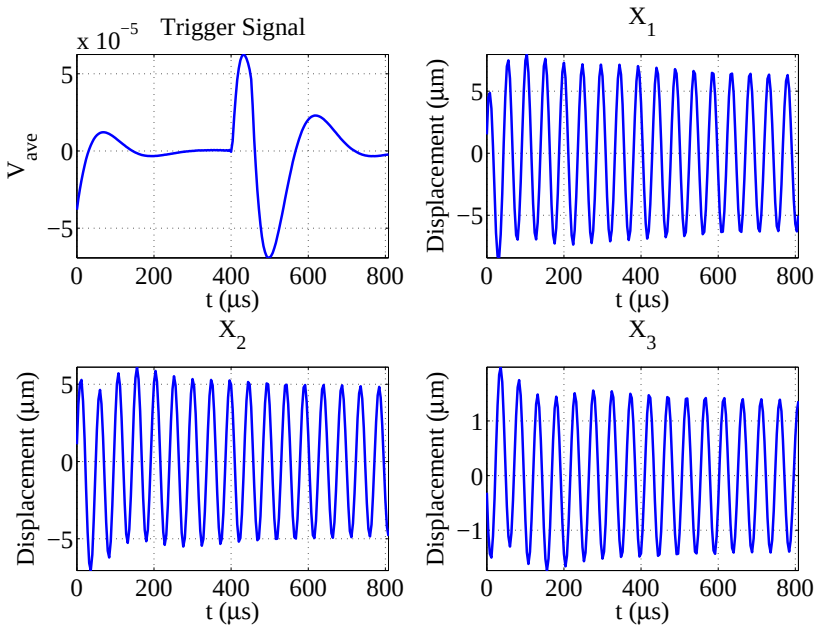

Fig. 5.12 Filtered displacements from three points on the Commercial Piezoelectric Actuator with Monolithic Horn attached through a steel stud set to 16Nm.

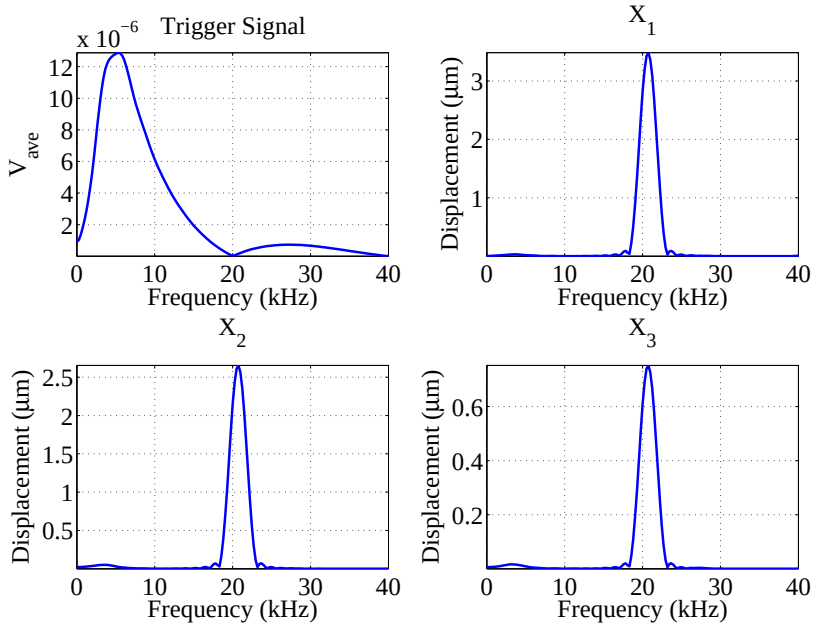

Fig. 5.13 Filtered Fast Fourier Transforms of obtained displacements from three points on the Commercial Piezoelectric Actuator with Monolithic Horn attached through a steel stud set to 16Nm.

rest again. An observation window that contains all of this information would be ideal for the force identification scheme because edge effects due to enforced periodicity would not influence the estimations. Obtaining response data from rest avoids the need to explicitly consider the initial conditions in the DTFM formulation. The signals are integrated and corrected to give the results in Figure 5.15. The integration of the excitation signal shows that the filtering has not corrected the transition from and to the quiescent period of the record. However the chosen parameters for the filter were found to obtain the best case of correction.

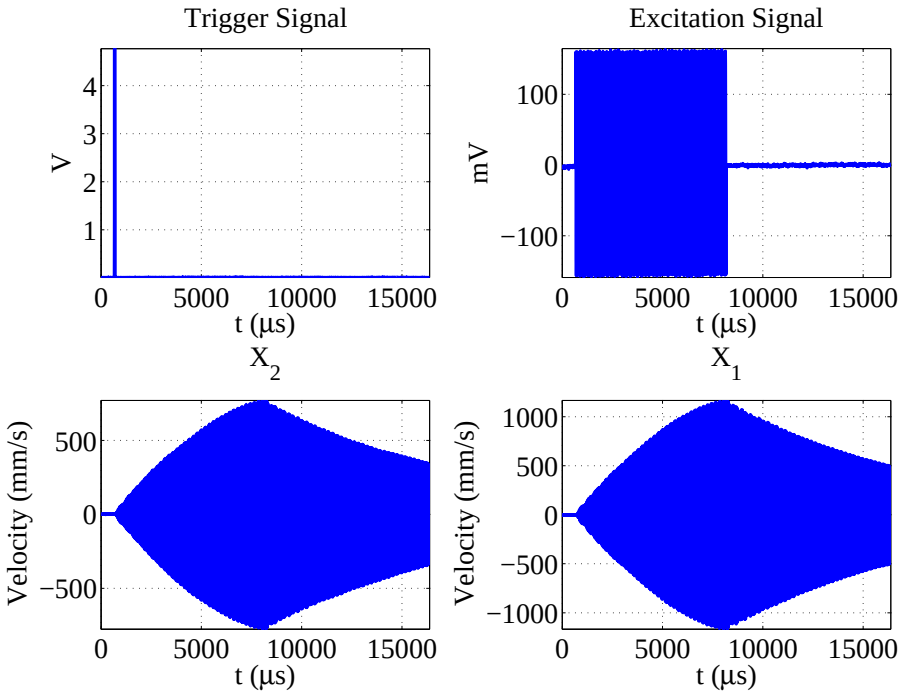

Fig. 5.14 Typical velocity measurements obtained from two points on the In-House Piezoelectric Actuator with Monolithic Horn attached through a steel stud set to 16Nm.

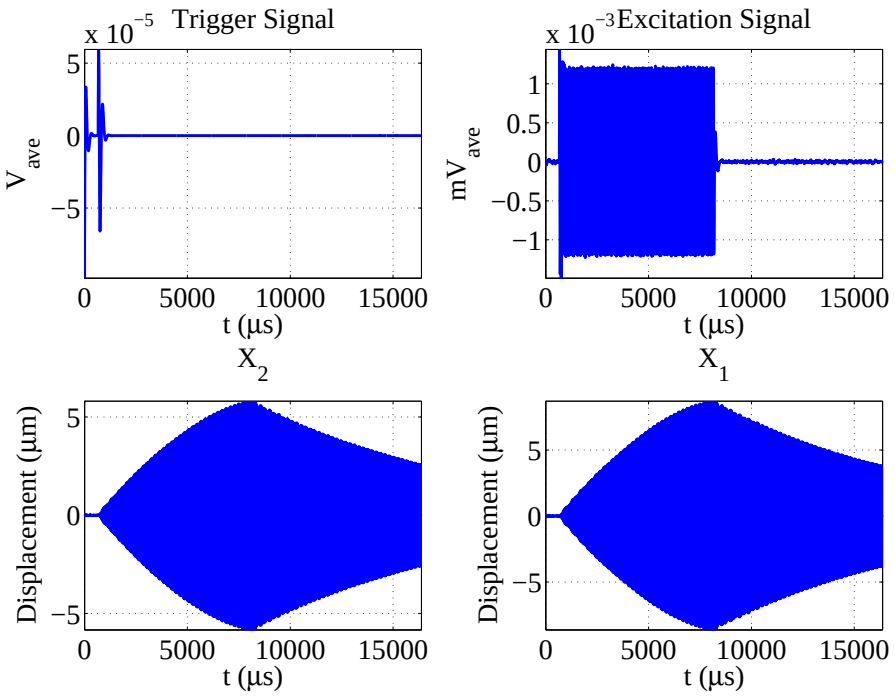

Fig. 5.15 Obtained displacements measurements from two points on the In-House Piezoelectric Actuator with Monolithic Horn attached through a steel stud set to 16Nm.

5.4 Experimental results

5.4.1 Digital Image Correlation measurements

Full field displacement and strains are estimated from the images that are recorded by the high speed camera through DIC. These estimations are required to form hysteresis loops to reveal the characteristics of either the CPA or IHPA test assembles throughout several cycles of vibration. The limitations of the DIC measurement set up must be separated from these observations. The comparison between the DIC and LDV results depends on the assumption that the displacement field has longitudinal amplitude that is consistent across the transverse dimension of the observed area. Averaging the axial signals along this direction yields an estimate of the axial displacement. These displacement field observations are influenced by the uniformity of illumination and its intensity throughout the camera acquisition time. Reflections of the flash lamp output can be observed as shifts in the histogram during the progression of images. Significant shifts can also be observed at the end of the acquisition

period and are attributed to the response of the CCD sensor.

Before any measurements are taken, the noise floor for each configuration is estimated by recording the speckle pattern in its unloaded state. Figure 5.16 shows the reference image, from a set of images, obtained from recording the CPA with the MH attached for no applied excitation. A subset size of 14×14 pixels is chosen for a grid of control points that are distributed over the Region of Interest (ROI) with a spacing of 7 pixels. Reducing either of these parameters tends to produce spurious results. The length of the flat is measured as 20.9mm and the number of pixels that correspond to this are counted in MATLAB as shown in Figure 5.16a. A scale of μm/pixel is defined for all of the measurements that are associated with this configuration. An initial grid of control points is specified over the entire speckle pattern as shown in Figure 5.16b. In order to compare the DIC and LDV measurements it must be possible to specify the y-coordinate of the speckle pattern that is associated with the location of the LDV measurement. The distance from the top of the flat to the location of the LDV is measured and this is used to specify a fraction in the y-axis of the ROI. However the initial grid covers portions of the horn at the start and the end of the flat, which appear to protrude over the speckle pattern, due to perspective errors inherent in the camera images. Therefore two rows of pixels are removed from the top and the bottom of the grid. Also, for rod-like behaviour it is desirable that the grid is more slender, so 4 columns of pixels are removed from the left and the right of the grid. The modified grid is shown in Figure 5.16c.

The DIC of the unloaded CPA with the MH attached is carried out over the full 102 available images. The computation of the displacement field is carried out and it is recommended to apply some smoothing to the field before the strain field is calculated. Spatial smoothing provides robustness against noise and reduces edge effects when the displacement at the edges of the ROI are reflected. The spatial smoothing is applied by masking the displacements, at groups of control points, through a Gaussian distribution that is located at the centre of the chosen kernel. The number of smoothing passes can be specified to average the displacements over a number of iterations. To assess the noise floor of the unloaded tests, the displacement in each direction is averaged over time. These are then plotted for a constant kernel size of 11 and an increasing number of smoothing passes. The results are shown in Figure 5.17. These suggest that there are limitations in the response of the camera sensor at the beginning and end of the total acquisition period. Subsequent correlations for this set up are limited to images 14-79 and three smoothing passes are applied. From the measured location of the LDV, the fraction of the ROI of the speckle pattern is calculated,

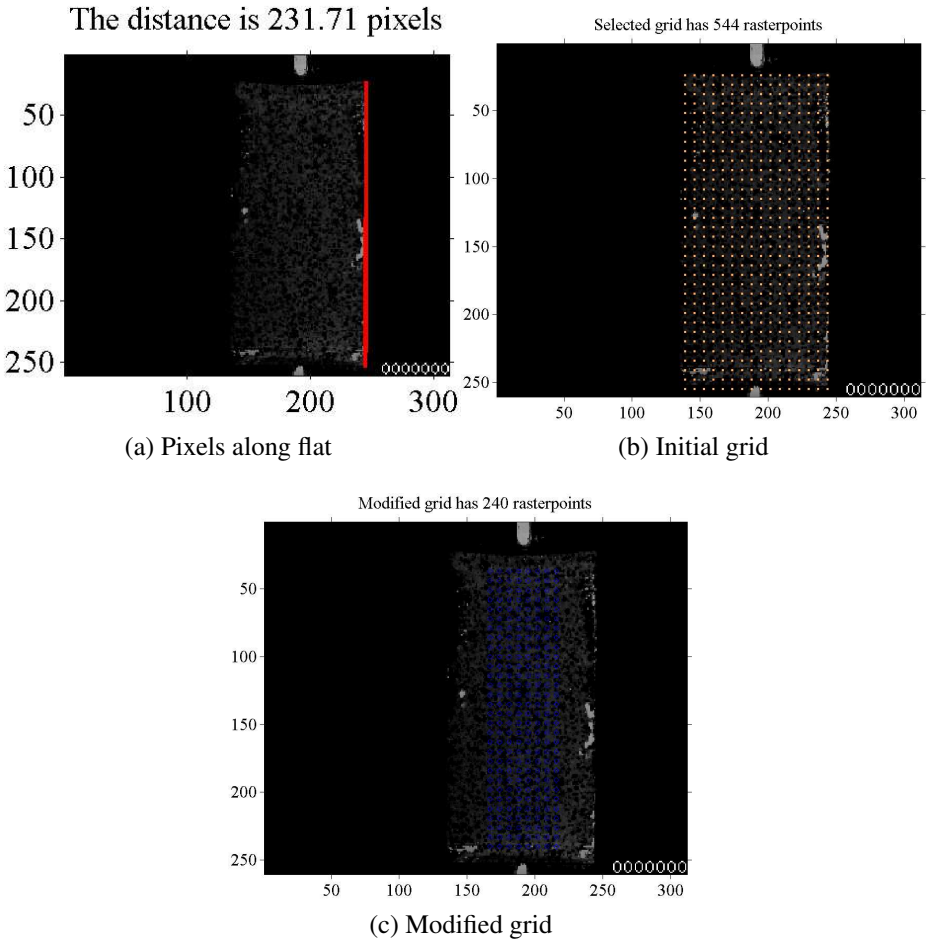

(a) Pixels along flat

(b) Initial grid

(c) Modified grid

Fig. 5.16 Defining the grid of control points.

and the average vertical displacement is obtained for the pixels that are located horizontally over this fraction. The results are shown in Figure 5.18 and demonstrates the non uniformity of the displacement field. This is consistent over the window of acquisition. Edge effects can be seen at the top and bottom of the flat, however these are situated close to the transition from the flat to the cylindrical rod where projection errors are most significant. The influence of these edge effects on the overall average axial (vertical) displacement is minimal and the displacements towards the middle of the ROI remain close to the range that is given by the line average in Figure 5.18b.

When applying the DIC method to obtain strain fields, it is assumed that displacements are continuous over the ROI. When the Jointed Horns (JH) are tested it is necessary to choose a portion of the speckle pattern that is above or below the bearing surface of the axial joint. The LDV is always focussed onto a point that is below the bearing surface. The ROI will

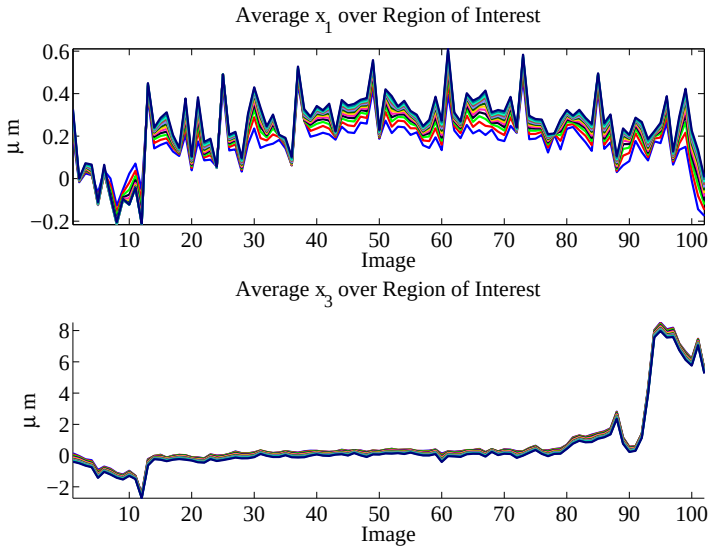

(a) Images 1-102

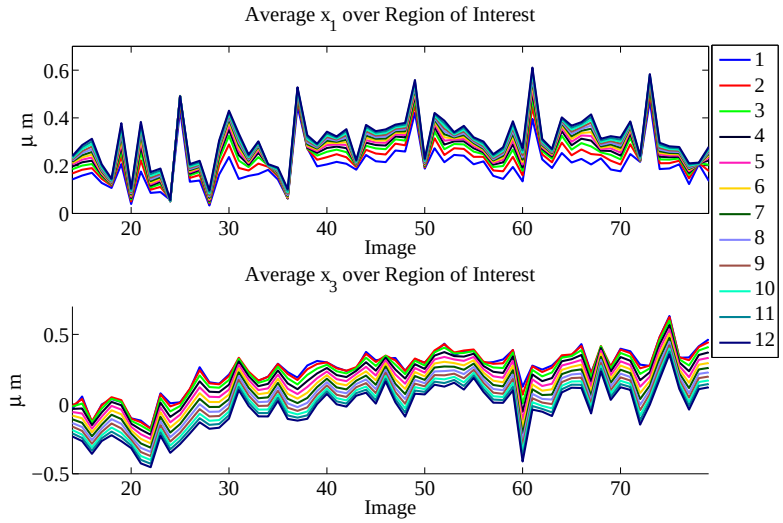

(b) Images 14-79

Fig. 5.17 Average displacement in each direction for the time window observed by the high speed camera with an increasing number of spatial smoothing passes applied to the images before taking the average displacement.

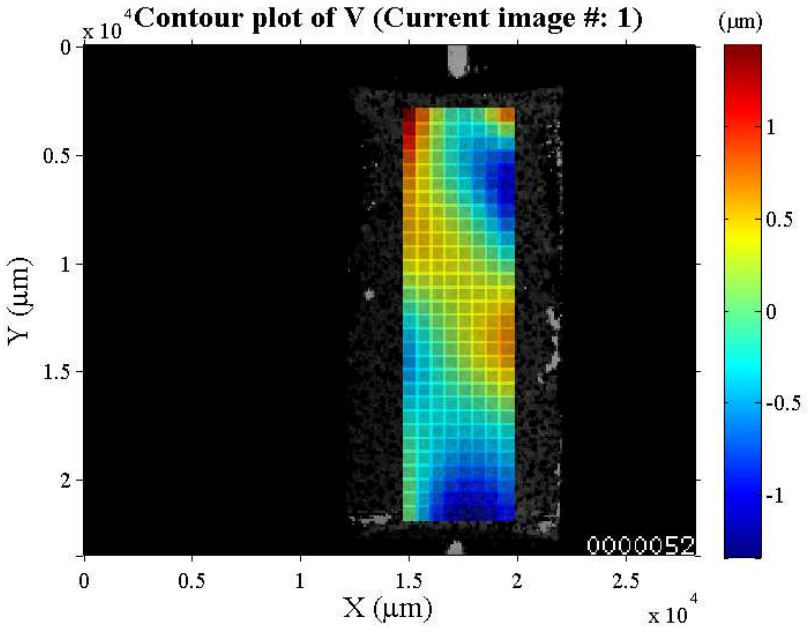

(a) Unloaded u_3 contour

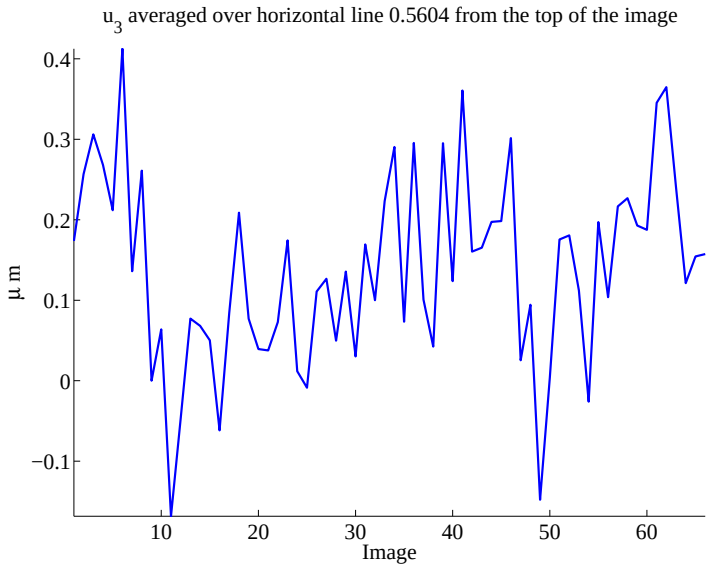

(b) Average u_3 at X_2

Fig. 5.18 Noise floor Digital Image Correlation reading for the Commercial Piezoelectric Actuator with Monolithic Horn attached subject to no excitation.

always be defined as the lower portion of the flat on each of the speckle patterns that are shown in Figure 5.1.

Exchanging the horn that is attached to the piezoelectric actuator can result in damage to the speckle pattern because a custom made torque adapter grips the horn by the flat during tightening. Before tests with the IHPA each speckle pattern is removed completely with an acetone solution and is then reapplied. The noise floor for the MH, when it is attached to the IHPA, is shown in Figure 5.19. A comparison to Figure 5.18 shows that the noise level in both cases is consistent, despite the reapplication of the speckle pattern and any differences in alignment between the two cases.

Commercial Piezoelectric Actuator

The CPA is tested with each of the MH or JHs attached. Each assembly is excited through the Sonic Systems power supply that locks onto the maximum phase of the impedance of the CPA to optimise the transfer of electrical power. The level of excitation is set from an analogue dial which gives a nominal reading of the peak amplitude in microns for the CPA with no tool attached to its front mass. Each of the results that follow are labelled for the setting of this analogue dial. This does not correspond to the output of the device, but is provided to show that more or less power has been supplied to it between tests of the same HPU assembly. The power supply cannot be triggered automatically, so the excitation of the device cannot be synchronised with the rest of the apparatus. Instead it is activated manually and then the camera and the oscilloscope acquisition is triggered before the power supply can be deactivated again. Continuous excitation is associated with softening overhang behaviour in the frequency response of the device, so a minimal excitation period is desirable. As a result it is not possible to separate the influence of heating of the device from the results obtained through this set up. Instead it is assumed that the behaviour of the axial joint will be more prevalent in the results than the other known nonlinearities of the device.

A reliable acquisition window of images 14-79 is identified by obtaining the displacement field for the assembly with no excitation signal applied. This gives an acquisition window of $T = 260\mu s$ over which it is expected that approximately five cycles will be captured. The expected noise level has been given in Figure 5.18 as $\pm 1\mu m$. However this estimate is dominated by the edge effects that are inherited when DIC is applied. The overall noise floor is unavoidable when assessing the strain field. The displacements that are derived through the DIC method, for the MH tests, are given in Figure 5.20 . The corresponding spectra are

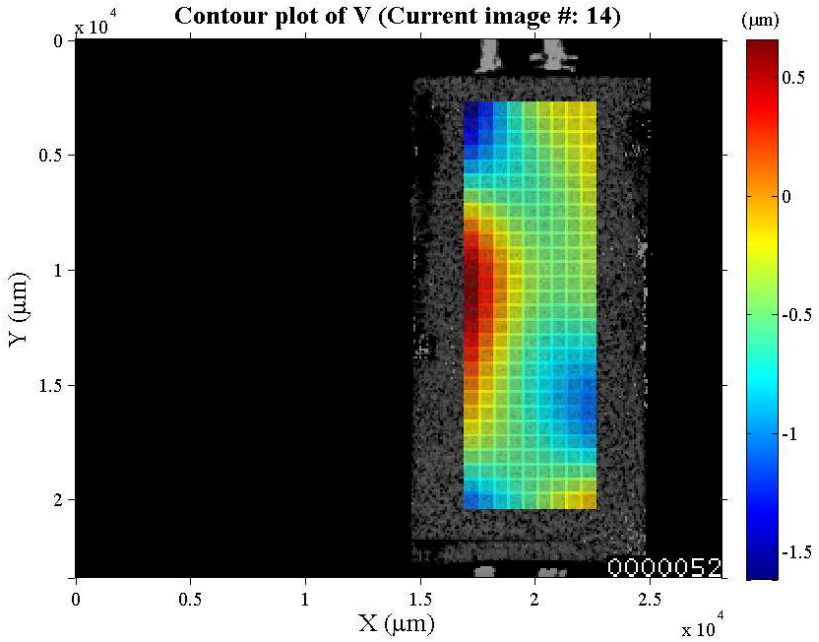

(a) Unloaded u_3 contour

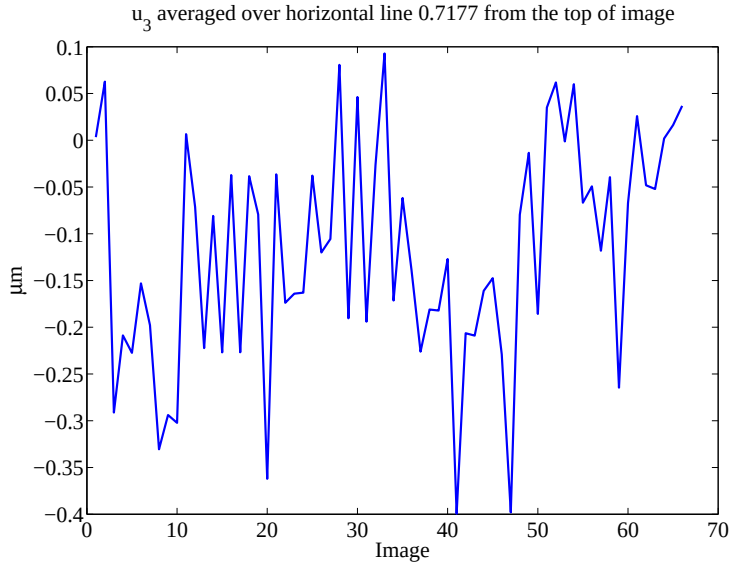

(b) Average u_3 at X_2

Fig. 5.19 Noise floor Digital Image Correlation reading for the In-House Piezoelectric Actuator with Monolithic Horn attached subject to no excitation.

given in Figure 5.21 . The spectra have been calculated by applying the MATLAB `fft()` function to the product of the displacement signal and the `hann()` window. The definition of each FFT is increased artificially by padding the acquisition period with trailing zeros up to 512 samples. Due to the very short time window, the resolution bandwidth of the FFT is limited to 3.8kHz. However the Complex Modal Indicator Function (CMIF), displayed in Figure 4.7, suggests that this is sufficient to distinguish the resonance of the MH due to the 2nd longitudinal mode at 20.8kHz. As the excitation to the assembly is increased, the displacement spectrum remains centred close to the expected frequency.

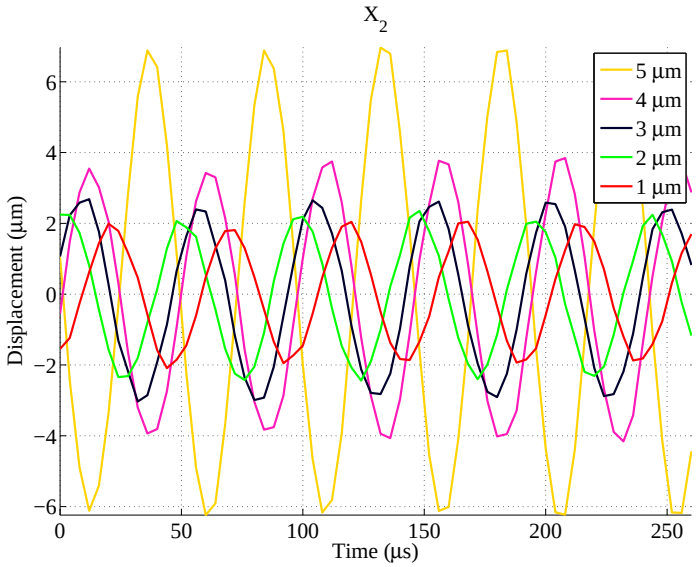

Fig. 5.20 Digital Image Correlation estimates of displacement for the Commercial Piezoelectric Actuator with the Monolithic Horn attached.

A limited number of experimental runs is shown when testing each of the JHs because increasing the power to each assembly tends to saturate the output. This suggests that the frequency behaviour of the electrical impedance of the device is changing as the power level is increased. This implies a change to the frequency behaviour of the mechanical assembly itself. If this is associated with an overhang frequency behaviour then it should possible to observe energy transfer to other frequencies in the spectrum. Another limiting factor to the experiment is that the saturation of the amplitude is accompanied by audible high pitched squealing from the device. Future experiments should involve JHs with an operating resonance that is above 20kHz.

The displacements obtained from testing each JH are shown in Figures 5.24-5.27. Clear low frequency modulation of the primary resonance frequency can be observed in most

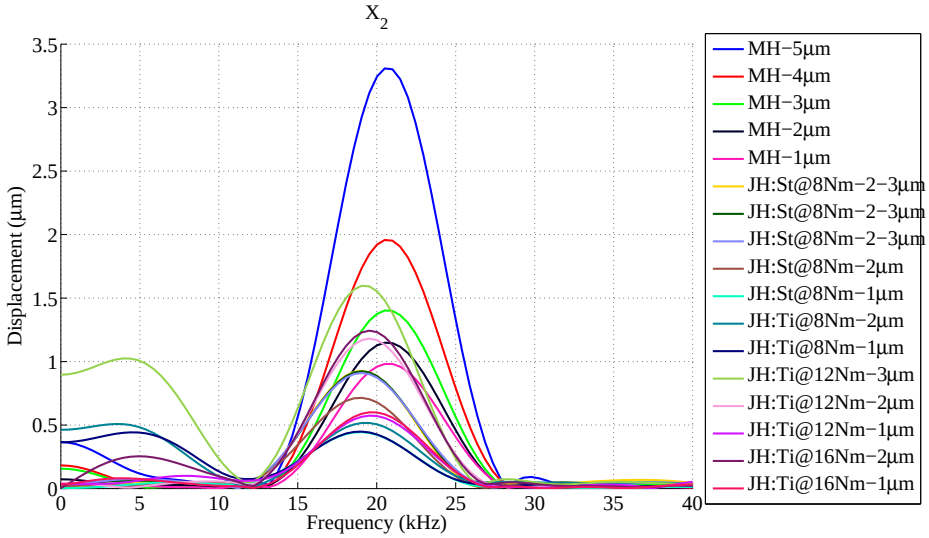

Fig. 5.21 Digital Image Correlation estimates of displacement spectra for the Commercial Piezoelectric Actuator with the each horn attached.

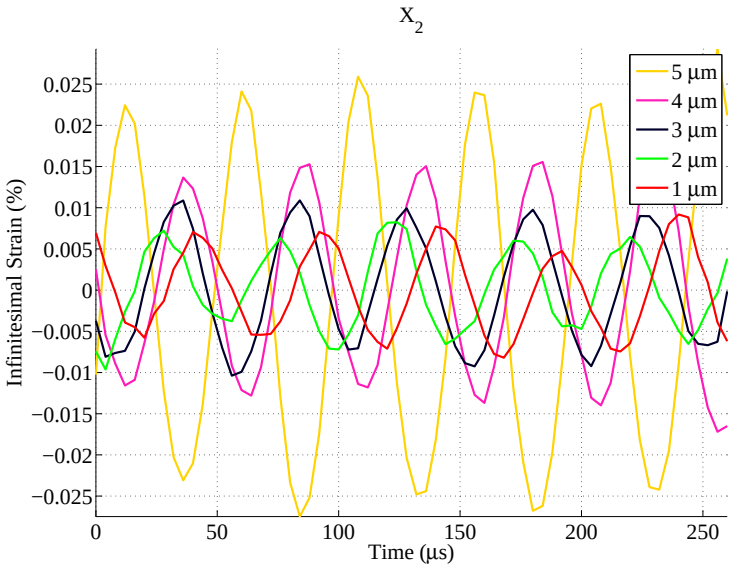

Fig. 5.22 Digital Image Correlation estimates of strain for the Commercial Piezoelectric Actuator with the Monolithic Horn attached.

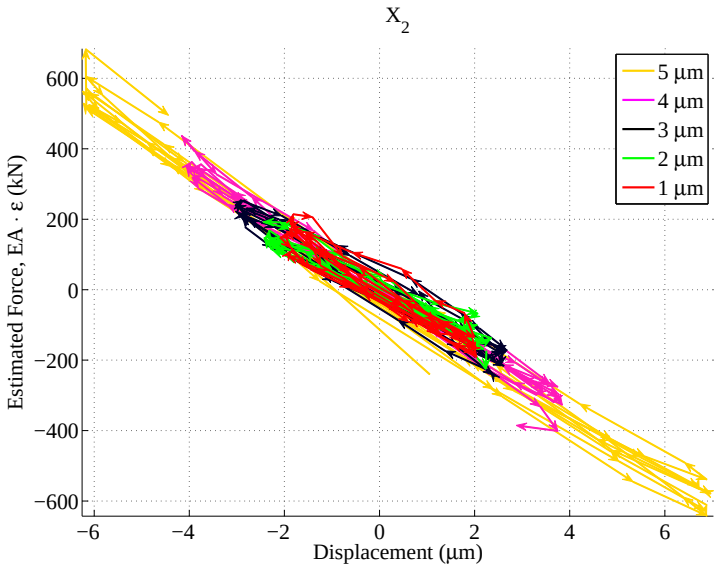

Fig. 5.23 Digital Image Correlation estimates of hysteresis loops for the Commercial Piezoelectric Actuator with the Monolithic Horn attached.

of the tests. The DIC measurement window is assessed when no power is applied to the device to ensure that the modulation is not associated with the illumination of the speckle pattern. However, if the modulation is associated with a vibration mode that contributes to out of plane motion, then this will distort the measurement of the axial displacement. The CMIF in Chapter 4 shows that modes other than those associated with longitudinal motion could not be detected reliably above the noise level of the EMA. The spectra in Figure 5.21 display the limited resolution FFT estimate of each of the primary resonances. Each resonance is centred close to the equivalent minimum impedances that were given in Figure 4.1. The spectra that are found from the clearly modulated displacements produce a low frequency component that is centred close to 5kHz. This is most significant in the spectrum that is obtained from testing the JH featuring a titanium cap that has been tightened to 12Nm. When this ultrasonic component is excited at the 3µm setting, the spectrum of the displacement shows a clear peak close to 4kHz, as well as a primary resonance at 19kHz.

The strain field has also been estimated for each test. The MH and JH results are given in Figure 5.22 and Figures 5.28-5.31 respectively. The latter shows that noise inherent in the displacement field is significant to the strain estimations. The force through the cross section is estimated from the derived strain, S, according to $F = EAS$. This is appropriate for the MH strain field because for small vibrations the Young's Modulus should be linear.

However, when testing each JH, the stiffness that is local to the cross section, will feature a gradient due to the prestress applied through the tension of the stud. The discussion in Chapter 4 showed that determining the nature of the prestress, by means of the suggested framework, remains an open question. The hysteresis loops that are drawn from the MH results in Figure 5.23 are expected to be elliptical, however a higher sample rate is required to observe the shape of the velocity reversal points to confirm this. The JH loops in Figures 5.32-5.35 are contaminated by noise, so it is difficult to discern the characteristic shape of the loop. Each average strain trace has been smoothed with the MATLAB moving average filter `smooth()`, for a span of 10%, in order to reduce the high frequency noise. The hysteresis loop from the 12Nm horn suggests that the loop is deviating from the shape of the equivalent MH loop. The loading-unloading curve between the velocity reversal points appears to have a cubic form and the loop exhibits pinching, which is associated with a loss of stiffness during the vibration cycle.

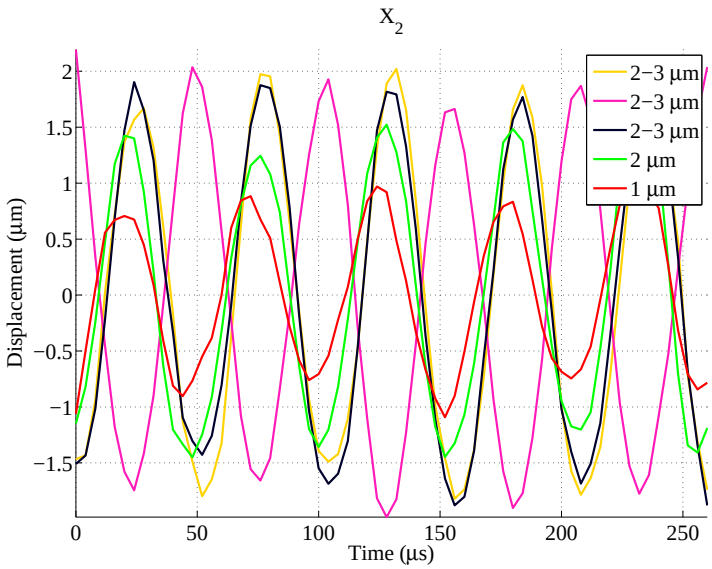

Fig. 5.24 Displacement estimated by Digital Image Correlation for the Commercial Piezoelectric Actuator with the Jointed Horn attached which features a Steel stud set to 8Nm.

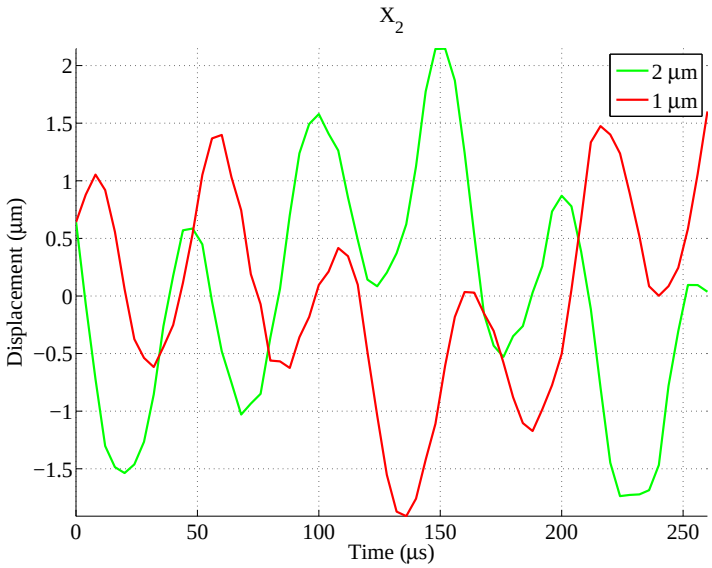

Fig. 5.25 Displacement estimated by Digital Image Correlation for the Commercial Piezoelectric Actuator with the Jointed Horn attached which features a Grade 5 Titanium stud set to 8Nm.

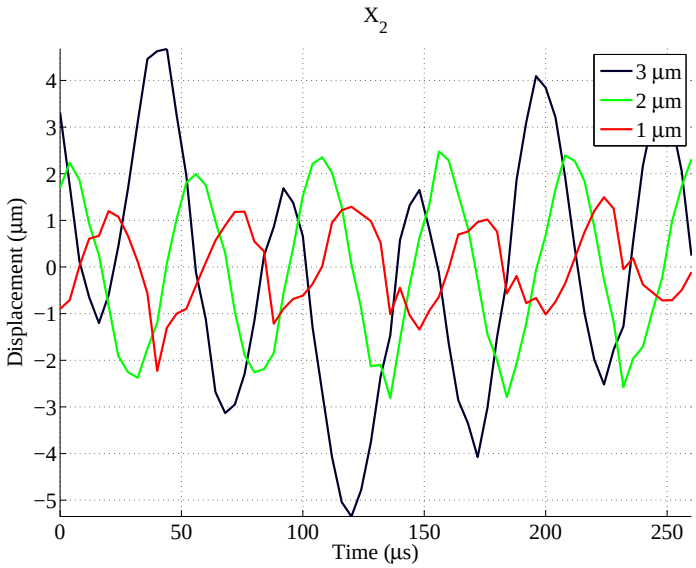

Fig. 5.26 Displacement estimated by Digital Image Correlation for the Commercial Piezoelectric Actuator with the Jointed Horn attached which features a Grade 5 Titanium stud set to 12Nm.

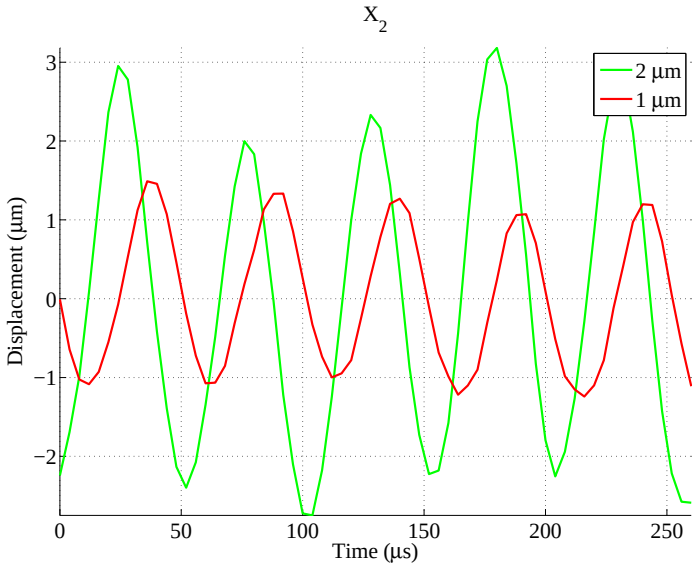

Fig. 5.27 Displacement estimated by Digital Image Correlation for the Commercial Piezoelectric Actuator with the Jointed Horn attached which features a Grade 5 Titanium stud set to 16Nm.

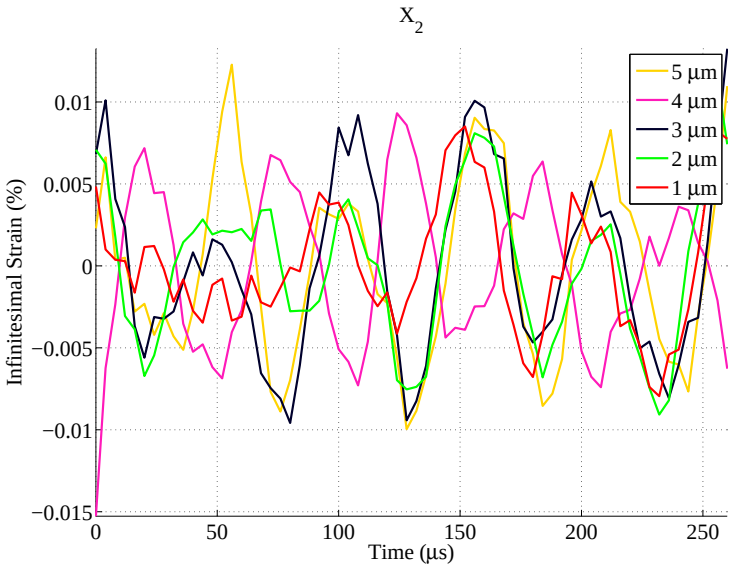

Fig. 5.28 Strain estimated by Digital Image Correlation for the Commercial Piezoelectric Actuator with the Jointed Horn attached which features a Steel stud set to 8Nm.

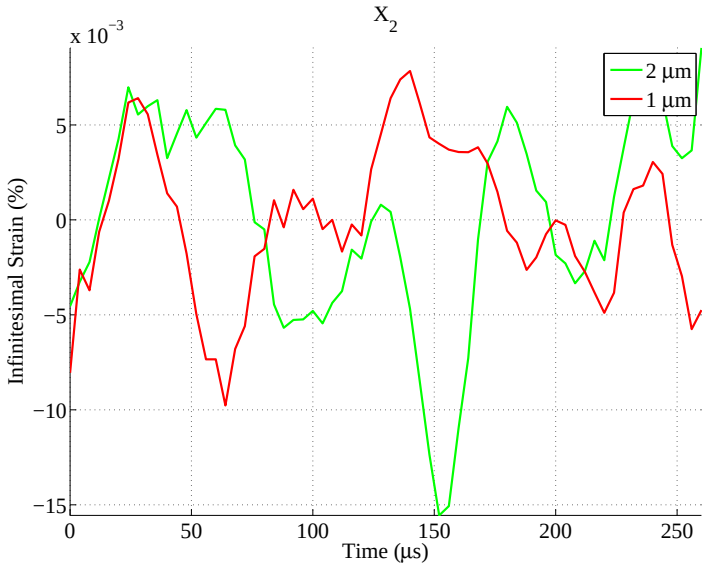

Fig. 5.29 Strain estimated by Digital Image Correlation for the Commercial Piezoelectric Actuator with the Jointed Horn attached which features a Grade 5 Titanium stud set to 8Nm.

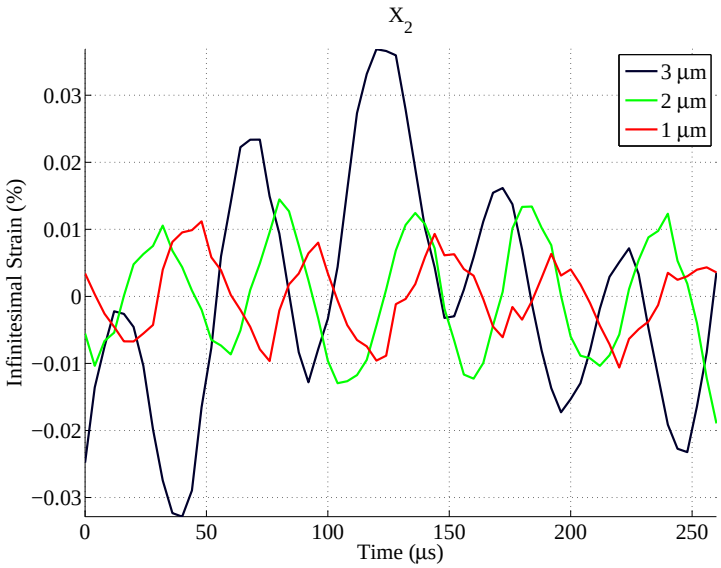

Fig. 5.30 Strain estimated by Digital Image Correlation for the Commercial Piezoelectric Actuator with the Jointed Horn attached which features a Grade 5 Titanium stud set to 12Nm.

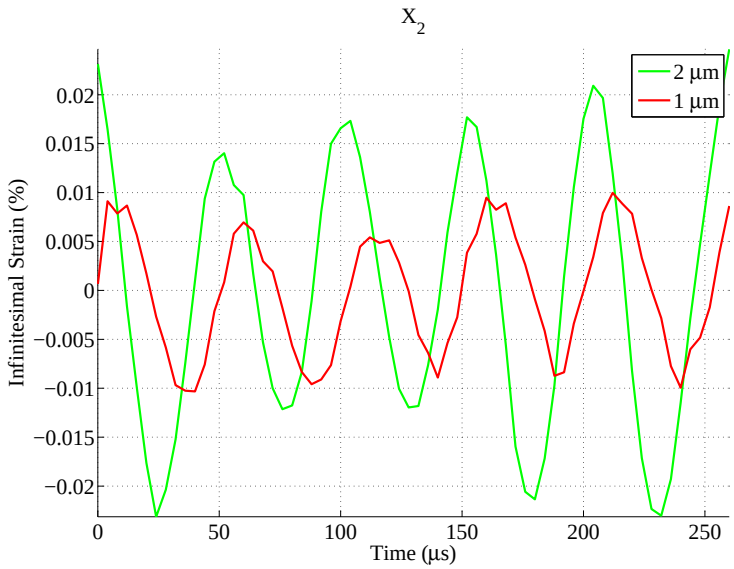

Fig. 5.31 Strain estimated by Digital Image Correlation for the Commercial Piezoelectric Actuator with the Jointed Horn attached which features a Grade 5 Titanium stud set to 16Nm.

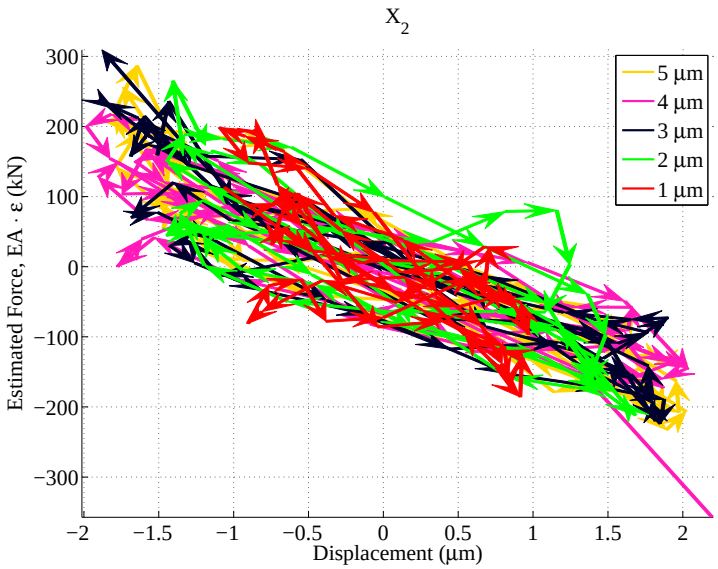

Fig. 5.32 Hysteresis loops estimated by Digital Image Correlation for the Commercial Piezoelectric Actuator with the Jointed Horn attached which features a Steel stud set to 8Nm.

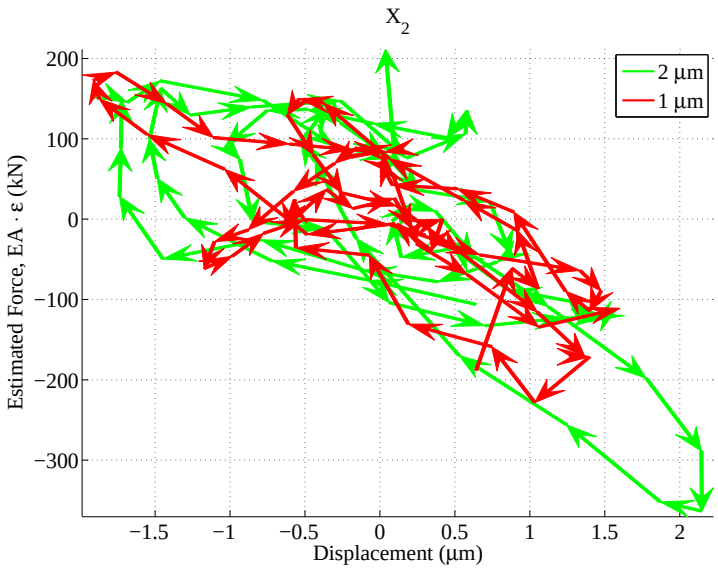

Fig. 5.33 Hysteresis loops estimated by Digital Image Correlation for the Commercial Piezoelectric Actuator with the Jointed Horn attached which features a Grade 5 Titanium stud set to 8Nm.

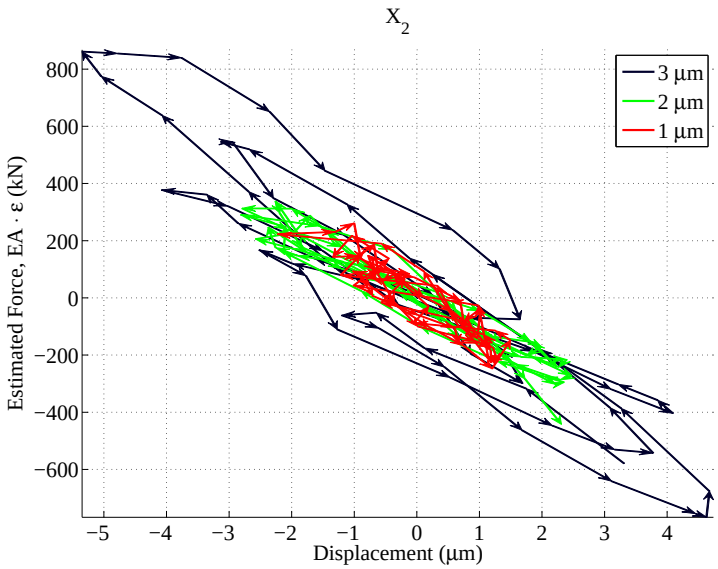

Fig. 5.34 Hysteresis loops estimated by Digital Image Correlation for the Commercial Piezoelectric Actuator with the Jointed Horn attached which features a Grade 5 Titanium stud set to 12Nm.

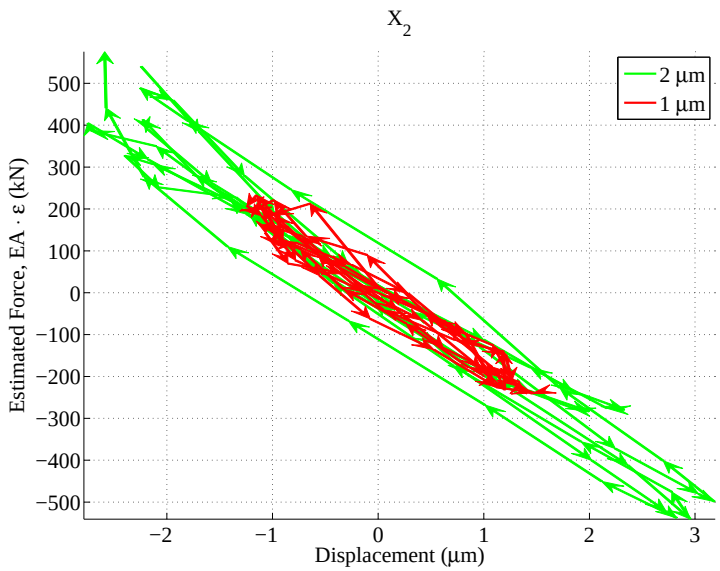

Fig. 5.35 Hysteresis loops estimated by Digital Image Correlation for the Commercial Piezoelectric Actuator with the Jointed Horn attached which features a Grade 5 Titanium stud set to 16Nm.

In-House Piezoelectric Actuator

A limitation of applying the force identification scheme to the CPA test data is that a number of geometric parameters had to be estimated, within some known constraints, because full access to the true geometry is not possible without damaging the device. Real time observation of the transient electrical behaviour is not available through its matching power supply. In order to remedy this problem, the IHPA was manufactured as a simplified version of the CPA. A comparison of the modal behaviour between the two actuators, in Section 4.4, demonstrated that the vibration of the CPA is dominated by its longitudinal modes whereas the IHPA features bending or torsional modes that are closely spaced to its longitudinal modes. This is undesirable because a rod-like description of the assembly is intended.

Each run of the experiment involves attaching either the MH or one of the JHs to the IHPA and then defining a peak to peak amplitude, V_{pk-pk}, of sinusoidal voltage from the function generator. The voltage signal consists of 160 cycles at the resonant frequency of the HPU assembly that is close to 20kHz. The average power, P_{mean}, that is produced by the waveform generator is estimated based on the nominal amplitude of this signal and is given for each setting in Table 5.3. The output channel from the function generator, the BNC cables used for connecting each channel and both of the input and output channels of the amplifier

have an impedance of $|Z_0| = 50\Omega$. The voltage is amplified by the 2200L Radio Frequency power amplifier, which is manufactured by Electronics and Innovation. This is a broadband amplifier that covers a spectrum of 10kHz to 12MHz and has a set gain of $L_{dB} = 53$dB. The manual states that it features a highly linear design and will not oscillate even if the source and load impedance are mismatched. The amplifier produces Class A linear output up to 200W (P_1dB). At this point the output power has deviated from linearity by -1dB. The input power for the rated output is 1mW, after which the gain will compress, as the input power rises. Once this departure from a linear gain is -3dB, the saturated power is given as 250W minimum for the 10kHz-10MHz frequency range. The amplified power, $P_{@|Z_0|}$, of each excitation signal is given in Table 5.3 on the assumption that the output impedance is equal to Z_0. Figure 4.5 shows the varying load impedance, Z_L, that the amplifier is likely

Table 5.3 Summary of the average power at the input and output terminals of the power amplifier.

V_{pk-pk} (mV)	P_{mean} (mW)	$P_{@\|Z_0\|}$ (W)
100	0.025	4.988
200	0.100	19.95
300	0.225	44.89
400	0.400	79.81
450	0.506	101.0

to encounter when it is required to drive each HPU assembly. Each assembly is excited at low voltages in order to minimise the heating of the piezoceramic elements. Due to the mismatch between the load impedance and the output impedance of the amplifier, a portion of the forward power will be absorbed, as it is reflected backwards. This reflected power can be read from the amplifier display, but cannot be recorded real time. The forward power from the amplifier is not observed because the high output voltage involved would have damaged the oscilloscope. This could be remedied through the use of a high voltage probe with the oscilloscope. The power that is reflected back to the amplifier can be estimated through the reflection coefficient: $|\Gamma_Z| = \left|\frac{Z_O - Z_L}{Z_O + Z_L}\right|$. This gives a mapping of the forward power that is delivered to the load [116]:

$$P_+ = 10^{0.1\left[10log_{10}\left(1-|\Gamma_Z|^2\right)+10log_{10}\left(P_{@|Z_0|}\right)\right]} \tag{5.15}$$

Data from the impedance analysis in Figure 4.5 is assumed in order to calculate the expected power that will be delivered to each HPU assembly. The absolute minimum impedance

from each trace is listed in Table 5.4 along with the subsequent reflection coefficient. If the V_{pk-pk} = 300mV signal is amplified linearly, below the P_1 limit, and the load and amplifier are impedance matched, $Z_L = Z_0$, then power delivered to the IHPA terminals is: P_+ = 44.89W. However, if the impedance of the load is taken from Figure 4.5, when any one of the ultrasonic horns is attached, then the full power is not transmitted. The HPU device has been disassembled and reassembled between each measurement of the load impedance and before each transient measurement that has been obtained. The same protocol of assembly has been followed each time, but some variation of the impedance spectrum is expected. Figure 5.36 shows the expected transmitted power to the device. Small changes to the impedance spectrum of the device can result in a dramatic change in the level of power that is reflected back to the amplifier. This is especially true when the MH is tested, whereas the equivalent JH test will achieve a lesser variation in reflected power. Clearly, for the purpose of this experiment, direct observation of the voltage at the terminals to the IHPA is best. Without this a new impedance matching circuit would need to be produced after assembling the HPU device for each ultrasonic horn in the test. Otherwise the described estimation of power transfer must be assumed.

Table 5.4 Summary of the minimum impedance that is associated with the dominant axial behaviour for each In-House Piezoelectric Actuator test assembly and the subsequent power reflection coefficient.

Horn	Horn Joint	Impedance Magnitude, $\|Z_L\|$ (Ω)	Reflection Coefficient, Γ_Z
JH	St@8Nm	26.52	0.307
JH	Ti@8Nm	28.60	0.272
JH	Ti@12Nm	10.01	0.666
JH	Ti@16Nm	7.711	0.733
MH	-	3.613	0.865

The relationships that have been assumed, to estimate the power transfer to an HPU assembly, are summarised through the schematic in Figure 5.37. The function generator produces a waveform with a peak-to-peak voltage, V_{pk-pk}, given in Table 5.3. The average power, P_{mean}, that is produced at the input to the power amplifier, is estimated from the Root Mean Square voltage, V_{RMS}. The linear gain of the power amplifier, L_{dB}, is added to the decibel value of the power at the input and the reflected power is removed through the reflection coefficient, Γ_Z, to give the forward power P_+. The transformation of the voltage at the terminals to the piezoelectric actuator, V, to the interface force at node 6, $q(\tau)$, is not expected to produce a good estimation from the simplistic electro-mechanical relationship. However

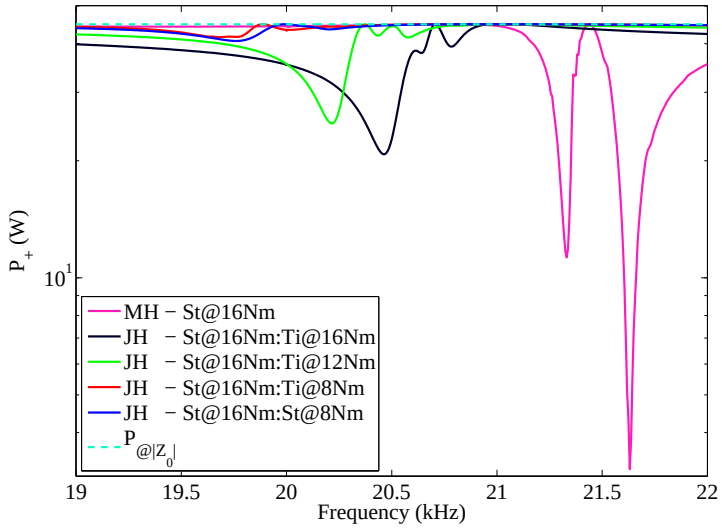

Fig. 5.36 Power transmitted from the amplifier estimated for each measured impedance of ultrasonic assembly made with the In-House Piezoelectric Actuator

some estimation of the input to a JH HPU assembly is required to find a least squares estimation of the joint force. It is assumed that the linear calibration model provides a suitable means of estimating the force at the piezoelectric stack from the response of the IHPA with the MH attached. This force is written as: $q_6^{MH}(\tau)$ and the unknown force at the same location of the IHPA with a JH attached is written as: $q_6^{JH}(\tau)$. The model in Figure 5.37 implies that, within the limitations of the one dimensional model, the ratio of the two forces is as follows:

$$\frac{q_6^{MH}\left(\omega_2^{MH}\right)}{q_6^{JH}\left(\omega_2^{JH}\right)} = \frac{|Z_L|^{JH}}{|Z_L|^{MH}} \sqrt{\frac{|Z_L|^{MH}\left(P_+^{MH}\right)}{|Z_L|^{JH}\left(P_+^{JH}\right)}} \tag{5.16}$$

where the constants are assumed when ω_2 is the resonant frequency of the 2$^{\text{nd}}$ longitudinal mode of the MH or the JH assembly, and the force at node 6 of the MH assembly has been estimated for the same V_{pk-pk} excitation voltage that has been applied to produce the response of the JH assembly. Therefore the problem that remains is that $\omega_2^{MH} \neq \omega_2^{JH}$, so solving Equation (5.16) for the JH force will not produce an appropriate estimate its input force. If it is assumed that the estimate will scale the MH force, so that it is close to the unknown input force, then this does provide a route to finding the least squares difference between the forces, that are developed in each HPU assembly, without directly addressing the nature of the axial joint. The principal resonance frequency of the JH assembly is known. It is possible to downsample the scaled MH force and adopt this as the input to the

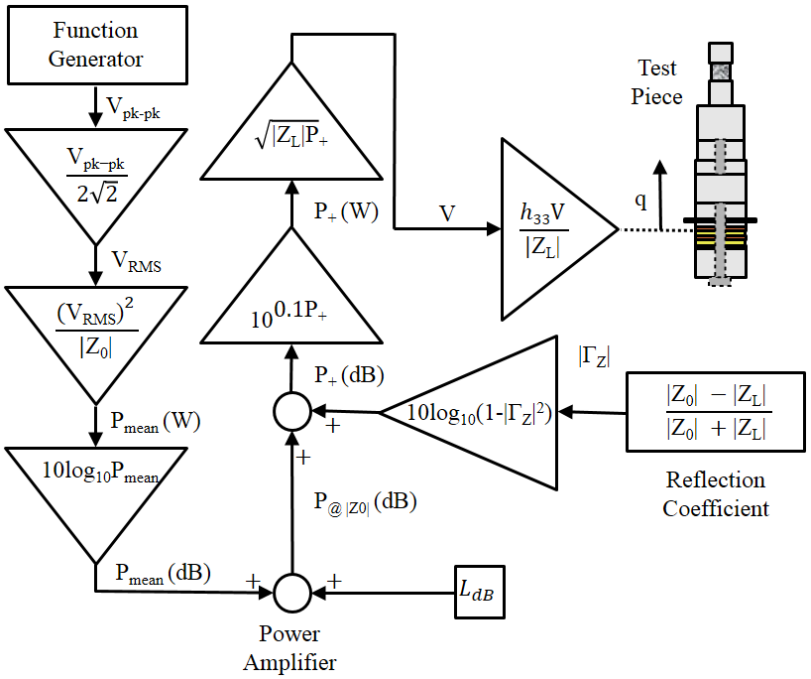

Fig. 5.37 Model of the average power delivered to the In-House Piezoelectric Actuator.

least squares force identification. Clearly an impedance matching circuit between the power amplifier and the HPU device will reduce the number of assumptions that are required. However, in attempting to isolate the joint force, a comparison between equivalent monolithic and jointed HPU assemblies will always need to be excited at two distinctly separate resonant frequencies in order to produce large enough amplitudes of vibration to facilitate either the DIC or force estimation procedures. Therefore it is not possible to simplify the force estimation by assuming that the same input force is seen by both assemblies.

A transfer function model that allows for detailed electromechanical transient relationships is necessary to make progress. The current scheme does not provide access to the transient electrical characteristics of the piezoelectric stack. This is essential to understanding the input behaviour of the HPU assembly and needs to be observed directly. Knowledge of this input behaviour is vital to isolating the behaviour of the axial joints and this will also require a detailed model of the strain that is generated by each piezoceramic disk. To achieve this, the method in Chapter 3 needs to increase in complexity because a higher mode waveguide theory is required to give a more reasonable estimate of the rod-like behaviour of the piezoelectric stack when it is described through a one dimensional model.

The proceeding chapters discuss the possibility of fitting a simplified hysteresis model to

the hysteresis loops that are identified in this chapter. In order to reduce model fitting errors it is desired that the response of the assembly is recorded from rest up to the number of samples that may be processed through the force identification program. The sample rate is the same that was chosen for the high speed camera records. This gives approximately 5000 samples, at 250kS/s, which will be observed through laser vibrometry. To obtain the best results, through the DIC method, the limited number of camera samples are aligned with the portion of the acquisition window where the level of displacement is greatest. Despite the overall noise floor, which is given in Figure 5.19 as 2µm pk-pk, the lowest displacement shown in Figure 5.38 is in phase with the rest of the measurements. This noise floor includes edge effects that are inherent to the results processed through DIC. For each measurement the resonance was found by tuning the excitation frequency from the function generator. The resonance condition of the MH assembly did not vary noticeably as the input voltage was increased. Each spectrum is centred close to the 2nd longitudinal mode that was identified through the modal analysis in Table 4.5.

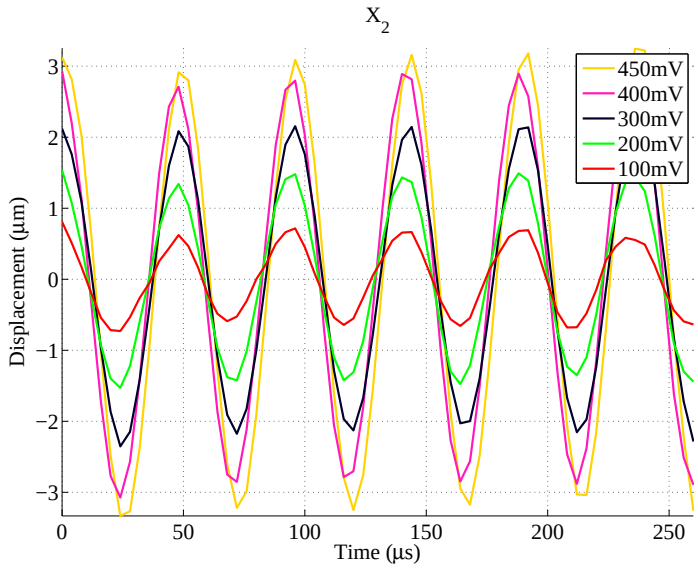

Fig. 5.38 Digital Image Correlation displacement estimates for the In-House Piezoelectric Actuator with the Monolithic Horn attached.

The displacements that are measured from each JH assembly are shown in Figure 5.42-5.45. Overall the displacements achieved with the IHPA are smaller than those found from the equivalent CPA tests. The impedance mismatch is the limiting factor. Above 100mV pk-pk the noise in the displacements is negligible. The spectra that are shown in Figure 5.39 suggest that the operating mode, estimated through the EMA in Table 4.6, has reduced

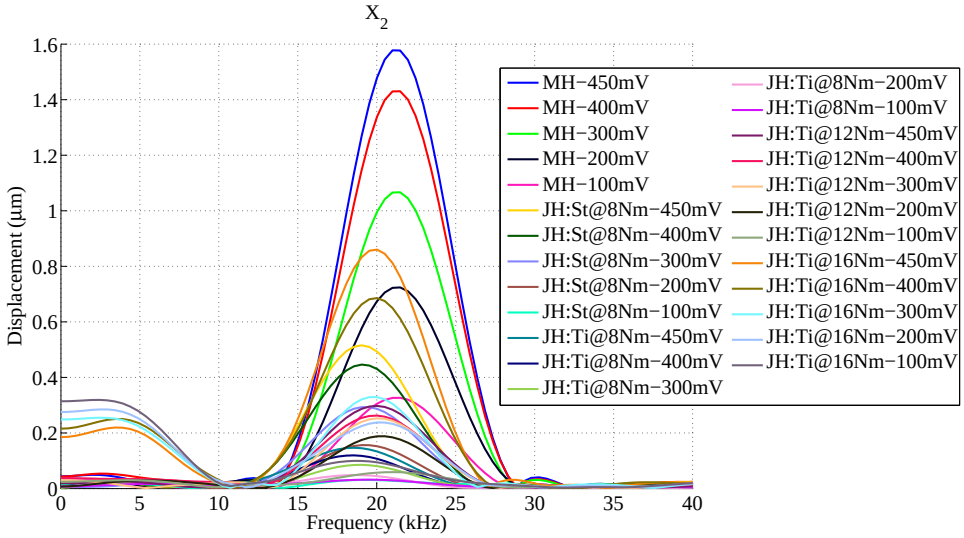

Fig. 5.39 Digital Image Correlation displacement spectra estimates for the In-House Piezoelectric Actuator with the Monolithic Horn attached.

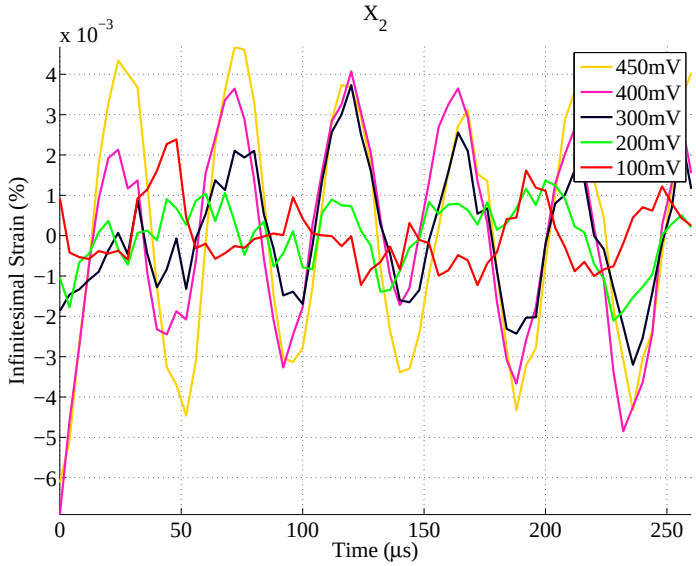

Fig. 5.40 Digital Image Correlation strain estimates for the In-House Piezoelectric Actuator with the Monolithic Horn attached.

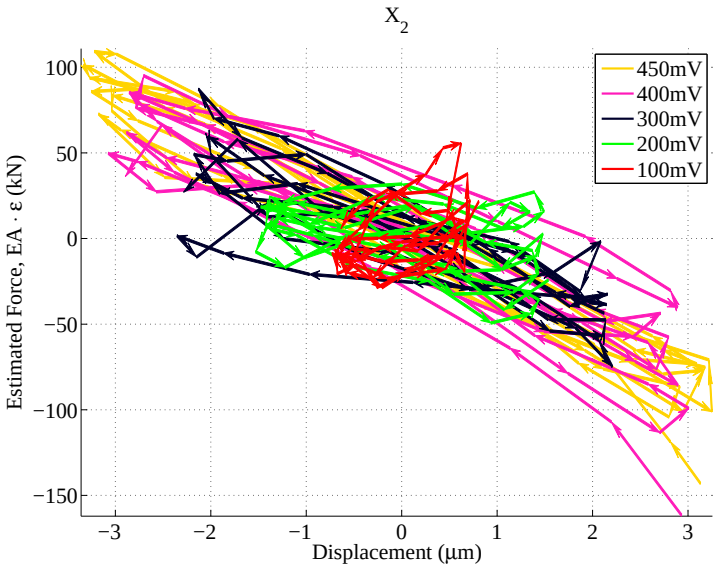

Fig. 5.41 Digital Image Correlation hysteresis loop estimates for the In-House Piezoelectric Actuator with the Monolithic Horn attached.

in frequency as the amplitude of the voltage is increased. For each JH test, the resonance condition varied for increasing input voltage. This was identified manually by tuning the frequency of the excitation signal, but it is not always clear from the limited resolution spectra. The spectra measured from the IHPA follow a similar pattern to the spectra of the CPA with the JHs attached. There is some suggestion of low frequency components that accompany the primary resonance. For the JH with a titanium cap, which is set to 16Nm, a primary resonance component of 19.73kHz was identified manually and the spectrum features a frequency component that is centred close to 4kHz.

The strain estimations in Figure 5.40 show that, due to the small displacements observed, the noise floor is significant. A modest degree of smoothing has been applied through a moving average filter with a span of 10%. Higher degrees of smoothing will induce an error at the start of the time window and this is encountered in the 400mV pk-pk and 450mV pk-pk strain readings. The poor strain estimations yield hysteresis loops that are noisy when the excitation voltages that are lower than 300mV pk-pk are evaluated in Figure 5.41. The remaining hysteresis loops appear to have a reduced strain rate at the velocity reversal points, but steady state vibrations have not been reached, so the loop deviates over time instead of tracing over a similar path, as shown in Figure 5.23. The sample rate limitation means that there are not enough points where the hysteresis has been recorded close to the velocity reversal points, and the points that have been found, suffer from significant noise. Without

this information it is not possible to determine the hysteresis loop from transient vibrations. The outlier points in the loops are associated with the limitations of the DIC or with the moving average filter at the spatial or temporal boundaries of the data respectively.

The JH strains in Figures 5.46-5.49 are mostly contaminated by noise and this is prevalent in the derived hysteresis loops in Figures 5.50-5.53. Modulation of the forcing frequency is significant in the strains. The hysteresis loops appear to be too noisy to be able to infer the form of a hysteresis loop that is associated with the axial joint behaviour. The hysteresis loops that are associated with the JH, with a Grade 5 Titanium stud set to 16Nm, appear to translate significantly over the observation window and are displayed in Figure 5.53. The lighting conditions of the speckle patterns appeared to be stable throughout the tests. However inspection of this set of results revealed a systematic error as each set of image records was contaminated with additional reflections from the flash lamps. Although the set up was not altered significantly between this test and the previous tests, the speckle pattern was more reflective in this case.

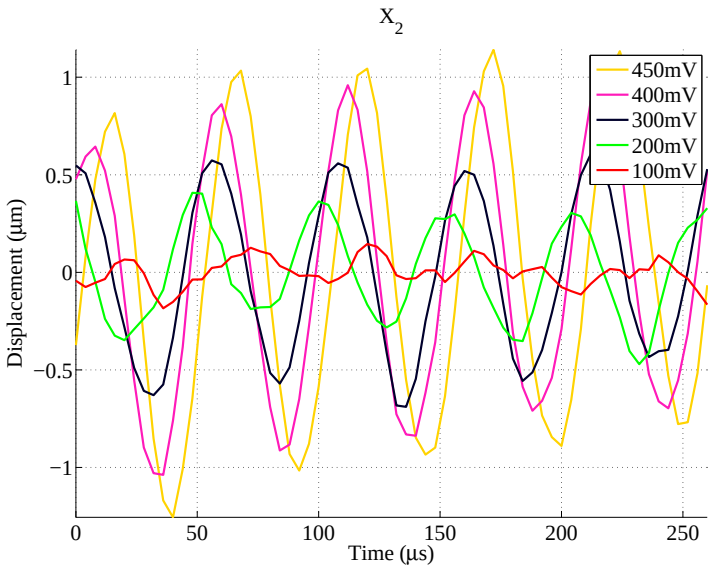

Fig. 5.42 Displacement estimated by Digital Image Correlation for the In-House Piezoelectric Actuator with the Jointed Horn attached which features a Steel stud set to 8Nm.

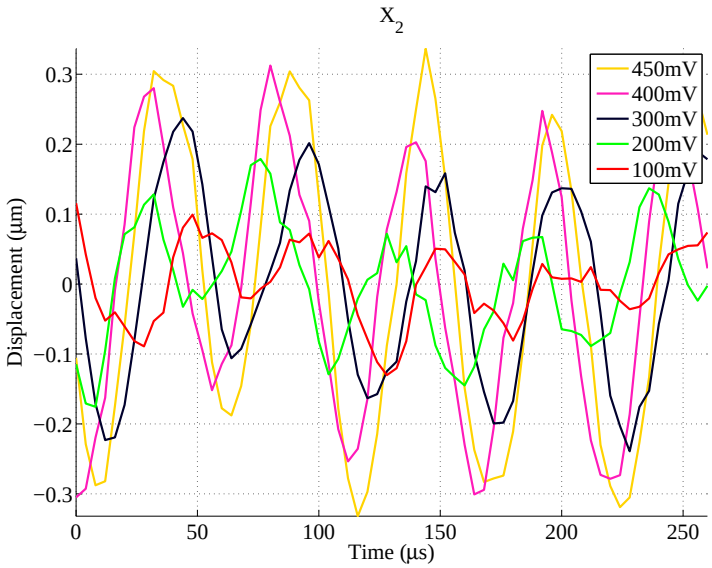

Fig. 5.43 Displacement estimated by Digital Image Correlation for the In-House Piezoelectric Actuator with the Jointed Horn attached which features a Grade 5 Titanium stud set to 8Nm.

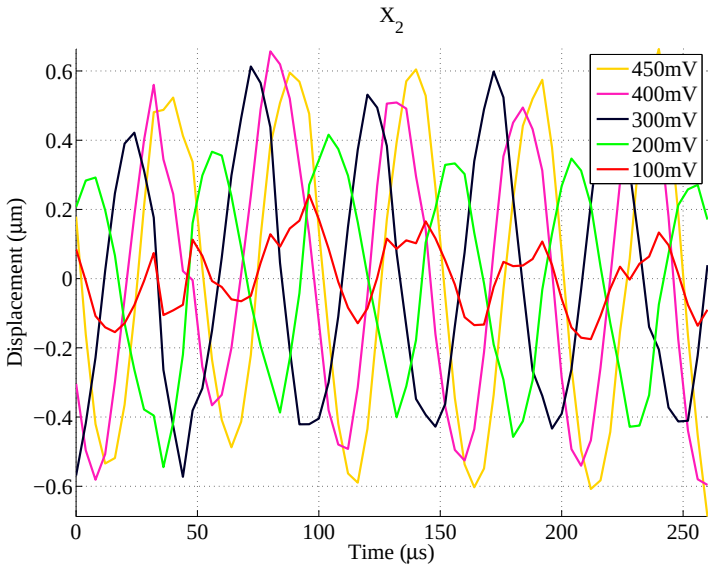

Fig. 5.44 Displacement estimated by Digital Image Correlation for the In-House Piezoelectric Actuator with the Jointed Horn attached which features a Grade 5 Titanium stud set to 12Nm.

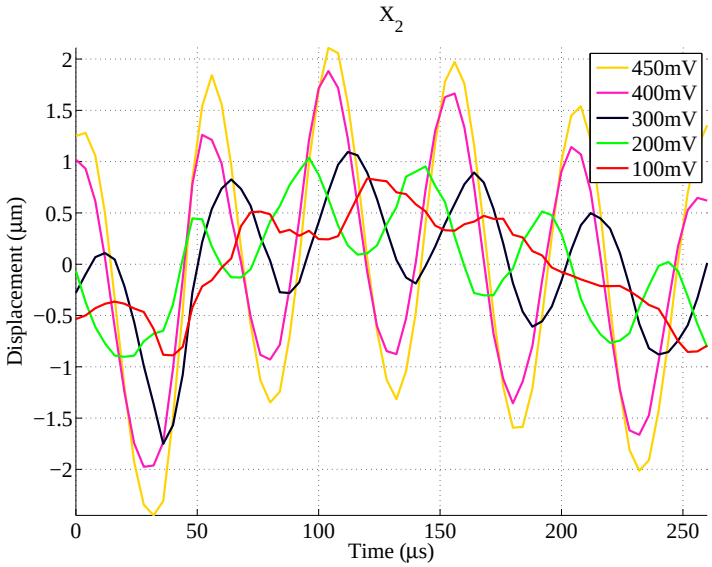

Fig. 5.45 Displacement estimated by Digital Image Correlation for the In-House Piezoelectric Actuator with the Jointed Horn attached which features a Grade 5 Titanium stud set to 16Nm.

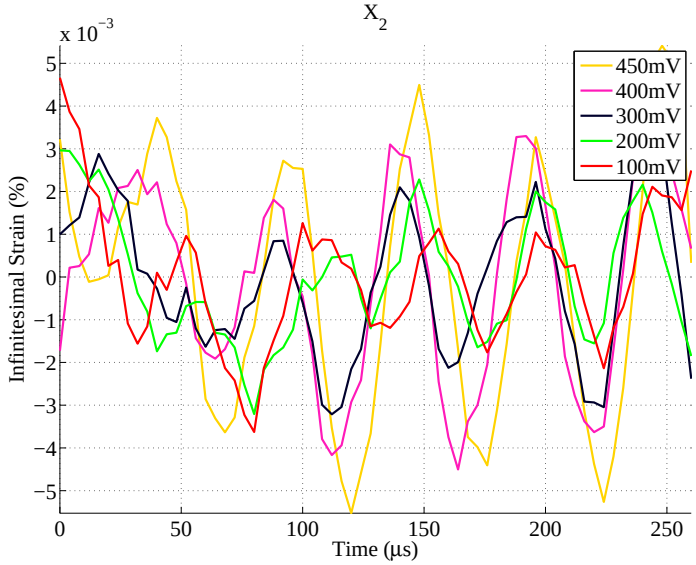

Fig. 5.46 Strain estimated by Digital Image Correlation for the In-House Piezoelectric Actuator with the Jointed Horn attached which features a Steel stud set to 8Nm.

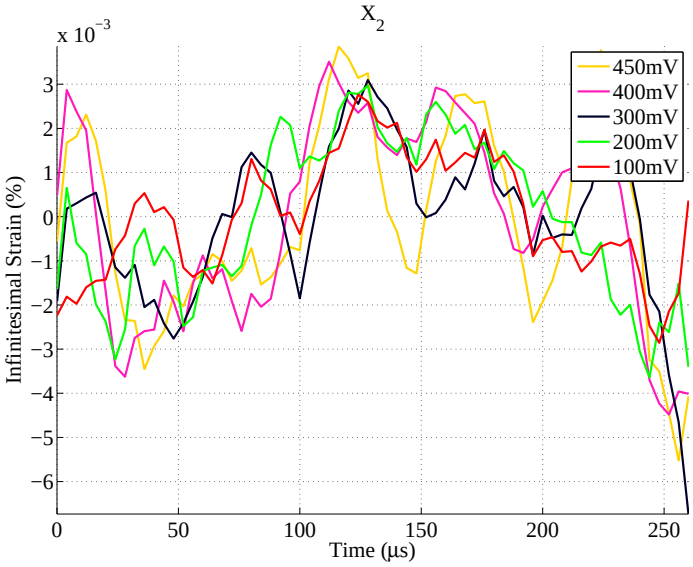

Fig. 5.47 Strain estimated by Digital Image Correlation for the In-House Piezoelectric Actuator with the Jointed Horn attached which features a Grade 5 Titanium stud set to 8Nm.

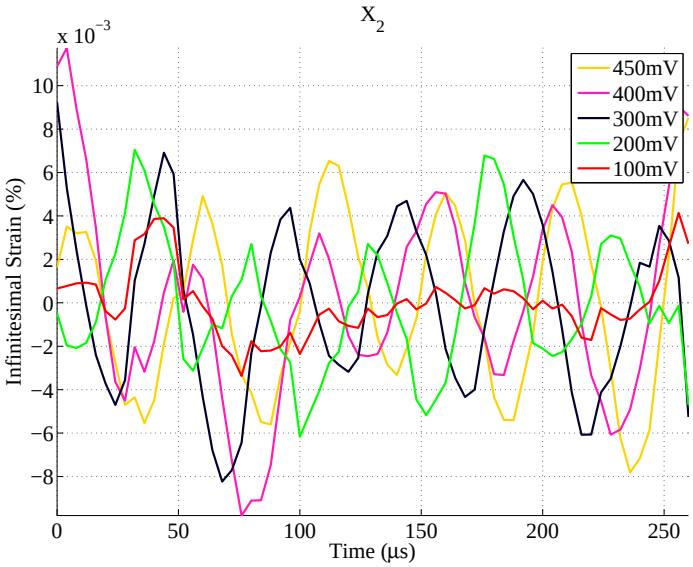

Fig. 5.48 Strain estimated by Digital Image Correlation for the In-House Piezoelectric Actuator with the Jointed Horn attached which features a Grade 5 Titanium stud set to 12Nm.

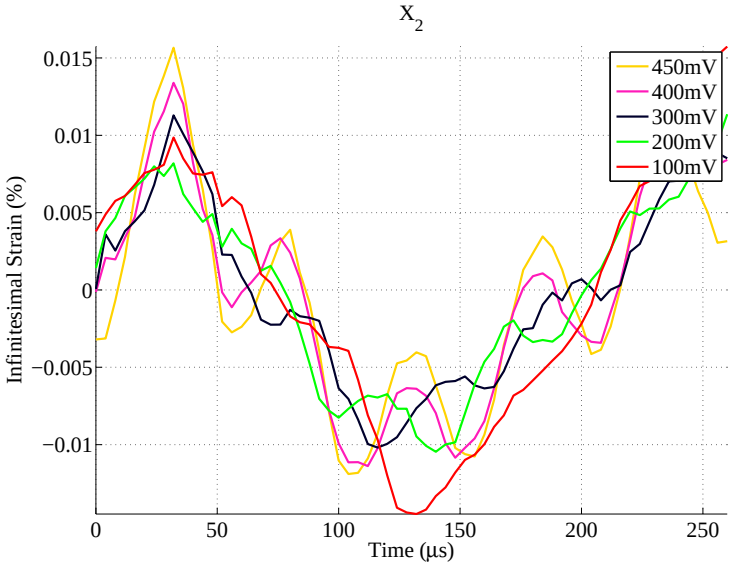

Fig. 5.49 Strain estimated by Digital Image Correlation for the In-House Piezoelectric Actuator with the Jointed Horn attached which features a Grade 5 Titanium stud set to 16Nm.

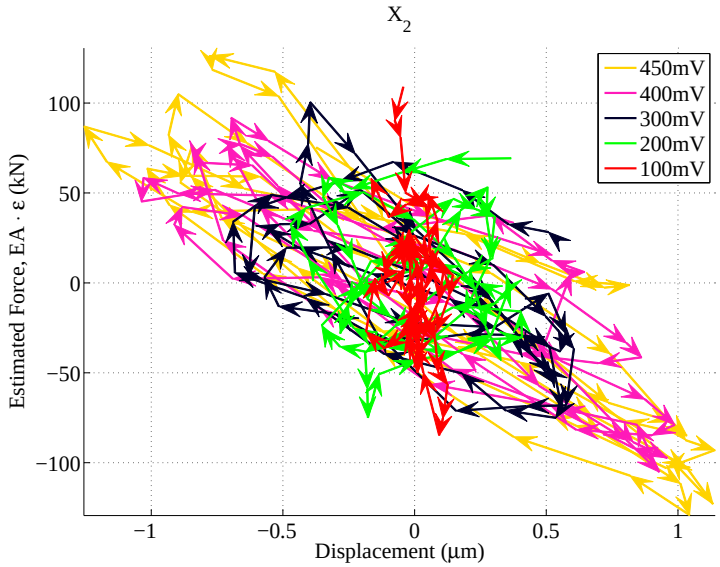

Fig. 5.50 Hysteresis loops estimated by Digital Image Correlation for the In-House Piezoelectric Actuator with the Jointed Horn attached which features a Steel stud set to 8Nm.

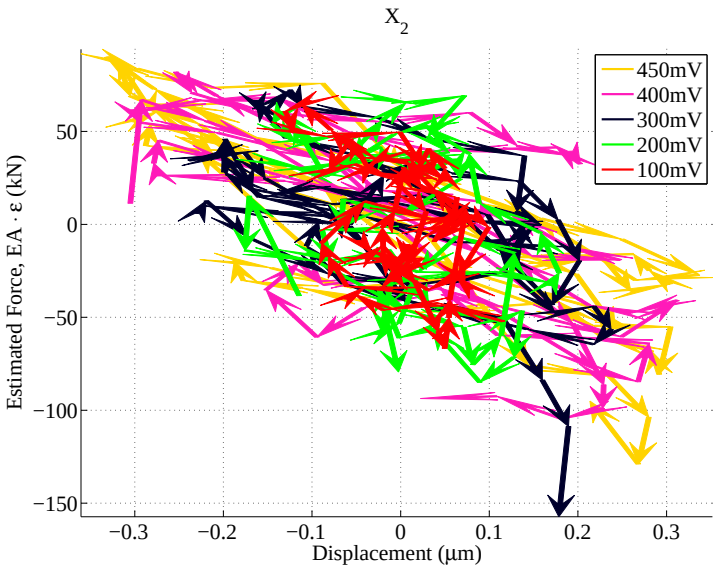

Fig. 5.51 Hysteresis loops estimated by Digital Image Correlation for the In-House Piezoelectric Actuator with the Jointed Horn attached which features a Grade 5 Titanium stud set to 8Nm.

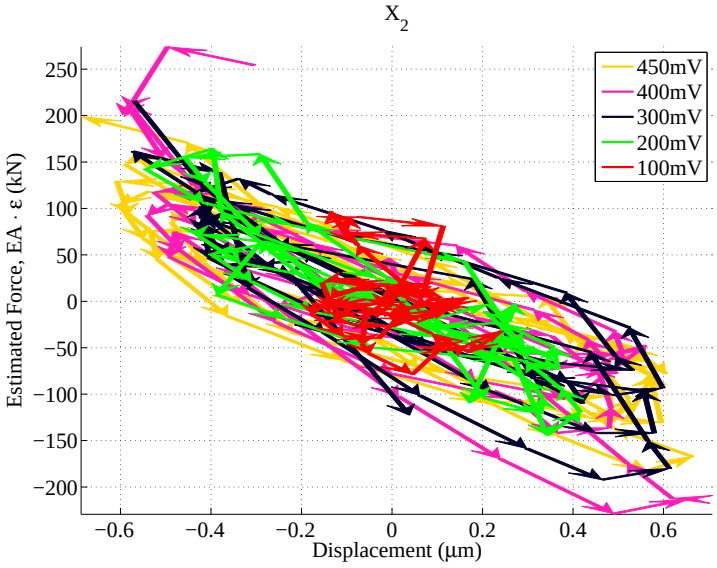

Fig. 5.52 Hysteresis loops estimated by Digital Image Correlation for the In-House Piezoelectric Actuator with the Jointed Horn attached which features a Grade 5 Titanium stud set to 12Nm.

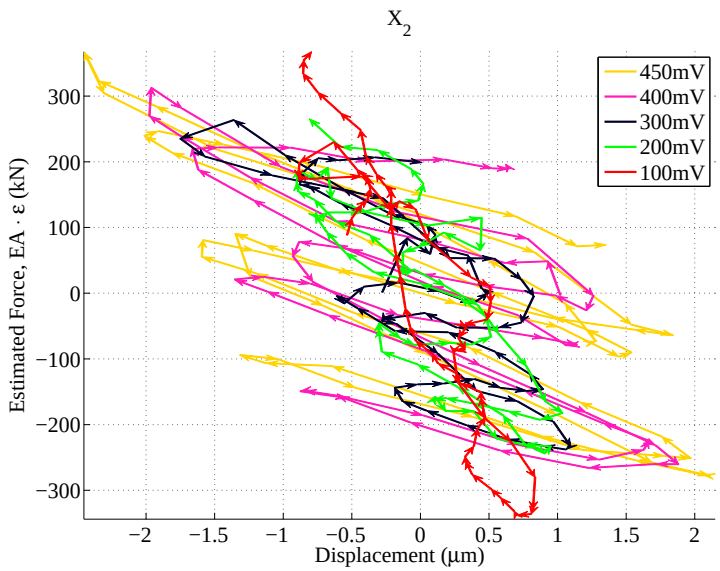

Fig. 5.53 Hysteresis loops estimated by Digital Image Correlation for the In-House Piezoelectric Actuator with the Jointed Horn attached which features a Grade 5 Titanium stud set to 16Nm.

5.4.2 Laser vibrometry measurements

When testing the CPA or the IHPA assemblies the LDV measurements have 202 or 4098 samples respectively. However, in order to compare the LDV readings with the synchronous DIC estimations, the plots that follow are limited to the acquisition time window of the DIC records. Also the CPA and IHPA assemblies are measured by three and two lasers simultaneously. This section displays the measurements taken at location X_2 only, however the additional measurements at the remaining locations will be introduced with the force identification results.

Commercial Piezoelectric Actuator

Figures 5.54-5.59 show the laser vibrometry results measured from testing each ultrasonic horn when it is attached to the CPA. The displacement spectra displayed in Figure 5.55 have been obtained by applying the FFT to the 202 samples obtained for each measurement. When the FFT is applied, the signal is padded with trailing zeros up to 512 points. The displacements have been windowed by a Hann function, in order to reduce the side lobes of the FFT, and the obtained spectra have been smoothed with a moving average filter for a span of 2%. The spectrum peaks that are obtained from testing the MH agree within 10Hz

of the 2nd longitudinal mode that was identified through EMA in Table 4.3. This small error shows that the protocol of disassembling and reassembling the HPU assembly is appropriate for the experiment.

The spectra for the JH:St@8Nm do not deviate in frequency as the excitation voltage is increased. The extent that this can be discerned is limited by resolution of the FFT. The short acquisition window gives a resolution bandwidth limited to 1.2kHz. The spectra are centred closely to the minimum impedance of the equivalent assemblies in Table 4.1. For the limited resolution FFT, the spectra of the JH:Ti@8Nm responds at the same frequency as the JH:St@8Nm, but with reduced displacement amplitude. The frequency of the minimum impedance for both test assemblies agree within 0.4% of Table 4.1. The test of the JH:Ti@12Nm appears to soften in frequency as the amplitude is increased from the 1μm to the 2μm setting. From the limited resolution of the FFT it is not possible to identify the shift in frequency precisely, however the frequency appears to be centred on 19.6kHZ then shifts to 19.5kHz, with the increase in power to the device. This is 400Hz less than equivalent minimum impedance in Table 4.1. Once the amplitude is increased to 3μm, the frequency drops more noticeably, close to 19.29kHz. There is clear low frequency modulation of the operating frequency in the displacement that is shown in Figure 5.58. The spectrum of this displacement suggests that there exists a low frequency component to the displacement close to 4.88kHz. It was also observed that increasing the amplitude to the device, in all of the JH tests, increased the loudness of audible shrieking that was produced during the experiment. The final two spectra are obtained from testing the JH:Ti@16Nm horn. The frequency components for both of the amplitude settings are very similar to the equivalent components from the JH:Ti@12Nm test. The amplitude is smaller in this case, however the response from the 2μm setting has a low frequency component that is noticeable above the sidebands of the other spectra. This component is centred closely with the low frequency component from the 3μm test of JH:Ti@12Nm.

In-House Piezoelectric Actuator

The measurements that are obtained from testing each ultrasonic horn with the IHPA are given in Figures 5.60-5.65. Each measurement consists of 4096 samples from which the displacement spectra are calculated through the MATLAB FFT function; with no trailing zeros added. This gives a resolution bandwidth of 62Hz and each spectrum has been widowed and smoothed equivalent to the CPA spectra. The resonance condition for the MH

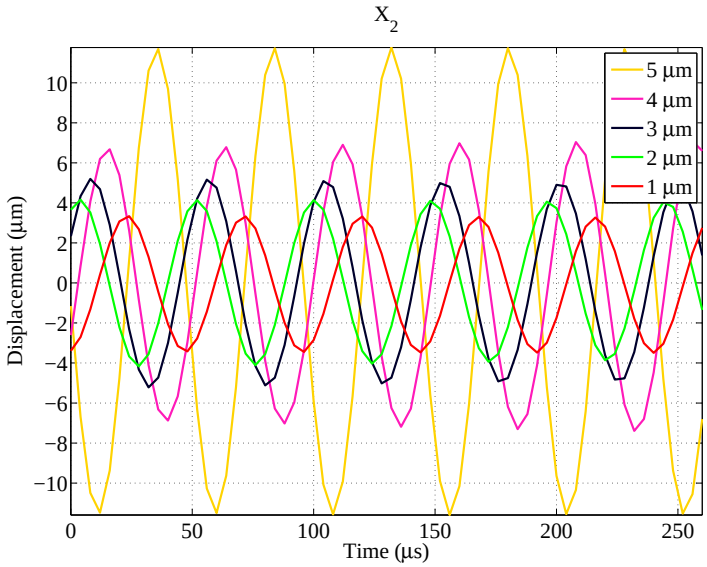

Fig. 5.54 Displacement measurements by laser vibrometry for the Commercial Piezoelectric Actuator with the Monolithic Horn attached.

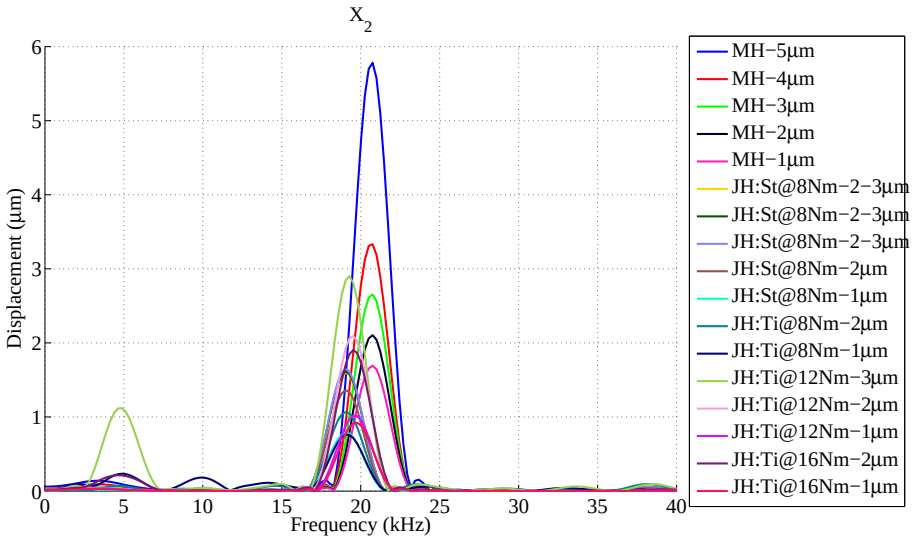

Fig. 5.55 Displacement spectra measurements by laser vibrometry for the Commercial Piezoelectric Actuator with each horn attached.

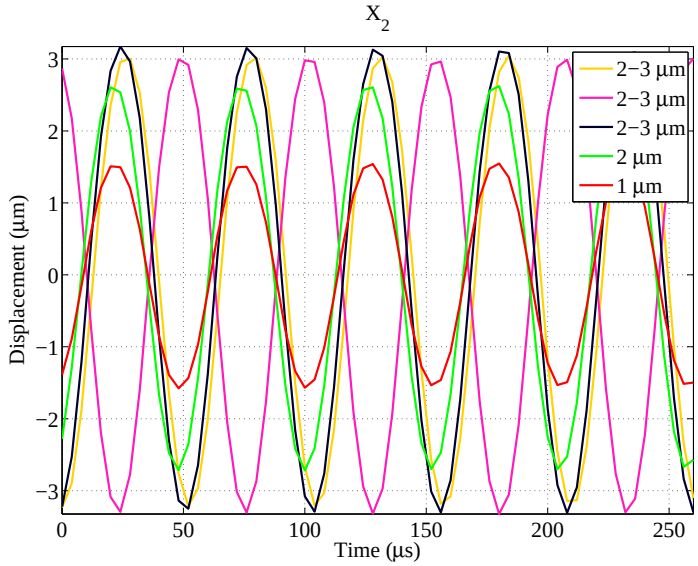

Fig. 5.56 Displacement measurements by laser vibrometry for the Commercial Piezoelectric Actuator with the Jointed Horn attached which features a Steel stud set to 8Nm.

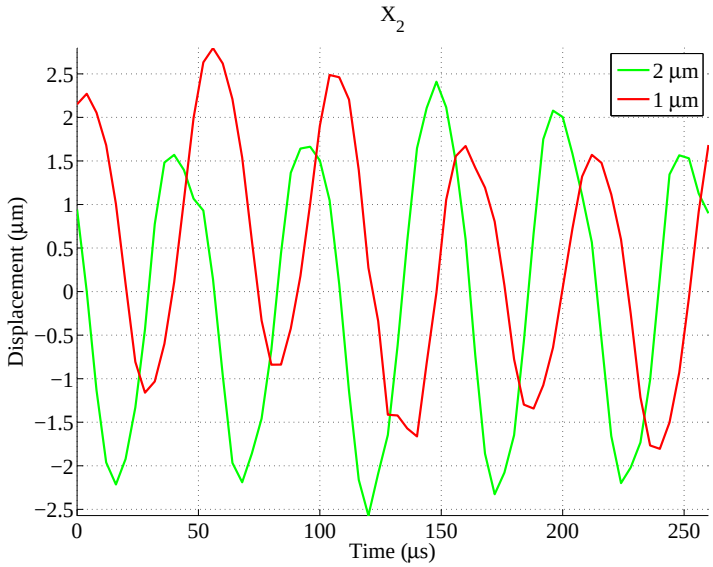

Fig. 5.57 Displacement measurements by laser vibrometry for the Commercial Piezoelectric Actuator with the Jointed Horn attached which features a Grade 5 Titanium stud set to 8Nm.

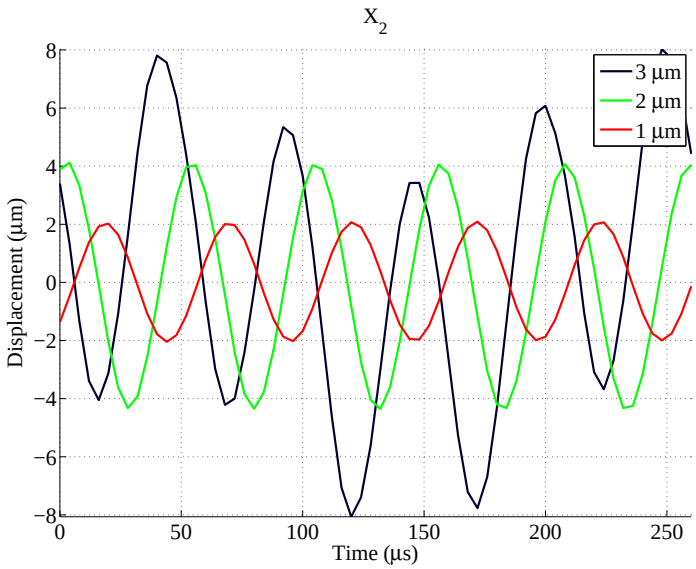

Fig. 5.58 Displacement measurements by laser vibrometry for the Commercial Piezoelectric Actuator with the Jointed Horn attached which features a Grade 5 Titanium stud set to 12Nm.

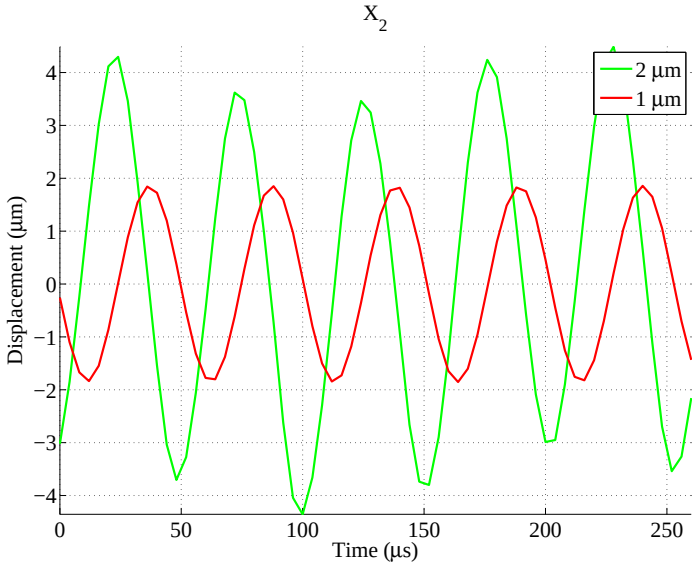

Fig. 5.59 Displacement measurements by laser vibrometry for the Commercial Piezoelectric Actuator with the Jointed Horn attached which features a Grade 5 Titanium stud set to 16Nm.

operating mode remains close to the same frequency setting of the function generator as the peak-to-peak voltage setting is increased. This was adjusted at steady state vibration of the assembly, however the displacements that are shown do not reach steady state within the limited observation window. Over the region where the LDV and camera acquisition coincide, it is found that the displacement spectrum agrees within 100Hz of the operating mode frequency that was obtained through EMA in Table 4.5. The EMA results for each JH, with Grade 5 Titanium threads, are compared to the equivalent spectrum that is produced at the lowest voltage setting. It is found that the 12Nm horn agrees within 10Hz of the EMA results, whereas 8Nm and 16Nm settings are within 500Hz and 800Hz respectively.

Errors are inevitable when disassembling and reassembling each HPU configuration and the spectra are assessed over the transient, and not the steady state region of the signal, as they are for the EMA. The error in the linear calibration model, which is given in Table 4.13, only achieves agreement to the EMA results within 900Hz. This error in the reference point cannot be circumvented by the force identification scheme. It is clear from each JH with a 8Nm or 12Nm setting that as the excitation voltage is increased, and the resonance condition is subsequently tuned, the operating mode appears to soften and the amplitude tends to saturate. Without an impedance matching circuit for each individual horn that is attached to the IHPA, in its current tightened state, it is not possible to separate the nonlinear behaviour of the power amplifier from the vibration amplitude of the device. The introduction of impedance matching circuits would represent an additional change to the apparatus that must be modelled if the MH assembly is to be compared to each JH assembly. Within the one dimensional model it is reasonable to assume an estimate of the power transfer that is given in Figure 5.36.

Low and high frequency components of the displacement spectra in Figure 5.55 have been magnified in Figure 5.66. The CPA tests of the horns demonstrated clear modulation in the displacement of the JHs under high power excitation. However, in this case, the IHPA displacements in Figures 5.56-5.59 have not achieved this modulation. Without the automatic impedance matching of the CPA tests, the IHPA tests do not develop as high amplitude displacement fields in the JHs. The low frequency component of the CPA is not reproduced. Alternatively, this could have been an artefact of the CPA power supply. The IHPA spectra show very small frequency components that were clearly not detectable below the noise floor of the equivalent DIC tests, or under the sidebands of the limited resolution spectra. The low amplitude of these harmonics suggests that they may have been produced through harmonic distortion during the amplification of the function generator waveform. The power

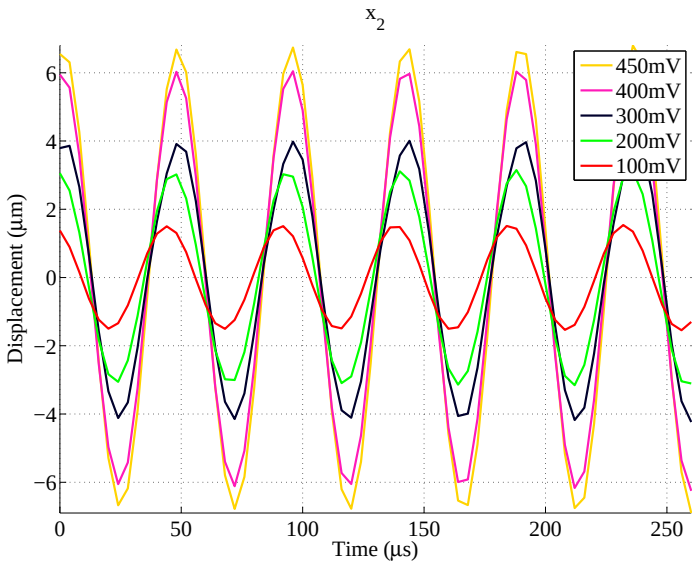

Fig. 5.60 Displacement measurements by laser vibrometry for the In-House Piezoelectric Actuator with the Monolithic Horn attached.

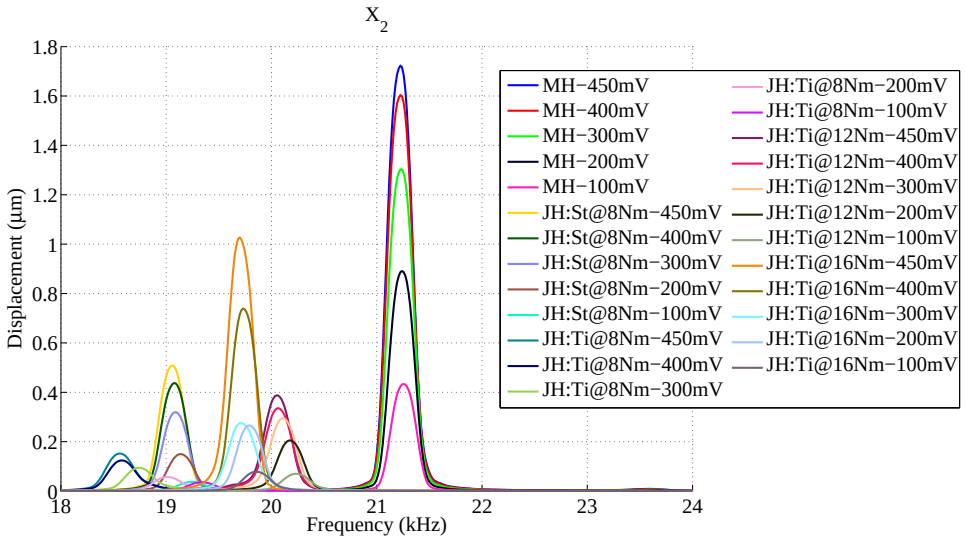

Fig. 5.61 Displacement spectra measurements by laser vibrometry for the In-House Piezoelectric Actuator with each horn attached.

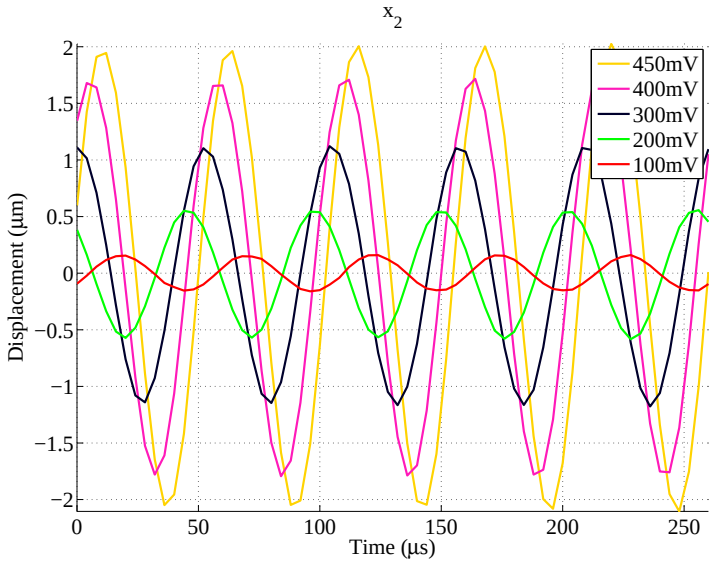

Fig. 5.62 Displacement measurements by laser vibrometry for the In-House Piezoelectric Actuator with the Jointed Horn attached which features a Steel stud set to 8Nm.

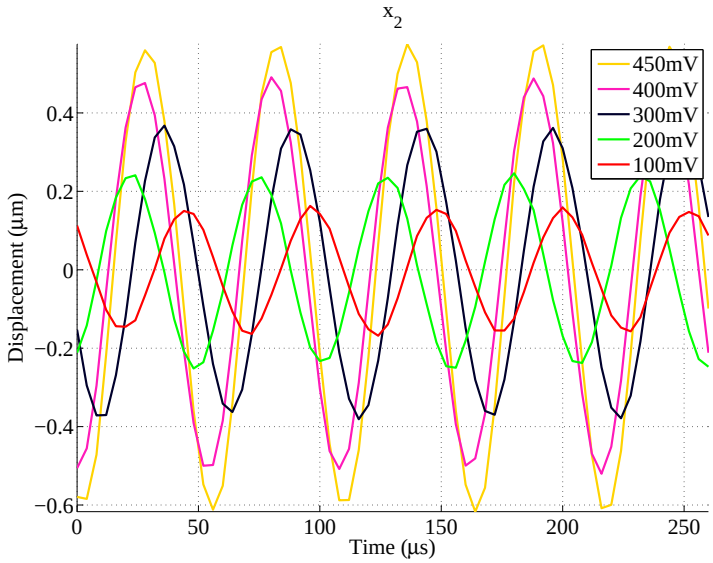

Fig. 5.63 Displacement measurements by laser vibrometry for the In-House Piezoelectric Actuator with the Jointed Horn attached which features a Grade 5 Titanium stud set to 8Nm.

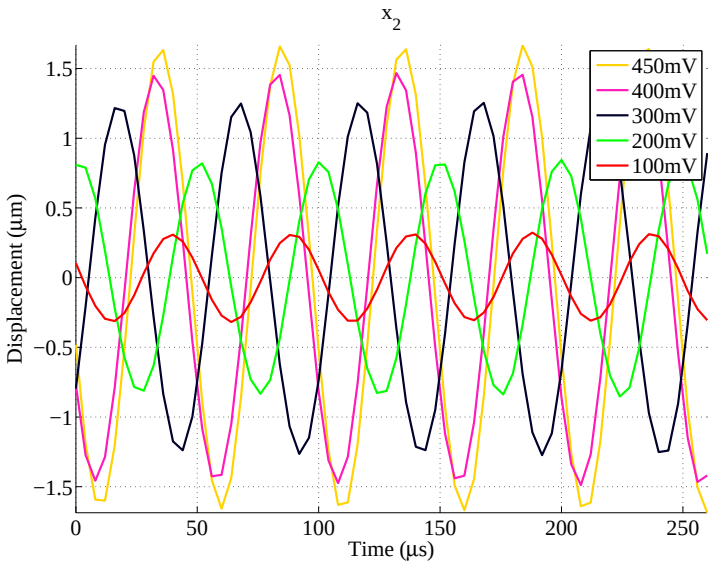

Fig. 5.64 Displacement measurements by laser vibrometry for the In-House Piezoelectric Actuator with the Jointed Horn attached which features a Grade 5 Titanium stud set to 12Nm.

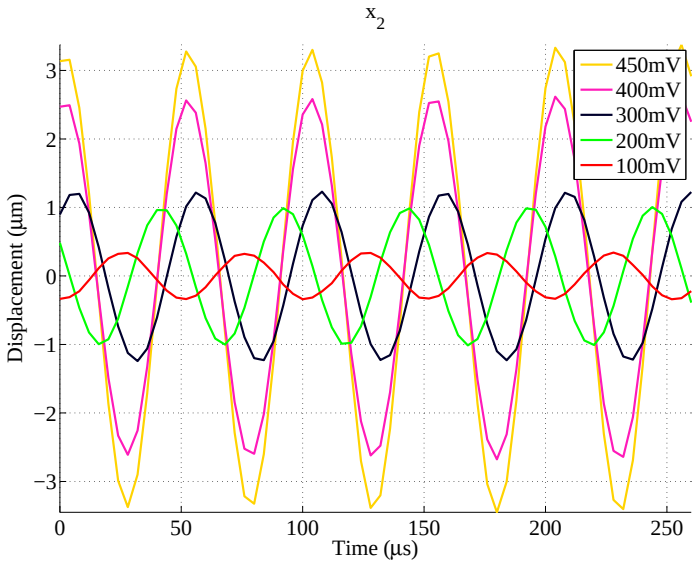

Fig. 5.65 Displacement measurements by laser vibrometry for the In-House Piezoelectric Actuator with the Jointed Horn attached which features a Grade 5 Titanium stud set to 16Nm.

amplifier manual states harmonic distortion of < -25 dBc at 200W output. The high frequency components are detected with greater amplitude. This may relate to the discussion of CAN that was given in Section 2.7. In which case the observed frequency behaviour would be an indication of slapping at the interface.

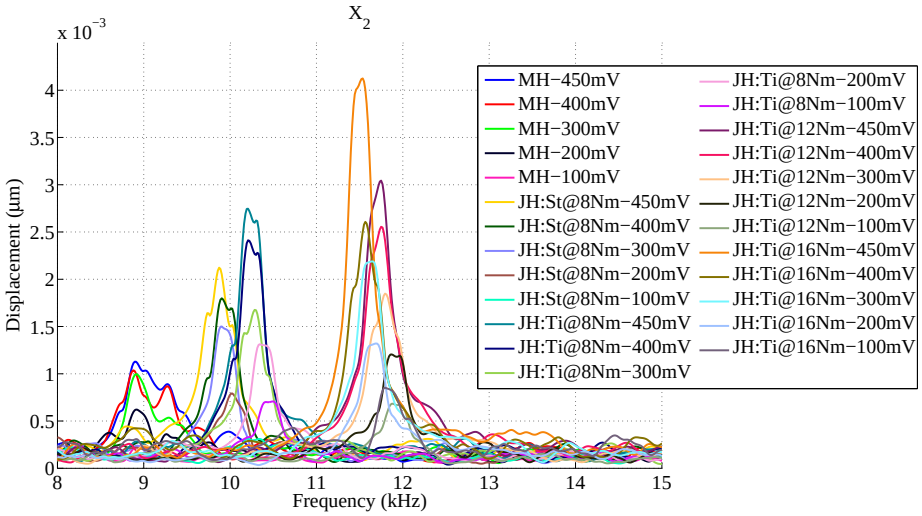

(a) Low

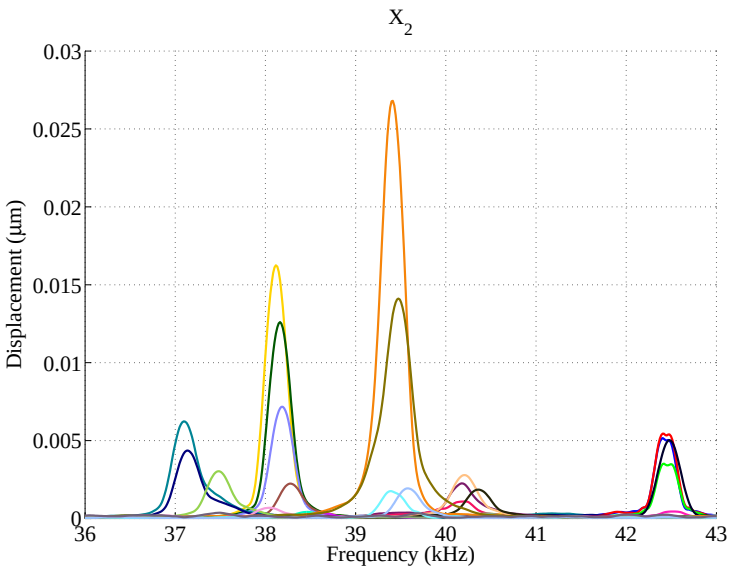

(b) High

Fig. 5.66 Frequency components observed in the displacement spectra for the In-House Piezoelectric Actuator with each horn attached.

5.4.3 Discussion

Both the force identification scheme, and the DIC method, rely on displacement data to obtain estimates of the axial force occurring in the HPU assembly. Data has been obtained for both computations through High Speed Imaging (HSI) and Laser Doppler Vibrometry (LDV) at synchronised samples. The tests carried out with the CPA achieve optimal power transfer to the each of the ultrasonic horns through the impedance matching power supply. The displacements that are found when the CPA drives the MH are given in Figures 5.20 and 5.54. The phase of the three smallest displacements are obtained through the FFT. These indicate the equivalence between the results obtained through the two test methods and are displayed in Figure 5.67a. A small phase error is expected between the results because the noise floor of the DIC is more significant. A cross correlation of the signals does not identify a delay between the traces for each amplitude setting in the test. This indicates that the time windows for each measurement scheme have been aligned appropriately. It is clear that the amplitudes of each set of results do not agree well and the DIC readings are significantly lower than the equivalent results obtained through LDV. A comparison of the LDV measured results to the DIC results is given in Figure 5.67b. Each of the DIC results has been scaled by a constant, which is limited to two significant figures, to give the best match to the equivalent LDV result. The LDV measurements do not require any smoothing whereas the DIC displacements require smoothing in order to compute the strain field reliably. Therefore some disparity in amplitude is expected. Despite this, the comparison of a different number of smoothing passes that were applied to the DIC results, in Figure 5.17, does not account for the difference of up to 4μm that is found.

The DIC axial displacement is computed as an average of the axial displacements at the control points that are within approximately 0.5mm of the centre line of the rod. To improve the slenderness of this average, the set of control points was defined so that the ROI had length that was more significant than its width. However this calculation will suffer from edge effects that give spurious displacements at the outer grid points. Averaging the axial displacements over the width should minimise the influence of the edge effects. The calculation of the displacement field also suffers from a bias due to the illumination of the measurement area. The influence of this is part of the noise floor assessment that was given in Figure 5.18. It is clear that noise can account for a ±1μm variation in the displacement results. Although the average of the axial displacements might not suffer all of this noise.

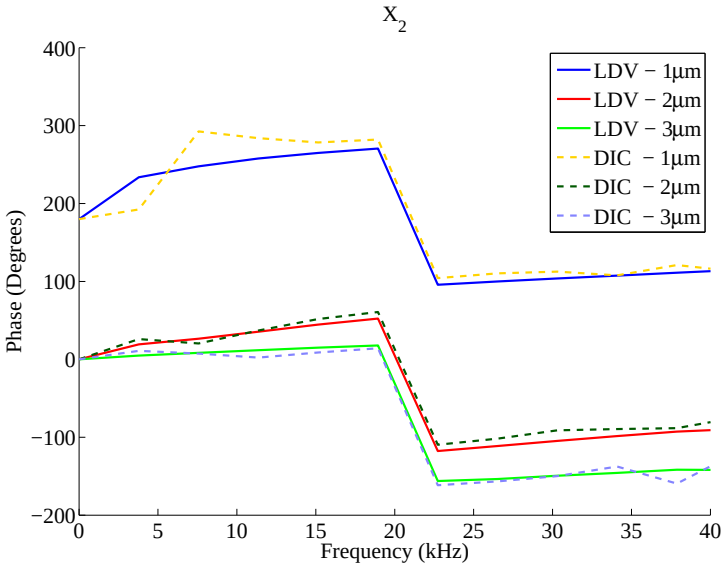

(a) Phase

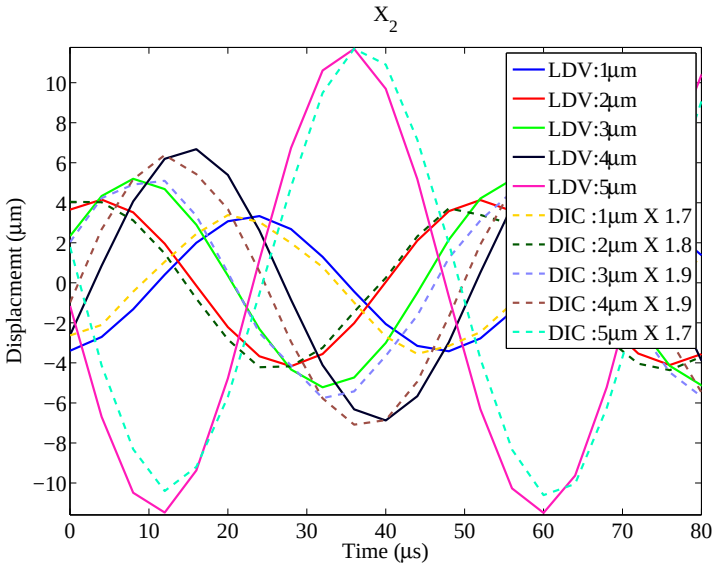

(b) DIC results scaled

Fig. 5.67 Comparison of displacements obtained through laser vibrometry and Digital Image Correlation (DIC) for tests of the Monolithic Horn attached to the Commercial Piezoelectric Actuator.

Finally the discussion of the ideal pinhole camera model in Section 5.2.3 suggests that out of plane displacements will induce a projection error into the images that are acquired by the high speed camera. Equation (5.1) suggests that this projection error will tend to distort the image as the magnification of the surface changes. This distortion will translate points of the perceived speckle pattern proportional to the movement of the surface to and from the focal point of the camera.

5.5 Force estimation

The force estimation scheme has been detailed in Chapter 3. It is applied to the LDV data, that is given in Section 5.4.2, with reference to the linear calibration models that have been developed in Chapter 4. In Section 5.4 the observations that were shown are from the flat portion of each horn, however the tests of the CPA and the IHPA assemblies featured measurements of axial velocity at 3 and 2 different locations respectively. The locations have been listed in Table 5.1 as X_1, X_2 or X_3. The additional displacements have been obtained simultaneously to the readings from X_2 and have been processed as shown in Section 5.3.2. Deconvolution of the force from more than one location will improve the condition of the least squares regularised solution because this involves the addition of the impulse response matrices that are related to each location [71]. When the inverse problem is formed through the measurements at two locations Equations (3.99) and (3.100) become:

$$\boldsymbol{N}(\tau_q) = \left[\boldsymbol{g}(X_1, x_a, x_b, t_p, \tau_q) + \boldsymbol{g}(X_2, x_a, x_b, t_p, \tau_q)\right]^{-1} \left\{\boldsymbol{G}(X_1, t_p, \tau_q) + \boldsymbol{G}(X_2, t_p, \tau_q)\right\} \quad (5.17)$$

The addition of the impulse response matrices, $\boldsymbol{g}$, will tend to produce a matrix that has a better condition number than either of its components. These components will contain very small values which are summed together. This will tend to improve the ratio of the smallest to the largest value in the matrix that is produced. However, applying this constraint is more likely to result in an unstable least squares solution, due to modelling errors. These descend from the limitations of the linear calibration and the restrictions imposed by the one dimensional waveguide theory. Furthermore, the introduction of more than one set of results adds to the overall measurement noise that must be accepted by the inversion. Inverse problems are characterised by their sensitivity to noise. As a result, small changes in the data to the problem can be amplified to large changes in the solution. The desired information can then be masked by measurement noise.

5.5.1 Linear calibration force

To make progress with the joint identification problem, it has to be assumed that when the MH is attached to either the CPA or the IHPA, the linear calibration model for each assembly is sufficient to describe its behaviour. The limitations of each model have been discussed in Chapter 4 and include discrepancies between its eigenvalues and eigenfunctions with the EMA results. This assumption implies that a linear calibration force can be found, for each assembly, as the least squares solution to the deconvolution of force from the LDV measurements. Where the spatial distribution of the force must be specified. In an attempt to associate this force estimation with the electrical excitation, that is input to the assembly, the expression in Equation (4.9) was defined. This assumes that the input to the assembly is an electrical boundary condition that results in an interface force at the front of the PZT stack. This is located at node 5 or 6 for the CPA or IHPA assembly respectively. The boundary load is estimated for each designated electrical excitation. Equations (3.96) and (3.98) can be restated as:

$$\boldsymbol{q}_i(\tau_q) = \boldsymbol{g}(X_m, t_p, \tau_q)^{-1}\boldsymbol{u}^{MH}(X_m, t_p) \qquad \text{For m = 1, 2 or 3} \tag{5.18}$$

where:

$$\boldsymbol{g}(X_m, t_p, \tau_q) = \begin{pmatrix}1 & 0\end{pmatrix} \cdot 2 \sum_{k=1}^{\infty} \boldsymbol{U}(x, j\omega_k)\boldsymbol{Q}_k \left(\sum_{q=1}^{p} sin\omega_k(t_p - \tau_q)\Delta t \begin{pmatrix}1\\0\end{pmatrix} \right) \tag{5.19}$$

The electrical excitation to the IHPA is adjusted at the input to the power amplifier via a waveform generator. The real time voltage that is applied to the terminals of the PZT stack is not observed, however it is possible to check the validity of Equation (4.9) by applying some understanding of the operating characteristics of the amplifier. Therefore the model of the input force is discussed as a comparison of the expected power applied at the terminals to the identified input force based on a boundary load at node 6. The expected input power to the IHPA terminals was discussed in Section 5.4.1 with reference to the schematic given in Figure 5.37. The linear calibration models are also applied to estimate the force at X_2, on the flat, so that the hysteresis loops at this location can be evaluated. These can then be compared to equivalent data from the DIC results.

Commercial Piezoelectric Actuator

The displacement of the MH attached to the CPA has been measured at the three locations X_1, X_2 and X_3, which were given in Table 5.1. The results are shown in Figure 5.68. Each of these correspond to the vibration at the front face and the flat of the MH, as well as the front mass of the CPA, respectively. Each trace is associated with the steady state vibrations of the HPU assembly for a nominal setting of its power supply in microns. The displacements were obtained through Omega Integration, and filtering of velocity measurements, following the discussion in Section 5.3.2. The noise floor was estimated to be 20nm by observing the unloaded device. Initially a direct application of Equations (5.18) and (5.19) is applied to form an estimate of the boundary load at node 5, $\boldsymbol{q}_5(\tau_q)$, which corresponds to the front of the piezoelectric stack. The least squares solutions to the boundary load through forward substitution are shown in Figure 5.69. These are very unstable when derived from the displacements at each of the positions. Deconvolution of the force from the displacement at X_2 yields a solution at a higher frequency than is expected.

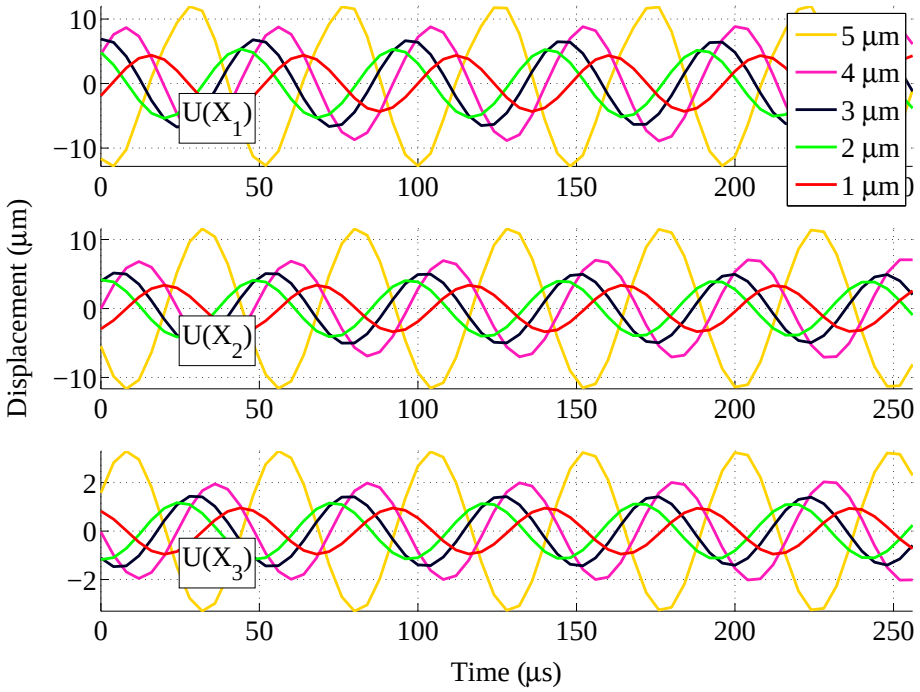

Fig. 5.68 Displacement measured through laser vibrometry at three locations on the Commercial Piezoelectric Actuator with the Monolithic Horn attached.

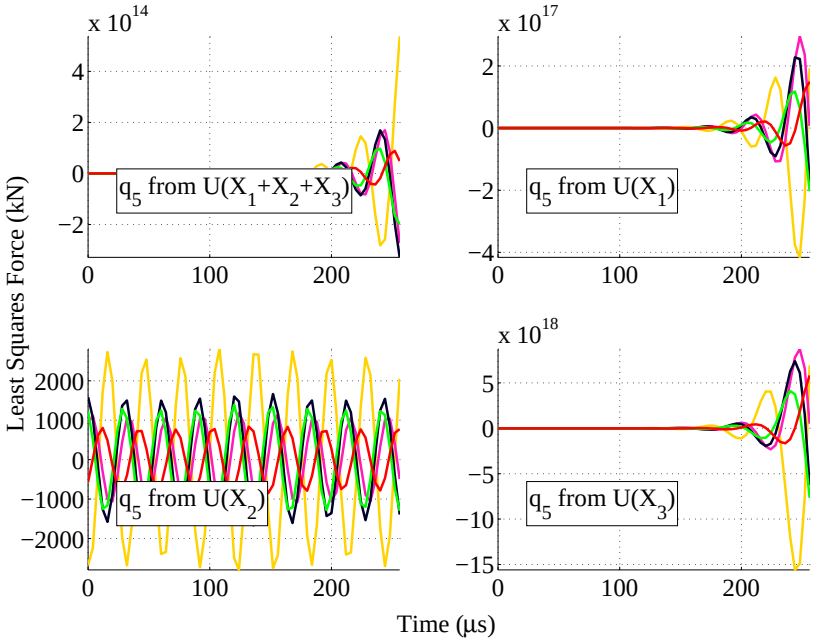

Fig. 5.69 Least square solution estimates through Forward Substitution of the boundary load $q_5(\tau_q)$ deconvolved from the response, $U(X_m)$, of the Monolithic Horn when it is attached to the Commercial Piezoelectric Actuator.

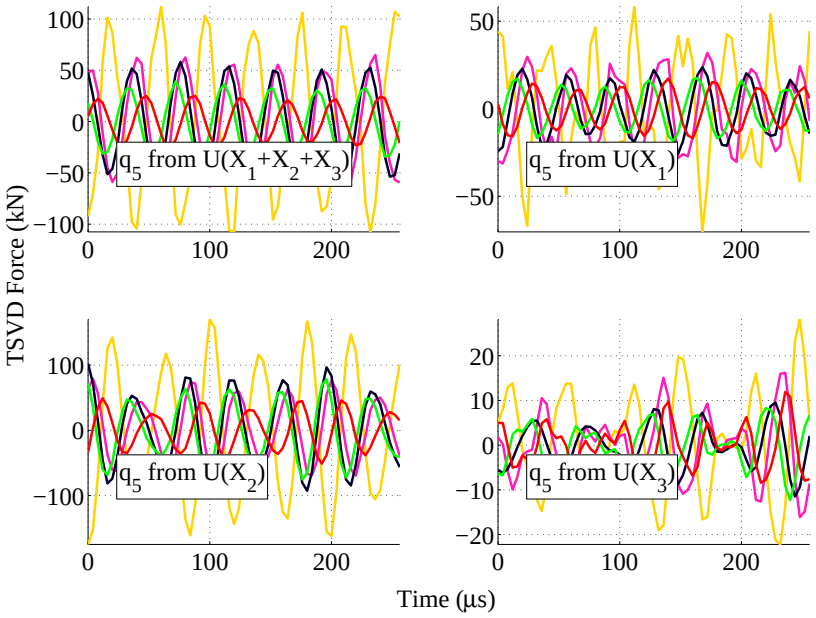

Fig. 5.70 Least square solution estimates through Truncated Singular Value Decomposition of the boundary load $q_5(\tau_q)$ deconvolved from the response, $U(X_m)$, of the Monolithic Horn when it is attached to the Commercial Piezoelectric Actuator.

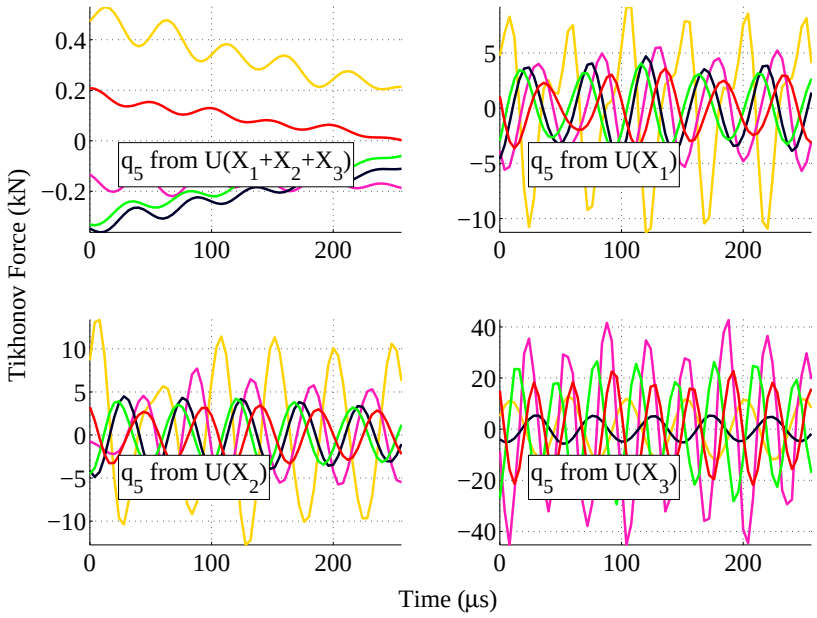

Fig. 5.71 Least square solution estimates through Tikhonov regularisation of the boundary load $q_5(\tau_q)$ deconvolved from the response, $U(X_m)$, of the Monolithic Horn when it is attached to the Commercial Piezoelectric Actuator.

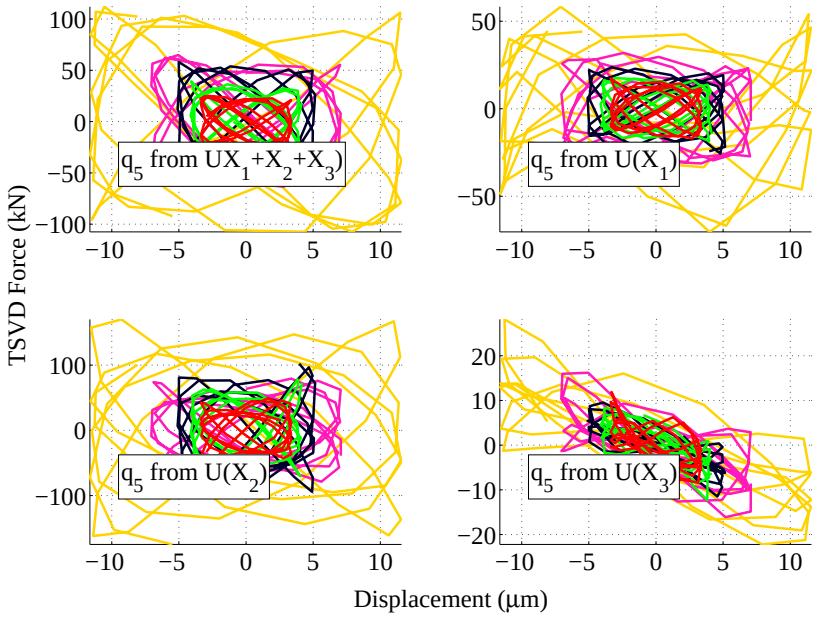

Fig. 5.72 Hysteresis loops for the boundary load $q_5(\tau_q)$ deconvolved from the response, $U(X_m)$, of the Monolithic Horn when it is attached to the Commercial Piezoelectric Actuator.

TSVD regularisation produces the results in Figure 5.70. The phase of each result agrees more closely with the equivalent strain trace that was obtained through the DIC analysis in Figure 5.22. This makes sense for excitation at the second longitudinal mode. The input force is obtained at the front of the piezoelectric stack, which is located in the negative x-direction from the first node of vibration. The DIC strain has been estimated over a front that is in the positive x-direction from the second node of vibration. Future iterations of this experiment might benefit from making use of the symmetry of the axial motion more exactly. At the very least this provides a route to verifying the phase of the force estimations at DTFM node 5 and location X_2 through the DIC results. The force is deconvolved by summing the impulse response matrices, and the displacement vectors, associated with all three locations. This agrees closest with the forces that are obtained from the displacement at X_2, however it is less modulated. The largest amplitude estimates appear to dominate the information from all three locations. For the force estimations it has been assumed that damping is negligible in the linear calibration model, so it cannot dissipate energy, and the transfer function will contain very sharp spectral behaviour. The regularised solutions have amplitude that depends on an arbitrary choice of regularisation tolerance and this can result in large variation of the force estimation. In the case of the CPA linear calibration, some of the hidden components were modelled based on guesses of geometric and material parameters. Access to this information is required to gain any confidence in the estimated forces. It is also limited by the ability of the model updating tool to find a linear calibration model that has a resonance close to the operating mode of the assembly. The difference in the amplitude of the force, from the three separate locations, questions the validity of the linear model in this case.

The singular values that are associated with the impulse response matrix in Equation (5.19) are given in Figure 5.73. The impulse response matrices are formed numerically in MATLAB. As a result they are subject to truncation errors. Viewing the computed singular values of the impulse response matrix is a relevant, but not rigorous, method of comparing the estimations that are associated with different impulse response matrices. When the displacements at location X_1 or X_3 are adopted, to estimate the boundary load, they feature a similar instability. This is indicated by the jump in magnitude of the singular values towards the end of the acquisition window. This drop in the singular values will have a disproportionate influence on the condition number of each of these impulse response matrices. This can be smoothed out of the inverse problem by choosing a tolerance for the TSVD regularisation that sets a threshold above these outlier points. In comparison, the remaining plots of singular values decrease smoothly with time.

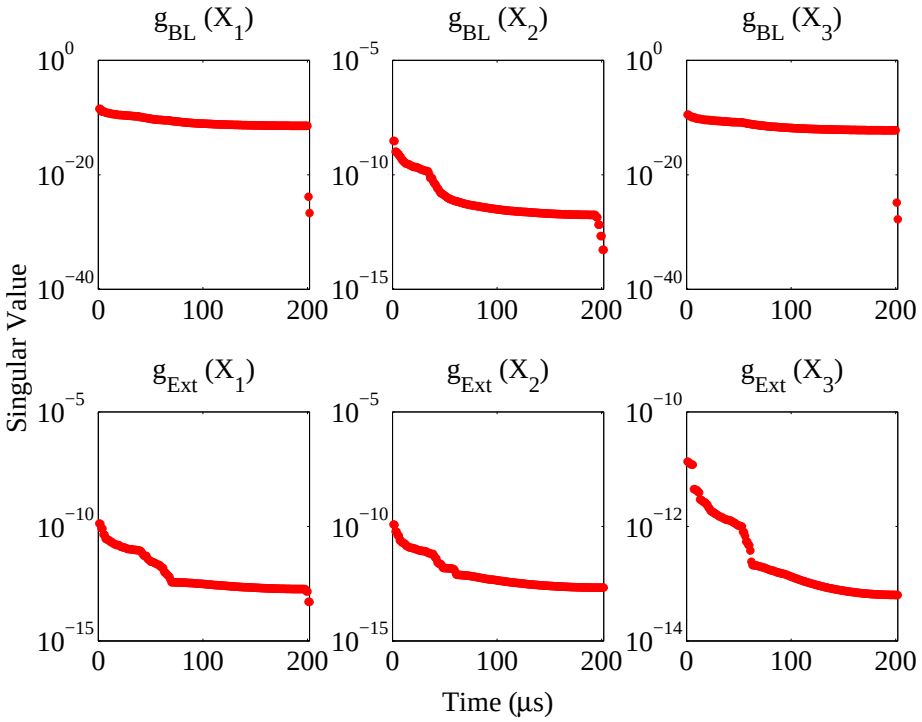

Fig. 5.73 Singular values of each impulse response matrix that forms the transfer function from the boundary load g_{BL} or the external force g_{Ext} to a measurement location at either the front of the horn X_1, the flat X_2 or the front mass X_3.

Tikhonov regularisation produces the results that are shown in Figure 5.71 . The amplitude of the obtained forces are much smaller than the TSVD results suggest. There is a greater disagreement in phase between these solutions than there is for the TSVD solutions. The hysteresis loops in Figure 5.72 are formed by accepting the TSVD force as the best estimate. However, for steady state vibration of the HPU device, the loops are not elliptical as expected. This suggests that the modelling errors are too significant to obtain a good estimate of the input force that is associated with the nominal amplitude set at the power supply to the HPU device. It is possible that butterfly type hysteresis loops could be a feature of the electro-mechanical relationship. The piezoelectric stack contains PZT rings, which are ferroelectric. As long as the temperature of the PZT does not exceed its Curie temperature, it will feature a remanent polarisation. However the polarisation orientations can still be switched by mechanical or electrical loads [117]. This results in butterfly type hysteresis loops in the strain-electric field loop. Drinčić *et al.* [118] has shown that 2-1 maps exist that can transform single hysteresis loops into multiple hysteresis loops with opposite orientations.

The estimation of the input force involved regions of the linear calibration model that could not be observed directly. However the estimation of the force close to location X_2, on the flat portion of the MH, involves geometry and material parameters that can be measured directly. It is assumed that the force is distributed uniformly over the flat from x_a to x_b, as defined in Table 5.2. The solution to this force is obtained through forward substitution in Figure 5.74. This yields a higher frequency solution than is expected when the impulse response matrix is associated with location X_1. When the force is deconvolved from the sum of all three locations the forward substitution it is dominated by this solution. The solutions that are associated with the remaining two locations appear to be closer in frequency to the DIC strains shown in Figure 5.22. However the amplitude of each solution suffers from significant levels of distortion and subsequent fluctuations in amplitude.

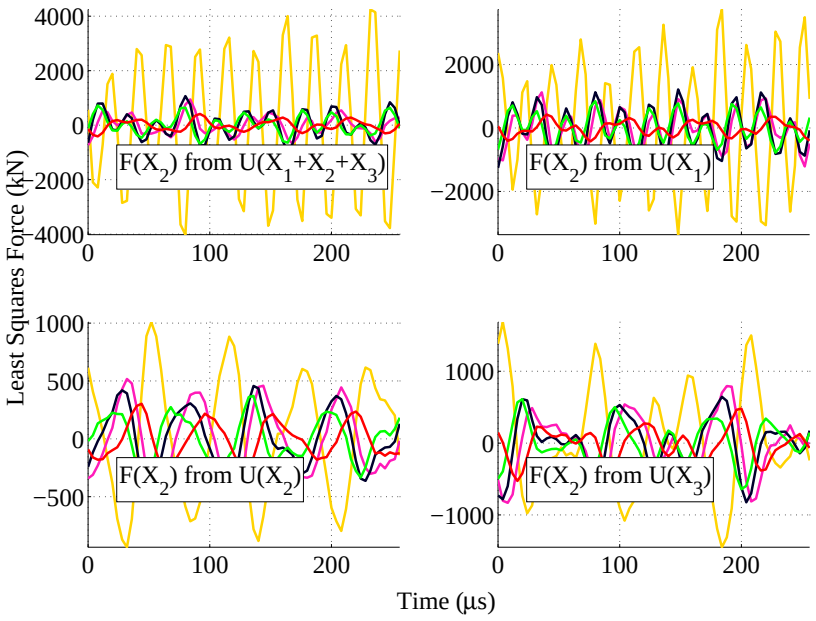

Fig. 5.74 Least square solution estimates through Forward Substitution of the external force, $N(x,\tau)$, at location X_2, when it is deconvolved from the response, $U(X_m)$, of the Monolithic Horn when it is attached to the Commercial Piezoelectric Actuator.

The forces that are obtained through TSVD regularisation are given in Figure 5.75. These agree reasonably with the phase of the DIC Strains. The regularised solutions have amplitude that depends on an arbitrary choice of regularisation tolerance. This can result in some variation of the force estimation. The force estimation from the sum contribution of all of the measurement locations is comparable to the forces associated with locations X_1 and X_2. This suggests that, within the limits of the linear calibration model, the most likely

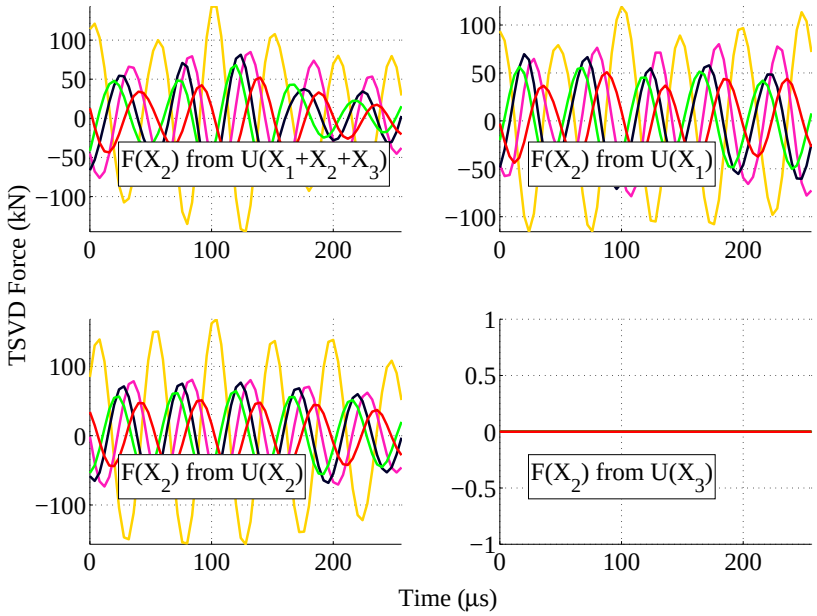

Fig. 5.75 Least square solution estimates through Truncated Singular Value Decomposition of the external force, $N(x,\tau)$, at location X_2, when it is deconvolved from the response, $U(X_m)$, of the Monolithic Horn when it is attached to the Commercial Piezoelectric Actuator.

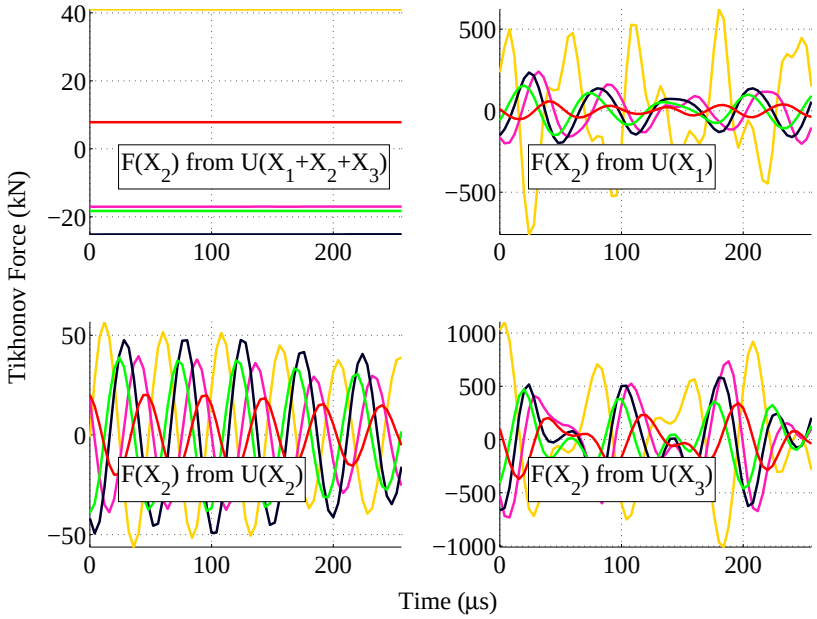

Fig. 5.76 Least square solution estimates through Tikhonov Regularisation of the external force, $N(x,\tau)$, at location X_2, when it is deconvolved from the response, $U(X_m)$, of the Monolithic Horn when it is attached to the Commercial Piezoelectric Actuator.

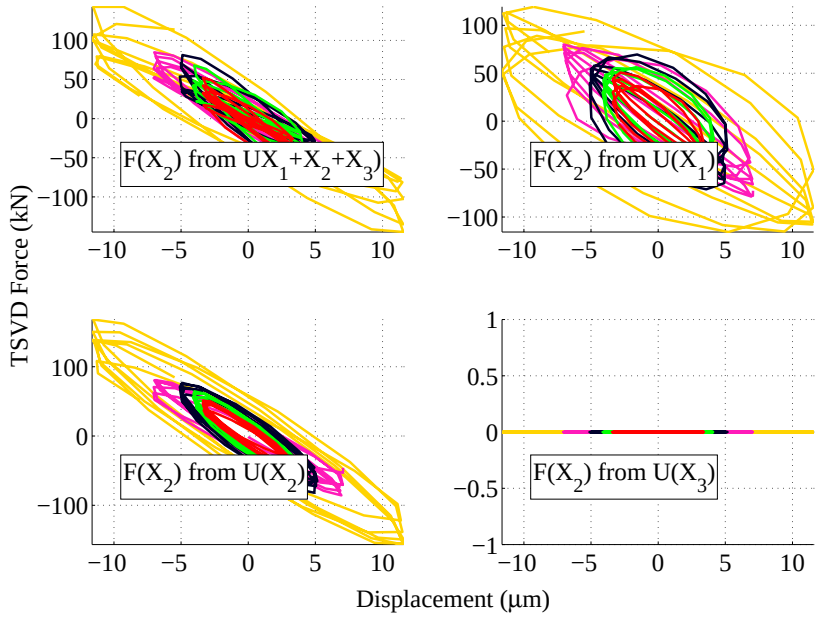

Fig. 5.77 Hysteresis loops for the external force, $N(x,\tau)$, at location X_2, when it is deconvolved from the response, $U(X_m)$, of the Monolithic Horn when it is attached to the Commercial Piezoelectric Actuator.

solution has been identified. Only zero solutions were identified from the measurements at X_3. This is the only location where the laser was not focussed onto a planar face of the HPU assembly. Therefore it is possible that there were errors in the alignment, and as a result, the noise will be more significant. This location is also closest to the portions of the assembly that were hidden by the casing of the piezoelectric actuator. Therefore the modelling error over this portion might have an influence on the impulse response matrix associated with X_3.

The force solutions that are obtained through Tikhonov regularisation are shown in Figure 5.76. There is no agreement between any of the forces that are derived from the four possible impulse response matrices. This suggests that the errors in the obtained linear calibration model are too significant to produce reliable force estimates. The force estimates associated with location X_2 do match the phase of the DIC strains very well. However the amplitude of the force that is associated with each level of excitation to the device does not appear to be in proportion to the DIC strains. The hysteresis loops for location X_2 are drawn from the TSVD regularised forces and shown in Figure 5.77. The loops from the impulse response matrix that is associated with location X_2 appear elliptical as expected. However, the linear calibration model did not feature any energy dissipation terms in the formulation

of its waveguides. Therefore the area that is enclosed by the hysteresis loops is attributed to errors in the estimation of the force. The LDV measurements feature extremely low levels of noise, so these errors must descend from the modelling error that is associated with the linear calibration model. Full access to the geometrical and material parameters of the assembly is required to reduce this error. It is likely that this level of error will obscure any information that might be deconvolved from the measurements of the jointed assemblies.

In-House Piezoelectric Actuator

The displacement of the MH, when it is attached to the IHPA, is measured at the two locations, X_1 and X_2, which are specified in Table 5.1, from Section 5.2.2, for the radiating end and the flat of the MH respectively. The displacements are given in Figure 5.78. The noise floor was observed by measuring the velocity of the assembly in its unloaded state. The displacement was obtained by the Omega Integration, and filtering, that was described in Section 5.3.2. The resulting noise floor estimate is 20nm. Direct application of Equations (5.18) and (5.19) will form the least squares solution to the boundary load at node 6. The results for each nominal amplitude of excitation are found through forward substitution in Figure 5.79. Any estimation of the input force $\boldsymbol{q}_6(\tau_q)$, that is deconvolved from the response at X_2, is obscured by noise and the remaining results are unstable. The same characteristics were observed through simulation in Section 4.5.3. This shows that forward substitution is not a suitable route to finding a solution, so the regularisation methods are necessary.

The Truncated Singular Value Decomposition (TSVD) regularised solutions are given in Figure 5.80 and the same solution is identified whether the displacements at one or two locations are considered. The singular values of the impulse response matrix in Equation (5.19) are given in Figure 5.83. It is clear that the singular values of the impulse response matrix, that is associated with location X_1, suffers a significant drop in magnitude towards the end of the time window. This indicates a failure of Hadamard's continuity criteria and suggests that the inversion of this matrix will be very ill-conditioned. Comparatively, the singular values that are associated with location X_2 drop relatively smoothly. They saturate over time instead of dropping abruptly. When both of these matrices are combined the new matrix will still be dominated by the significantly smaller singular values, which are associated with location X_1. This will result in a very large condition number.

The interface forces are obtained through the Tikhonov regularisation method and displayed

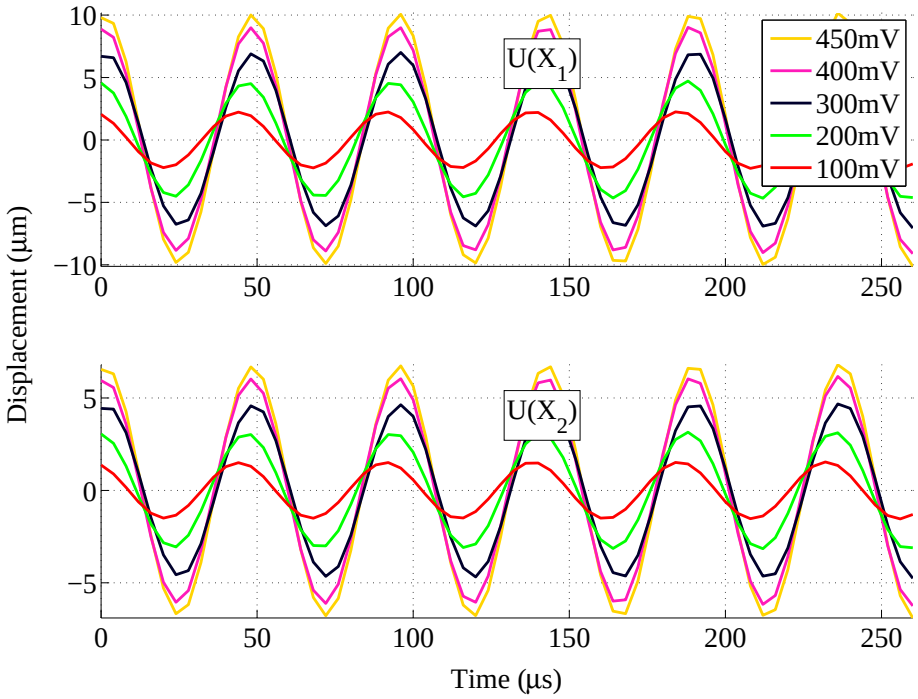

Fig. 5.78 Displacement measured through laser vibrometry at two locations on the In-House Piezoelectric Actuator with the Monolithic Horn attached.

in Figure 5.81. When the force is estimated from a single location, the results approximately match to the TSVD regularised solutions. However, the estimations that are associated with two locations, find solutions that are only a fraction of the other solutions. The Tikhonov solutions obtained from one and two locations are applied to the linear calibration model. When the maximum amplitude solution is selected in both cases, the displacements shown in Figure 5.84 are obtained. The measured displacements are recovered by applying the force that was obtained from the response at one location. The force obtained from two responses does not reproduce the correct amplitude displacements. It is clear that the Tikhonov force, that is derived from two locations, has converged onto a minimum that is not a true solution. The solution that is identified from one location is one of many potential solutions to the inverse problem. The only way to judge whether this estimation is realistic is to have an equivalent result to which it can be compared. Such a comparison can only be made for the force generated at location X_2, on the flat, because the DIC results are only associated with this location.

Figure 5.85 displays the least squares solution to the estimated force, occurring at X_2 on the flat, of the linear calibration model. The spatial distribution of the force is specified

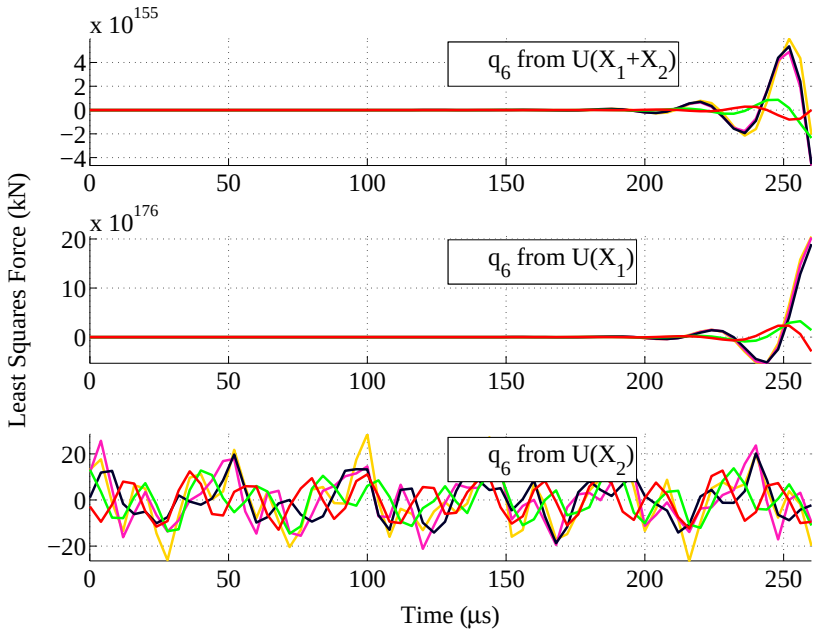

Fig. 5.79 Least square solution estimates through Forward Substitution of the boundary load $q_6(\tau_q)$ deconvolved from the response, $U(X_m)$, of the Monolithic Horn when it is attached to the In-House Piezoelectric Actuator.

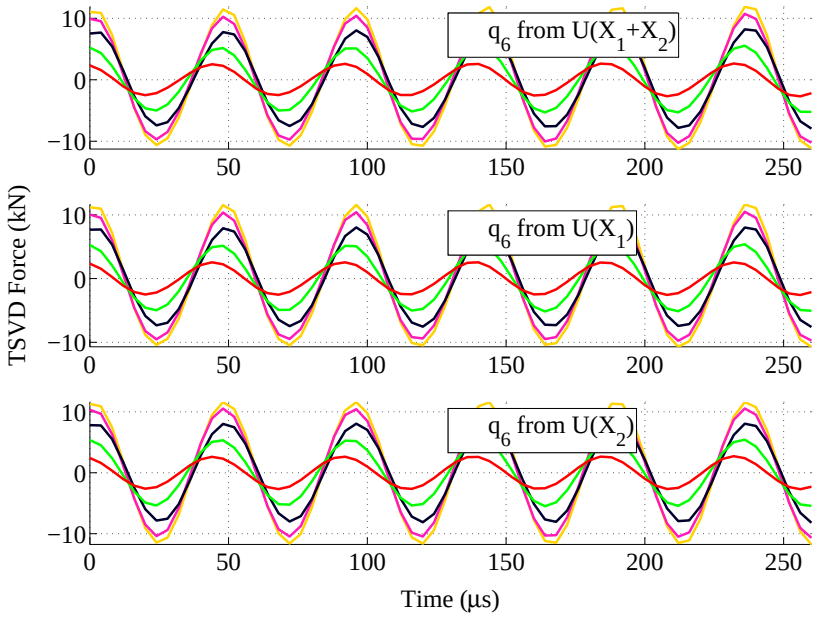

Fig. 5.80 Least square solution estimates through Truncated Singular Value Decomposition of the boundary load $q_6(\tau_q)$ deconvolved from the response, $U(X_m)$, of the Monolithic Horn when it is attached to the In-House Piezoelectric Actuator.

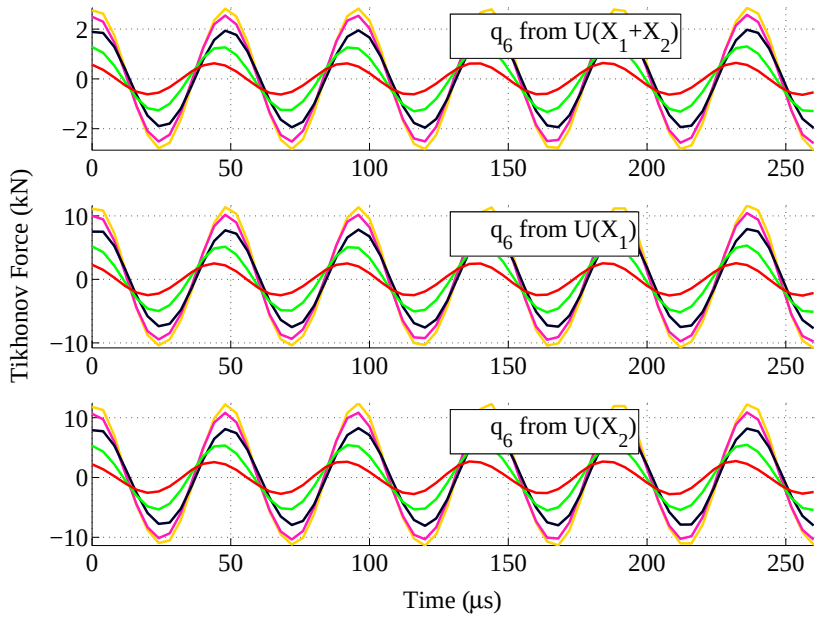

Fig. 5.81 Least square solution estimates through Tikhonov Regularisation of the boundary load $q_6(\tau_q)$ deconvolved from the response, $U(X_m)$, of the Monolithic Horn when it is attached to the In-House Piezoelectric Actuator.

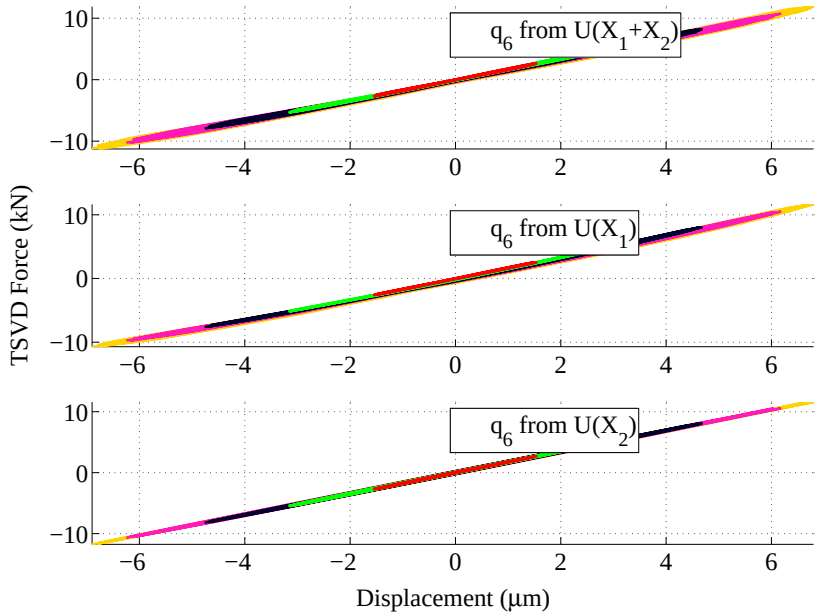

Fig. 5.82 Hysteresis loops for the boundary load $q_6(\tau_q)$ deconvolved from the response, $U(X_m)$, of the Monolithic Horn when it is attached to the In-House Piezoelectric Actuator.

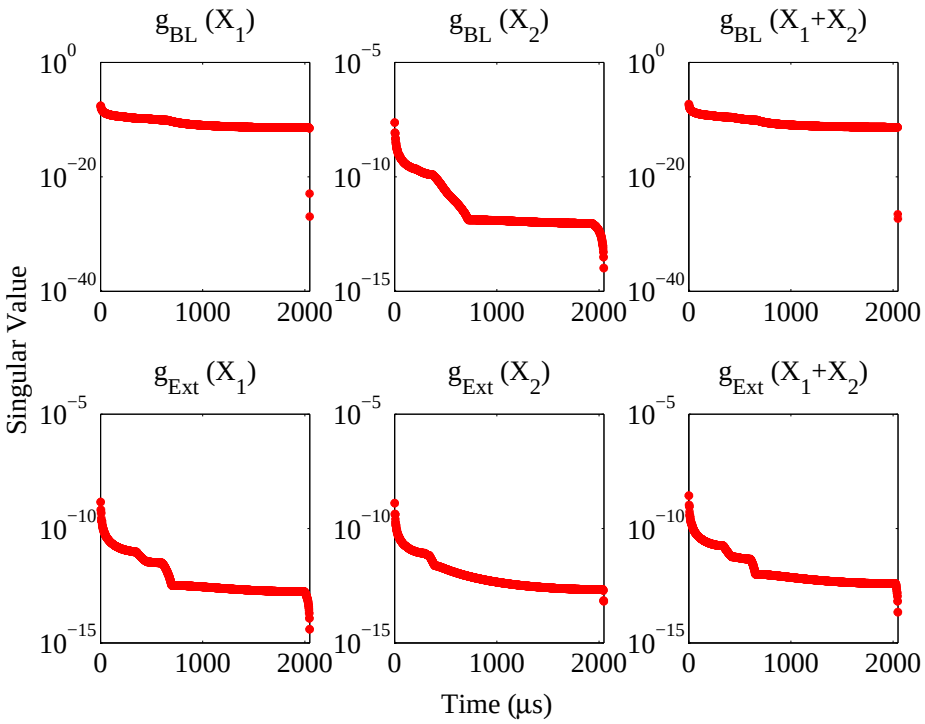

Fig. 5.83 Singular values of each impulse response matrix that forms the transfer function from the boundary load g_{BL} or the external force g_{Ext} to a measurement location at either the front of the horn X_1 or the flat X_2.

as uniform, between the x locations x_a and x_b, where the parameter values are listed in Table 5.1. The average strain at X_2 was estimated through DIC and is given in Figure 5.40. Although the DIC strains are very noisy, it is clear that their phase agrees well with the least squares solution for the majority of the acquisition window. The DIC strains were converted to forces, through the Young's Modulus of Grade 5 Titanium, and the subsequent hysteresis loops were shown in Figure 5.41. If the values at the extremes of the acquisition window are excluded, then the largest strain signal implies a peak amplitude of 100kN. The least squares solution has a peak amplitude that is close to 200kN, but overall the waveform resembles a sawtooth shape, which would not the expected from this mechanical vibration. In comparison, the TSVD regularised solution shows smooth sinusoidal solutions that agree with the phase of the DIC estimations. There is good agreement whether the solutions are associated with a single location, or two locations. The peak amplitude of each trace, that is associated with the highest electrical excitation, falls within 180 ± 10kN. The estimations that are obtained through Tikhonov regularisation are shown in Figure 5.87. The estimations that are associated with one location agree well with the TSVD solutions,

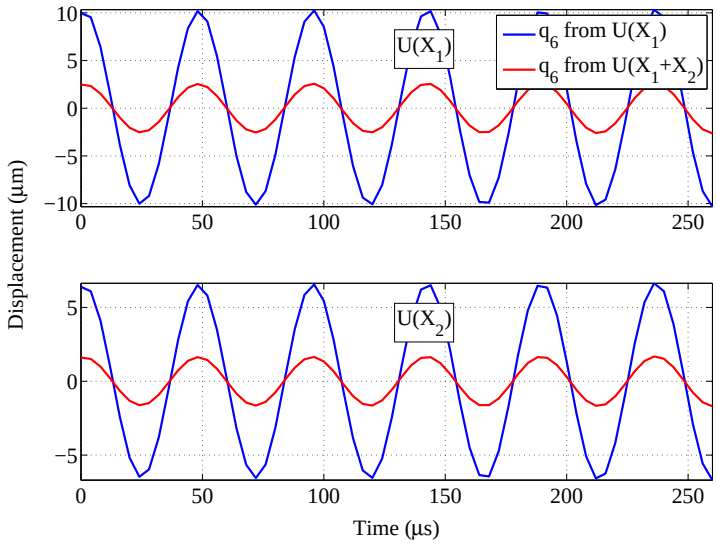

Fig. 5.84 Comparison of the displacements found when the Tikhonov input force is applied to the linear calibration model of the In-House Piezoelectric Actuator with the Monolithic Horn attached.

although the amplitudes can be up to 10kN higher. The results that are associated with two locations converge onto a minimum that does not represent a solution. The hysteresis loops are formed from the TSVD solutions and are shown in Figure 5.88. No damping has been applied to the waveguide model, so any deviation from the straight line loading-unloading path, is the result of noise. It is assumed that the mechanical energy dissipation of the linear calibration model is small in comparison to the dissipation of an equivalent jointed assembly.

5.5.2 Joint force

The input force that is developed by the piezoelectric stack in the HPU assemblies remains unknown. Very restrictive assumptions were required to make an estimation of this force through the distributed parameter system. The linear calibration forces that were retrieved in the previous section offer the best estimate to how an equivalent jointed system would behave if the joint did not exist. There are limitations in both the phase and the amplitude of this estimation if it is assumed to be the input when the joint is included. When a joint is introduced into an ultrasonic horn the overall mechanical impedance of the HPU device will be modified. This loss of stiffness will manifest as a change to the frequency of the operating

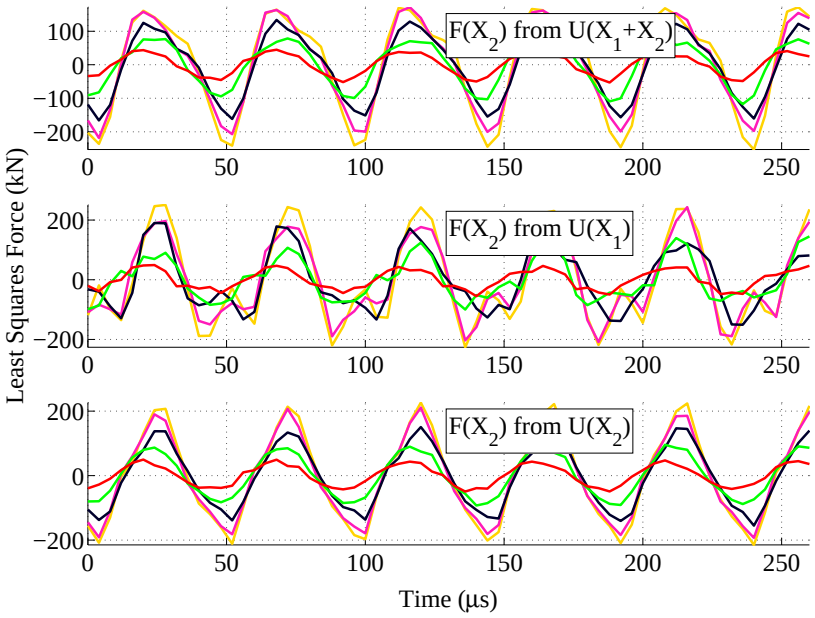

Fig. 5.85 Least square solution estimates through Forward Substitution of the external force, $N(x,\tau)$, at location X_2, when it is deconvolved from the response, $U(X_m)$, of the Monolithic Horn when it is attached to the In-House Piezoelectric Actuator.

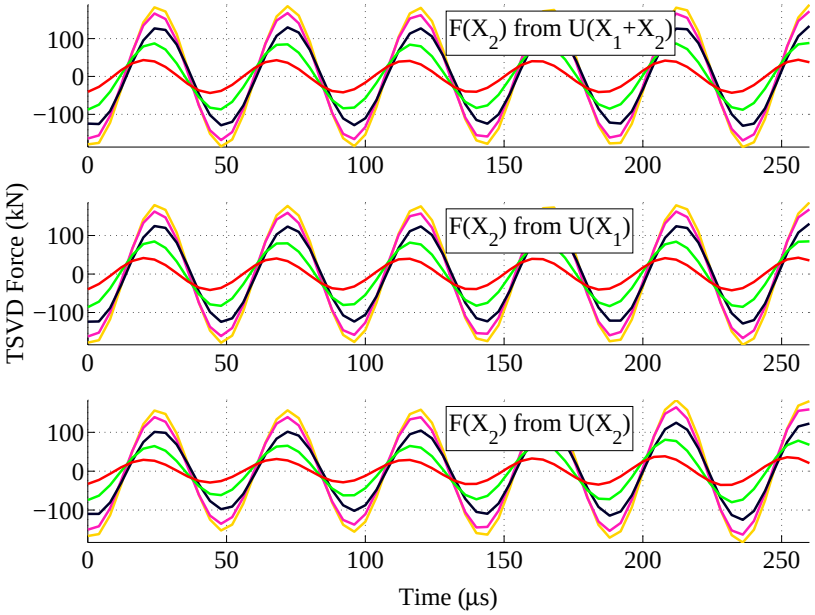

Fig. 5.86 Least square solution estimates through Truncated Singular Value Decomposition of the external force, $N(x,\tau)$, at location X_2, when it is deconvolved from the response, $U(X_m)$, of the Monolithic Horn when it is attached to the In-House Piezoelectric Actuator.

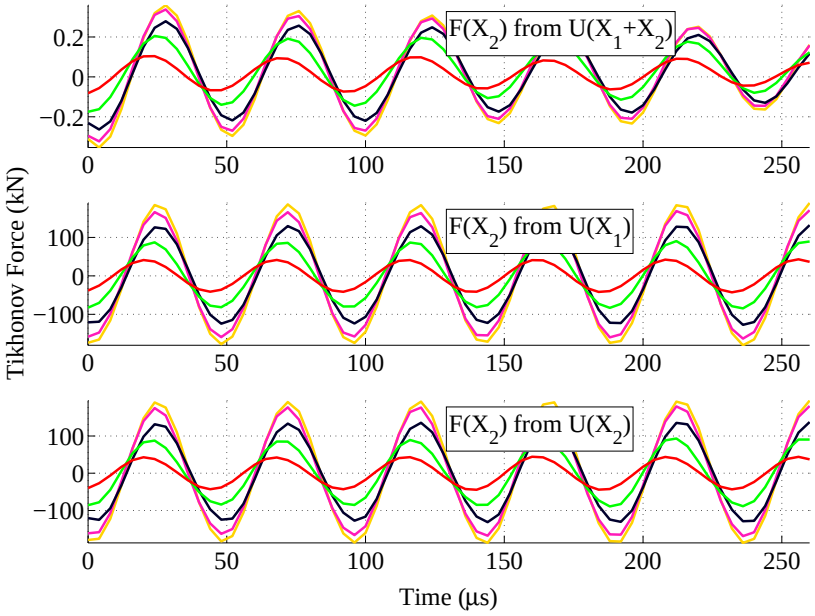

Fig. 5.87 Least square solution estimates through Tikhonov Regularisation of the external force, $N(x,\tau)$, at location X_2, when it is deconvolved from the response, $U(X_m)$, of the Monolithic Horn when it is attached to the In-House Piezoelectric Actuator.

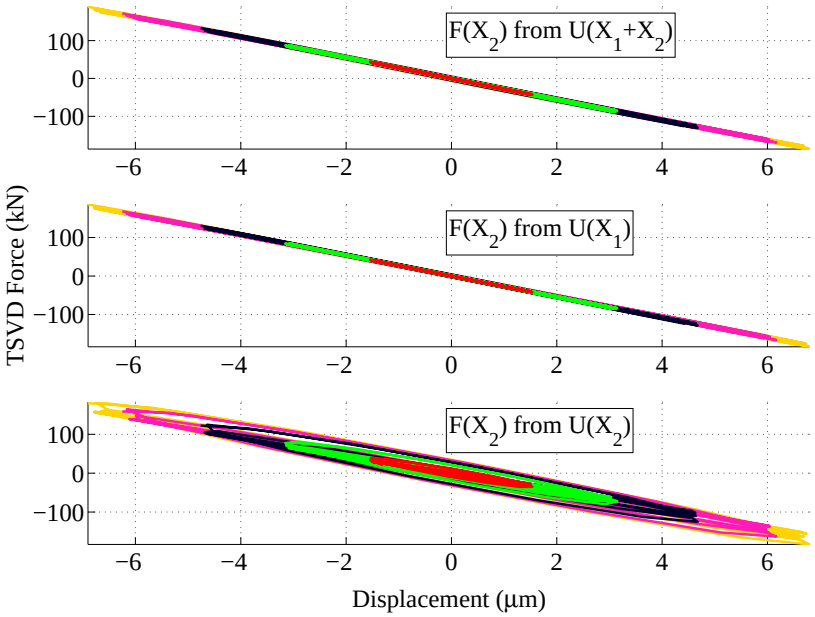

Fig. 5.88 Hysteresis loops for the external force, $N(x,\tau)$, at location X_2, when it is deconvolved from the response, $U(X_m)$, of the Monolithic Horn when it is attached to the In-House Piezoelectric Actuator.

vibration mode of the assembly, as long as its mode shape remains axial. Therefore any estimation of the input force to the JH, from a test of the MH, will contain a phase error. This represents a serious limitation to the linear calibration scheme. However, this issue is superseded by the limitations of updating the linear calibration model that were discussed in Chapter 4. It was found that the information that was known about the model, and that could be measured through the EMA, was not sufficient to identify a unique distributed parameter model. Therefore the model was updated through an evolutionary scheme to minimise the error between the model and EMA measured eigenvalues. For the operating mode, this error was not reduced to a degree where the change in frequency to the assembly, as a result of including the additional joint, would be discernible from the modelling error.

The amplitude error, which is inherent to the estimated input, also descends from the mismatch in mechanical impedance. Figure 5.37 shows that the potential difference across the piezoelectric stack depends on its electrical impedance. The discussion in Section 4.3 shows how the mechanical behaviour of the joint modifies the electrical impedance of the piezoelectric stack. Furthermore, if no impedance matching circuitry is included between the power amplifier and the piezoelectric stack, then power will be reflected back to the amplifier. This is the case for the tests of the IHPA. Tests of its MH and JH assemblies have been performed when the excitation signal from the function generator has the same amplitude. However the power that is drawn by the piezoelectric stack will not be equivalent. Therefore the amplitude of the input force is not interchangeable between the two assemblies.

To produce an estimate of the joint force it must be accepted that the linear calibration is the best estimate that is available as an input to the JH. The addition of a sensor would modify the HPU assembly significantly and would introduce further mechanical impedance into the problem. An exact distributed parameter model with higher complexity is required to accurately simulate the linear behaviour of the piezoelectric stack. A comparison of the tests of the MH and JH assemblies in Section 5.4.2 were enough to demonstrate that the addition of the axial joint can produce nonlinear dynamical behaviour that is not encountered in the equivalent MH assembly. Perhaps it is possible to isolate this behaviour whilst accepting the phase error in the input to the jointed assembly. It was also suggested that the amplitude of this input should be corrected through Equation (5.16). This employs the relative change in the electrical impedance of the operating mode that can be determined from the results in Section 4.3.

The formulation of the linear calibration model does not feature any form of energy dissipation. The issue with applying viscous damping, in order to approximate material damping,

was introduced in Section 4.5.2. Without this, it is expected that attempting to isolate the JH hysteresis will also include the hysteresis of the monolithic assembly. In some hysteresis loops, that were obtained through the estimate of the input force in Section 5.5.1, it was found that the regularised solution can appear elliptical. Without a damping model, the area that is enclosed by this type of hysteresis loop must be attributed to the error that is associated with the degree of the regularisation.

The analysis that follows makes use of the linear calibration models that were defined in Chapter 4. The response of both of the actuators has been measured with the MH attached. The estimated input force in Section 5.5.1 has been deconvolved from this and the results have been listed for each nominal power supply setting. It has already been discussed that when each setting is applied to the JH assembly, the input force that is developed is not equivalent. If there are nonlinear dynamic phenomena, that descend from the joint, then perhaps these can still be observed when the joint force is deconvolved from the linear calibration model, with the estimated input force, for the same nominal power setting. This is the rationale for the direct application of the force estimation that was expressed in Equation (3.99). This implicitly assumes that the same input force is applied to both the MH and the JH assembly. Then the joint force is deconvolved from the linear calibration model. The output is taken as the difference in the measured responses of the two assemblies. When this process is applied to the JH responses it is referred to as the *displacement calibration*.

The JH assembly is not capable of achieving the same input force as the MH assembly because of its increased mechanical impedance. To account for this, the amplitude of the estimated input force, from Section 5.5.1, is scaled through the expression in Equation (5.16). This is based on Figure 5.37. The joint force is deconvolved from the difference between the measured JH response and the estimated response of the linear calibration model, when it is loaded by the scaled input. This is computed through the expressions in Equations (3.96)-(3.98). When this method is applied to the JH responses it is referred to as the *force calibration*.

Commercial Piezoelectric Actuator

The responses that have been measured when each JH is attached to the CPA have already been given in Figures 5.56-5.59. Only half of the samples that were measured for steady state vibrations have been displayed. For an initial estimate of the joint behaviour, the displacement calibration has been applied. It has already been shown that regularisation

methods are required to obtain a stable solution. When TSVD regularisation is applied the singular values below the tolerance, $\epsilon = 3.1623 \times 10^{-13}$, are considered to be negligible. When Tikhonov regularisation is applied the regularisation parameter is selected through the L-curve method. It is typically of the order $\Gamma_{X_m} \approx \times 10^{-17}$ to $\Gamma_{X_m} \approx \times 10^{-20}$. Where X_m is the measurement location where $m = 1$, 2 or 3.

The TSVD regularised solutions to the displacement calibration are shown in Figures 5.89-5.92 and the subsequent hysteresis loops are displayed in Figures 5.93-5.96. Each set of results gives the force when it is estimated from the response at each location, as well as the sum of all of the responses. It was not possible to retrieve any solutions from the readings at location X_3, which are taken from the front mass of the CPA. The best source of a comparison, to the results that are obtained, are the equivalent strain readings that were found through the DIC. These results were given in Figures 5.28-5.31 from which the amplitude can be discerned from the associated hysteresis loops in Figures 5.32-5.35. There is little agreement between the amplitudes of force that are estimated through both methods. This is expected because the DIC strains have been transformed to force through an assumed constant Young's modulus, which does not represent the true stiffness behaviour of the observed area. There are significant errors in assuming that the JH is excited by the same input force as the MH. The DIC hysteresis loops also drift from the origin more substantially than the joint force estimation suggests. The regularised solutions feature the correct number of cycles when compared to the equivalent DIC results.

The JH with a steel stud, which is set to 8Nm, was tested for more nominal power settings than the JHs with a Grade 5 Titanium stud. The joint forces developed in this horn are estimated by summing all three responses and the obtained solutions appear to follow a similar pattern to the equivalent DIC results. There is also low frequency modulation behaviour that is equivalent between both data sets. However it is not possible distinguish this completely from the errors that are associated with each method. For the same tightness, but a Grade 5 Titanium stud, the DIC strain estimations were very poor due to the very low amplitude of the observed displacement field. As a result, it is not possible to form a comparison with the regularised solutions. However the frequency of the solutions is consistent. This suggests that the closest least squares solution, that is available through the estimation, has been found. For the JH, with a stud that is set to 12Nm, there is no agreement between the estimated amplitudes. The DIC result, for the highest nominal power setting, drifts significantly from the origin. There is some suggestion of this in the hysteresis loops that are formed from the regularised solution when it is estimated from the sum of all of

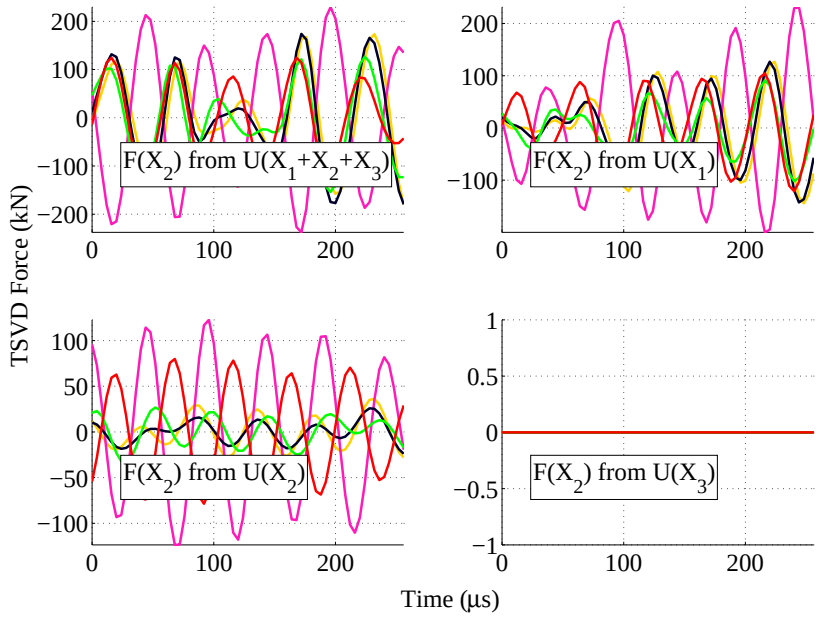

Fig. 5.89 Truncated Singular Value Decomposition regularised solution of the force at X_2 from the linear calibration $u^{JH}(X_2) - u^{MH}(X_2)$ for the Commercial Piezoelectric Actuator with the Jointed Horn attached which features a Steel stud set to 8Nm.

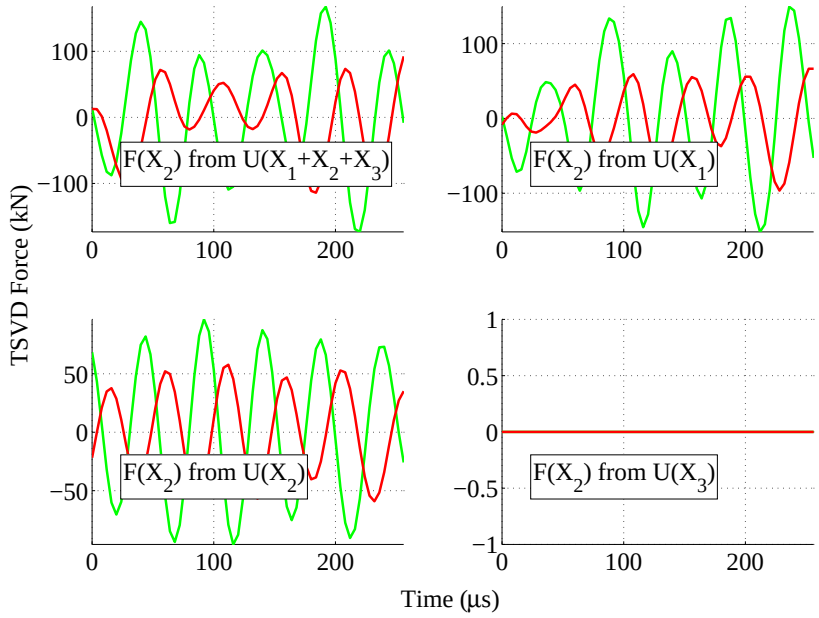

Fig. 5.90 Truncated Singular Value Decomposition regularised solution of the force at X_2 from the linear calibration $u^{JH}(X_2) - u^{MH}(X_2)$ for the Commercial Piezoelectric Actuator with the Jointed Horn attached which features a Grade 5 Titanium stud set to 8Nm.

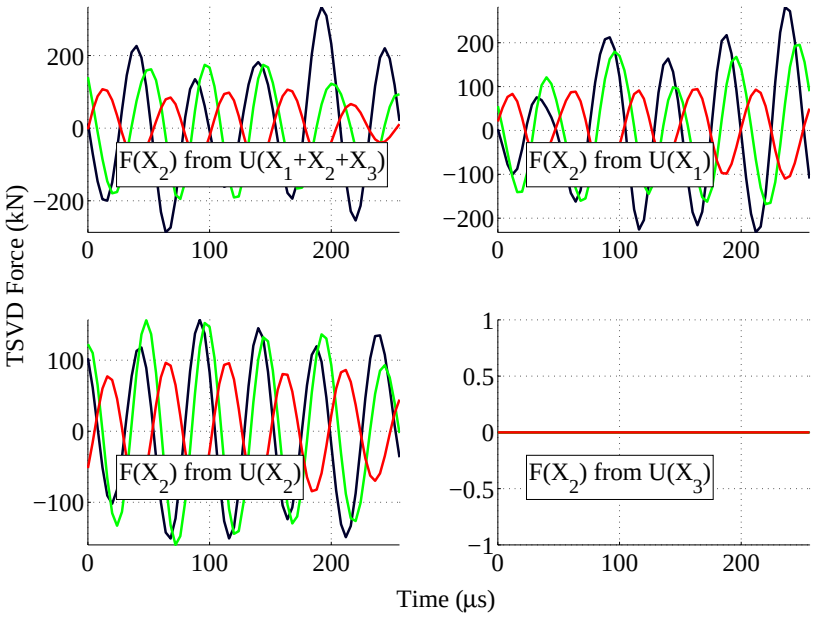

Fig. 5.91 Truncated Singular Value Decomposition regularised solution of the force at X_2 from the linear calibration $u^{JH}(X_2) - u^{MH}(X_2)$ for the Commercial Piezoelectric Actuator with the Jointed Horn attached which features a Grade 5 Titanium stud set to 12Nm.

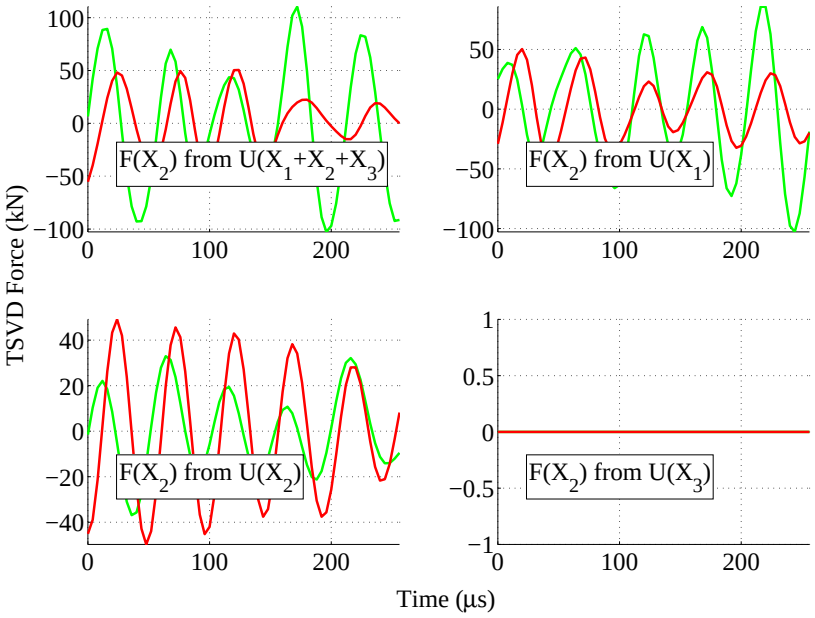

Fig. 5.92 Truncated Singular Value Decomposition regularised solution of the force at X_2 from the linear calibration $u^{JH}(X_2) - u^{MH}(X_2)$ for the Commercial Piezoelectric Actuator with the Jointed Horn attached which features a Grade 5 Titanium stud set to 16Nm.

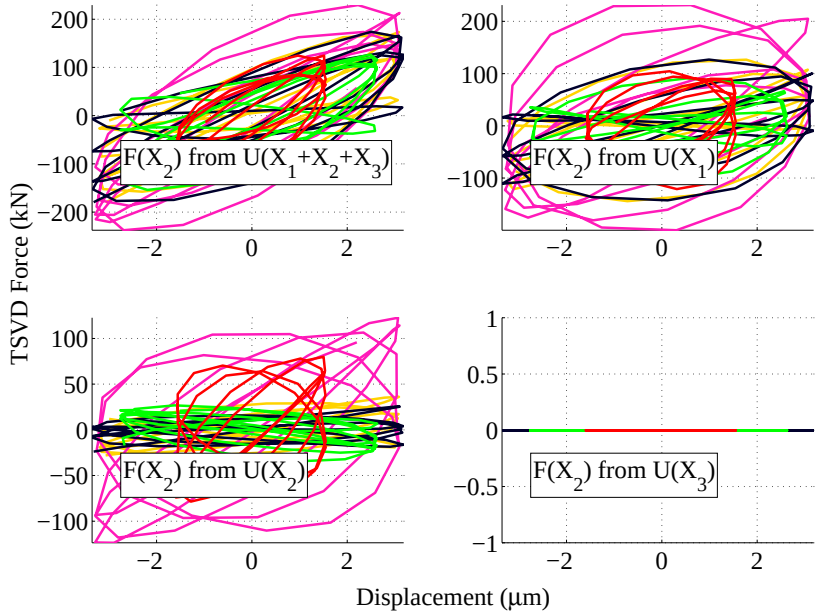

Fig. 5.93 Hysteresis loops at X_2 from the linear calibration $u^{JH}(X_2) - u^{MH}(X_2)$ for the Commercial Piezoelectric Actuator with the Jointed Horn attached which features a Steel stud set to 8Nm.

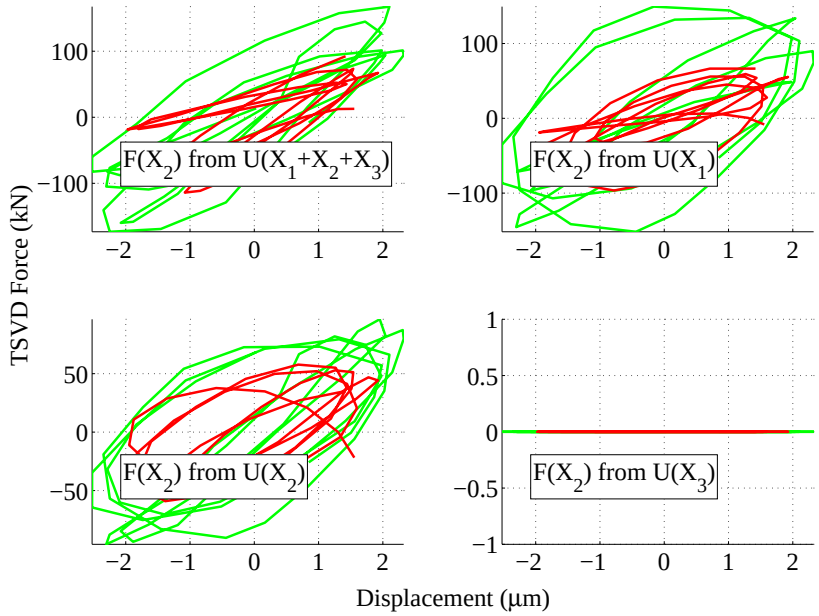

Fig. 5.94 Hysteresis loops at X_2 from the linear calibration $u^{JH}(X_2) - u^{MH}(X_2)$ for the Commercial Piezoelectric Actuator with the Jointed Horn attached which features a Grade 5 Titanium stud set to 8Nm.

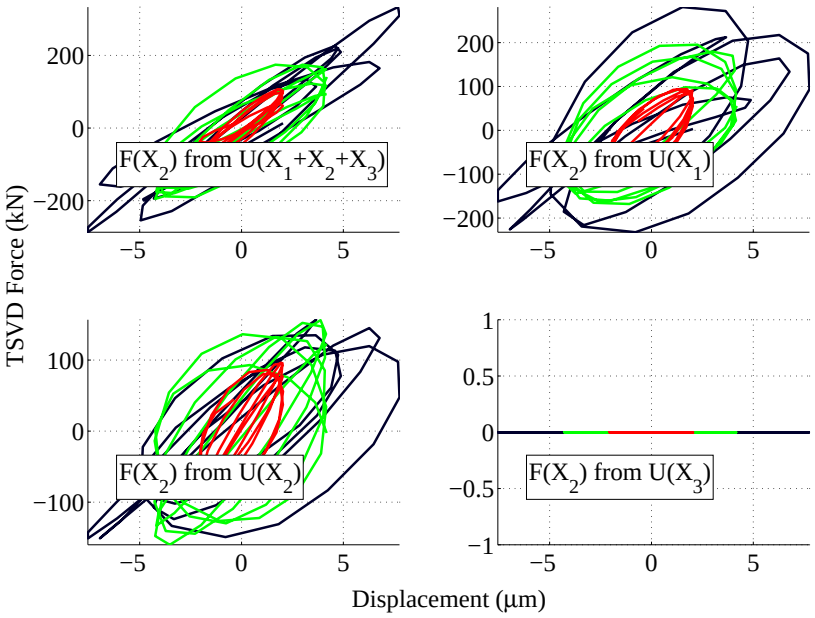

Fig. 5.95 Hysteresis loops at X_2 from the linear calibration $u^{JH}(X_2) - u^{MH}(X_2)$ for the Commercial Piezoelectric Actuator with the Jointed Horn attached which features a Grade 5 Titanium stud set to 12Nm.

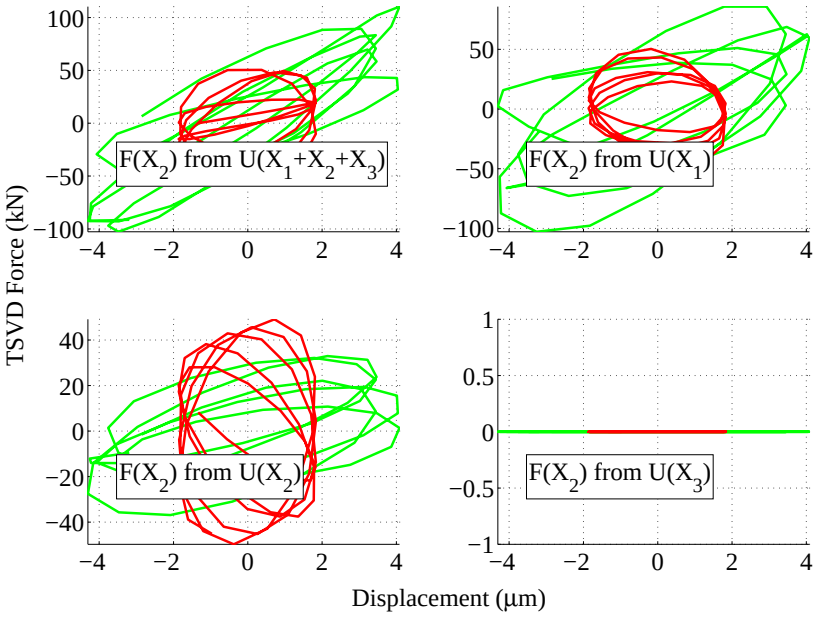

Fig. 5.96 Hysteresis loops at X_2 from the linear calibration $u^{JH}(X_2) - u^{MH}(X_2)$ for the Commercial Piezoelectric Actuator with the Jointed Horn attached which features a Grade 5 Titanium stud set to 16Nm.

the responses. This solution also clearly displays a similar level of signal modulation to the equivalent DIC strain result. Although there is a significant phase error between the observations. This modulation is not as significant for the lower amplitude settings. This could show that it is not a result of the regularisation strategy. When the tightness is set to 16Nm the disagreement in the estimated amplitude is significant. The regularised solutions that are associated with the response at X_1 agree best with the DIC results. For the solutions that are associated with the sum of all of the responses, the highest power setting result appears to be modulated differently from the DIC result. Also the solution that is associated with this setting, and found from X_2 only, is found to be smaller than the solution that is measured for a lower power setting. Overall it is expected that the force estimations that are associated with the sum of all three responses are the most reliable solutions that are available. All of these were recovered with frequency that is comparable to the equivalent DIC results. However, the DIC results and the regularised solutions contain very few samples, which means that the resolution bandwidth of the Fast Fourier Transform (FFT) is very poor. The resolution of the DIC results was 3.8kHz and the discrepancy between the two data sets is expected to be within the error of the linear calibration, which is 1kHz. Therefore it is not possible to reliably state the frequency error of the joint force estimation.

An equivalent set of estimations of the joint force are formed using Tikhonov regularisation. In each case the optimal value for the regularisation parameter is chosen through the L-curve method. The estimated forces are shown in Figures 5.97-5.100 and the subsequent hysteresis loops are displayed in Figures 5.101-5.104. Only constant force solutions are obtained when the regularised solutions are found by summing all three displacement responses. This could suggest that the errors of the linear calibration model and the estimated input force are too limiting to produce a reasonable estimate of the joint force. For each set of results, that is associated with an individual JH, there is a considerable difference in amplitude when it is found from locations X_1 and X_3 compared to X_2. This might explain the failure to develop a reasonable estimate from the sum of all three locations. Figure 5.97 shows the solutions that are associated with X_2 for the JH with a steel stud, which is set to 8Nm. These agree well with the equivalent TSVD solutions that were obtained from the sum of the displacements at all three locations. In this case the amplitude modulation is not as prevalent as it was before, which might suggest that those TSVD solutions were over regularised. These solutions resemble the pattern of the DIC results, but feature a phase error. The amplitude of the regularised solutions is also less than half the amplitude of the DIC results.

The hysteresis loops, which are shown in Figure 5.101, follow a similar pattern to the hys-

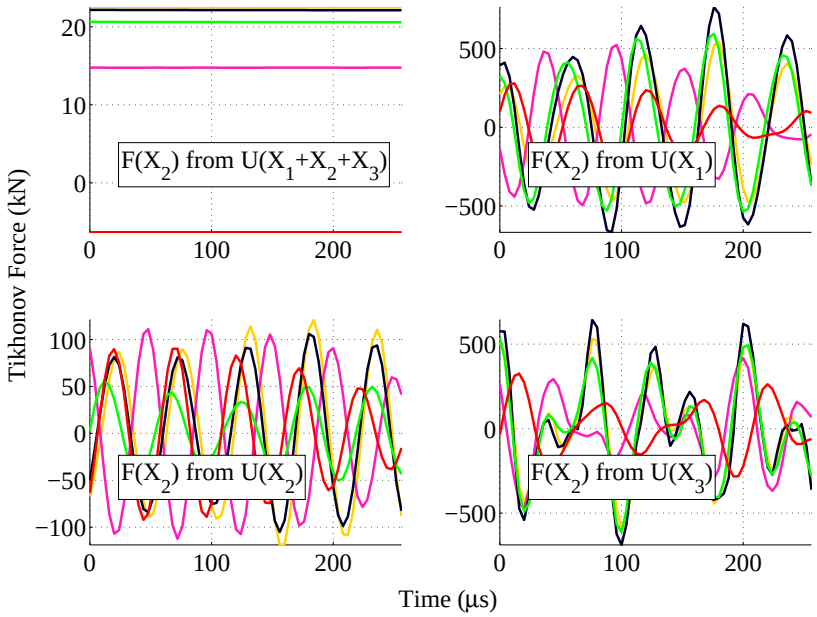

Fig. 5.97 Tikhonov Regularised solution of the force at X_2 from the linear calibration $u^{JH}(X_2) - u^{MH}(X_2)$ for the Commercial Piezoelectric Actuator with the Jointed Horn attached which features a Steel stud set to 8Nm.

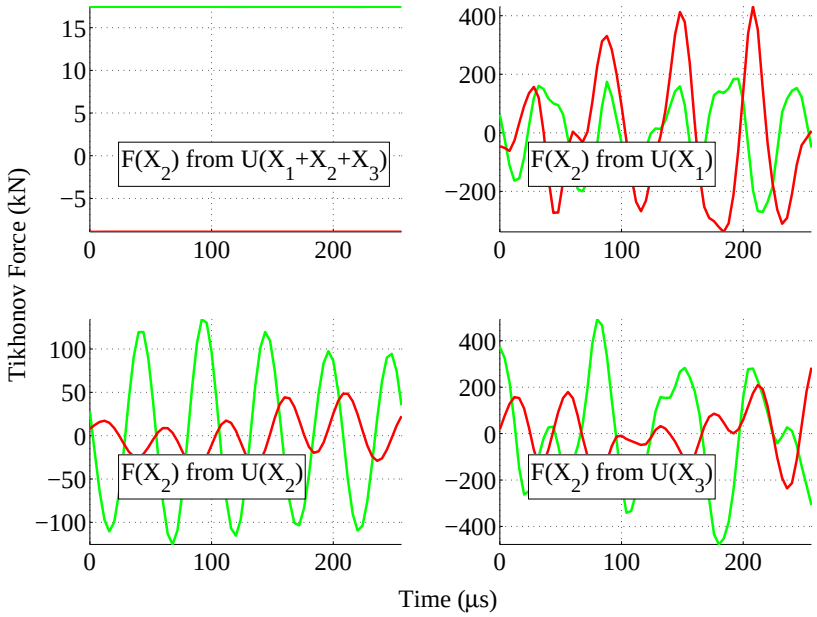

Fig. 5.98 Tikhonov Regularised solution of the force at X_2 from the linear calibration $u^{JH}(X_2) - u^{MH}(X_2)$ for the Commercial Piezoelectric Actuator with the Jointed Horn attached which features a Grade 5 Titanium stud set to 8Nm.

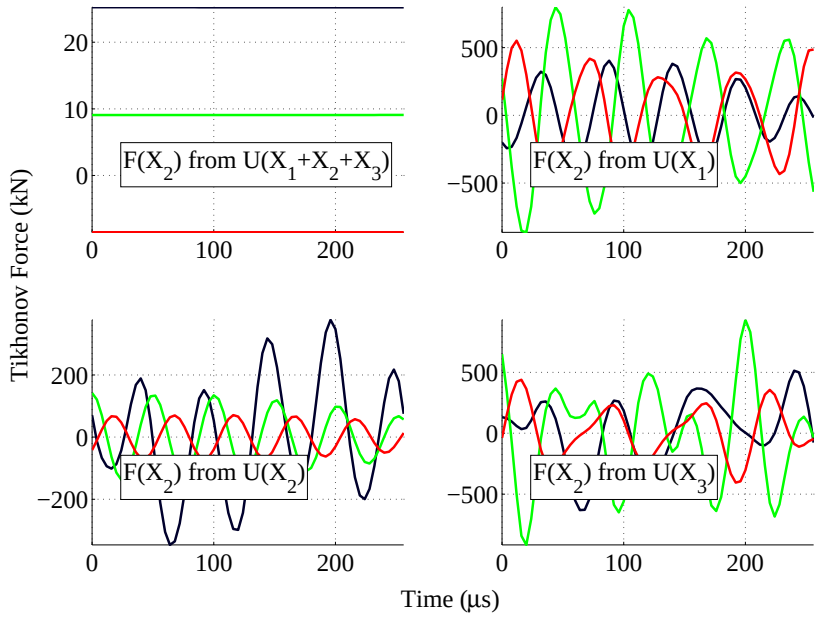

Fig. 5.99 Tikhonov Regularised solution of the force at X_2 from the linear calibration $u^{JH}(X_2) - u^{MH}(X_2)$ for the Commercial Piezoelectric Actuator with the Jointed Horn attached which features a Grade 5 Titanium stud set to 12Nm.

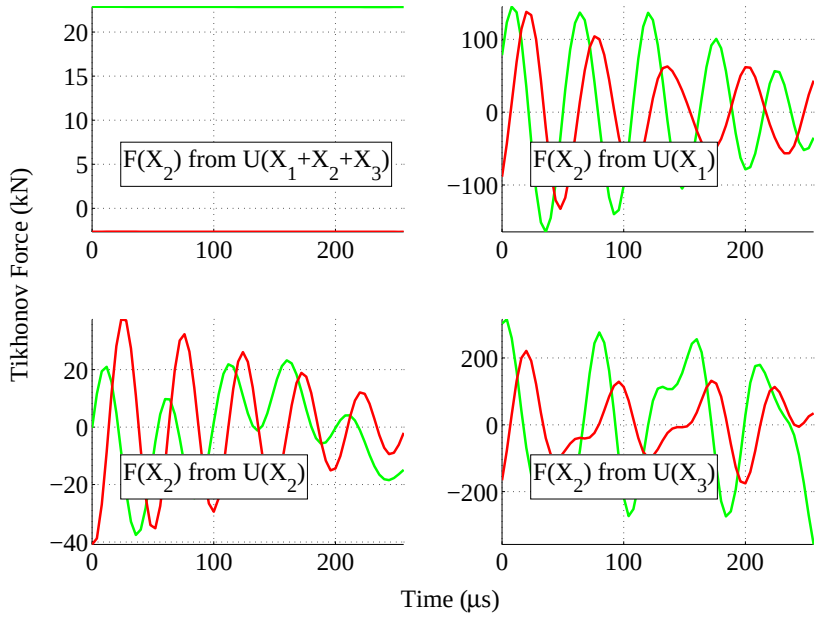

Fig. 5.100 Tikhonov Regularised solution of the force at X_2 from the linear calibration $u^{JH}(X_2) - u^{MH}(X_2)$ for the Commercial Piezoelectric Actuator with the Jointed Horn attached which features a Grade 5 Titanium stud set to 16Nm.

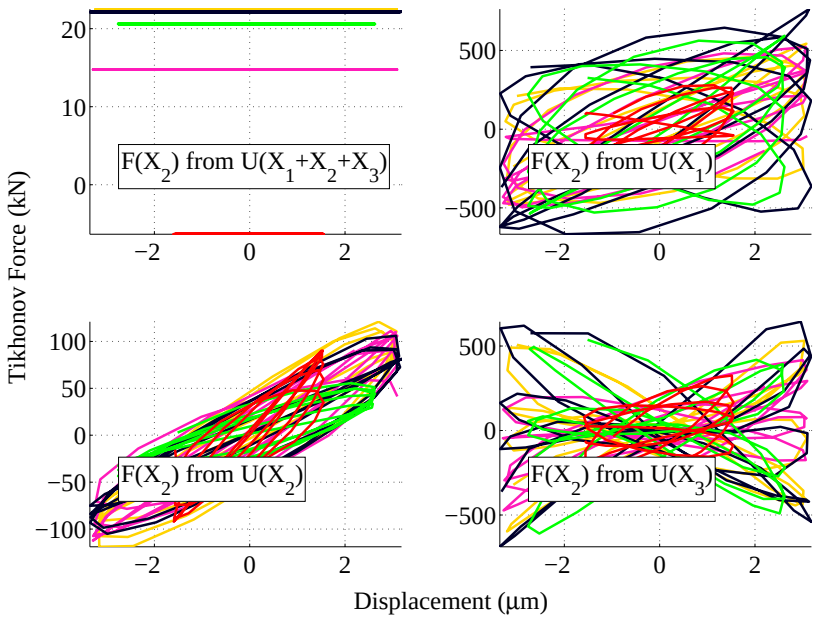

Fig. 5.101 Hysteresis loops at X_2 from the linear calibration $u^{JH}(X_2) - u^{MH}(X_2)$ for the Commercial Piezoelectric Actuator with the Jointed Horn attached which features a Steel stud set to 8Nm.

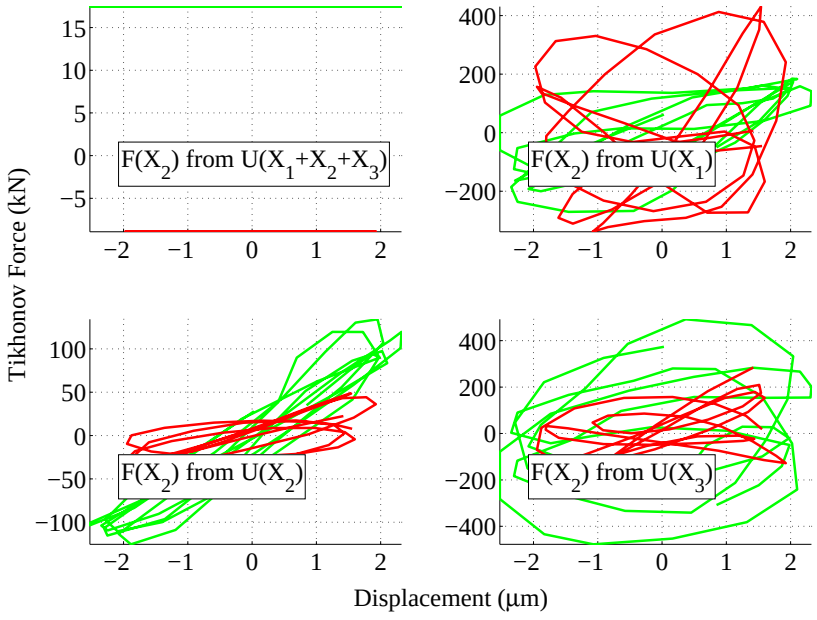

Fig. 5.102 Hysteresis loops at X_2 from the linear calibration $u^{JH}(X_2) - u^{MH}(X_2)$ for the Commercial Piezoelectric Actuator with the Jointed Horn attached which features a Grade 5 Titanium stud set to 8Nm.

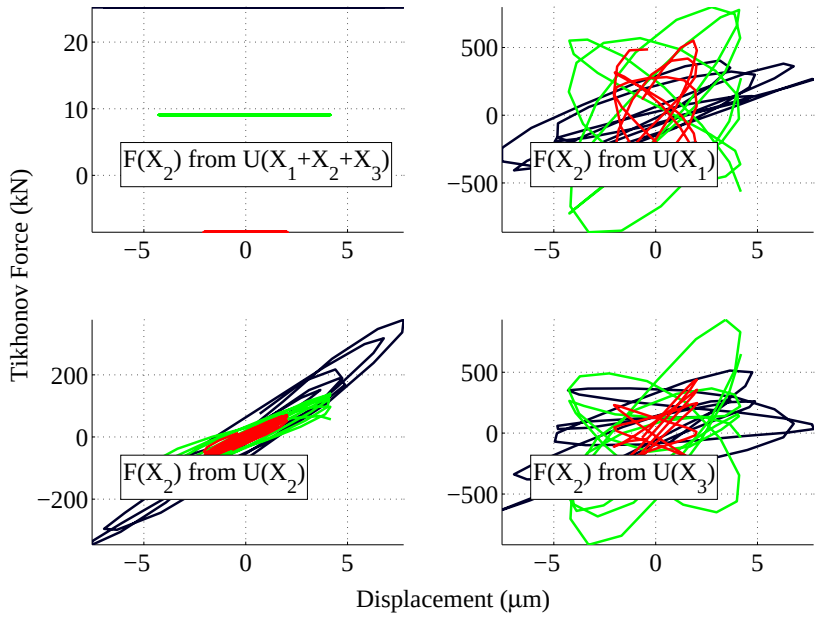

Fig. 5.103 Hysteresis loops at X_2 from the linear calibration $u^{JH}(X_2) - u^{MH}(X_2)$ for the Commercial Piezoelectric Actuator with the Jointed Horn attached which features a Grade 5 Titanium stud set to 12Nm.

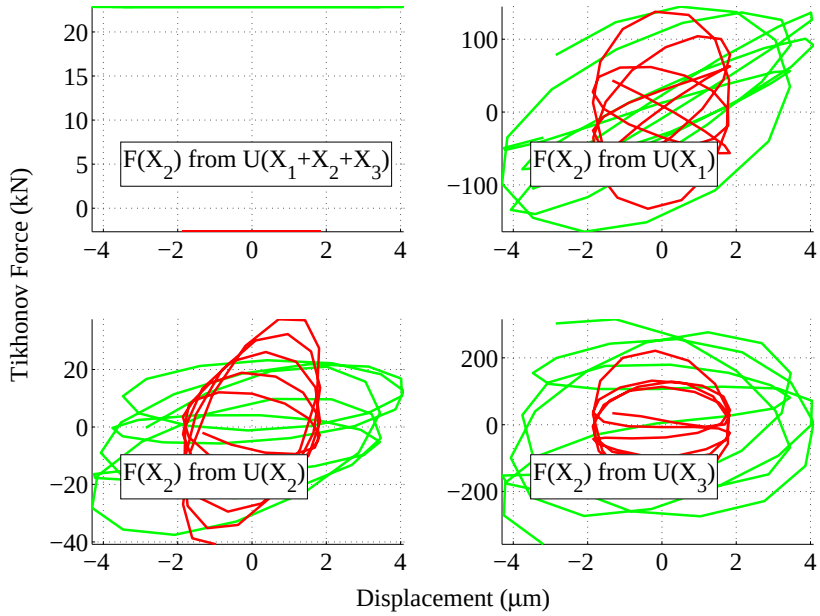

Fig. 5.104 Hysteresis loops at X_2 from the linear calibration $u^{JH}(X_2) - u^{MH}(X_2)$ for the Commercial Piezoelectric Actuator with the Jointed Horn attached which features a Grade 5 Titanium stud set to 16Nm.

teresis loops found through the DIC. The DIC loops are too noisy to discern detailed characteristics of the loops, but the regularised solutions draw smooth loops when only the response at X_2 is considered. The Tikhonov estimates are more consistent than the TSVD regularised loops because the regularisation parameter has been optimised each time. For a JH with the same tightness, but a Grade 5 Titanium stud, the solutions associated with X_2 agree most closely to the best TSVD results. It is difficult to compare the form of the solutions to the DIC results, which were very noisy. When the tightness of the joint is increased to 12Nm the regularised solutions associated with location X_2 are most consistent with the equivalent DIC and TSVD results. The solutions with the other locations do not make sense because the largest amplitude vibrations are not associated with the largest amplitude forces. The solutions that are associated with X_2 resemble the pattern of the DIC results with a phase error. Despite the difference in amplitude, the hysteresis loops are qualitatively similar in both cases. When the tightness is increased to 16Nm, it is the results that are associated with location X_1 that appear to agree better with the DIC and TSVD results. However the hysteresis loops are far noisier than the DIC hysteresis loops suggests. Overall the Tikhonov solutions should be a clearer indication of the appropriateness of the joint force estimation. Due to the variable quality of the solutions it is very difficult to develop any confidence in the results. However this can be expected given the lack of details on the construction of the CPA. It is unlikely that the force calibration method would improve the estimations considerably.

In-House Piezoelectric Actuator

The responses that have been measured, when each JH is attached to the IHPA, have already been given in Figures 5.62-5.65. Only a small number of samples have been shown for the observation time window at which the HPU device has reached its working amplitude. Initially the displacement calibration has been applied to estimate the joint force. The tolerance of the TSVD regularised solutions is maintained at $\epsilon = 3.1623 \times 10^{-13}$. The results from this are consistent whether one or two responses are involved in the deconvolution, so Tikhonov regularisation was not applied. This would offer a small correction to the obtained amplitudes because the regularisation parameter can be optimised. However in Section 5.5.1 it converged on solutions that were incorrect in some cases.

Figures 5.105-5.108 display the regularised solutions, at X_2, that are deconvolved from the difference in the response of the MH and JH assembly for the same amplitude setting of the

function generator. Each set of results are similar in phase when each JH is tested and the force is deconvolved from the response at one or two locations. Clearly this is the result of the linear calibration dominating the computation because it is expected that the joint force would reduce in frequency for a looser joint. The equivalent DIC strain results, which are shown in Figures 5.46-5.49, are extremely noisy despite the application of a moving average filter. These show that the regularised solutions have an extra half cycle and do not demonstrate any low frequency modulation. However, it should be noted that the DIC results are expected to feature some low frequency modulation due to the noise floor that is related to the illumination of the speckle pattern.

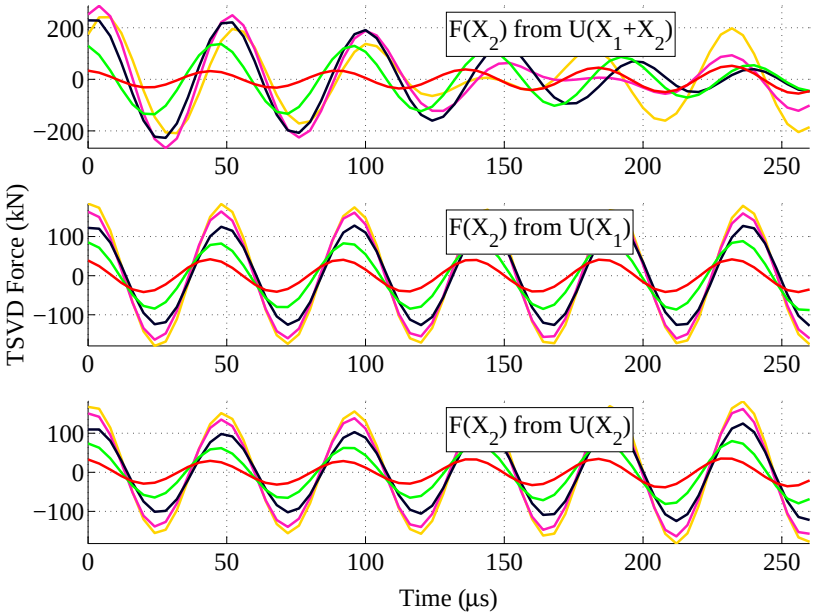

Fig. 5.105 Truncated Singular Value Decomposition regularised solution of the force at X_2 from linear calibration $u^{JH}(X_2) - u^{MH}(X_2)$ for the In-House Piezoelectric Actuator with the Jointed Horn attached which features a Steel stud set to 8Nm.

The results from the JH with a steel stud, that is set to 8Nm, are shown in Figure 5.105. When the regularised solutions are found from the sum of the responses at two locations they converge on a solution that is approximately double the solutions that are evaluated from the response at one location. The amplitude of the solutions derived from the response at one location agree better with the estimations given by the DIC hysteresis loops in Figure 5.50. The equivalent solutions that were obtained from testing the MH are shown in Figure 5.86. It is clear that the JH solutions only represent a shift in phase of the MH solutions with little change in the amplitude. However, a comparison of the DIC measured hysteresis loops, for

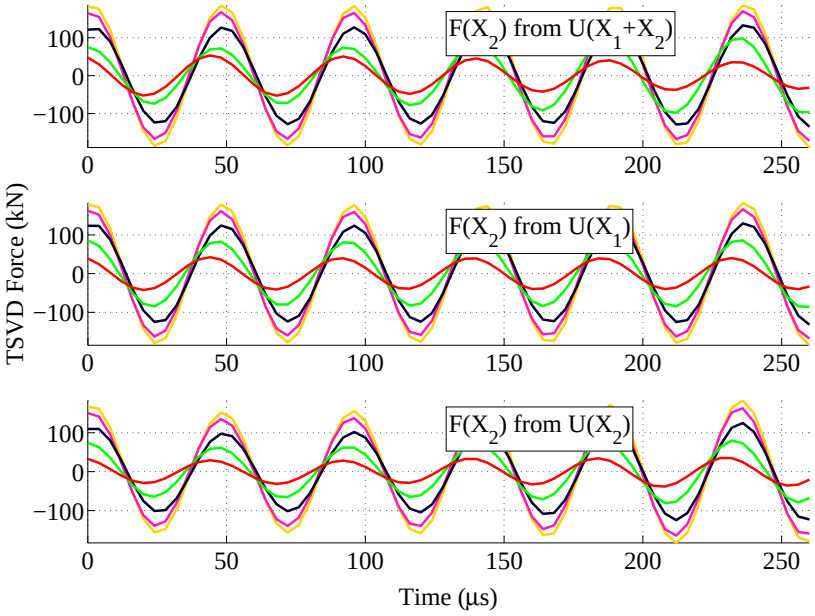

Fig. 5.106 Truncated Singular Value Decomposition regularised solution of the force at X_2 from linear calibration $u^{JH}(X_2) - u^{MH}(X_2)$ for the In-House Piezoelectric Actuator with the Jointed Horn attached which features a Grade 5 Titanium stud set to 8Nm.

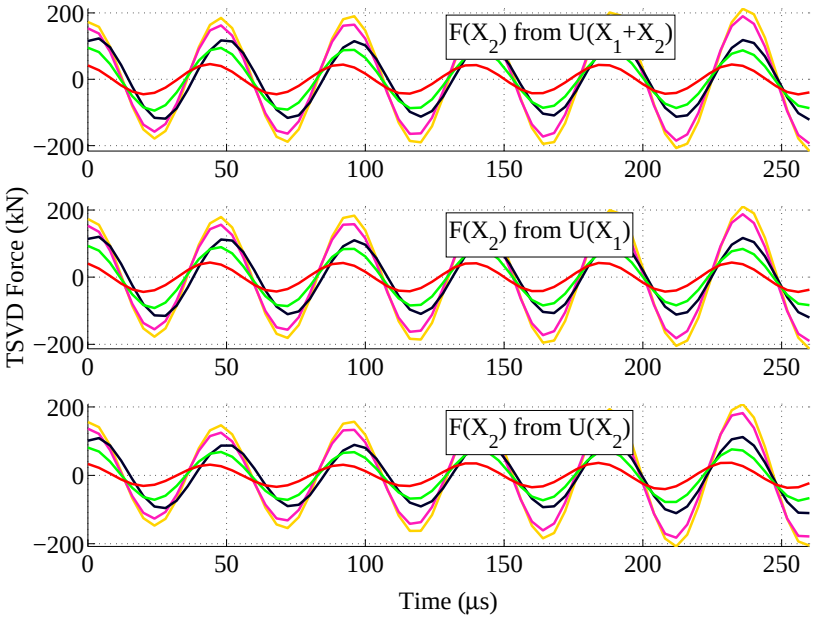

Fig. 5.107 Truncated Singular Value Decomposition regularised solution of the force at X_2 from linear calibration $u^{JH}(X_2) - u^{MH}(X_2)$ for the In-House Piezoelectric Actuator with the Jointed Horn attached which features a Grade 5 Titanium stud set to 12Nm.

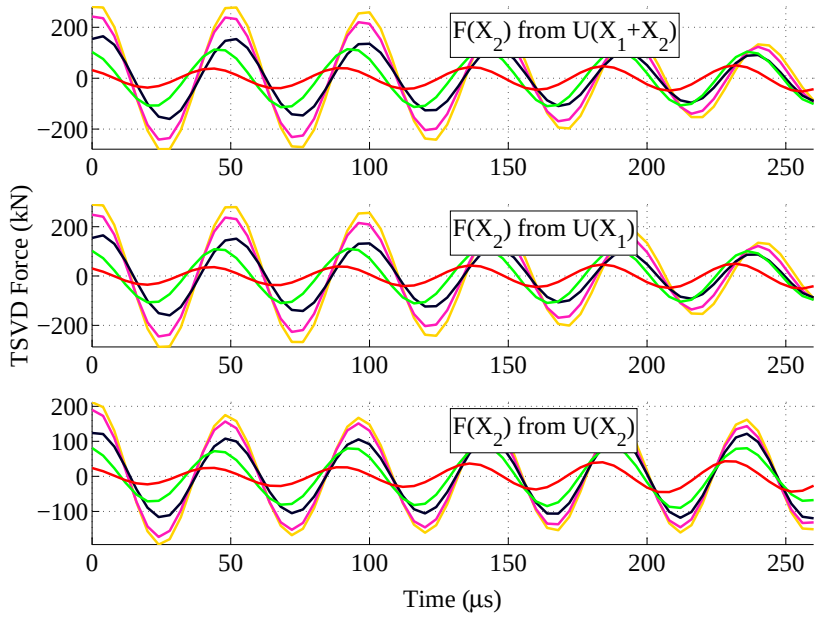

Fig. 5.108 Truncated Singular Value Decomposition regularised solution of the force at X_2 from linear calibration $u^{JH}(X_2) - u^{MH}(X_2)$ for the In-House Piezoelectric Actuator with the Jointed Horn attached which features a Grade 5 Titanium stud set to 16Nm.

the MH and JH assemblies in Figures 5.41 and 5.50, suggested that they did achieve similar amplitudes of force when the same excitation voltage was set at the function generator. Despite this, the displacement responses that were measured from the JH assembly were approximately 1/3 of the equivalent responses of the MH assembly.

If the steel stud is replaced with a Grade 5 Titanium stud, and set to the same tightness, then the regularised solutions are displayed in Figure 5.106. The forces that are deconvolved from the response at one location are approximately the same as the equivalent results for the previous JH assembly. However when the forces are deconvolved from the sum of two locations, this time, the solutions are very similar to the forces when they are deconvolved from one location. The JH with a titanium stud represents less of a deviation from the MH than the JH with a steel stud because the acoustic matching of the joint will be improved when there is no material change. However the electrical impedance results in Table 4.1 have already shown that the discrepancy between the impedance minima of the two assemblies is minimal. The DIC results, that were obtained from testing the titanium stud JH, suggests that the force developed at the joint will be reduced in comparison to the JH with a steel stud. The displacement responses are also considerably reduced. Overall the similarity between the JH results for 8Nm tightness, and the MH results, suggests that the linear

calibration is masking the joint force behaviour that is of interest.

When the tightness is increased to 12Nm the joint force estimates increase beyond the amplitude of the linear calibration forces. The phase of the solutions remains very similar to the previous solutions. The amplitude of the force estimates is comparable to the equivalent DIC results, however these were derived from displacements that are approximately double the amplitude of the DIC displacement field. The regularised solutions appear to be the same whether they are associated with the response at one or two locations. When the joint tightness is 16Nm the phase of the regularised solutions is not modified noticeably, but the amplitude increases. The impedance analysis results in Section 4.3 suggested that the 12Nm JH achieved a sharper response and would therefore develop greater amplitude than the 16Nm JH. However, the response of the 16Nm JH is greater than the 12Nm JH, when it is found for an equivalent voltage from the function generator, through laser vibrometry and DIC. It is not possible to form a comparison between the DIC strain results and the regularised solutions of the 16Nm JH because of a systematic error in the DIC results. As a result, the strain estimations are significantly modulated and the hysteresis loop translates over time on the force-displacement plane. It was found that the speckle pattern that was applied to the 16Nm JH was more reflective than the other speckle patterns in the test. Therefore transient artefacts influence the estimation of the displacement field and are amplified in the strain estimation.

The force estimation is summarised in the schematic that is shown in Figure 5.109. This demonstrates that the force identification method is limited in a very specific way when it is applied to an HPU device. Clearly it requires that both the MH and the JH assembly is excited through the same input signal. However, the resonance bandwidth if very narrow for each assembly, so applying the excitation signal at the resonance frequency of either of the assemblies, to both of the assemblies, will result in two responses that can and cannot be measured reliably above the noise floor of the equipment. Therefore both of the HPU assemblies must be forced at their resonance frequency in order to obtain the data that is necessary for the force estimation. If an equivalent experiment could be executed when the operating resonance of the MH has a greater bandwidth, then detuning the input frequency from this resonance to the resonance of the JH assembly would produce reliable displacement data for both tests. Therefore the best estimation of the input force to the JH is considered to be the regularised force that is estimated from the response of the MH assembly.

The current input forces are scaled so that Equation (5.16) is solved for $q_6^{JH}\left(\omega_2^{JH}\right)$. This requires the ideal output power of the amplifier, which is given in Table 5.3, and the mag-

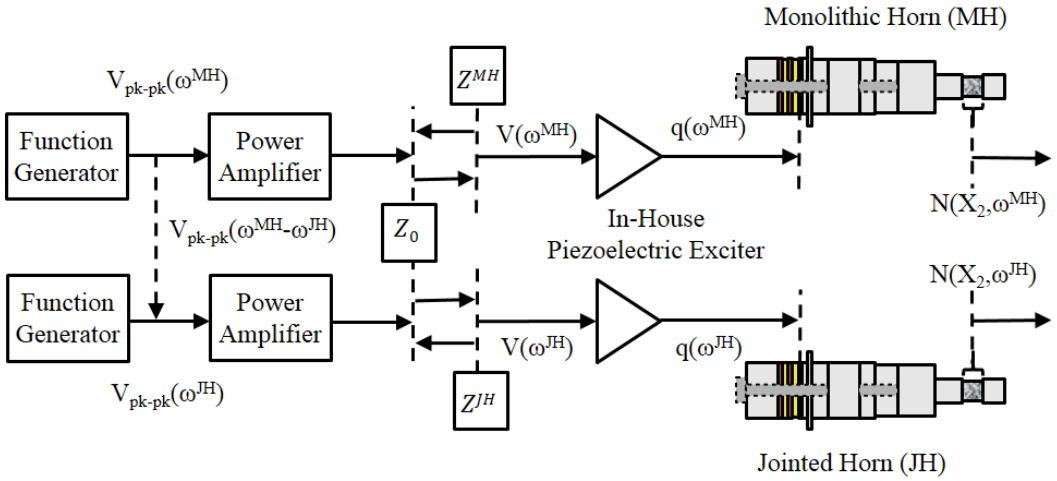

Fig. 5.109 Summary of the comparison between the Monolithic Horn and the Jointed Horn test assembly.

nitude of the minimum impedance at the operating mode for the MH and JH assemblies, which are given in Table 5.4. The scaled input forces are applied to deconvolve the joint force. The results are shown in Figures 5.110-5.113. It is expected that the amplitude estimate for the force is improved, but without a correction to the phase error of the input force to the JH assembly, the characteristics of the joint remain obscured by the linear calibration. The hysteresis loops shown in Figures 5.114-5.117 represent the least squares solution to the energy dissipation between the two HPU systems, but this also inherits the modelling errors of the linear calibration.

5.5.3 Discussion

It is clear that the input force that is developed in the piezoelectric stack of an HPU assembly that features a JH is not linear because it is functionally dependent on the behaviour of the joint. The linear calibration force that has been assumed has limited application to the force identification scheme because it relies on the monolithic HPU assembly. This cannot have the same operating frequency as a jointed HPU assembly and therefore it cannot be implemented to deconvolve the desired information from the experimental configuration. Increasing the complexity of the DTFM model, so that it can accurately describe linear piezoelectric material behaviour, is the best approach to developing the force identification scheme. This requires that the DTFM is extended to waveguides that are governed by coupled equations of motion. The linear calibration forces, that were deconvolved from

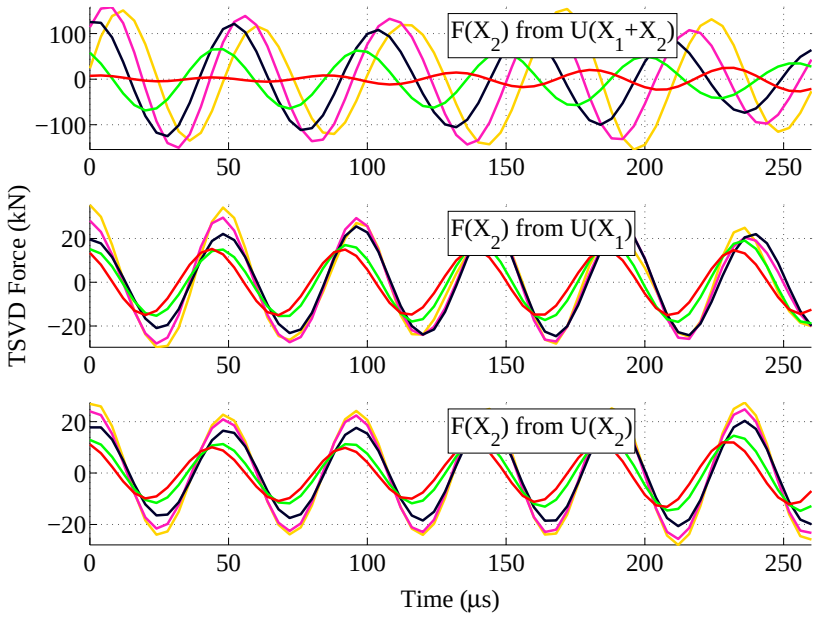

Fig. 5.110 Truncated Singular Value Decomposition regularised solution of the force at X_2 from the scaled linear calibration $q_6(X_2,\tau)$ for the In-House Piezoelectric Actuator with the Jointed Horn attached which features a Steel stud set to 8Nm.

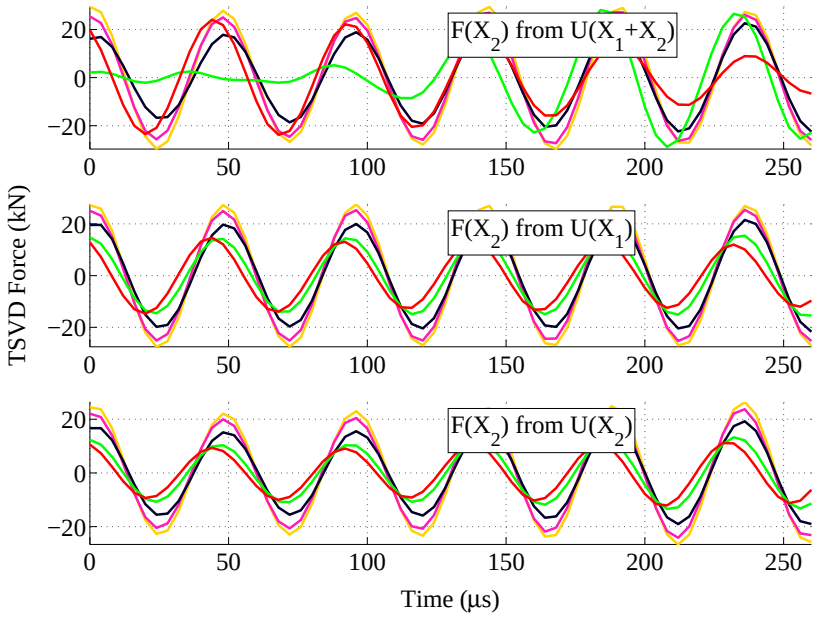

Fig. 5.111 Truncated Singular Value Decomposition regularised solution of the force at X_2 from the scaled linear calibration $q_6(X_2,\tau)$ for the In-House Piezoelectric Actuator with the Jointed Horn attached which features a Grade 5 Titanium stud set to 8Nm.

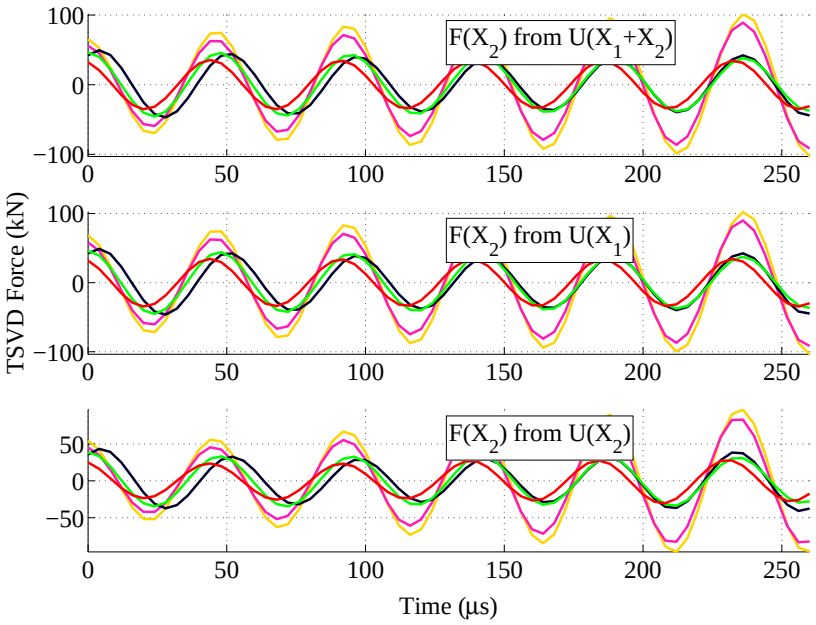

Fig. 5.112 Truncated Singular Value Decomposition regularised solution of the force at X_2 from the scaled linear calibration $q_6(X_2,\tau)$ for the In-House Piezoelectric Actuator with the Jointed Horn attached which features a Grade 5 Titanium stud set to 12Nm.

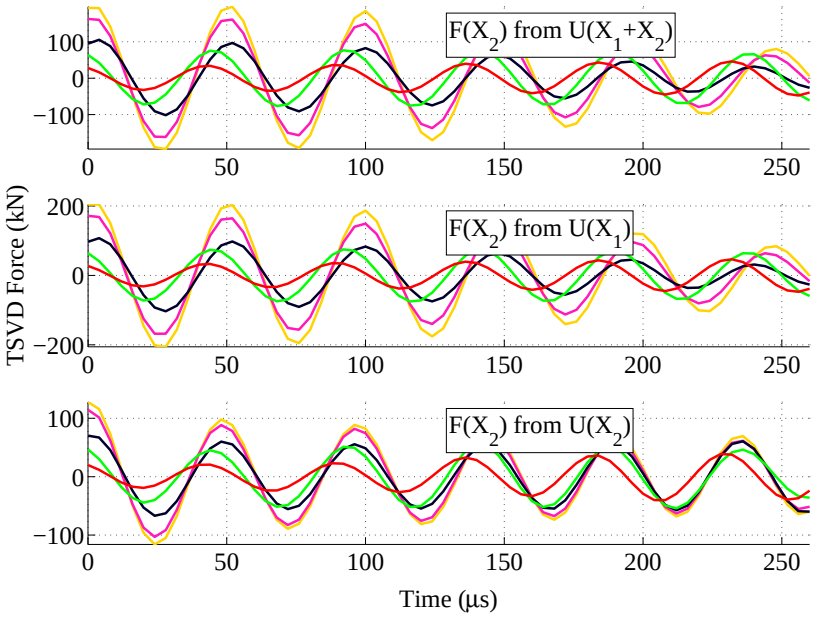

Fig. 5.113 Truncated Singular Value Decomposition regularised solution of the force at X_2 from the scaled linear calibration $q_6(X_2,\tau)$ for the In-House Piezoelectric Actuator with the Jointed Horn attached which features a Grade 5 Titanium stud set to 16Nm.

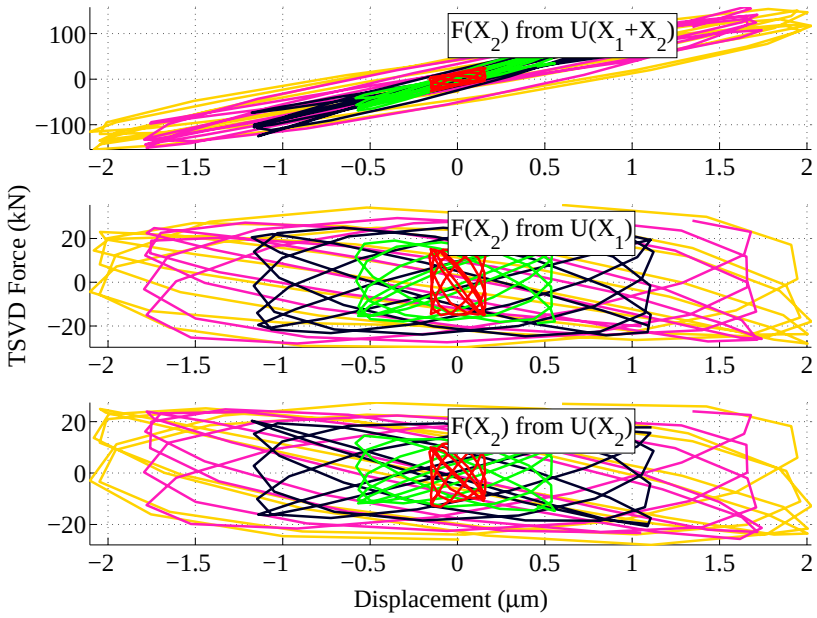

Fig. 5.114 Hysteresis loops at X_2 from the scaled linear calibration $q_6(X_2, \tau)$ for the In-House Piezoelectric Actuator with the Jointed Horn attached which features a Steel stud set to 8Nm.

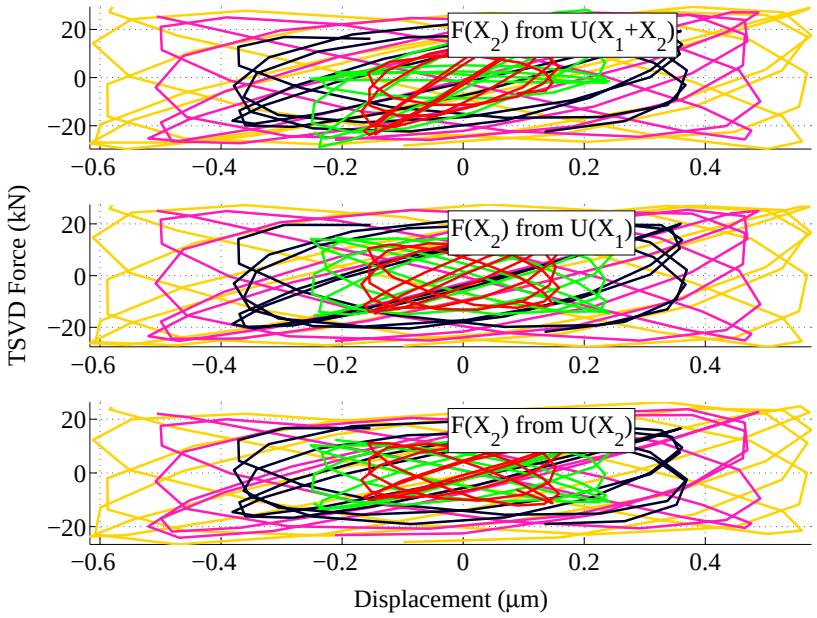

Fig. 5.115 Hysteresis loops at X_2 from the scaled linear calibration $q_6(X_2, \tau)$ for the In-House Piezoelectric Actuator with the Jointed Horn attached which features a Grade 5 Titanium stud set to 8Nm.

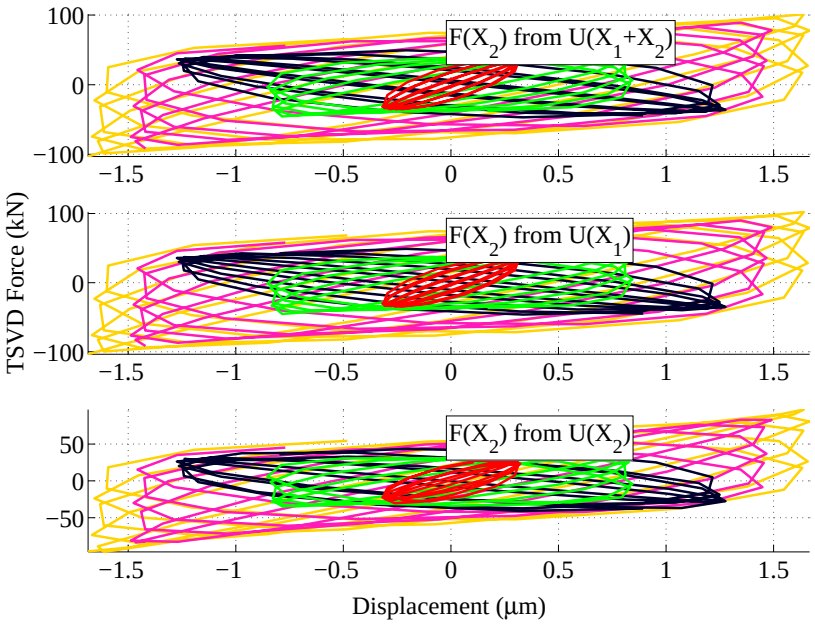

Fig. 5.116 Hysteresis loops at X_2 from the scaled linear calibration $q_6(X_2, \tau)$ for the In-House Piezoelectric Actuator with the Jointed Horn attached which features a Grade 5 Titanium stud set to 12Nm.

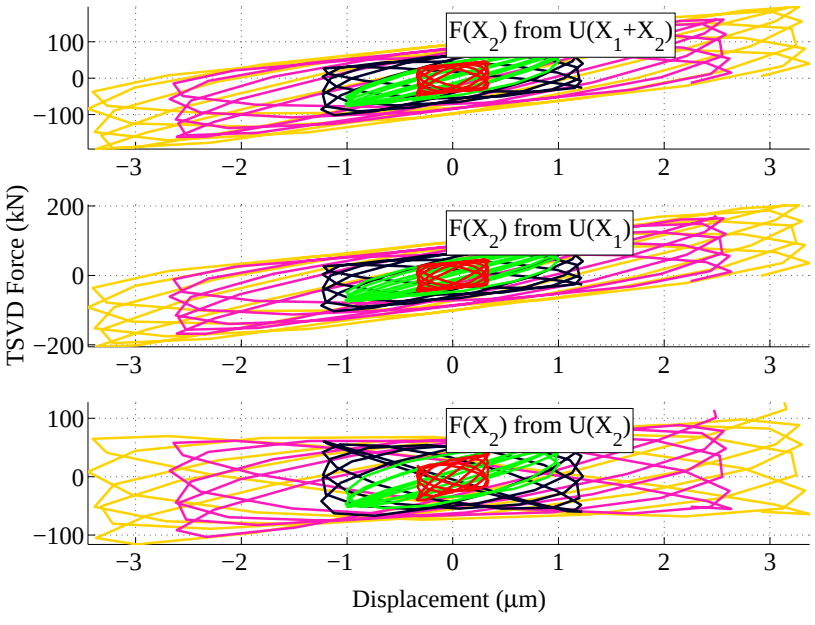

Fig. 5.117 Hysteresis loops at X_2 from the scaled linear calibration $q_6(X_2, \tau)$ for the In-House Piezoelectric Actuator with the Jointed Horn attached which features a Grade 5 Titanium stud set to 16Nm.

the tests of the monolithic assemblies, were assumed as the input force to the jointed assemblies. For the CPA, the regularised solutions were inconsistent whether the TSVD or Tikhonov regularisation method was applied. This is likely the result of the estimations that were required to define the linear model of the CPA from the limited information that was available. Despite the poor quality of the equivalent DIC results, it was clear that the frequency of the regularised solutions was reasonable. The phase errors were not significantly greater than the error between the DIC strain measurements of the monolithic and jointed assemblies. Any agreement between the forces estimated through DIC or the force identification scheme is likely a coincidence due to difference in amplitude between the DIC and the LDV measured displacements.

The regularised solutions that are found from the IHPA tests are mostly consistent. Although the geometry of the IHPA could be measured directly, there were still errors in the linear calibration model that were as significant as the equivalent errors in the CPA model. Despite this, the regularised solutions appear to be well behaved.When the solutions are found by assuming that the same input force has been applied to both the monolithic and jointed assemblies, they are dominated by the signals that would be obtained if the force was deconvolved from the response of the monolithic assembly only. The input force is scaled, using impedance data, and the joint force is deconvolved. This makes the consistency of the regularised solutions worse.

5.6 Outcomes

Numerical tests of the force identification scheme from Chapter 3 were presented in Chapter 4. However physical experiments are required to understand the repercussions of accepting the one mode waveguide theory and the discrepancies in updating the linear calibration models. Digital Image Correlation (DIC) is employed as another means to estimating the force occurring within a High Power Ultrasonic device (HPU). Each ultrasonic horn features a pair of symmetrical flats. Each flat is observed simultaneously through High Speed Imaging (HSI) and Laser Doppler Vibrometry (LDV). Unloaded tests of the HPU assemblies give a comparison of the noise floor that is expected. The DIC noise floor is limited by the resolution of the camera and the uniformity of illumination over the test area throughout the observation window. Increasing the length of the flat portions of the horns would increase the working distance of the camera lens. This will reduce the impact of out of plane

alignment or motion, which was not reconciled in the tests. Analysis of the pinhole camera model did not suggest that the errors would be significant. The DIC and Laser Doppler Vibrometer (LDV) derived displacements agreed well in phase and not amplitude. The amplitude error is reasonably consistent as the excitation to the HPU assembly is increased. It is difficult to identify the source of this error, but it is suggested that the projection errors must be significant. The use of a 3D DIC set-up would remove this error, as well as the need to have flat portions on the ultrasonic horns.

The observation of each Jointed Horn (JH) is severely limited by the impedance mismatch between the HPU assembly and the power amplifier. This can be minimised through impedance matching circuitry. Direct measurement of the high power signal that is applied to the piezoelectric stack would be beneficial for comparison between measurements and is required if the distributed parameter model is extended to include detailed piezoelectric behaviour. If the force estimation scheme was based on velocity, instead of displacement measurements, then this would reduce the error involved in post processing of the LDV observations. The LDV observations featured low and high harmonics that were half or double the operating frequency, of the HPU assembly, respectively. The amplitude of the high harmonics was more significant.

The input force to the HPU device was estimated at the foremost node, of the piezoelectric stack, through the linear calibration models. The force was deconvolved based on the displacement observations of one or multiple locations. Forward substitution tended to produce asymptotic behaviour in the window of reconstruction. The Truncated Singular Value Decomposition (TSVD) and Tikhonov regularisation methods produced signals close to the frequency that was expected. The CPA linear calibration produced regularised solutions that were significantly modulated and there was no consistency in the estimation of the amplitude. This could descend from the mismatch in the model due to limited information about its assembly. The hysteresis loops did not trace a closed path for the steady state vibration. The IHPA linear calibration produced regularised solutions that were consistent. The Tikhonov regularised solution that was based on two locations converged onto a minimum that was not a true solution. This indicates that modelling errors may still be too significant for a reliable estimation of force. The hysteresis loops dissipated no energy, however this is expected because there was no damping in the distributed parameter model. The estimation of force at the flat, in each of the linear calibration models, behaved very similarly to the estimation of the input force. However the CPA results did draw closed loops. The amplitude of the CPA results did not agree with the equivalent DIC results. However the IHPA results

were comparable.

The input signals that were obtained through the linear calibration schemes will feature errors in phase and amplitude due to the change in the impedance of the HPU device upon the introduction of an axial joint. The sharp response in the spectral characteristics of a jointed assembly means that it will have to be excited at a frequency that is lower than the operating frequency of its equivalent monolithic assembly. To test whether this error in the phase of the input force is acceptable it was assumed that the jointed assembly had been excited with the same signal as the monolithic assembly. This involves deconvolving the force from the linear calibration model and the difference in the displacement vectors of the monolithic and jointed assemblies. The noise in the DIC estimations of strain made it difficult to draw any conclusion of the validity of the joint force estimations. The frequency of the regularised solutions was reasonable. The CPA results were inconsistent and when all three locations were included, in the estimation, the result was unstable. The IHPA results were consistent, but they may have been dominated by the linear calibration signals. The input force was scaled using the impedance measurement data. The joint forces were deconvolved when this is applied to the linear calibration model and the response of the jointed assembly is applied. This does provide a qualitative change in the joint force estimations.

Chapter 6

The dynamic response of the Bouc-Wen model for hysteresis

6.1 Introduction

Phenomenological models are useful tools for the investigation of damping behaviour in systems that are complicated to model through their constitutive equations. A model of this nature will provide no insight into the physics of the system, however it can lead to an understanding of its dynamic behaviour if the limitations to the model are understood. This modelling strategy involves combining some physical understanding of the system with a black box approach to identifying the parameters of the model. Some authors call this "semi-physical" modelling [119]. In order to make use of a phenomenological model, it is vital to understand the characteristics that it is capable of simulating and the consistency of its behaviour with physical rules. Idealised patterns can be found in the damping mechanisms, that are shared by typical engineering systems, when they are exposed to different types of excitations and environments. Damping of a system might be related to, but is not limited to, the energy dissipation in a volume of macro-continuous media, the interaction of distinctly separate components or electro-mechanical and electro-magnetic processes.

A thorough discussion of the idealization of damping phenomena can be found in Lazan [120]. Here, inelastic behaviour is classified as rate dependent/independent and recoverable/nonrecoverable. Rate dependence refers to the reliance of the stress-strain relationship on the rate of loading or the rate of straining. The recoverability is the propensity of the

system to gain back the amount of strain that it has lost with time. The units that are used to define the damping properties of nonlinear systems depend on energy dissipation. Therefore the damping of different systems may be compared through the damping energy dissipation per cycle of stress, or the ratio of the damping energy to the strain energy. In general, a system is said to exhibit hysteresis when there is a characteristic looping behaviour found in the relationship between its input and output. If this relationship is rate independent then the loop will remain the same as the frequency of the input is varied. The energy dissipation is calculated by finding the area enclosed by the loading-unloading loop. However this area is not enough to fully understand the dynamic response of the system exhibiting the loop. The shape of the loop is also important.

The Bouc-Wen (BW) model has been used to simulate the hysteresis behaviour of components in various fields of engineering. This preliminary study considers the steady state response of the model, as it is subjected to harmonic excitation, and aims to develop the understanding necessary to fit it to the behaviour of a normally loaded joint in a High Power Ultrasonic (HPU) system. The formulation of the model is explored and the response is found using analytical and numerical techniques. The closed form expressions of the model are derived and these can be used to fit the model to a measured hysteresis loop. The expressions depend on the parameters that define the BW model. Interpreting the behaviour of these parameters is important in relating the model to a physical experiment because the parameters are not straightforwardly related to measurable physical quantities. A local sensitivity analysis, through a one-factor-at-a-time method, is completed to gain some qualitative and quantitative insight into the influence of each of the model parameters. The parameters that are specific to the BW formulation are: A, β, γ and n [121]. When the BW model is part of a Mass Spring Damper (MSD) system it is common to introduce a further parameter, α, which is used to tune the contribution of a hysteretic and nonhysteretic spring to the overall stiffness behaviour. It is found that the parameter A scales the limits of the hysteresis loop and influences the natural frequency of the system. The ratio of β to γ controls the stiffness behaviour of the loop, where increasing β reduces the amplitude of the response. Increasing parameter n causes the hysteresis loop to tend towards bilinear stiffness behaviour and changes in α are shown to cause large variability in the restoring force behaviour.

Bouc [122] proposed the hysteretic semi-physical model, which was later generalised by Wen [121], as a method to analyse the response of a system to random excitation. It represents the inelastic behaviour of a system through the notion of intrinsic time. Therefore it

is considered to belong to the class of endochronic models that were introduced by Valanis [123]. The functional shown in Figure 6.1a was supplied by Bouc to describe the hysteresis phenomenon and this example shows that four values of z are related to a single value of u. However u is a function of time, t, so the value of z at the instant t will not only depend on the value of the displacement u at t, but also on the past values of u.

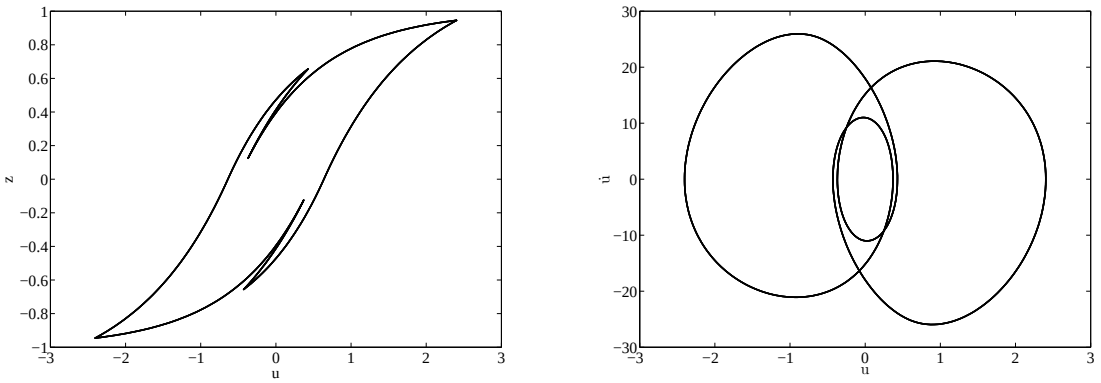

(a) Bouc's hysteresis functional

(b) Phase portrait

Fig. 6.1 Response of the Bouc-Wen model when it is incorporated into the equation of motion of a mass-spring-damper system that is excited harmonically.

Wen's generalisation of Bouc's initial model decomposes the restoring force of a nonlinear hysteretic system into two components:

$$Q(\dot{u},u) = g(\dot{u},u) + z(u) \tag{6.1}$$

where g is a generally nonlinear nonhysteretic component, that is a function of instantaneous displacement and velocity, and z is a hysteretic component that is a function of the time history of the displacement. The function $g(\dot{u},u)$ is a polynomial that can be used to express a large class of symmetric loading-unloading forces:

$$g(\dot{u},u) = h(\dot{u}) + f(u) \tag{6.2}$$

where:

$$h(\dot{u}) = a_0 \text{sign}(\dot{u}) + a_1\dot{u} + a_2|\dot{u}|\dot{u} + a_3\dot{u}^3 + \ldots \tag{6.3}$$

$$f(u) = b_0 \text{sign}(u) + b_1 u + b_2|u|u + b_3 u^3 + \ldots \tag{6.4}$$

The signum function is expressed as sign() and a and b are constants. The restoring force model also requires that u and z satisfy the following differential equation:

$$\begin{aligned} \dot{z} &= -\beta|\dot{u}|z^n - \gamma\dot{u}|z^n| + A\dot{u} && \text{for n odd} \\ \dot{z} &= -\beta|\dot{u}|z^{n-1}|z| - \gamma\dot{u}z^n + A\dot{u} && \text{for n even} \end{aligned} \tag{6.5}$$

where A, β, γ and n are constants that are used to tune the hysteresis loop. Bouc's original formulation of $\dot{z}$ has the variables β and γ named as α and β respectively. The initial stiffness of the hysteresis response is specified by A, the parameters β and γ determine the shape of the hysteresis loop and the smoothness of the loop is controlled by n.

The BW model has the potential versatility to describe the behaviour of screwed threaded joints through very few parameters. It can be applied to represent the yielding behaviour of the restoring force at an interface. If the behaviour of joints is considered to be analogous to the plasticity of materials, then yielding is associated with the frictional behaviour of the interface. An austere joint model is required to analyse structures that contain many joints and will provide a method to carry out an analysis of the structural damping behaviour subject to various excitations. Oldfield *et al.* [25] apply the BW model to represent a detailed Finite Element (FE) model of a bolted joint that is created using Abaqus FE software. The FE model is used to generate response data that is obtained from a joint when it is subjected to a dynamically applied torque. The model is then tuned using four parameters to approximate the FE hysteresis response. It is found that the BW model is particularly efficient in representing the smooth transition from a small amount of microslip in the joint to the point at which macroslip occurs. Oldfield *et al.* [25] finds that the BW model fits the FE hysteresis data at the velocity reversal points and gives a similar estimation of the energy dissipation due to the joint. However it does not have the required flexibility to match the stiffness behaviour of the loading-unloading curve.

The bolt in the study by Oldfield *et al.* [25] is accommodated by a clearance hole and does not feature detailed modelling of the screw threads. This is appropriate for a joint that is subjected to a dynamic torque. In-depth consideration of the slip behaviour at the bearing surface is most relevant. This is related to the distribution of preload through the joint, which is expected to be conical, originating at the bolt head or nut and meeting at the interface. This joint admits the installation of force transducers between the bolt head or nut and the prestressed components. Therefore it is possible to relate applied torque to preload at these locations. In the case of the HPU device, the distribution of the prestress through

the axial joint depends on the contacts at the threaded surfaces. Therefore an appropriate FE model should feature detailed modelling of the threads. This level of detail will considerably increase the complexity of computing the dynamic response of the device. These difficulties are considered out with the scope of the current study, but could be attempted as future work.

The BW model has been adapted in a variety of ways to suit the needs of many areas in engineering. A modification that has been widely used in the modelling of structural elements is the Bouc-Wen-Baber-Noori model [124]. This provides the facility to simulate a greater variety of hysteresis loops through 13 shape parameters. The additional parameters are used to describe pinching in the loop as well as strength and stiffness degradation. This model was modified by Foliente [125] to develop models of wood joints with yielding plates, yielding nails and yielding bolts. Wee *et al.* [126] investigate an alternative formulation of the BW model to describe the rubber to metal interface of the guide roller system found in elevators. In order to represent the nonlinear rate-dependent stick-slip phenomena, found in their experiments, they incorporate m^{th} power velocity damping into the model. This provides better performance in characterising the complicated behaviour observed in experiments than the original BW model. Other modified versions of the BW model exist in relation to studies of wire cable vibration isolators [127], magnetorheological dampers, [128], and Teflon bearings in base isolation [129].

The overall aim of this work is to identify a BW model that follows the behaviour of a screwed threaded joint in an HPU system. As a precursor to defining this model it is essential to appreciate the influence that each parameter has on its dynamic response. Developing this sensitivity analysis will indicate the limitations of the original formulation of the model with respect to the obtained experimental data. This preliminary analysis involves developing a qualitative understanding of the range of hysteresis loops that can be simulated and attempts to derive constraints that can be made on the values of identified parameters. An attempt at drawing further conclusions is made by quantifying the influence of each parameter on the response by evaluating the root-mean-square-error.

6.2 Formulation of the model

Assume that a single degree of freedom system has the nonlinear equation of motion:

$$m\ddot{u} + f(u, \dot{u}, t) = F \tag{6.6}$$

where m is the inertial mass of the system, u is displacement, t is time, F is applied external load and f is a function made up of nonlinear stiffness and damping terms. The dot accents represent differentiation with respect to time. A hysteresis loop can be obtained by plotting f against u. This will characterise the energy dissipation in this system by supplying information about the rate of energy dissipation, the amount of energy loss, the stiffness of the joint and the range of displacements that will be produced by an applied load.

A nonlinear bolt model can be formed through the BW model. The equation of motion stated in Equation (6.6) can be recast for displacement $u(t)$ and has an expression $f(u, \dot{u}, t)$ that consists of a linear viscous damper as well as a nonhysteretic and a hysteretic spring [130]. The springs and linear damper are connected in parallel and this gives the equation of motion:

$$m\ddot{u}(t) + c\dot{u}(t) + \alpha k_i u(t) + (1-\alpha)k_i z(t) = F(t) \tag{6.7}$$

where k_i is the stiffness coefficient and $0 \leq \alpha \leq 1$ is a weighting parameter that determines the percentage of the restoring force that descends from each spring [131]. The post yield stiffness is defined as $k_f = \alpha k_i$.

The hysteretic component in Equation (6.5) can be restated in the following concise form:

$$\begin{aligned} \dot{z} &= \left[A - z^n\left(\beta sign(\dot{u}) + \gamma sign(z)\right)\right]\dot{u} && \text{for n odd} \\ \dot{z} &= \left[A - z^n\left(\beta sign(\dot{u}\cdot z) + \gamma\right)\right]\dot{u} && \text{for n even} \end{aligned} \tag{6.8}$$

6.3 Response of the model

6.3.1 Closed form expressions

A hysteresis loop can be formed by finding the closed form solutions to Equation (6.8), over branches that are separated by velocity reversal points, and locations where the loop intersects an axis. These branches descend from the discontinuous sign functions, which depend on the value of n that is selected to represent the smoothness of the loop, as well as the values of $\dot{u}$ and z. An example loop is shown in Figure 6.2. Closed form expressions can be formed by rewriting Equation (6.8) as:

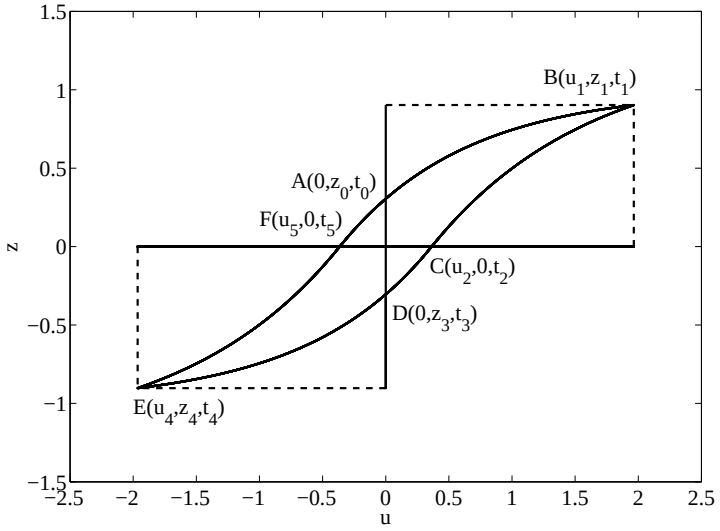

Fig. 6.2 The Bouc-Wen functional separated into branches that can be described through closed form expressions.

$$\frac{dz}{du} = A \pm (\beta \pm \gamma) z^n \tag{6.9}$$

Table 6.1 shows the form of Equation (6.9), for each branch of the hysteresis loop, when n is even. Before any energy has been dissipated in this system the hysteretic displacement z is zero. In relation to the joint this can be thought of as the point before any microslip has taken place. Therefore Equation (6.8) is expressed as:

$$\dot{z} = A\dot{u} \tag{6.10}$$

Table 6.1 Sign changes for the shape parameters in branches of the hysteresis loop

Branch	$sgn(\dot{u})$	$sgn(u)$	u domain	$sgn(z)$	z domain	$\frac{dz}{du}$ for n even
AB	+	+	$u \in [0, u_1]$	+	$z \in [z_0, z_1]$	$A-(\beta+\gamma)z^n$
BC	-	+	$u \in [u_1, u_2]$	+	$z \in [z_1, 0]$	$A+(\beta-\gamma)z^n$
CD	-	+	$u \in [u_2, 0]$	-	$z \in [0, z_3]$	$A-(\beta+\gamma)z^n$
DE	-	-	$u \in [0, u_4]$	-	$z \in [z_3, z_4]$	$A-(\beta+\gamma)z^n$
EF	+	-	$u \in [u_4, u_5]$	-	$z \in [z_4, 0]$	$A+(\beta-\gamma)z^n$
FA	+	-	$u \in [u_5, 0]$	+	$z \in [0, z_0]$	$A-(\beta+\gamma)z^n$

This implies that the parameter A can be thought of as the contact stiffness of the interface before any microslip has occurred. When the gradient of the hysteresis loop reaches zero, Equation (6.9) becomes:

$$\frac{dz}{du} = A \pm (\beta \pm \gamma) z_y^n = 0 \tag{6.11}$$

Therefore z_y is considered to be the load required for the joint to yield because at this point the gradient of the loop is zero, so the joint response exhibits perfect plastic behaviour. Equation (6.11) can be rearranged for each branch of the loop, that is represented in Table 6.1, to determine the sign of the shape parameters. The obtained expressions can then be integrated over their displacement domain for arbitrary values of the shape parameters.

6.3.2 State space representation

Fitting the hysteresis functional directly to experimental data through, Equation (6.9), does not allow the BW model to describe the observed system over the passage time. Instead an alternative representation of the system can be found by adopting the functional to describe the hysteretic component of a spring in a single degree of freedom oscillator. Equations (6.7) and (6.8) are transformed into state space form as follows:

$$\begin{Bmatrix} x_1(t) = u(t) \\ x_2(t) = \dot{u}(t) \\ x_3(t) = z(t) \end{Bmatrix} \tag{6.12}$$

$$\begin{Bmatrix} \dot{x}_1(t) \\ \dot{x}_2(t) \\ \dot{x}_3(t) \end{Bmatrix} = \begin{Bmatrix} x_2(t) \\ -\frac{1}{m}\left[c x_2(t) + \alpha k_i x_1(t) + (1-\alpha) k x_3(t) - F(t)\right] \\ (A - |x_3(t)|^n [\beta sign(x_2(t) \cdot x_3(t)) + \gamma)]) x_2(t) \end{Bmatrix} \tag{6.13}$$

The state space representation gives a nonlinear system of ODEs that can be solved numerically. This is carried out using the `ode5()` (Dormand-Prince) solver in MATLAB, which is used to solve initial value problems for ODEs. This is a fixed step solver so the step size has to be set to allow the integration of the model to complete. At $t = 0$: $x_1 = x_2 = x_3 = 0$. The Simulink model used to carry out the integration is displayed in Figure 6.3. This is used to compute the continuous states at the current time step from the states at the previous time steps and the state derivatives.

There are two possible solution vectors to the system:

$$\begin{Bmatrix} y_1(t) = u(t) \\ y_2(t) = \dot{u}(t) \\ y_3(t) = z(t) \end{Bmatrix} \tag{6.14}$$

or:

$$\begin{Bmatrix} y_1(t) = u(t) \\ y_2(t) = \dot{u}(t) \\ y_3(t) = f(u(t), \dot{u}(t), z(t)) \end{Bmatrix} \tag{6.15}$$

where:

$$f(u, \dot{u}, z) = c\dot{u}(t) + \alpha k_i u(t) + (1 - \alpha) k_i z(t) \tag{6.16}$$

The relevance of distinguishing between these two options is that $f(u, \dot{u}, z)$ is a measurable force whereas the hysteretic displacement, $z(t)$, is a variable that is intrinsic to the model, but is not measurable. The study by Oldfield *et al.* [25] involves fitting the behaviour of the hysteretic displacement to the restoring torque that is measured from a cyclically loaded joint. This meant that only four parameters were identified when the model was fitted to the experimental data. The solution vector expressed in Equation (6.15) requires additional model parameters to be identified. However this adds flexibility to the model and provides a foundation for testing the modifications to it that may allow it to mimic the stiffness behaviour of the joint more accurately.

6.3.3 Analytical solutions

The parameters to the BW model can be determined by developing closed analytical relationships to the branches of the loop that is shown in Figure 6.2. A procedure to finding these is given by Sireteanu *et al.* [132]. This is summarised here for the purpose of fitting

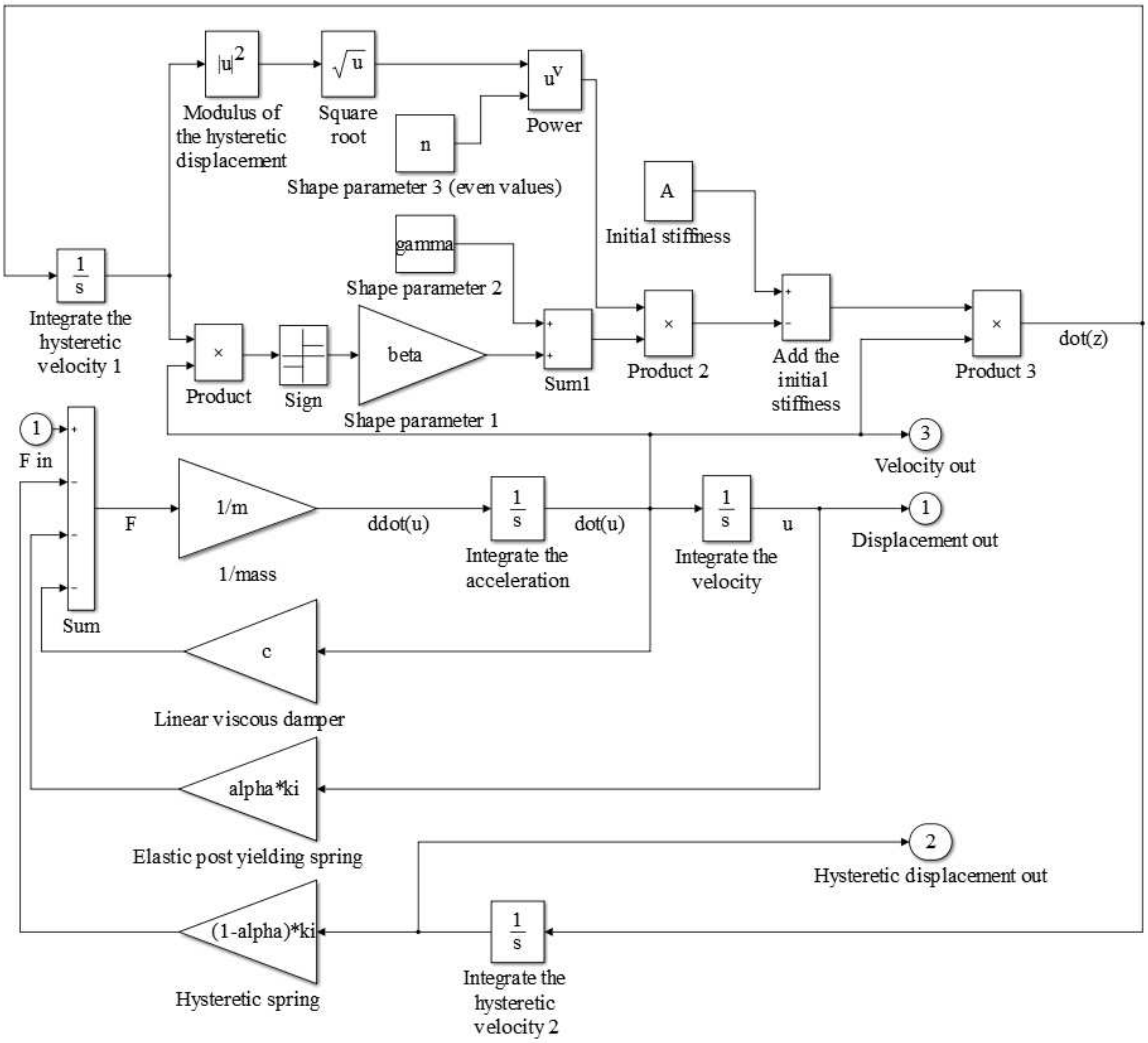

Fig. 6.3 Simulink model used to carry out the integration

the BW model to the hysteresis loops that are obtained through the DIC analysis. If it is assumed that the observed loop is symmetrical, then it is fully described by the branch ABCD, which has rotational symmetry with branch DEFA. The BW model that forms this loop is described by Equation (6.8). The parameters are determined for its steady state vibrations under harmonic loading. This represents a loop with a constant limit cycle, whilst the system is in equilibrium. The following loop axis crossing points must be recorded in order to identify the loop parameters:

$$A(0,z_0),\ C(u_2,0),\ D(0,z_3) \tag{6.17}$$

It is also necessary to know the velocity reversal point in the loop:

$$B(u_1, z_1) \tag{6.18}$$

Analytical solutions to Equation (6.8) can be found for $n = 1$ or $n = 2$. Numerical solutions can be found for arbitrary values of n, but for any parameter fitting method the function must be predefined. The form of Equation (6.8), for each branch, can be determined from Table 6.1. To simplify this analysis the following temporary substitutions are made:

$$\sigma = \beta + \gamma, \delta = \beta - \gamma \tag{6.19}$$

The expressions for $\frac{dz}{du}$ in Table 6.1 are integrated, for $n = 2$, to obtain the following closed form solutions:

1. AB: $\dot{x} > 0, \quad z > 0$

$$\frac{z_1 - z_0}{A} = u_1 \qquad (\sigma = 0) \tag{6.20}$$

$$\frac{\sqrt{\frac{\sigma}{A}}(z_1 - z_0)}{1 - \frac{\sigma}{A} z_1 z_0} = tanh\Big(\sqrt{A\sigma} u_1\Big) \qquad \left(\sigma > 0 \implies z_1 < \sqrt{\frac{A}{\sigma}}\right) \tag{6.21}$$

$$\frac{\sqrt{\frac{|\sigma|}{A}}(z_1 - z_0)}{1 + \frac{|\sigma|}{A} z_1 z_0} = tan\Big(\sqrt{A|\sigma|} u_1\Big) \qquad (\sigma < 0) \tag{6.22}$$

2. BC: $\dot{x} < 0, \quad z > 0$

$$\frac{z_1}{A} = u_1 - u_2 \qquad (\delta = 0) \tag{6.23}$$

$$\sqrt{\frac{\delta}{A}} z_1 = tan\Big(\sqrt{A\delta}(u_1 - u_2)\Big) \qquad (\delta > 0) \tag{6.24}$$

$$\sqrt{\frac{\delta}{A}} z_1 = tanh\Big(\sqrt{A\delta}(u_1 - u_2)\Big) \qquad \left(\delta < 0 \implies z_1 < \sqrt{\frac{A}{|\delta|}}\right) \tag{6.25}$$

3. CD: $\dot{x} < 0, \quad z < 0$

$$\frac{z_3}{A} = -u_2 \qquad (\sigma = 0) \tag{6.26}$$

$$\sqrt{\frac{\sigma}{A}} z_3 = tanh\left(-\sqrt{A\sigma} u_2\right) \qquad \left(\sigma > 0 \implies |z_3| < \sqrt{\frac{A}{\sigma}}\right) \tag{6.27}$$

$$\sqrt{\frac{|\sigma|}{A}} z_3 = tan\left(-\sqrt{A|\sigma|} u_2\right) \qquad (\sigma < 0) \tag{6.28}$$

The parameter identification is carried out through the following steps:

(I) Check for $\sigma = 0$:

(i) Combine Equations (6.20) and (6.26) to yield the following expression:

$$\frac{z_1 - z_0}{u_1} + \frac{z_3}{u_2} = 0 \tag{6.29}$$

(ii) If this is true then either of the Equations (6.20) or (6.26) can be rearranged to find A. It also implies that $\beta = -\gamma$, so $\delta \neq 0$.

(iii) Assume that $\delta > 0$ and substitute A into Equation (6.24). Therefore solve the following transcendental equation in δ through a Newton iterative scheme:

$$z_1 \sqrt{\frac{1}{A}\delta} - tan\left((u_1 - u_2)\sqrt{A\delta}\right) = 0 \tag{6.30}$$

(iv) If no solution is found then apply the same initial guess to the transcendental equation for $\delta < 0$ from Equation (6.25):

$$z_1 \sqrt{\frac{1}{A}\delta} - tanh\left((u_1 - u_2)\sqrt{A\delta}\right) = 0 \tag{6.31}$$

(v) If no solution is found then restart the analysis with a new initial guess for δ. Otherwise solve Equation (6.19) for γ and subsequently find $\beta = -\gamma$.

(II) Assume that $\sigma > 0$:

(i) To find σ most reliably all of the information that is available must be applied. Therefore a transcendental equation is formed by combining Equations

(6.21) and (6.27). These represent branch AB and CD respectively. Following Sireteanu *et al.* [132] the square root terms are removed through the substitution of:

$$\theta = \sqrt{A|\sigma|} \tag{6.32}$$

$$\phi = \sqrt{\frac{|\sigma|}{A}} \tag{6.33}$$

(ii) Equations (6.21) and (6.27) are combined to eliminate ϕ and the remaining transcendental equation is solved for θ:

$$[z_1 - z_0]tanh(-\theta u_2) - \left[z_3 - \frac{z_1 z_0}{z_3} tanh^2(-\theta u_2)\right] tanh(\theta u_1) = 0 \tag{6.34}$$

(iii) Substitute the obtained θ into Equation (6.27) to find ϕ:

$$\phi = \frac{1}{z_3} tanh(-\theta u_2) \tag{6.35}$$

(III) If no solution has been obtained assume that $\sigma < 0$:

(i) A transcendental equation is formed by combining Equations (6.22) and (6.28) to eliminate ϕ:

$$[z_1 - z_0]tan(-\theta u_2) - \left[z_3 + \frac{z_1 z_0}{z_3} tan^2(-\theta u_2)\right] tan(\theta u_1) = 0 \tag{6.36}$$

(ii) Substitute the obtained θ into Equation (6.28) to find ϕ:

$$\phi = \frac{1}{z_3} tan(-\theta u_2) \tag{6.37}$$

(IV) If no solution to σ is obtained then a new initial guess must be chosen for the Newton iterative scheme. Otherwise Equations (6.32) and (6.33) can be solved simultaneously to yield σ and A.

(V) Parameter A can then be substituted into Equation (6.30) and the transcendental equation is solved to find δ. If no solution is found then the same process is repeated for the expression in Equation (6.31). Failure of this requires that a new initial guess is

chosen for the Newton iterative scheme.

(VI) Finally with σ, δ and A determined β and γ can be found from Equation (6.19).

(VII) The obtained parameters are applied to compare the analytical solution to the observed data. Each branch is integrated in the positive displacement direction for the identified model. A significant error between the solution and the data prompts new initial guesses to be asserted at each of the stages where a transcendental equation must be solved by the Newton iterative scheme. If the solution draws smooth curves between the specified coordinates at points A-D then it is likely that an optimal solution has been identified. The sensitivity analysis that follows will demonstrate the range of flexibility of the Bouc functional to follow loading- unloading data. Additional terms must be added to the functional to allow it to follow paths that are associated with pinching, strength and stiffness degradation and asymmetry in an experimentally obtained hysteresis loop.

The algorithm I-VII is written as a concise set of MATLAB functions that are given in Appendix A. The parameters are determined based on searches for the roots of the transcendental functions. The MATLAB root searching function `fzero()` is applied for this purpose and requires an initial guess for two very differently scaled parameters: δ and θ when $n = 2$. If a solution cannot be found under these conditions then the algorithm is executed with $n = 1$. In this case the scale of the guesses is not so different because they are made for the parameters: δ and σ. It is observed that when $n = 2$, branches BC and EF will tend to converge on either a horizontal or vertical asymptote. This is the nature of the solution that is posed with the `tanh()` function. The initial guess must be very close to obtain a fit to this branch if a solutions exists. Comparatively the $n = 1$ solution for these branches will converge over a much larger variation of the initial guess to the transcendental equation.

The loops that are obtained through the DIC analysis, in Section 5.4.1, are recorded when the HPU assembly is operating at steady state equilibrium. Each of the loops from testing the Jointed Horns (JH), in Figures 5.32-5.35, are generated serially so that each cycle can be observed. These figures clearly show that each of the loops did not follow a closed path of the form in Figure 6.2. It is likely that this is due to limitations in the measurement set up and the DIC computation. It may also be attributed to the behaviour of the HPU assembly. Its power supply is actively matching to the impedance of the device and this will change the power that is delivered. Approximately 5 cycles should be captured, but it is not

possible to average these to get an estimate of the loop because this would not capture the nature of the obtained loops appropriately. Therefore each of the 5 loops has been tested with the BW analytical fitting algorithm to determine whether any of the loops adhere to the physical observations that were used to define the BW model. The parameters u_{1-5} and z_{0-4} are obtained for one observed cycle of displacement and strain behaviour. Due to the smoothing of the strain signals, the loop behaviour at the beginning and end of the time window follows outlier points that should not be included. Table 6.2 gives the samples out of the DIC observation window that have been employed to draw the hysteresis loops in Figures 6.4-6.7. There is no guarantee that the loop will not drift from the origin because of the level of noise in the observed strain signals, as well as the apparent modulation of both the observed displacement and strains. This is most evident in the loop from the test of the JH, that is tightened to 12Nm, for 3μm of nominal output. A very clear closed loop was found offset from the origin. In this case the loop has been centred on the point that gives the average between the displacement and the force at both of the velocity reversal points.

When it is assumed that $n = 2$ there are two solutions for A, β and γ, which are given in Table 6.2. These are produced for the branches ABCD and DEFA, which are half loops separated by the vertical axis. The plot in Figure 6.4 can be produced by integrating the model for each half loop. Both halves of the loop obtain a reasonable fit for branches AB, CD, DE and FA. However branches BC and EF tend to converge on an asymptotic solution, which can only be integrated with limited success. There is also a continuity error between the two solutions, where branch AB meets branch FA, at the vertical axis. This occurs because the integration of each branch is carried out in the direction of positive displacement. The integrated solution to each branch will always begin at its smallest displacement value and, if the identified solution is not a good fit to the data, then this will be manifested in the integrated solution to the force that is associated with the greatest displacement value for the branch.

If it is assumed that $n = 1$, then there is a greater error between the analytical solution and the data for branches AB and DE, as shown in Figure 6.5. The parameter values are given in Table 6.2. The analytical solution to Branch CD is fitted to the data with negligible difference. The solutions to branches BC and DE do not fit to the velocity reversal points of the data. When the $n = 1$ solution is applied to branch FA it appears to have greater error with the data than the equivalent $n = 2$ solution. However the discontinuity error between the two halves of the loop, which are separated by the vertical axis, has not occurred between

branches FA and AB. Instead this error is between branches CD and DE. The area of the loop that is enclosed by the intersections of the branches AB, BC and CD is closer to the area enclosed by the data than the $n = 2$ solution. The same results can be said for the solution to the left hand side of the vertical axis. Branch CD is a worse fit because the loop appears to be pinched close to the origin. Pinching of a hysteresis loop is associated with the loss of stiffness at some point between the velocity reversal points of the loop. Out of the modifications that have been made to the BW model, to fit experimental observations, pinching requires the most additional parameters to simulate. Foliente [125] modulated the Bouc functional with a pinching function to describe the loss of stiffness in wooden structures assembled by joints as cyclic loading is applied. A detailed sensitivity analysis of a such a system is also given by Ma *et al.* [131]. In the case of the hysteresis behaviour observed from the JH@12Nm horn, there is too much noise in the strain estimation to be sure that pinching behaviour is a characteristic of this system.

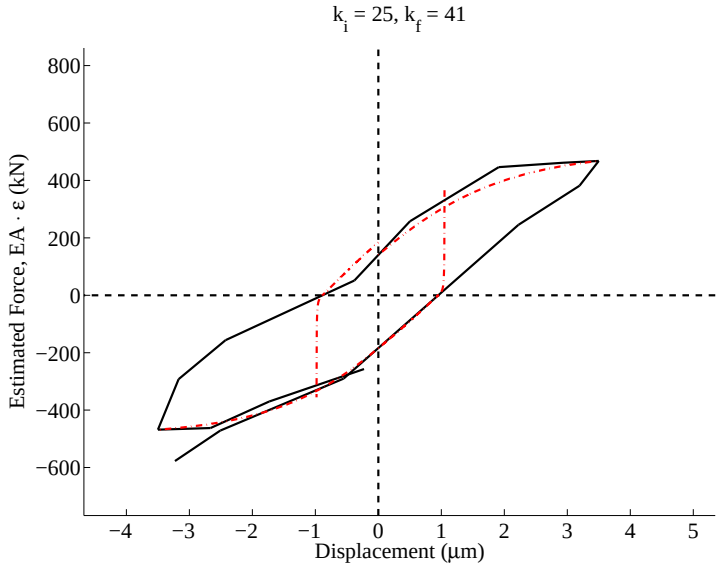

Fig. 6.4 Analytical solution of the Bouc-Wen model for $n = 2$ (- -) to fit experimentally obtained hysteresis loops for the Commercial Piezoelectric actuator, with the Jointed Horn set to 12Nm attached, and excited at 3μm (–). Experimental data is limited to samples k_i to k_f out of the window of observation.

Many of the attempts to fit the BW model to the DIC data have not been shown because they resulted in loops similar to those shown in Figures 6.4 and 6.5. Often it is possible to find a reasonable solution for one half of the loop whilst the other half results in asymptotic solutions. Figure 6.6 shows the data from testing JH@12Nm set to 1μm nominal excitation. A closed loop could not be obtained, but all of the required parameters were identified. In

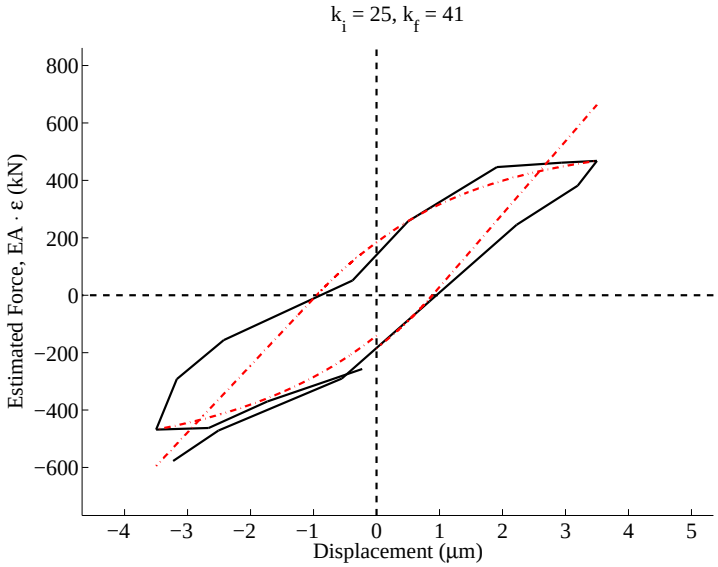

Fig. 6.5 Analytical solution of the Bouc-Wen model for $n = 1$ (- -) to fit experimentally obtained hysteresis loops for the Commercial Piezoelectric actuator, with the Jointed Horn set to 12Nm attached, and excited at 3μm (–). Experimental data is limited to samples k_i to k_f out of the window of observation.

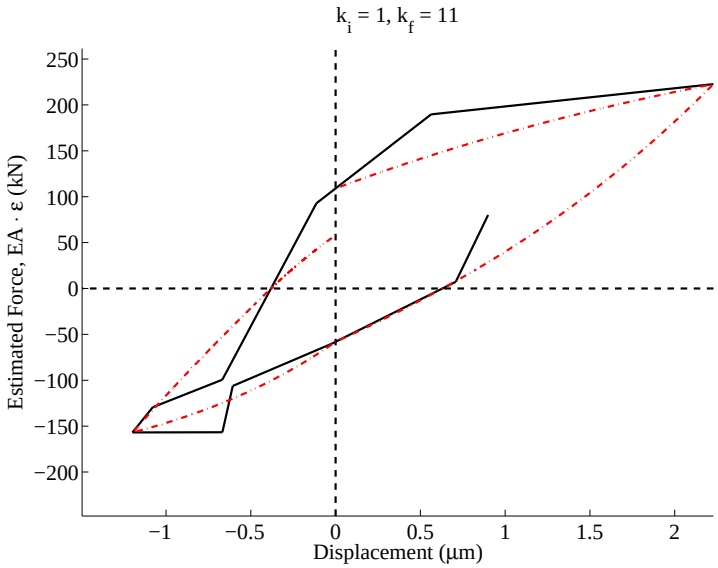

Fig. 6.6 Analytical solution of the Bouc-Wen model for $n = 1$ (- -) to fit experimentally obtained hysteresis loops for the Commercial Piezoelectric actuator, with the Jointed Horn set to 12Nm attached, and excited at 1μm (–). Experimental data is limited to samples k_i to k_f out of the window of observation.

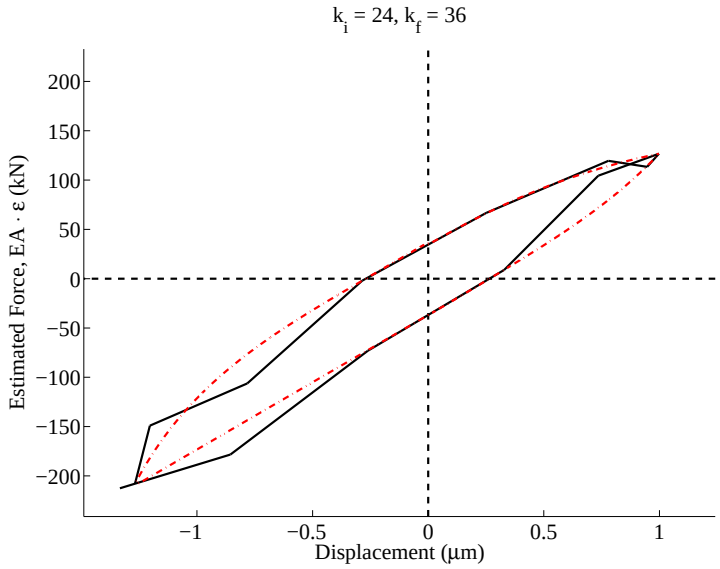

Fig. 6.7 Analytical solution of the Bouc-Wen model for $n = 2$ (- -) to fit experimentally obtained hysteresis loops for the Commercial Piezoelectric actuator, with the Jointed Horn set to 16Nm attached, and excited at 1µm (–). Experimental data is limited to samples k_i to k_f out of the window of observation.

Table 6.2 Parameters identified for selected Digital Images Correlation results from observing the response of assemblies made with the Commercial Piezoelectric Actuator

Torque	Excitation	Samples		u > 0				u < 0			
(Nm)	(µm)	k_i	k_f	n	A	β	γ	n	A	β	γ
12	3	25	41	2	202.7	0.586	-0.585	2	218.0	0.604	-0.603
12	3	25	41	1	254.0	0.237	0.237	1	233.2	0.204	0.204
12	1	1	11	1	100.8	0.338	-0.049	1	177.4	0.507	0.315
16	1	24	36	2	141.6	0.006	-0.001	2	136.4	0.004	-0.004

this case a solution is obtained for both halves of the loop when $n = 1$ and the parameters are given in Table 6.2. There is a clear continuity error between the solution where branches AB and FA meet. This will not be a problem when the model is applied to describe real time hysteresis behaviour because only one solution to the model will be implemented for both sides of the loop, which are separated by the vertical axis. To describe asymmetric loop behaviour, the functional can be modified following Wang & Wen [133].

The clearest limitation of applying the model so far is that the loops appear to have a force gradient, which is higher than the model is tracking, based on the selected velocity reversal point. However, these loops have been derived by assuming a constant linear modulus for the material throughout the duration of the measurement time window. It is reasonable to assume that the obtained data will exhibit a higher force gradient; especially close the velocity reversal point. If it is assumed that the data is the best estimate that is possible, then the BW model should be modified to follow the obtained loading-unloading pattern. Under these circumstances the stiffness degradation behaviour of the Bouc-Wen-Baber-Noori model [124] might produce a loop that is closer. This requires the Bouc functional to be scaled by another function that depends on one additional loop parameter. If this does not produce the desired effect then another option is to adopt the power velocity damping model from Wee *et al.* [126]. This has been applied to describe the rubber to metal interface found in the guide roller system of an elevator system. This significantly modifies the Bouc functional, but only requires two additional parameters to choose the power of the damping element and a delta function that is estimated by a Gaussian distribution. This also means that the model will now have rate dependent behaviour.

The closest match between the BW model and the DIC results is obtained for JH@16Nm for 1μm nominal excitation. It is assumed that $n = 2$ and the fit is shown in Figure 6.7 and the parameters are given in Table 6.2. The clearest limitation here is that it seems physically unrealistic if the branches DEFA do not have rotational symmetry with the branches ABCD. Instead the axis of symmetry is at 45° to the left of the vertical axis. Therefore the continuity between both halves of the loop is not consistent. The functional in Figure 6.2 was drawn by integrating the BW model. It is clear that a loop of this shape would describe the current experimental data well if it was matched so that its velocity reversal points and axis crossing points were closer to those of the data. However a solution of this type was not identified through the inverse parameter identification method. Therefore, in the following chapter, the velocity observed from each experimental test of a JH, attached to the IHPA, will be minimised with the velocity of the state space representation of the BW model through a

numerical optimisation.

6.4 Sensitivity Analysis

A parameter sensitivity analysis of the BW model will indicate how much influence each variable has on its dynamic response. It may also be applied creatively to indicate the usefulness of modifications to the model when fitting it to experimental data. It is important to observe any conditions that lead to non-physical behaviour in order to validate the model. In the following analysis the degree that a change in a parameter affects the output of the model is assessed qualitatively and quantitatively through two independent analyses. Both analyses take the form of a simple one-factor-at-a-time method, where one parameter is varied whilst the others are fixed at nominal values. The nominal values are chosen arbitrarily in order to show the versatility of the model and are not related to the physical system that is to be modelled. This method will only address the sensitivity of the model to these chosen base values and not over the entire parameter space.

6.4.1 Base values

The base values to the one-factor-at-a-time sensitivity analysis have been chosen by adhering to the constraints that have been defined by the other authors. These are discussed further in Section 7.3.1. This indicates that the simulated responses are physically consistent. However the remainder of the decision making is made arbitrarily, such that the results will graphically display the versatility of the model. To achieve this, the qualitative analysis will demonstrate this versatility graphically, for a large change in the base values, whereas the quantitative analysis will involve varying each parameter ±50%. The chosen base values are given in Table 6.3.

The two values of k_i refer to the qualitative analysis and the quantitative analysis where it was 632Nm^{-1} and 1776.5Nm^{-1} respectively. This base value was changed in order to display a better picture of the behaviour of the model in the frequency domain in the second analysis. The model was excited through a frequency range of $1 - 5$Hz and the natural frequency of

Table 6.3 Base values of parameters for sensitivity analysis

Parameter	Value	Units	Description
m	1	kg	Inertia of the system
c	0.1	$\mathrm{Nsm^{-1}}$	Linear viscous damping coefficient
k_i	632 or 1776.5	$\mathrm{Nm^{-1}}$	Stiffness of the linear elastic spring
α	0.2	–	Ratio of post yield stiffness to pre-yield stiffness
A	1	$\mathrm{Nm^{-1}}$	Initial stiffness at loading
β	0.1	–	Shape parameter for hysteresis loop
γ	0.9	–	Shape parameter for hysteresis loop
n	1	–	Sharpness of yield

the single degree of freedom system can be estimated from:

$$\omega_k = \frac{1}{2\pi}\sqrt{\frac{\alpha k_i}{m}} \tag{6.38}$$

This gives: $k_i = 632\mathrm{Nm^{-1}} \rightarrow \omega_k \approx 1.79\mathrm{Hz}$ and $k_i = 1776.5\mathrm{Nm^{-1}} \rightarrow \omega_k \approx 3\mathrm{Hz}$.

The aim of this study is to analyse the steady state behaviour of the BW model to harmonic excitation. The linear viscous damper can be used to ensure that the model reaches steady state for the given base values in a manageable amount of time. This is important because large amounts of data must be stored in order to extract the hysteresis loops and frequency response when varying each parameter. The step response of the system is found to check that an appropriate value of c has been chosen, so that the settling time falls within the time window for each simulation. Only the last 2^{12} sample points are stored for the solution vector in order to reduce data storage further and speed up simulation times. This number of sample points was chosen because MATLAB's FFT function is more efficient for an input vector with 2^r components, where r is a positive integer.

6.4.2 Method

For each run of the sensitivity analysis one of the original BW parameters is varied whilst all other parameters remain fixed. To do this a MATLAB script is used to perform frequency sweeps by running the Simulink model displayed in Figure 6.3. The steps in the script can be summarised as follows:

Input script

1. Assign the integration step: This was controlled by varying the number of sample points by increasing r for 2^r. Generally a value of 2^{16} was required for the time window defined by $t = 0 - 2^6$s. Increases in the excitation frequency would require a decrease in the integration time step.

2. Assign the frequency sweep: The model was excited at each discrete sample frequency defined by the frequency range $1 - 5$Hz in 2^6 points.

3. Assign the excitation: The excitation amplitude remains constant throughout each run so that the energy content of the force is approximately equal as the excitation frequency is varied. This facilitates the comparison of responses at different frequencies for changing parameters.

4. Assign base parameters

5. Assign sensitivity step: The parameter to be varied is chosen at this point.

6. Write simulation parameters: All write functions in the script produce text files that can be stored as a record of the simulation.

7. Start for loop for each iteration: This will run the frequency sweep for each value of the parameter that is being varied.

8. Start frequency sweep: This will run the Simulink model at each discrete frequency defined by step 2.

9. Run the Simulink model

10. Store solution vector: An array for the last 2^{12} samples of u, $\dot{u}$ and z is created and the data is stored here for each discrete frequency.

11. Next frequency in sweep

12. Store solution vector for iteration: Each array for u, $\dot{u}$ and z is written to text files.

13. Next iteration

This will yield a set of solution vectors for a set of iterations. All of the data is stored in text files that can be read by a separate MATLAB script. This script will plot the hysteresis loops and the loading-unloading curves at a discrete frequency for the number of iterations in the

sensitivity analysis. This can be utilised to assess the qualitative behaviour of the hysteresis loop when one parameter is varied. The script is also implemented to plot the frequency response of the displacement u over the frequency sweep.

Plotting script

1. Assign the frequency sweep vector
2. Start for loop for each iteration
3. Import data for iteration
4. Plot hysteresis loop and loading-unloading curve: These are plotted for a discrete frequency that is chosen arbitrarily.
5. Plot the frequency response of the displacement: Take the FFT of u at each discrete frequency in the sweep. Then extract the maximum value each time and plot it against the excitation frequency.
6. Next iteration

The methods used here were only sufficient to perform frequency sweeps in one direction.

The frequency sweep method that has been implemented here is a simple approach to analysing the steady state behaviour of the model. A wide range of alternative numerical methods could be applied to this problem with the benefit of reducing the computation times. Wong *et al.* [134] consider the methods used to analyse nonlinear steady state oscillations and resolve to apply the Galerkin/Levenberg-Marquart procedure to the BW model. They introduce frequency/time domain alternation and FFT techniques into this frequency domain procedure. They do this to overcome the limitations of numerical integration, such as numerical instabilities, that will occur if the time step is not chosen adequately and the unlikelihood that unstable responses and subharmonic resonances will be captured. This method obtains the steady state response directly and does not depend on computing the transient response until steady state.

Quantifying results

The scripts described in Section 6.4.2 are sufficient to carry out the qualitative analysis of the model. An additional script is implemented to quantify the influence of varying each parameter. This script quantifies the one-factor-at-a-time method as is suggested by Ma *et al.* [131]. To do this define the base values of the sensitivity analysis as: $[y_1, y_2, y_3]^T$ and when one parameter is changed let the solution vector be: $[x_1, x_2, x_3]^T = [u, \dot{u}, f(u, \dot{u}, z)]^T$. For each change in a parameter calculate the root-mean-square-error:

$$e = \left[\sum_{i=1}^{M} \left\{ (x_{1i} - y_{1i})^2 + (x_{2i} - y_{2i})^2 + (x_{3i} - y_{3i})^2 \right\} \right]^{1/2} \tag{6.39}$$

where M is the number of sample points taken in the time window. The error is evaluated for the response at the discrete frequency that was used when plotting the hysteresis loop that is equivalent to this analysis.

6.4.3 Qualitative analysis of the Bouc-Wen functional

The response of the BW functional is assessed qualitatively by inspecting the hysteresis loops produced when each of the original model parameters is varied independently. For each parameter the simulation is carried out at three amplitudes of excitation: 2^8N, 2^{10}N, 2^{12}N.The hysteresis loops have been extracted for a discrete frequency in the frequency sweep. Choosing a frequency that is close to a peak in the frequency spectrum will not produce loops that are centred on $(u, z) = (0, 0)$, so they are extracted for the response at 5Hz.

The base values used in this sensitivity analysis of: $n = 1$, $A = 1$ and $\beta + \gamma = 1$ imply that a change in A will be equivalent to a change in the yield load z_y:

$$z_y = A \tag{6.40}$$

where:

$$z_y = \pm \left(\frac{A}{\beta + \gamma} \right)^{1/n} = \pm 1 \tag{6.41}$$

This is demonstrated in Figures 6.8a- 6.8e. Figures 6.8b show that a change in A influences the saturation of the amplitude and the natural frequency. However the sensitivity of the

natural frequency with A reduces for higher excitation amplitudes.

The condition $\beta = 1 - \gamma$ guides the results that are shown in Figure 6.9. The hysteresis loop can be varied to give a loading stiffness that is quadratic or cubic up to the point of velocity reversal. A lower ratio of β:γ increases the likelihood of jump phenomenon occurring. The frequency range of the multi-valued response region decreases with increasing amplitude of excitation. When $\beta > \gamma$ the loading stiffness is quadratic up the the point of velocity reversal. The frequency sweep in Figure 6.9b shows that increasing the ratio of β:γ tends to reduce the amplitude of the response.

The results for changing parameter n are shown in Figure 6.10. As n is increased the hysteresis loop tends towards a elastic-perfect plastic response. The Simulink model that is used to produce the plots is based on the form of the BW functional in Equation (6.8), which is stated as valid for even values of n. However, the simulation does form closed hysteresis loops for odd values of n. Figure 6.10b shows that increasing n tends to saturate the amplitude of the response without increasing the bandwidth of the overhang frequency behaviour.

A change in α will adjust the contribution between the hysteretic and nonhysteretic spring to the restoring force of the system. This modifies the linear estimate of the natural frequency of the system according to Equation (6.38) and the results are given in Figure 6.11. It is also clear that a change in α will scale area of the hysteresis loop because it is varying the energy dissipation in the system.

6.4.4 Quantitative analysis of the hysteresis model

A simple method is implemented here to quantify the influence that each parameter has locally on the system response. By following the method explained in Section 6.4.2, a spider diagram is generated as the root-mean-square-error for each change in a parameter ±50% from its base value. The previous section focussed on the assessing the hysteresis loop that is generated by plotting z against u, however z cannot be measured directly through experiment. It is more practical to consider the restoring force $f(u, \dot{u}, z)$ that is expressed in Equation (6.16). For each simulation the amplitude of excitation is set to 2^{10}N. The linear spring is set to $k_i = 1776.5\text{Nm}^{-1}$ which gives $\omega_k \approx 3$Hz. Again the hysteresis loops are extracted for the response at 5Hz.

The results are shown in Figures 6.12-6.15 and the influence of each parameter can be observed directly from the spider diagram displayed in Figure 6.16 for the solution vector Equation (6.15). The analysis is repeated for the solution vector in Equation (6.14) where the hysteretic displacement z is considered instead of the restoring force $f(u,\dot{u},z)$. A change in parameter A in both cases is equivalent to a change in z_y, which adjusts the yielding behaviour of the hysteresis loop. Clearly this parameter has the strongest influence on the energy dissipation of the response. When the restoring force response is considered, instead of the hysteretic displacement, the model will clearly be more sensitive to changes in α. The difference between the influence of n and the ratio β:γ in both cases is greater when the restoring force is considered.

6.4.5 Discussion

The sensitivity analysis does not develop any understanding of how the parameters interact. Given the constraints that have been applied here it is clear that the influence of each parameter cannot be separated, so understanding the interactions between the parameters is important. Further work should be carried out to develop a global sensitivity analysis on the model. The parameter A clearly has a greater scale of influence on the model than the other parameters. However it is widely accepted that it is redundant and considering the yield load is more practical. The influence of β and γ was not separated here, but it was shown that they define the stiffness behaviour of the loading-unloading curve. For high values of n the hysteresis loop tends towards a bilinear oscillator. The parameter α becomes more important when the restoring force of the model is considered in the solution vector.

The range of possible modifications to the model have been explored in other studies and are numerous and varied. Before any modifications to the model can be analysed, through a sensitivity analysis, it is important to have the experimental hysteresis loops that are characteristic of the system to be modelled. It is clear that considering the restoring force, instead of purely the hysteresis functional, is a step forward in modelling bolted joints. This bridges the gap between the abstract functional, and the experimental data, because the restoring force can be measured directly. Each modification will require further parameters to be identified, and this adds complexity and cost to the identification process.

A limitation of the method applied in MATLAB is that the frequency sweeps have only been performed in one direction. Therefore the jump behaviour, that is known to occur, in

the response of this model, has not been shown. This should be addressed in future analyses and developing this understanding can be used to evaluate the validity of the model in simulating the nonlinear behaviour that is known to occur in HPU devices. The model has been analysed over a narrow bandwidth of the low frequency range, and observes the primary resonance of the system, whilst capturing at least one subharmonic. This becomes energised through the nonlinear hysteresis functional. If the model is to be applied to simulate the behaviour of a joint in an HPU device, then it will be necessary to include a portion of the high frequency range. This will extend the bandwidth of the analysis so that it covers 0-40kHz.

6.5 Outcomes

This study analysed the steady state behaviour of the Bouc-Wen model under harmonic loading. Some of the versatility of the model has been has been demonstrated by conducting a local sensitivity analysis using a one-factor-at-a-time method. The frequency domain analysis of the model is facilitated by incorporating Bouc's functional into the equation of motion of a Mass-Spring-Damper. Analysing closed form expressions of Bouc's functional leads to a greater understanding of its describing parameters and their ability to form hysteresis loops that are physically consistent. Analytical solutions are derived under the condition that the shape parameter $n = 2$. The sensitivity analysis is carried out using numerical integration and the Fast Fourier Transform in MATLAB. The shape parameter A is shown to define the initial stiffness of the system as well as effect the scaling of the hysteresis loop and the frequency of the response. The ratio of the shape parameters β:γ contribute most significantly to the stiffness behaviour of the hysteresis loop. This manifests as softening stiffness behaviour in the sensitivity analysis. A higher value of β tends to reduce the amplitude of the response. For increasing values of n, the response tends towards a bilinear oscillator. The parameter α varies the ratio of hysteretic to nonhysteretic spring and is more significant if the restoring force of the system is considered in the solution vector. This study has highlighted the key areas that have to be addressed in order to apply the Bouc-Wen model to physical problems.

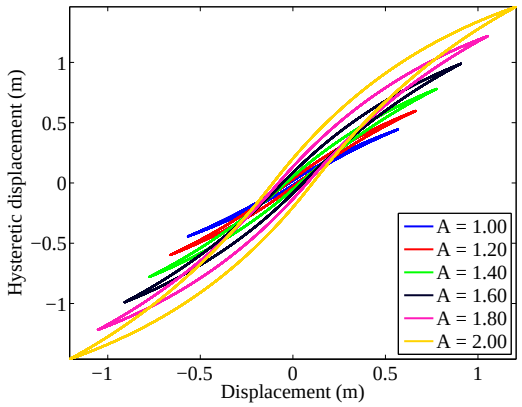

(a) $y(t) = \{u(t),\ z(t)\}$ for $F(t)@2^8$N

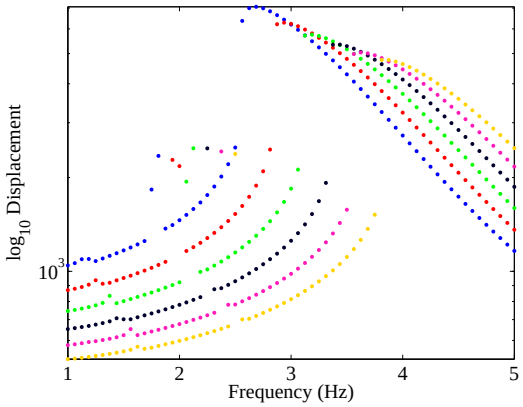

(b) $u(\omega)$ for $F(\omega)@2^8$N

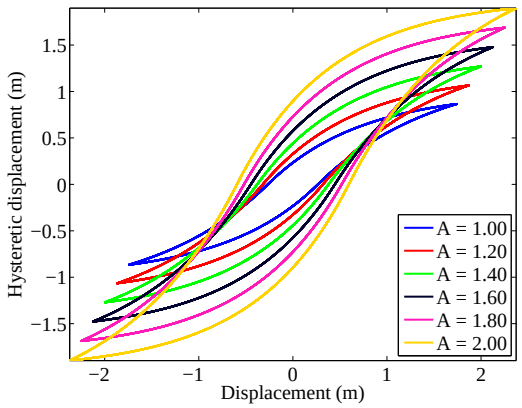

(c) $y(t) = \{u(t),\ z(t)\}$ for $F(t)@2^{10}$N

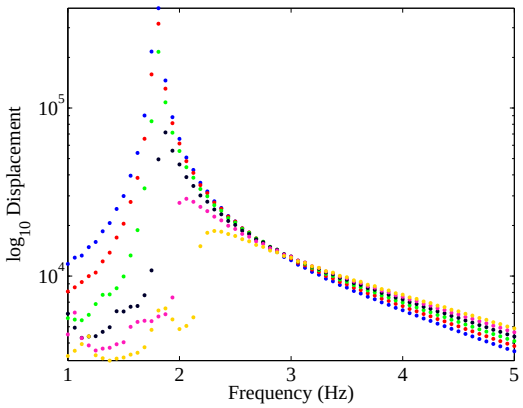

(d) $u(\omega)$ for $F(\omega)@2^{10}$N

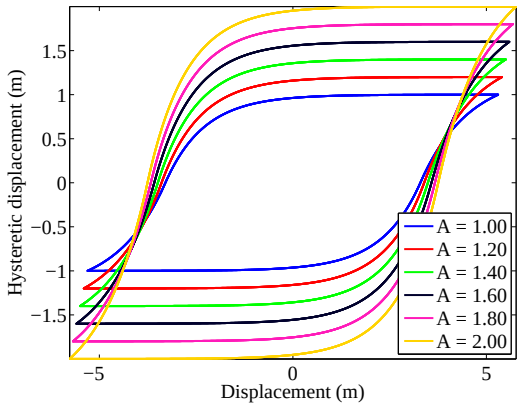

(e) $y(t) = \{u(t),\ z(t)\}$ for $F(t)@2^{12}$N

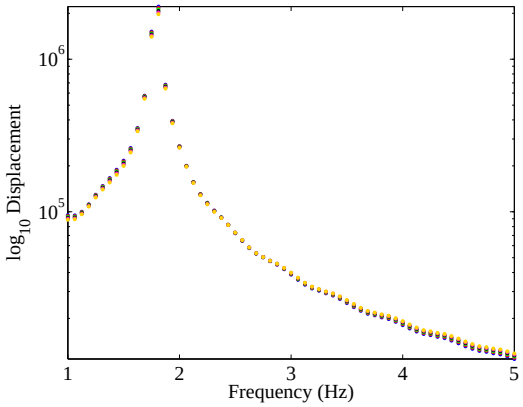

(f) $u(\omega)$ for $F(\omega)@2^{12}$N

Fig. 6.8 Varying A for three different amplitudes of input excitation.

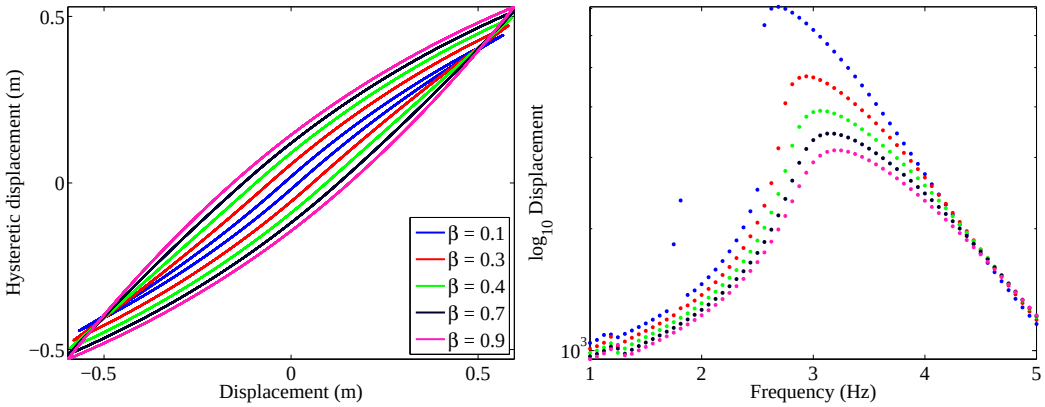

(a) $y(t) = \{u(t), z(t)\}$ for $F(t)@2^8$N (b) $u(\omega)$ for $F(\omega)@2^8$N

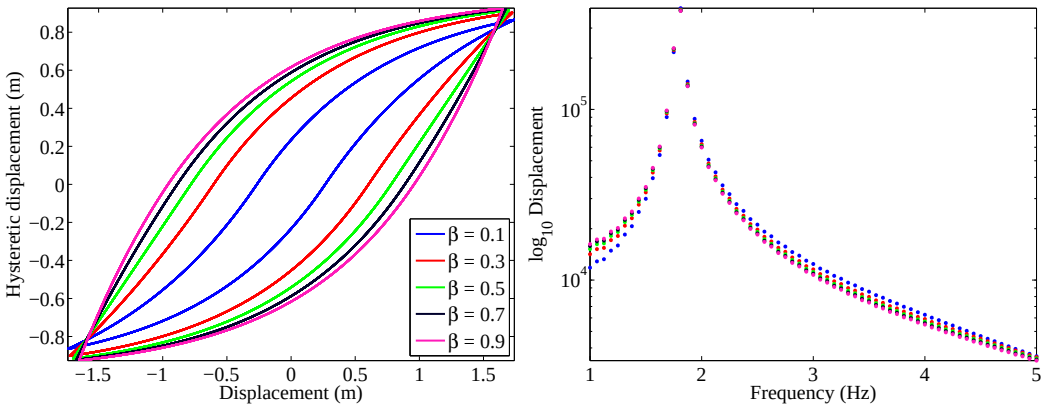

(c) $y(t) = \{u(t), z(t)\}$ for $F(t)@2^{10}$N (d) $u(\omega)$ for $F(\omega)@2^{10}$N

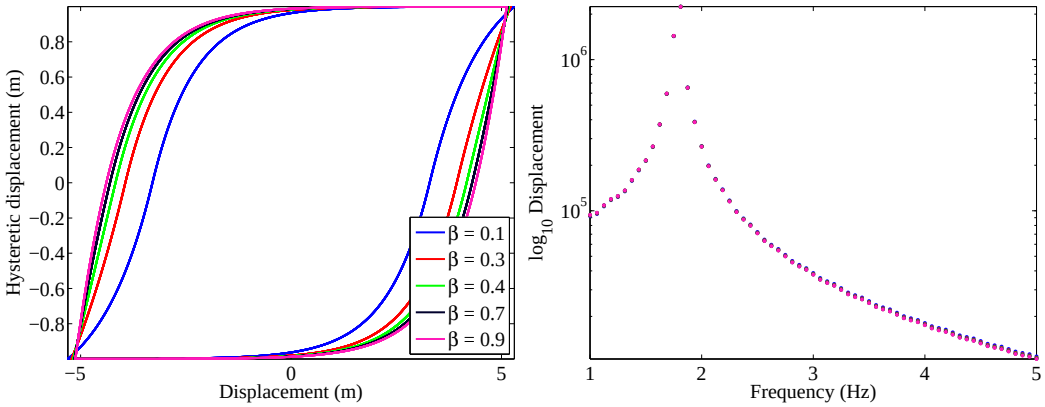

(e) $y(t) = \{u(t), z(t)\}$ for $F(t)@2^{12}$N (f) $u(\omega)$ for $F(\omega)@2^{12}$N

Fig. 6.9 Varying the ratio of β to γ for three different amplitudes of input excitation

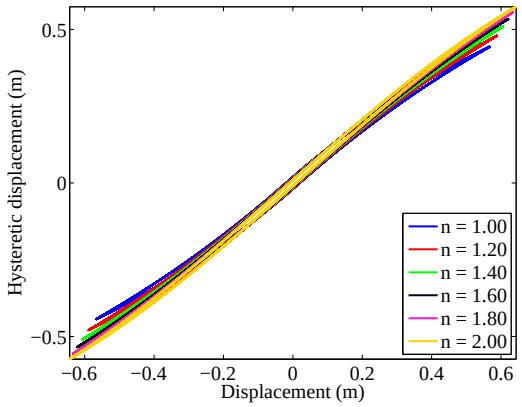

(a) $y(t) = \{u(t), z(t)\}$ for $F(t)@2^8$N

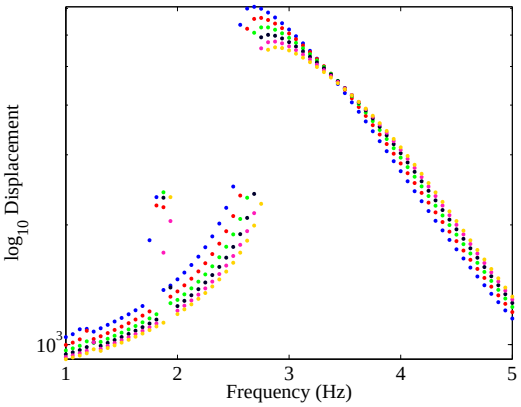

(b) $u(\omega)$ for $F(\omega)@2^8$N

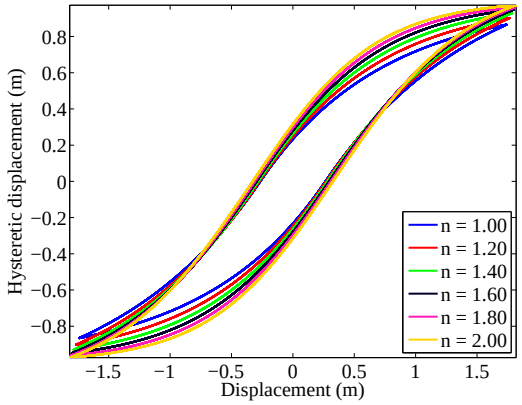

(c) $y(t) = \{u(t), z(t)\}$ for $F(t)@2^{10}$N

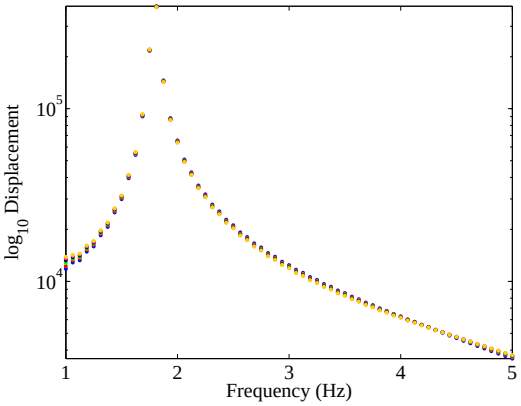

(d) $u(\omega)$ for $F(\omega)@2^{10}$N

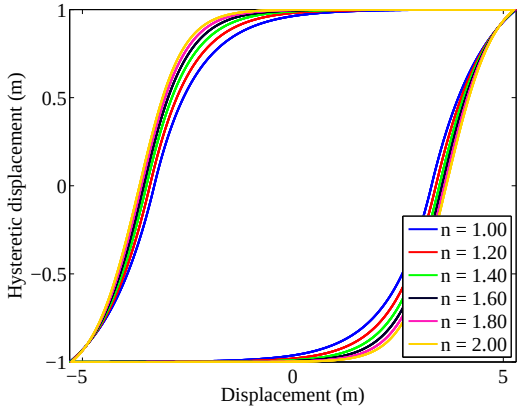

(e) $y(t) = \{u(t), z(t)\}$ for $F(t)@2^{12}$N

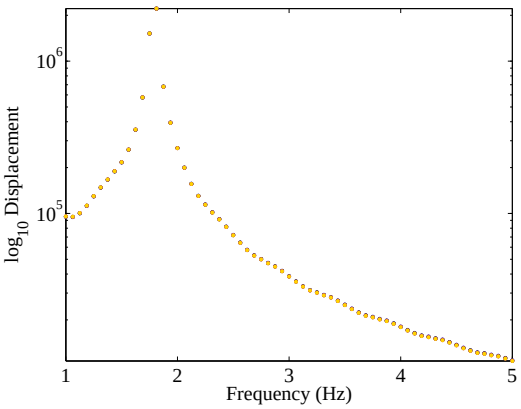

(f) $u(\omega)$ for $F(\omega)@2^{12}$N

Fig. 6.10 Varying n for three different amplitudes of input excitation

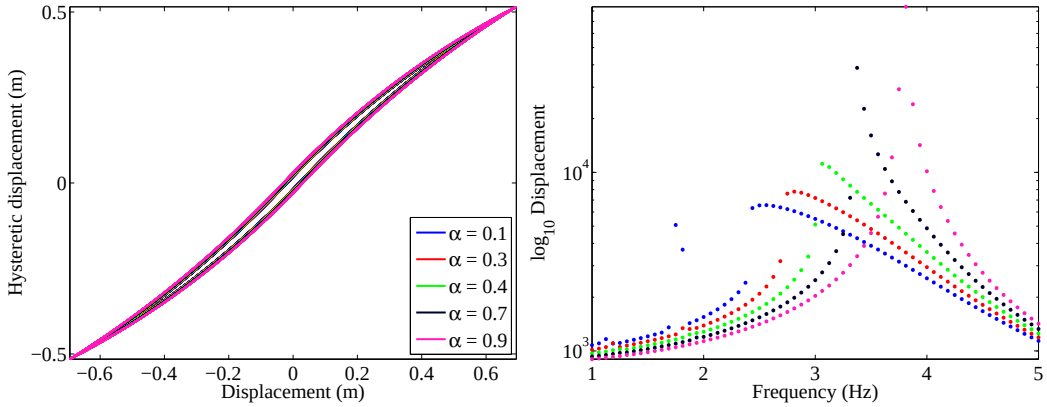

(a) $y(t) = \{u(t), z(t)\}$ for $F(t)@2^8$N (b) $u(\omega)$ for $F(\omega)@2^8$N

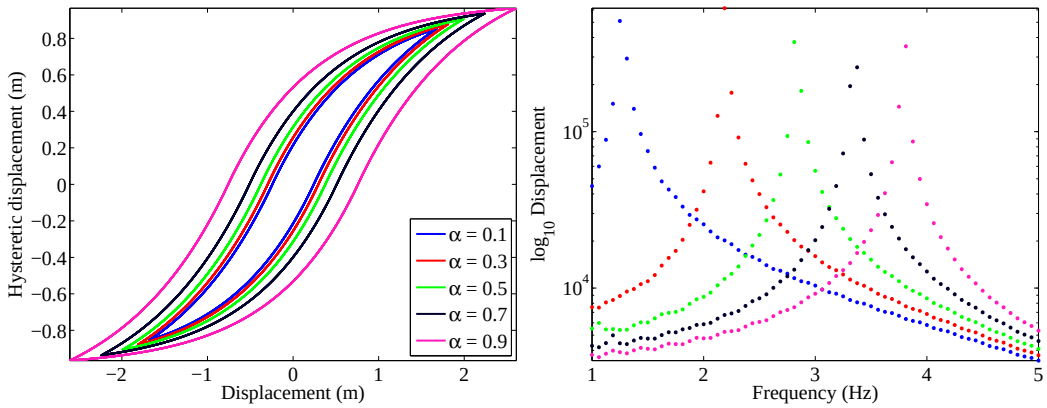

(c) $y(t) = \{u(t), z(t)\}$ for $F(t)@2^{10}$N (d) $u(\omega)$ for $F(\omega)@2^{10}$N

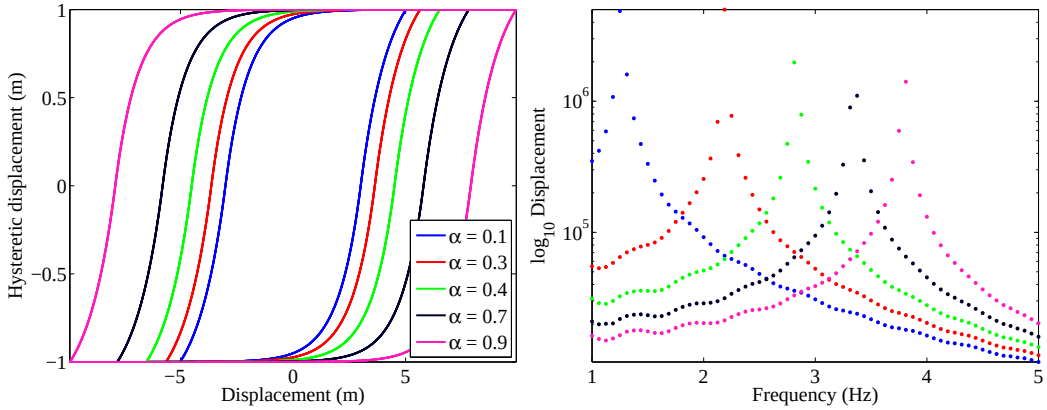

(e) $y(t) = \{u(t), z(t)\}$ for $F(t)@2^{12}$N (f) $u(\omega)$ for $F(\omega)@2^{12}$N

Fig. 6.11 Varying α for three different amplitudes of input excitation.

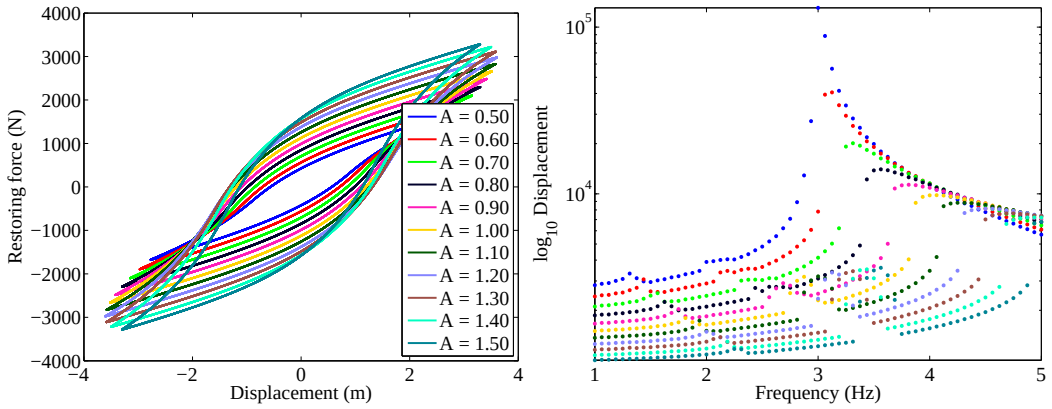

(a) $y(t) = \{u(t),\ f(u(t), \dot{u}(t), z(t))\}$ for $F(t)@2^{10}$N (b) $u(\omega)$ for $F(\omega)@2^{10}$N

Fig. 6.12 Varying $A \pm 50\%$ from its base value.

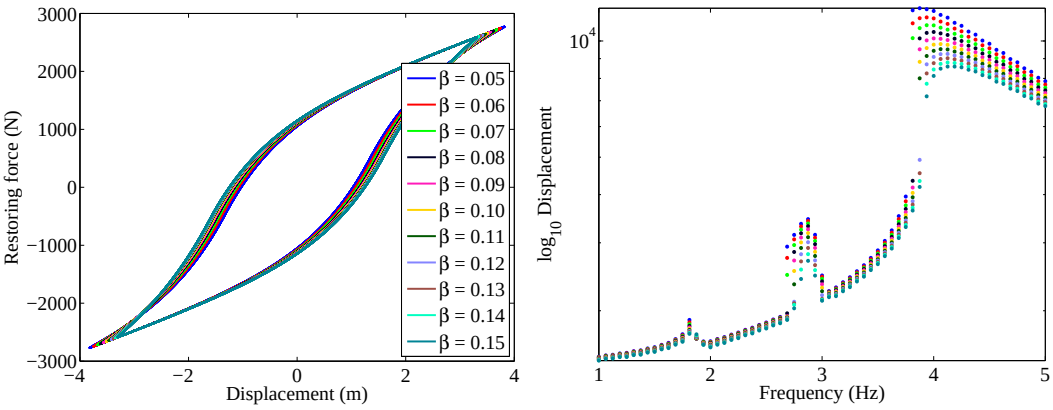

(a) $y(t) = \{u(t),\ f(u(t), \dot{u}(t), z(t))\}$ for $F(t)@2^{10}$N (b) $u(\omega)$ for $F(\omega)@2^{10}$N

Fig. 6.13 Varying the ratio of β:γ $\pm 50\%$ from its base value.

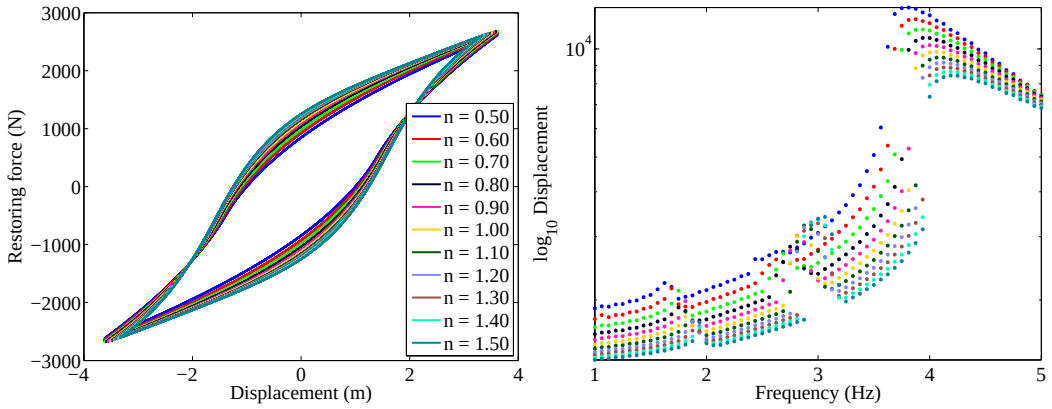

(a) $y(t) = \{u(t),\ f(u(t), \dot{u}(t), z(t))\}$ for $F(t)@2^{10}$N (b) $u(\omega)$ for $F(\omega)@2^{10}$N

Fig. 6.14 Varying $n \pm 50\%$ from its base value.

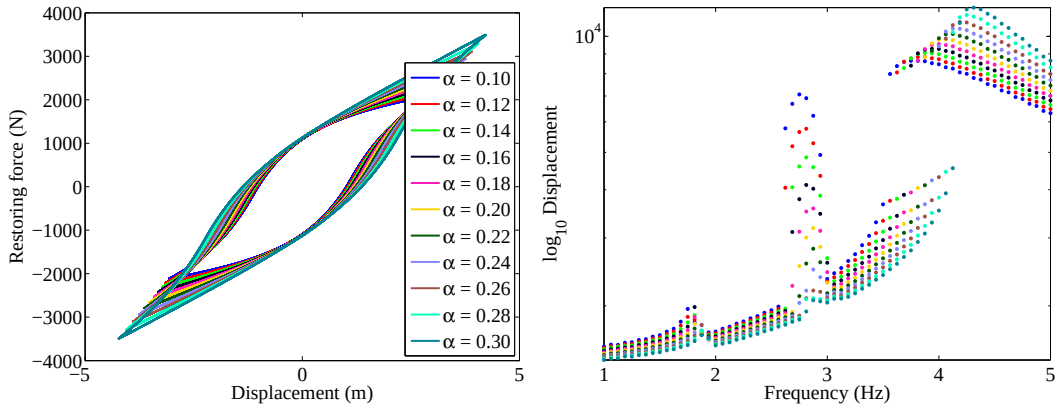

(a) $y(t) = \{u(t),\ f(u(t), \dot{u}(t), z(t))\}$ for $F(t)@2^{10}$N (b) $u(\omega)$ for $F(\omega)@2^{10}$N

Fig. 6.15 Varying $\alpha \pm 50\%$ from its base value.

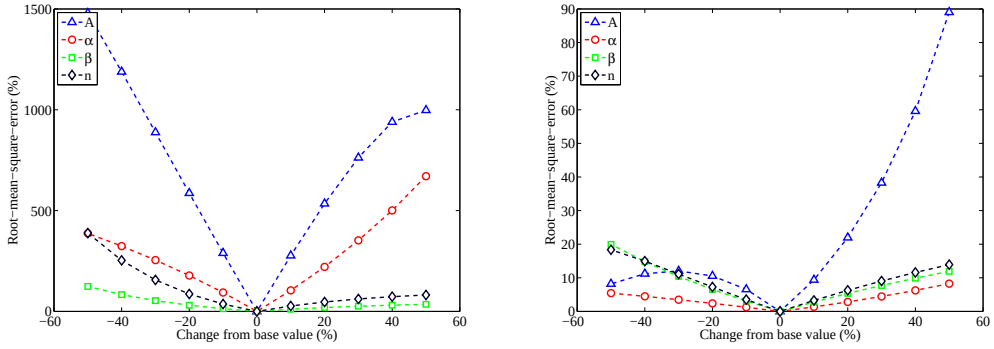

(a) $y(t) = \{u(t),\ f(u(t), \dot{u}(t), z(t))\}$ (b) $y(t) = \{u(t),\ z(t)\}$

Fig. 6.16 The one-factor-at-a-time method assessed though the root-mean-square-error for the two solution vectors.

Chapter 7

Estimation of the Bouc-Wen model parameters from experimental results

7.1 Introduction

There are two approaches that may be considered when applying the Bouc-Wen (BW) model to simulate the hysteresis behaviour of an unknown system. The first approach concerns fitting the Bouc functional to a hysteresis loop that retains a smooth continuous shape over the time window of observation. Many vibrating systems will draw loops over a similar loading-unloading path when their response is recorded at steady state. This will yield the velocity reversal points and the intersection points, at the orthogonal axis, following the discussion in Section 6.3.3. An attempt can then be made to identify the model parameters through the functions provided in Appendix A. When the Bouc functional in Equation (6.8) is applied directly, instead of interfacing it with a single degree of freedom oscillator, this will be referred to as the *limit cycle* identification approach. On the other hand, if the system's transient behaviour has been observed, then an *evolutionary* identification approach can be adopted to find a suitable BW model description. To achieve this, the BW model facilitates the replacement of the linear spring, in a Mass-Spring-Damper (MSD) system, with a pre-yield and a post-yield spring connected in parallel. The state space representation of this system can be integrated for a large number of parameter vectors, as part of a minimisation scheme, that tends towards the best model description for a chosen fitness function. In this case there are two options for the fitness function. It can either be a least squares minimisation between the displacements produced by the state space model and

obtained through laser vibrometry, or it can be a cost function that is computed based on Dynamic Time Warping (DTW). The solution vector for the evolutionary approach involves terms that are not featured in the limit cycle approach. In this case, it has been assumed that the observed hysteresis loop corresponds to the solution vector for the restoring force that is given in Equation (6.15). Whereas, the limit cycle approach relates the observed hysteresis loop directly to the Bouc functional.

If the BW model is to be applied as part of a control system to a High Power Ultrasonic (HPU) device, then its transient behaviour may be applied to produce a control signal that is related to the hysteresis behaviour. Evolutionary algorithms would need an initial learning time period before they could settle on a reasonable estimate of the model parameters. If the requirement is to test whether the BW model is suitable for describing an observed vibration phenomenon, then the limit cycle approach can be utilised to determine if the model has the suitable design space to fit the observed hysteresis behaviour. If the parameter identification method, which is discussed in Section 6.3.3, results in a solution that has discontinuities between the branches of the hysteresis loop, or converges on asymptotic or erroneous solutions, then the model is either not suitable or must be modified. The constraints on the parameter identification of the evolutionary approach are not as strong as they are for the limit cycle approach. Therefore, it is more likely that the evolutionary approach will converge onto a minimum solution that is not the global minimum.

Both of the mentioned approaches are relevant to the experimental data that has been obtained from testing the HPU assemblies. To isolate the behaviour of the screwed threaded connection, it is necessary to observe the system as it is subjected to burst excitations. The number of cycles in the excitation signal to the system is limited in order to minimise the influence of the temperature change. This occurs when the device is excited continuously. It is known that this temperature change will contribute towards softening overhang behaviour in the frequency response of the system. The temperature increase will be most pronounced in the piezoelectric stack. Applying high power excitation signals to the stack is associated with another source of softening overhang behaviour in the frequency response of the device. This is known to descend from the constitutive behaviour of the piezoelectric material.

The scheme to isolate the behaviour of a screwed threaded axial joint relies on being able to assume that the device can be described with a linear model, over some operating range, when the joint is omitted. New vibration phenomena should be encountered when the equivalent device, with a joint included, is tested over the same operating range. The use of burst

excitations allows the system to be at rest initially in the time window, so that zero initial conditions can be assumed. The system can then be observed over transients that are associated with it progressing to and from steady state to rest. This is also beneficial when estimating a force in the distributed parameter system. However this force identification problem is limited by the memory capacity of the system running the MATLAB code. This means that it can only be applied to a relatively small number of samples, which may not allow the system to progress from zero to steady state, and back to zero, for the sample rate that is required. Comparatively, the evolutionary identification of the BW model can cope with a greater number of samples because it is only required to compute the fitness function by operating on two 1D arrays.

The Commercial Piezoelectric Actuator (CPA) cannot be excited using burst excitations because this can damage its internal electronics. Therefore, the In-House Piezoelectric Actuator (IHPA) was manufactured for the purpose of this test. The response of this actuator, with either a Jointed Horn (JH) or the Monolithic Horn (MH) attached, has been recorded through laser vibrometry during the experiment in Chapter 5. The power spectrum of each horn, attached to the IHPA, is shown in Figure 7.1. This is performed through the same apparatus that was utilised for the Experimental Modal Analysis (EMA) and is shown in Figure 4.6. The excitation signal is defined as a sinusoid with frequency nearby to the 2^{nd} longitudinal mode. This mode was identified through the EMA in Tables 4.5 and 4.6. The MH exhibits a very narrow bandwidth response close to its 2^{nd} longitudinal mode at its damped resonant frequency ω_p^{MH}. To find a basis of comparison, for the recorded power spectra, it is useful to calculate the Q factor [135], according to: $Q = \frac{f_r}{\Delta f_{\sqrt{2}}}$. Here $\Delta f_{\sqrt{2}}$ is a bandwidth that begins and ends with the frequencies at either side of the resonant frequency f_r, at which $\sqrt{2}$ of the amplitude at f_r is reached. This indicates the energy loss, per cycle, relative to the stored energy of the resonator. The Q factors are estimated from the power spectrum that is obtained by testing each horn when it is attached to the IHPA. The results are given in Table 7.1. These are used to estimate the damping ratio $\zeta = \frac{1}{2Q}$ for the single degree of freedom oscillator.

A comparison of the power spectra for the JH and MH assemblies are shown in Figure 7.1. The power spectra do not suggest that there is a frequency where the bandwidth of each assembly will produce enough amplitude to be observable above the noise floor. If this condition could be realised, then the same loading condition could be assumed for both systems. It would then be feasible to deconvolve the force at the axial joint from the difference in the equivalent response of each assembly. The current alternative approach is

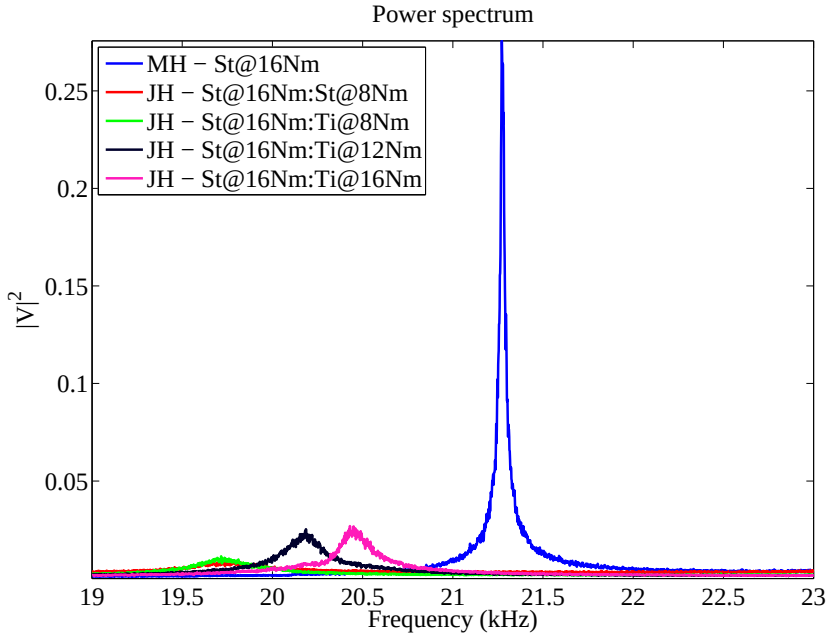

Fig. 7.1 Power spectrum of each ultrasonic horn attached to the In-House Piezoelectric Actuator.

to take the tests of the MH as a calibration experiment. The influence of the joint in a JH is referred to, relative to this, through a least squares solution. This means that it is not possible to purely isolate the axial joint behaviour, however it may be possible to form a useful basis of comparison on the strain that a JH can develop in its piezoelectric stack combined with the behaviour of the axial joint.

7.2 Estimation of the simplified linear calibration model

The Monolithic Horn (MH) is attached to the In-House Piezoelectric Actuator (IHPA) and the assembled device is excited close to the primary resonance, which has been associated with its 2nd longitudinal mode through Experimental Modal Analysis (EMA). The configuration of the HPU assembly from the force identification test, and the EMA in Chapter 4, is shown in Figure 7.2. This displays the assembly being supported at its flange, at which a node of vibration is approximately located. This arrangement is excited at the damped resonant frequency ω_p^{MH} and is described by the following MSD model:

$$f\left(u^{MH}, \dot{u}^{MH}\right) = c\dot{u}^{MH} + \alpha k_i u^{MH} = q^{MH}(t) - m\ddot{u}^{MH} \tag{7.1}$$

Table 7.1 Computation of the quality factor for each horn attached to the In-House Piezoelectric Actuator

Horn	Joint	f_r (kHz)	$\Delta f_{\sqrt{2}}$ $f_{\sqrt{2}} < f_r$ (kHz)	$\Delta f_{\sqrt{2}}$ $f_{\sqrt{2}} > f_r$ (kHz)	Q	ζ ($\times 10^{-3}$)
MH	-	21.272	21.265	21.285	1064	0.47
JH	St@8Nm	19.722	19.550	19.960	48	10.4
JH	Ti@8Nm	19.716	19.630	19.800	123	4.07
JH	Ti@12Nm	20.190	20.120	20.240	168	2.98
JH	Ti@16Nm	20.430	20.400	20.520	170	2.94

Fig. 7.2 In-House Piezoelectric Actuator, with the Monolithic Horn attached, supported at its flange.

where $f\left(u^{MH}, \dot{u}^{MH}\right)$ is the restoring force of the system, u^{MH} represents the observed displacement at a point on the flat of the MH and m, c and k_i are the inertial mass, linear damping and linear stiffness coefficients respectively. An additional coefficient α determines the ratio of pre-yield stiffness to post-yield stiffness of an element that is composed of a nonhysteretic and a hysteretic spring connected in parallel. In the case of the MH, α is set to 1, where values < 1 will introduce the Bouc functional into the formulation. Finally, $q^{MH}(t)$ is the input force to the linear system, which has been estimated previously through the distributed parameter model.

A value of $Q = 1064$ was determined from the power spectrum test of the MH. This yields an estimated damping ratio of $\zeta = \frac{1}{2Q} = 4.7 \times 10^{-4}$. The mass of the lumped parameter system is $m = 880.66$g and the contribution for each of the main components is given in Table

7.2. It was not possible to obtain an estimate of the modal mass that is associated with the operating vibration mode. The Frequency Response Functions that were measured in the Experimental Modal Analysis, which is discussed in Section 4.4, were not obtained for an input force excitation. Instead a random voltage signal has been recorded before it is then amplified and applied to the piezoceramic stack of the device. Therefore the measured mode shapes cannot be employed to estimate the modal mass. An alternative is to make use of the mode shapes that were computed through the Distributed Transfer Function model. However these are based on a comparison with incomplete measured mode shapes. In Section 4.5.1, it was already shown that the influence of prestress on the material parameters of the model is unknown. This limits the accuracy of the DTFM mode shapes. The effective modal mass should indicate the significance of a vibration mode. The Complex Modal Indicator Function in Figure 4.15 suggests that the 2^{nd} longitudinal (operating) mode of the assembly is most dominant. Therefore, as an initial guess, the full mass of the assembly has been assumed as the modal mass in the current model. However the analysis could be improved with a better estimate. If it is assumed that $\zeta = 4.7 \times 10^{-4}$ then the undamped natural frequency is found from:

Table 7.2 Mass of the components in the ultrasonic assembly

Component	Mass (g)
In-House Piezoelectric Actuator	590.00
Monolithic Horn	282.78
Threaded steel rod	7.88

$$\omega_k^{MH} = \frac{\omega_p^{MH}}{\sqrt{1-2\zeta^2}} \tag{7.2}$$

where the stiffness and damping coefficients are:

$$k_i = \left(m\omega_k^{MH}\right)^2 \tag{7.3}$$

$$c = 2\zeta\sqrt{mk_i} \tag{7.4}$$

The displacement of the assembly was measured during the experiment in Chapter 5 and the obtained spectra were shown in Figure 5.61. The damped resonant frequency is found and the MSD relationships are applied to form the initial model in Table 7.3. The full signal records are given in Figure 7.3b for a range of peak-to-peak input voltages. These were

applied at resonant frequencies that were identified by manually tuning the frequency of the function generator. The input forces that were deconvolved from the DTFM model, for these displacement records, are given in Figure 7.3a. In this case the set of forces that have been assumed are obtained with reference to the sum of the displacement signals at X_1 and X_2 through the pseudoinverse, by means of Truncated Singular Value Decomposition (TSVD).

Table 7.3 Initial Mass-Spring-Damper models of the In House Piezoelectric Actuator with the Monolithic Horn attached.

Voltage (mV)	ω_p^{MH} ($\times 2\pi \times 10^3$ rads^{-1})	ζ ($\times 10^{-4}$)	ω_k^{MH} ($\times 2\pi \times 10^3$ rads^{-1})	k_i (GNm^{-1})	c (Nsm^{-1})
100	21.255	4.7	21.255	15.71	110.6
200	21.240	4.7	21.240	15.69	110.5
300	21.225	4.7	21.225	15.66	110.4
400	21.225	4.7	21.225	15.66	110.4
450	21.225	4.7	21.225	15.66	110.4

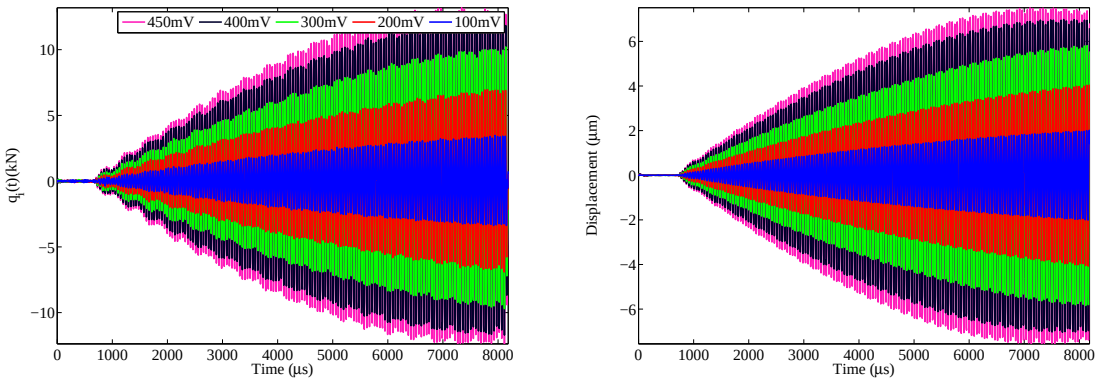

(a) Force

(b) Displacement

Fig. 7.3 Input and output signals of the resonance being described by the Mass-Spring-Damper model.

Equation (7.1) is solved through the function `ode45()` in MATLAB for the parameters given in Table 7.3. This produces the displacements given in Figure 7.4a. If it is assumed that the Q factor gave an appropriate value for the damping ratio then these results suggest that there are significant errors in the scale of the input forces. The displacement solutions are clearly unrealistic for the given device. The formulation of the DTFM model in

Chapter 3 included a retarding force that is proportional to velocity. The nature of this dissipation was discussed through simulation in Chapter 4. This demonstrated that the model did not dissipate energy as a result of increasing this dissipative force. Instead the response was distributed according to an exponential trend over the observation window. The initial MSD model would only be acceptable if the input force was computed through an inverse method that has more realistic dissipation behaviour. There was some agreement about the level of force that was estimated at the flat on the MH when the DIC results were compared to the force identification results. In this case the identification was carried out for an undamped distributed parameter system. The input forces in the current chapter were computed through the same assumptions. However, they were identified at the foremost point of the piezoeceramic stack and could not be verified through DIC. Instead of introducing further complexity into the force identification scheme the estimated forces are not modified. The damping of the MSD model will be identified so that the error descending from the estimated input force is minimised. Therefore the damping ratio must be corrected for each model.

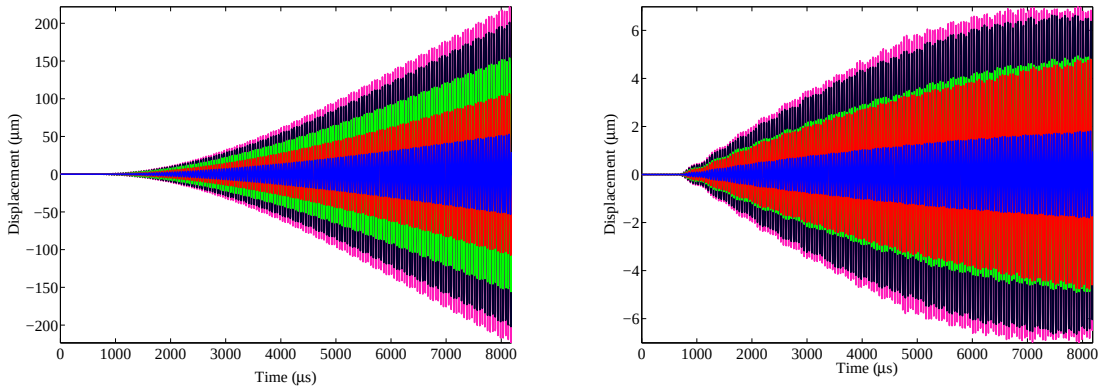

(a) Initial (b) Improved

Fig. 7.4 Response of the Mass-Spring-Damper models.

7.2.1 Mean Squared Error

The damping ratio ζ is estimated for each test of the IHPA with the MH attached. This can be achieved by varying ζ and observing the response of the MSD as it compares to the measured response. To automate this process, and quantify the outcome, a fitness function must be defined to quantify the error between the measured and the simulated response.

The first fitness function that is considered is the Mean Squared Error (MSE). This can be expressed as follows:

$$\text{MSE} = \frac{100}{N\sigma_u^2}\sum_{p=1}^{N}\left(u_p - \check{u}_p\right)^2 \tag{7.5}$$

where N is the number of samples, σ_u^2 is the variance of the measured displacement u and $\check{u}$ is the displacement predicted by the MSD.

Each pair of input and output signals are associated with a peak-to-peak voltage level as shown in Figure 7.5. The MSE is calculated for each pair as ζ is varied and the results are shown in Figure 7.5a. This shows that this fitness function is not suitable for the given data. The unsuitability most likely descends from the relationship between the pair of input and output signals. The input signal has been estimated as a L-2 norm. Therefore the error between the signals has already been smoothed artificially before the fitness function has been applied. This clearly demonstrates the limited information that is available through the estimate of the inverse DTFM model. An alternative approach is to develop a minimisation scheme is by considering Dynamic Time Warping (DTW).

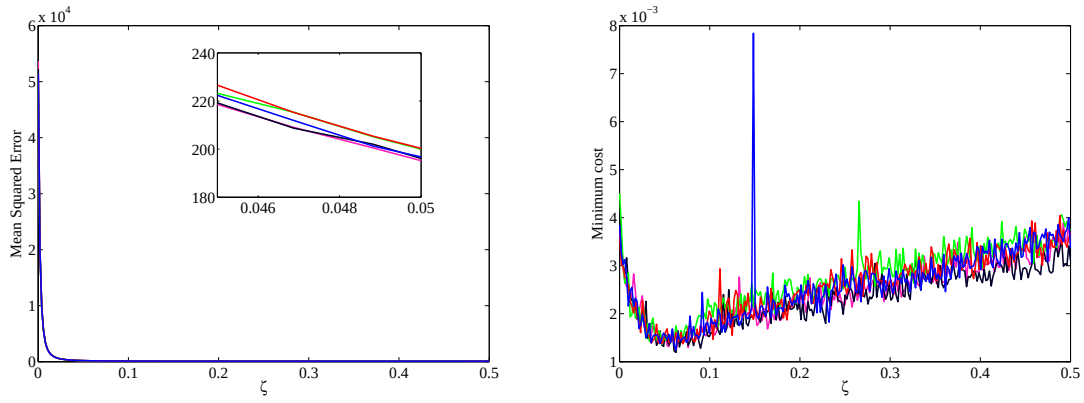

(a) Mean Squared Error

(b) Dynamic Time Warping

Fig. 7.5 Comparison of fitness functions to estimate ζ.

7.2.2 Dynamic Time Warping

Dynamic Time Warping (DTW) is an algorithm that has been applied in an effort to recognise the same word when it is spoken at two different speeds. The difference between these two speeds is a nonlinear function of time that has to be minimised for the same transient

phenomenon. Typically this is considered as mapping a test pattern onto a reference pattern through dynamic programming [136]. Most studies of this area come from computer science and are specifically interested in recognising spoken or written words [137]. However there are examples of it being applied to engineering systems for the correction of phase aberration in ultrasonic imaging [138], the indication of malfunctions in manufacturing processes [139], and for detecting mechanical anomalies in circuit breakers [140]. The application of DTW for speech recognition was superseded by the application of hidden Markov models and examples of this in the engineering literature are more prevalent [141].

To illustrate the DTW algorithm consider the following vibration signals:

$$\begin{aligned} \mathbf{A} &= \{\mathbf{a}_1, \mathbf{a}_2, \ldots, \mathbf{a}_p, \ldots, \mathbf{a}_P\} \\ \mathbf{B} &= \{\mathbf{b}_1, \mathbf{b}_2, \ldots, \mathbf{b}_q, \ldots, \mathbf{b}_Q\} \end{aligned} \tag{7.6}$$

where $\mathbf{a}_p$ and $\mathbf{b}_q$ are vectors containing portions of the spectrum of the signal with p and q as time indices and P and Q are the size of vectors $\mathbf{A}$ and $\mathbf{B}$. If it is assumed that there is some underlying transient phenomena in both sets of data, then they will be linked through the time deviation function. When $P = Q$ this warping function can be written as:

$$q = w(p) \tag{7.7}$$

This links the short time features of the signals. These can be found using the MATLAB function `spectrogram()`. This automates the process of taking Short Time Fourier Transforms (STFT) of the vibration signal by segmenting it by a specified length of window which can overlap with neighbouring windows. In this case a Hann window with a length of 512 samples has been applied over the entire time period and these overlap by 75%. The form of the warping function will minimise the time gap and this can be represented as a cost function:

$$D(\mathbf{A}, \mathbf{B}) = \frac{1}{N} \sum_{p=1}^{N} d(\mathbf{a}_p, \mathbf{b}_{q=w(p)}) \tag{7.8}$$

where $d(\mathbf{a}_p, \mathbf{b}_{q=w(p)})$ corresponds to the distance of one portion of the spectrum of the signal. Landry *et al.* [140] compare three possible forms of this distance and conclude that the Euler formula yields the best results to align their signals. Instead of calculating a cost function directly, Turetsky & Ellis [142] assemble a Similarity Matrix (SM) to align raw audio of a song to its MIDI transcription. The SM must be traversed by a Dynamic Programming algorithm in order to determine the magnitude of the cost function between the two signals.

It is formed by computing the cosine distance between the spectra **A** and **B** as follows:

$$\mathrm{SM}(p,q) = \frac{\mathbf{A}(p)^T\mathbf{B}(q)}{|\mathbf{A}(p)||\mathbf{B}(q)|} \tag{7.9}$$

Viewing this matrix, when it is scaled to the full range of a chosen colour map, reveals a chequerboard pattern that shows the segment boundaries and repeated phases between the signals. The presence of a strong diagonal line indicates good alignment between the two signals. To generate this diagonal, signal **B** must be warped to match signal **A**, by minimising the time deviation that is found through Dynamic Programming. To assume that there is a minimum cost, which is associated with the maximum similarity of the signals, the SM must be scaled through: S_{max}-SM. Here S_{max} is the maximum value of the SM. Dynamic programming is the process of breaking the overall time deviation between the two signals into smaller steps. The overall cost is accumulated by summing all of these steps. Each element of the SM is evaluated recursively to find the minimum cost path from the origin to (P-1, Q-1). The results that follow have been produced using the functions for the SM and Dynamic Programming that can be obtained from Ellis [143].

The MSE fitness function in Section 7.2.1 is replaced with the DTW technique in order to compute a fitness function that is based on the time deviation between the signals. The fitness landscapes in Figure 7.5b are generated by varying ζ from 0 - 0.5 for each set of input-output data. This reveals a clear minimum despite the level of noise in the fitness function. The topology of three minimum cost matrices are displayed as colour maps in Figure 7.6. These are computed from the data set that is associated with the last row in Table 7.3 for the 450mV voltage signal. The minimum cost path is computed through Dynamic Programming and is displayed as a red line. When $\zeta = 0$, the path is offset from the diagonal of the matrix and the remainder of the path is horizontal. This indicates dissimilarity between the signals. The difference between $\zeta = 0.057$, the optimal identified value, and $\zeta = 0.05$ is not clear because of the strong diagonal that is identified in both cases. However the diagonal in the optimal case is predominant in its colour map. With ζ at the optimum value, the improvement in the fitting of the MSD model to the input-output data is clear. The comparison of the first and last 1000 samples, between the MSD simulated and measured displacements, are shown in Figure 7.7 for the 450mV model in Table 7.3. Clearly the DTW technique does not act to minimise the amplitude difference between the two signals, however for the specified window of transient observation, minimising the time deviation does appear to give a reasonable estimate.

Figure 7.7 features a constant phase error between the integrated solution to the Mass-Spring-Damper model (MSD) model in Equation (7.1) and the measured response of the In-House Piezoelectric Actuator (IHPA) with the Monolithic Horn (MH) attached. These are both associated with the results for the 450mV excitation signal. The estimated input force, which was deconvolved for this assembly in Chapter 5, has been applied to the MSD model. It is possible that the phase error occurs due to the uncertainty in the damped resonant frequency of the model that was assumed in Table 7.4. This was located by tuning the frequency of the function generator, which produces the voltage signal that is applied to the piezoceramic stack, before it is amplified. The damped resonant frequency was found when the response at the front of the assembly achieved maximum amplitude after the frequency was varied nearby to the operating mode. This mode was identified through the Experimental Modal Analysis in Chapter 4. The damped resonant frequency was obtained by applying the Fast Fourier Transform (FFT) to the measured response. This was recorded over 4096 samples and a Hann window was applied. This gives a resolution bandwidth of 61Hz, which suggests the uncertainty in the subsequent frequency estimate. This FFT is shown in Figure 5.61 and the frequency at which the response is maximum was listed as the damped resonant frequency in Table 7.4. This uncertain frequency is taken forward to define the MSD model. The input force has been deconvolved from the response of the IHPA with the MH attached in Chapter 5. However, due to the memory requirement of forming the 2D convolution matrix, only the first 1024 samples of the response data was operated on to obtain a TSVD regularised solution of the same size. The resolution bandwidth of this signal is therefore 244Hz. The FFT of the TSVD regularised solution for the 450mV signal has a peak at 21.240kHz. This demonstrates a 15Hz disparity with the damped resonant frequency that was identified for this voltage. Furthermore the FFT of the force signal demonstrates amplification of high frequency noise that is not as prevalent in the equivalent displacement signal, which was taken from location X_2 that is given in Table 5.1 of Chapter 5. Despite this disparity between the damped resonant frequency of the MSD model and the frequency of the linear calibration force, the limitation in applying the force signal to deconvolving the joint force has already been discussed. There is an unknown phase error between the linear calibration signal and the expected input signal to the Jointed Horn. An equivalent problem exists in attempting to identify the BW model parameters from the linear calibration signals. However a better estimate is not currently available, so the MSD model is accepted as the best guess until the experiment can be improved through future iterations. The identification of ζ values through the DTW was not sufficient to remove this phase error in the case of the linear MSD model.

Each set of input-output data is minimised, through the DTW cost function, with the MATLAB function `fminbnd()`. This minimises a single variable continuous function over a fixed interval. The interval is set as $\zeta \in (0, 0.5)$ and the remaining variables are set according to the values in Table 7.3 and the discussion in Section 7.2. The resulting MSD models are given in Table 7.4 and the standard deviation of ζ is 6×10^{-3}. The displacements estimated by the improved MSD models are given in Figure 7.4b. Each trace can be compared to the measured results that are given in Figure 7.3b. Clearly the results are not ideal because the amplitude difference cannot be minimised due to the relationship between the estimated input force and the measured output displacement for the assumed linear system.

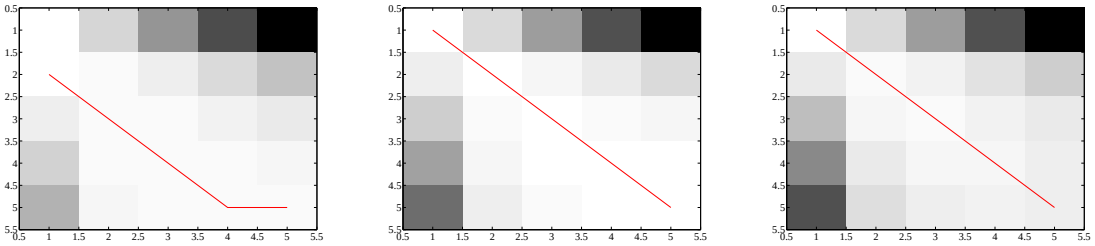

(a) $\zeta = 0$ (b) $\zeta = 0.057$ (c) $\zeta = 0.05$

Fig. 7.6 Comparison of the minimum cost matrix for ζ.

Table 7.4 Improved Mass-Spring-Damper models of the In-House Piezoelectric Actuator with the Monolithic Horn attached.

Voltage (mV)	ω_p^{MH} ($2\pi \times 10^3$rads^{-1})	ζ ($\times 10^{-2}$)	ω_k^{MH} ($2\pi \times 10^3$rads^{-1})	k_i (GNm^{-1})	c ($\times 10^2$Nsm^{-1})
100	21.255	5.86	21.328	15.82	138.3
200	21.240	4.51	21.283	15.79	106.2
300	21.225	6.28	21.309	15.66	148.1
400	21.225	5.57	21.291	15.76	131.2
450	21.225	5.70	21.294	15.77	134.3

7.3 Estimation of the simplified axial joint model

Each JH is attached to the IHPA and excited close to its primary resonance. This is close to the 2nd longitudinal mode that was identified through the EMA in Table 4.6. The peak

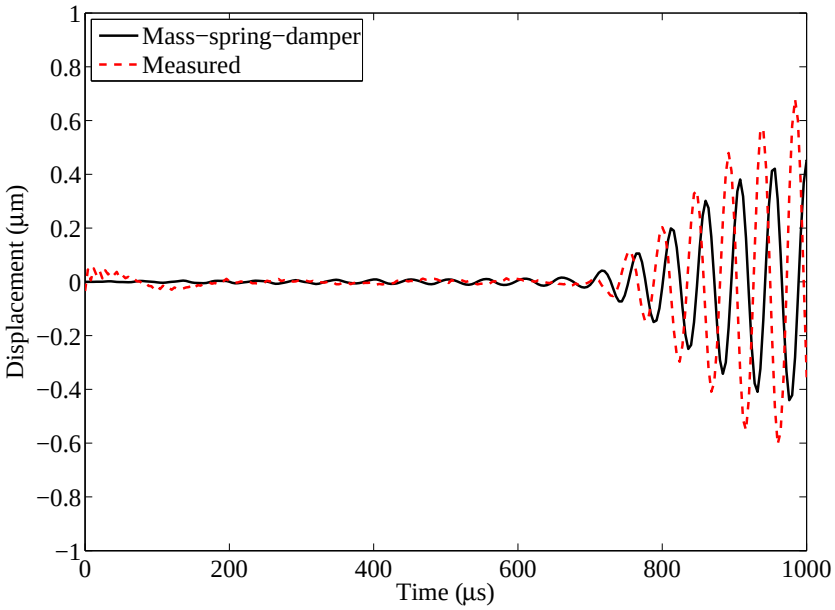

(a) Intital 1000 samples

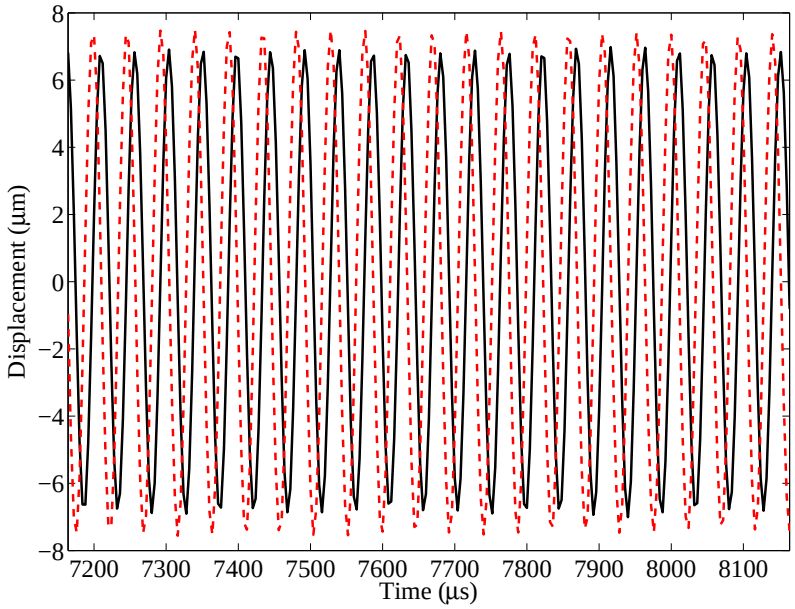

(b) Final 1000 samples

Fig. 7.7 Comparison of the measured and the mass-spring damper responses for 450mV excitation over the observation time window.

response is found by sweeping the frequency of the excitation voltage down, from the EMA result, whilst viewing the response signals from each of the Laser Doppler Vibrometers (LDV). These displacement measurements have already been discussed in Section 5.4.2. The displacement measured from the flat of each horn, or location X_2, is employed in the following analysis.

The results from Section 7.2 are thought of as the linear calibration to this experiment. They define the starting point to the identification of the axial joint model in each set of equivalent JH results. However, in the case of both the calibration and the joint model, the input force has been estimated through the force identification scheme that was given in Chapter 3. Therefore the input to the simplified linear model inherits the inaccuracies that were quantified through the Transcendental Eigenvalue Problem in Section 4 as well as the level of regularisation that was applied to estimate the force from the distributed parameter model. In the case of the simplified joint model, the true input force is unknown. It is assumed that this force follows a similar pattern to the force that was deconvolved from the linear model. However, it is clear from the EMA results that the frequency would be lower due to the loss of axial stiffness in the overall system. Under ideal conditions, if the joint could be tightened to the extent that its internal and external threads would fuse, then the MH would be recovered. The loss of axial stiffness that is introduced by the axial joint also corresponds to a change to the electrical impedance behaviour of the HPU device. Before the linear estimated force is applied as the approximate input to a JH, it must be scaled according to the linear power draw of the device from the power amplifier. This relationship is depicted in Figures 5.37 and 5.109. The following relationship has been applied to scale the input force to a JH:

$$q^{JH}(t) = \frac{q^{MH}(t)}{\frac{|Z^{JH}|}{|Z^{MH}|}\sqrt{\frac{|Z^{MH}|}{|Z^{JH}|}P_{Ratio}}} \tag{7.10}$$

where:

$$P_{Ratio} = \frac{10^{0.1\left[10log_{10}\left(P_{@Z_0}\right)+10log_{10}\left(1-|\Gamma|^2_{Z^{MH}}\right)\right]}}{10^{0.1\left[10log_{10}\left(P_{@Z_0}\right)+10log_{10}\left(1-|\Gamma|^2_{Z^{JH}}\right)\right]}} \tag{7.11}$$

where q^{JH} and q^{MH} are the assumed input forces to a JH assembly and the MH assembly respectively. The impedances of these assemblies are Z^{JH} and Z^{MH}. The power reflected back to the power amplifier is determined by the reflection coefficient, which is given as $|\Gamma|_Z$ in Figure 5.37. The output impedance of the power amplifier is $|Z_0| = 50\Omega$ and the impedance associated with the HPU assembly is the load impedance $|Z_L|$. The forward power from the amplifier when the output impedance equals the load impedance is given as

$P_{@Z_0}$ in Table 5.3.

To model the axial joint it is assumed that $\alpha < 1$ and this implies that Equation (7.1) is the modified form of the BW model for hysteresis that follows:

$$f\left(u^{JH}, \dot{u}^{JH}, z\right) = c\dot{u}^{JH} + \alpha k_i u^{JH} + (1-\alpha) k_i z = q^{JH}(t) - m\ddot{u}^{JH} \tag{7.12}$$

$$\dot{z} = \left[A - z^n \left(\beta sign\left(\dot{u}^{JH} \cdot z\right) + \gamma\right)\right] \dot{u}^{JH} \tag{7.13}$$

where u^{JH} is the simulated displacement of the HPU system when the axial joint behaviour is significant in its response. The parameters of the BW model have been discussed in Chapter 6. The values of the parameters α, A, β, γ and n are not necessarily related to physical quantities. It is assumed that the parameters m, k_i and c are known. The MSD model, that is defined by these, acts as a reference point for the estimation of the remaining unknown parameters.

7.3.1 Properties of the Bouc-Wen model of hysteresis

The BW model is extremely versatile as it can capture many different forms of hysteresis behaviour based on known input-output data. This is very useful, however it poses a problem when the model is required to behave very closely to the actual system. The highly nonlinear nature of the identification problem can make it very difficult to achieve a very good fit to the data. The performance of any identification scheme will rely on its ability to explore the design space and make sufficient progress with converging onto an appropriate minimum. The balance of these requirements must be considered over the run time of the identification scheme. Before any parameter estimation scheme is applied, it is important to simplify the nature of the design space as far as possible. The main points to consider can be found in the survey by Ismail *et al.* [119], where the physical and mathematical properties of the model are explored. The physical behaviour of the model can be summarised as follows:

- Bounded Input-Bounded Output stability: This is important because structural and mechanical systems are open loop stable and it is stated that this is true for fixed values of the parameters A, β, γ and n of $0 < \alpha < 1$ and the initial hysteretic displacement $z(0)$ is a real value.

- Consistency with the asymptotic motion of physical systems: As $t \to \infty$; $u(t) \to$ constant and $\dot{u}(t) \to 0$. For every initial condition $u(0)$, $\dot{u}(0)$ and $z(0)$ the signals $u(t)$, $\dot{u}(t)$

and $z(t)$ have derivatives that are continuous.

- Passivity: When the BW model represents a mechanical system, the integral of the limit cycle, which is given by a plot of $(u(t),\ f(u(t), \dot{u}(t), z(t))$, gives the energy dissipated by the system. Therefore the system does not produce energy.

- Thermodynamic admissibility: Erlicher & Point [144] proved that a specific form of the BW model obeyed the 2nd Law of Thermodynamics under the following parameter constraints: $n > 0, \beta > 0, -\beta \leq \gamma \leq \beta$. The form of the hysteresis function is the same as has been applied in this study, so it is reasonable to assume these constraints.

- Accordance with Drucker and Il'iushin stability postulates: Charalampakis & Koumousis [145] have shown that the BW model can produce negative energy dissipation in the form of displacement drift and force relaxation when it is subjected to short unloading- reloading paths. They correct this by introducing a stiffening factor into the hysteresis expression. Casati [146] shows that only positive energy dissipation will occur as long as the following parameter constraints are applied: $n = 1, \beta + \gamma > 0$ and $\gamma - \beta \leq 0$. Also the constraints that were applied for Thermodynamic admissibility imply that it adheres to Drucker's postulate.

- Consistency with the hysteresis property: The output must depend on the sign of the derivative of the input. Ismail *et al.* [119] have shown that the BW model will adhere to this under the following constraint:

$$\max_{t \geq 0}(u(t)) \leq \frac{(1-\alpha)z_0}{\alpha} \tag{7.14}$$

where:

$$z_0 = \sqrt[n]{\frac{A}{\beta + \gamma}} \tag{7.15}$$

The mathematical properties of the BW model are concerned with the existence and the uniqueness of its solutions. Ikhouane *et al.* [147] state that Equation (7.13) locally satisfies the Lipschitz condition for some time interval as long as $n > 1$. This property is not verified for $0 \leq n < 1$, so the solutions to this model may not be unique. It is clear from Equation (7.15) that a constraint $n \geq 1$ will greatly simplify the design space because now the value of z_0 cannot increase through the manipulation of n.

Ikhouane & Rodellar [148] demonstrate that two BW descriptions produce exactly the same input-output behaviour when β & γ for each system are related by a positive constant to the power n. Therefore an infinite number of BW descriptions exist for the same input-output behaviour. Ikhouane & Rodellar [148] present a normalised BW model, which reduces the redundancy of parameters through the transformation:

$$v(t) = \frac{z(t)}{z_0} \tag{7.16}$$

where z_0 is given in Equation (7.15). This yields the following set of parameters with constraints: $\rho_v = \frac{A}{z_0} > 0$, $\sigma_v = \frac{\beta}{\beta+\gamma} \geq 0.5$, $\kappa_u = \alpha k_i > 0$ and $\kappa_v = (1-\alpha)k_i z_0 > 0$. If the initial condition $v(0)$ adheres to $|v(0)| \leq 1$ then $|v(t)| \leq 1$ for all $t \geq 0$. Therefore $z(t)$ has been scaled to unity and the normalised BW model achieves a bijective relationship between its input-output behaviour and its parameters.

This model description was implemented for the parameter identification of the JH. The following ranges of values were assumed for each parameter: $\kappa_u \in (0, k_i)$, $z_0 \in (0, 200)kN$, $\kappa_v \in (0, k_i z_0)$, $\rho_v \in (0, 1)$, $\sigma_v \in (0, 1)$ and $n \in (0, 9)$. The scale of possible values for κ_v meant that the design space was much more costly to traverse. An alternative strategy to remove the parameter redundancy of the BW model was given by Ma *et al.* [131]. They show that the response of the model is invariant to parameter A and setting $A = 1$ does not alter the functional dependence of the loop. This is applied for the analysis of each JH assembly because it reduces the complexity of the design space and implies that only β and γ may be required to assume very large values. The merit of considering the physical and mathematical properties of the BW model is to set up intervals, on each of the unknown parameters, with the aim of simplifying the design space. A parameter identification scheme can then be selected to traverse this restricted space.

The parameters of the BW model are identified for some input-output behaviour that is expected to exhibit hysteresis. The proposed input must be applied to the model at each step of time, that is involved in the identification process, in order to produce a predicted output. This is problematic when the desire is to speed up the integration by implementing an ODE solver with an adaptive time step. Therefore, each time the input is applied to the model, it is interpolated to estimate the magnitude of the input that matches to the time step of the solver. This output is compared to measured data and the difference between the two signals is quantified. The Mean Squared Error (MSE) in Equation (7.5) will be applied to compare the measured and simulated displacements. The Dynamic Time Warping (DTW)

scheme discussed in Section 7.2.2 will not provide any information about the discrepancy between the amplitudes of the signals, so it will not be applied. An identification scheme must be assumed to minimise the error between the predicted and measured response. Due to the highly nonlinear nature of the BW model this is not a straightforward task. It is non-differentiable and if its limit cycle cannot be directly measured, then its parameters must be identified based on temporal data.

7.3.2 Identification of dynamic systems

The identification of dynamic systems is discussed in the monograph by Isermann & Münchhof [149]. They discuss theoretical and experimental modelling as approaches to obtaining a mathematical description to a system. A system is a circumscribed collection of processes with behaviours that are not mutually exclusive. Theoretical modelling is concerned with known physical laws that may be found from balance equations, equations of state, phenomenological equations or interconnection equations. In each of these cases the model will have a certain structure with defined parameters. Simplifying assumptions will be required to solve the model for the most predominant physical effects. Experimental modelling relies on a mathematical description that is derived from measurements. A Priori assumptions are required to make progress and these must be made based on some previous theoretical analysis or from empirical evidence. An identification method is applied to the input and output signals to define a relationship between them. However this relationship will always be incomplete. If the model has D dimensions then it will only be possible to observe it on less than D occasions [150]. Furthermore, each of these observations will be contaminated by measurement noise. However these are the only estimates that are available through the chosen measurement system. The theoretical and experimental modelling techniques should not exist in isolation from one another because the analysis of each of these models, in tandem, should feedback into the overall system analysis.

The combined theoretical/experimental modelling analysis so far can be summarised as follows. It is assumed that the physical laws of the axial joint will follow the BW model, but it may be difficult to estimate appropriate parameters to complete the description. The response of the jointed HPU assemblies have been measured reliably, but if these responses contain beat phenomenon, then the functional relationship will need to be reconsidered. The exact input is unknown, but based on the analysis of the monolithic HPU assemblies, it is assumed to be a linear signal with a fundamental frequency that is equal to the sec-

ond axial mode of the jointed HPU assembly. The internal state that is required to describe frictional processes means that they have to be modelled in the time domain. They are described through nonlinear functional relationships that represent non-continuously differentiable processes. If the underlying model structure is linear in its parameters then these can be identified through a direct estimation method. This has been demonstrated through the force estimation scheme. However, in cases where this is not possible, an iterative parameter estimation method must be employed. This is the case for the BW model, which is nonlinear in parameters.

7.3.3 Iterative parameter estimation methods

Iterative parameter estimation methods involve the numerical minimisation of a cost, fitness or objective function. This function must define a basis on which the error between a measured and predicted signal can quantified and it should be real and positive to produce minima. Depending on the application, the influence of large errors on the cost function might be weighted differently to smaller errors. For this reason it can be helpful to consider a range of possible cost functions, such as: Least squares, Huber, Bisquare, L1-L2 and absolute value [149]. The elementary algorithms, which are applied to minimise a cost function, solve the unconstrained optimisation problem. Therefore parameter estimation can be performed, with no knowledge of the nature of the parameters, by restarting the optimisation for a wide range of initial values and then evaluating the behaviour of the search of the design space. However when the design space is complex many local minima can exist that stop the minimisation from progressing to the global minimum.

To improve the efficiency of the parameter estimation it is preferable, or sometimes necessary, to define boundaries on the parameter space. In some cases knowledge of the boundaries can transform a multi-dimensional problem into a one dimensional problem. This is the case when the Transcendental Eigenvalue Problem is solved for the distributed parameter model of the HPU device. Knowledge of the expected eigenvalues can be applied to enclose a single minimum of the cost function. This is an example where the gradient of the cost function is explicitly available. As a result it is possible to search for the minimum with increasing accuracy as higher order derivatives of the gradient are employed. In this case the minimum has been identified through the Newton method, which is a second order method. Second order methods require knowledge of the second derivative of the cost function and other examples are the Quasi-Newton, Gauss-Newton and the Levenberg-Marquart

algorithms. The Gradient Descent method is an example of a first order method. The preceding methods can estimate parameters in a multi-dimensional design space when the cost function is differentiable. However when this is not permitted, by the structure of the process, more general parameter estimation approaches are necessary. This is the case for the BW model because it is nonlinear in its parameters and it features a discontinuous auxiliary equation.

Zeroth order optimisation methods require only the discrete value of the cost function when it is evaluated for a certain parameter set. In order to progress towards a solution the chosen algorithm must be capable of learning how to improve the parameter set throughout the course of the optimisation. The desire to optimise models of engineering systems from limited information lead to the field of Evolutionary Programming. This is a subset of Artificial Intelligence where the algorithms are biologically inspired. The algorithms act on mechanisms such as reproduction, mutation, recombination and selection to allow a population of individual solutions to progress towards meeting the criteria of the optimisation problem. Successful optimisation depends on achieving a good balance in the exploration and exploitation of the design space. When the design space is complex more diversity in the population will be required to locate the global minimum solution. Too much specialisation in the population may result in early convergence onto a local minimum that does not represent a good solution. When an algorithm suffers from this it is sometimes necessary to restart the search multiple times to obtain the desired solution. Sacrificing specialisation for exploration comes with the cost that the obtained solution may not be truly optimised despite being on the correct track. Evolutionary algorithms have been successfully applied to a diverse range of fields because they do not make any assumptions about the nature of the design space. As a result, a great deal of algorithms are available. However only a few are prevalent in the engineering literature. These include: the Genetic Algorithm (GA), Differential Evolution (DE) and Particle Swarm Optimisation (PSO). A number of variations of each of these are also available.

Initially each of the three Evolutionary Algorithms populates the design space with random solution vectors. Each parameter that features in the solution should be constrained by upper and lower bounds. However, in the case of the BW model, this can be difficult because it is not possible to relate all of the parameters to physical or mathematical constraints. An over-constrained parameter might limit the ability of the model to describe the experimental observations. Both the MATLAB GA and PSO functions, `ga()` and `particleswarm()` respectively, can make progress towards a minimum with no parameter constraints. How-

ever, as a result, it is difficult to gain confidence that the potential design space has been explored sufficiently.

To perform DE in MATLAB a standalone package produced by Buehren [151] was employed. This requires definite boundaries to each parameter as well as the quantisation over the specified range. This quantisation is strongly tied to the flexibility of the search. This is demonstrated clearly when Equations (7.14)-(7.15) are considered. If $0 \leq \alpha \leq 1$, $A = 1$, $-\beta \leq \gamma \leq \beta$ and n is set to 1, then the amplitude $z_0 \propto \frac{1}{\beta+\gamma}$. The dominator has the constraints $0 < \beta + \gamma \leq 2\beta$. Therefore the largest value that z_0 can take in this case depends on the quantisation of β and γ. Buehren [151] states that a side effect of the boundary constraints on the parameters is that the boundary values might be favoured throughout the optimisation scheme.

Both the GA and DE involve the participation of three operators: selection, crossover and mutation [82, 152]. Selection increases the prevalence of the fittest solutions, which will be evaluated in the next iteration. Crossover recombines solutions to produce new potential solutions for the next iteration. Mutation creates a new potential solution by applying random changes to a previous solution. PSO operates differently. Each solution is held by a particle that traverses the design space. By updating its velocity vector it reaches a new solution at each iteration. This is calculated from the current fitness value of the particle, the best fitness value so far and the best fitness value that has been identified out of all of the particles. The velocity vector is also modified by vectors of random variables that are uniformly distributed over the interval (0,1). The particles are attracted to solutions, but remain on the move.

The GA and DE are defined through stochastic behaviour that is distinctly different to PSO. The GA selection operator acts on a probability that is found based on the fitness of a solution compared to the average fitness for the whole population. The DE selection operator owes more to crossover and mutation. It maintains a pair of vector populations of size N_p over g_{max} iterations for D parameters. One population contains the current solutions that have been accepted through the selection operator and is represented as follows:

$$\begin{aligned} \boldsymbol{P}_{\boldsymbol{x},g} &= \left(\boldsymbol{x}_{i,g}\right), \quad i = 0,1,\ldots,N_p-1, \quad g = 0,1,\ldots,g_{max} \\ \boldsymbol{x}_{i,g} &= \left(\boldsymbol{x}_{j,i,g}\right), \quad j = 0,1,\ldots,D-1 \end{aligned} \tag{7.17}$$

The other population is composed of trial solutions that are produced by recombining a current solution with a mutated vector, that is synthesised from randomly chosen vectors.

This population is denoted by:

$$\begin{aligned} \boldsymbol{P}_{\boldsymbol{u},g} &= \left(\boldsymbol{u}_{i,g}\right), \quad i = 0,1,\ldots,N_p-1, \quad g = 0,1,\ldots,g_{max} \\ \boldsymbol{u}_{i,g} &= \left(\boldsymbol{u}_{j,i,g}\right), \quad j = 0,1,\ldots,D-1 \end{aligned} \tag{7.18}$$

A trial solution will only be accepted by the selection operator if it has better fitness than current solution from which it was synthesised. If the current solution does not improve, then it will be replaced upon the next iteration, so that the process does not stagnate. The mutated vector $\boldsymbol{v}_{i,g}$ is constructed as follows:

$$\boldsymbol{v}_{i,g} = \boldsymbol{x}_{r0,g} + F \cdot \left(\boldsymbol{x}_{r1,g} - \boldsymbol{x}_{r2,g}\right) \tag{7.19}$$

These form the mutated population, $\boldsymbol{P}_{\boldsymbol{v},g} = (\boldsymbol{v}_{i,g})$, where r0, r1 and r2 and indexes to three random vectors in the current population and F is a real and positive scaling factor that is understood to be the rate at which the population evolves. Mutation is the first step in DE after initialisation. The GA performs mutation as the last step to producing a new population. The operator makes relatively small random changes to the solution vector under the guidance of some probabilistic criteria. Before a new trial solution is produced, the DE crossover operator copies a portion of the mutant vector into the current solution vector:

$$\boldsymbol{u}_{i,g} = \boldsymbol{u}_{j,i,g} = \begin{cases} v_{j,i,g} & \text{if} \left\{ rand_j(0,1) \leq Cr \text{ or } j = j_{rand} \right\} \\ x_{j,i,g} & \text{otherwise} \end{cases} \tag{7.20}$$

where $Cr \in (0,1)$ is the cross over probability that controls how much of the mutant vector is assigned, $rand_j(0,1)$ is a random number that is uniformly distributed over the interval and j_{rand} is a random index that is selected from $(0,1,\ldots,N_p-1)$. When there is high correlation between parameters, the value of Cr should be selected closer to 1. The GA crossover operator is concerned with a direct recombination of current solutions to produce new potential solutions. This can be achieved through a variety of methods [82].

The DE algorithm by Buehren [151] will be applied to fit the BW model to the transient response of the IHPA with a JH attached. This code features 10 DE variants. The classic implementation of the DE is denoted as *DE/rand/1/bin* [152]. This indicates that *random* base vectors $\boldsymbol{x}_{r0,g}$ are chosen to form the mutated population $\boldsymbol{P}_{\boldsymbol{v},g}$. In this case only *1* vector difference is added to the base vector. The crossover criteria is set to inherit parameters from the mutated vector following a *binomial* distribution. Variations on this involve choosing the base vector that has the *best* fitness value in the population or alternating between both

options of the base vector throughout the simulation, *rand-best*. Buehren [151] includes the option to add *2* vector differences and an *exponential* distribution in the cross over step. Charalampakis & Dimou [153] apply three variants of the DE to a BW identification problem. They find that the DE variants outperform variants of the GA and PSO algorithms. The best performing DE was *DE/rand-best/1/bin* and the classic DE did improve on this after a larger number of function evaluations.

The analysis of the experimental data from Chapter 5 is carried out with either *DE/rand/1/bin* or *DE/rand-best/1/bin*. The number of population members will always be equal to 10 times the number of parameters in the former case or 20 times for the latter. The stopping criteria specifies that the simulation terminates when the MSE, in Equation (7.5), is equal to unity. If this is not achieved then it would be best to stop it based on the number of completed iterations. However, each evaluation of the fitness function requires integration of the model. Initially the MATLAB solver `ode45()` was applied. A small proportion of function evaluations took a significant amount of time to complete because the ODE became stiff. This appears to be due to the scaling between the input and output. The solver was replaced with `ode15s()`. This improved the performance of the search to some extent, however some function evaluations resulted in very small time steps or solutions involving matrices that were close to singular. The mean function evaluation time is seconds long, but the overall processing time of the simulation is dominated by solutions that take significantly longer to evaluate. The maximum number of iterations is set to 20 for the classic DE and 50 for the alternative DE. Throughout the simulations it was not clear how the parameters might be bounded to avoid costly integrations. Therefore the task is to evaluate whether the experimental data is allowing the DE to tend towards a meaningful solution. The optimal solution may not be found, but some understanding of the parameter boundaries can be developed. One additional constraint, that will always be applied, is a penalty function to coerce the DE towards a solution that satisfies: $-\beta \leq \gamma \leq \beta$. The penalty function modifies the MSE once it has been computed for a particular parameter vector. The form given in Kyprianou *et al.* [154] is applied:

$$\text{MSE} = \begin{cases} \text{MSE} + 20\left(\frac{\beta+\gamma}{\beta}\right)^2 & \text{for} \quad \gamma < -\beta \\ \text{MSE} & \text{for} \quad -\beta \leq \gamma \leq \beta \\ \text{MSE} + 20\left(\frac{\beta-\gamma}{\beta}\right)^2 & \text{for} \quad \gamma > \beta \end{cases} \tag{7.21}$$

7.3.4 Application of the function generator input

Due to the generality of the BW model there is an alternative strategy to analysing its behaviour with respect to the measurements made from each JH assembly. So far it has been necessary to employ a mechanical input because the best way to isolate the axial joint behaviour is through the observation of its force-displacement hysteresis loops. However the electrical and mechanical behaviour of the HPU system cannot be separated. Low & Guo [155] employ the Bouc functional from Equation (6.8) to account for the hysteresis behaviour of a three layer piezoelectric biomorph beam. The behaviour of both the beam assembly, and its materials, is assumed to be elastic, so parameter n is set to unity. The functional is modified so that the internal state z is balanced with the product of the input voltage, V, and an effective piezoelectric coefficient, d_e. It can be expressed as:

$$\dot{z} = \left[A d_e - z^n \left(\beta sign\left(\dot{V} \cdot z \right) + \gamma \right) \right] \dot{V} \tag{7.22}$$

The most notable feature of this modification is that the hysteresis behaviour is no longer a function of the displacement of the hysteresis oscillator. Instead the time derivative of the voltage signal is required. In the case of the jointed assemblies, it will not be sensible to assume that $n = 1$, so this parameter has been retained for this analysis. The equation of motion takes the following form:

$$f\left(u^{JH}, \dot{u}^{JH}, z\right) = c\dot{u}^{JH} + \alpha k_i u^{JH} + (1-\alpha) k_i z = \alpha k_i d_e V - m\ddot{u}^{JH} \tag{7.23}$$

Figure 7.8 and shows the form of typical input signals to the monolithic and jointed assemblies. The same number of cycles was selected as the frequency was varied, so the length of the input signal varies as the resonant frequency is tracked. However, out of the entire observation window, this discrepancy is minimal. Figure 7.9 shows the voltage-displacement loops, for both systems, when the excitation voltage is 450mV pk-pk. A clearer comparison of the hysteresis loops, that are drawn by each assembly, can be shown if the observation window from the Digital Image Correlation (DIC) results is assumed. The parameters for this are given in Table 5.2 and the hysteresis loops for each assembly are shown in Figure 7.10. The majority of these results show elliptical hysteresis loops that might be better described through linear viscous damping than the BW model. The results that are obtained from testing the jointed assembly, when it is set to 8Nm through Grade 5 Titanium threads, appear to feature the sharp velocity reversal points, that are associated with the BW model. The resonant frequency tracking results, which were given in Figure 5.61, show that the res-

onance condition reduced from 19.333kHz to 18.555kHz as the voltage was increased from 100mV to 450mV. An equivalent set of tests were performed for the jointed assembly set to 8Nm through a steel stud. The frequency change in this case was 19.241kHz to 19.058kHz. The resonant frequency tracking tests of the monolithic assembly suggested that it was appropriate to assume that the piezoelectric material was operating with linear behaviour. The limited number of excitation cycles that were applied to it suggests that the temperature change was negligible. Therefore it is expected that the resonant frequency shifts are can be attributed to the behaviour of the joint.

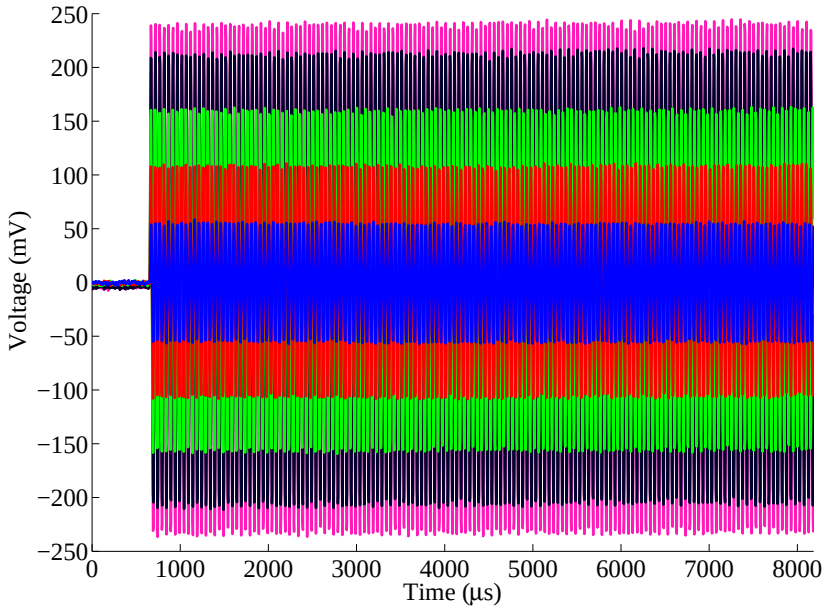

Fig. 7.8 The input voltage signals applied to the In-House Piezoelectric Actuator with the Jointed Horn attached. The joint is set to 12Nm through Grade 5 Titanium threads.

The hysteresis loops that are shown in Figure 7.10 suggest that the expected form of hysteresis behaviour cannot be observed from most of the voltage-displacement loops. The measured voltage is not the direct voltage that is applied to the piezoelectric stack. Therefore the desired hysteresis behaviour is obscured by the interaction between the piezoelectric stack and the power amplifier. This loss of information occurs because the device is not impedance matched to the amplifier, so some power is reflected backwards. There will also be phase errors due to harmonic distortion from the amplification process. The frequency settings of the function generator and the FFTs of the recorded displacements, from the jointed assemblies that were shown in Figure 5.61, agree within 15Hz for every result. It is

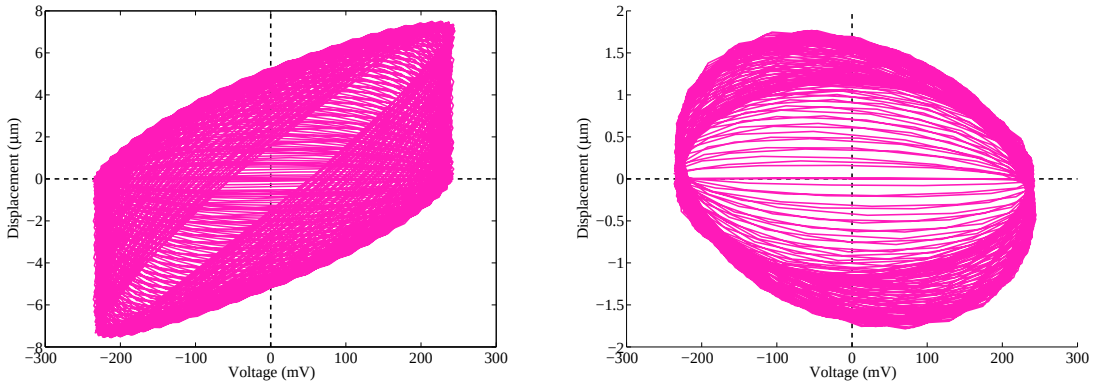

(a) Monolithic assembly

(b) Jointed assembly Ti@12Nm

Fig. 7.9 The voltage-displacement loops for the High Power Ultrasonic assemblies excited at 450mV pk-pk.

well known that piezoelectric actuators feature a strong capacitive driven reactance [156]. Therefore a matching circuit must be employed that can balance this with an inductor. A transformer is also required to step down the resistance of the actuator to match with the amplifier. The impedance results from testing the IHPA assembly are shown in Figure 4.5. These give an indication of the information that is lost by not observing the direct voltage that is applied to the piezoelectric stack. However hysteresis behaviour represents the phase lag between the input and output to the system. The experimental observations do not demonstrate how this lag is influenced by the impedance mismatch.

The results found from testing the loosest JH, with Grade 5 titanium threads, demonstrate voltage-displacement behaviour that is expected of a piezoelectric actuator. This assembly has the minimum impedance mismatch to the power amplifier. Parameter estimation through the limit cycle method, that was given in Section 6.3.3, will indicate the appropriateness of the BW model for this data. The algorithm that is given in Appendix A was applied and the BW model parameters that are given in Table 7.5 were found. The solutions are based on one cycle of vibration, which is selected within an observation window, that coincides with the high speed camera measurements. These are displayed in Figure 7.11. It was not possible to identify any solutions for the highest nominal voltage setting.

The identified solutions converged quickly for parameter $n = 2$. However only one solution was identified for $n = 1$. The analytical fit was carried out for one half of the loop and the dashed line shows the rest of the measured loop. The velocity reversal points occur when the displacement is maximum or minimum. The solutions for 300mV and 400mV do not follow

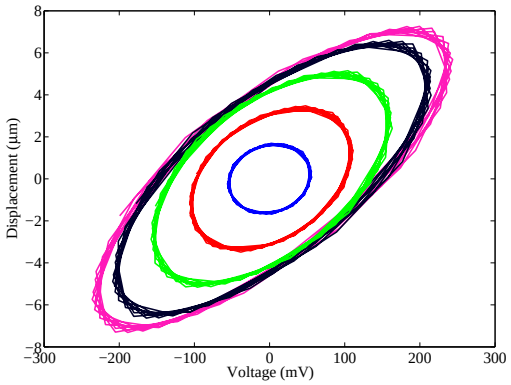

(a) Monolithic assembly

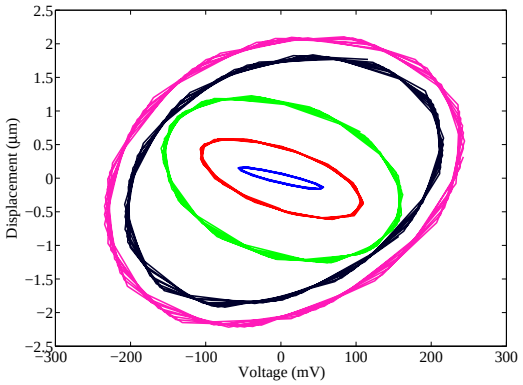

(b) Jointed assembly St@8Nm

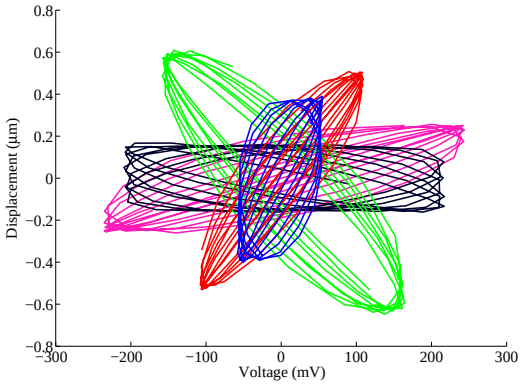

(c) Jointed assembly Ti@8Nm

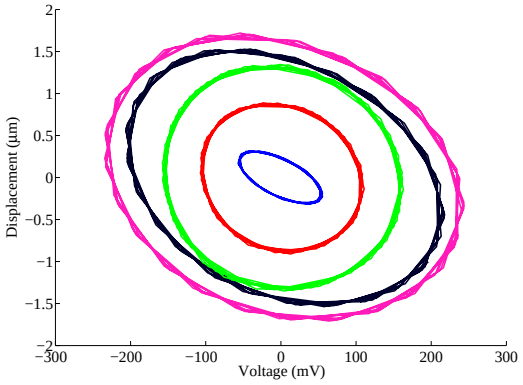

(d) Jointed assembly Ti@12Nm

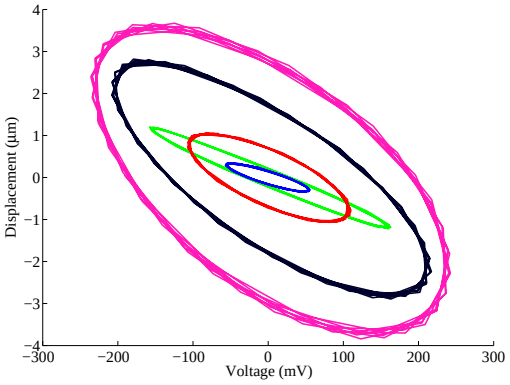

(e) Jointed assembly Ti@16Nm

Fig. 7.10 The voltage-displacement loops for the High Power Ultrasonic assemblies over the observation window of the high speed camera.

the loops well because the measurements follow an elliptical path. However these points are the most difficult to observe reliably as it would take a very high sample rate to reliably indicate their true locations. The experimental data is taken from transient measurements, so there is some drift in the hysteresis loop. For all of the results the analytical fit is always on top of the data, apart from the unloading portion of the 400mV result, which deviates clearly. The other dotted lines, that are not tracked, represent a cycle that was not part of the fitting process. A temporal fitting scheme is necessary to accurately fit to this data. The scaling of the identified parameters may be a useful guide to applying DE to the model that was given in Equations (7.23) and (7.22). If it is assumed that $A = 1$ then:

$$z_y = \pm\left(\frac{1}{\beta+\gamma}\right)^{1/n} \tag{7.24}$$

Calculating z_y for each of the results in Table 7.5, when $n = 2$, yields values within the range $0.5 - 8\times10^{-7}$. When $A = 1$, $\beta+\gamma = z_y^n$. It is assumed that $n \geq 1$, in which case $\beta+\gamma$ would be of the order $\times10^{-7}$. The quantisation rate of these parameters will need to be of this order. If $n = 2$ then this quantisation rate is of the order $\times10^{-14}$. However when Low & Guo [155] made use of the BW model they assumed that A was replaced by Ad_e. Parameter d_e is derived based on the linear theory of piezoelectricity, for a uniform electric field, through expressions related to Equations (3.15). From their detailed analysis they find a value of d_e of order $\times10^{-6}$ and identify that parameter A is of order $\times10^{-1}$. However, the applied voltage was directly observed, whereas the voltage in the current study undergoes some unknown transformation before it is applied to the piezoelectric stack. The term Ad_e will increase the complexity of the design space, which was reduced by setting $A = 1$. However sensible bounding of d_e will mean that this term is no longer redundant. It is not thought that setting A to unity will reduce the flexibility of the model. Based on the observations in Table 7.5, the assumption that d_e is of order $\times10^{-6}$, implies that β and γ might range from $\pm0.5 - 10\times10^{7}$.

The limit cycle analysis is employed to establish the parameter boundaries for the BW model in Equations (7.22) and (7.23). The parameter estimation is carried out through the classic DE by means of the Buehren [151] algorithm. The time derivative of the voltage input signal, $\dot{V}$, is found through omega differentiation. The identification is based on an observation window of the DIC results, which gives the loops in Figure 7.10c. The samples in Figure 7.11 are increased to cover 1328-1429. The inertial mass, m, is obtained from Table 7.2 and the initial stiffness, k_i, and damping coefficient, c, from the linear calibration in Table 7.4 are

Table 7.5 Parameter estimation of the Bouc-Wen model parameters from voltage displacement data through the limit cycle method

Nominal voltage (mV pk-pk)	Samples	A	β	γ	n
100	1398-1413	6.044×10^{-6}	1.025×10^{8}	-7.186×10^{7}	2
200	1398-1413	4.939×10^{-6}	4.327	-0.787	1
200	1398-1413	4.760×10^{-6}	1.403×10^{7}	-5.996×10^{6}	2
300	1398-1413	4.373×10^{-6}	1.003×10^{8}	-9.092×10^{7}	2
400	1329-1345	7.833×10^{-7}	2.812×10^{8}	-2.603×10^{8}	2

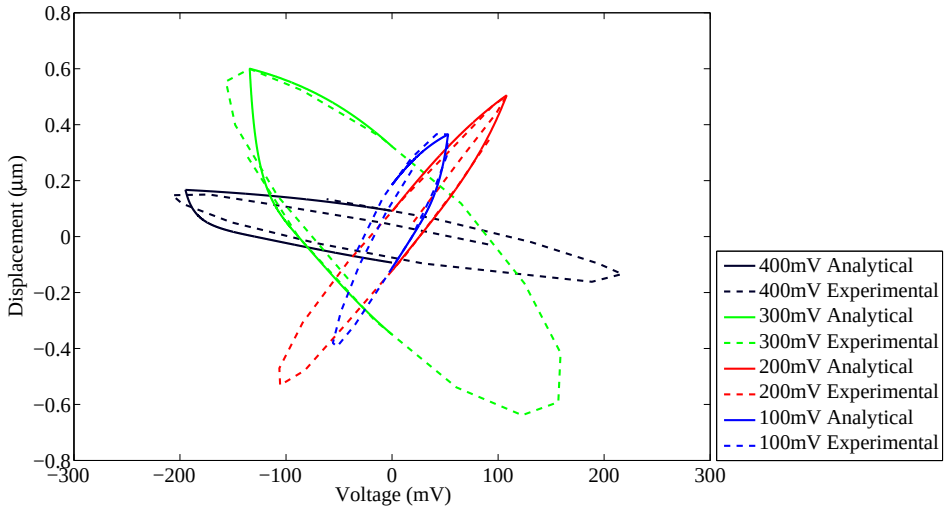

Fig. 7.11 Analytical fitting of the Bouc-Wen model to the voltage-displacement hysteresis loops of the jointed High Power Ultrasonic assembly featuring the axial joint set to 8Nm through Grade 5 Titanium threads.

assumed. The initial guesses and boundaries for the parameters are given in Table 7.6. The identification was carried out for all of the measurements of the JH with Grade 5 Titanium threads set to 8Nm.

The set of results that are associated with the 400mV setting obtained a solution that was not physical. The remaining voltage settings found an appropriate solution with similar characteristics. However due to the stiffness of the ODE, for a small proportion of parameter sets, it was difficult to run the DE for many iterations in a manageable time scale. The function evaluation history of each simulation does not suggest that the DE is converging onto the obtained solution because the population remains diverse across the parameter

Table 7.6 Parameter estimation of the Bouc-Wen model parameters from voltage-displacement data through Differential Evolution

Parameter	Initial guess	Boundaries		Quantisation	Identified values
		Lower	Upper		
d_e	4.76×10^{-6}	4.00×10^{-6}	5.00×10^{-6}	1×10^{-8}	4.02×10^{-6}
α	0.90	0	1.00	1×10^{-2}	0.38
β	1.40×10^{7}	1.00×10^{7}	2.00×10^{7}	1×10^{5}	1.90×10^{7}
γ	-6.00×10^{6}	-2.00×10^{7}	2.00×10^{7}	1×10^{5}	-2.80×10^{6}
n	2.00	1.00	3.00	1×10^{-2}	1.40

range. However the form of the transient response of the model is the same in each case. The best function evaluation value of 2.7 is found for the results associated with 300mV input. The parameter vector is given in Table 7.6. However this was discovered in the first if 6 iterations, which covered 302 function evaluations, before the time limit of three hours was exceeded. This three hours is not real clock time. When the integration becomes stiff the high loading of the computer memory significantly increases the processing cost. The investigation by Charalampakis & Dimou [153] required at least 2000 analyses to obtain the best results through the classic DE.

The response of the best solution is displayed in Figure 7.12. The BW model response clearly overshoots the displacement data before settling to a steady state. The data does not reach steady state however. The hysteresis loops are limited to the samples of the DIC observation window. The model gives an average of the measured loop. The minimisation was limited to this time window and the model matches the data very closely for these samples. Therefore the solution has been optimised sufficiently. However, for the remainder of the total time window, the model and data are always out of phase. Fitting the model for the total time window tended to result in a solution that was not physical.

Viewing the evaluation values, throughout the DE simulation, can indicate the behaviour of the parameters. These results are shown in Figure 7.13. Most of the results suggest undulating behaviour of the fitness function and suggests that more information is required to define each of the parameters. However parameter α features a clear minimum close to 0.6. Despite this, the value was found to be 0.38. Direct observation of the voltage that is directly applied to the piezoelectric stack is required. The phase errors between the input and the output of the power amplifier appear to mask the information that is required to identify the BW model successfully.

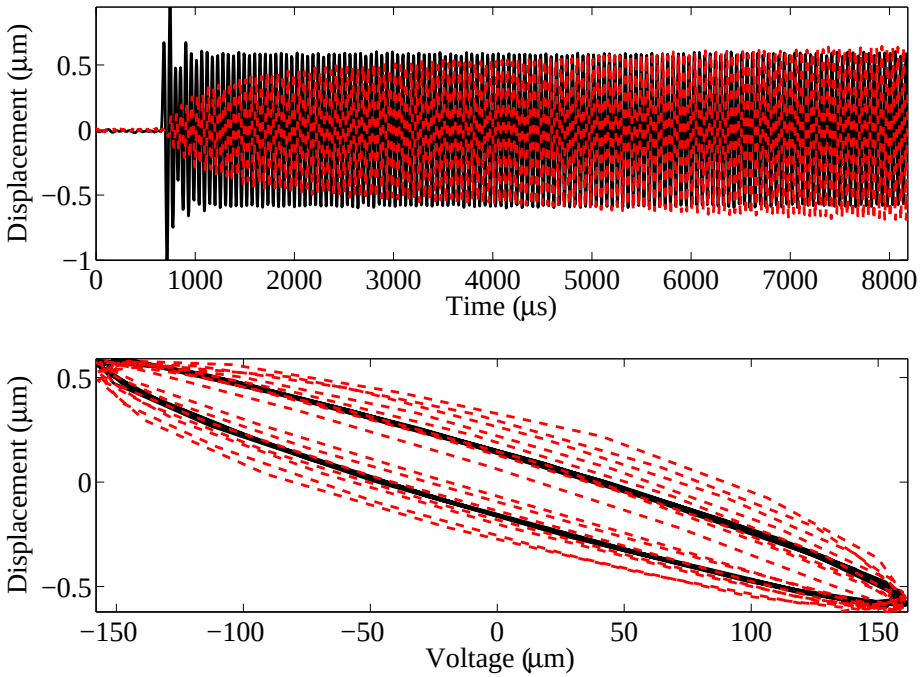

Fig. 7.12 Transient solution to the Bouc-Wen model relating the input voltage to the transient response for the Jointed Horn set to 8Nm through Grade 5 Titanium threads. The nominal input voltage was 300mV and the measured and numerical responses are denoted by (- -) and (–) respectively. The hysteresis loops are limited to the samples of the Digital Image Correlation observation window.

7.3.5 Application of the linear calibration input

The linear calibration force is obtained from the response of the IHPA with the MH attached. The force is then scaled through the impedance data in Figure 4.5 using Equation (5.16). This is the assumed input to the BW model that produces the output response that is recorded when a JH is attached to the IHPA. This would have been acceptable, if it was possible to measure this response reliably, when the jointed assembly is excited at the same frequency as the monolithic assembly. However, due to the sharp spectral behaviour of HPU devices, this is not possible. As a result, the jointed assembly was excited at a frequency that obtained a maximum output response. The frequency was swept down from the frequency of the second axial mode in Table 4.6 to locate this maximum. Therefore the assumed linear calibration force is erroneous. There is an unknown phase error between this force and the true input force developed by the jointed system. This masks the nature of the joint from the force identification scheme in Chapter 3. Under these circumstances the only

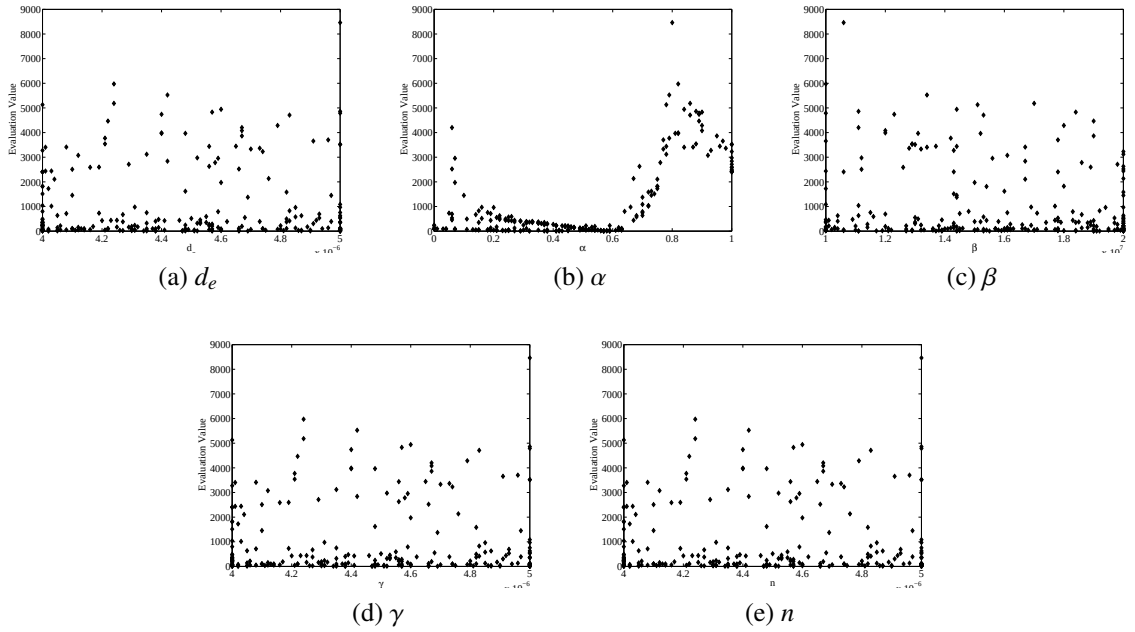

Fig. 7.13 Evaluation of the fitness function against parameter values for the Differential Evolution simulation of the Jointed Horn with Grade 5 Titanium threads set to 8Nm and excited at 300mv.

remaining option is to assume that the input signal is very noisy. It has already been shown that constraints on the BW model parameters are available to indicate a physically viable solution. Is it possible to find a solution to the parameter identification problem that is useful based on a very noisy input and a measured output?

Many of the deconvolved joint force results in Figures 5.114-5.117 and the measured voltage-displacement loops in the previous section were double loops for most of the LDV observation window. Restricting the window to a small number of samples can provide single loops. It may be possible to transform the BW description so that it can describe double loops. However the ability of the BW model to describe a single loop is still relevant to this problem. For the measured voltage-displacement loops, the only results that do not draw double loops, are obtained from the jointed assembly, that is set to 12Nm, when it is excited nominally at 100mV or 300mV. The 300mV loop is shown in Figure 7.14. The DE strategy is set to *DE/rand-best/1/bin* to encourage the best exploration of the design space and the initial guesses and parameter boundaries are set according to Table 7.7. No maximum time was set in this case and the DE run is terminated at 50 iterations. The population size was set to 80. The best value of the fitness function improved from 55 to 36 over the 50 iterations.

The response for the best parameter vector is shown in Figure 7.15. It is qualitatively different to the measured response and the hysteresis loop exhibits chaotic behaviour. The fitting of the response over the DIC observation time window does appear to be minimised within the boundaries of the simulation. The evaluation values are given against each parameter in Figure 7.16. The most extreme values have been omitted in order to best display whether each parameter displays clear minima. The distribution of the α fitness values agrees well with the obtained solution. Small values of n are favoured by the DE as the design space for values greater than 1.2 is relatively unexplored. The values of β and γ have been attempted reasonably uniformly between their boundaries. This suggests that the data does not contain enough information to estimate these parameters. The DE simulation is problematic because the BW model becomes a stiff system of differential equations for some parameter vectors. The simulation time is dominated by the solution time, or failure, on these occasions. Heine [157] asserted that the computation time to solve the Bouc-Wen-Baber-Noori model was greatly reduced if the force and displacement were of the same order of magnitude. The hysteresis loops were measured as force in (kN) against displacement in (mm). For a HPU device the displacement will always be of the order of (μm) and the force might be hundreds of (kN). Possibly the BW system would be less stiff to integration if the force was of the order of (MN).

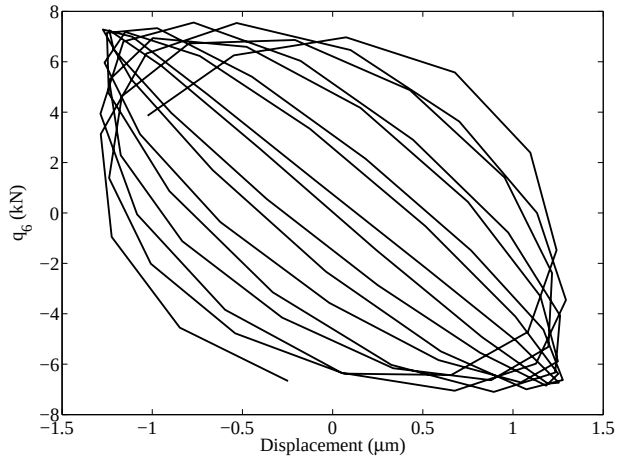

Fig. 7.14 The linear calibration force to the In-House Piezoelectric Actuator against its response with the Jointed Horn set 12Nm attached.

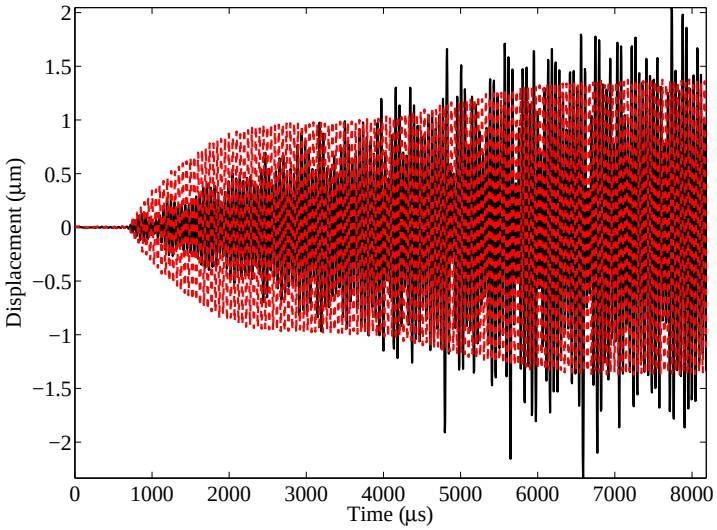

(a) Full observation window

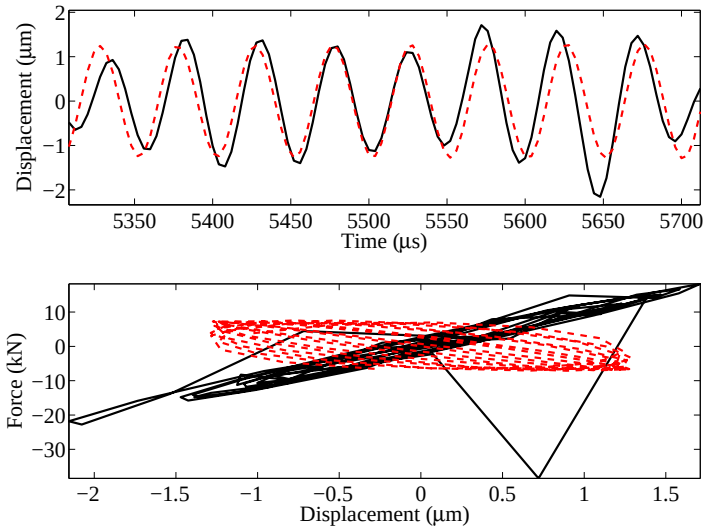

(b) Digital Image Correlation observation window

Fig. 7.15 Transient solution to the Bouc-Wen model relating the linear calibration force to the transient response for the Jointed Horn set to 12Nm through Grade 5 Titanium threads. The nominal input voltage was 300mV and the measured and numerical responses are denoted by (- -) and (–) respectively. The hysteresis loops show the measured response against the assumed input force (- -) with the simulated response against the simulated restoring force (–).

Table 7.7 Parameter estimation of the Bouc-Wen model parameters from linear calibration force-displacement data through Differential Evolution

Parameter	Initial guess	Boundaries		Quantisation	Identified values
		Lower	Upper		
α	0.460	0	1	1×10^{-3}	0.661
β	1.7400×10^{7}	0	1.0000×10^{9}	1×10^{3}	8.88443×10^{8}
γ	1.6200×10^{7}	-1.0000×10^{9}	1.0000×10^{9}	1×10^{3}	-8.70903×10^{8}
n	1.000	1.000	3.000	1×10^{-3}	1.060

7.4 Application of a synthesised input

It is assumed that the input should take the form of the linear calibration force. The frequency of this signal must be adjusted to the match the frequency of excitation that was applied to the jointed system. This can be achieved by manipulating the FFT of the signal, but this will reduce the number of samples in the signal. Instead a signal is synthesised as a modulated sine wave. This takes the form:

$$\boldsymbol{q} = \left[\mathbf{0} \quad C\,sin(\omega_p \boldsymbol{T})\right] \circ sin(\omega_m \boldsymbol{T}) \tag{7.25}$$

where $\mathbf{0}$ is a vector of 163 zeros that represents the time before the function generator signal is triggered. C is the maximum amplitude of the linear calibration force that was deconvolved from the first 2047 samples of the response of the IHPA with the MH attached. The damped resonant frequency ω_p is the frequency at which the maximum response of the JH assembly was found through adjusting the function generator. The sample times are held in the vector $\boldsymbol{T}$ from 0 to $2047\times4\mu$s and ω_m is the frequency of the modulation signal. The Hadamard product is denoted by $\circ$. This is known as Element-wise multiplication in MATLAB and is applied so that each sample of the sine wave is scaled by the equivalent sample of the modulation signal. Following Section 7.2.2, the cost between the synthesised signal and the linear calibration force is computed as a nonlinear time warp function. The value of ω_m is adjusted until the cost is minimised through the MATLAB function `fminbnd()`. The search is constrained $\in (1,100)$Hz. The synthesised signal and the linear calibration signal are given in Figure 7.17 for the JH set to 12Nm at 100mV nominal excitation.

With the assumed input-output data, the analysis of the previous section is repeated. However, the initial guess in Table 7.7, is replaced with the values that were identified in the

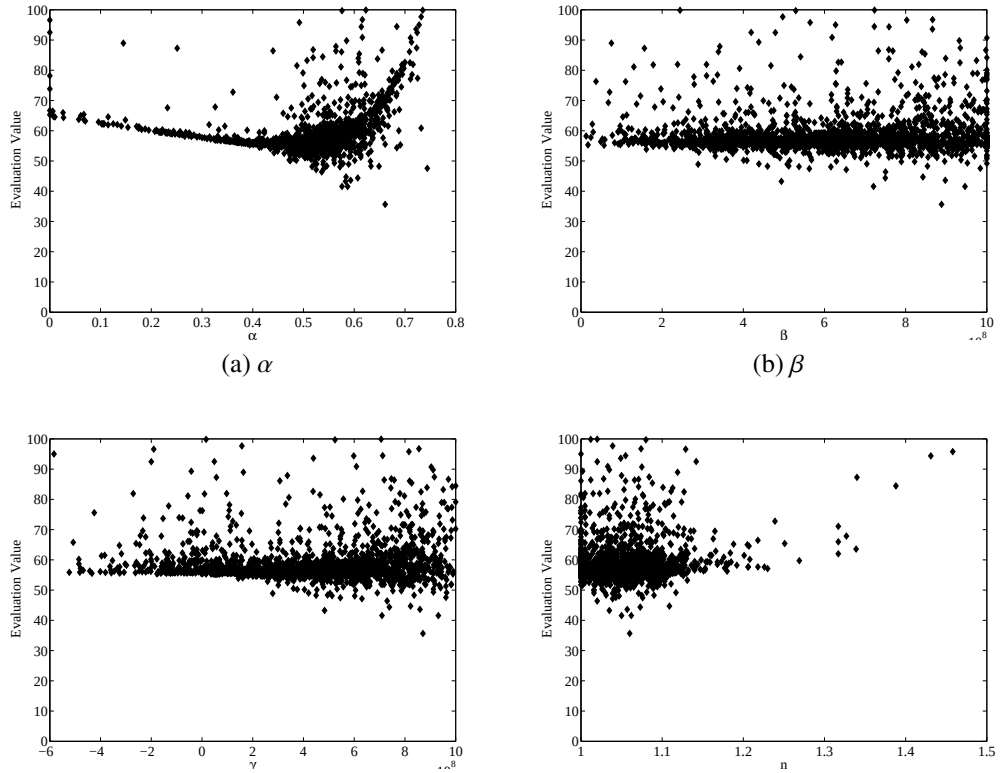

(a) α (b) β

(c) γ (d) n

Fig. 7.16 Evaluation of the fitness function against parameter values for the Differential Evolution simulation of the Jointed Horn with Grade 5 Titanium threads set to 12Nm and excited at 300mv.

last section. The fitness function is computed from the first 2047 samples instead of being limited to the DIC observation window. The best fitness value improves from 55 to 35 over 50 iterations. The following solution vector is obtained: $\alpha = 0.937$, $\beta = 4.97929 \times 10^8$, $\gamma = -7.35116 \times 10^8$, $n = 1.230$. This yields the solution given in Figure 7.18. This shows that the BW model can produce a response signal that mimics the envelope of the response data. However, instead of following the measured response in overshooting the steady state portion of the signal, the simulated response undershoots. A closer look at the simulated response shows that it only fits the measured response intermittently. Without reliable DIC measurements, or successful force deconvolution for the joint, it is not possible to verify the BW simulated hysteresis loop. Figure 7.19 maps the evaluation values of the fitness function against the parameter values. Parameter α shows a clear minimum at 0.93 and this matches to the best solution vector. There is not a clear minimum in the case of β or γ, so it is not possible to say that the best solution has optimised these parameters and this is due to the

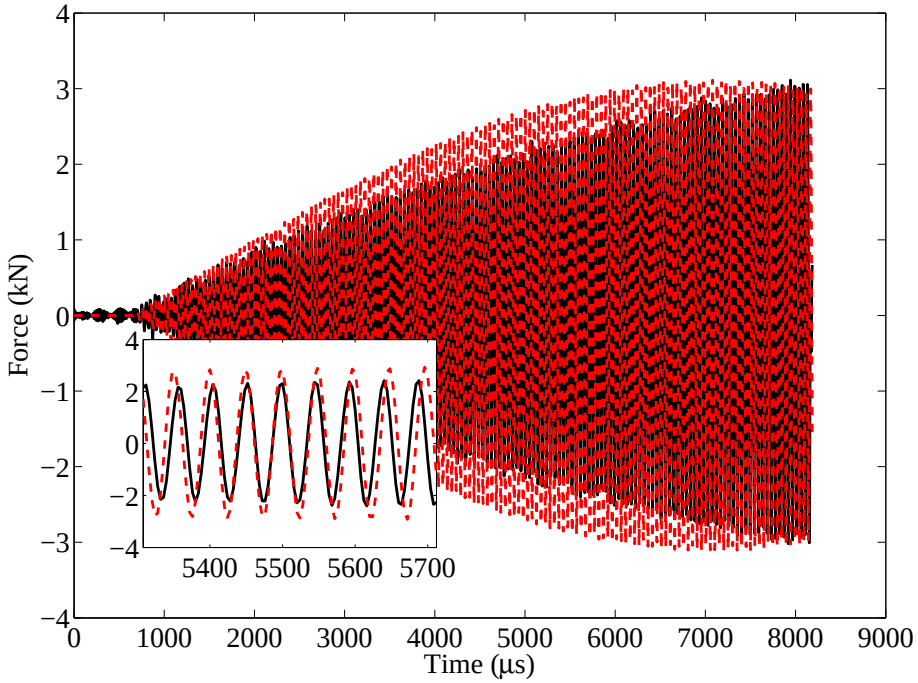

Fig. 7.17 The synthesised input (- -) against the linear calibration force (–). The inset matches to the observation window of the Digital Image Correlation.

error in assuming the synthesised input. The search for parameter n was clearly restricted to a very limited range and the input-output data does not lead to a reliable minimum.

7.5 Frequency sweeps

The frequency behaviour of an HPU device, around its operating mode, is critical to its application because the frequency of the excitation signal will continually be adjusted to maximise the output of the device. As the excitation frequency is swept upwards, or downwards, it may drive the system to instability as a result of overhang frequency behaviour. In Chapter 6 it was demonstrated that the BW model can mimic this overhang behaviour in the same way that the Duffing equation was employed by Lim [5] in his open loop linearisation scheme. The BW model improves on this because it is capable of reproducing physical hysteresis behaviour, as shown in Oldfield [24]. It is clear that the axial joint in a HPU device modifies its impedance characteristics significantly. It has not been possible to isolate the nature of the hysteresis at this joint. However regular operation of the device will require

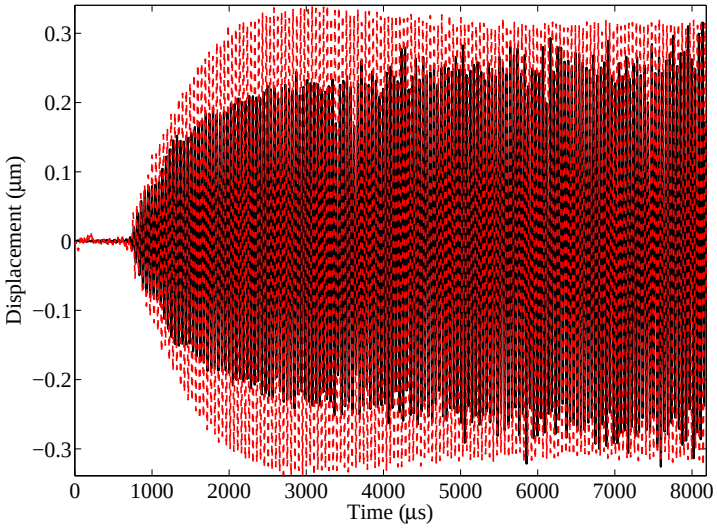

(a) Full observation window

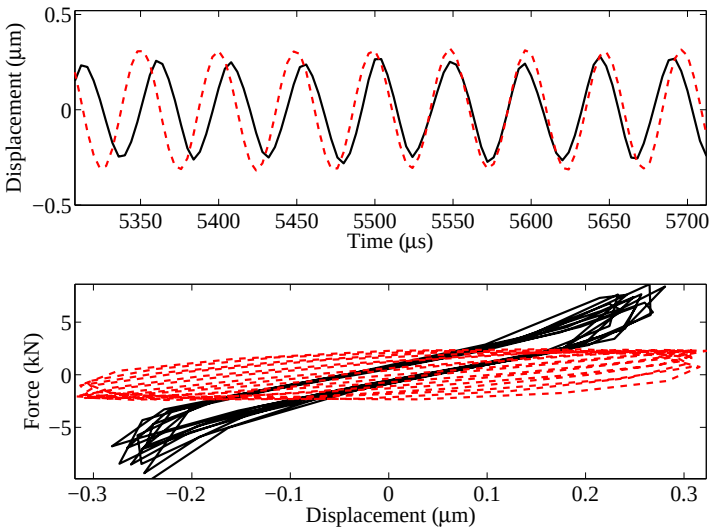

(b) Digital Image Correlation observation window

Fig. 7.18 Transient solution to the Bouc-Wen model relating the synthesised input force to the transient response of the Jointed Horn set to 12Nm through Grade 5 Titanium threads. The nominal input voltage was 100mV and the measured and numerical responses are denoted by (- -) and (−) respectively. The hysteresis loops show the measured response against the sythesised input force (- -) with the simulated response against the simulated restoring force (−).

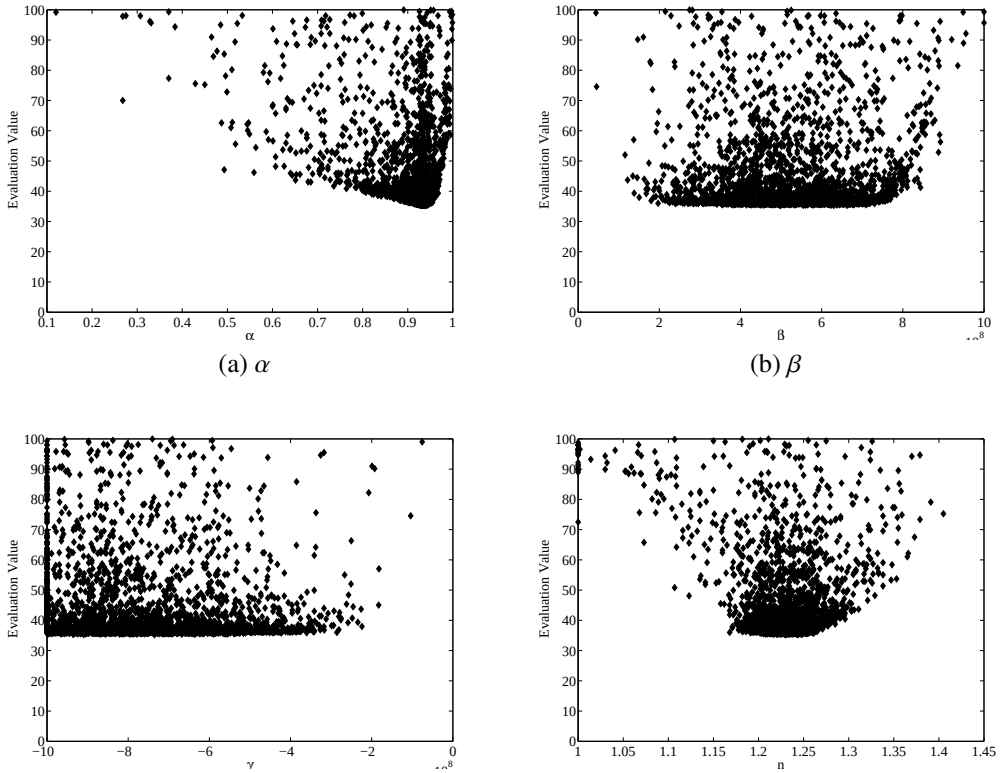

(a) α (b) β

(c) γ (d) n

Fig. 7.19 Evaluation of the fitness function against parameter values for the Differential Evolution simulation of the Jointed Horn with Grade 5 Titanium threads set to 12Nm and excited at 100mv.

that the voltage-displacement hysteresis behaviour is captured. The real time voltage that is applied to the stack must be captured and the output at its radiating surface must be measured. The BW model represents a concise way to relate these two signals and a suitable description will give access to the frequency behaviour of the device at low computational cost.

The current set of experiments did not capture the direct voltage that was applied to the piezoelectric stack. The function generator output was recorded. If the power amplifier does not modify this signal significantly then it should still be possible to capture the voltage-displacement relationship of the HPU device with the BW model. The BW model that was identified in Section 7.3.4 is adopted. This gave a good estimate of the hysteresis behaviour over the DIC observation window. However there was no evidence to suggest that the parameters β and γ had been optimised. The tests of the IHPA with the 8Nm JH, with Grade 5 Titanium threads, demonstrated that the resonance condition tended to reduce

as the excitation voltage was increased. Therefore it is expected that an appropriate BW model should produce a softening stiffness overhang behaviour. The BW model in Table 7.6 is excited by a sinusoidal input:

$$q = C sin(\omega_n T) \tag{7.26}$$

where $C = 164$mV is the maximum amplitude of the measured voltage from the function generator, ω_n is a discrete frequency $\in (5,45) \cdot 2\pi \times 10^3 \text{rads}^{-1}$, which is sampled every $40.0404 \cdot 2\pi \cdot \text{rads}^{-1}$, and T is time. The BW model is solved using `ode15s()`, for each value of ω_n, to find the displacement response of the model. The samples of the DIC observation window are extracted and a Hann window is applied before the FFT is taken. The frequency at which the FFT obtains its maximum is selected. This is repeated for every ω_n, in the range, to produce the frequency sweep that is displayed in Figure 7.20. The frequency sweep displays a peak at a much lower frequency than expected, so the BW description is not successful. Slight hardening overhang behaviour is exhibited. The frequency sweep also exhibits sidebands suggesting that more samples are required for the FFT of the response.

The frequency sweep is performed for the model that was identified, with the linear calibration input applied, in Table 7.7. The constant for the sinusoidal input is the maximum value of the linear calibration force: $C = 8$kN. The frequency sweep is shown in Figure 7.21 and no clear overhang behaviour is demonstrated. The displacement response of this model did not match the experimental response as well as the previous example. The BW model cannot form a relationship between the estimated input to the linear calibration model and the response of the jointed system. This relationship does not relate to the measured response because the excitation frequency was adjusted to match the resonance condition of the jointed system.

The synthesised input in Section 7.4 was the best guess of the mechanical input produced by the piezoelectric stack from limited information. The BW model, that was identified, produced a response that agreed qualitatively better with the measured response than the previous examples. The nature of the hysteresis loop deviated from the ellipse shape. This is expected for jointed systems. However the input-output data did not extract a clear trend in the values of β and γ as desired. The frequency sweep of this model is shown in Figure 7.22 and demonstrates hardening overhang behaviour. This type of behaviour would be expected in the response of a bar horn, as part of an HPU device that is excited at high

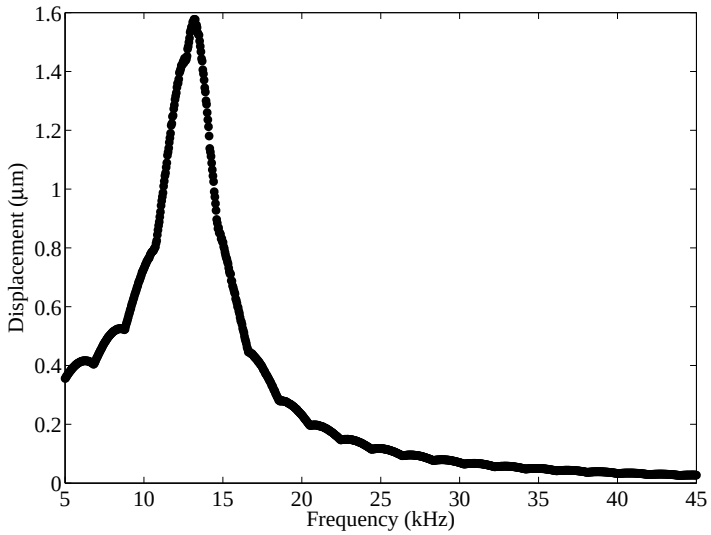

Fig. 7.20 Frequency sweep of the Bouc-Wen model derived from the application of the function generator input.

power levels [6]. It does not exhibit the second harmonics that are expected of the axial joint.

7.6 Discussion

It is clear that a lack of understanding of the input to the jointed HPU systems limits the application of the BW model. The BW model that was identified, when the function generator input was applied, did not feature a primary resonance that was close to the resonance of the experimental data. Hardening instead of softening overhang behaviour was identified. However, resonance tracking had already demonstrated that the resonance softened as the excitation power was increased. The model that was identified, as a result of applying the linear calibration input, was unstable and did not match to any expected joint behaviour. The best estimation of a synthesised input to a jointed system suggested hardening overhang behaviour and also featured unstable regions.

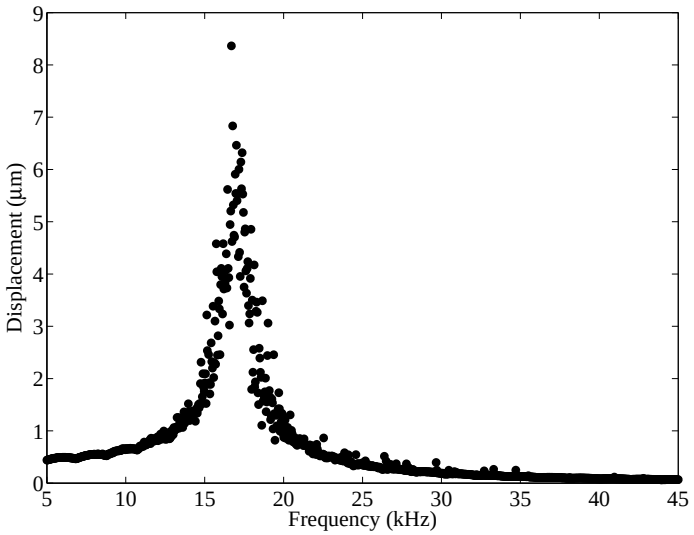

Fig. 7.21 Frequency sweep of the Bouc-Wen model derived from the application of the linear calibration force.

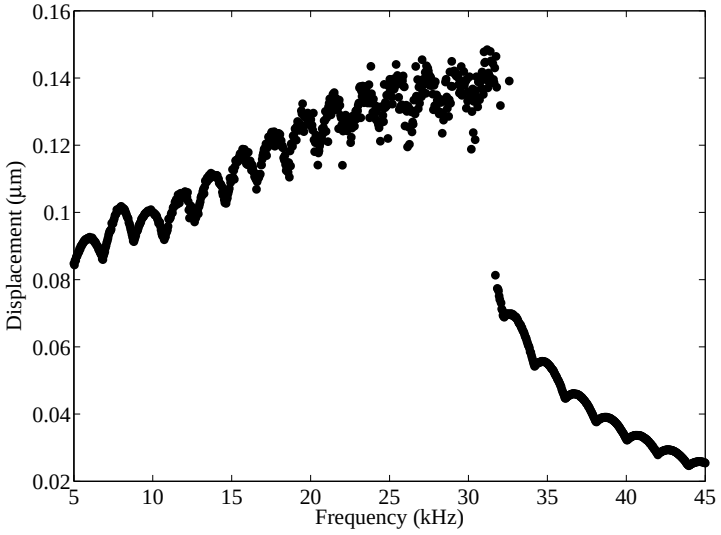

Fig. 7.22 Frequency sweep of the Bouc-Wen model derived from the application of the synthesised input.

7.7 Outcomes

The electromechanical nature of HPU devices makes it very difficult to isolate the behaviour of an axial joint through a comparison to an equivalent monolithic system. The power draw of a monolithic system is significantly greater than the jointed system when impedance

matching circuitry, between the device and the power amplifier, is not employed. The resonance condition of the monolithic system, will be reduced in the equivalent jointed system, due to the loss of stiffness at the bearing surface. The power spectrum analysis demonstrated that the jointed system must be excited close to this resonance in order to be observable above the noise floor. The frequency response of the monolithic system is much sharper and this means that it cannot be excited at the same frequency as the resonance of the jointed system.

Q factors were calculated from power spectrums of the monolithic and jointed HPU assemblies. This gave an estimate of the damping ratio for each monolithic system to form a linear calibration model. The resonance tracking results were employed to find the stiffness, but the solution of each Mass-Spring-Damper (MSD) model was not physically realistic for the HPU device. The damping ratios were corrected under the assumption that this would account for the erroneous amplitude of the estimated input signals. The Mean Squared Error (MSE) was calculated for each set of input-output data, that was applied to the MSD model, as the damping ratio was modified. This demonstrated that the estimated input signals did not contain the information required to estimate the damping ratio. The best approximation of the damping ratio was found by applying a Dynamic Time Warping scheme to each MSD model. This produced a reasonable fit, so that the linear calibration models could be employed as a starting point to identifying the Bouc-Wen (BW) model description of a jointed HPU system.

The linear calibration force is scaled before it is applied to a jointed HPU system to account for the power that is reflected due to the impedance mismatch between the device and the power amplifier. Before carrying out the identification, of the BW model, it is important to restrict its design space to promote good physical and mathematical properties. The following constraints were applied to the parameters: $A = 1$, $0 < \alpha < 1$, $\beta > 0$, $-\beta \leq \gamma \leq \beta$, $n \geq 1$. This implies that any identified models will be open loop stable and consistent with the asymptotic motion of physical systems. Signals will have derivatives that are continuous and the system will not produce energy. Also the number of potential models is reduced by fixing A.

The BW models are identified through Differential Evolution (DE), which requires many potential models to be integrated and compared through the MSE fitness function. The DE simulation time is dominated by occasions where the parameter vector results in a stiff set of BW model equations. It is likely that this is due to the scaling of the input and the output signals and would be improved if these were of the same order. As a result, the

Matlab solver `ode15s()` was applied. There is uncertainty in the correct input that should be applied to the BW model to identify it from the response of a jointed HPU system. Three inputs are considered, none of which features all of the requirements of the input behaviour to the jointed system. The voltage that was produced by the function generator was recorded before it is amplified linearly and applied to the piezoelectric stack. It is possible to make a reasonable estimate of the amplitude of the voltage at the piezoelectric stack, however the phase error that is introduced during the amplification is unknown.

The BW model is modified for the voltage-displacement relationship, so that the hysteresis functional is in terms of the time derivative of the voltage. The measured voltage-displacement loops appear as double loops over the transient response of the jointed system. Over the observation window of the Digital Image Correlation (DIC) measurements it is possible to isolate elliptical loops. The loops of the system featuring the jointed horn, set to 8Nm through Grade 5 Titanium threads, represents the most intuitive data for a BW model fit. The analytical fitting of the Bouc functional to this data produced reasonable solutions for the 100mV - 400mV results when $n = 2$. The value of A relates to a value of d_e that is a reasonable equivalent constant for the piezoelectric material. This is based on the study by Low & Guo [155]. The analytical fitting is employed as a guide to setting the parameter boundaries of the DE analysis. A suitable model is identified, by limiting the MSE, to consider the observation window that is associated with the DIC measurements. However the identified model does not mimic the initial portion of the response of the jointed system. The BW model produces a hysteresis loop that gives the average hysteresis behaviour over the limited time window. The evaluation values of the fitness function, during the DE analysis, does not suggest any clear minimum behaviour occurring in any of the parameters other than α. It was expected that the frequency sweep behaviour of this model would exhibit softening overhang behaviour because as the input voltage was increased, to each jointed system, the resonance condition tended to diminish in frequency. The BW model from the voltage-displacement loop suggests hardening overhang behaviour. However the resonance of the model is much lower in frequency than the tests of the jointed system demonstrated. These results are shown from the FFTs of the measured signals in Figure 5.61.

The linear calibration input is scaled, for the expected power draw of the jointed system, and is then applied to the BW model. The DE identification process is applied to minimise the MSE between the measured and predicted outputs. There will be a significant phase error in the input signal that descends from the loss of stiffness in the linear calibration model as a joint is introduced. The identified model features a chaotic response. However the error in

the model has been minimised over the DIC observation window. Again, the only clear minimum in the parameters is found for α. The frequency sweep of the model suggests unstable behaviour around the resonance. To correct the phase error of the linear calibration force a synthetic input is adopted. The model for this input is an amplitude modulated sine wave. The modulation frequency is computed by minimising the MSE between the linear calibration force and the synthetic input as the modulation frequency is adjusted. The BW model, that is identified from this input, produces a response that is smaller and noisier in amplitude than the measured response. This only matches intermittently over the DIC observation window. The hysteresis loop of the model appears to be reasonable, but without better DIC results, it is not possible to verify this result. The frequency sweep of this model features significant hardening overhang behaviour, but it also undulates unrealistically.

It is clear that a better definition of the input to the jointed systems is required to make progress with this analysis. The DIC results must also be improved if any results are to be verified. Assuming a voltage-displacement form of the BW model is more intuitive for HPU devices. However a mechanical input is required to truly isolate the behaviour of an axial joint.

Chapter 8

Conclusions and future work

8.1 Conclusions

The open loop control of High Power Ultrasonic (HPU) devices requires understanding of the nonlinear behaviour of its serially connected subsystems. The nature of these subsystems depends on the constitutive behaviour of axial screwed threaded joints and piezoelectric materials. It is well documented that softening frequency overhang behaviour descends from the latter during high voltage excitation. Detailed study of the axial joint in an HPU device is less prevalent in comparison. The axial joints are key to the operation of the device because the piezoelectric stack must be held under a prestress in order to do meaningful work with its output. The applicability of this piezoelectric actuator depends on the attachment, or removal, of a variety of ultrasonic horns and tools, which are connected serially through axial joints.

Discussions of the axial joint in an HPU device were summarised in the literature review. This introduced the idea of the critical stress amplitude at the bearing surface. This represented a trade-off where encouraging the energy dissipation at the axial joint, through loosening, will sharply diminish the relative amplitude of the response to the measurement noise floor. Studies where frequency sweeps of the device had been performed, for changing joint tightness, suggested that loosening contributed to softening overhang behaviour. This increased the bandwidth of the instability region due to a hysteresis loop in the frequency response.

Studies of axial joints, that are of the type found in HPU devices, are not common in the

bolted joint literature. Instead the expected vibration behaviour and modelling schemes were assumed from studies of bolted lap joints. Discussion of these interface suggested a variety of physical mechanisms that determine their dynamics. Slap processes appeared to be most relevant to axial joint behaviour. These occur at high vibration amplitudes when parts of the interface experience dynamic contact. As a result, energy is transferred to higher frequencies than those that excited the slap process. In the case of HPU devices, they will not resonate if there is significant play in the joint, so the slap process occurs between the asperities of the surfaces in contact. It is likely that a 3D constitutive model of this contact behaviour would be obtrusively complex for dynamic analysis. A summary of the literature on phenomenological models for friction suggested that adopting one of these could give insight to the dynamic behaviour of the axial joint and would represent a significant reduction in the analysis cost. The Bouc-Wen (BW) model is adopted for its versatility. Observation of the force-displacement hysteresis loop at the axial joint is required to identify this model. However the axial joint is inaccessible to direct measurement and force sensors are not available, to respond linearly, at the operating frequency of the HPU device. A number of joint or force identification schemes are detailed in the bolted joint literature based on frequency or impulse response models. These appear to offer the most likely route to the data that is desired. It is suggested that the best lead on developing such a method is to apply the following concept. A set of identical test assemblies must be produced that can be described by a linear model over some operating range. Each of these are named the monolithic assembly. When one of these is modified, to introduce an axial joint, it becomes a jointed assembly. The difference in the response of this system and the monolithic system yields a signal. The behaviour of the joint is estimated from this signal by means of deconvolution through the linear model.

The Distributed Transfer Function Method (DTFM) is introduced as a framework to developing a hybrid analytical-experimental scheme for estimation of the axial joint force. This is selected over the Fast Fourier Transform (FFT) based Spectral Element Method (SEM) because it has access to the Transcendental Eigenvalue Problem (TEP). This can be exploited for the purpose of updating model parameters. This is important because other components in the assembly are modified by prestress of unknown magnitude and distribution. Modification of the axial joint, that is of interest, will change the impedance behaviour of the HPU device. This represents a significant reduction in the power draw of a jointed assembly when compared to the equivalent monolithic assembly. Discussion of a piezoelectric rod element is included to provide an approximation of the force that is produced by the piezoelectric stack for an applied voltage. This gives an idea of how a change of impedance modifies

the force that is output at the front of the stack. Overall the DTFM framework cannot simulate piezoelectric behaviour because it can only make use of one equation of motion to describe a waveguide. Indirect estimation of the joint force will always be incomplete. The Truncated Singular Value Decomposition (TSVD) and Tikhonov regularisation methods are introduced as a means to arriving at a stable solution from the ill-posed problem.

Jointed Horns (JH) and a Monolithic Horn (MH) are manufactured and attached to a Commercial Piezoelectric Actuator (CPA) or an In-House manufactured Piezoelectric Actuator (IHPA). Electrical impedance analysis demonstrates that four resonances are found in the 0-40kHz range. The resonances of the JH assembly are adjusted, towards those of the MH assembly, as the joint is tightened. Experimental Modal Analysis (EMA) confirms that these resonances are dominated by axial motion. This yields the one dimensional axial mode shapes of the system. The linear calibration models are formed to describe the behaviour of the monolithic assemblies. These are the CPA or the IHPA with the MH attached. The DTFM model of each assembly features unknown parameters. These are estimated through a minimisation between the eigenvalues of the model and the natural frequencies that were found through EMA. This is carried out through the Genetic Algorithm (GA), however this does not give any insight to the nature of the unknown parameters because of the multitude of available solutions. Despite this, the DTFM and measured mode shapes give a reasonable comparison of the node locations for each axial mode. Simulations of the indirect force estimation scheme demonstrates that errors in the parameters of the linear model can lead to significant errors in the estimations after regularisation. The introduction of a retarding force that is proportional to velocity was not reasonable in the scheme.

Experimental tests of the force estimation scheme are required to determine whether reasonable solutions can be obtained despite the simplifications required for the DTFM model. These solutions must be verified through an independent method before the scheme is considered acceptable. Digital Image Correlation (DIC) is adopted for this purpose. The data for both methods must be acquired simultaneously to make the comparison. The DIC and Laser Doppler Vibrometer (LDV) derived displacements agree well in phase, but not in amplitude. It is likely that this is due to projection errors, which were exasperated by the close working distance of the camera lens. This was necessary to focus the measurement area so that it made full use of the resolution of the high speed camera. The DIC strain field is derived from the displacement field through Finite Elements (FE) that deform according to a bicubic interpolated surface. The average axial force is recovered from the cross sectional stiffness at the axial location of the LDV measurement. The DIC hysteresis loops are

very noisy and do not form the closed force-displacement loops that are required for the identification of the axial joint model. The results are noisier for the IPHA jointed assemblies because they do not develop sufficient response due to impedance mismatch with the power amplifier. The LDV displacement measurements featured low and high harmonics. However due to the impedance mismatch it was not possible to determine whether loosening the joint contributed to second harmonics. These may have been generated through the amplification process.

The input force to the HPU device is deconvolved from the linear calibration model and the measurement of the monolithic assembly at one or more locations. Reasonable solutions are obtained when regularisation is applied. The CPA solutions, that are derived from different response locations, are inconsistent and significantly modulated. This suggests that errors in updating the linear calibration model, or its formulation, mask the input. The IHPA results were more consistent for the different response combinations. If the obtained linear calibration forces were applied, to the jointed systems, then they would erroneous in phase, and amplitude, due to the impedance of the jointed system relative to the monolithic assembly. The amplitude is scaled, through impedance measurements of both systems, by assuming capacitive behaviour of the piezoelectric stack. The phase of the input signal to the jointed system cannot be obtained. For the IHPA jointed assemblies the joint force is estimated directly from the difference in the response of the monolithic and equivalent jointed systems. It is also estimated by scaling the linear calibration force and reapplying it to the linear calibration model. The obtained hysteresis loops appear to be reasonable, but are possibly dominated by the linear calibration signal. Without improved DIC results it is not possible to verify these loops.

The BW model features a hysteresis functional that is defined through 4 parameters that are not explicitly related to physical measurements. This functional is introduced into a Mass-Spring-Damper (MSD) through an additional parameter. This parameter detunes the stiffness of the MSD to introduce a percentage contribution of a hysteretic spring force to its nonhysteretic spring force. A set of MATLAB functions is produced to fit the branches of the Bouc functional to experimental data through transcendental equations that are derived analytically for $n = 1$ or $n = 2$. It is determined that the DIC derived hysteresis loops are not consistent with the Bouc functional. To gain further understanding of the parameters a sensitivity analysis of the BW model is completed. This demonstrates the behaviour of the hysteresis loop as each of the parameters are changed one at a time. The model is also excited to steady state, for a range of discrete frequencies, to reveal its frequency response.

This is repeated to demonstrate the influence of each of the parameters on the overhang frequency behaviour. Parameter A defines the initial stiffness of the hysteresis loop and determines the scale of the loop or frequency response when $\beta + \gamma = 1$. The ratio β:γ determines the bandwidth of the region of hysteresis in the frequency response. As parameter n is increased, the BW model tends towards a bilinear oscillator. Parameter α modifies the location of the resonance.

The power spectrum analysis of the test assemblies demonstrates that it is not possible to assume the same input signal, to both the monolithic and jointed assemblies, and achieve measurements of the response above the noise floor of the LDV. The damping ratios of the IHPA, with the MH attached, are estimated from the Q-factor. This resonance is then described through a MSD system. However the response of this system is not physically realistic. The input was deconvolved from the linear calibration model and the response of the monolithic assembly. No damping was assumed in this estimation. The damping ratio is corrected so that the linear calibration force can be assumed. The Mean Squared Error (MSE) cannot be applied to estimate the damping ratio because the input was formed as a minimum L-2 norm solution. Therefore Dynamic Time Warping (DTW) is applied to minimise the time warping between the measured response and the model response. This gives a damping ratio that is reasonable, but does not minimise the amplitude error.

A review of the BW model literature yields parameter constrains that simplify the design space from which solutions to the model will be identified. The identification requires a zeroth order iterative solver. Differential Evolution (DE) is applied to the experimental data for the MSE fitness function. A modified form of the BW model is considered that makes it amenable to voltage-displacement loops. Most of the voltage-displacement data draws elliptical loops. The Jointed Horn (JH), which is set to 8Nm through Grade 5 Titanium threads, forms loops that are fitted by the analytical solutions to the Bouc functional when $n = 2$. These results are applied to form boundaries on β and γ. Either parameter A or $\beta + \gamma$ should be constrained well to restrict the search of the design space. Applying DE to identify the BW model parameters is very costly because the search is dominated by parameter vectors that result in a stiff system of equations. The minimisation does not progress well when it is based on the entire observation of the transient data. Instead the fitness function is computed for the samples that coincide with the DIC observation window. The identified BW model does not perform well for the initial transient portion of the measured response, however its steady state response gives a reasonable average of the voltage-displacement loop over the DIC observation window. The unmodified form of the BW model does not

provide a relationship between the linear calibration force and the response of a jointed HPU assembly. However the DE is successful in minimising the MSE over the DIC measurement window. The best guess of the input to a jointed assembly is formed by assuming a sine wave with a modulation frequency that produces a signal that has a minimal MSE with the linear calibration force. The BW model that is identified does not match the measured response at the beginning of the observation window, but its envelope is more reasonable than the previous example. However this could be a result of the form of the synthesised input. The model does not produce a signal that matches to the phase of the measured response. The hysteresis loop appears to be sensible, but the DIC data is not good enough for any verification. The pattern of the DE search for each of the inputs follows a similar pattern. A clear minimum can be found for α, but neither β or γ demonstrate a minimum to suggest that the identified values are meaningful. The frequency sweeps of each of the models feature regions of instability where hardening overhang behaviour is exhibited.

8.2 Future work

The study of an axial joint in a High Power Ultrasonic (HPU) system consists of a series of sub-problems. The indirect estimation of the joint force depends on the limitations that are inherited from these interrelated problems. Successful force estimation is required to identify a model of the dynamic behaviour of the axial joint. However this must be preceded by an improved definition of the input to the jointed system.

The literature review should be developed further to consider studies of bolted joints that follow a Bayesian framework. A discussion of these methods towards structural dynamics is given in Yuen [66] and a number of studies that follow these principles have been summarised in Ibrahim & Petit [35]. Implementation of these ideas will avoid the naive estimations that can be recovered from ill-posed inverse problems.

The form of the Distributed Transfer Function Method (DTFM) that was adopted could not be applied to describe higher order waveguide theories or realistic piezoelectric behaviour. It can be extended to describe 2D material behaviour through the interpolation between 1D strip displacements, Yang & Zhou [158]. Another approach towards this is the Finite Difference DTFM from Yang & Yang [159]. These would improve the description of the HPU assemblies, which have symmetry around their longitudinal axis, at the portions housing an axial screwed threaded stud. The Fast Fourier Transform (FFT) based Spectral Element

Method (SEM) by Doyle [52] is already formulated for higher order waveguide theories. The FFT based method evolved into the Spectral Finite Element Method (SFEM) discussed in Gopalakrishnan *et al.*[160]. This represents an alternative route to developing the inverse problem. A further development to this is the replacement of the FFT with a Wavelet Transform (WT) as discussed in Mitra & Gopalakrishnan [161]. This overcomes the limitation of the FFT in producing reflections as a result of its enforced periodicity.

The DTFM features explicit formulation of the Transcendental Eigenvalue Problem (TEP) for the distributed parameter system. Singh [64] followed on from the analytical work that is summarised in Gladwell [65] to develop an Inverse TEP scheme for a one dimensional beam element. This provides a route to identifying a unique distributed parameter model from the resonant and antiresonant frequencies of a fixed-free beam. The TEP in section 3.7 can be employed to develop an Inverse TEP for the current distributed rod model. The unique distributed rod can be recovered from the resonant frequencies of the fixed-free and fixed-fixed rods. However the fixed-fixed frequencies can be obtained as the anti-resonant frequencies of the fixed-free rod. Updating the parameter of a DTFM rod through a scheme of this nature represents the optimal distributed model for the joint force estimation. However this is still an ill-posed problem that requires regularisation to achieve a stable solution. This would be suitable for the impact testing of a long slender rod. However applying a fixed boundary condition to a HPU device will not allow it to resonate. Therefore an alternative scheme is required that is based on boundary conditions that are relevant to this device. This may involve an open or short circuit at the piezoelectric stack or creating a range of assemblies based on the torque that is applied to the bolt that prestresses the piezoceramic rings.

Only a small number of test assemblies were manufactured for this study. Multiple copies of each assembly should be tested in future iterations of the experiment. Assemblies with a greater applied torque would identify the tightness at which the jointed assembly does not tend towards the monolithic assembly. An In-House manufactured Piezoelectric Actuator (IHPA) that behaves more like the Commercial Piezoelectric Actuator (CPA) is required. Impedance matching circuits should also be designed for each assembly. Better minimisation of the error between the linear calibration model and the Experimental Modal Analysis (EMA) of the monolithic assembly is required. However, successful incorporation of linear damping in the model should make it more robust for the force identification scheme. This linear damping can only be identified with a better definition of the input to the system. Forming the relationship between the input voltage and the output response is the most

intuitive option.

Ideally 3D Digital Image Correlation (DIC) should be applied to estimate the displacement and strain fields at the axial joint. This removes the need for the flat portion. However, without the availability of this flat for gripping by a torque wrench adapter, it is difficult to reliably set the tightness of the axial joint. If the jointed assemblies are impedance matched then it is more likely that the 2D DIC set up will be sufficient. The area close to the axial joint should be focussed onto the sensor of the camera. A telescopic lens should be introduced to reduce the influence of projection errors on the measurements. It may also be beneficial to apply a finer speckle pattern through an airbrush.

When the transient response of each test assembly is measured it would be beneficial to observe the real time potential difference across the piezoelectric stack by means of a high voltage probe. This data is required to define the input to the jointed systems. It will also illuminate the relationship between the second harmonic and the axial joint tightness. The force identification is best understood when it is deconvolved from the response at multiple locations.

Hysteresis loops that are characteristic of the behaviour of axial joints in HPU systems are required to make progress. This data will indicate whether the Bouc-Wen (BW) model should be modified to better describe the observations. The sensitivity analysis could be extended to investigate these modifications. However it is likely that the best sensitivity analysis requires a zeroth order iterative scheme. Running Differential Evolution for a diverse population will map the parameter behaviour more effectively. Further investigation of the conditions through which the BW system becomes stiff is required to reduce the computational cost of the iterative evolutionary analysis. Identifying the parameters β and γ that are associated with an axial joint system remains an open problem.

8.3 Summary of Contribution

The aims of the investigation of the axial joint in a High Power Ultrasonic device were set out in Section 1.1. These have been satisfied throughout this study as follows:

(I) The Bouc-Wen (BW) model is introduced as a simplified approach to modelling the dynamic behaviour of the axial joint in a High Power Ultrasonic (HPU) device. Numerical simulations of the model demonstrate that it can describe the softening over-

hang behaviour that has been observed in the response of HPU devices. It can also describe the generation of multiple subharmonics that are thought to descend from Contact Acoustic Nonlinearity (CAN) [162]. Experimental data is obtained to identify the model parameters through Differential Evolution (DE). The results of the simulation demonstrated that the information required to find the model parameters was not present in the data. This exhibited the difficulties in measuring appropriate response data from the HPU test assemblies and in determining an appropriate input signal to the BW model of the HPU system.

(II) A new force estimation scheme is established for deconvolving the force at an axial joint in a rod-like assembly with distributed parameters. This closed form scheme is based on a recent formulation of the Distributed Transfer Function Method (DTFM). It is shown that the scheme requires further development to describe the thick rod-like wave guides that are required to model the HPU assembly. The scheme is applied to experimental data through a set of MATLAB scripts and functions. Regularisation methods are applied to obtain stable force estimations through the model.

(III) A Commercial Piezoelectric Actuator (CPA) and an equivalent In-House manufactured Piezoelectric Actuator (IHPA) are tested with equivalent jointed and unjointed horns. Each Jointed Horn (JH) contains an additional axial joint that is not present in the Monolithic Horn (MH) and has been set with a calibrated torque wrench. Electrical impedance analysis and Experimental Modal Analysis (EMA) is carried out for a range of assemblies with a piezoelectric actuator and ultrasonic horn. This demonstrates the behaviour of the assembly as the additional axial joint is tightened or removed completely. It also shows the modal data that is available for updating a linear model of the HPU device with the current experimental apparatus.

(IV) It is demonstrated that the major limitation in applying the hybrid force estimation scheme to the HPU device is that it is not possible to excite the device with the exact same input signal in order to be able to deconvolve the joint force. This is due to the narrow bandwidth behaviour of the HPU system as well as the difficulty in generating sufficient vibration amplitude in the jointed HPU assemblies.

(V) Digital Image Correlation (DIC) using images obtained with an ultra-high speed camera is introduced as a viable alternative to observing the hysteresis behaviour at the axial joint in the HPU test assemblies. The limitations of the DIC scheme mean that the axial hysteresis behaviour can only be estimated either side of the axial joint. It

is shown that much higher vibration amplitudes are required, than is developed in the jointed HPU assemblies, in order to compute reliable full field strains. A direct comparison between the DIC displacement estimations and equivalent measurements, which are obtained through Laser Doppler Vibrometry, suggest that further development of the experimental configuration is required to obtain reliable displacement measurements. Recommendations are made to improve this analysis.

References

[1] M. P. Cartmell, F. C. N. Lim, A. Cardoni, and M. Lucas, "Optimisation of the vibrational response of ultrasonic cutting systems," *IMA Journal of Applied Mathematics*, vol. 70, no. 5, pp. 645–656, October 2005.

[2] X. Bao, Y. Bar-Cohen, Z. Chang, B. Dolgin, S. Sherrit, D. Pal, S. Du, and T. Peterson, "Modeling and computer simulation of Ultrasonic/Sonic Driller/Corer (USDC)," *Ultrasonics, Ferroelectrics and Frequency Control, IEEE Transactions on*, vol. 50, no. 9, pp. 1147–1160, 2003.

[3] E. Ungar, "The status of engineering knowledge concerning the damping of built-up structures," *Journal of Sound and Vibration*, vol. 26, no. 1, pp. 141–154, 1973.

[4] C. Beards and J. Williams, "The damping of structural vibration by rotational slip in joints," *Journal of Sound and Vibration*, vol. 53, no. 3, pp. 333–340, 1977.

[5] F. C. N. Lim, "A preliminary investigation into the effects of nonlinear response modification within coupled oscillators," Ph.D. dissertation, University of Glasgow, 2003.

[6] A. Cardoni, "Characterising the dynamic response of ultrasonic cutting devices," Ph.D. dissertation, University of Glasgow, 2003.

[7] A. Mathieson, "Nonlinear characterisation of power ultrasonic devices used in bone surgery," Ph.D. dissertation, University of Glasgow, 2012.

[8] N. Aurelle, D. Guyomar, C. Richard, P. Gonnard, and L. Eyraud, "Nonlinear behavior of an ultrasonic transducer," *Ultrasonics*, vol. 34, no. 2, pp. 187–191, 1996.

[9] P. Green, K. Worden, K. Atallah, and N. Sims, "Performance of linear and nonlinear resonant frequency energy harvesters under uncertain loading conditions," *USD2010: 3rd International Conference on Uncertainty in Structural Dynamics - Leuven, Belgium*, 2010.

[10] M. Lucas, A. Gachagan, and A. Cardoni, "Research applications and opportunities in power ultrasonics," *Proceedings of the Institution of Mechanical Engineers, Part C: Journal of Mechanical Engineering Science*, vol. 223, no. 12, pp. 2949–2965, 2009.

[11] H. Kumehara, K. Morimura, K. Maruyama, and I. Yoshimoto, "Characteristics of threaded joints in ultrasonic vibration systems." *Bulletin of Japanese Society of Mechanical Engineers*, vol. 27, no. 223, pp. 117–123, 1984.

[12] G. Chakraborty, A. Mallik, and H. Hatwal, "Normal modes and near-resonance response of beams with non-linear effects," *Journal of Sound and Vibration*, vol. 210, no. 1, pp. 19–36, 1998.

[13] C. Hartwigsen, Y. Song, D. McFarland, L. Bergman, and A. Vakakis, "Experimental study of non-linear effects in a typical shear lap joint configuration," *Journal of Sound and Vibration*, vol. 277, no. 1-2, pp. 327–351, 2004.

[14] X. Ma, L. Bergman, and A. Vakakis, "Identification of bolted joints through laser vibrometry," *Journal of Sound and Vibration*, vol. 246, no. 3, pp. 441–460, 2001.

[15] H. Ouyang, M. Oldfield, and J. Mottershead, "Experimental and theoretical studies of a bolted joint excited by a torsional dynamic load," *International Journal of Mechanical Sciences*, vol. 48, no. 12, pp. 1447–1455, 2006.

[16] H. Ahmadian and H. Jalali, "Generic element formulation for modelling bolted lap joints," *Mechanical Systems and Signal Processing*, vol. 21, no. 5, pp. 2318–2334, 2007.

[17] D. Segalman, T. Paez, D. Smallwood, A. Sumali, and A. Urbina, "Status and integrated road-map for joints modeling research," Sandia National Laboratories, Tech. Rep., 2003.

[18] J. Oden and J. Martins, "Models and computational methods for dynamic friction phenomena," *Computer Methods in Applied Mechanics and Engineering*, vol. 52, no. 1-3, pp. 527–634, 1985.

[19] F. P. Bowden and D. Tabor, *The friction and lubrication of solids*. Oxford: The Clarendon Press, 1954.

[20] J. F. Archard, "Surface topography and tribology," *Tribology*, vol. 7, no. 5, pp. 213 – 220, 1974.

[21] J. A. Greenwood and J. B. P. Williamson, "Contact of nominally flat surfaces," *Proceedings of the Royal Society of London. Series A, Mathematical and Physical Sciences*, vol. 295, no. 1442, pp. 300–319, 1966.

[22] C. Andrew, J. Cockburn, and A. Waring, "Metal surfaces in contact under normal forces: some dynamic stiffness and damping characteristics," *Archive: Proceedings of the Institution of Mechanical Engineers, Conference Proceedings 1964-1970 (Vols 178-184), Various Titles Labelled Volumes A to S*, vol. 182, no. 311, pp. 92–100, 1967.

[23] B. Wikie and J. Hill, "Stick-slip motion for two coupled masses with side friction," *International Journal of Non-Linear Mechanics*, vol. 35, no. 6, pp. 953–962, 2000.

[24] M. Oldfield, "Harmonic excitation of bolted joints," Ph.D. dissertation, University of Liverpool, 2004.

[25] M. Oldfield, H. Ouyang, and J. Mottershead, "Simplified models of bolted joints under harmonic loading," *Computers and Structures*, vol. 84, no. 1-2, pp. 25–33, 2005.

[26] D. Canudas, "A new model for control of systems with friction," *IEEE Transactions on Automatic Control*, vol. 40, no. 3, pp. 419–425, 1995.

[27] H. Olsson, K. Åström, C. C. D. Wit, M. Gäfvert, and P. Lischinsky, "Friction models and friction compensation," *European Journal of Control*, vol. 4, pp. 176–195, 1998.

[28] S. Andersson, A. Söderberg, and S. Björklund, "Friction models for sliding dry, boundary and mixed lubricated contacts," *Tribology International*, vol. 40, no. 4, pp. 580–587, 2007.

[29] K. Valanis, "Fundamental consequences of a new intrinsic time measure. plasticity as a limit of the endochronic theory," University of Iowa, Tech. Rep., 1978.

[30] L. Gaul and J. Lenz, "Nonlinear dynamics of structures assembled by bolted joints," *Acta Mechanica*, vol. 125, no. 1, pp. 169–181, 1997.

[31] S. Basava and D. Hess, "Bolted joint clamping force variation due to axial vibration," *Journal of Sound and Vibration*, vol. 210, no. 2, pp. 255–265, 1998.

[32] R. Zadoks and X. Yu, "An investigation of the self-loosening behavior of bolts under transverse vibration," *Journal of Sound and Vibration*, vol. 208, no. 2, pp. 189–209, 1997.

[33] D. Hess and S. Sudhirkashyap, "Dynamic analysis of threaded fasteners subjected to axial vibration," *Journal of Sound and Vibration*, vol. 193, no. 5, pp. 1079–1090, 1996.

[34] D. Karnopp, "Computer simulation of stick-slip friction in mechanical dynamic systems," *Journal of Dynamic Systems, Measurement, and Control*, vol. 107, no. 1, pp. 100–103, 1985.

[35] R. Ibrahim and C. Pettit, "Uncertainties and dynamic problems of bolted joints and other fasteners," *Journal of Sound and Vibration*, vol. 279, no. 3-5, pp. 857–936, 2005.

[36] J. Tsai and Y. Chou, "The identification of dynamic characteristics of a single bolt joint," *Journal of Sound and Vibration*, vol. 125, no. 3, pp. 487–502, 1988.

[37] Y. Ren and C. Beards, "Identification of joint properties of a structure using FRF data," *Journal of Sound and Vibration*, vol. 186, no. 4, pp. 567–587, 1995.

[38] S. Hong and C. Lee, "Identification of linearised joint structural parameters by combined use of measured and computed frequency responses," *Mechanical Systems and Signal Processing*, vol. 5, no. 4, pp. 267–277, 1991.

[39] W. Li, "A new method for structural model updating and joint stiffness identification," *Mechanical Systems and Signal Processing*, vol. 16, no. 1, pp. 155–167, 2002.

[40] H. Jalali, H. Ahmadian, and J. Mottershead, "Identification of nonlinear bolted lap-joint parameters by force-state mapping," *International Journal of Solids and Structures*, vol. 44, no. 25-26, pp. 8087–8105, 2007.

[41] H. Kashani and A. Nobari, "Identification of dynamic characteristics of nonlinear joint based on the Optimum Equivalent Linear Frequency Response Function," *Journal of Sound and Vibration*, vol. 329, no. 9, pp. 1460–1479, 2010.

[42] J. Rivière, G. Renaud, S. Haupert, and M. Talmant, "Nonlinear acoustic resonances to probe a threaded interface," *Journal of Applied Physics*, vol. 107, p. 124901, 2010.

[43] V. Aleshin and K. V. D. Abeele, "Preisach analysis of the Hertz-Mindlin system," *Journal of the Mechanics and Physics Of Solids*, vol. 57, pp. 657–672, 2009.

[44] S. Hirsekorn, "Nonlinear transfer of ultrasound by adhesive joints - a theoretical description," *Ultrasonics*, vol. 39, no. 1, pp. 57–68, 2001.

[45] S. Biwa, S. Nakajima, and N. Ohno, "On the acoustic nonlinearity of solid-solid contact with pressure-dependent interface stiffness," *Journal of Applied Mechanics*, vol. 71, pp. 508–519, 2004.

[46] X. Guo, D. Zhang, and J. Wu, "Quantitative evaluation of contact stiffness between pressed solid surfaces using dual-frequency ultrasound," *Journal of Applied Physics*, vol. 108, no. 3, p. 034902, 2010.

[47] J. Richardson, "Harmonic generation at an unbonded interface–i. planar interface between semi-infinite elastic media," *International Journal of Engineering Science*, vol. 17, no. 1, pp. 73–85, 1979.

[48] B. Yang, "Transfer functions of constrained/combined one-dimensional continuous dynamic systems," *Journal of Sound and Vibration*, vol. 156, no. 3, pp. 425–443, 1992.

[49] B. Yang, *Stress, strain, and structural dynamics: an interactive handbook of formulas, solutions, and MATLAB toolboxes*. Access Online via Elsevier, 2005, vol. 1.

[50] B. Yang, "Exact transient vibration of stepped bars, shafts and strings carrying lumped masses," *Journal of Sound and Vibration*, vol. 329, no. 8, pp. 1191–1207, 2010.

[51] M. Shatalov, I. Fedotov, H. Tenkam, and T. Fedotova, "Theory of longitudinally polarised piezocomposite rod based on Mindlin-Herrmann model," *11^{th} Pan-American Congress of Applied Mechanics. Foz do Iguaçu, PR, Brazil*, 2010.

[52] J. F. Doyle, *Wave propagation in structures: Spectral analysis using Fast Discrete Fourier Transforms*. Springer (New York), 1997.

[53] A. Żak and M. Krawczuk, "Assessment of rod behaviour theories used in Spectral Finite Element Modelling," *Journal of Sound and Vibration*, vol. 329, no. 11, pp. 2099–2113, 2010.

[54] V. D. Lupi, "The use of mathematically exact solutions of structural dynamics models for structural control design," Ph.D. dissertation, Massachusetts Institute of Technology, Dept. of Aeronautics and Astronautics, 1992.

[55] D. Fotiadis, G. Foutsitzi, and C. Massalas, "Wave propagation modeling in human long bones," *Acta mechanica*, vol. 137, no. 1-2, pp. 65–81, 1999.

[56] T. M. Kamel and G. de With, "Poling of hard ferroelectric PZT ceramics," *Journal of the European Ceramic Society*, vol. 28, no. 9, pp. 1827–1838, 2008.

[57] U. Güven, "Love-Bishop rod solution based on strain gradient elasticity theory," *Comptes Rendus Mécanique*, 2013.

[58] H. F. Tiersten, *Linear piezoelectric plate vibrations: Elements of the linear theory of piezoelectricity and the vibrations of piezoelectric plates*. Plenum Press, 1969.

[59] Q.-H. Qin, *Advanced Mechanics of Piezoelectricity*. Springer, 2013.

[60] C. Lanczos, *The variational principles of mechanics*. Courier Dover Publications, 1970, vol. 4.

[61] C. R. R. Nave, http://hyperphysics.phy-astr.gsu.edu/hbase/electric/elewor.html#c1, acessed 3rd April, 2014.

[62] C.-T. Chen, *Linear System Theory and Design*. Oxford University Press, Inc., 1998.

[63] K. V. Singh and Y. M. Ram, "Transcendental eigenvalue problem and its applications," *AIAA Journal*, vol. 40, no. 7, pp. 1402–1407, 2002.

[64] K. V. Singh, "The Transcendental Eigenvalue Problem and its application in system identification," Ph.D. dissertation, Citeseer, 2003.

[65] G. M. Gladwell, *Inverse Problems in Vibration*, 2nd ed. Springer Netherlands, 2005.

[66] K.-V. Yuen, *Bayesian methods for structural dynamics and civil engineering*. John Wiley & Sons, 2010.

[67] F. D. M. Neto and A. J. da Silva Neto, *An Introduction to Inverse Problems with Applications*. Springer Berlin Heidelberg, 2013.

[68] J. L. Mueller and S. Siltanen, *Linear and Nonlinear Inverse Problems with Practical Applications*. SIAM, 2012, vol. 10.

[69] J. Hadamard, "Sur les problèmes aux dérivées partielles et leur signification physique," *Princeton University bulletin*, vol. 13, no. 49-52, p. 28, 1902.

[70] P. C. Hansen, "Analysis of discrete ill-posed problems by means of the L-curve," *SIAM review*, vol. 34, no. 4, pp. 561–580, 1992.

[71] M. Martin and J. Doyle, "Impact force identification from wave propagation responses," *International Journal of Impact Engineering*, vol. 18, no. 1, pp. 65–77, 1996.

[72] W. P. Mason, *Electromechanical transducers and wave filters*. D. Van Nostrand Co., 1948.

[73] B. Fu, "Piezoelectric actuator design via multiobjective optimization methods," Ph.D. dissertation, 2005.

[74] B. Mortimer, T. du Bruyn, J. Davies, and J. Tapson, "High power resonant tracking amplifier using admittance locking," *Ultrasonics*, vol. 39, no. 4, pp. 257–261, 2001.

[75] U. Wiklund and I. Hutchings, "Investigation of surface treatments for galling protection of titanium alloys," *Wear*, vol. 251, no. 1, pp. 1034–1041, 2001.

[76] K. V. Singh, "Transcendental Inverse Eigenvalue Problems in damage parameter estimation," *Mechanical Systems and Signal Processing*, vol. 23, no. 6, pp. 1870–1883, Aug. 2009.

[77] M. Dilena and A. Morassi, "The use of antiresonances for crack detection in beams," *Journal of Sound and Vibration*, vol. 276, no. 1-2, pp. 195–214, Sep. 2004.

[78] Avitabile, http://sdasl.uml.edu/umlspace/mspace.html, acessed 8th May, 2014.

[79] P. Avitabile, "Experimental Modal Analysis," *Sound and Vibration*, vol. 35, no. 1, pp. 20–31, 2001.

[80] D. J. Ewins, *Modal testing: theory and practice*. Research studies press Letchworth, 1984, vol. 79.

[81] C. Shih, Y. Tsuei, R. Allemang, and D. Brown, "A frequency domain global parameter estimation method for multiple reference frequency response measurements," *Mechanical Systems and Signal Processing*, vol. 2, no. 4, pp. 349–365, 1988.

[82] M. Mitchell, *An introduction to Genetic Algorithms*. MIT press, 1998.

[83] I. Automation Creations, http://www.matweb.com/, accessed 27th May 2014.

[84] E. W. Weisstein. (2014, Feb) Circular segment. MathWorld. Wolfram Web Resource. [Online]. Available: http://mathworld.wolfram.com/CircularSegment.html

[85] J. Shigley, C. Mischke, and R. Budynas, *Mechanical Engineering Design*. McGraw-Hill, 2004.

[86] H. Al-Budairi, "Design and analysis of ultrasonic horns operating in longitudinal and torsional vibration," Ph.D. dissertation, University of Glasgow, 2012.

[87] A. Albareda, R. Perez, J. A. Casals, J. E. Garcia, and D. A. Ochoa, "Optimization of elastic nonlinear behavior measurements of ceramic piezoelectric resonators with burst excitation," *Ultrasonics, Ferroelectrics and Frequency Control, IEEE Transactions on*, vol. 54, no. 10, pp. 2175–2188, 2007.

[88] K. Spak, G. Agnes, and D. Inman, "Comparison of damping models for space flight cables," in *Conference Proceedings of the Society for Experimental Mechanics Series*, F. N. Catbas, S. Pakzad, V. Racic, A. Pavic, and P. Reynolds, Eds. Springer New York, 2013, pp. 183–194–.

[89] MathWorks, "mldivide (r2013a)," http://www.mathworks.co.uk/help/matlab/ref/mldivide.html, 2014, acessed 29th May, 2014.

[90] N. J. Higham, "The accuracy of solutions to triangular systems," *SIAM Journal on Numerical Analysis*, vol. 26, no. 5, pp. 1252–1265, 1989.

[91] MathWorks, "Pseudoinverse (r2013a)," http://www.mathworks.co.uk/help/matlab/ref/pinv.html, 2014, acessed 29th May, 2014.

[92] D. Wang, M. Lucas, and K. Tanner, "Characterising the strain and temperature fields in a surrogate bone material subject to power ultrasonic excitation," *Strain*, vol. 49, no. 5, pp. 409–419, 2013.

[93] D. Lecompte, S. Bossuyt, S. Cooreman, H. Sol, and J. Vantomme, "Study and generation of optimal speckle patterns for DIC," in *Proceedings of the annual conference and exposition on experimental and applied mechanics*, vol. 3, 2007, pp. 1643–9.

[94] N. Otsu, "A threshold selection method from gray-level histograms," *Automatica*, vol. 11, no. 285-296, pp. 23–27, 1975.

[95] T. Goji Etoh, D. Poggemann, G. Kreider, H. Mutoh, A. J. P. Theuwissen, A. Ruckelshausen, Y. Kondo, H. Maruno, K. Takubo, H. Soya, K. Takehara, T. Okinaka, and Y. Takano, "An image sensor which captures 100 consecutive frames at 1000000 frames/s," *Electron Devices, IEEE Transactions on*, vol. 50, no. 1, pp. 144–151, 2003.

[96] F. Pierron, R. Cheriguene, P. Forquin, R. Moulart, M. Rossi, and M. Sutton, "Performances and limitations of three ultra high-speed imaging cameras for full-field deformation measurements," *Applied Mechanics and Materials*, vol. 70, pp. 81–86, 2011.

[97] W. Peters and W. Ranson, "Digital imaging techniques in experimental stress analysis," *Optical Engineering*, vol. 21, no. 3, pp. 213 427–213 427, 1982.

[98] T. Chu, W. Ranson, and M. Sutton, "Applications of digital-image-correlation techniques to experimental mechanics," *Experimental Mechanics*, vol. 25, no. 3, pp. 232–244, 1985.

[99] M. Sutton, C. Mingqi, W. Peters, Y. Chao, and S. McNeill, "Application of an optimized digital correlation method to planar deformation analysis," *Image and Vision Computing*, vol. 4, no. 3, pp. 143–150, 1986.

[100] W. Peters, W. Ranson, M. Sutton, T. Chu, and J. Anderson, "Application of digital correlation methods to rigid body mechanics," *Optical Engineering*, vol. 22, no. 6, pp. 226 738–226 738, 1983.

[101] H. Bongtae and D. Post, "Geometric Moiré," in *Springer Handbook of Experimental Solid Mechanics*. Springer, 2008, pp. 601–626.

[102] D. Post and H. Bongtae, "Moiré interferometry," in *Springer Handbook of Experimental Solid Mechanics*. Springer, 2008, pp. 627–654.

[103] Y. Gan and W. Steinchen, "Speckle methods," *Springer Handbook of Experimental Solid Mechanics*, pp. 655–674, 2008.

[104] R. J. Pryputniewicz, "Holography," *Springer Handbook of Experimental Solid Mechanics*, pp. 675–700, 2008.

[105] C. Sciammarella, "Optical techniques that measure displacements: A review of the basic principles," in *Optical Measurements, Modeling and Metrology*. Springer, 2011, vol. 5, pp. 155–180.

[106] M. Sutton, J. Yan, V. Tiwari, H. Schreier, and J. Orteu, "The effect of out-of-plane motion on 2D and 3D Digital Image Correlation measurements," *Optics and Lasers in Engineering*, vol. 46, no. 10, pp. 746–757, 2008.

[107] E. Jones, "Improved Digital Image Correlation," https://www.mathworks.co.uk/matlabcentral/fileexchange/43073-improved-digital-image-correlation--dic-, Aug 2013, acessed 29th May, 2014.

[108] C. Eberl, "Digital Image Correlation and tracking," http://www.mathworks.com/matlabcentral/fileexchange/12413-digital-image-correlation-and-tracking, Sep 2006, acessed 29th May, 2014.

[109] C. Eberl, D. Gianola, and K. Hemker, "Mechanical characterization of coatings using microbeam bending and Digital Image Correlation techniques," *Experimental mechanics*, vol. 50, pp. 85–97, 2008.

[110] M. A. Sutton, J.-J. Orteu, and H. W. Schreier, "Image correlation for shape, motion and deformation measurements: Basic concepts, theory and applications," *Springer Science and Business Media, New York*, 2009.

[111] B. Pan, K. Qian, H. Xie, and A. Asundi, "Two-dimensional Digital Image Correlation for in-plane displacement and strain measurement: A review," *Measurement Science and Technology*, vol. 20, no. 6, pp. 062 001–, 2009.

[112] H. W. Schreier, J. R. Braasch, and M. A. Sutton, "Systematic errors in Digital Image Correlation caused by intensity interpolation," *Optical Engineering*, vol. 39, no. 11, pp. 2915–2921, 2000.

[113] P. Cheng, M. A. Sutton, H. W. Schreier, and S. R. McNeill, "Full-field speckle pattern image correlation with b-spline deformation function," *Experimental Mechanics*, vol. 42, no. 3, pp. 344–352, 2002.

[114] D. A. Tortorelli, *Solid mechanics: Analysis and design with the Finite Element Method.* Urbana, IL USA: Electronic Publication, 2010.

[115] J. Barlow, "Optimal stress locations in Finite Element models," *International Journal for Numerical Methods in Engineering*, vol. 10, no. 2, pp. 243–251, 1976.

[116] J. Smith, "Application note # 49 RF amplifier output voltage, current, power and impedance relationship," AR RF/Microwave Instrumentation, Tech. Rep., 2009.

[117] L. Wang, R. Melnik, and F. Lv, "Stress induced polarization switching and coupled hysteretic dynamics in ferroelectric materials," *Frontiers of Mechanical Engineering*, vol. 6, no. 3, pp. 287–291, 2011.

[118] B. Drinčić, X. Tan, and D. S. Bernstein, "Why are some hysteresis loops shaped like a butterfly?" *Automatica*, vol. 47, no. 12, pp. 2658–2664, 2011.

[119] M. Ismail, F. Ikhouane, and J. Rodellar, "The hysteresis Bouc-Wen model, a survey," *Archives of Computational Methods in Engineering*, vol. 16, pp. 161–188, 2009.

[120] B. Lazan, *Damping of materials and members in structural mechanics*. Pergamon Press, 1968.

[121] Y. K. Wen, "Method for random vibration of hysteretics systems," *Journal of the Engineering Mechanics Division*, vol. 2, pp. 249–263, 1976.

[122] R. Bouc, "Modéle mathématique d'hystérésis," *Acustica*, vol. 24, pp. 16–25, 1971.

[123] K. C. Valanis, "A theory of viscoplasticity without a yield surface. part 1. general theory," *Archives of Mechanics*, vol. 23 (4), pp. 517–533, 1971.

[124] T. T. Baber and M. N. Noori, "Random vibration of degrading, pinching systems," *Journal of Engineering Mechanics*, vol. 111, no. 8, pp. 1010–1026, 1985.

[125] G. C. Foliente, "Hysteresis modeling of wood joints and structural systems," *Journal of Structural Engineering*, vol. 121, no. 6, pp. 1013–1022, 1995.

[126] H. Wee, Y. Y. Kim, H. Jung, and G. N. Lee, "Nonlinear rate-dependent stick-slip phenomena: Modeling and parameter estimation," *International Journal of Solids and Structures*, vol. 38, no. 8, pp. 1415 – 1431, 2001.

[127] Y. Q. Ni, J. M. Ko, C. W. Wong, and S. Zhan, "Modelling and identification of a wire-cable vibration isolator via a cyclic loading test," *Proceedings of the Institution of Mechanical Engineers, Part I: Journal of Systems and Control Engineering*, vol. 213, no. 3, pp. 163–172, 1999.

[128] B. F. Spencer, S. J. Dyke, M. K. Sain, and J. D. Carlson, "Phenomenological model for magnetorheological dampers," *Journal of Engineering Mechanics*, vol. 123, no. 3, pp. 230–238, 1997.

[129] M. Constantinou, A. Mokha, and A. Reinhorn, "Teflon bearings in base isolation ii: Modeling," *Journal of Structural Engineering*, vol. 116, no. 2, pp. 455–474, 1990.

[130] A. Charalampakis and V. Koumousis, "On the response and dissipated energy of Bouc-Wen hysteretic model," *Journal of Sound and Vibration*, vol. 309, no. 3 - 5, pp. 887 – 895, 2008.

[131] F. Ma, H. Zhang, A. Bockstedte, G. C. Foliente, and P. Paevere, "Parameter analysis of the differential model of hysteresis," *Journal of Applied Mechanics*, vol. 71, no. 3, pp. 342–349, 2004.

[132] T. Sireteanu, M. Giuclea, and A. M. Mitu, "An analytical approach for approximation of experimental hysteretic loops by Bouc-Wen model," *Proceedings of Romanian Academy, Series A*, vol. 10, no. 1, 2009.

[133] C.-H. Wang and Y.-K. Wen, "Evaluation of pre-northridge low-rise steel buildings. i: Modeling," *Journal of Structural Engineering*, vol. 126, no. 10, pp. 1160–1168, 2000.

[134] C. W. Wong, Y. Q. Ni, and S. L. Lau, "Steady-state oscillation of hysteretic differential model. i: Response analysis," *Journal of Engineering Mechanics*, vol. 120, no. 11, pp. 2271–2298, 1994.

[135] E. I. Green, "The story of Q," *American Scientist*, pp. 584–594, 1955.

[136] F. Itakura, "Minimum prediction residual principle applied to speech recognition," *Acoustics, Speech and Signal Processing, IEEE Transactions on*, vol. 23, no. 1, pp. 67–72, 1975.

[137] R. Martens and L. Claesen, "Dynamic programming optimisation for on-line signature verification," in *Document Analysis and Recognition, 1997., Proceedings of the Fourth International Conference on*, vol. 2. IEEE, 1997, pp. 653–656.

[138] A. Brenner, K. Eck, G. Engelhard, and T. Noll, "Phase aberration correction using Dynamic Time Warping," in *Ultrasonics Symposium, 1995. Proceedings., 1995 IEEE*, vol. 2. IEEE, 1995, pp. 1361–1365.

[139] S. B. Dolins and J. Reese, "A curve interpretation and diagnostic technique for industrial processes," *Industry Applications, IEEE Transactions on*, vol. 28, no. 1, pp. 261–267, 1992.

[140] M. Landry, F. Léonard, C. Landry, R. Beauchemin, O. Turcotte, and F. Brikci, "An improved vibration analysis algorithm as a diagnostic tool for detecting mechanical anomalies on power circuit breakers," *Power Delivery, IEEE Transactions on*, vol. 23, no. 4, pp. 1986–1994, 2008.

[141] J. M. Lee, S.-J. Kim, Y. Hwang, and C.-S. Song, "Diagnosis of mechanical fault signals using continuous hidden Markov model," *Journal of Sound and Vibration*, vol. 276, no. 3, pp. 1065–1080, 2004.

[142] R. J. Turetsky and D. P. Ellis, "Ground-truth transcriptions of real music from force-aligned midi syntheses," *ISMIR 2003*, pp. 135–141, 2003.

[143] D. Ellis, "Dynamic Time Warp (DTW) in MATLAB," http://www.ee.columbia.edu/~dpwe/resources/matlab/dtw/, 2003, acessed 24th September 2014.

[144] S. Erlicher and N. Point, "Thermodynamic admissibility of Bouc-Wen type hysteresis models," *Comptes Rendus Mécanique*, vol. 332, no. 1, pp. 51 – 57, 2004.

[145] A. Charalampakis and V. Koumousis, "A Bouc-Wen model compatible with plasticity postulates," *Journal of Sound and Vibration*, vol. 322, pp. 954 – 968, 2009.

[146] F. Casciati, "Stochastic dynamics of hysteretic media," *Structural Safety*, vol. 6, no. 2, pp. 259–269, 1989.

[147] F. Ikhouane, V. M. nosa, and J. Rodellar, "Dynamic properties of the hysteretic Bouc-Wen model," *Systems and Control Letters*, vol. 56, no. 3, pp. 197 – 205, 2007.

[148] F. Ikhouane and J. Rodellar, "On the hysteretic Bouc-Wen model," *Nonlinear Dynamics*, vol. 42, no. 1, pp. 79–95, 2005.

[149] M. Isermann, R. & Münchhof, *Identification of Dynamic Systems: An Introduction with Applications*. Springer Berlin Heidelberg, 2011.

[150] H. U. Voss, J. Timmer, and J. Kurths, "Nonlinear dynamical system identification from uncertain and indirect measurements," *International Journal of Bifurcation and Chaos*, vol. 14, no. 06, pp. 1905–1933, 2004.

[151] M. Buehren, "Differential Evolution," http://www.mathworks.com/matlabcentral/fileexchange/18593-differential-evolution, Feb 2008, acessed 26th November, 2014.

[152] K. Price, R. M. Storn, and J. A. Lampinen, *Differential Evolution: A practical approach to global optimization*. Springer, 2006.

[153] A. Charalampakis and C. Dimou, "Comparison of Evolutionary Algorithms for the identification of Bouc-Wen hysteretic systems," *Journal of Computing in Civil Engineering*, pp. –, 2013.

[154] A. Kyprianou, K. Worden, and M. Panet, "Identification of hysteretic systems using the Differential Evolution algorithm," *Journal of Sound and Vibration*, vol. 248, no. 2, pp. 289 – 314, 2001.

[155] T. Low and W. Guo, "Modeling of a three-layer piezoelectric bimorph beam with hysteresis," *Journal of Microelectromechanical Systems*, vol. 4, no. 4, pp. 230–237, 1995.

[156] J. A. Gallego-Juárez and K. F. Graff, *Power Ultrasonics: Applications of High-Intensity Ultrasound*. Elsevier, 2014.

[157] C. P. Heine, "Simulated response of degrading hysteretic joints with slack behavior," Ph.D. dissertation, 2001.

[158] B. Yang and J. Zhou, "Semi-analytical solution of 2-D elasticity problems by the Strip Distributed Transfer Function Method," *International Journal of Solids and Structures*, vol. 33, no. 27, pp. 3983–4005, Nov. 1996.

[159] Y. Yang and B. Yang, "Semi-analytical solution of two-dimensional elasticity problems by Finite Difference Distributed Transfer Function Method," *International Journal of Structural Stability and Dynamics*, vol. 10, no. 02, pp. 315–334, Jun. 2010.

[160] S. Gopalakrishnan, A. Chakraborty, and D. R. Mahapatra, *Spectral Finite Element Method: Wave propagation, diagnostics and control in anisotropic and inhomogeneous structures*. Springer, 2007.

[161] M. Mitra and S. Gopalakrishnan, "Spectrally formulated Wavelet Finite Element for wave propagation and impact force identification in connected 1-D waveguides," *International Journal of Solids and Structures*, vol. 42, no. 16-17, pp. 4695–4721, Aug. 2005.

[162] B. Korshak, I. Y. Solodov, and E. Ballad, "Dc effects, sub-harmonics, stochasticity and memory for contact acoustic non-linearity," *Ultrasonics*, vol. 40, no. 1, pp. 707–713, 2002.

Appendix A

MATLAB estimation of the Bouc-Wen model from limit cycle data

All of the following MATLAB functions must be present in the MATLAB directory to fit the Bouc-Wen model to the steady state vibration of a hysteretic system.

```
function [A, beta, gamma] = IdentBWSymm(u1, u2, z0, z1, z3, n, ...
    varargin)
% Analytical solution to the Bouc-Wen model for n = 1 or 2
% Requires 6 inputs
% u1 - Displacement at the velocity reversal point.
% u2 - Displacement when the hysteretic displacement is 0.
% z0 - Hysteretic displacement when the displacement is 0 for z0 < z3.
% z1 - Hysteretic displacement at the velocity reversal point.
% z3 - Hysteretic displacement when the displacment is 0 for z3 < z0.
% n  - Parameter for the Bouc functional. Analytical solutions are ...
    supplied only for n = 1 (odd functional) or n = 2 (even ...
    functional).
if u1 < u2
    error('IdentBWSymm requires that u1 < u2');
elseif z3 > z0
    error('IdentBWSymm requires that z3 > z0');
elseif z1 < z0
    error('IdentBWSymm requires that z1 < z0');
elseif n > 2
    error('IdentBWSymm requires that n = 1 or 2');
```

```
18 elseif n < 1
19     error('IdentBWSymm requires that n = 1 or 2');
20 end
21 % Up to 2 optional inputs specify the starting point for the root ...
      finding function
22 % n = 1 => varargin = [delta_i, sigma_i]
23 % n = 2 => varargin = [delta_i, theta_i]
24 % Each of the optional inputs can be a scalar starting point, for ...
      the root search, or an interval specified by [...].
25 numvarargin = length(varargin);
26 if numvarargin > 2
27     error('IdentBWSymm:TooManyInputs requires at most 2 optional ...
          inputs');
28 end
29 % Default optional inputs
30 optargs = {-1 1};
31 % Overwrite defaults with the optional inputs
32 optargs(1:numvarargin) = varargin;
33 if n == 1
34     [delta_i, sigma_i] = optargs{:};
35 else
36     [delta_i, theta_i] = optargs{:};
37 end
38 % Initiate checks for a solution
39 checkFlag = 1;
40 % checkFlag = 1 => assume sigma = 0
41 %           = 2 => assume sigma > 0 if no solution is found then ...
      assume sigma < 0
42 %           = 3 => sigma and A are known then assume delta > 0 if ...
      no solution is found then assume delta < 0
43 %           = 4 => A, beta and gamma are known
44 %           = 5 => New guess for delta_i, sigma_i or theta_i ...
      indicated by error message
45 while checkFlag < 4
46     switch(checkFlag)
47         case 1
48             LHS = (z1-z0)/u1;
49             RHS  = -z3/u2;
50             if LHS == RHS
51                 sigma = 0;
52                 A = RHS;
53                 checkFlag = 3;
```

```
54              else
55                  checkFlag = 2;
56              end
57          case 2
58              switch(n)
59                  case 1
60                      try
61                          h = @(sigma) sigmaP1(u1, u2, z0, z1, z3, ...
                                sigma);
62                          sigma = fzero(h,sigma_i);
63                          A = -(sigma*z3)/(1-exp(-sigma*u2));
64                          checkFlag = 3;
65                      catch
66                          disp('No solution obtained for sigma. Try ...
                                a new sigma_i')
67                          checkFlag = 5;
68                      end
69                  case 2
70                      try
71                          h = @(theta) thetaP(u1, u2, z0, z1, z3, ...
                                theta);
72                          theta = fzero(h,theta_i);
73                          phi = (1/z3)*tanh(-theta*u2);
74                          A = theta/phi;
75                          sigma = A*phi^2; sigma = abs(sigma);
76                          checkFlag = 3;
77                      catch
78                          try
79                              k = @(theta) thetaN(u1, u2, z0, z1, ...
                                    z3, theta);
80                              theta = fzero(k,theta_i);
81                              phi = (1/z3)*tan(-theta*u2);
82                              A = theta/phi;
83                              sigma = A*phi^2; sigma = abs(sigma);
84                              checkFlag = 3;
85                          catch
86                              disp('No solution obtained for theta. ...
                                    Try a new theta_i')
87                              checkFlag = 5;
88                          end
89                      end
90              end
```

```
91          case 3
92              try
93                      switch(n)
94                          case 1
95                              f = @(delta) deltaP1(u1, u2, z1, A, ...
                                    delta);
96                          case 2
97                              f = @(delta) deltaP2(u1, u2, z1, A, ...
                                    delta);
98                      end
99                      delta = fzero(f,delta_i);
100                     checkFlag = 4;
101             catch
102                     try
103                         switch(n)
104                             case 1
105                                 g = @(delta) deltaN1(u1, u2, z1, ...
                                        A, delta);
106                             case 2
107                                 g = @(delta) deltaN2(u1, u2, z1, ...
                                        A, delta);
108                         end
109                         delta = fzero(g,delta_i);
110                         checkFlag = 4;
111                     catch
112                         disp('No solution obtained for delta. Try ...
                                a new delta_i')
113                         checkFlag = 5;
114                     end
115             end
116             if checkFlag == 4
117
118                 gamma = (abs(sigma) - delta)/2;
119                 beta = sigma - gamma;
120
121             end
122     end
123 end
124 if checkFlag == 5
125     [A, beta, gamma] = deal(0);
126 end
127 % Replace any results that are not a number with a zero
```

```
A(isnan(A))=0;
beta(isnan(beta))=0;
gamma(isnan(gamma))=0;
% Return an empty array if all results are nonzero
checkPlot = find([A beta gamma] == 0, 1);
% Plot the solution
if isempty(checkPlot) == 1
    N = 2^10;
    [uAB, uBC, uCD, zAB, zBC, zCD] = IntegrateBW(u1, u2, z0, z3, ...
        A, beta, gamma, n, N);
    figBW = figure; set(figBW,'Color',[0.55 0.35 ...
        0.75],'Position',[50 50 1200 850]); hold on;
    plot(uAB,zAB,'k'); plot(uBC,zBC,'k'); plot(uCD,zCD,'k');
end
end
```

```
function f = sigmaP1(u1, u2, z0, z1, z3, sigma)
    e1 = exp(-sigma*u1);
    e2 = exp(-sigma*u2);
    f = z1 + z3 + e2*((z0*e1)-z1)-e1*(z0+z3);
end
```

```
function f = thetaP(u1, u2, z0, z1, z3, theta)
    c1 = z1-z0;
    c2 = z3;
    c3 = z1*z0/z3;
    t1 = tanh(-theta*u2);
    t2 = tanh(theta*u1);
    f = (c1*t1) - (c2-(c3*t1^2))*t2;
end
```

```
function f = thetaN(u1, u2, z0, z1, z3, theta)
    c1 = z1-z0;
    c2 = z3;
    c3 = z1*z0/z3;
    t1 = tan(-theta*u2);
    t2 = tan(theta*u1);
    f = (c1*t1) - (c2+(c3*t1^2))*t2;
```

```
end
```

```
function f = deltaP1(u1, u2, z1, A, delta)
    f = (A/(A+delta*z1)) - exp(delta*(u2-u1));
end
```

```
function f = deltaP2(u1, u2, z1, A, delta)
    f = z1*sqrt(abs(delta)/A) - tan((u1-u2)*sqrt(A*abs(delta)));
end
```

```
function f = deltaN1(u1, u2, z1, A, delta)
    f = (A/(A-abs(delta)*z1)) - exp(-abs(delta)*(u2-u1));
end
```

```
function f = deltaN2(u1, u2, z1, A, delta)
    f = z1*sqrt(1/A*abs(delta)) - tanh((u1-u2)*sqrt(A*abs(delta)));
end
```

```
function [uAB, uBC, uCD, zAB, zBC, zCD] = IntegrateBW(u1, u2, z0, ...
    z3, A, beta, gamma, n, N)
% Integrate the Bouc functional over branch AB, BC and CD with ode45
% Branch AB
    u = 0:u1/(N-1):u1;                          % Displacement ...
        interval
    f = @(u, z) BWAB(z, A, beta, gamma, n);     % Anonymous branch ...
        function
    [uAB, zAB] = ode45(f,u,z0);                 % Solve for ...
        initial z0
% Branch BC
    u = u2:(u1-u2)/(N-1):u1;
    f = @(u, z) BWBC(z, A, beta, gamma, n);
    [uBC, zBC] = ode45(f,u,0);
% Branch CD
    u = 0:u2/(N-1):u2;
    if mod(n,2) == 0                            % n is even
```

```
14          f = @(u, z) BWevenCD(z, A, beta, gamma, n);
15          [uCD, zCD] = ode45(f,u,z3);
16      else                                            % n is odd
17          f = @(u, z) BWoddCD(z, A, beta, gamma, n);
18          [uCD, zCD] = ode45(f,u,z3);
19      end
20  end
```

```
1  function f = BWAB(z, A, beta, gamma, n)
2      f = A - ((beta + gamma)*z^n);
3  end
```

```
1  function f = BWBC(z, A, beta, gamma, n)
2      f = A + ((beta - gamma)*z^n);
3  end
```

```
1  function f = BWevenCD(z, A, beta, gamma, n)
2      f = A - ((beta + gamma)*z^n);
3  end
```

```
1  function f = BWoddCD(z, A, beta, gamma, n)
2      f = A + ((beta + gamma)*z^n);
3  end
```